TOWARD A SEISMIC RESISTANT STEEL STAGGERED TRUSS FRAMING SYSTEM (STF)

by

RA'ED KHALIL MOHAMMAD AL-MAZAIDH

DISSERTATION

Submitted in partial fulfillment of the requirements
for the degree of Doctor of Philosophy at
The University of Texas at Arlington
May 2020

Arlington, Texas

Supervising Committee:

Shih-Ho Chao, Supervising Professor.

Samantha Sabatino.

Suyun Ham.

Himan Hojat Jalali.

Madan Mehta.

Acknowledgements

I would like to express my deep and sincere gratitude to my research supervisor, Professor Shih-Ho Chao for giving me the opportunity to do research and providing invaluable guidance throughout this research. His dynamism, vision, sincerity, and motivation have deeply inspired me. He has taught me the methodology to carry out the research and to present the research works as clearly as possible. It was a great privilege and honor to work and study under his guidance.

Special gratitude is also due to the committee members Dr. Samantha Sabatino, Dr. Suyun Ham, Dr. Himan Hojat Jalali, and Dr. Madan Mehta. My gratitude also goes to faculty and staff at the University of Texas at Arlington for their support and kindness.

I would like to acknowledge the Gate Precast Company in Pearland, Texas for providing the hollow-core prestressed precast concrete planks, the Nelson Stud Welding, Incorporation in Irving, Texas for providing the shear studs and welding them on the steel beams, and the Forterra Pipe and Precast in Grand Prairie, Texas for providing cement and sand.

I would also like to thank our research group Dr.Ghassan Almasabha, Dr. Kyoung-Sub Park, Dr.Chatchai Jiansinlapadamrong, Seyed Missagh Shamshiri Guilvayi, , and Ashish Karmacharya for their support in constructing and testing throughout this research.

I am extremely grateful to my parents for their love, prayers, caring and sacrifices for educating and preparing me for my future. I am very much thankful to my wife and my children for their love, understanding, prayers and continuing support to complete this research work.

April 1, 2020

Abstract

TOWARD A SEISMIC RESISTANT STEEL STAGGERED TRUSS FRAMING SYSTEM (STF)

Ra'ed Khalil Mohammad Al-mazaidh, PhD

The University of Texas at Arlington, 2020

Supervising Professor: Dr. Shih-Ho Chao

The Staggered Truss Framing (STF) system is a type of steel structural system used in mid- to high-rise buildings. It was initially developed in the 1960s in order to create a steel framing system that has low floor-to-floor height (9 to 10 ft.) and wide column-free space (60 to 80 ft.). This system consists of a series of story-high trusses spanning the total width between two rows of exterior columns and arranged in a staggered pattern on adjacent column lines.

Due to the staggered layout, lateral seismic force transfer in the STF system is also in a staggered manner from the top of the structure; therefore, the lower floor's diaphragm and its connections are carrying increasingly larger load due to the accumulative inertia forces all the way from the top level of the building. Nevertheless, STF's seismic behavior is nearly unknown and extensive analytical and three-dimensional experimental studies and collapse simulations are needed in order to understand its seismic behavior.

The main objectives of this study are to investigate the cyclic behavior of the connection between precast hollow-core slab diaphragm to steel truss in the STF system, to present a design procedure for the STF system, and to evaluate the seismic performance of the proposed modified STF by nonlinear time-history (NTH) analyses.

Large-scale experiments were tested under cyclic loading protocols. The results showed that the prestressed precast hollow-core slab and its connection to the steel chord of the STF system has insufficient strengths to resist high shear forces. On the other hand, Finite Element Analyses (FEA) showed that some interior connections are under the effect of double shear.

Nonlinear analyses show that STF system with the modified configurations including multi-panel Vierendeel panels in the middle of trusses with addition of vertical members in the non-truss levels can effectively improve the ductility and seismic behavior of steel trusses. It also has clearly defined yield mechanism and structural fuses compared with the conventional STF system. Furthermore, the STF system no longer primarily depends on staggered manner via the diaphragms to transfer the lateral forces, as in the conventional STF system. Nonlinear analyses also showed that using the horizontal trusses as a diaphragm can effectively transfer the seismic forces along the longitudinal direction.

Table of Contents

List of Illustrations

List of Tables

Chapter 1

Introduction

1.1 Overview

The Staggered Truss Framing system (STF system) was developed at the Massachusetts Institute of Technology (MIT) in the 1960s (Goody et al.,1967; Scalzi, 1971). This system was originally developed to achieve a very efficient structural framing system to resist wind loads, and at the same time, provide versatility of floor layout with large open areas. The result was an economical steel framing system for mid-to high-rise buildings (6 to 25 stories tall) that was simple to fabricate and erect with low floor-to-floor heights and large column-free spaces (Figure 1-1).

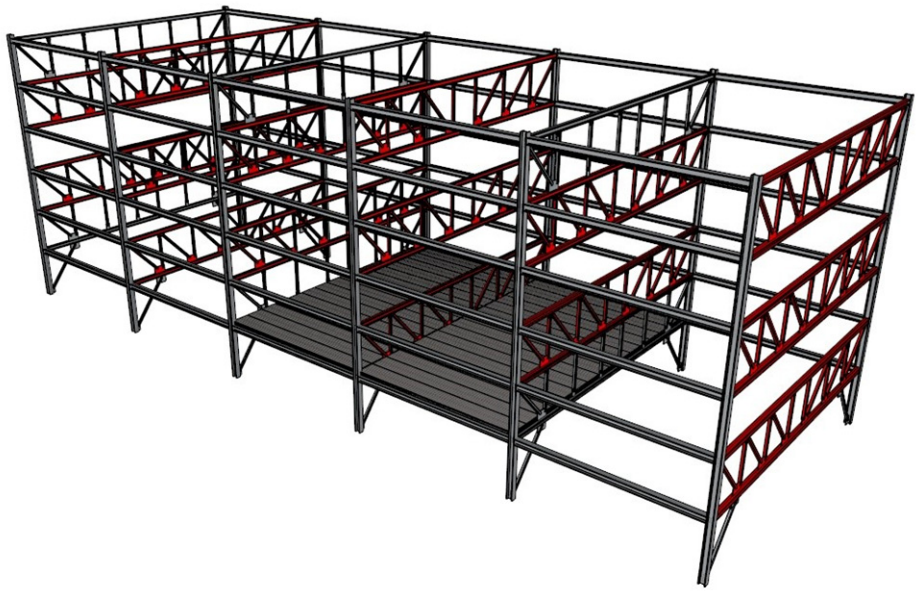

Figure 1-1 Overview of the conventional Staggered Truss Framing system (STF system).

STF system has become a popular system in the U.S. in regions of low seismicity for residential apartments, hotels, motels, dormitories, hospitals, and other structures for which a low floor-to-floor height is desirable (Brazil, 2000; Wexler and Lin, 2003). Although STF system were originally developed for low seismic regions, the high lateral stiffness and light weight structural frames make this system attractive for use in highly seismic regions.

However, the diaphragms and their connections to the chords of trusses are critical to the lateral load path of this system. In lower stories, they almost transfer the entire shear base of the building. That makes the study of their behavior and design as important as the trusses and columns in this system.

This chapter presents the features, advantages, load path, and the seismic behavior of STF system. The proposed modified STF system and the issues that limit using this system in moderate to high seismic areas are discussed. Furthermore, the objectives of the research and outline of the dissertation are also included.

1.2 Features of STF system

This system uses story-high trusses to span along the entire transverse direction of the building, and either moment or braced frames are used in the longitudinal direction of the building. Moreover, the trusses are arranged in a “staggered pattern” wherein trusses are placed at alternating levels at alternating column lines (Figure 1-2).

Exterior columns support the ends of the trusses and they are oriented with their strong axis resisting lateral forces in the longitudinal direction of the building. Therefore, large column-free space (60 to 80 ft) is available in each direction. Typically, the truss has an opening at the center of the truss to serve as a corridor or a passageway to run perpendicular to the truss. This opening can be achieved by eliminating the diagonal. In

this case, the shear is carried by Vierendeel action of the bottom and top chords and the truss vertical member (Taranath,2012).

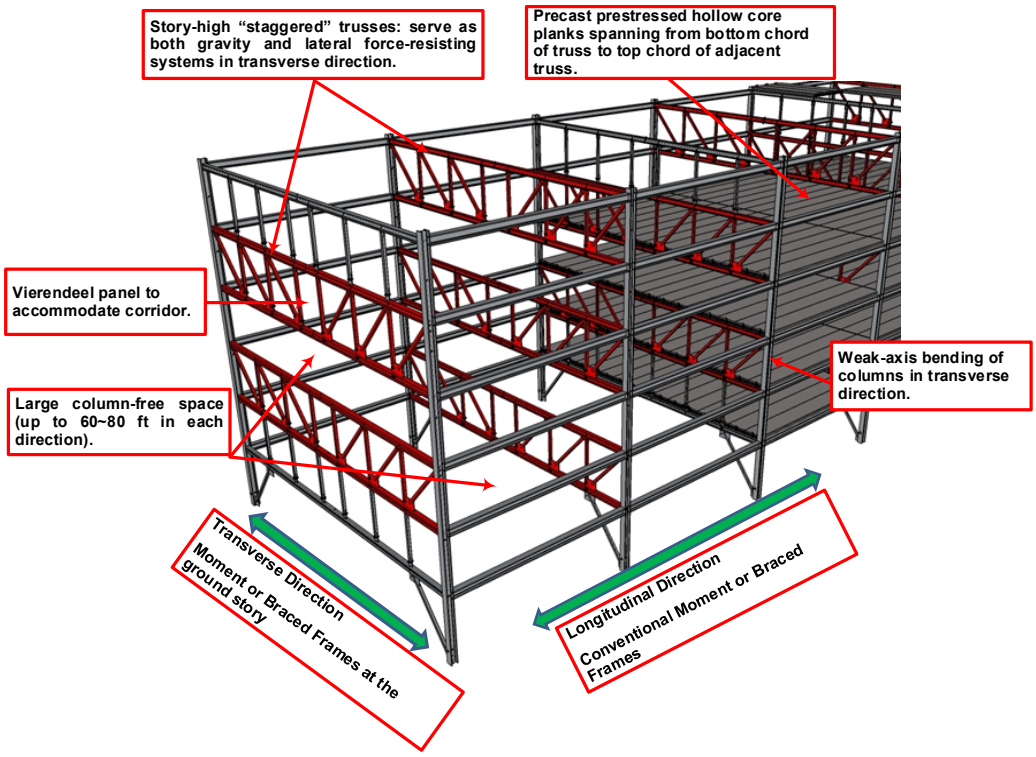

Figure 1-2 Features of Staggered Truss Framing (STF) System.

The floor in this system acts as a diaphragm, and it typically consists of pre-stressed precast hollow-core slabs spanning from the bottom chord of one truss to the top chord of the adjacent truss. Prestressed hollow-core slabs are used because of their reduced weight and long spans, low maintenance cost, and fast speed of construction. Additionally, they also have better control of deflection and flexural cracking, acoustical and heat transfer control, and excellent fire resistance.

1.3 Advantages of STF system

The staggered truss frame system has many advantages which make it one of the preferred systems (Figure 1-3). This system uses story-high trusses in a staggered pattern which provides large column-free areas and low floor-to-floor heights. Typically (8'-8" to 10") a low floor-to-floor-height is achieved and (60-80) feet large column-free spaces in each direction are available.

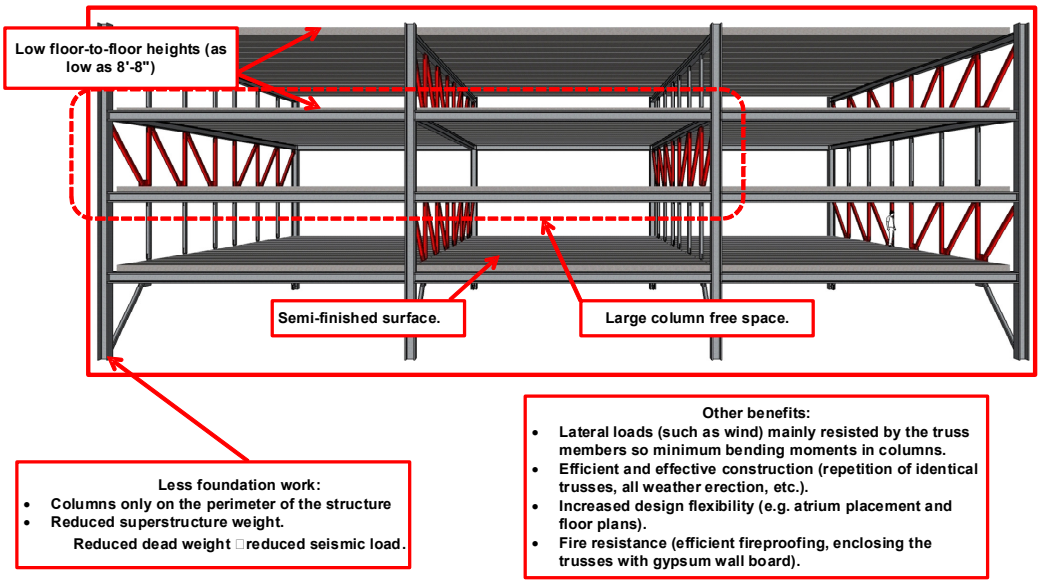

Figure 1-3 Advantages of Steel Staggered Truss Frame System (STF system).

As a result of large column-free spaces, in which there are no interior columns and the columns are located only on the perimeter of a structure, a greater flexibility in laying out floor plans is achieved. Moreover, the foundations are on the column lines only and two strip footings might be used. Thereby, having fewer columns and foundations offers faster fabrication and reduces costs.

Since the floor slab can be carried out by using concrete planks (typically prestressed hollow-core), the time of construction is reduced and little to no finishing is

needed. However, the weight of this system which includes the concrete planks, the steel frames and foundations is less than equivalent concrete system. This advantage decreases the superstructure weight and thereby reduces the seismic load.

Fire resistance is another advantage, for several reasons. First, the steel is localized to the trusses, which only occur at every 58-to-70-feet on a floor, so the fireproofing operation can be completed efficiently. Furthermore, the trusses are typically placed within demising walls and it is possible that the necessary fire rating can be entirely by enclosing the trusses with gypsum wallboard. Finally, if spray-on protection is desired, the applied thickness can be kept to a minimum due to the compact nature of the truss elements.

1.4 Load path in STF system under seismic load

To understand the load path of the STF system under seismic loads, assume that we have the two following frame systems as illustrated in Figure 1-4. In the first system (a), there are two floors. The first floor consists of a truss frame and all the frames in the ground level are moment frames connected by a rigid diaphragm. In the second system, the difference is that the ground floor consists of two trusses frames at exterior ends and a non-truss frame at interior connected by rigid diaphragm. The second system represents the arrangement of the trusses frames in the STF system.

Both systems are modeled using RISA-3D program and one-unit lateral load is applied on the truss of the first floor. The results showed that in the first system, when the lateral force at the upper level is transmitted to the lower level, 40% of the load transfers to the bay below, and 60% of the lateral force transfers to the adjacent bays via diaphragm.

In the second system, when the lateral force at the upper level is transmitted to the lower level, only 10% of the force transfers to the bay below because the lateral stiffness of the story immediately below the truss floor is much smaller. However, most of the lateral

force (90%) is transferred to the adjacent bays through the diaphragms because the lateral stiffness is much higher.

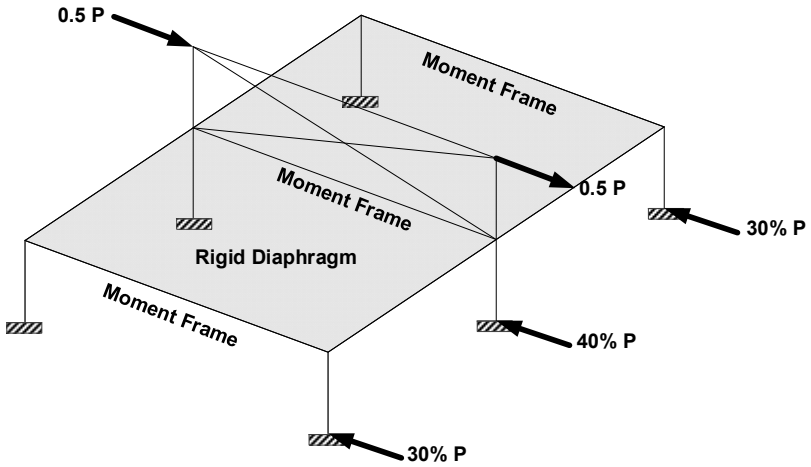

(a)

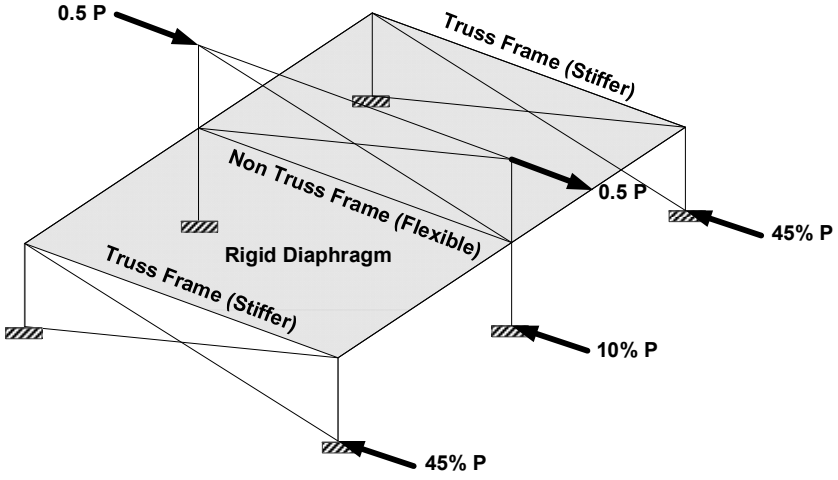

(b)

Figure 1-4 Load transfer in (a) Moment frames. (b) stiffer and flexible truss frames.

It can be concluded from the above analysis and discussion that unlike all the other seismic force resisting systems (SFRSs), the lateral force transfers in STF system is in a "staggered" pattern which can be illustrated by the simple system shown in Figure 1-5.

The seismic forces in the STF system is transferred through a combination of concrete floor slab diaphragms and vertical truss web elements (Moore,2005). As shown in Figure 1-5, the seismic force inertia is developed at the floor diaphragm of the upper story, then it is distributed through the diaphragm to the upper truss chord (Blue arrows).This force is transferred through the vertical truss webs to the bottom chord of the truss in the next floor.

Since the diaphragm of the lower story has its own inertia force (Green arrows), this force combines with the force from the above story (Blue arrows) and the resultant (Red arrows) is distributed again through the diaphragm of the lower level as a shear force to the top chord of the adjacent trusses (Black arrows).

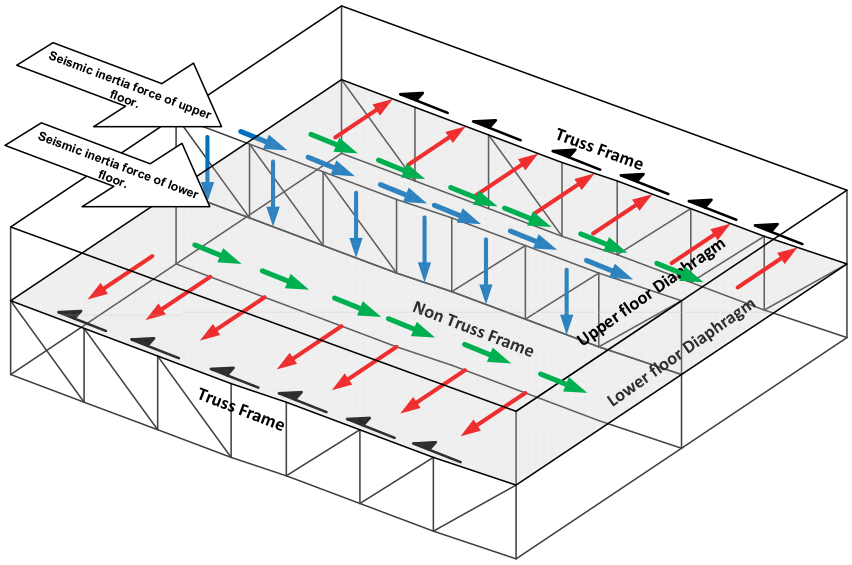

Figure 1-5 Seismic Load path in staggered truss system (the upper floor diaphragm is not shown for clarity).

1.5 Seismic behavior of STF system under seismic load

The nonlinear analyses showed that the STF structure has a large capacity of energy absorption and ductile deformation capability. Moreover, the energy is dissipated through the chord members in the central open panel of the truss (Hanson et al,1972.).

Under seismic load in the transverse direction, this Vierendeel panel would be subject to high deformations. So that, it should be designed to dissipate energy through flexural yielding.

Seismic behavior and energy dissipation mechanisms of the steel trusses in STF systems are very similar to that of Special Truss Moment Frames (STMF) (Taranath, 2012; Chao,2012, Simasathien et al., 2014a; Simasathien, 2016). Figure 1-6 (a), (b) shows the yield mechanism and plastic hinges formation in the STMF and the STF, respectively.

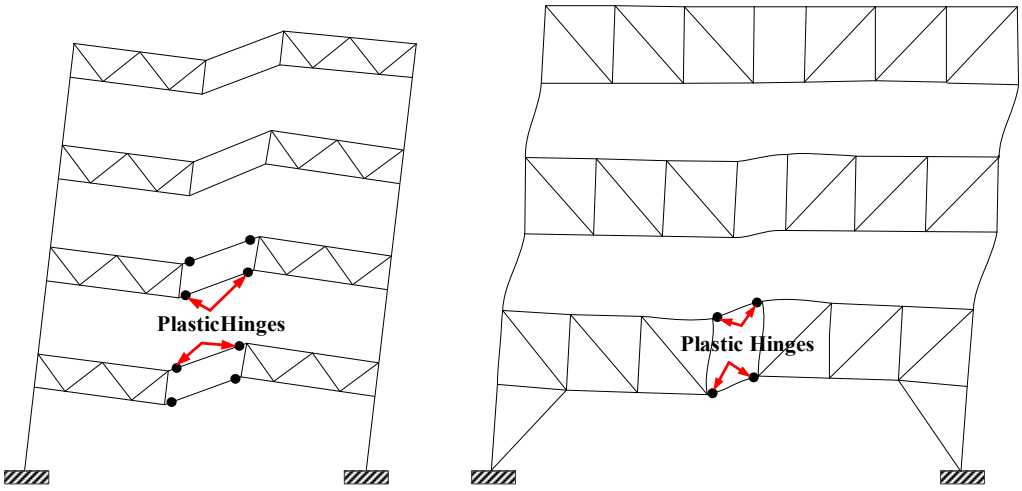

Figure 1-6 Yield mechanism and plastic hinges formation in (a)Special Truss Moment Frame system (STMF). (b) Staggered Truss framing system (STF).

1.6 Issues of STF system in the areas of moderate to high seismic action

The STF system is highly effective to resist the lateral loading which is caused by wind and earthquake in the direction of trusses (Hanson et al. ,1972; Wexler and Lin, 2003). However, there are attributes in the STF system that limit using of this system in areas of moderate to high seismicity. These attributes can be summarized as follows:

- The stability of gravity system due to the fact that the gravity and lateral loads are resisted by the same trusses.
- The lower floor's diaphragm and its connections are carrying an increasingly larger diaphragm force due to the accumulative inertia forces all the way from the top level of the building.
- Large deformation "kink" in columns at the flexible "non-truss" level under lateral loads and large rotation at the ends of the chord members in the single Vierendeel panels which in turns limits the overall drift capacity of the system as shown in Figure 1-7.
- Large openings on the floor, e.g., staircases or elevators, affect the shear transfer across the diaphragms.

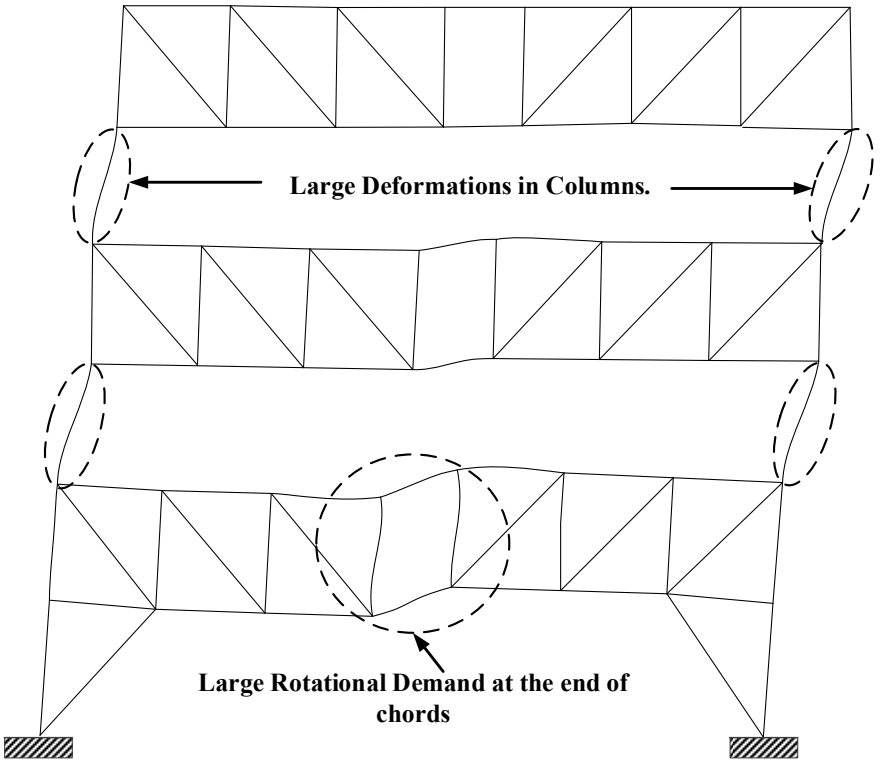

Figure 1-7 The large rotational demand at the ends of chords and the large deformation in the columns of the conventional STF system (Simasathien et al ,2014a).

1.7 Proposed modified STF system

The same modifications that are proposed by Simasathien et. al (2014a) to enhance the seismic performance of the STF system, which are discussed in chapter 2 (Literature Review), will be kept in this research. However, for architectural purposes, the bracing members (Kickers) that are proposed in their models at the ends of the non-story levels to minimize the column deformations that occur due to relatively smaller story stiffness are replaced by vertical members as shown in Figure 1-8.

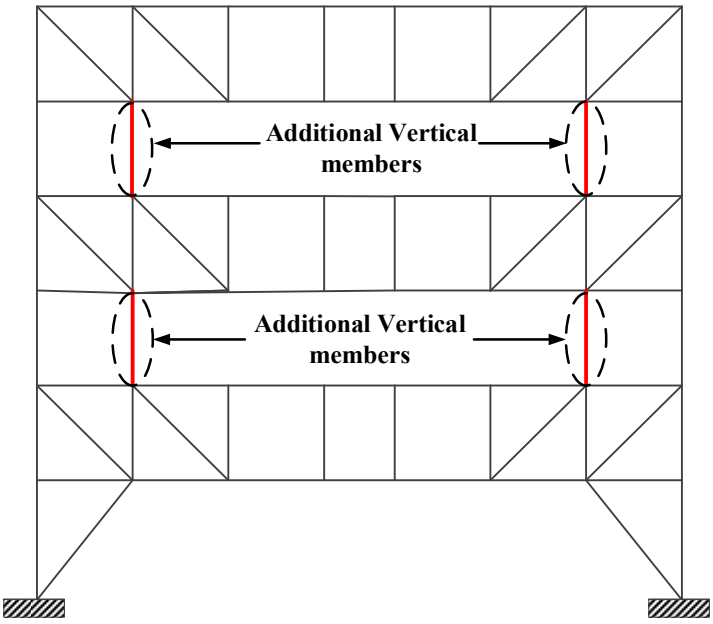

(a)

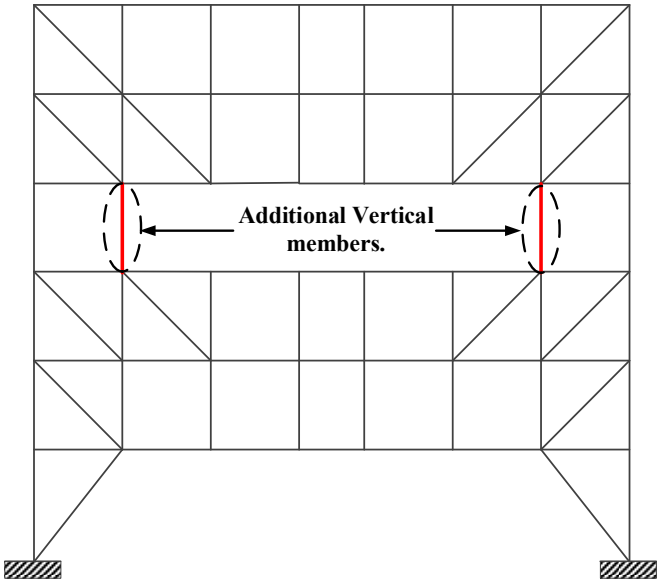

(b)

Figure 1-8 6-story STF prototype building with modified STF system (Vertical members at ends): (a) odd bay; (e) even bay.

On the other hand, the layout of the horizontal steel trusses which was proposed by (Simasathien et. al ,2014a) in their models to transfer the in-plane shear to STF system through direct axial forces in the truss members was modified by adding additional members as shown in Figure 1-9 :

- To increase the stiffness of the steel diaphragm.
- To decrease the members' axial forces and consequently decrease the axial force demands on the connections.
- To decrease the deflections which are due to the large spans of beams.

However, the proposed details for the connections between the members of horizontal truss, the horizontal truss members and the chords members, the horizontal truss members, and the beams in the longitudinal direction are presented in this study and they are shown in Figure 1-10 and Figure 1-11.

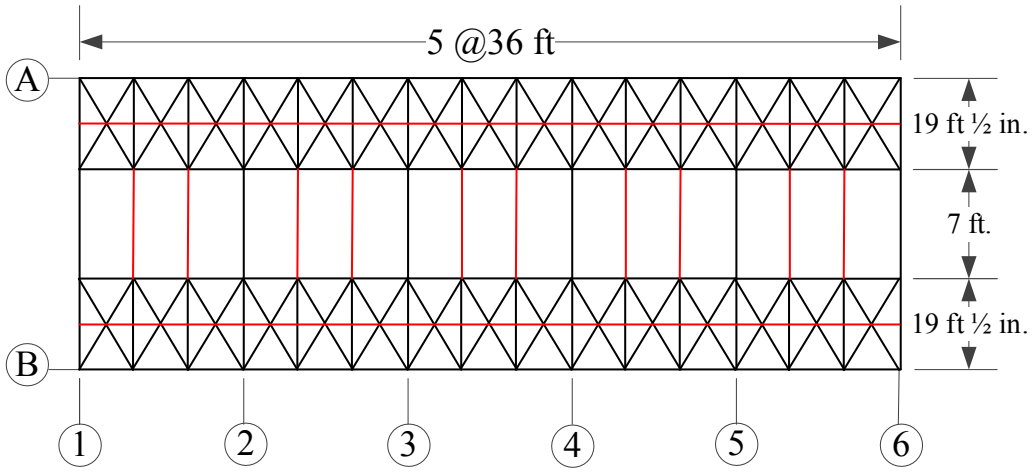

Figure 1-9 Modifification on the layout of horizontal trusses(The additional members are shown in red color).

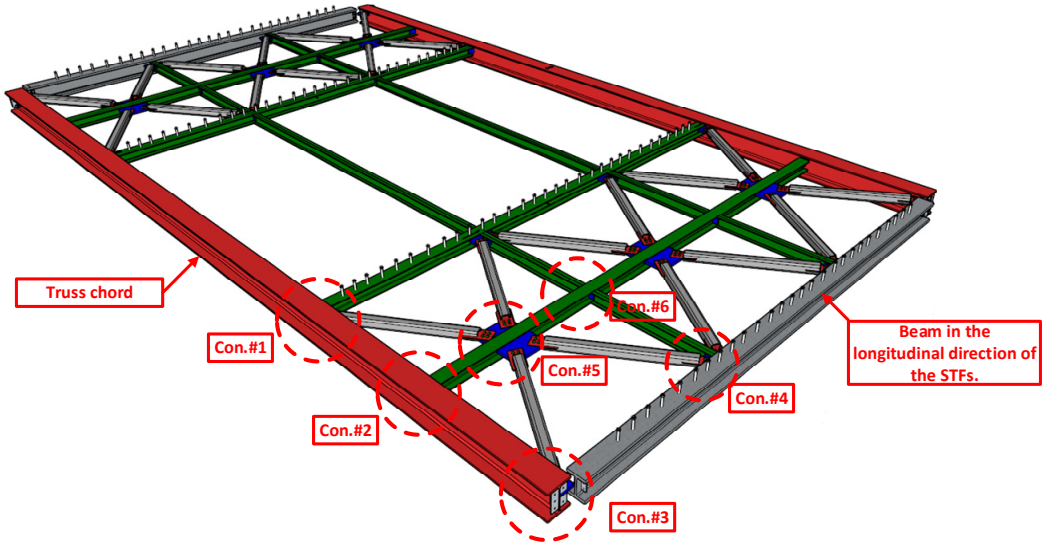

Figure 1-10 Overview of the modiified horizontal trusses with their connections to the truss chords and the beams in the longitudinal direction.

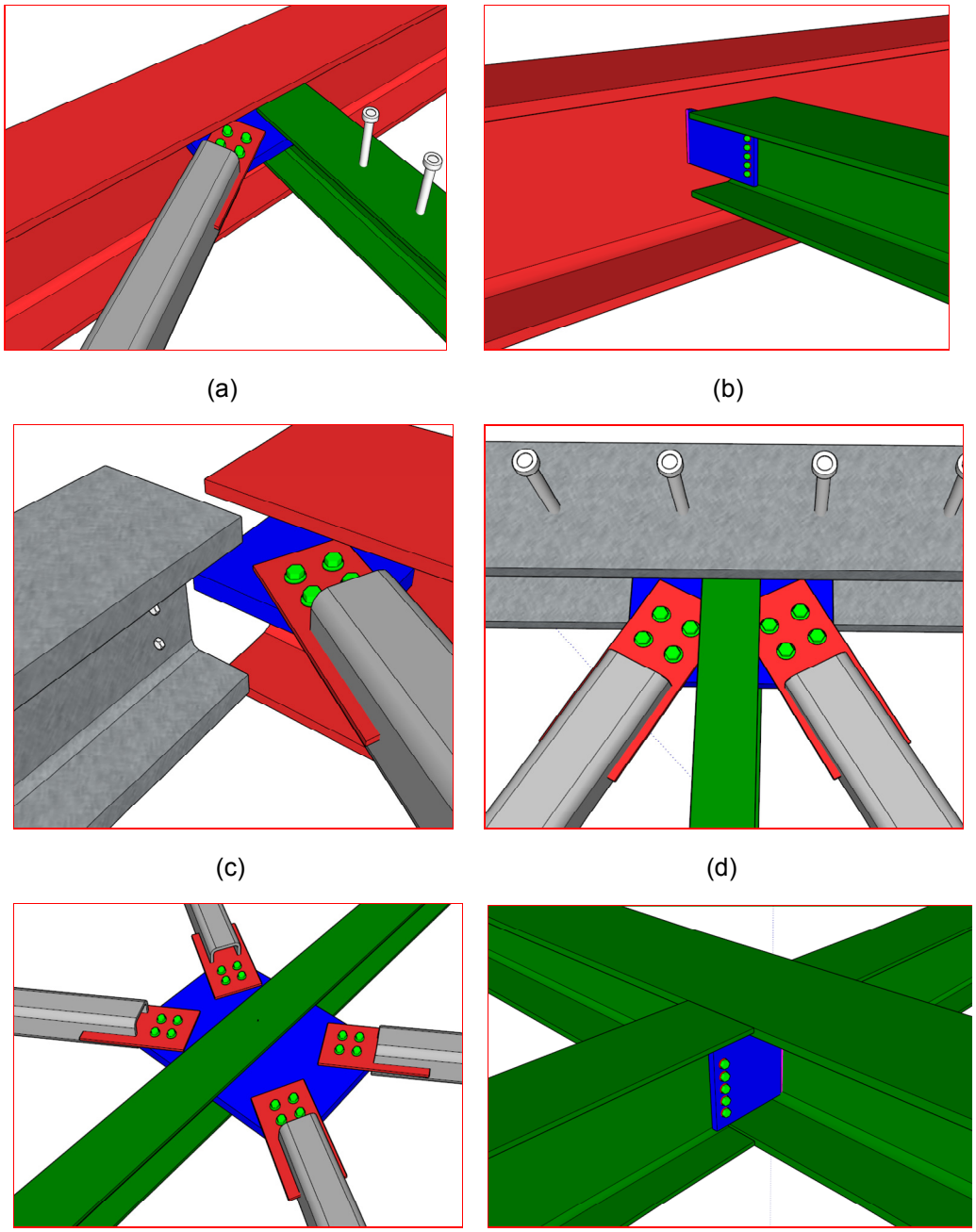

Figure 1-11 Details of connections: (a) connection #1,(b) connection #2, (c)connection #3,(d) connection #4, (e) connection #5, (f) connection #6.

1.8 Research objectives

In the first part of this research, five large-scale experimental tests were conducted for the connection between precast hollow-core slab diaphragm to steel truss in the STF system that is subjected to cyclic loading. The main objectives of this part are:

- To evaluate the behavior of the connection under cyclic loading.
- To determine the shear strength and deformation in the connections.
- To determine if the hollow-core slabs and the diaphragm-to-truss connections could sustain large shear due to major earthquakes.

In the second part, the proposed modified STF system, which was discussed in section 1.7 above, will be designed and investigated under cyclic ground motions. The modified model will be compared with a conventional STF model. Furthermore, mid-to high-rise STF buildings are designed and Finite Element Analysis (FEA) was carried out for a modified STF structure.

The primary objective of this part:

- To present a design procedure for the STF system.
- To evaluate the seismic performance of the modified STF by nonlinear time-history (NTH) analyses.
- To compare the seismic behavior and performance of the modified STF system with the conventional one.
- To study and understand the force transfer mechanism across trusses members, and the slab diaphragm in the conventional and modified STF systems.
- To determine the shear demands in the connections between precast hollow-core slab diaphragm to steel truss members.
- To evaluate the effect of shear (γ) and bending (ϕ) on the slab and the connection as well.

1.9 Dissertation outline

- Chapter 2 presents a review of the previous research on STF system in addition to the behavior and strength of the shear studs under cyclic loading.
- Chapter 3 presents a comprehensive review of the experimental program for the tests of in-plane shear deformation of the connection between the precast hollow-core slab diaphragm to steel truss in STF system under cyclic loading.
- Chapter 4 describes, analyzes, and discusses the individual test results for each specimen.
- Chapter 5 presents the PERFORM 3D modeling and the members properties that are used to design and evaluate the seismic performance of the STF models.
- Chapter 6 presents a design procedure for the modified STF system and a seismic performance evaluation of the proposed modified layout for mid-to high-rise STF buildings.
- Chapter 7 discusses the results on the non-linear analyses based on the modeling and the design procedure which were discussed in chapter 5 and chapter 6, respectively.
- Chapter 8 discusses the modeling and the results of the Finite Element Analysis (FEM) which was carried out to investigate the stress transfer mechanism across trusses members and the slabs, the shear demands in the connections between precast hollow-core slab diaphragm to steel truss members, and the bending deformation.
- Chapter 9 presents the summary and conclusions for this research.

Chapter 2

Literature Review

2.1 Introduction

Studies on the Staggered Truss Framing system (STF) are limited. Most of them are technical articles in magazines discuss, in general, the conceptual design and the construction details of some STF buildings. Although some of articles discuss the process of analysis and force path calculation, little information is provided regarding to the behavior of this system under high seismic forces particularly on the high in-plane precast hollow-core slab diaphragm which is typically used in the STF system. Moreover, there is no test data available in this subject. However, very little attention was paid to either connection demands or post yielding behavior related to overall stability or energy dissipation.

This chapter presents the history of STF system and the previous studies and technical articles on the STF system. Furthermore, the AISC steel design guide series No.14, which covers the design and construction of the STF system is included.

The previous research on the seismic behavior and design of STF system is also presented in this chapter. However, since the shear force in the typical connection transfers between the precast prestressed hollow-core slab to the steel chord through the shear studs, the literature of the behavior and strength of the shear studs is also included in this chapter.

2.2 The history of STF system.

By 1960, for several varying reasons, such as low floor-to floor heights, the flat-slab concrete structural system eliminated structural steel as a competitive material in high-rise buildings. Due to the high concern of the USS (United States Steel Corporation), the ARL (Applied Research Laboratory) was ordered to produce ideas to help re-acquire a portion of that market. ARL research consultant and MIT (Massachusetts Institute of Technology) graduate, Bob Hossli, was impressed by the work designed and tested by the architectural team at MIT headed by Marvin Goody and Albert Dietz (Hossli and Flucker,2013).

Therefore, he suggested that MIT propose for a research project to develop a steel structural system competitive and cost-effective compared to the flat-slab concrete structural system for high-rise buildings. Structural engineer William “Bill” James LeMessurier and architect Marvin Goody accepted to develop a steel structural system with these requirements in mind.

After many meetings with slow progress, William “Bill” James LeMessurier had a thought. He suggested that thought to his MIT team. He proposed a new structural steel system called “Staggered Truss Framing for High-Rise Buildings” as illustrated in Figure 2-1.

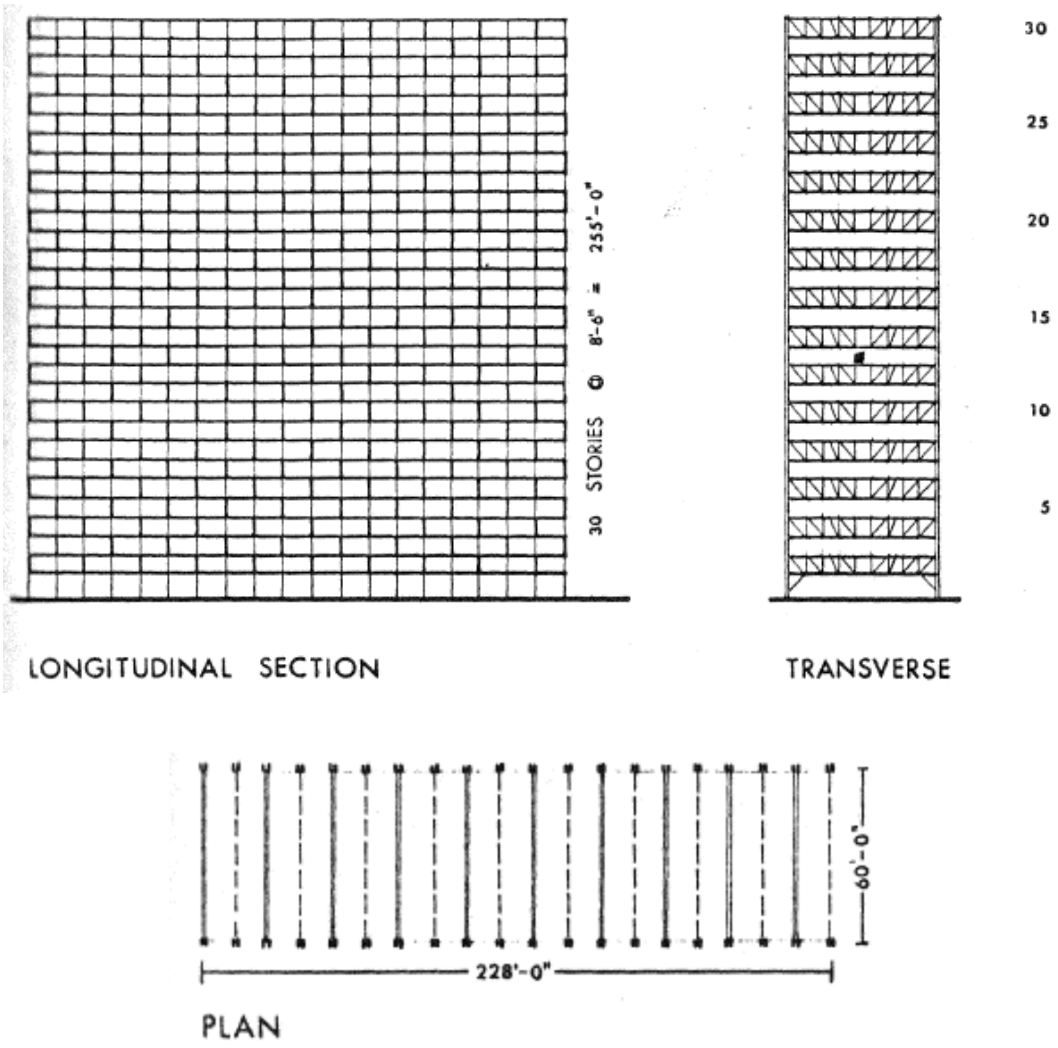

Figure 2-1 The structural geometry the proposed STF system by the MIT team,1967

Without much protest, the MIT team accepted the answer as the solution to the charge. The Steel Staggered Truss Framing System was presented to the United States Steel corporation (USS) in January of 1967. Proving to be successful, the ARL and USS's construction marketing department officially considered this system. In June 1966, upon hearing the news, the American Institute of Steel Construction (AISC) invited William

LeMessurier to present and describe the concept at the annual Engineering Conference in Boston.

The first STF building was constructed in 1968. The building was carried out by Bakke and Kopp, Inc. in St. Paul, Minnesota. Seventeen-story apartment building for elderly with $ 2.3 million cost. The length of the trusses is 50 ft. and their depth are 9 ft. 4 in. and the free space between the trusses is 45 ft. 4 in.

2.3 Previous studies and technical articles on the STF system.

Scalzi (1971) summarized the design considerations which were included in the MIT's team report. He discussed the theory and design requirements for each component, advantages, fabrication, and erection of this system. The author explained the features of this system, for instance the arrangement of trusses, columns and floors. Moreover, he summarized the advantages of this system which make it effective and economic.

However, the author demonstrates the major design factors that should be considered in the design of floor which are in-plane shear strength and stiffness, as well as resisting the gravity loads. Furthermore, the columns are designed to resist the axial loads only, because the lateral loads are resisted by diagonals of the trusses, so that the loads affect as direct axial on the columns and there is no local bending effect. As a result, the webs of the columns can be turned perpendicular to the trusses direction. The author listed some steel sections that can be used in the fabrication of the system, for example wide flange, tees and channels.

As STF system began to use in Canada, Stringer (1982) presented a paper to review the design aspects and the construction measures of this system. The Delta bow valley inn hotel, in Calgary, 21 floor levels, which is the first STF system in Canada was described generally in this paper.

Leffler (1983) presented a procedure for the hand calculation of wind drift and checking the overturning moment which is due to the wind forces for the STF structure. The author explained that in a detailed example and compared the results with finite-element computer analysis. The results showed that this hand calculation methodology is accurate since the difference between this procedure and computer analysis is less than 1.5%.

Cohen (1986) demonstrated why the STF system was chosen among other systems for a project. The project is a STF high-rise hotel (442 ft. height) located on the oceanfront in Atlantic City. The author summarized the conceptual design, the selection process, and the construction details. However, the design process faced problems and some decisions were made to solve these issues such as the design of the floor diaphragm.

The diaphragm is an important structural element especially in the lower stories which is prone to high cumulative shear force. Consequently, a solid composite concrete slab system was selected as shown in Figure 2-2. This system consists of a precast prestressed solid concrete slab covered by cast-in-place concrete. In order to ensure a sufficient bond between the two surfaces, the top surface of the precast solid slab was roughened and reinforced by horizontal ties. These planks are tapered at the ends and can span over 30 ft.

Regarding to the connection between the planks and the chord, ¾" diameter shear connectors were used by welding them to the steel chord. Moreover, the large area which due to the tapered ends of the planks was filled by the cast-in-place concrete. However, using this composite system of slab increases the weight of the structure and consequently increases the seismic load.

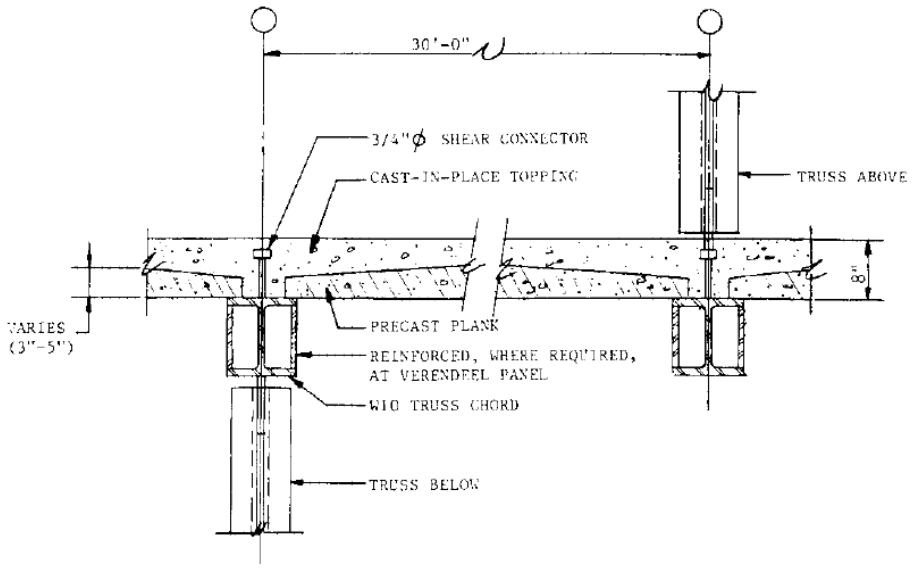

Figure 2-2 The solid composite concrete slab system and the connection detail for STF high-rise hotel in Atlantic City (Cohen,1986).

Hassler (1986) addressed the details of construction for STF project. The project is a 13-story hotel contains with about 170,000 ft^2. The author demonstrated the fabrication, field erection, and the end of the paper showed the cost of the building which is 14.31$/$ft^2$ at that time.

McNamara (1999) presented one of the biggest STF high-rise building. It is the Aladdin hotel in Las Vegas, a 38-story building that replaced the old Aladdin Hotel, which was demolished in March 1998. The STF system was selected for this project because of many advantages and the major reason is that the STF is the most economical system. The author briefly discussed the geometry of the building, the foundations, and some details of the trusses and the planks.

According to the author, STF is not stiff enough to resist the lateral loads which are primarily the wind load. Therefore, two braced core structures and four separate bracing were designed to resist the lateral loads. Regarding to the seismic design, the system was

designed for a peak ground acceleration of 0.2g. Moreover, a complete spectrum analysis was performed for the three-dimensional structure and the diaphragm action of the plank was simulated. On the other hand, the seismic connections were designed for unreduced seismic forces. Additionally, Finite Element Analysis (FEA) was utilized for the floor blank system to ensure the elastic behavior under seismic action.

Brazil (2000) discussed the reason of choosing the STF to construct the Embassy Suites which is a largest newly built hotel in New York City. The reason is the estimated cost showed that using STF system will save more than $2 million. The design of the truss members for this building is not controlled by the lateral forces according to the author. However, conventional Chevron bracing was used to resist the lateral load in the longitudinal direction.

Levy (2000) presented a brief detail about another STF building in New York City. It is Baruch College Academic Center, fifteen stories from the ground level. The author discussed, in general, some details such as foundations, steel trusses, and gladding. The lateral forces, wind and seismic, were resisted in transverse direction by the trusses whereas the braced frames used in the longitudinal direction.

Marstellar (2002) presented detail drawings for the six-story STF system. The drawings also include the connection of blank-chord member. Pollak (2003) focused on the fabrication and the constructions procedures for the Clayton Park Apartments complex in White Plains, NY. The building, which is only 8-story depends on stiffness of the trusses and some braces.10-inch-thick concrete blanks are used for spans 27 feet or 36 feet.

2.4 AISC Steel Design Guide Series No.14 (Staggered Truss Framing Systems)

The AISC has published a design guide for the staggered truss system in December 2001 (AISC Steel Design Guide Series No.14). This design guide covers the design and construction of this system. It includes truss member design, diaphragm design, connection design, mechanical design considerations, erection considerations and fire protection considerations.

Based on this guide, the STF system is highly effective to resist the lateral loading which is caused by wind and earthquake in the direction of trusses. Furthermore, the system's stiffness provides the appropriate drift control against the lateral load. However, in the longitudinal direction, a lateral force resisting system must be used such as moment frame or bracing system. This system can also provide an excellent amount of capacity for energy absorption and ductile deformation for high seismic uses.

Although this guide includes a chapter on seismic design, it only recommends using a more conservative value of response modification factor (R= 3·0) for seismic design. However, it does not consider the other seismic behavior factors, like overstrength and ductility factors and the system behavior related to the seismic forces. Therefore, this system cannot be designed and used in active seismic areas.

2.5 Previous research on the seismic behavior and design of STF system.

The most crucial publications about the seismic behavior of STF system originated from the University of Michigan-Ann Arbor. Gupta (1971) investigated the inelastic seismic behavior of the STF structure which is designed by the procedure in the Uniform Building Code, 1970 edition. The following parameters also considered in this research: (1) viscous damping in the structure, (2) input ground motion to the structure, (3) number of stories in the structure, (4) width of the central panels on the trusses, and (5) condition in the bottom story of the structure (open or not). The researcher used the following series of STF

structures in his study: (1) a 40-story structure, (2) a 20-story standard structure, (3) a 20-story structure with the central panels of the trusses larger than the width in the standard structure, (4) a 20-story structure with the bottom story open and a 10-story structure. The North-South component of the El Centro earthquake of 1940 or this earthquake with the acceleration ordinates increased by 1.5 times were used in the analysis.

Twenty three-story building which is subjected to the gravity and lateral loads was analyzed. A truss was modeled to calculate the forces and to design the members. However, bilinear hysteresis type was assumed at the ends of central panels members and the stiffness was assumed to be 5% of the elastic stiffness as shown in Figure 2-3. The lateral load was increased, and the plastic hinges were formed at the bottom chords and top chords respectively as it can be seen in Figure 2-4.

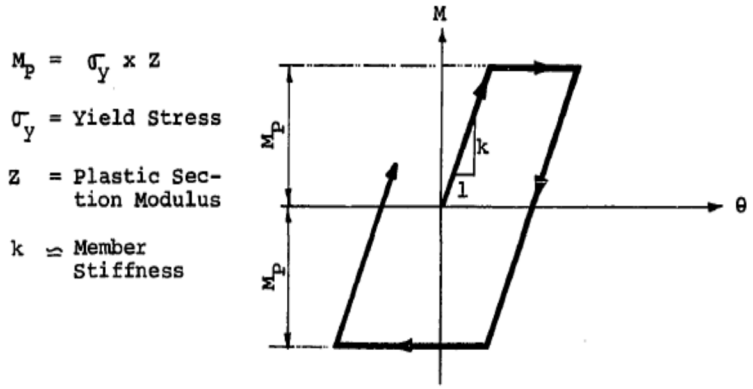

Figure 2-3 Elasto-Plastic form of bilinear moment rotation hysteresis (Gupta,1971).

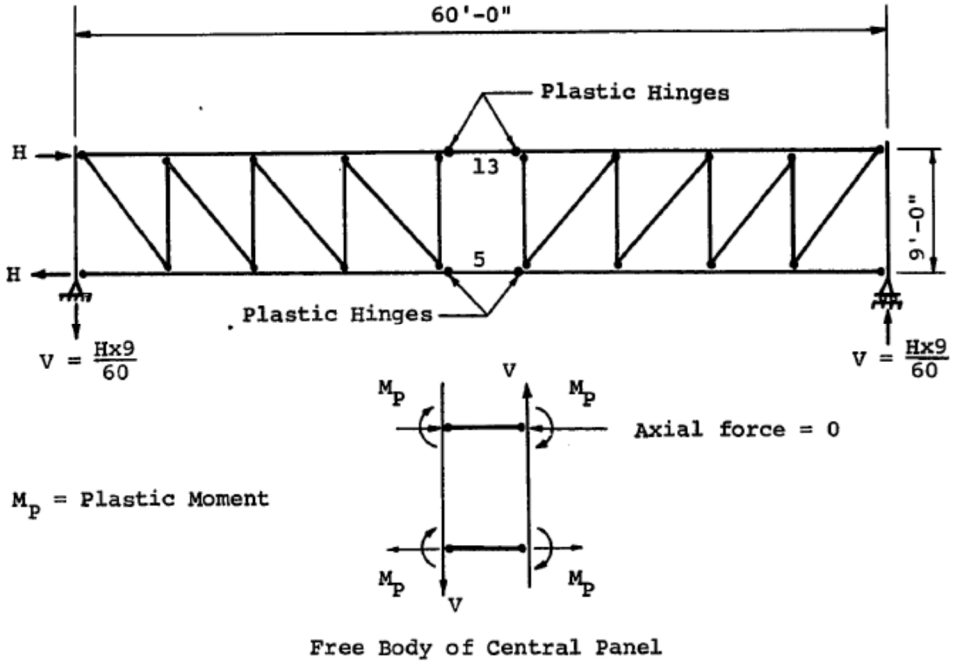

Figure 2-4 Failure mechanism of the truss (Gupta,1971).

The author had a difficulty of deriving mathematically model to compute the inelastic dynamic for these structures. This difficulty is due to three dimensions behavior of the STF system because of staggered arrangement of the trusses, and the large number of the members. To overcome these issues, an equivalent truss was developed. This equivalent truss has less structural members, but equal strength and stiffness compared with the actual truss as illustrated in Figure 2-5. The mechanism of failure which mentioned above was taken into consideration when this truss was developed.

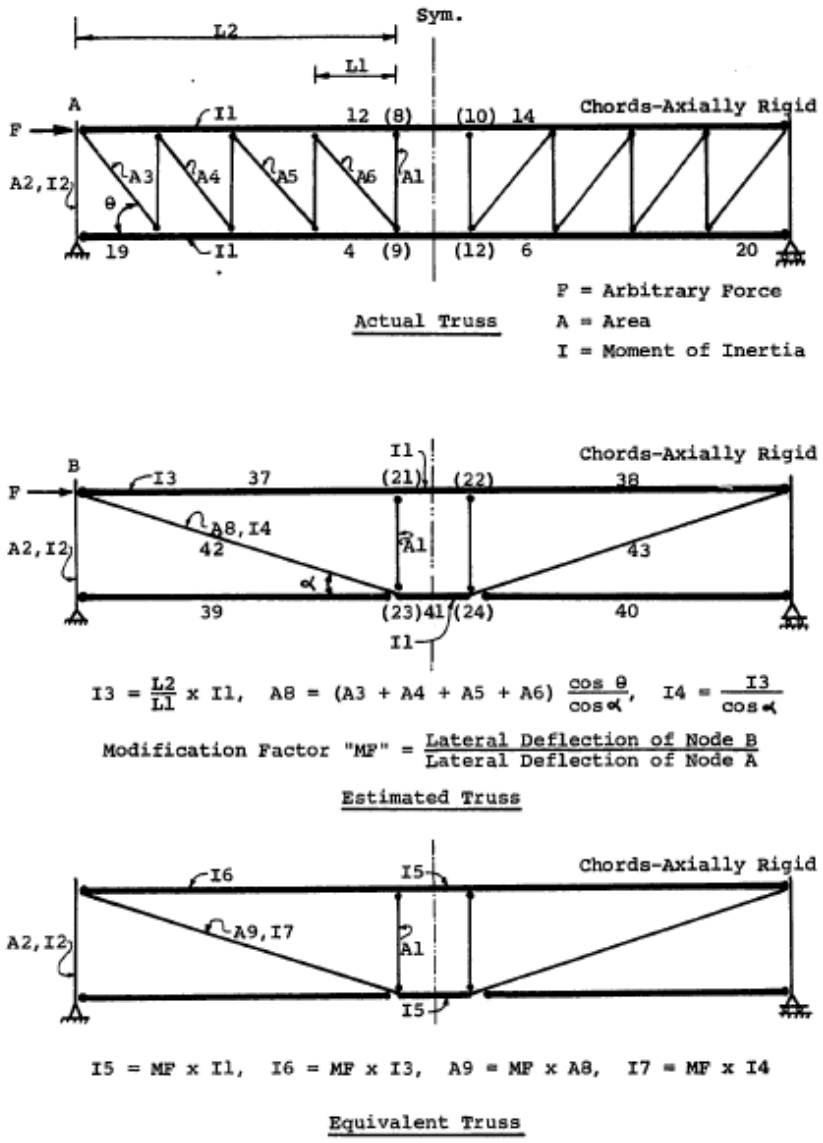

Figure 2-5 The Actual and equivalent trusses (Gupta,1971).

Gupta found that the values of the seismic coefficients which are determined by the Uniform Building Code are not large enough to resist the earthquakes that used in his study. The results of analysis showed that the columns carry high axial load with minor end moments and most of them reached the yielding. Moreover, the yielding members are the

chords in the central panel of the trusses. However, if 5% of the critical viscous damping is added, 50% of the maximum ductility ratios are reduced.

The researcher noticed that the increase in the inelastic activity is higher than 50% when the ground motion is increased by 50% in many stories. On the other hand, the base shear coefficient of the taller buildings is smaller than the shorter buildings. The width of the central panel has an important effect on the inelastic response of the STF structure was also noticed. In other words, the wider the central panel reduces the ductility requirements, the columns axial forces, and the lateral stiffness of the structure compared with the standard one.

Gupta's research laid a foundation for Hanson and others to develop a design procedure for earthquake loading for STF. Hanson et al. (1972,1973,1974) explained in detail the design procedure of STF under earthquake loading. First, a 40-story building which is subjected to gravity and lateral loads was analyzed and designed for the elastic limit and ultimate limit state. Second, the inelastic dynamic response of this building which is under the effect of the El Centro and 1.5 times the El Centro 1940 NS accelerogram was checked. Moreover, both are compared to the same response of the UBC designed building.

The results showed that the STF is an effective structural system to resist the earthquake loading, and its response behavior is a combination of braced frame and moment frame system. According to the researcher, the design of the floor diaphragm and its connection is important because the horizontal shear force is transmitted by them in this system. Furthermore, the floor diaphragm of the high-rise buildings needs to be thicker because of high amount of shear forces.

The inelastic dynamic response results showed that the STF structure has a large capacity of energy absorption and ductile deformation capability. This energy dissipates

through the chord members in the central open panel of the truss. This inelastic response makes this system effective in the design for buildings in active seismic areas compared with other seismic resistance systems that are used there.

Gupta and Goel (1972) as well as Hanson and Berg (1974) placed major importance on the analysis methodology and elastic behavior of steel trusses. However, very little attention was paid to either connection demands or post yielding behavior related to overall stability or energy dissipation.

Moore (2005) discussed the possibility of using Staggered Truss Framing system (STF system) in the areas of moderate-high seismic hazard. He provided and evaluated the technical publications which discussed the STF in many aspects. There are few papers and articles and most of them developed before 1987, little information was provided considering the effect of large seismic forces.

The author explained in detail the seismic behavior of STF system and the general seismic force path. Based on his paper, the load is transferred in staggered pattern. Furthermore, STF system transfers seismic loads by the concrete diaphragms and vertical trusses and the ductility will be provided by Vierendeel panel. However, the design of Vierendeel panels must consider that the dissipation of the seismic energy will occur through the flexural yielding.

Because there is lack of analytical and experimental data, field experience and comprehensive understanding, the author recommended to avoid using this system in the area of moderate to high seismic areas. However, for the development of future research, the author suggested a three-dimensional nonlinear response history analysis supported by experimental tests to use their results in the modeling of the structure.

Kim et al. (2007) designed and then investigated the seismic load-resisting capacities of 4, 10, and 30 stories of STF systems by pushover analysis. The authors also

designed conventional systems which are concentric braced frames (CBF) and moment-resisting frames (MRF) to compare their seismic performances with the STF systems.

According to the analysis results, the seismic load-resisting capacity of STF system is similar or higher than the Concentric Braced Frames (CBF) as it can be seen in Figure 2-6 . Furthermore, the results showed that nonlinear behavior of STF basically depends on the Vierendeel panel.

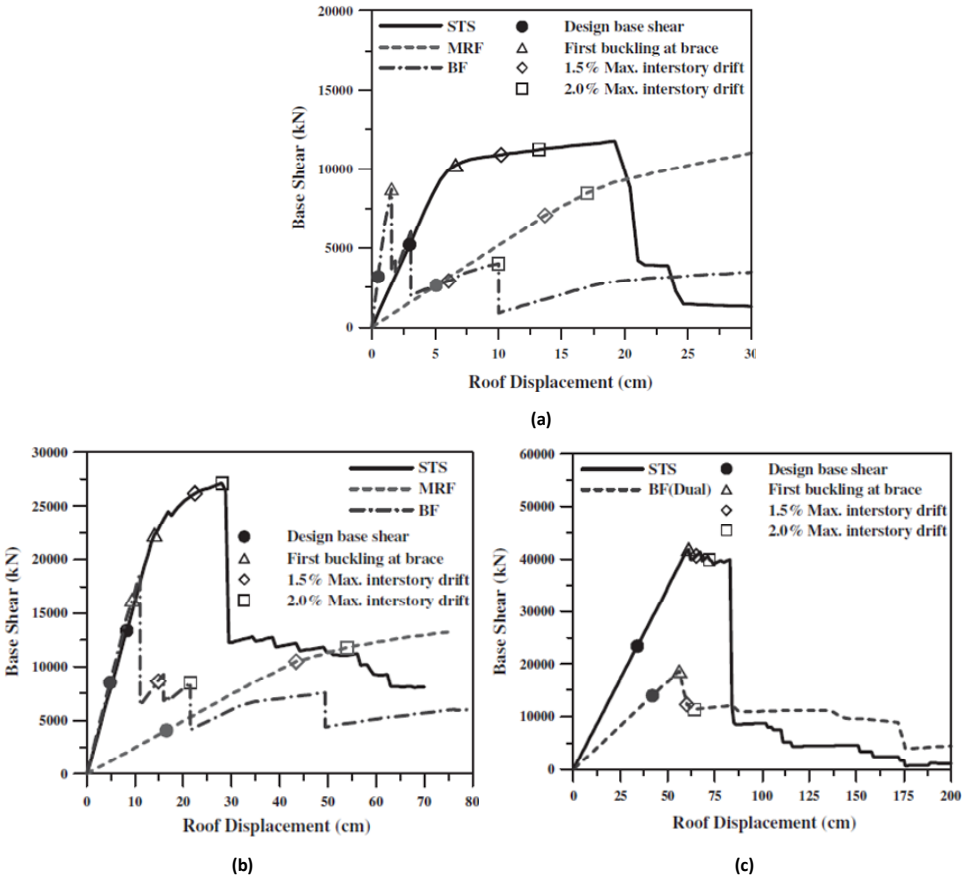

Figure 2-6 Pushover curves of the STF model structures (a) 4-story STF; (b) 10-story STF; (c) 30-story STF (Kim et al.,2007).

However, the 4-story (low-rise building) has adequate seismic load-resisting capacity. On the other hand, the analysis of 10-story (mid- rise building) and 30-story (high-rise building) showed that there is a brittle failure at the maximum capacity of the system.

In order to increase the lateral load-resisting capacity and the overall ductility of the STF system, the horizontal and vertical members in the Vierendeel panels were reinforced by increasing the moment of inertia by 30% ,50%, and 100% .

The results that are illustrated in Figure 2-7 showed that by reinforcing the horizontal members, the strength and stiffness increased slightly but the strength dropped early. On the other hand, by reinforcing the vertical members, the overall ductility increased in the 10- and 30-story structures significantly without early drop in the strength as shown in Figure 2-8.

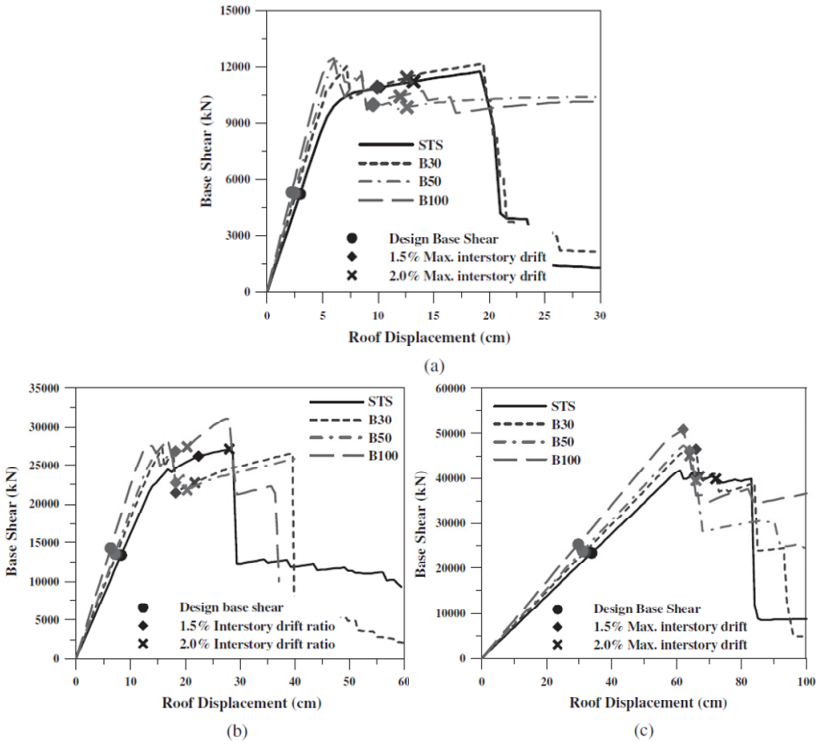

Figure 2-7 Pushover curves of the STS model structures with increased moment of inertia of horizontal members: (a) 4-story STF; (b) 10-story STF; (c) 30-story STF (Kim et al.,2007).

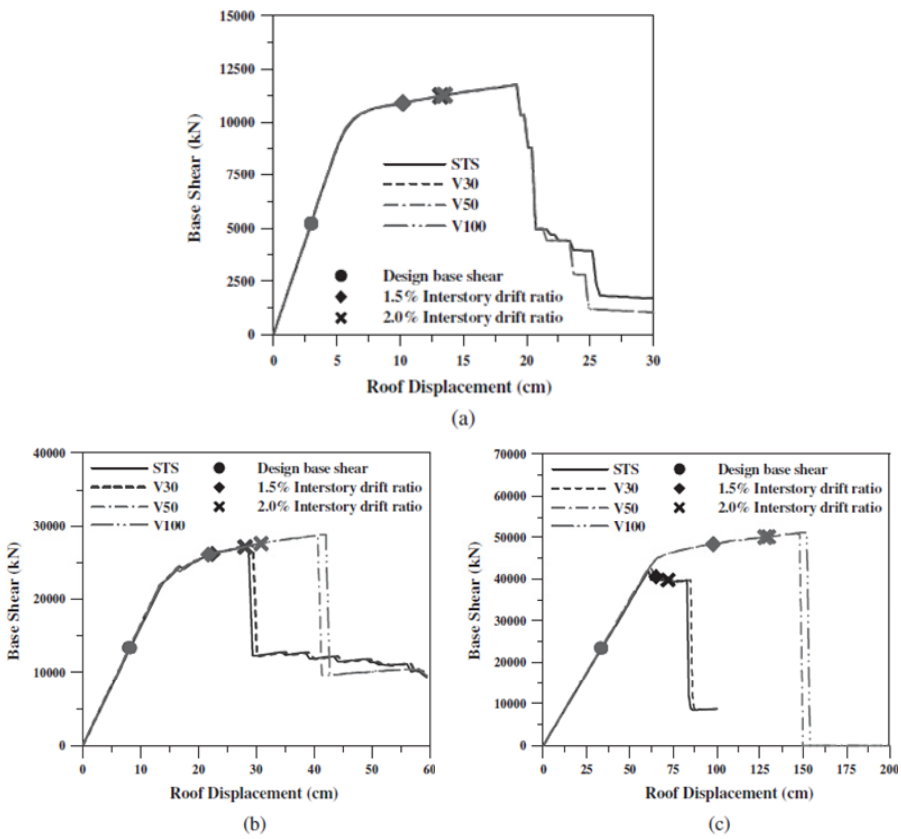

Figure 2-8 Pushover curves of the STS model structures after reinforcing vertical members: (a) 4-story STF;(b) 10-story STF; (c) 30-story STF (Kim et al.,2007).

The researchers also used different type of members, buckling-restrained braces (BRB), for all or part of the vertical and diagonal members of STF system. The results that are illustrated in Figure 2-9 show that the use of buckling restrained braces in the vertical members of the Vierendeel panels increased the system ductility.

However, in all prior studies the researchers only analyzed the two-dimensional behavior of steel trusses. Therefore, prior research failed to reveal the actual seismic behavior of STF system.

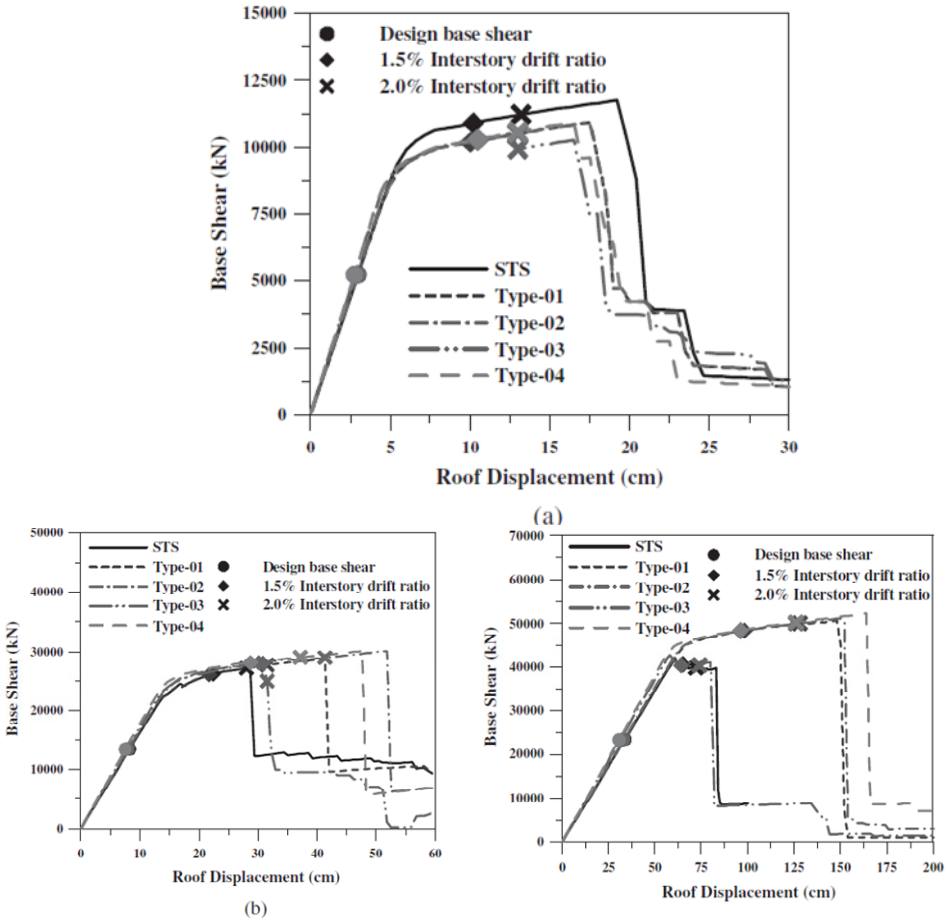

Scheme	BRB location
Type 01	Vertical members of Vierendeel panels
Type 02	All vertical members in truss
Type 03	All diagonal members in truss
Type 04	All vertical and diagonal members

Figure 2-9 Pushover curves of the STF model structures with BRB: (a) 4-story STS; (b) 10-story STS; (c) 30-story STF (Kim et al.,2007).

The seismology committee of the Structural Engineers Association of California (SEAOC),2009 recommends against use of the staggered truss system as a seismic force-resisting system in ASCE 7-02/05 Seismic Design Categories (SDCs) C through F and in 2001 CBC Seismic Zones 3 and 4.

The committee considers the assertions that mentioned in the AISC Steel Design Guide Series No.14 are apparently based on elastic analysis results and theoretical response estimates by Goel et al. (1973) and perhaps by an inappropriate extrapolation of inelastic behavior modes expected in special truss moment frames (Basha and Goel 1994).

The committee lists the following design and performance issues that need to be addressed by adequate testing and analysis:

- Identification of predictable inelastic mechanisms.
- Design forces and deformations in yielding Vierendeel panels and adjacent truss members.
- Design forces related to diaphragm-truss interaction, considering expected strength, stiffness, and ductility.
- Force distribution and inelasticity in precast diaphragms and topping slabs under high in plane forces.
- Force distribution and inelasticity in diaphragms under vertical displacements related to truss deflections and link deformation.
- Design of diaphragm-to-truss connections, considering cyclic loading and diaphragm or truss overstrength.
- Column design forces and ductility demands, considering dynamic truss-column interaction and sharing of columns by lateral and transverse systems.
- Vulnerability of the gravity system to failure of seismic-force-resisting members.
- Effects of openings and discontinuities in highly loaded diaphragms.
- Disproportionate effects of atypical and irregular building configuration.
- Axial and flexural interaction in truss chords, diagonals, and connectors.

Simasathien et al. (2014b) studied the issues which do not allow the STF system to be used in the regions that are prone to moderate or severe earthquakes. These issues are:

- The lateral force-resisting frames are the same as the gravity systems in the transverse direction.
- The large rotational demand at the end of the chord members in the Vierendeel panel, which limits the overall drift of the system and effects on the stability of the gravity system when they yield. In other words, in Figure 2-10, if the ratio of Ls/L is small, this in turn limits the overall drift capacity of the structure.
- The large deformation in the columns at the non-story levels as shown in Figure 2-10.
- The diaphragms and diaphragm-connections in lower stories have high cumulative in-plane shear force demands. Furthermore, the diaphragm-connection is subjected to large moment in the longitudinal direction.

The authors proposed an alternative layout to solve these issues as following:

- They modified the Vierendeel panels to span over three panels to increase the Ls/L ratio, which reduces the rotational demands in the Vierendeel panels.
- Braces (Kickers) were added to the non-truss levels.
- Additionally, horizontal steel trusses with precast hollow-core slabs to span over the transverse direction were proposed.

These modifications are illustrated in Figure 2-11 and

Figure 2-12. However, the horizontal steel trusses were proposed because they are an efficient structural form to transfer large shear through direct tension and compression in the truss members as shown in Figure 2-13.

The horizontal trusses use typical connections to transfer the diaphragm shear to STF system. Unlike the conventional STF systems, the hollow-core slabs are now arranged in the transverse direction because the horizontal trusses serve as transfer diaphragms. The prestressed hollow-core slabs are simply supported on the horizontal steel trusses without being connected to the STF system; therefore, they only transfer their own inertia forces. In addition, the horizontal steel trusses can be shifted away from the Vierendeel panels to avoid the direct gravity loading on the Vierendeel panels, thereby preventing the yielding members from resisting gravity loads.

Pinned connections are placed between the horizontal steel trusses and truss chords to minimize the bending moment induced by the lateral displacement in the longitudinal direction.

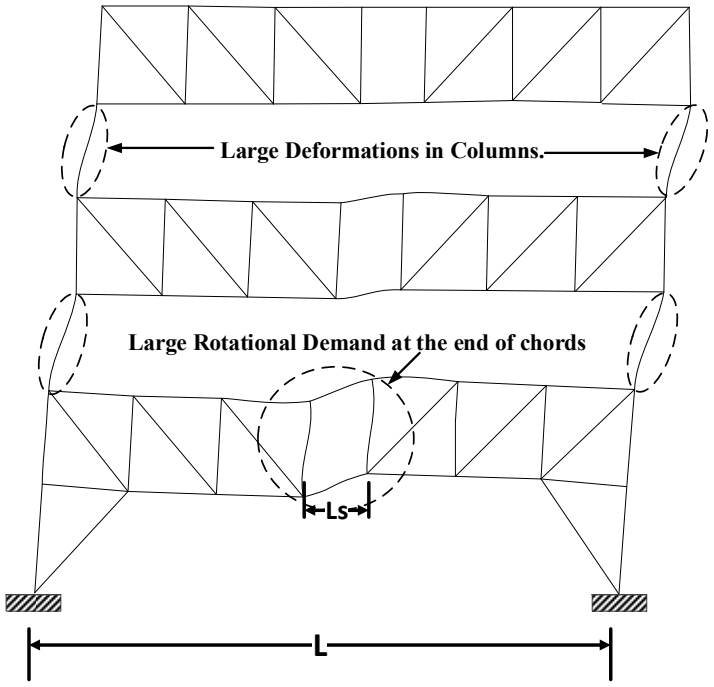

Figure 2-10 The large rotational demand at the ends of chords and the large deformation in the columns of the conventional STF system (Simasathien et al ,2014b).

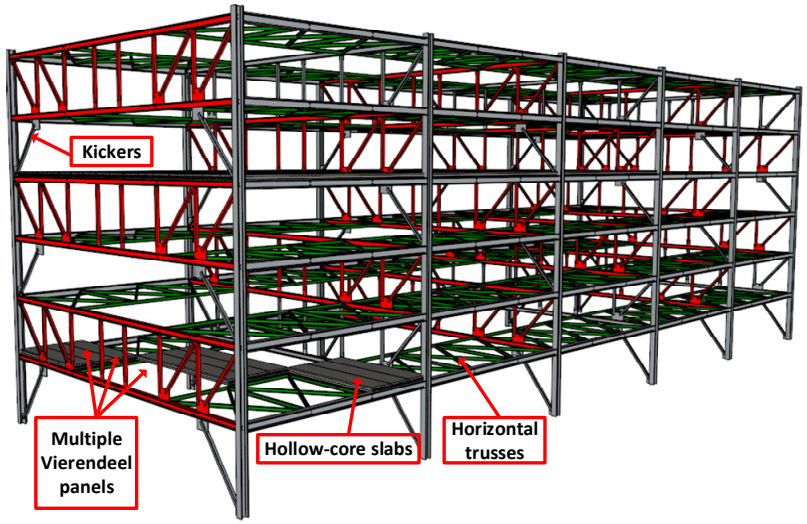

Figure 2-11 Overview of the modified STF which was proposed by (Simasathien et al ,2014b)

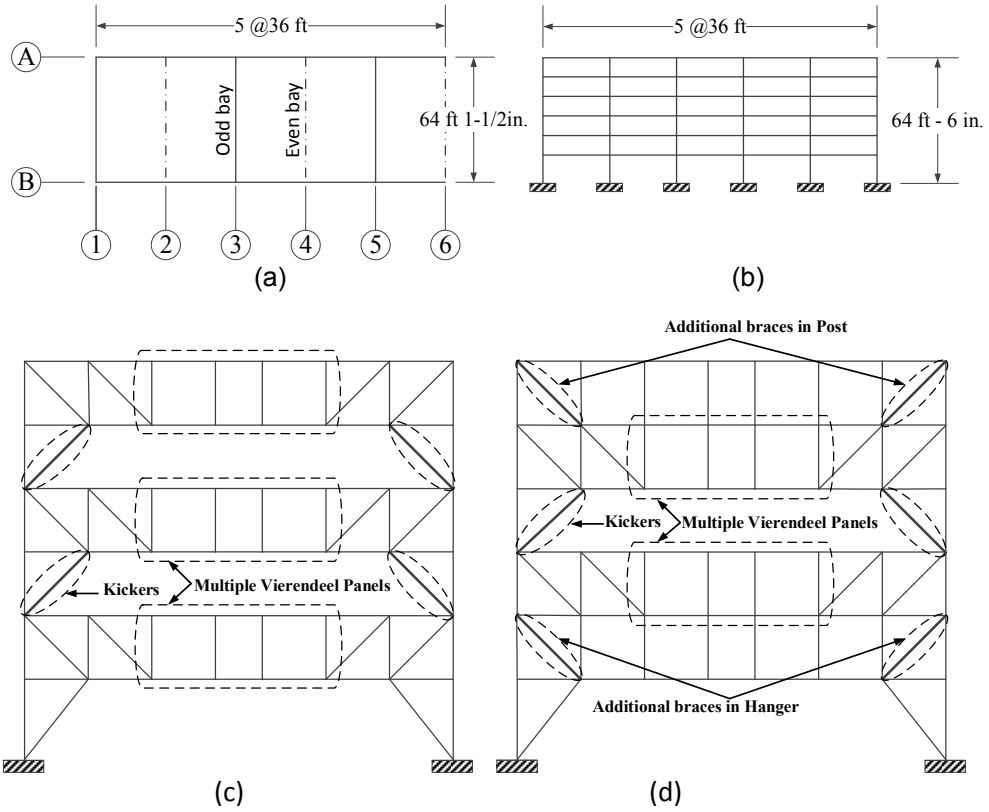

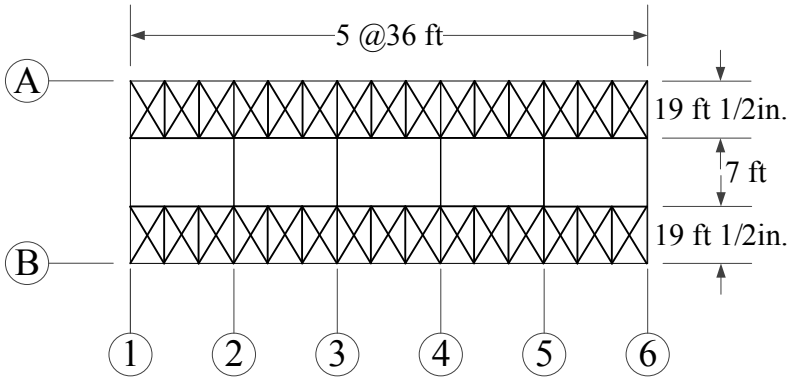

(e)

Figure 2-12 Structural geometry of the 6-story STF prototype buildings with modified STF system: (a) plan view (b) longitudinal side (moment frame) view (c) odd bay view; (d) even bay view (e) floor diaphragms with horizontal trusses (Simasathien et al ,2014b).

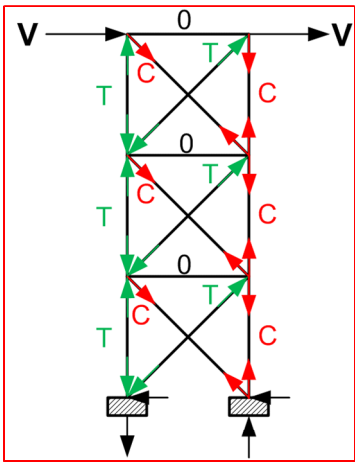

Figure 2-13 Transfer shear force in the truss members (Simasathien et al ,2014b).

Since the Vierendeel panels were modified to span over three panels, the seismic energy dissipation mechanism will be as shown in Figure 2-14. In this mechanism, the three Vierendeel panels members are the special segment (SS) in this system and the yielding members are the chords and the vertical members.

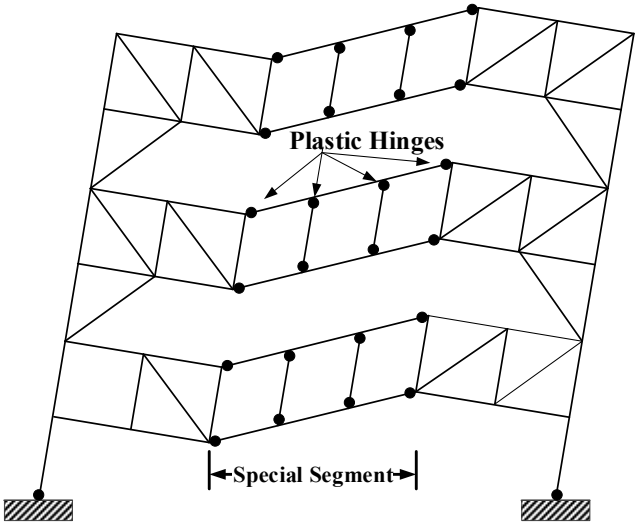

Figure 2-14 Yield mechanism and plastic hinges formation in the modified STF.

The prototype buildings of six story STF were designed in accordance with the spectrum specified in the 1997 NEHRP. Then, the members were designed elastically using a computer program, SAP 2000. Another computer program, PERFORM 3D, was utilized to investigate their seismic responses through a series of nonlinear time-history analyses for both the design basis earthquake (DBE, 10%probability of exceedance in 50 years) and the maximum considered earthquake (MCE, 2% probability of exceedance in 50 years) level ground motions in both the transverse and the longitudinal directions.

The results showed an increase in the overall drift, thereby decreasing the rotation of plastic hinges as a result of expanding the Vierendeel panels. Reduction in the deformation of the columns was noticed which was due to adding the braces in the non-story levels. One of the most significant results is adding the braces made new loads transfer paths. Therefore, high shear forces demand in diaphragms and connections were no longer an issue.

As a result of using horizontal trusses, the gravity loads were transferred out of Vierendeel panels. The results also demonstrated there is a relative uniform in the interstory drift values.

2.6 Shear studs in the composite steel beams

Shear studs are used in the composite steel beams to transfer the shear forces from the concrete slab to the steel beam by the mechanical action. They are welded to the flanges of the beam and the flexible behavior of the shear studs allows a high longitudinal slip between the concrete and the steel beam before reaching the ultimate limit state.

However, the shear studs have been investigated by many researchers to determine their shear strengths and behavior under monotonic and cyclic loading.

2.6.1 The behavior and strength of shear studs subjected to monotonic shear forces

Early composite beam research, using the push-off specimen, was conducted in 1956 by Viest at the University of Illinois. Viest tested 12 specimens to study the behavior of headed studs with varying the ratios of effective depth-to-stud diameter h_{ef}/d, where h_{ef} is the stud height from its base to the bottom of the stud head.

Three failure modes were observed: The first mode is the steel failure, where the yield stress of the headed stud is reached. The second is the concrete failure, where the concrete surrounding the headed stud crushed. The third mode of is the mixed failure of headed stud and concrete when maximum stresses are reached in headed stud and concrete element. Moreover, Viest proposed the first formula (Eq.1) to estimate the shear strength of headed studs of composite structures.

$$\left.\begin{array}{l} \text{If d<1 in., then } Q=5.225d^2 f_c^{'}\sqrt{\dfrac{4000}{f_c^{'}}} \\ \text{If d>1 in., then } Q=5d^2 f_c^{'}\sqrt{\dfrac{4000}{f_c^{'}}} \end{array}\right\} \quad \text{Eq.1}$$

Viest's equation was modified by Driscoll and Slutter (1961) (Eq.2). The researchers noticed that if the total height-to-diameter ratio (h/d) for studs embedded in normal-weight concrete equal to or larger than 4.2, the tensile strength determined the ultimate strength of the studs. On the other hand, if (h/d) is less than 4.2, the strength of studs was reduced because of fracture in the concrete.

$$\left.\begin{array}{l} \text{Long studs } (\dfrac{h}{d}) \geq 4.2\text{: } Q=\dfrac{932d^2\sqrt{f_c^{'}}}{A_s} \\ \text{Long studs } (\dfrac{h}{d}) < 4.2\text{: } Q=\dfrac{222hdf_c^{'}}{A_s} \end{array}\right\} \quad \text{Eq.2}$$

However, the first formula that adopted by the AISC Manual in 1993 (Eq.3) to compute the shear strength of headed studs was suggested by Ollgaard et al.,1971. The researchers tested 48 push-out tests in lightweight and normal-weight concrete with an effective embedment depth ratio, (h_{ef}/d =3.26). The failures were noticed in both the steel and concrete material.

$$Q = 0.5A_s\sqrt{f_c^{'}E_c} < A_s F_u$$

Where:

Q: Nominal strength of one stud shear connector embedded in a solid concrete slab;

A_s: Cross-sectional area of a stud shear connector;

f'_c :Specified compressive strength of concrete;

E_c: Modulus of elasticity of concrete; and

F_u: Specified minimum tensile stress of steel.

Pallarés and Hajjar (2010) collected and reviewed 391 monotonic and cyclic pushout tests data of steel headed shear studs subjected to shear force without use of a metal deck. After statistical reliability analysis, the researchers developed the following formula (Eq.5) for the limit states of steel failure and concrete failure of headed stud anchors subjected to shear force without the use of a metal deck.

$$P_u = \min \begin{Bmatrix} 17 f_c'^{0.45} E_c^{\,0.04} \\ 6.2 A_s (f_c' E_c)^{0.20} \\ 18 f_c'^{0.50} h^{0.20} \\ 9 \lambda f_c'^{0.50} h^{0.60} \end{Bmatrix} \text{ Concrete failure.} \qquad \text{Eq.5}$$

$$P_u = 0.65 F_u A_s \qquad \text{Steel failure.}$$

AISC (2016b) determines the nominal shear strength of one steel headed stud anchor embedded in a solid concrete using the following formula (Eq 6). When a formed deck is used ,R_g and R_P parameters depend on the deck properties. However, these parameters are 1.0 and 0.75 for solid slab (no formed steel deck).

$$Q = 0.5 A_s \sqrt{f_c' E_c} < R_g R_p A_s F_u \qquad \text{Eq.6}$$

Eurocode 4 (2004) defines the ultimate shear strength of a headed stud anchor embedded in a solid concrete slab by:

$$P_{RD} = \min\left\{\begin{array}{l}\dfrac{0.29\alpha d^2\sqrt{f_{ck}E_c}}{\gamma_v} \\ \dfrac{0.8F_u\pi d^2}{4\gamma_v}\end{array}\right\} \qquad \text{Eq.7}$$

With,

$$\alpha=\left\{\begin{array}{ll}0.2(\dfrac{h_{sc}}{d}+1); & (3\le\dfrac{h_{sc}}{d}\le 4) \\ 1.0 & ;(\dfrac{h_{sc}}{d}>4)\end{array}\right\}$$

Where,

f_{ck}: is the characteristic cylinder compressive strength of the concrete at the age considered, of density not less than 1750 kg/m^3;

E_c : is the modulus of elasticity for concrete;.

f_u: is the specified ultimate tensile strength of the material of the stud but not greater than 500 N/mm^2;

h_{cs}: is the overall nominal height of the stud.

d : is the diameter of the shank of the stud, 16 mm ≤d ≤25 mm;

γ_v: is the partial safety factor, and is taken as 1.25 at the ultimate limit state.

However, the formula that is required in the Eurocode to estimate the shear strength of stud in is not only determined by stud failure but also by concrete crush. Therefore, the Eurocode formula is more conservative than that in AISC (2016b).

Lam (2006) studied the capacities of headed stud shear connectors in composite steel beams with precast hollowcore slabs. Push test was carried out for seventy-two specimens to investigate the parameters that affect on the capacity of shear connector. However, the author noticed that the parameters which play a significant role in the capacity are the transverse reinforcement, strength of concrete, the width of the gap

between the planks, height and diameter of the stud and the end profile of the slab (i.e. square or chamfered end). On the other hand, no significant effect was observed for the slab thickness.

Additionally, the author proposed two equations to estimate the capacity of connector based on the parameters he studied. However, the steel failure equation is the same as that required by Eurocode 4 (2004), whereas two factors were added to the concrete failure equation. The first factor is (β) which takes into account the in-situ infill gap between the HCS, g_i, and is given by 0.5 (g_i /71+1) ≤ 1.0 and gi ≥30. The second factor is (ε) which takes into account the transverse reinforcement and is given by 0.5(ϕ /20 + 1) ≤1.0, where ϕ is the diameter of transverse reinforcement.

$$P_{RD} = \min\left\{\begin{array}{ll} \dfrac{0.29\alpha\beta\varepsilon d^2\sqrt{f_{ck}E_c}}{\gamma_v}, & \text{Concrete failure} \\ \dfrac{0.8F_u\pi d^2}{4\gamma_v}, & \text{Steel failure} \end{array}\right\} \qquad \text{Eq.8}$$

2.6.2 The behavior of shear studs subjected to cyclic shear forces

In general, the results available in literature show that the shear studs subjected to cyclic shear force have lower strength and ductility than those under monotonic shear force (McMullin and Astaneh-Asl, 1994; Civjan and Singh, 2003; Saari et al., 2004).

Makino (1984) conducted experiments on a one-third scale single-story, single-bay steel frames with reinforced concrete infills. The researchers found that the cyclic strength of the studs was almost 50% of the estimated strength from the formulas of Ollgaard et al.

Hawkins and Mitchell (1984) carried out push-out tests for twenty-three specimens of composite shear connections under monotonic and reversed cyclic loading. A ¾ -in.

diameter of shear stud was used and some of the specimens were tested with ribbed metal deck and others without. Four failure modes were observed in the metal deck stud shear connections: (1) stud shearing, (2) concrete pullout, (3) rib shearing, and (4) rib punching. The results showed the ultimate shear strengths with stud shear failure under reversed cyclic shear is approximately 17% lower than their monotonic strengths.

Gattesco and Giuriani (1996) tested four specimens; two of them were subjected to monotonic loading while the others subjected to cyclic loading. The results showed that the strengths of the two specimens under cyclic loading were reduced by 10%.

Bursi and Gramola (1999) tested two series of eleven push-type specimens under low-cycle high amplitude displacements. The test results showed both stiffness and strength of stud connectors were reduced because of yielding and fatigue cracking in the studs in addition to the propagation and coalescence of microcracks in concrete.

Civjan and Singh (2003) performed a set of experimental and analytical tests to investigate the behavior of shear studs subjected to fully reversed cyclic load. They found that there is a 40% reduction in the shear studs' strengths under reversed cyclic loading compared to monotonic strengths computed by AISC 2005. According to the authors, this reduction is due to the low-cycle fatigue of the shear stud, weld materials, and concrete degradation.

Ciutina and Stratan (2011) tested a series of ten experiments subjected to cyclic and monotonic loading by varying the type of connectors. The results demonstrated that the shear strengths of studs under cyclic loading were reduced in the range (10%-40%) as compared to the corresponding monotonic specimens. Furthermore, they concluded that the 25% reduction in the connector's shear resistance as requested by Eurocode 8 is sufficient for headed stud connectors.

The wide range of data which was compiled and documented by Pallarés and Hajjar, 2010 showed the 25% reduction of the shear studs which is requested by the AISC-341-05 is justified.

Chapter 3

Experimental Program

3.1 Introduction

Nonlinear analyses of a three-dimensional 6-story STF building model indicated that the hollow-core slab diaphragms and the diaphragm-to-truss connections is subjected to in-plane shear deformation ($\gamma = L_h/\Delta_h$) which is due to relative lateral drifts between trusses as shown in Figure 3-1 (Simasathien, 2016). Moreover, the nonlinear Finite Element Analysis (FEA) results showed that there is a double shear effect on some of these connections (Discussed in chapter 8) and single shear effect as well. Based on these results, five large-scale specimens were prepared and tested at the University of Texas at Arlington-Civil Engineering Laboratory Building (UTA-CELB).

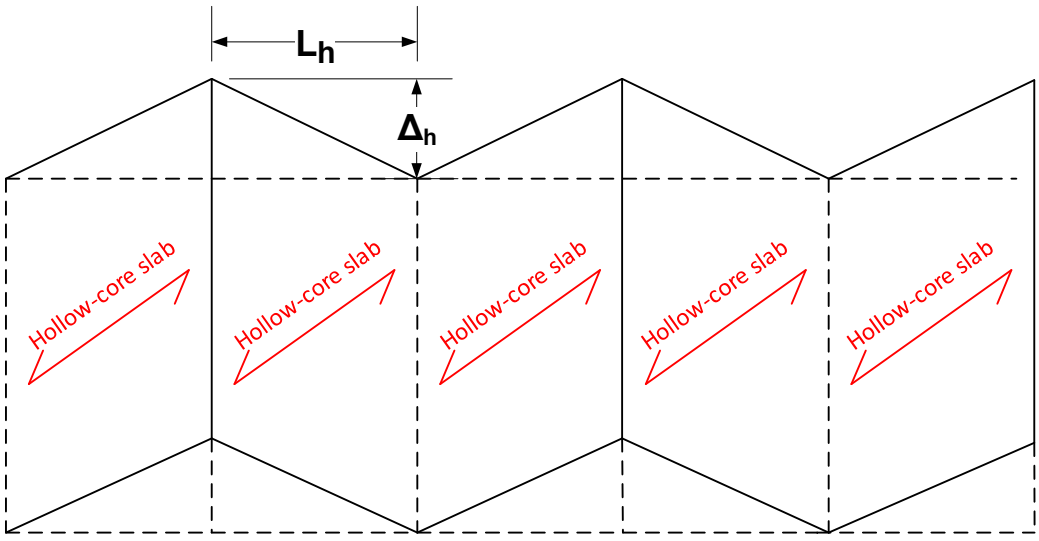

Figure 3-1 In-plane shear deformations in the hollow-core slab diaphragms and the diaphragm-to-truss connections.

The preparing, setup, and testing of all specimens are discussed in this chapter. The first specimen was tested monotonically, and the loading protocol was developed, then it was used in the following cyclic tests. However, based on the results of the first cyclic test, the number of shear studs and the detail of longitudinal rebars were modified in all following cyclic tests.

Additionally, the fourth specimen was tested with 2 in. reinforced concrete topping slab which casted over the hollow-core planks to investigate if that increases the shear strength of the planks and the connection as well. The last specimen was tested to investigate the shear strength of the connection and the planks under the effect of double shear. The results of these experiments are analyzed and discussed in Chapter 4.

3.2 Preliminary monotonic test for in-plane shear deformation

A preliminary monotonic test was carried out to determine the rigidity, strength, and ductility of the hollow-core slab diaphragm and the connection. Furthermore, the protocol loading for the next cyclic load specimens was developed based on the results of this test.

The specimen was tested using the setup which is shown in Figure 3-2 through Figure 3-5. The setup in the lab was first started by construction the concrete blocks and the post-tension of the blocks to the reaction floor of the lab, then welding the studs over the top flange of the middle steel beam. Furthermore, the setup included installing the steel beams and their supports in addition to install the precast prestressed hollow-core concrete planks. The strain gauges were attached to the specified locations on the steel rebars and the shear studs of the connection. The setup was ended by casting the connection then attaching the 100K actuator to the specimen and installing the LVDTs. However, all of these procedures will be discussed in detail in the following sections.

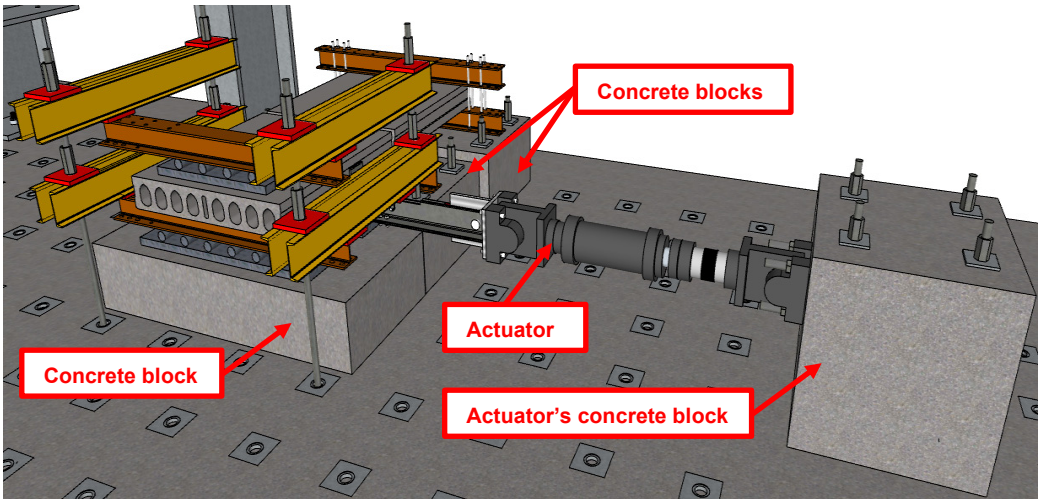

Figure 3-2 Overview setup drawing of the preliminary in-plane shear deformation monotonic specimen.

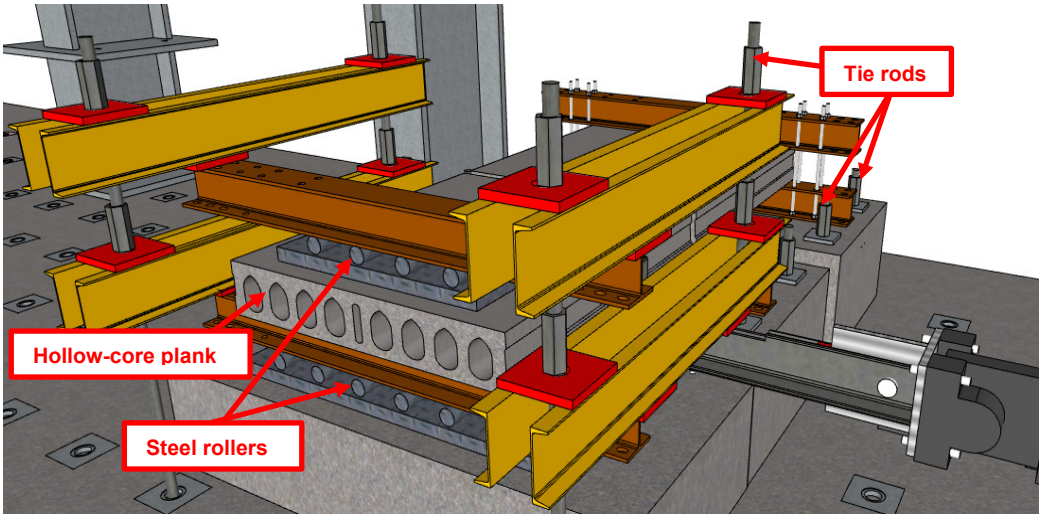

Figure 3-3 Isometric view drawing of the specimen setup.

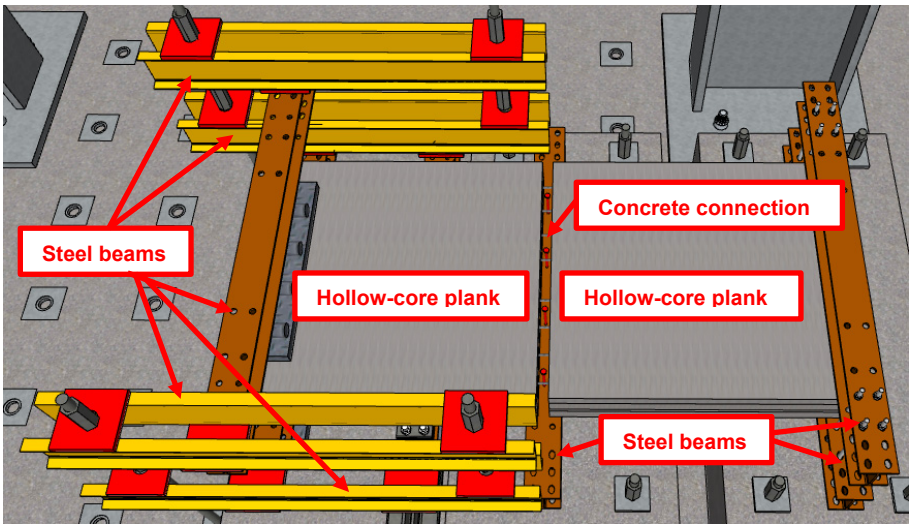

Figure 3-4 Top view drawing of the specimen setup.

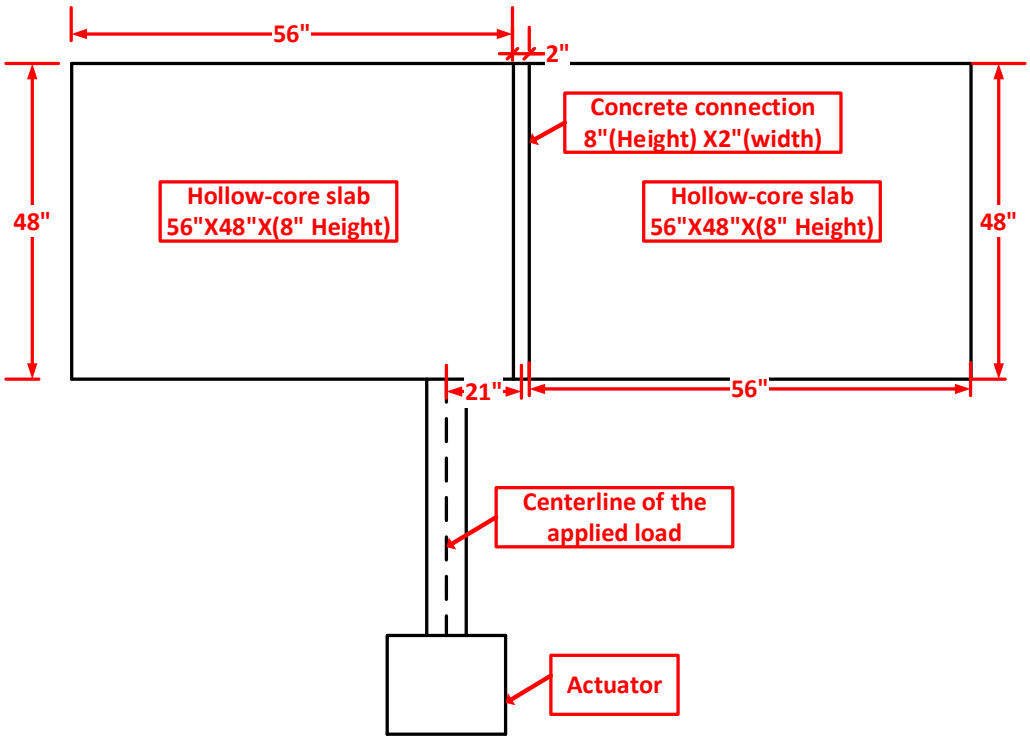

Figure 3-5 Schematic of the specimen's dimensions.

3.2.1 Concrete blocks construction

Four concrete blocks were first constructed, three of them were used to support the steel beams (discussed later) and the other one to support the 100K actuator during the test. Timber of cross section (2 in.x4 in.) and plywood of 5/8 in. thickness were used in the construction of the formworks of the concrete blocks as shown in Figure 3-6.

The plywood pieces were connected to the wood pieces by screws and the four sides were connected together by 1/4 in. diameter threaded rods to keep the formwork capable of resisting the hydrostatic pressure of the wet concrete during the cast. Figure 3-7 and Figure 3-8 show the construction of the formworks.

The dimensions of two blocks which were used to support the steel beams are 84”X40”X22” and the other is 84”X40”X17.5”, whereas the concrete block which was used to support the actuator is 45”X40”X40” as shown in Figure 3-9 and Figure 3- 10. Four steel cages were prepared, and Figure 3-11 shows one of them.

Figure 3-6 Picking up the timber of X-section 4”X2” and plywood of 5/8” thickness.

Figure 3-7 Preparing the sides of the formworks.

Figure 3-8 Connection the sides of the formwork together.

Figure 3-9 The formworks of the three concrete blocks that support steel beams.

Figure 3- 10 The formworks of the concrete block that supports the actuator.

Figure 3-11 Preparing the steel cages.

Four polyvinyl chloride (PVC) pipes of 2-1/2 in. diameter near the corners of each block were installed vertically. Additionally, the spaces between the pipes are 24 in. in the short direction and 72 in. the long direction which match with the typical reaction floor holes spaces in the lab. However, the spaces are 24 in. in both direction for the actuator's concrete block.

Plywood discs were used to keep the pipes fixed during the cast and the ends of the plastic pipes are confined by steel stirrups as shown in Figure 3-12 and Figure 3-14, respectively. These pipes are used to post-tension the supporting block to the reaction floor using threaded rods of 2 in. diameter. Moreover, fourteen PVC pipes of 1-1/2 in. diameter are also installed horizontally to be used for 1 in. threaded rods to support the actuator during the test as shown in Figure 3-14 .

Two wide flange steel beams of section W6X25 with ASTM 992 and length of 72 in. are used as a steel chord in the STF system. The beams are connected to the concrete blocks by ½ in. and ¾ in. diameter threaded rods. However, these steel beams are used temporarily in addition to some of timber wood pieces to support the threaded rods during the cast as shown in Figure 3-15.

Figure 3-16 shows the complete specimens' components before concrete casting. Ready-mix concrete with compressive strength 4000 psi was used to cast the specimens. Figure 3-17 through Figure 3-18 show the casting process and Figure 3-20 shows the specimens after remolding the formworks.

Figure 3-12 Installing the plywood discs to support the PVC pipes.

Figure 3-13 Stirrups at the ends of the PVC pipes.

Figure 3-14 Horizontal and vertical PVC pipes to support the blocks and the actuator.

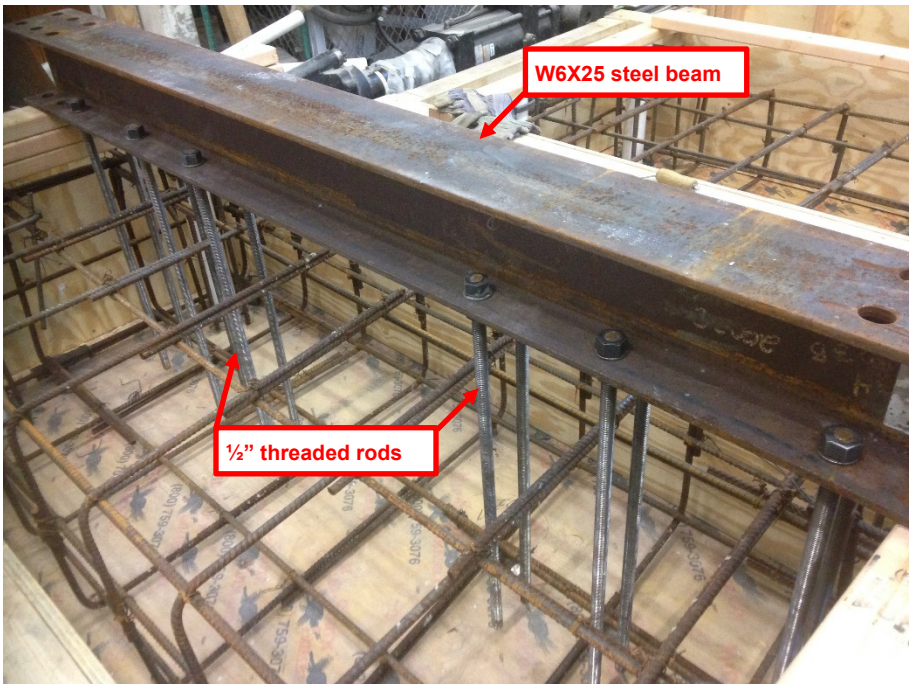

Figure 3-15 The threaded rods that used to support the steel beam.

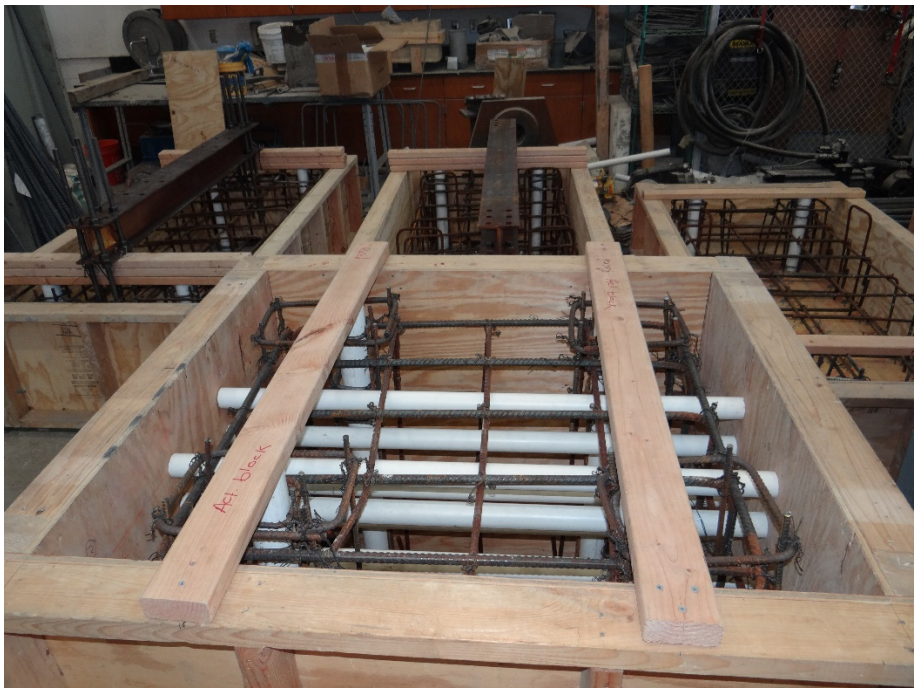

Figure 3-16 Complete specimens' components before concrete casting.

Figure 3-17 Concrete casting of the specimens.

Figure 3-18 Finishing the surface of the specimens after casting.

Figure 3-19 The specimens after finishing the casting.

Figure 3-20 The specimens after remolding the formworks.

The four concrete blocks were moved to specified locations in the lab, then each one of three blocks two of the 88”X40”X22” dimensions concrete block and the actuator’s block of the dimensions 45”X40”X40” were post-tensioned to the reaction floor by four 2 in. diameter threaded rods.

3.2.2 The concrete connection and its detail

The connection details which are proposed by Structural Prestressed Industries (SPI) Inc. was used in this test. Figure 3-21 shows the detail of the connection which consists of shear studs welded over a steel beam and # 4 steel rebars with length 48 in. is equally divided between the two sides. The connection of width 2 in. in addition to the holes of planks to the end of the steel rebars are filled with a grout.

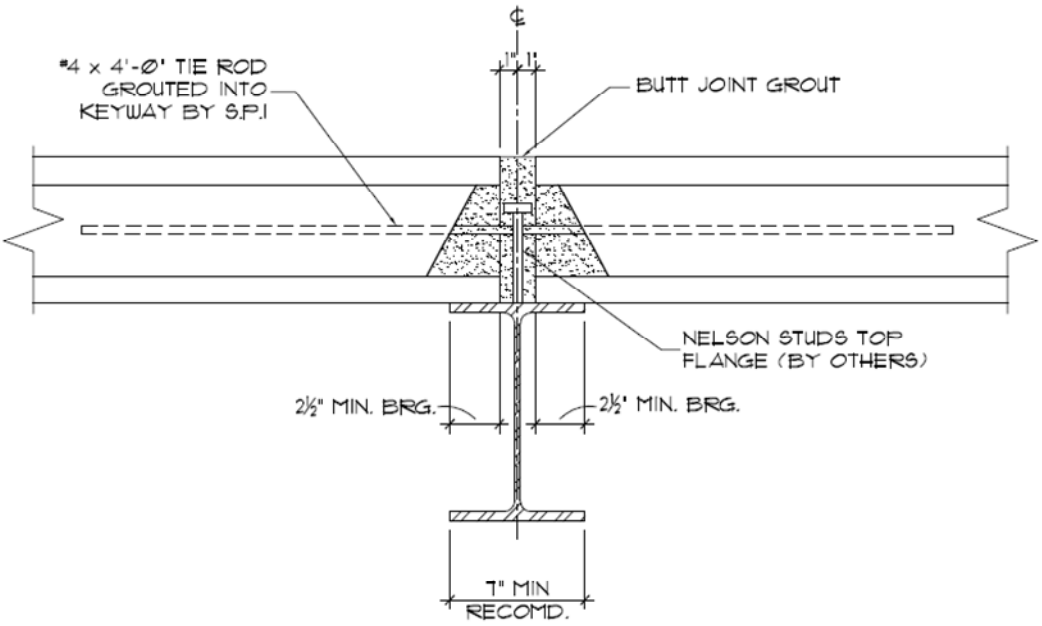

Figure 3-21 detail of the connection which proposed by Structural Prestressed Industries Inc. (SPI).

3.2.3 Shear studs welding process

Shear studs of 4 in. length and ¾ in. diameter (Figure 3-22) were welded on the top of the middle steel beam by Nelson Stud Welding, Inc. at Irving, TX. The equipment of welding are the welding machine, hand tool called the stud gun, and the ceramic ferrule as shown in Figure 3-23 and Figure 3-24. Ceramic ferrule is important for stud welding, it helps to shield the arc from the operator, minimizes the atmosphere that the flux must purge, forms the molten metal into the fillet, and its fillet vents allow weld gases to escape.

In this process the shear stud was placed with the stud gun and the ceramic ferrule placed on the base of stud. Then the shear stud was placed in contact with the top flange of the steel beam, a weld arc was drawn which melted the welding stud base and an area of the steel beam. The welding stud was then forced into the melted area and hold in place until the metals re-solidify. Figure 3-23 through Figure 3-27 show the shear stud welding process.

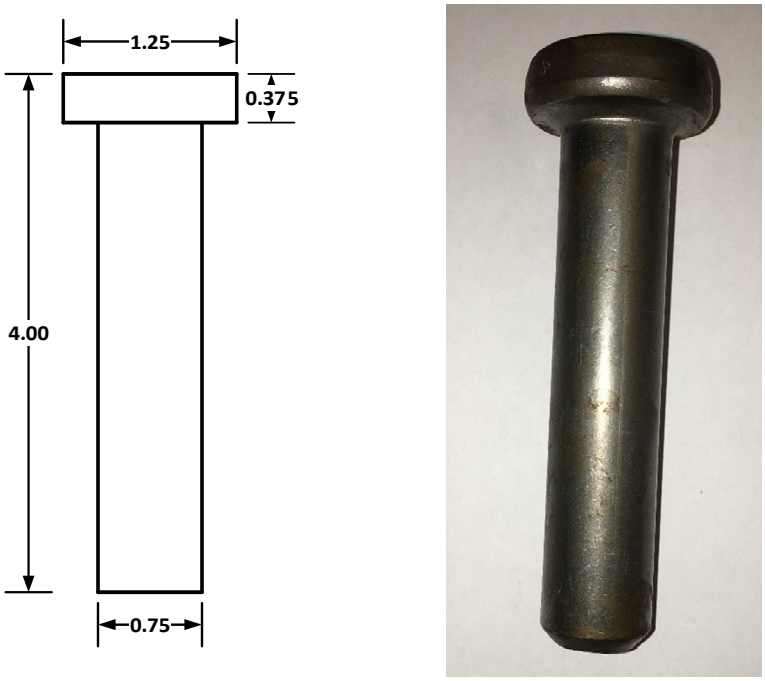

Figure 3-22 Shear stud dimensions in inch; picture of the shear stud

Figure 3-23 Welding machine.

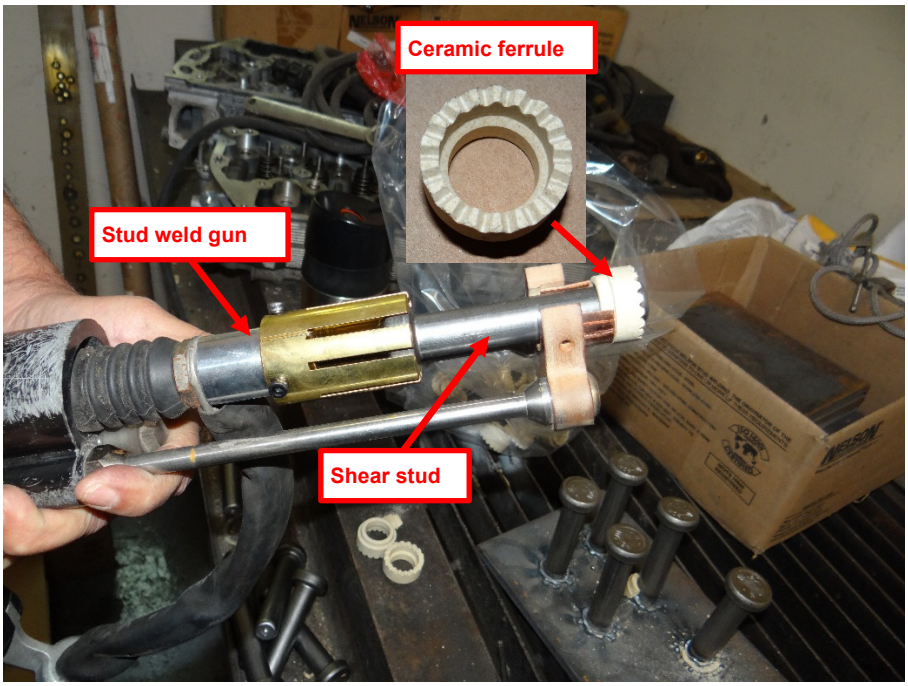

Figure 3-24 Welding equipment; Stud gun; ceramic ferrule.

Figure 3-25 Placing the shear stud in contact with the steel beam

Figure 3-26 Melting the welding stud base and the area of the steel beam and escaping the weld gases thought vents in the ceramic ferrule.

Figure 3-27 The shear studs and the welding area (in the frame) after completion of the welding process.

Four shear studs were used in this test, the number of shear studs were determined based on Denis lam equation, which was discussed in Chapter 2 and the following calculations show that.

$P = 0.29\alpha\beta\varepsilon d^2\sqrt{f^{'}E_c}/\gamma_v$ (Metric units)

$P = \dfrac{0.80 f_u \pi d^2}{4\gamma_v}$

α=$0.20(\dfrac{h}{d}+1)$, h:height of shear stud.

, d:diameter of shear stud.

β=$0.50(\dfrac{g}{71}+1)$,g:in-situ infill gap.

ε=$0.50(\dfrac{\phi}{20}+1)$, ϕ : diameter of transverse reinforcement.

$\gamma_v = 1.25$ safety factor.

$f_c^{'}$: Average strength of the in-situ and precast concrete.

E_c : Modulus of elasticity of the in-situ and precast concrete.

F_u : Minimum tensile strength of the shear stud.

$h = 3.875", d = 0.75" = 19mm.$

$g = 2" = 50.8mm, \phi = 12.7mm.$

$f_c^{'}$ (in-situ concrete)=2Ksi=13.79Mpa.

$f_c^{'}$ (precast concrete)=4Ksi=27.60Mpa.

$\Rightarrow f_c^{'}(Average) = 3Ksi = 20.70Mpa.$

$E_c(\text{in-situ concrete}) = 4700\sqrt{13.79} = 17453.4Mpa.$

$E_c(\text{precast concrete}) = 4700\sqrt{27.60} = 24691.78Mpa.$

$\Rightarrow E_c(Average) = 21072Mpa.$

α=$0.20(\dfrac{3.875}{0.75}+1) = 1.233$

β=$0.50(\dfrac{50.8}{71}+1)$=0.8577.

ε=$0.50(\dfrac{12.7}{20}+1)$=0.8175

$P = 0.29(1.233)(0.8577)(0.8175)(19)^2\sqrt{(20.7)(21072)}/1.25$

$= 47.82KN = 10.75Kips. \rightarrow Controls.$

$F_u = 65Ksi.$

$P = \dfrac{0.80(448.5)(\pi)(19)^2}{4(1.25)} = 81.4KN = 18.3Kips.$

Therefore, use 4 shear studs, the total shear resistance is 43Kips.

3.2.4 Precast prestressed hollow-core planks

Two precast prestressed concrete hollow-core planks which mostly used as a slab (diaphragm) in the STF system were used in this test. The thickness of this planks is 8 in., the width is 48 in. and the length is 56 in. and they were produced by Gate Precast Co. in Pearland, TX. Figure 3-28 shows the cross-section dimensions of the plank and Figure 3-29 shows the delivery of the planks at UTA-CELB.

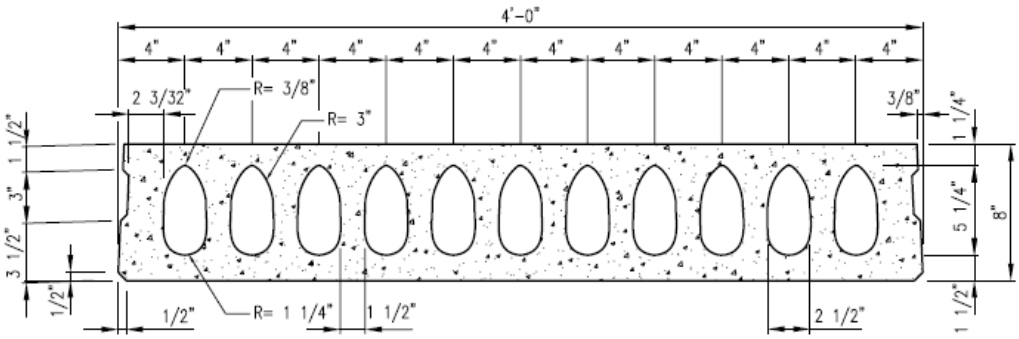

Figure 3-28 Cross section of the precast prestressed concrete hollow-core plank (Source: Gate precast company: Specification Details).

Figure 3-29 Delivery of the hollow-core planks at UTA-CELB.

3.2.5 Installing the steel beams and their supports

The two-steel beam were attached to two of concrete blocks throughout the ½" threaded rod which were already embedded in the concrete then the nuts were tightened strongly using the torque wrench. On the other hand, two supports were installed at the ends of the concrete hollow-core plank to restrain the horizontal displacement at exterior connection as shown in Figure 3-30 . However, the horizontal displacement on the other exterior side must be released to ensure that the connection will be under pure shear force. In order to achieve that, the hollow-core plank was supported by a steel beam over rollers and the rollers move horizontally over 2 in. greased steel plate to eliminate any frictional forces as shown in Figure 3-31.

Figure 3-30 Supports at one end of the concrete hollow core planks (Fixed side).

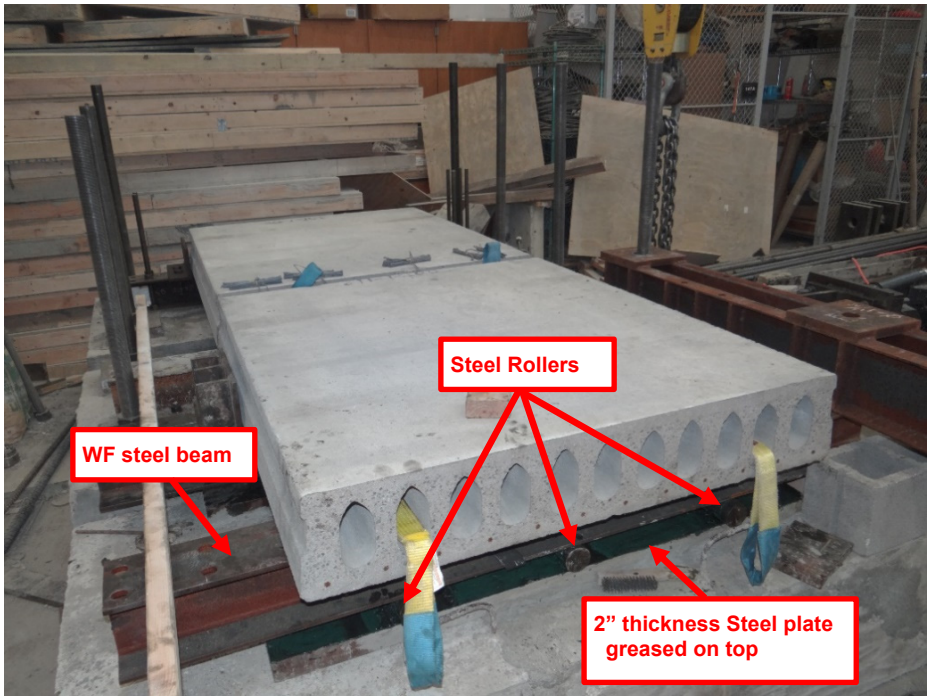

Figure 3-31 Supports at one end of the concrete hollow core planks (Roller side).

After installing the steel beams and their supports, the first hollow-core plank was installed in its place. It spanned between the middle steel beam to the fixed side steel beam. Then 11#4 -Grade 60 rebars installed in the openings of the planks as shown in Figure 3-32.

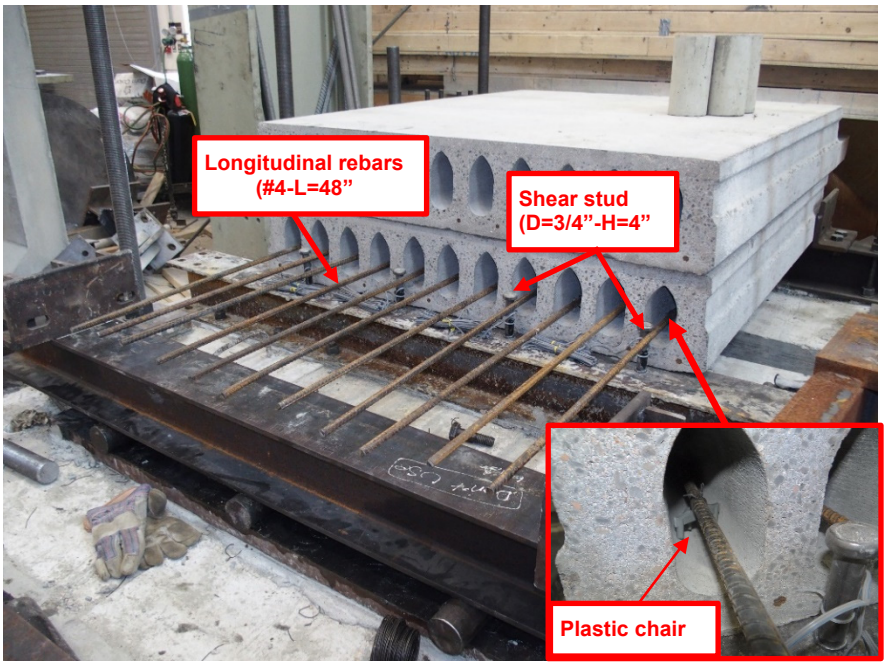

Figure 3-32 Installing the longitudinal rebars.

3.2.6 Strain gauges installing process and their locations layout

Strain gauges were attached slightly above the welding area of the stud as shown in Figure 3-33. The process starts by grinding the stud face, cleaning the face by acidic neutralizing agents, then attaching the strain gauge to smoothed stud face using the glue. M-coat A should be spread on top of the strain gauge and wait for at least 15 minutes to add M-coat B. After two hours, electrical tap and liquid sealant should be used to cover and preserve the coated strain gauges. Figure 3-34 shows the stain gauges locations layout.

Figure 3-33 Strain gauges installing process on the shear stud

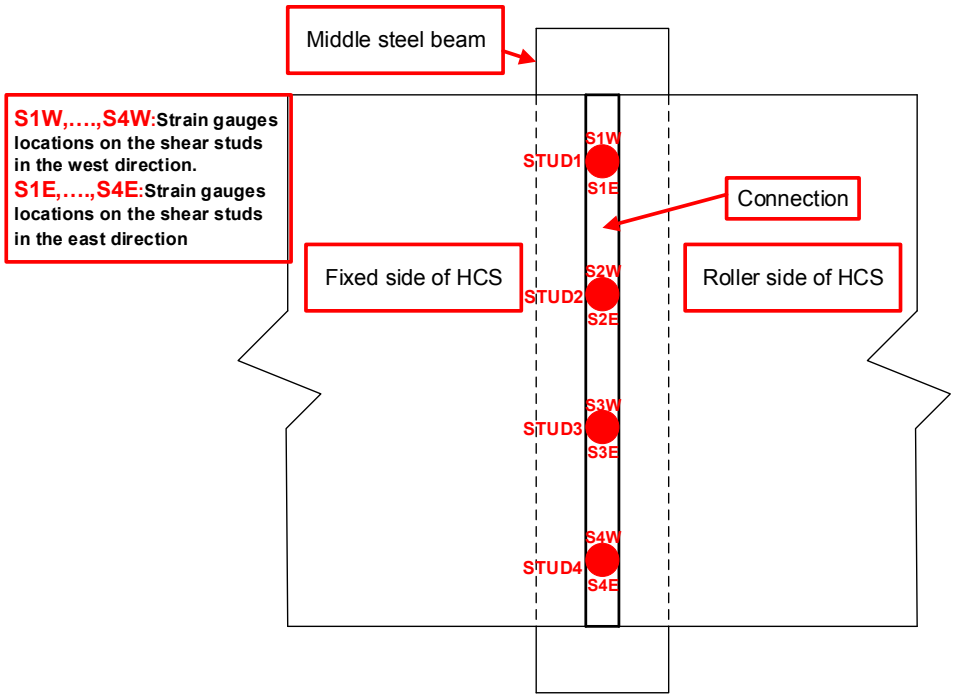

Figure 3-34 Strain gauges locations layout.

3.2.7 Casting of the connection

Sample of grout which is a mixture of cement, sand, and water was prepared and tested first. The compressive strength of the grout usually ranges from 2000 psi to 3000 psi at 28 days. However, the grout should be flowable to ensure filling the connection and the specified openings in the hollow-core panels. In order to ensure the ranged

compressive strength and the flowability, 1:3 cement to sand ratio was used, in addition to use 0.60 as W/C ratio. Thee cylinders (8”X4”) were tested after three days and the average compressive strength was 2700 psi which is in the range.

Based on this result, it was decided to test the specimen after three days from the casting of the connection. In order to stop flowing of the grout after the end of rebars and the ends of connection, pieces of foam boards which were prepared to have the same shape of the holes and the ends of connection as shown in Figure 3-35 and Figure 3-36, respectively. The casting of connection is shown in Figure 3-37 through Figure 3-39. Six cylinders ware taken and tested at the same day of testing the specimen (after three days from the casting of the connection).

Figure 3-35 Closing the holes in the planks at the ends of rebars.

Figure 3-36 Closing the ends of the connection.

Figure 3-37 Preparing the materials for casting the connection.

Figure 3-38 Filling the connection and the holes in the planks.

Figure 3-39 The connection after completion the casting.

3.2.8 Preparing for the test

In order to prevent the vertical displacements at the ends of the hollow-core panels which are due to uplift forces during the test, a steel beam was installed on the top of each side of the panels. The beam in the fixed side was attached to the ½" threaded rods and tighten using the wrench. However, the beam in the roller side was installed over rollers and 2 in. greased steel plate then it was fixed from the top by two steel beams. These two-steel beams were hold by four 2 in. threaded rods which were attached to the reaction floor. All these details are shown in Figure 3-40.

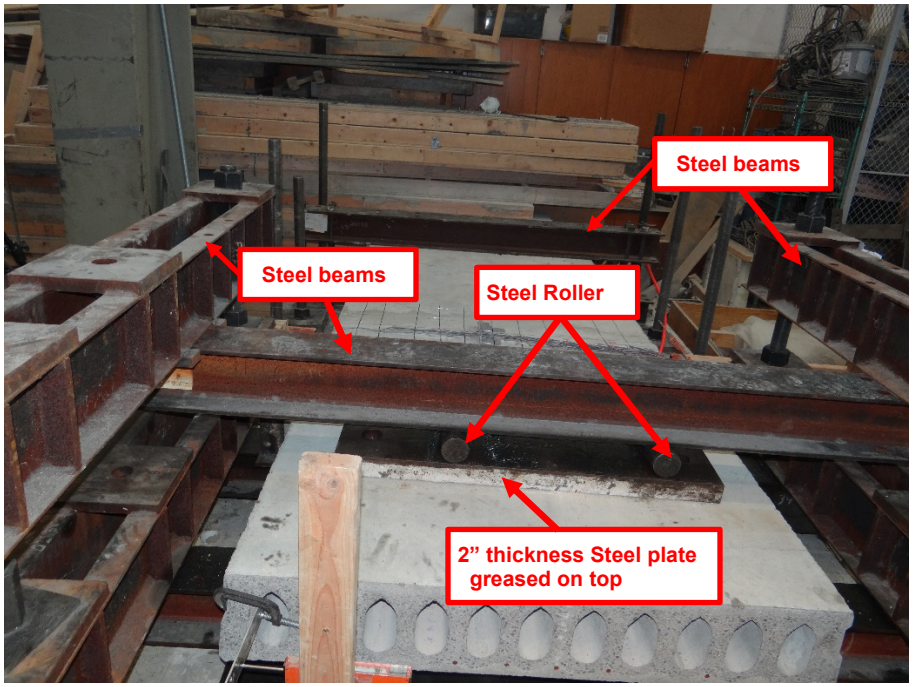

Figure 3-40 Supporting both ends of the planks against the uplift forces.

The concrete block of the actuator was post-tensioned to the reaction floor by four 2 in. threaded rods. The 100 Kips actuator was connected to the concrete block using 1 in. threaded rods as shown in Figure 3-41. Furthermore, it was supported from the back by

two post-tension threaded rods to prevent any horizontal displacement during the test as shown below in Figure 3- 42.

In order to apply the shear force, W6X25 steel beam attached underneath the hollow-core plank in the roller side at 21 in. distance from the center of the beam to the center of the connection. This beam was placed over steel rollers and the rollers move horizontally over 2 in. greased steel plate to eliminate any frictional forces and the steel plate was supported by the concrete block as shown in Figure 3-43. Furthermore, two stiff steel angles (L6”X4”X5/8”) were prepared and bolted to the steel beam, one of them at the first point of contact between the hollow-core and the steel beam and the other at end of contact as can be seen in Figure 3-44 .The purpose of both supports is to apply the shear force on the hollow-core panel and consequently on the connection.

The steel beam was then connected to the 100 Kips actuator via two steel angles (6”x4”X5/8”) as shown in Figure 3-45 and Figure 3-46.

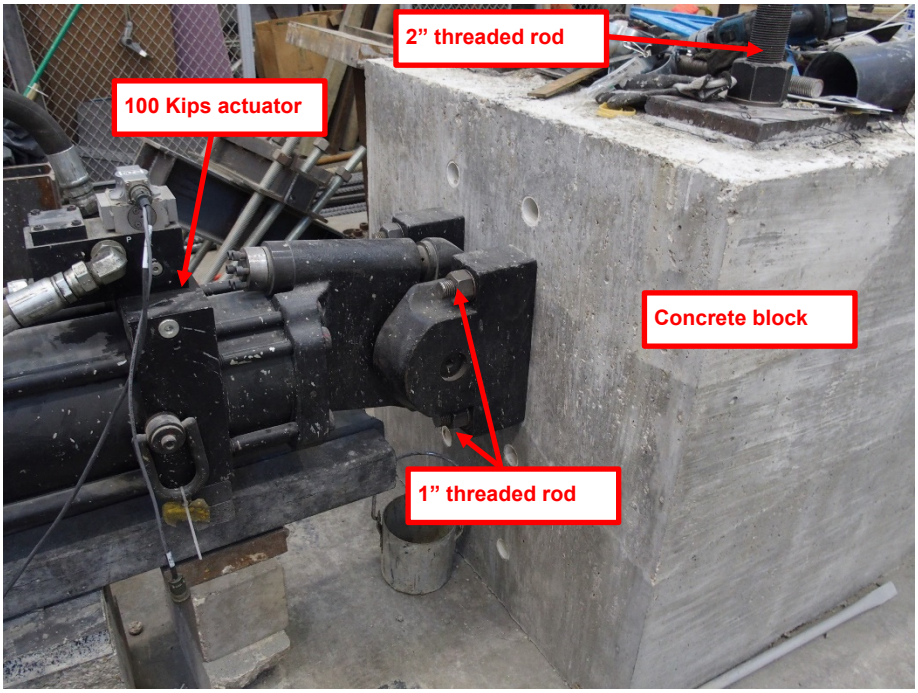

Figure 3-41 Connection the 100 Kips actuator to the concrete block.

Figure 3- 42 Supporting the actuator's concrete block from the back.

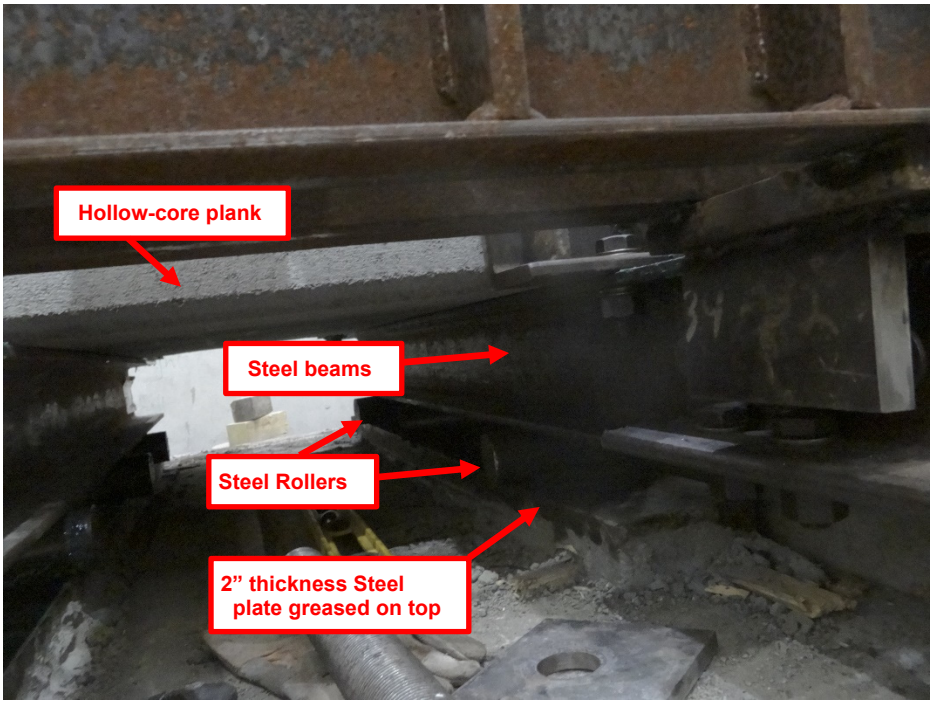

Figure 3-43 Detail of supported beam that used to apply the shear force.

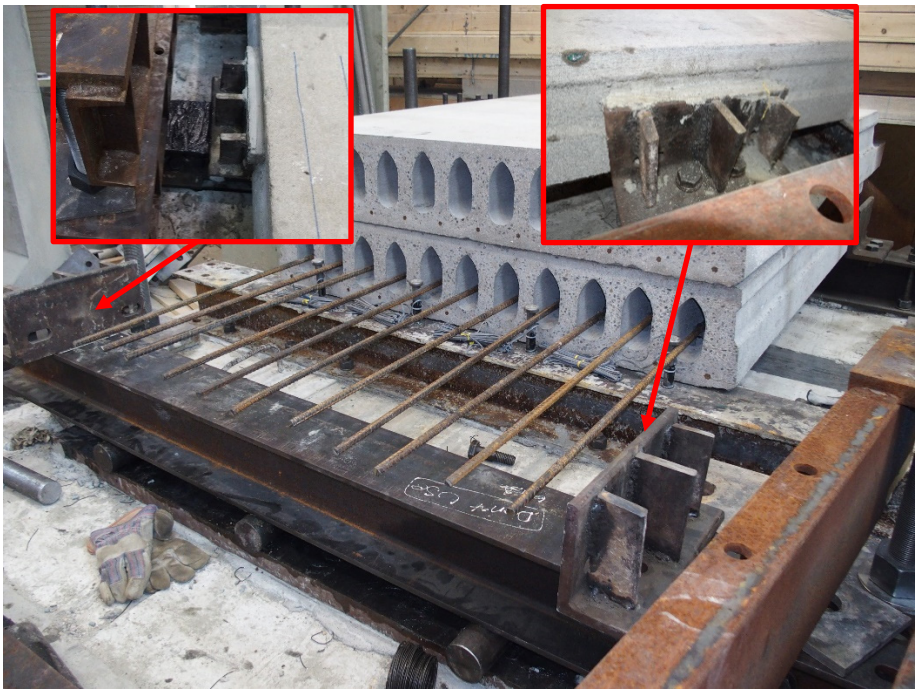

Figure 3-44 The two stiff supports that used to apply shear force.

Figure 3-45 Connecting the W6X25 steel beam to the two steel angles.

Figure 3-46 Details of connecting the actuator to the specimen.

Three Linear Variable Displacement Transducers (LVDTs) were used in this test as shown in Figure 3-47 and Figure 3-48. The first one (L1) was used to monitor if the steel beam of the connection moves during the test whereas the others (L2 and L3) to measure the displacements of the connection in fixed and roller sides, respectively. Additionally, L4 and L5 are used as backup LVDTs.

The strain gauges and LVDTs wires are attached to the blue wires which connected to four Data Acquisition (DAQ) sensors (version 8000). The four sensors connected together by an adaptor which has a port to connect to the laptop that has the DAQ software installed in as shown in Figure 3-49. The pictures of setup before testing can be seen in Figure 3-50 through Figure 3-52.

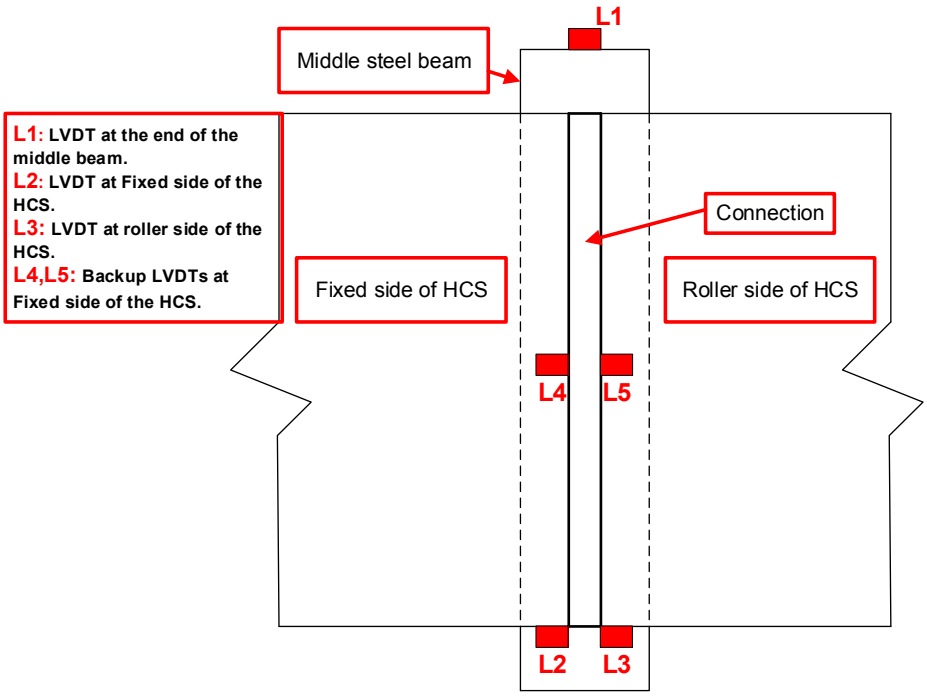

Figure 3-47 LVDTs locations layout.

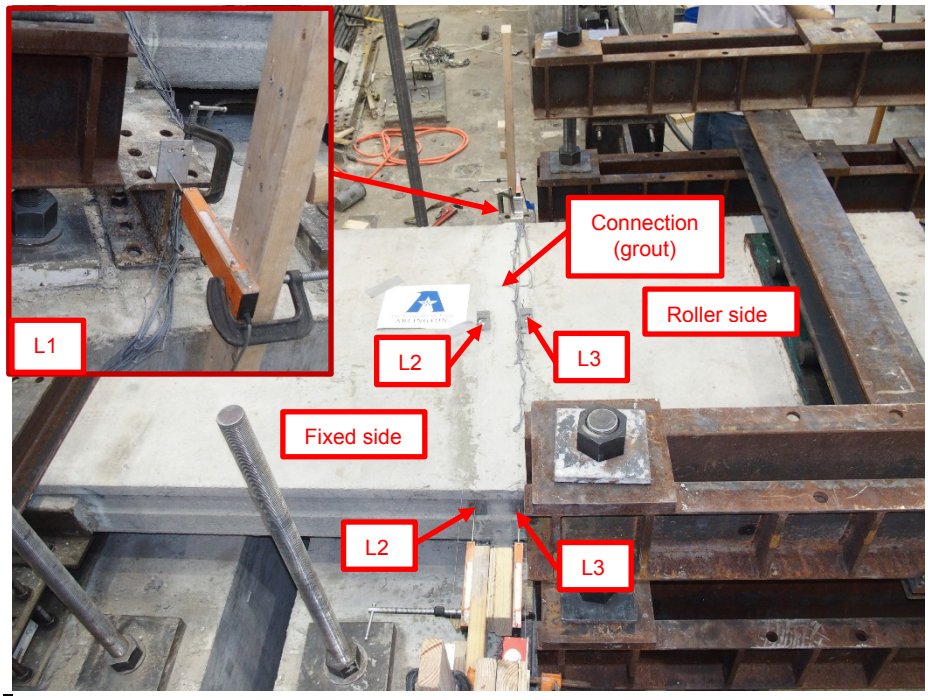

Figure 3-48 picture of LVDTs locations.

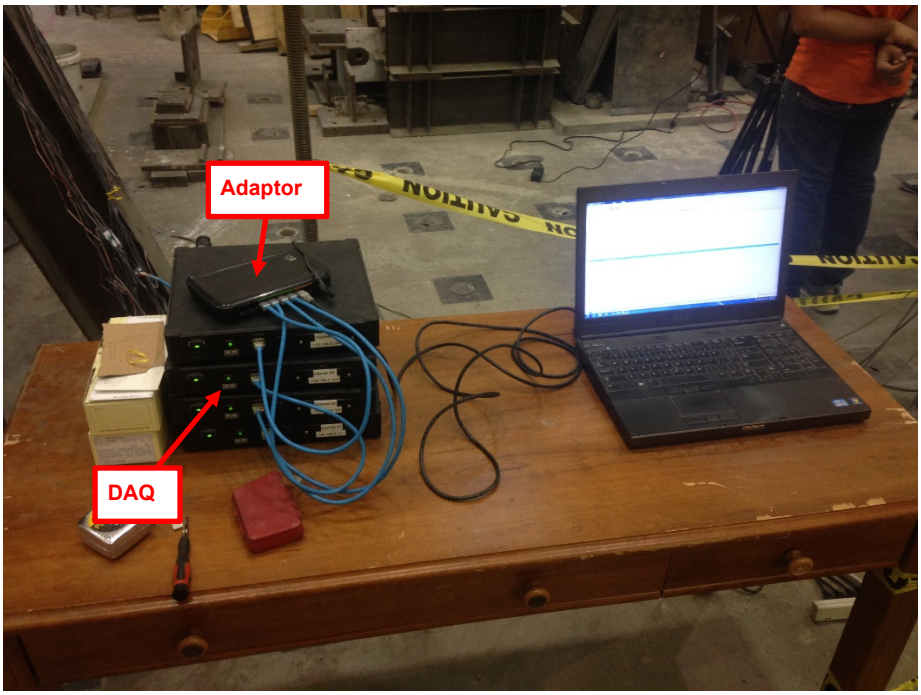

Figure 3-49 DAQ sensors; adaptor.

Figure 3-50 Overview setup before testing the specimen.

Figure 3-51 Top view of the setup before testing the specimen.

Figure 3-52 side view of the setup before testing the specimen.

3.3 Cyclic in-plane shear deformation test

The same setup procedures that were used in the preliminary monotonic in-plane shear deformation test were followed in this test. In addition to the four strain gauges that were used on the shear studs, fifteen strain gauges were attached to the longitudinal rebars to measure the strains in the rebars during this test and the installing process of the strain gauges on the longitudinal rebars can be seen in Figure 3-54. Furthermore, the backups LVDTs (L4 and L5) were moved to be in the other end of the connection. An additional LVDT (L6) was added on the right corner of the hollow-core panel in the roller side to measure the rotation. Figure 3-54 schematically show the locations of the strain gauges on the longitudinal rebars and the LVDTs.

Figure 3-55 and Figure 3-56 show pictures of the locations for the shear studs, longitudinal rebars, and the LVDTs. The overview of the setup before testing is shown in Figure 3-57.

Figure 3-53 Strain gauges installing process on the longitudinal rebars.

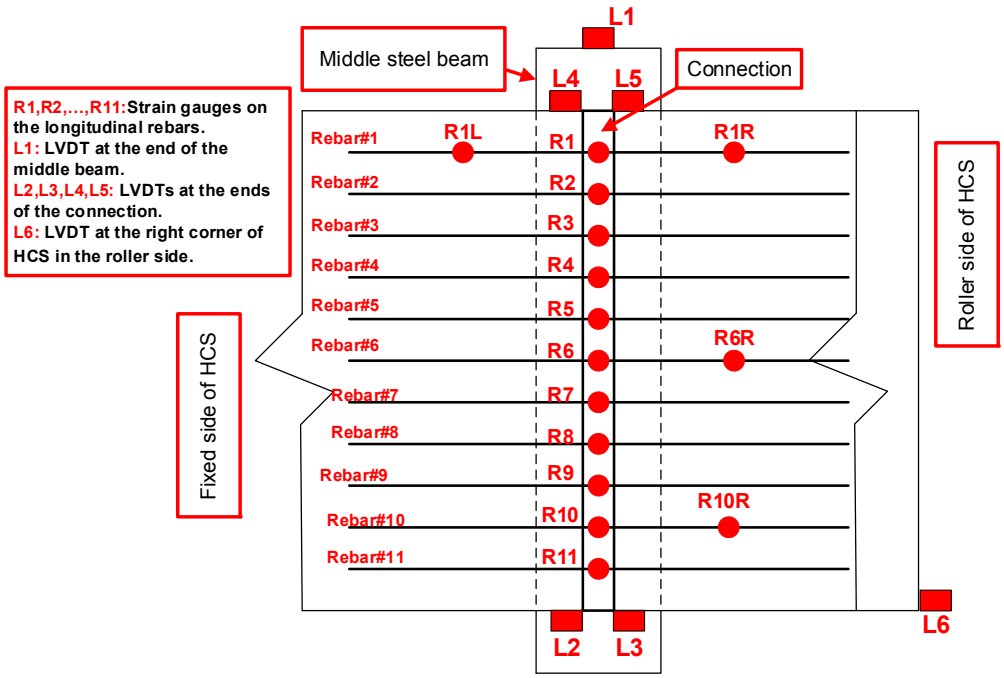

Figure 3-54 Strain gauges locations on the longitudinal rebars and LVDTs locations.

Figure 3-55 Picture of strain gauges locations on the longitudinal rebars and shear studs.

Figure 3-56 Pictures of LVDTs locations.

Figure 3-57 Overview of the setup before testing.

3.4 Cyclic in-plane shear deformation test (6 Studs+180º hooked rebars)

The same setup procedures that were used in the preliminary monotonic in-plane shear deformation test were followed in this test. However, based on the results of the previous cyclic in-plane shear deformation test, it was decided to increase the number of the shear studs to be six. Moreover, all longitudinal rebars were hooked up to 180º at the ends as shown in Figure 3-58.

The locations of the strain gauges for the longitudinal rebars and shear studs were kept the same as in the previous test and four new strain gauges were attached to the two new studs. Furthermore, two additional LVDTs were added to the specimen on the right and left middle sides of the connection as other backups to measure the deformation. Figure 3-59 and Figure 3-60 show strain gauges on the studs and LVDTs locations including the new LVDTs. The overview of the setup before testing is shown in Figure 3-61.

Figure 3-58 Hooked longitudinal rebar and its dimensions.

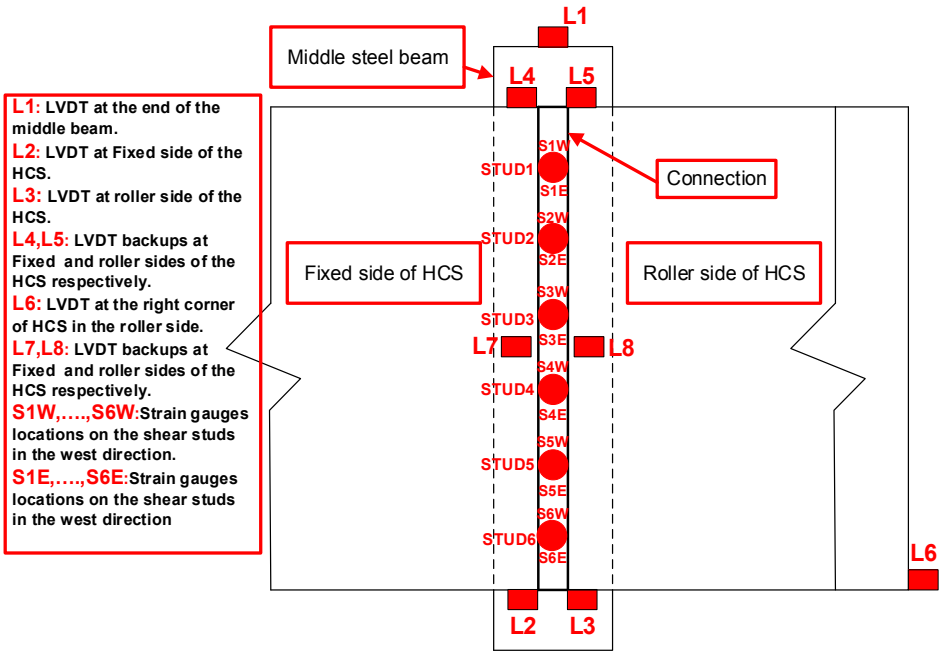

Figure 3-59 Locations layout of the studs' strain gauges and LVDTs.

Figure 3-60 Picture of strain gauges on the longitudinal rebars and shear studs.

Figure 3-61 Overview of the specimen before testing.

3.5 Cyclic in-plane shear deformation test (6 Studs,180º hooked rebars,2" topping)

The same setup procedures that were used in the previous tests followed in this test too. However, it was decided to add 2 in. concrete topping over the hollow-core panels to investigate if that increases the shear strength of the planks and the connection as well. Figure 3-62 and Figure 3-63 illustrate drawings of overview and sideview of the test setup.

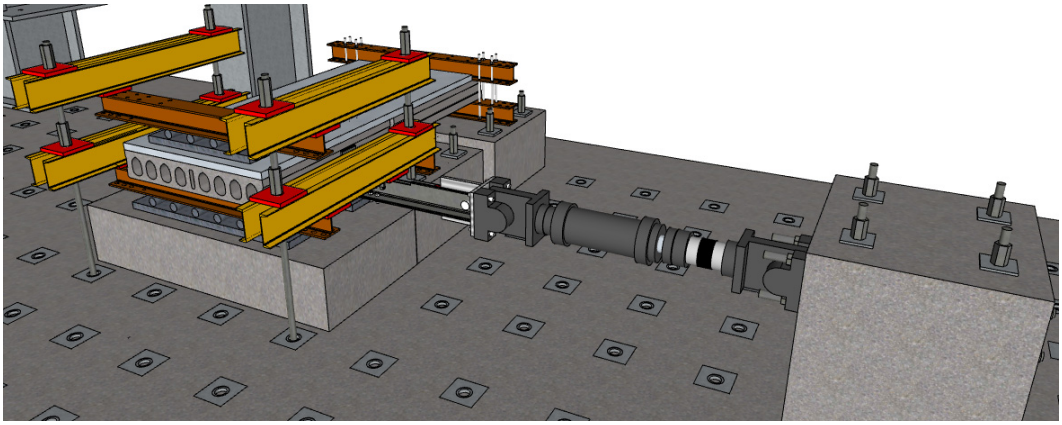

Figure 3-62 Overview drawing of the test setup.

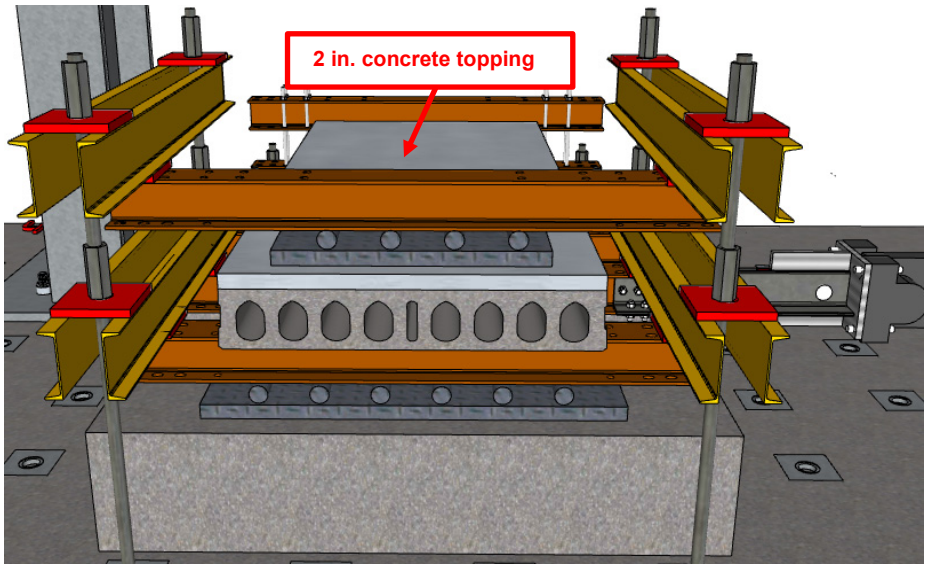

Figure 3-63 Sideview drawing of the test setup.

A specific concrete mix design was used to cast the 2 in. reinforced concrete topping slab to ensure the average compressive strength after three days is not less than 4 Ksi. The mix consisted of cement, coarse aggregate, sand, fly ash-c, silica fume, and water. The water to cement ratio (w/c) was 0.4 and a superplasticizer was used to increase the workability. A steel reinforcement mesh was used to control the cracks which due to shrinkage as seen in Figure 3-64 and Figure 3-65.

The plywood that was used to support the sides of the determined area of topping slab during the casting can be seen in Figure 3-64 too. The connecting was casted first based on the same mix design as in previous test. Then, the concrete topping slab was casted as shown in Figure 3-65 through Figure 3-67.

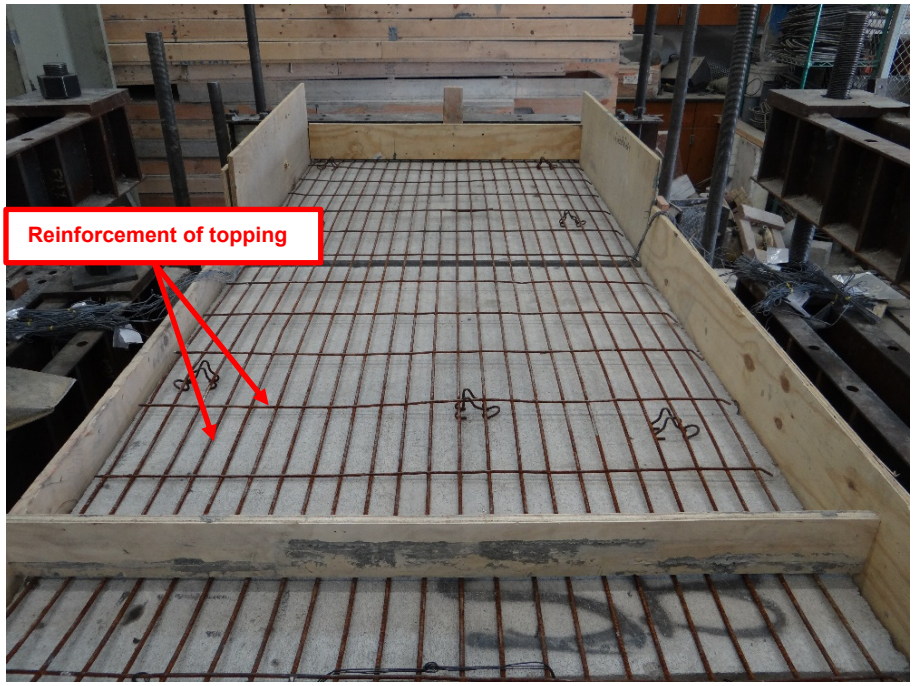

Figure 3-64 Steel reinforcement mesh of the concrete topping slab.

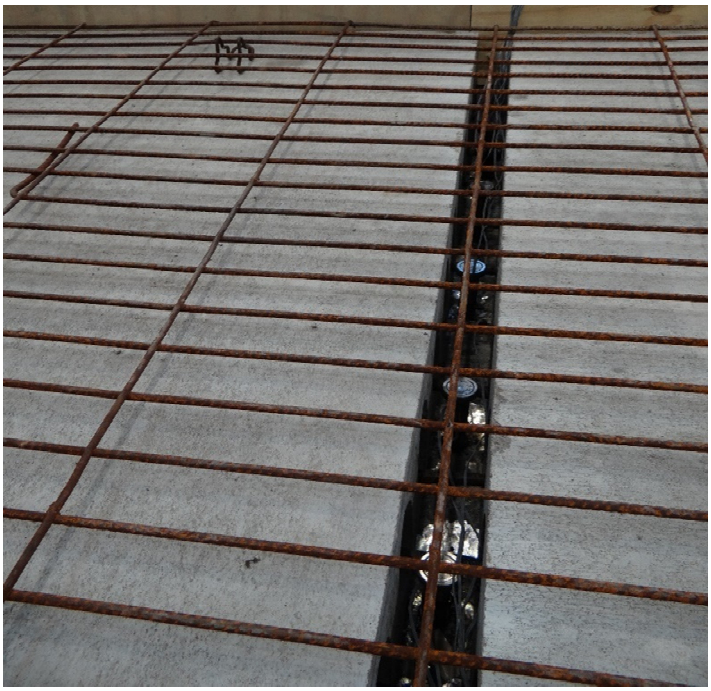

Figure 3-65 Steel reinforcement mesh of the concrete topping slab over the connection.

Figure 3-66 Casting the connection first then the concrete topping slab.

Figure 3-67 The concrete topping slab after completion casting.

The number of shear studs and their strain gauges locations in addition to the LVDTs locations were kept the same as in the previous test. On the other hand, all longitudinal rebars were hooked up to 180° at the ends as in the previous test, whereas the strain gauges for the longitudinal rebars were reduced to be six. Figure 3-68 shows layout locations of the rebars' strain gauges and LVDTs. Figure 3-69 and Figure 3-70 show overview and sideview of the test setup before testing, respectively.

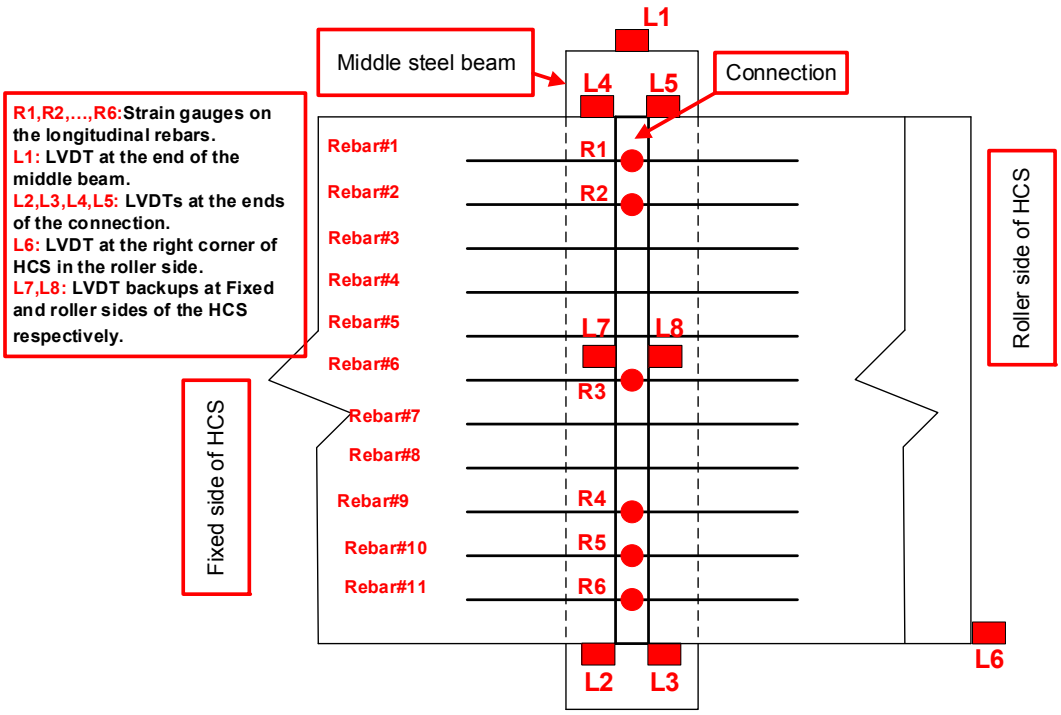

Figure 3-68 Layout locations of the rebars' strain gauges and LVDTs.

Figure 3-69 Overview of the specimen before testing.

Figure 3-70 Side view of the specimen before testing.

3.6 Cyclic in-plane shear deformation test (6 Studs,180^{o} hooked rebars) under double shear effect.

Based on the nonlinear Finite Element Analysis (FEA) results (Chapter 8) which showed that there is a double shear effect on some connection in the STF system, a new specimen was prepared and tested using the setup which is schematically shown in Figure 3-71 through Figure 3-74. Two concrete blocks (dimensions 84”X48”X22” and 84”x40”x22”) were constructed by following the same procedures as in section 3.2.1. Figure 3-75 shows the steel cages reinforcement and the formworks of the blocks. The first concrete block was used to support the exterior beam whereas the second was used to support the middle beam. The other concrete block which was used to support the other exterior beam is the same one that used in the previous tests (dimensions 84”X40X22”). However, the length of the middle beam that used in this test is 48 in.

Both exterior sides of the hollow-core panels were supported by two bottom and top steel beams. These beams were attached to the concrete blocks by ½” threaded rods, steel tubes, and 2 in. threaded rods. However, to prevent any frictional forces between the panels and the steel beams, the contact surfaces were greased as shown in Figure 3-76.

Figure 3-77 and Figure 3-78 show drawings of the assembly that used in order to apply the double shear forces on the connection. In this assembly, two steel angles (L6”X4”X5/8”) of length 105 in. are attached underneath the sides (48 in. side) of the two hollow-core planks along the connection sides as illustrated in Figure 3-79. One-inch space was kept between the middle beam and each steel angle beam to prevent and possible friction during the test.

Additionally, two stiff angles (L6”X4”X5/8”) were bolted to the steel angle beams at both sides of the beginning and end of the connection to apply the double shear force on the planks and consequently the connection as it can be seen in Figure 3-80 through Figure 3-83.

The two steel angle beams were connected to 100 Kips actuator which is supported by a concrete block. Moreover, steel rollers over 2 in. greased steel plates which is supported by the concrete block were installed to support the two steel angle beams at the beginning and end, and to achieve moving the specimen without frictional forces as shown in Figure 3-80 and Figure 3-82.

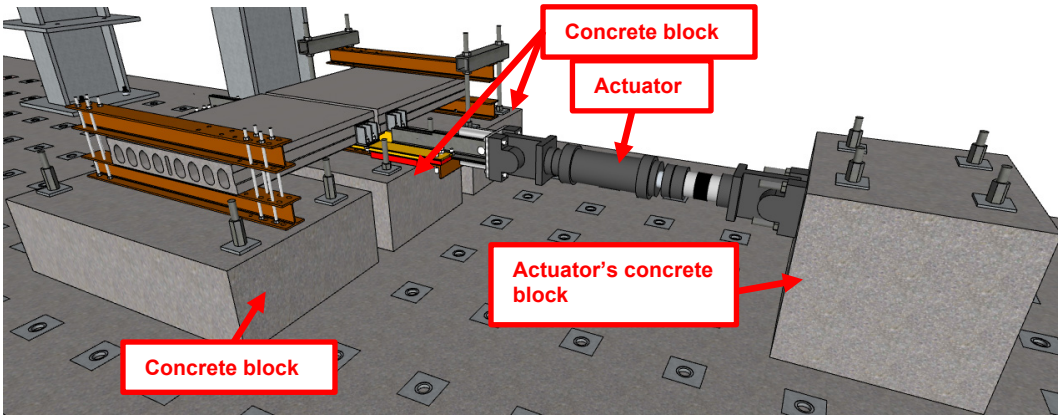

Figure 3-71 Overview drawing of the test setup.

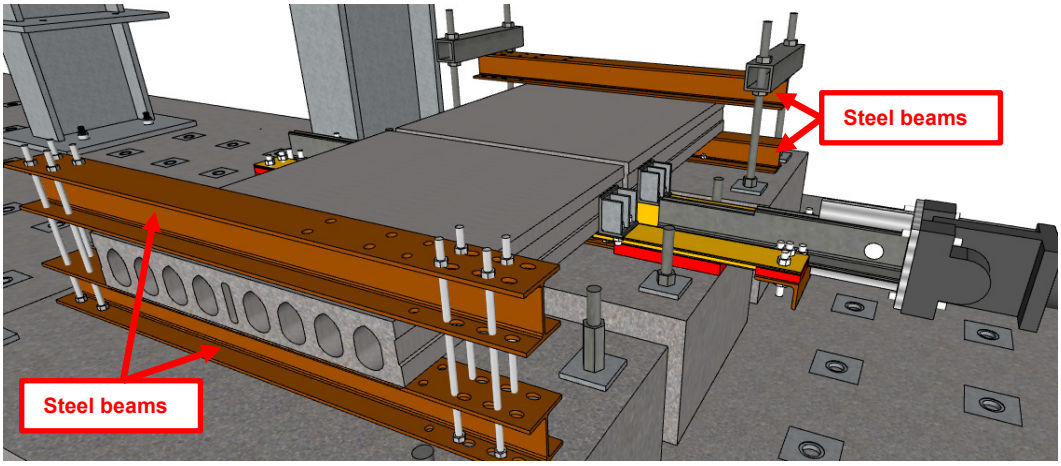

Figure 3-72 Isometric drawing of the test setup.

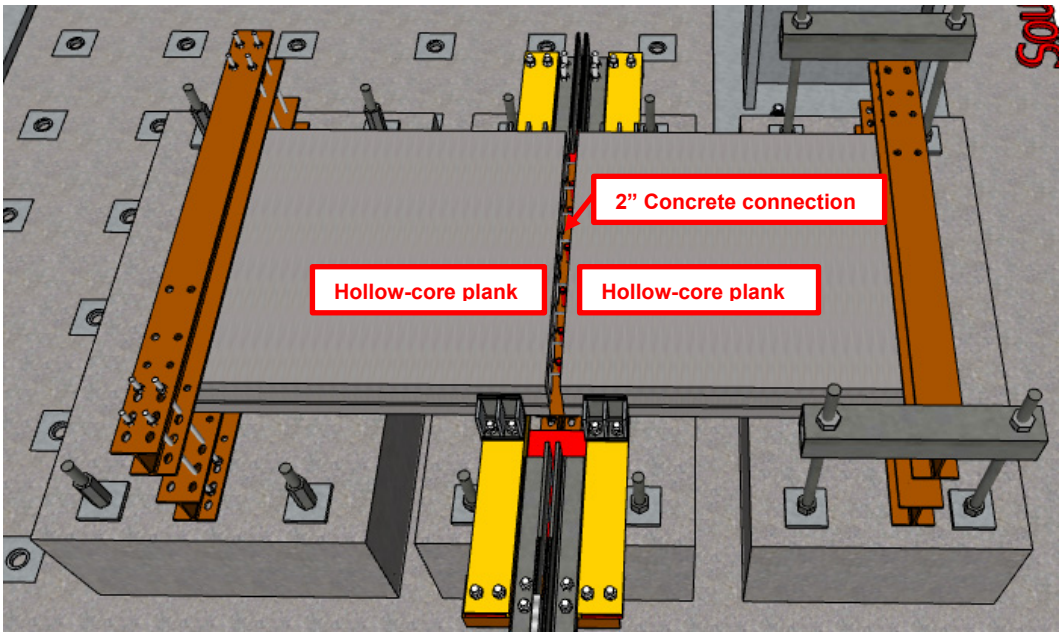

Figure 3-73 Top view drawing of the test setup.

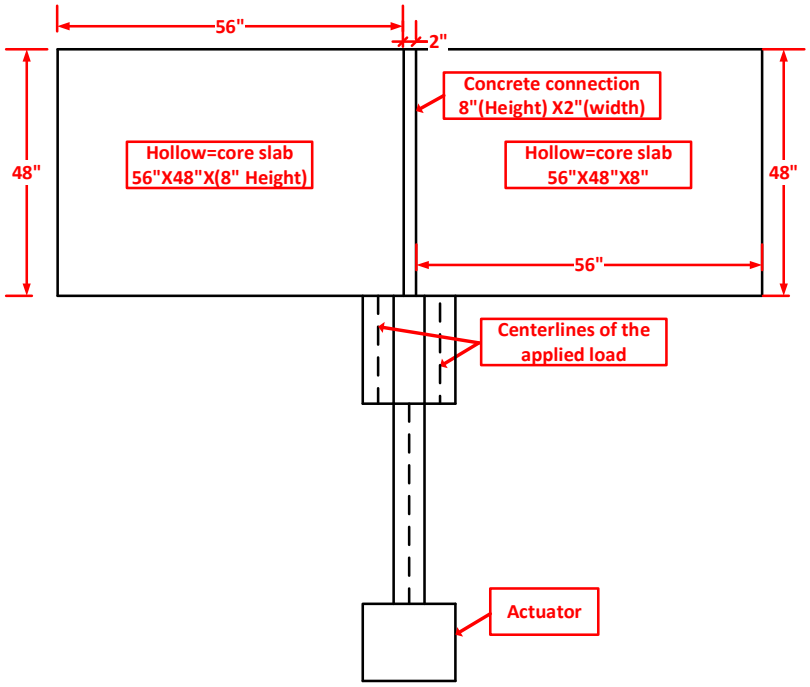

Figure 3-74 Schematic of the specimen’s dimensions.

Figure 3-75 steel cages reinforcement and the formworks of the blocks.

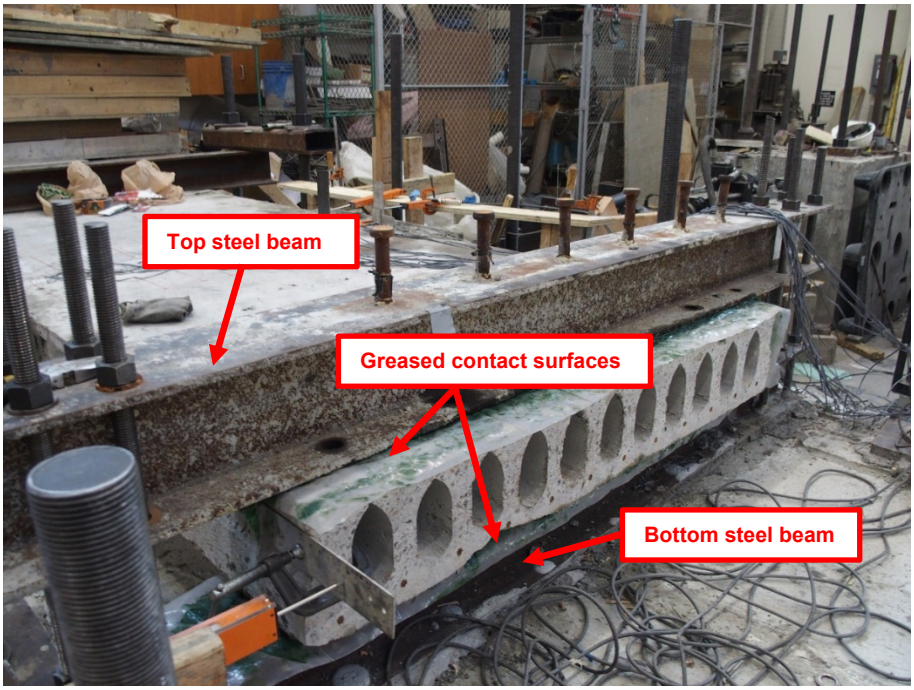

Figure 3-76 The exterior side of the specimen.

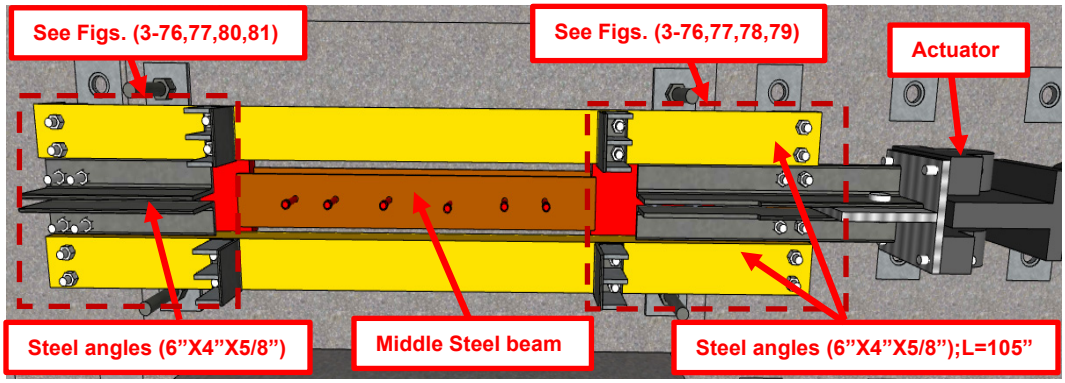

Figure 3-77 Top view of the assembly of applying the double shear forces on the connection (Hollow-core planks are not shown for clarity).

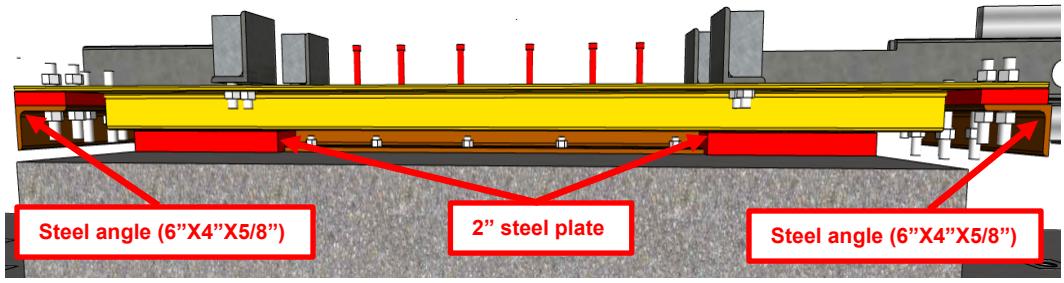

Figure 3-78 Sideview of the assembly of applying the double shear forces on the connection.

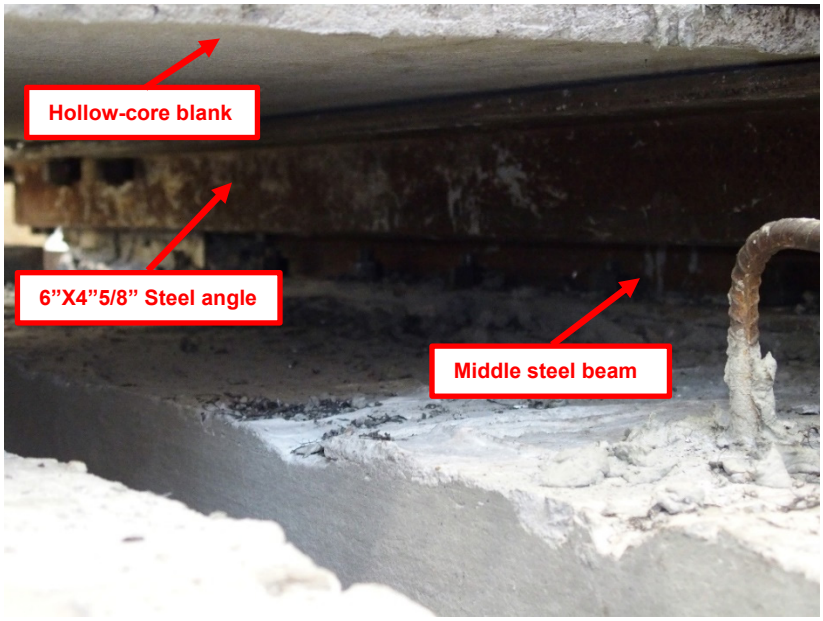

Figure 3-79 The 6”X4”X5/8” steel angle underneath the hollow-core panels.

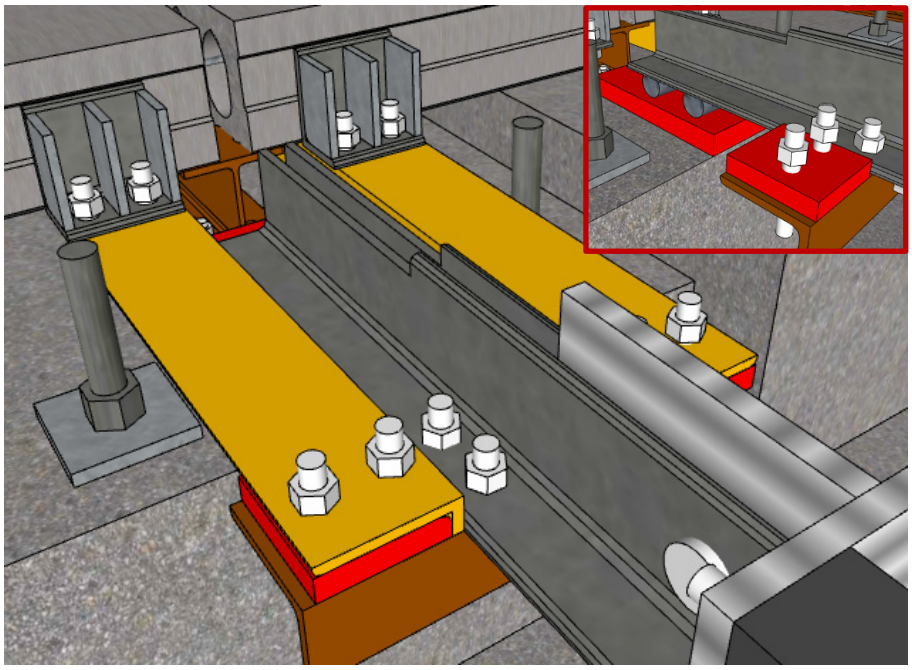

Figure 3-80 Part of the assembly at the beginning of connection (the steel angle beams - yellow color-are not shown in the framed drawing for clarity).

Figure 3-81 Picture of a part of the assembly at the beginning of connection.

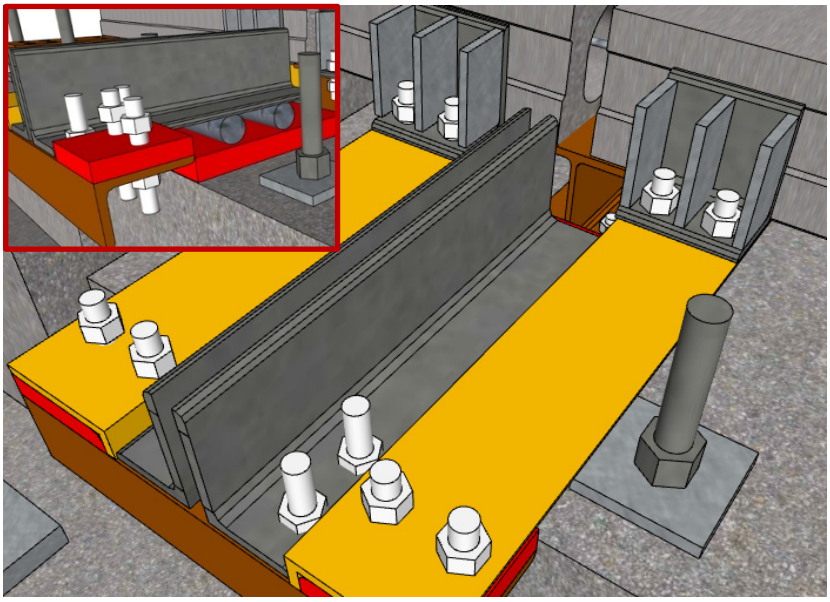

Figure 3-82 Part of the assembly at the end of connection (the steel angle beams -yellow color-are not shown in the framed drawing for clarity).

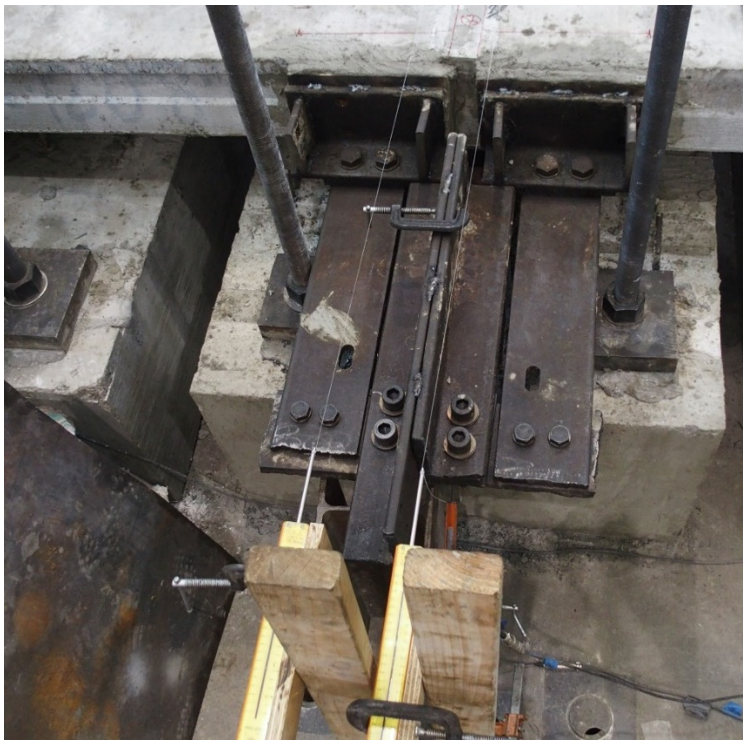

Figure 3-83 Picture of a part of the assembly at the end of connection.

Six shear studs (D=3/4";H=4") and hooked #4 longitudinal rebars were used in this specimen too. Therefore, the locations of strain gauges for studs and the longitudinal rebars were kept the same as in Figure 3-59 and Figure 3-68. However, since there are supports to apply the beginning and end of the connection, the locations of the LVDTs that measure the displacement of the connection were modified. Moreover, two additional LVDTs were added (L6,L7). The first one (L6) to measure the rotation of the second panel and the other one (L7) to measure if the middle concrete block moves during the test as illustrated in Figure 3-84 through Figure 3-90. Figure 3-91 through Figure 3-93 show overview and sideview of the test setup before testing.

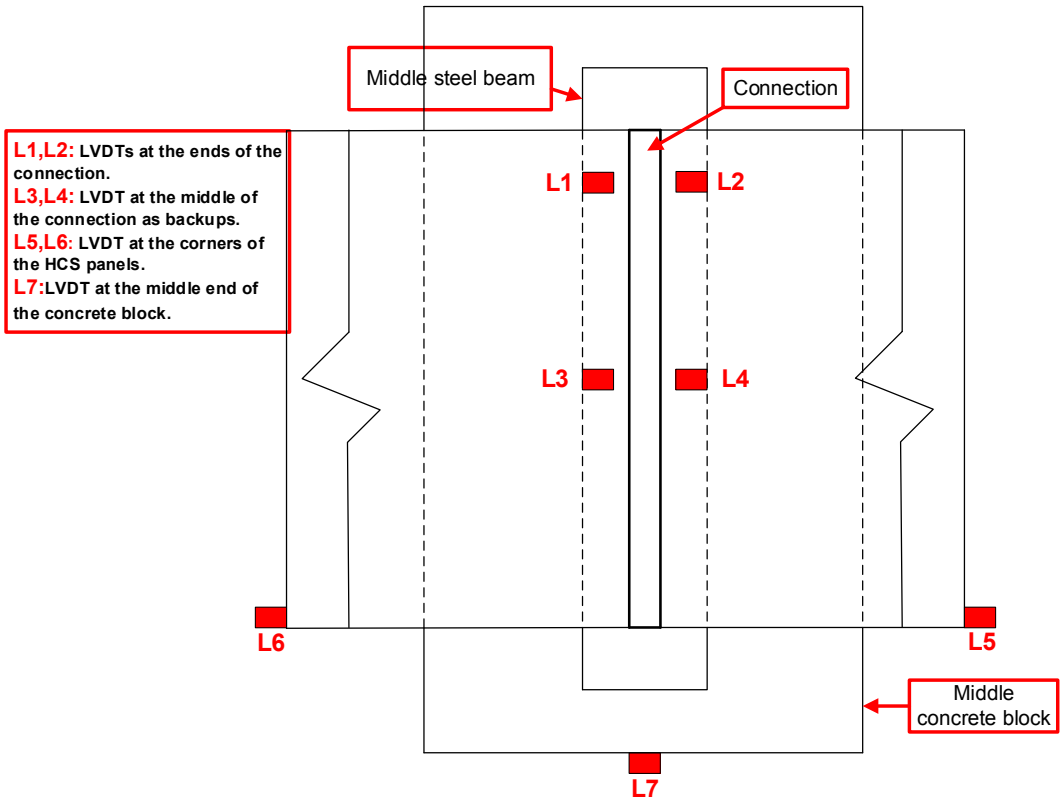

Figure 3-84 Locations of LVDTs.

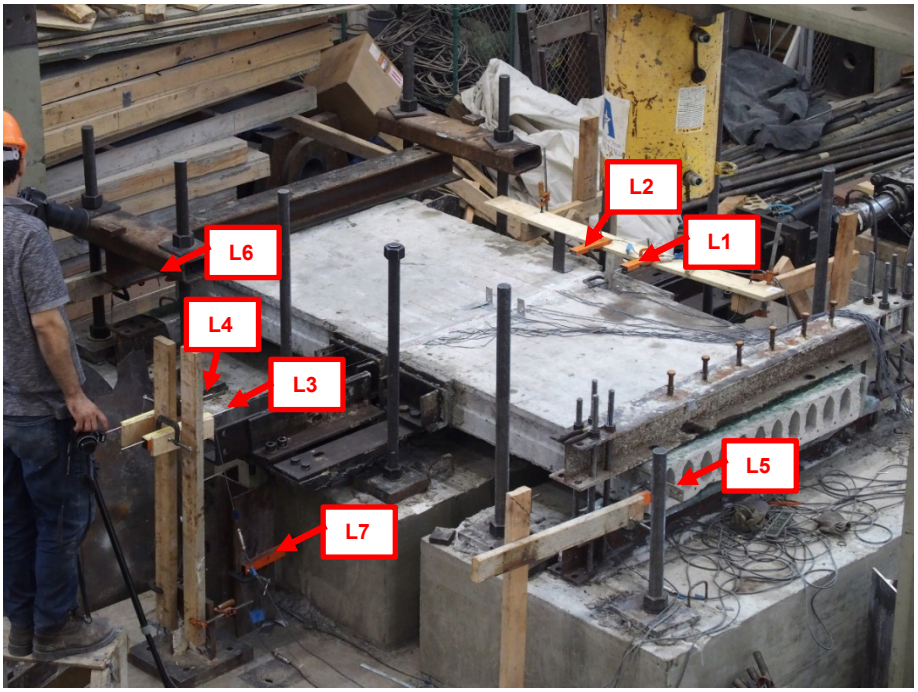

Figure 3-85 General picture of the locations of LVDTs.

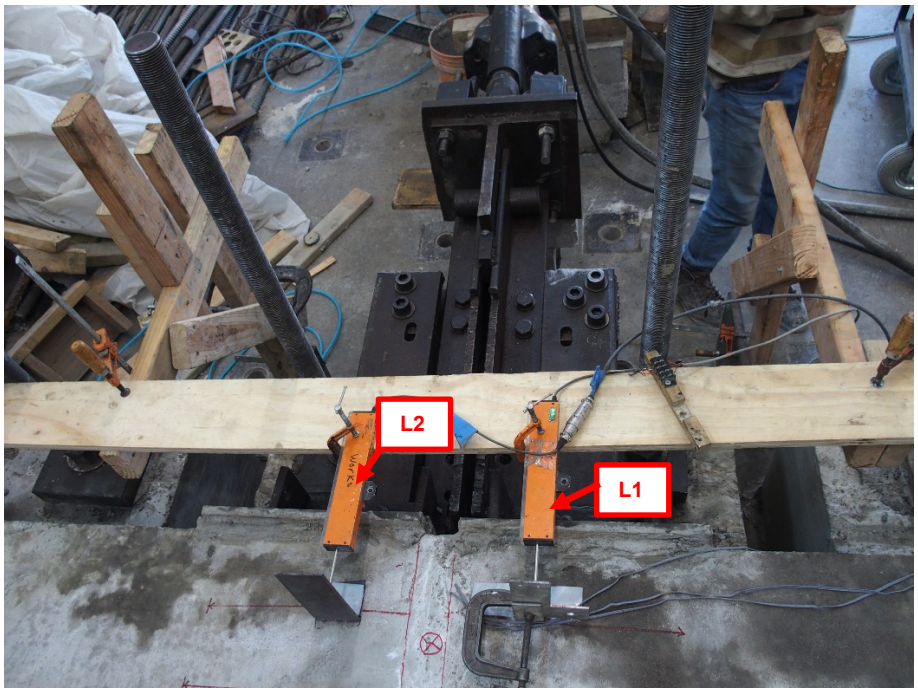

Figure 3-86 Picture of locations of LVDT1, LVDT2 (L1, L2)

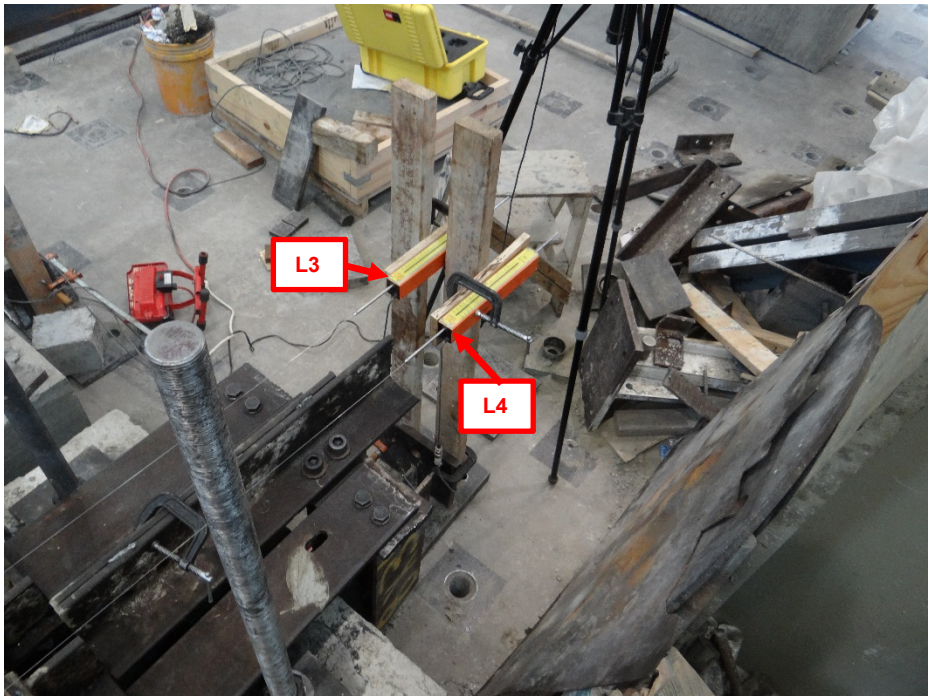

Figure 3-87 Picture of locations of LVDT3, LVDT4 (L3, L4).

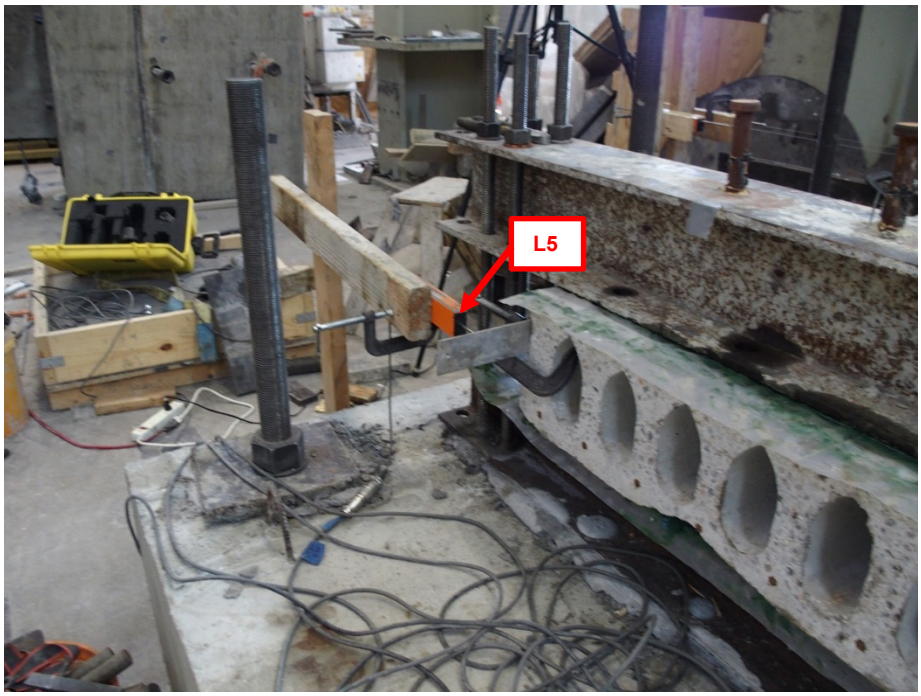

Figure 3-88 Picture of locations of LVDT5 (L5).

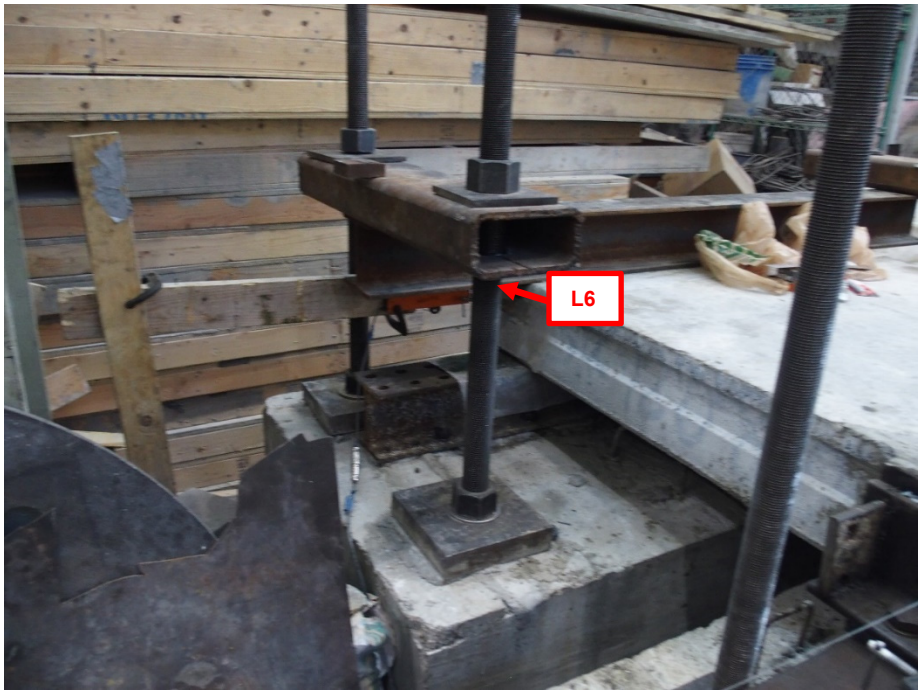

Figure 3-89 Picture of locations of LVDT6 (L6).

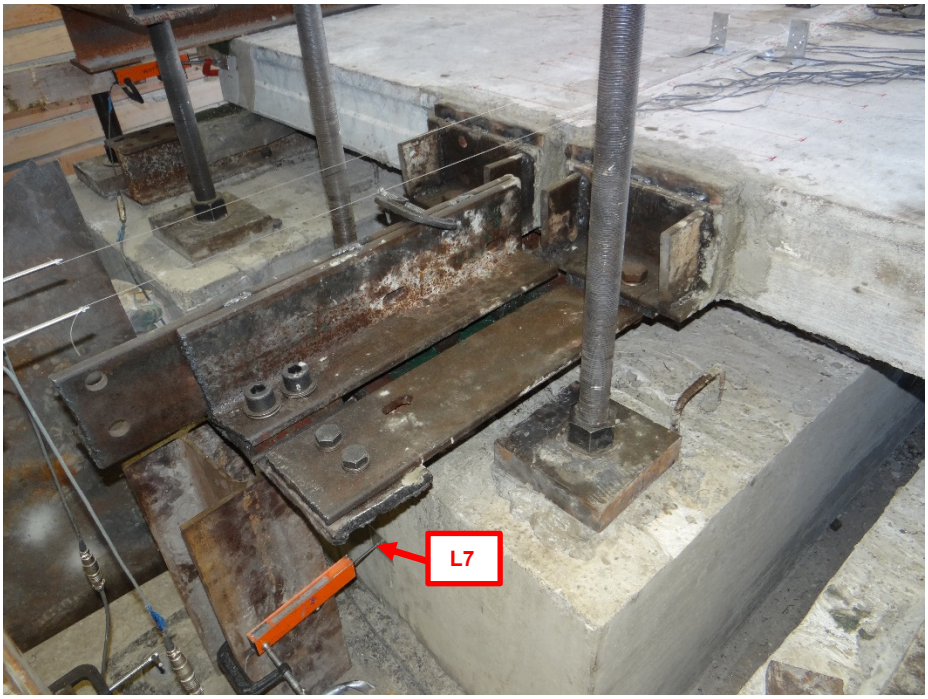

Figure 3-90 Picture of locations of LVDT7 (L7).

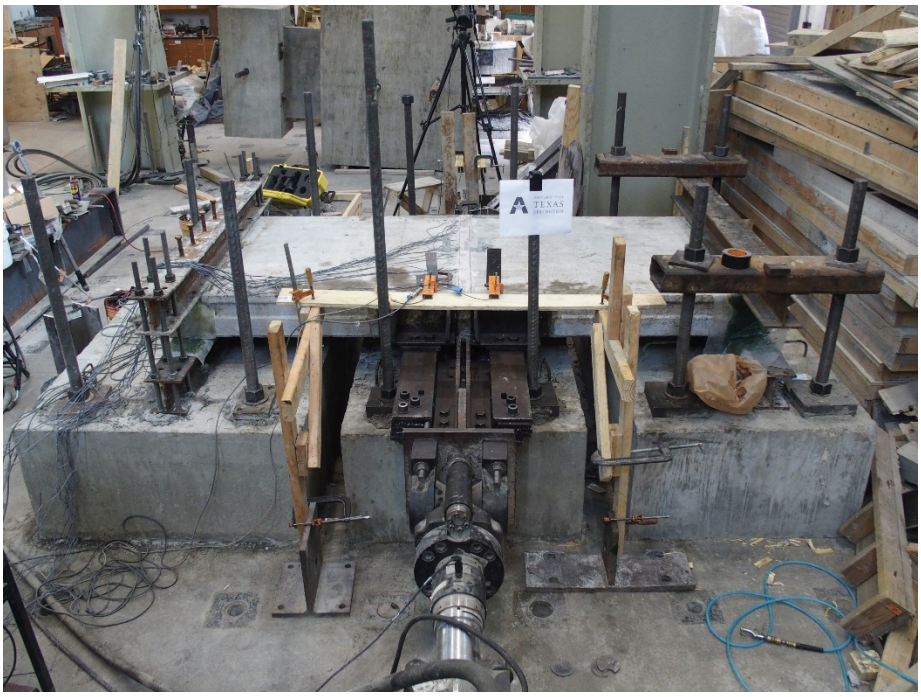

Figure 3-91 Front view of the specimen before testing.

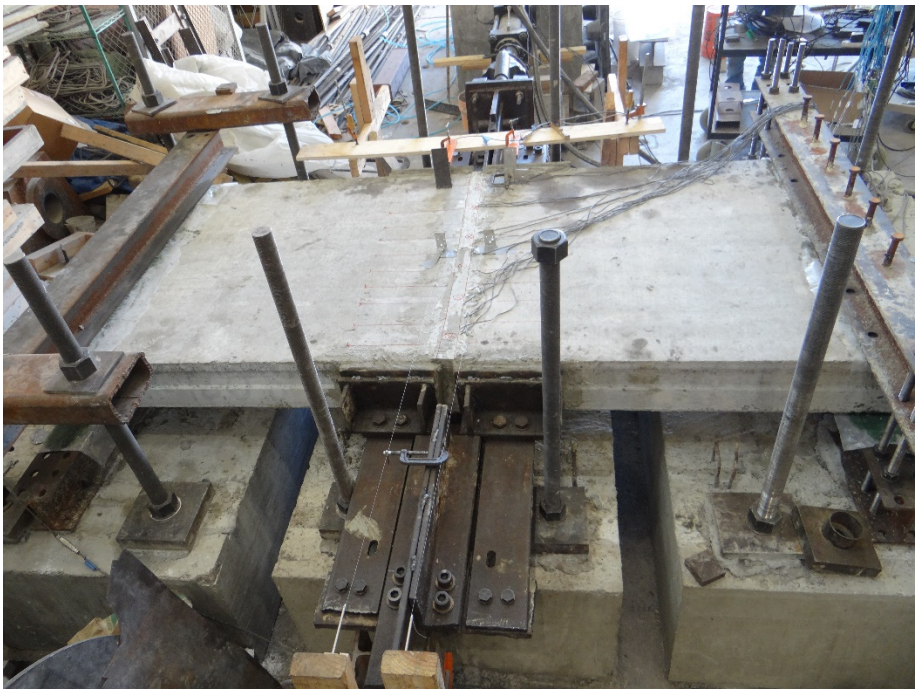

Figure 3-92 Back view of the specimen before testing.

Figure 3-93 Top view of the specimen before testing.

Chapter 4

Results and Discussion

4.1 Introduction

In this chapter the results of the experiments are presented and discussed with reference to the aim of the tests, which is to investigate the in-plane shear deformation of the connection between the precast hollow-core slab diaphragm to steel truss in STF system under cyclic loading.

The results of in-plane shear deformation under monotonic loading test were shown and discussed first. The loading protocol for the cyclic tests was constructed based on the results of this test which showed that the first crack was developed at 30 Kips and maximum shear capacity of the connection was 66.4 Kips.

The results of in-plane shear deformation under cyclic loading tests, which includes the change of some parameters such as the number of studs, the detail of reinforcement rebar, and the topping slab are then shown and discussed.

However, the behavior of the shear studs and the reinforcement rebars under monotonic and cyclic loading are presented. This behavior is supported by graphs which show the load-strain relationship during the tests.

4.2 Preliminary in-plane shear deformation under monotonic loading test

After completing the setup of the test as described in section 3.2 and shown in Figure 3-50 through Figure 3-52, the test was started by applying monotonic load. The load was first increased with increment 5 Kips, then checking the changes in the whole specimen. However, the increment was modified to be 2 kips based on the developing of cracks and some changes in the specimen.

4.2.1 Shear strength and deformation of the connection under monotonic load

It was noticed that the first crack occurred at 30 Kips and the displacement of the plank at the roller side is 0.0143 in. and the displacement of the plank at the fixed side is 0.0126 in., so the relative displacement is (0.0017 in.).

The crack started at the contact of the plank (roller side) with the connection, it's parallel to the direction of loading as shown in Figure 4-1 and the width of crack is 0.1 mm.

Figure 4-1 The first crack in the connection (at 30 Kips).

However, a propagation of the first crack was noticed at 34 Kips as it can be seen in Figure 4-2. The displacement of the plank at the roller side is 0.0173 in. and the displacement of the plank at the fixed side is 0.0157 in. Therefore, the relative displacement is (0.0016 in.).

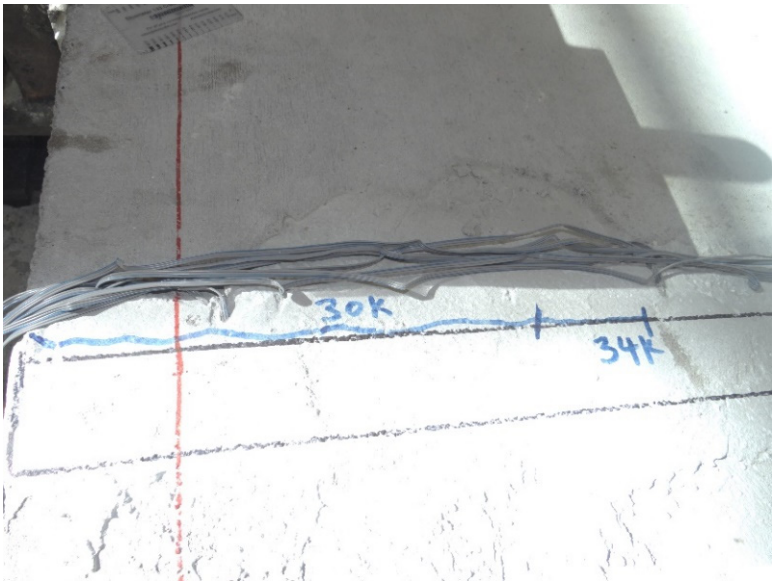

Figure 4-2 First crack propagation at 34 Kips.

A diagonal crack was observed at 38 Kips. It was in the grout of the connection that is surrounding the second shear stud as shown in Figure 4-3. The displacement of the plank at the roller side is 0.0228 in. and the displacement of the plank at the fixed side is 0.0193 in., so the relative displacement is (0.0035 in.).

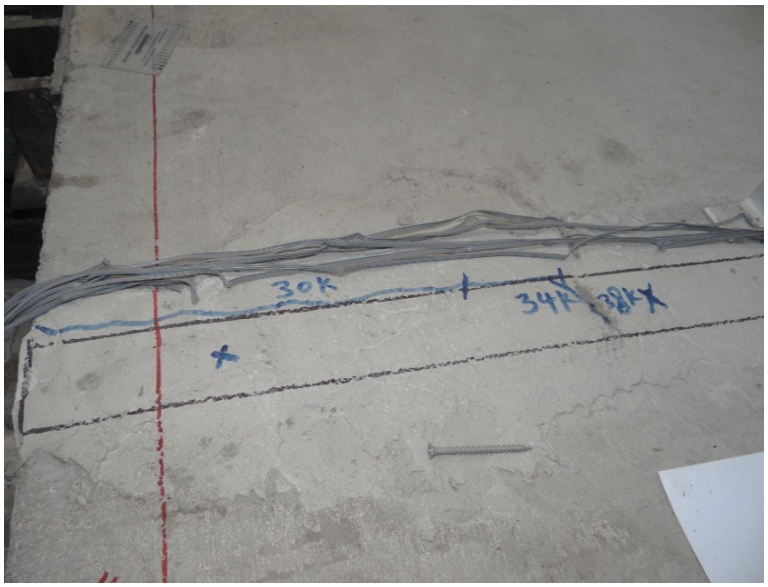

Figure 4-3 The diagonal crack in the grout of the connection at 34 Kips.

Another diagonal crack developed at 40 Kips in the grout of the connection as it can be seen in Figure 4-4. The displacement of the plank at the roller side is 0.026 in. and the displacement of the plank at the fixed side is 0.0213 in., so the relative displacement is (0.0047 in.).

Figure 4-4 the second diagonal crack in the grout of the connection at 40 Kips.

The crack at the contact of the plank (fixed side) with the connection started at 44 Kips as it can be seen in Figure 4-5. Additionally, the crack is parallel to the direction of loading. The displacement of the plank at the roller side is 0.0315 in. and the displacement of the plank at the fixed side is 0.0256 in., so the relative displacement is (0.0059 in.).

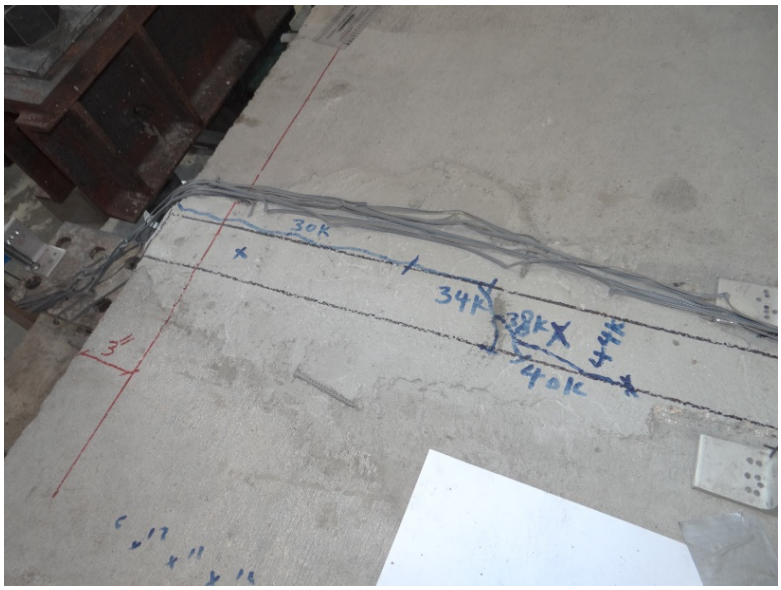

Figure 4-5 Starting the crack at the contact of the plank (fixed side) with the connection at 44 Kips.

The propagation of the crack in the fixed side was noticed at 50 Kips as illustrated in Figure 4-6. The displacement of the plank at the roller side is 0.0437 in. and the displacement of the plank at the fixed side is 0.0354", so the relative displacement is (0.0083 in.).

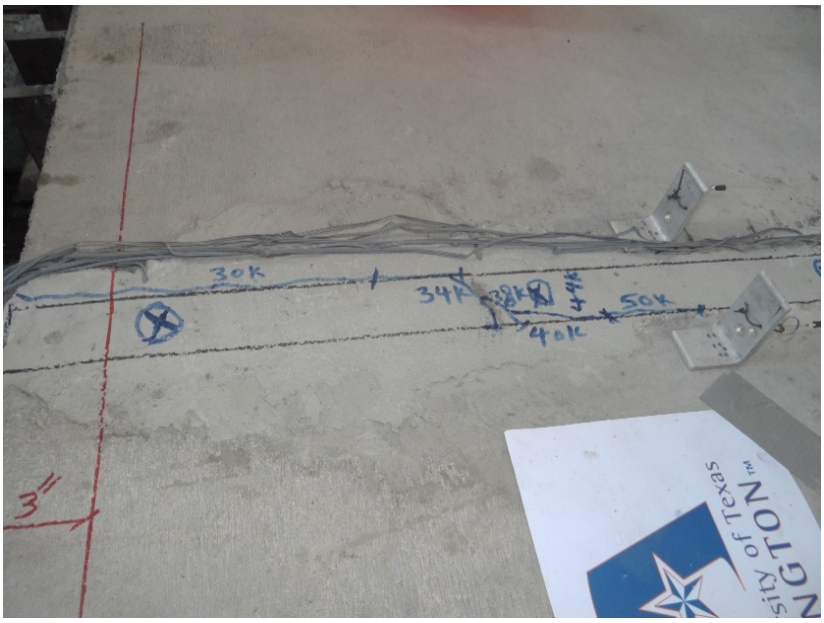

Figure 4-6 Crack propagation in the fixed side at 50 Kips.

A crack in the plank (fixed side) was noticed at 54 Kips, the crack is perpendicular to the direction of loading and parallel to the cores as illustrated in Figure 4-7. It occurred along the steel rebar which is inside the core of the plank. This crack is due to debonding between the steel rebar and the grout. the displacement of the plank at the roller side is 0.0594 in. and the displacement of the plank at the fixed side is 0.0488 in., so the relative displacement is (0.0106 in.).

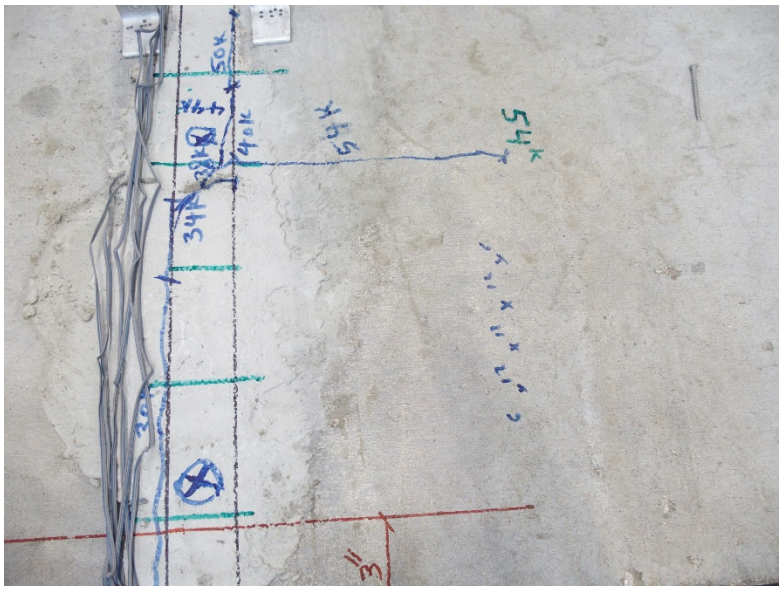

Figure 4-7 Starting the crack in the plank (fixed side) at 54 Kips.

The propagation of crack in the plank (fixed side) was noticed at 56 Kips as shown in Figure 4-8. The displacement of the plank at the roller side is 0.0701 in. and the displacement of the plank at the fixed side is 0.0591 in., so the relative displacement is (0.011 in.).

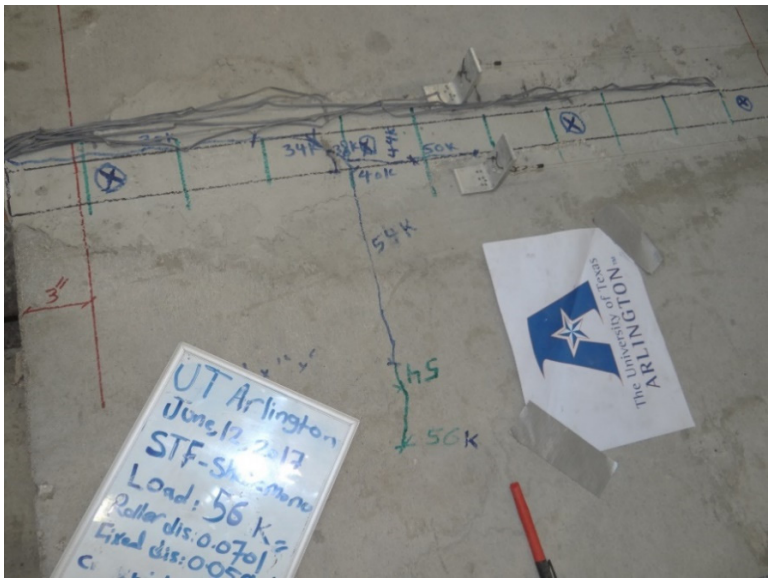

Figure 4-8 Crack propagation at 56 Kips.

When the load reached 60 Kips, the following cracks were observed:

- Propagation of the same crack in the plank (fixed side) along the steel rebar.
- New crack in the plank (fixed side), the crack is parallel to the direction of loading.
- Propagation of the crack which is at the contact of the plank (fixed side) with the connection.
- New diagonal cracks developed from the point of load to the first and second shear stud of the connection.

All of these developing and propagating of the cracks can be seen in Figure 4-9. The displacement of the plank at the roller side is 0.1232 in. and the displacement of the plank at the fixed side is 0.1051 in., so the relative displacement is (0.0181 in.).

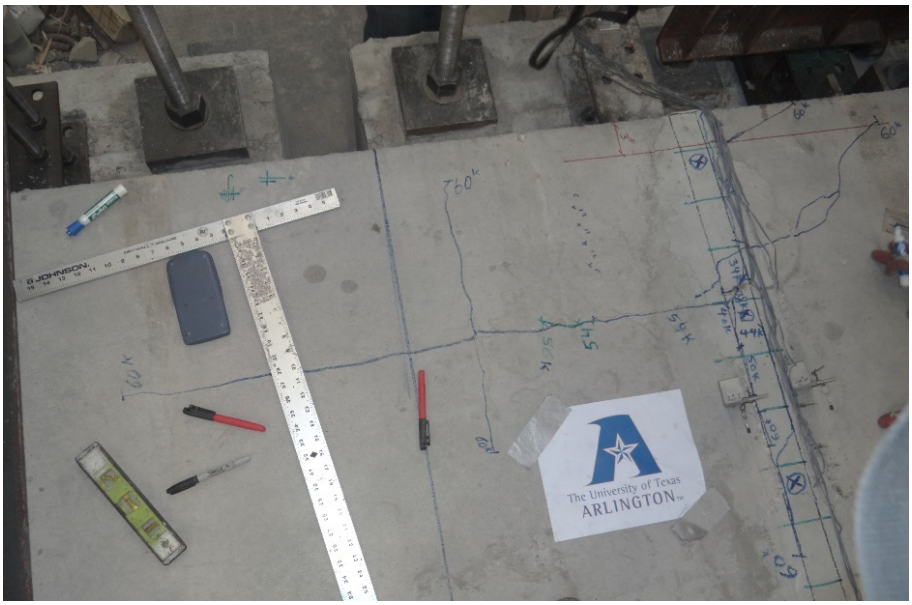

Figure 4-9 Developing and propagating of the cracks at 60 Kips.

Some propagation of cracks in both blanks were noticed at 62 Kips as shown in Figure 4-10 and Figure 4-11. The displacement of the plank at the roller side is 0.1531 in.

and the displacement of the plank at the fixed side is 0.1331 in., so the relative displacement is (0.02 in.).

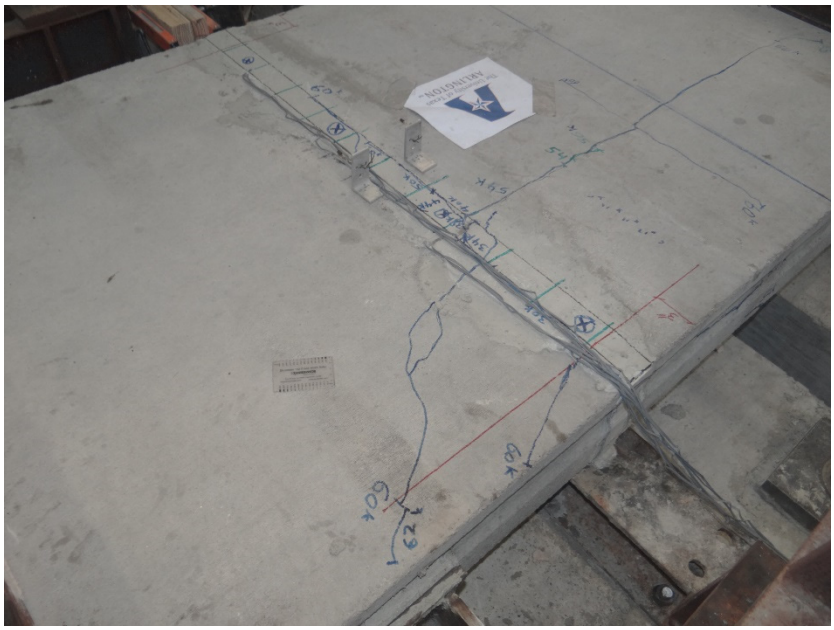

Figure 4-10 Top view of cracks propagation at 62 Kips.

Figure 4-11 Sideview of cracks propagation at 62 Kips.

A diagonal crack at the connection was noticed at 64K as shown in Figure 4- 12. The displacement of the plank at the roller side is 0.1921 in. and the displacement of the plank at the fixed side is 0.1673 in., so the relative displacement is (0.0248 in.).

Figure 4- 12 The diagonal crack at 64 Kips.

When the load reached 66K, many cracks were noticed, and the load started dropping:

- Propagation of the crack in the plank (fixed side) along the steel rebar.
- New cracks in the plank (fixed side) along the steel rebars developed.
- Propagation of the crack which is at the contact of the plank (fixed side) with the connection.
- Propagation and new diagonal cracks developed from the point of load to the first, second and third shear studs of the connection.

Figure 4-13 and Figure 4-14 show developing and propagating of cracks at 66 Kips . On the other hand, Figure 4-15 shows the failure in the planks due to debonding between grout and steel rebars. The displacement of the plank at the roller side is 0.2969 in. and the the displacement of the plank at the fixed side is 0.2611 in., so the relative displacement is (0.0351 in.).

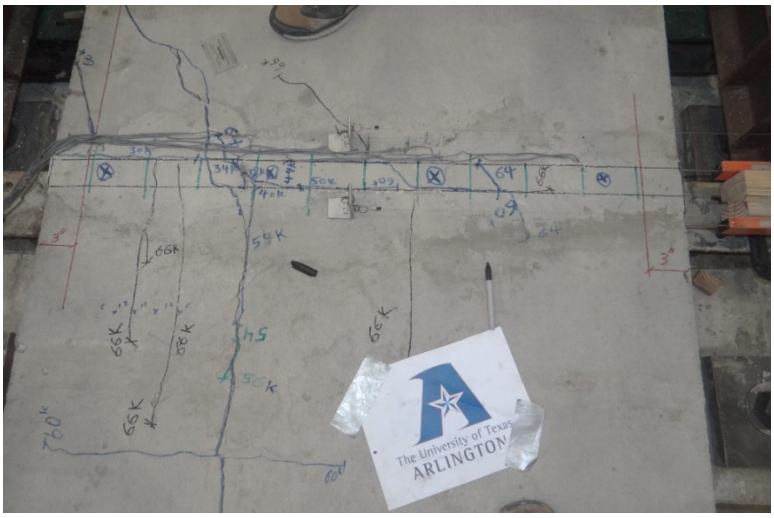

Figure 4-13 Top view of developing and propagating of cracks at 66 Kips.

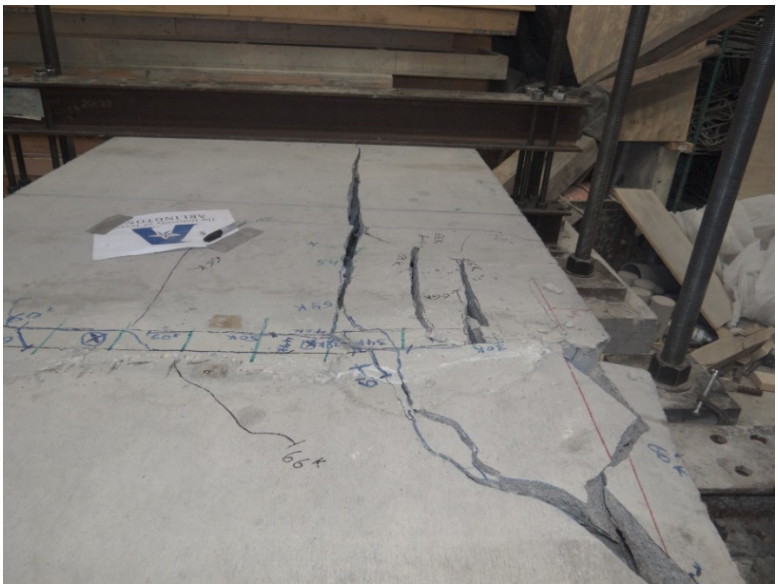

Figure 4-14 Sideview of developing and propagating of cracks at 66 Kips.

.

Figure 4-15 Failure in the planks due to debonding between grout and steel rebars.

The relative displacement of the connection represents the difference between displacement of the connection in the roller side and the fixed side. Based on Figure 4-16 which shows the locations of LVDTs, the relative displacement was calculated based on the following equation:

Relative disp.(in) =L3 (Roller side) reading(in.) - L2 (Fixed side) reading (in.).

L4 and L5 were used as backup LVDTs in this test and L1 was used to notice if the middle beam moves during the test. However, the readings of L1 showed that the middle beam did not move during the test.

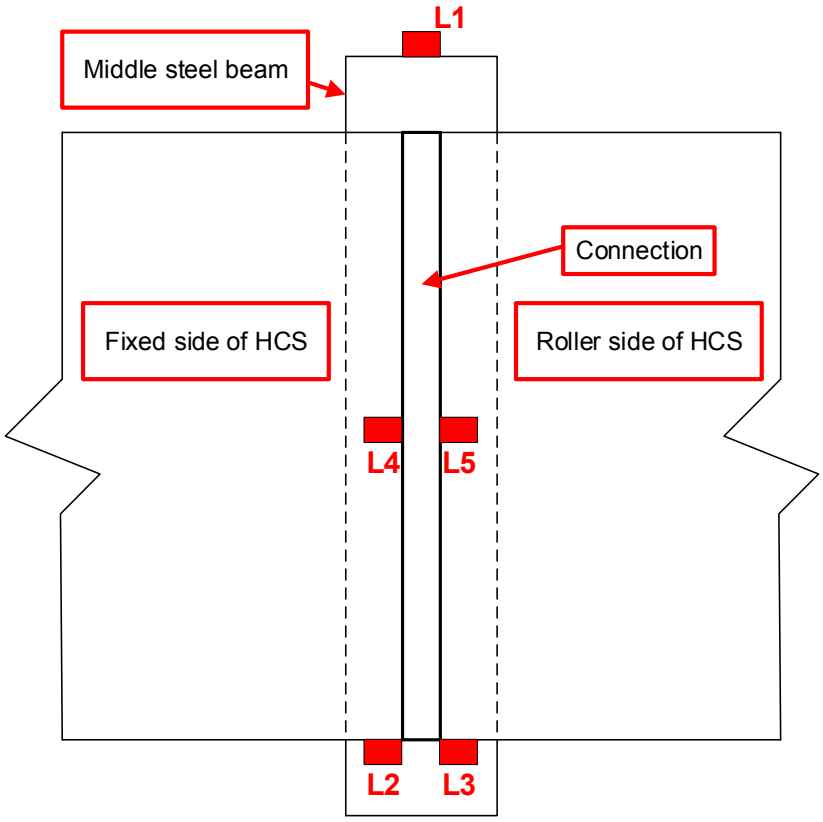

Figure 4-16 LVDTs locations.

Figure 4-17 shows the relationship between the applied load and the relative displacement of the connection. The maximum shear strength of the connection was 66.4 Kips and the relative displacement at the maximum shear strength was 0.035 in.

Six concrete cylinders were tested at the same day of test. The results showed that the average compressive strength of the grout is 2.6 Ksi. On the other hand, to check if the crack in the connection is due to the flexural moment, the following calculations were done.

$f_r = 7.5\sqrt{f_c^{'}}$

Where,

f_r : flexural strength of the concrete.

$f_c^{'}$: compressive strengh of concrete.

$\Rightarrow f_r = 7.5\sqrt{2600} = 0.328Ksi$

$f_b = \frac{MC}{I}$

where,

f_b : Allowable extreme fiber bending stress.

M : Maximum bending moment.

c : Distance from neurtal axis to extreme fiber.

I : Moment of ineertia.

$M = P * x$

P : Maximum applied shear force.

x : Distace from the centerline of applied shear to the centerline of connection.

Based of Figure 3-5:

$\Rightarrow$ M=$66.4 * 21 = 1361.20 in.Kip$

$I = \frac{1}{12} * b * h^3$

b : the height of the connection.

b : the width of the connection.

$\Rightarrow I = \frac{1}{12} * (8) * (2)^3 = 5.334 in^4$

$\Rightarrow f_b = \frac{1361.2 * (1)}{5.334} = 0.255Ksi < 0.328Ksi$

Based on these calculations, the cracks that developed during the test is due to pure shear only.

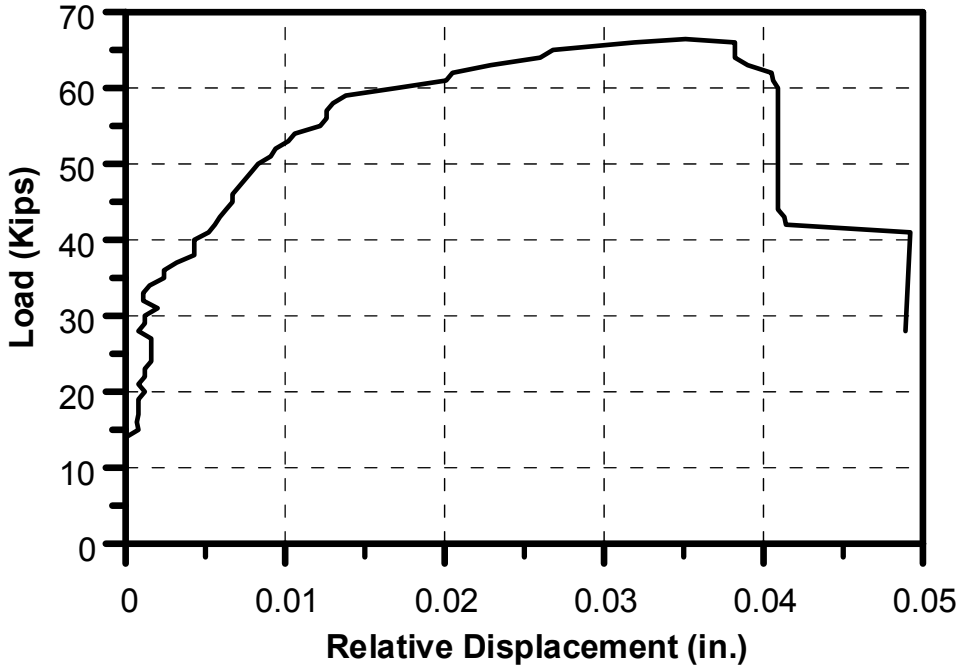

Figure 4-17 Load-relative displacement curve.

4.2.2 Results of strain gauges on shear studs

Based on the specifications of the shear stud, the yielding strength is 51 Ksi. Therefore, the yielding strain of the shear stud is calculated using Hook's law formula as shown below:

$$\varepsilon_y = \frac{F_y}{E_s}$$

Where: ε_s: Shear stud Stain.

E_s: Young's modulus of steel (29,000 Ksi).

F_y: Yielding strength of the shear stud (51 Ksi).

$$\varepsilon_y = \frac{51}{29{,}000} = 1759\ \mu$$

With reference to Figure 4-18 which shows the locations of the strain gauges on the shear studs, the results of strain gauges with applied shear load demonstrated that the shear stud #1, where the first crack occurred, started yielding first at 49 Kips as shown in Figure 4-19. However, the last shear stud that started yielding was # 3 at 65 Kips. Stud #2 and #4 started yielding at 59 Kips. Figure 4-20 through Figure 4-27 illustrate the load-strain curves for the four shear studs that used in this specimen.

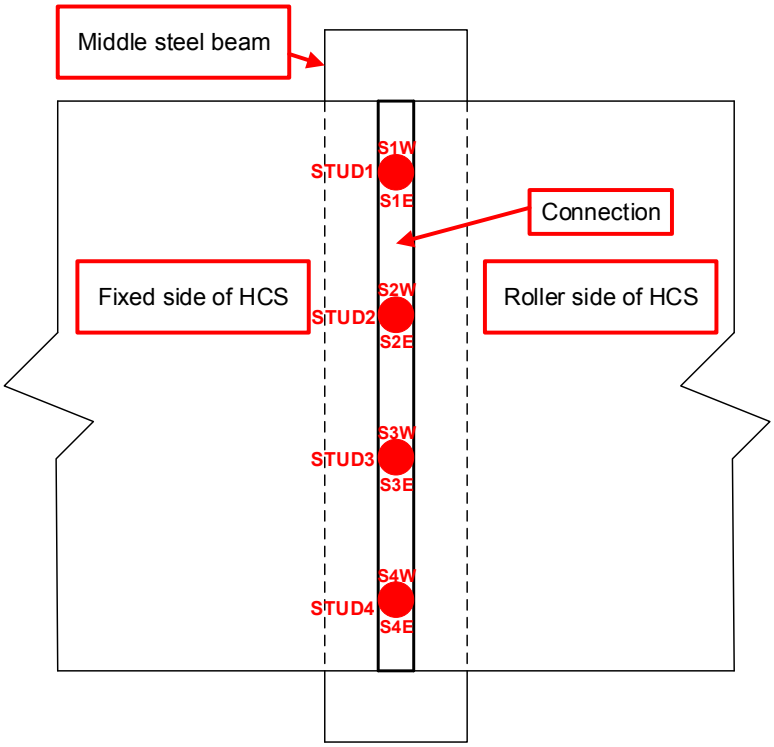

Figure 4-18 Locations of shear studs.

Figure 4-19 First Shear stud in the west direction, it started yielding at 49 kips.

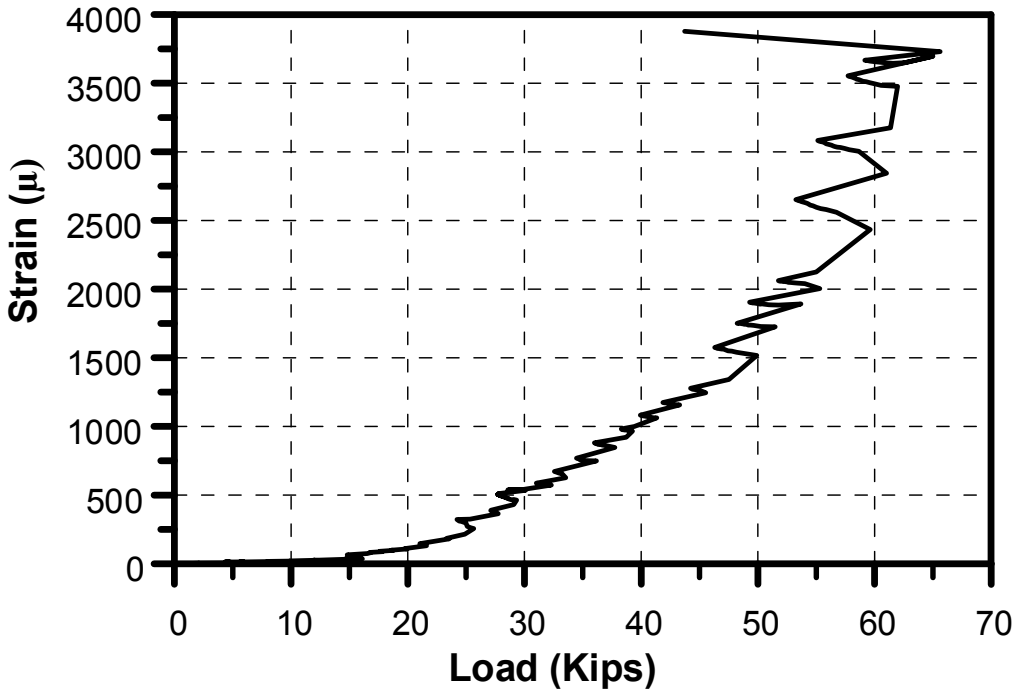

Figure 4-20 Load-strain curve for stud #1 (S1W).

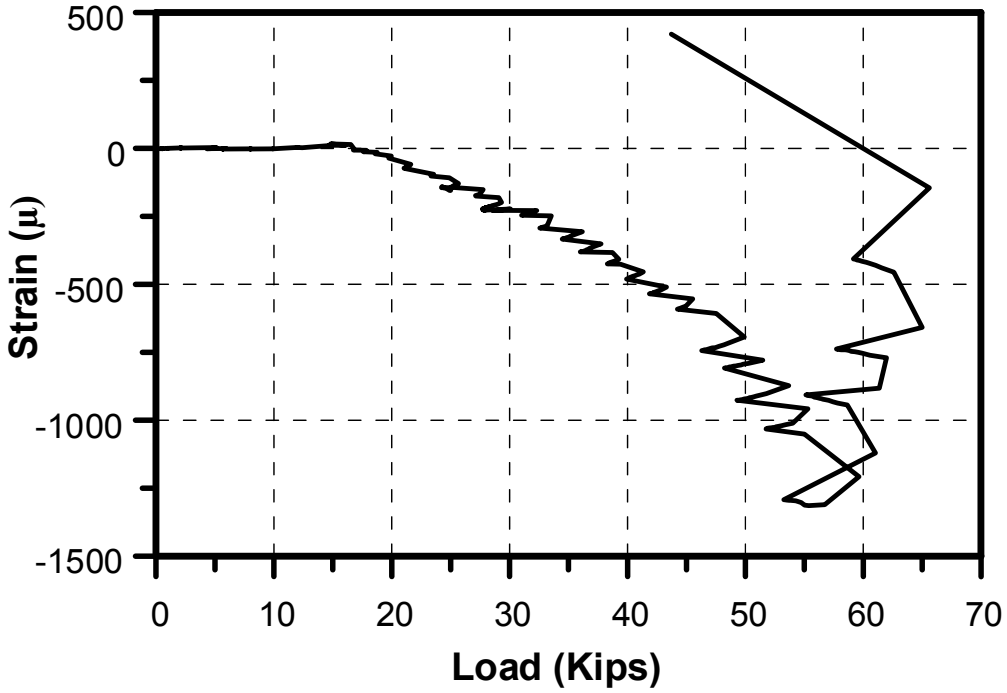

Figure 4-21 Load-strain curve for stud #1 (S1E).

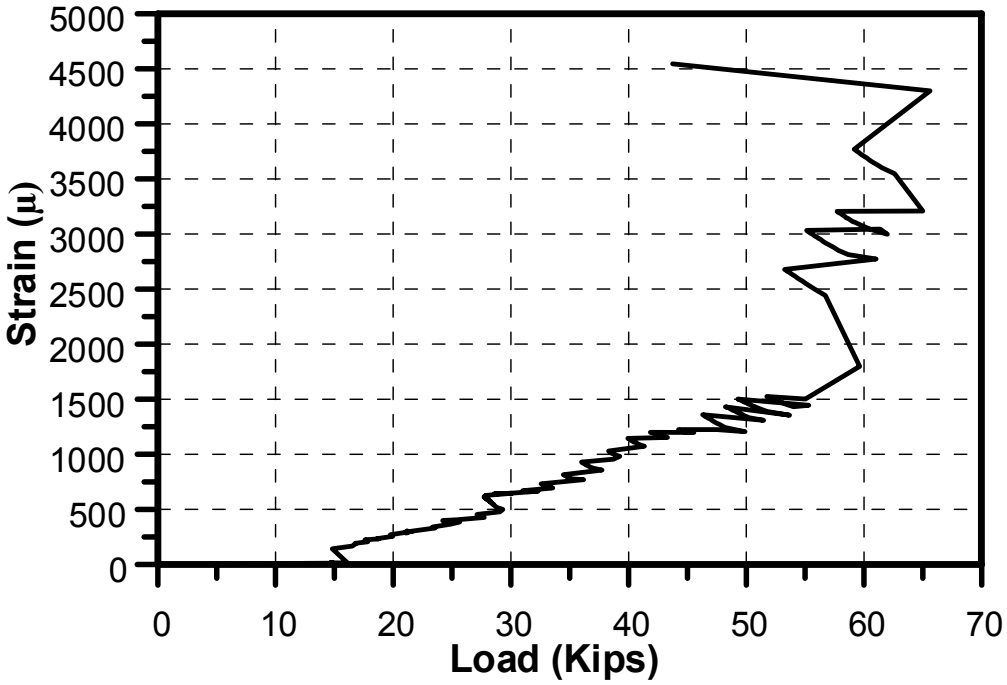

Figure 4-22 Load-strain curve for stud #2 (S2W).

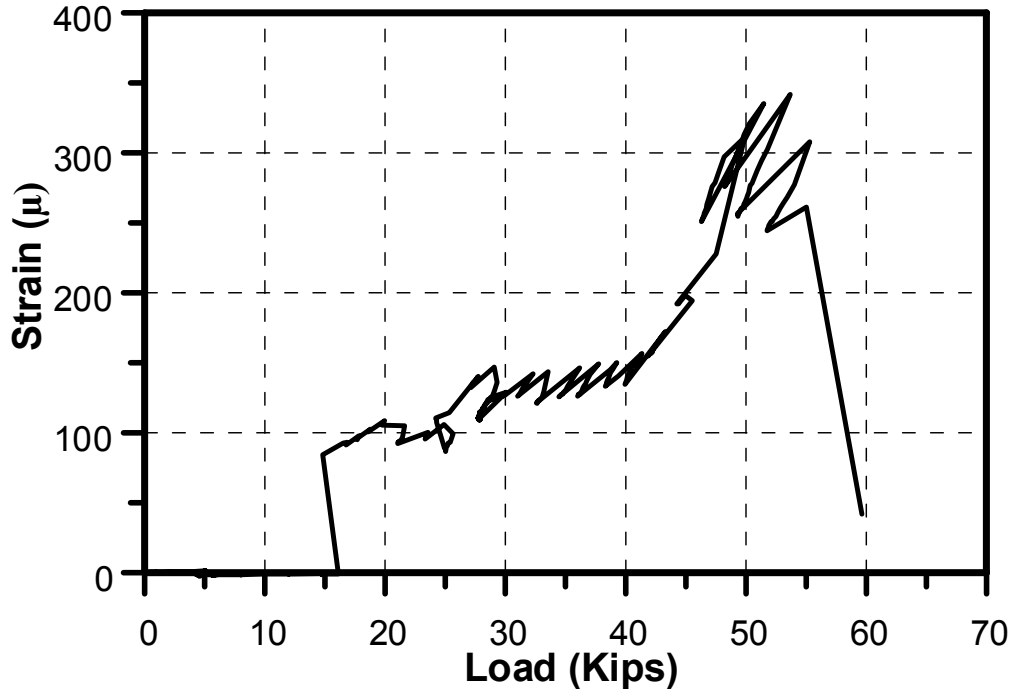

Figure 4-23 Load-strain curve for stud #2 (S2E).

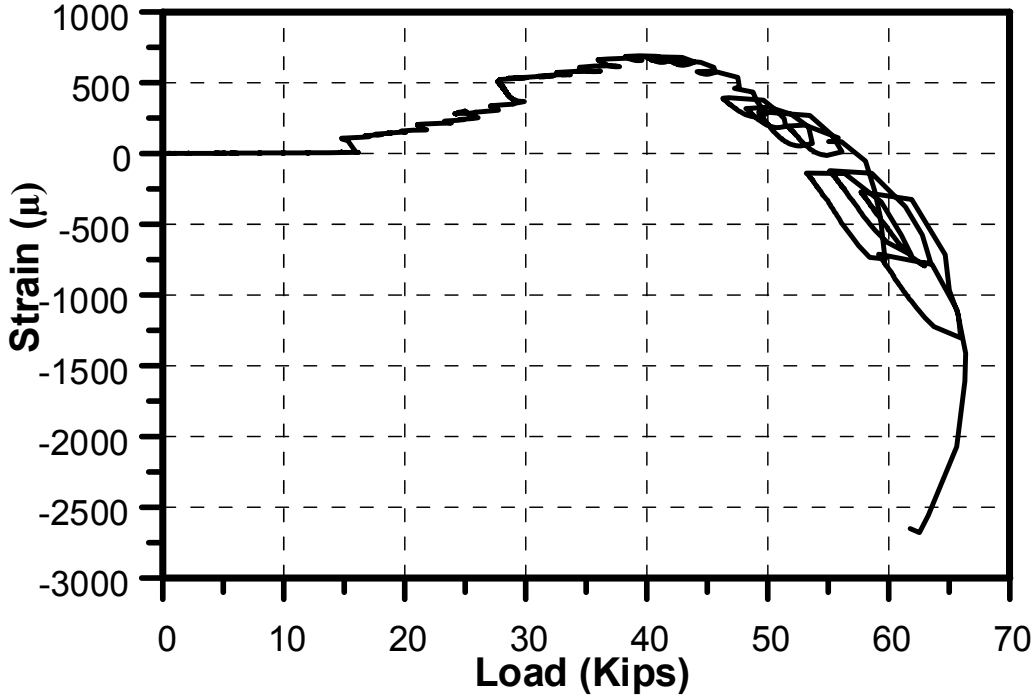

Figure 4-24 Load-strain curve for stud #3 (S3W).

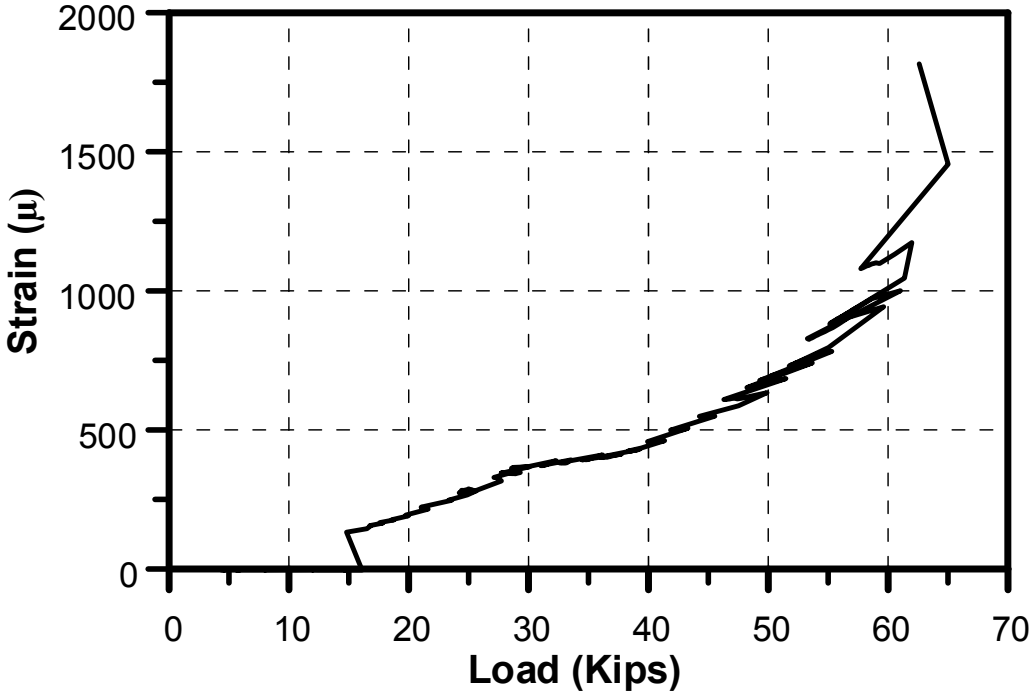

Figure 4-25 Load-strain curve for stud #3 (S3E).

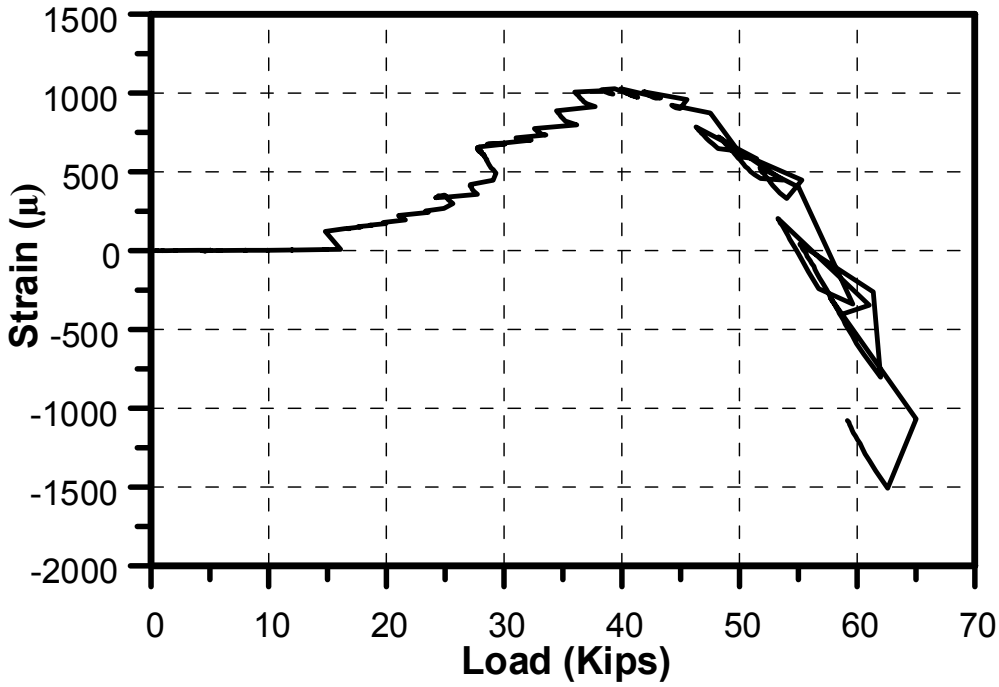

Figure 4-26 Load-strain curve for stud #4 (S4W).

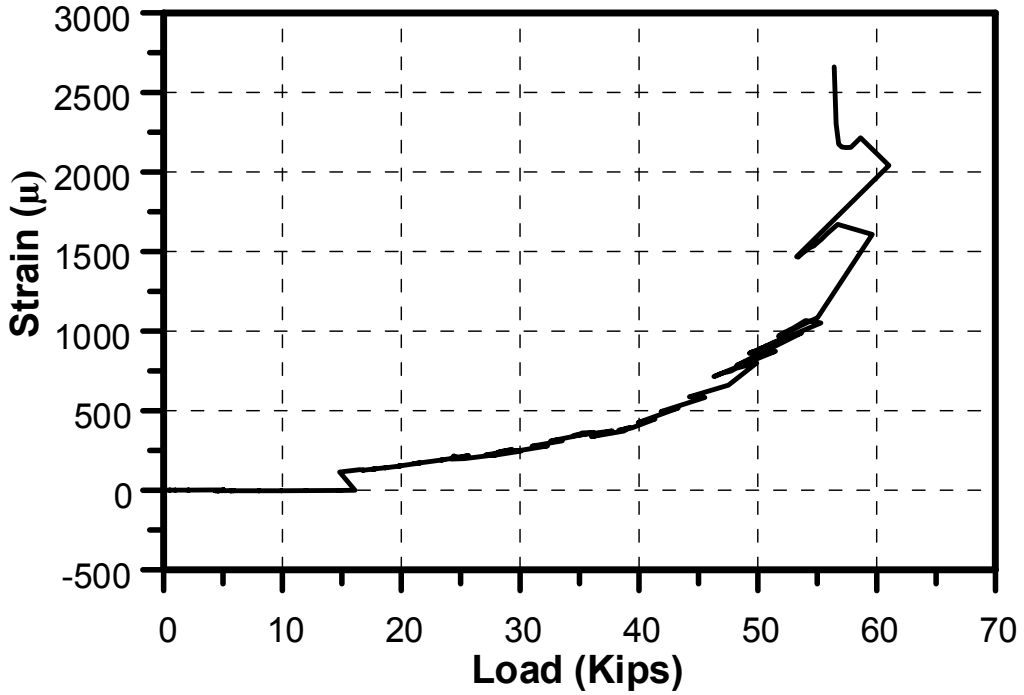

Figure 4-27 Load-strain curve for stud #4 (S4E).

4.2.3 Analysis and discussion of the results

Based on the test results, it was noticed that no crack occurred before 30 Kips. The relative displacement of the first crack at 30 Kips was 0.0017 in. Since the length of the connection is 4 ft., that means the shear resistance of the of the connection before onset the cracks is 7.5 Kips/ft.

The maximum load that the connection resisted before failure was 66.4 Kips and the relative displacement at that load was 0.0351". However, a failure in the grout that was surrounding the shear studs in the west direction was noticed. Moreover, the failure in the hollow core panel occurred along the steel rebars which is due to debonding between grout and steel rebars.

The shear stud in the west (Stud #1) yielded first at the same area that the first crack occurred. However, the other shear studs (Stud #2, Stud #3, and Stud #4) yielded at

load approximately close to the failure load of the whole specimen and a very sharp increase in the strain was observed which seems due to the fracture of these shear studs. Therefore, it can be concluded that the average yielding capacity of each shear stud is around 14.5 Kips.

The average compressive strength of the grout at the day of test is 2.6Ksi. Based of compressive strength of the grout =2.6ksi, the modulus of rupture =382psi, so no flexural crack is expected below 57 kips and flexural crack is expected above that since the maximum load is 66.4kips.

4.2.4 Developing of loading protocol

Based on the results of the preliminary in-plane shear deformation under monotonic loading test, the following loading protocol which is shown in Figure 4-28 was developed to test the in-plane shear deformation under monotonic loading experiments.

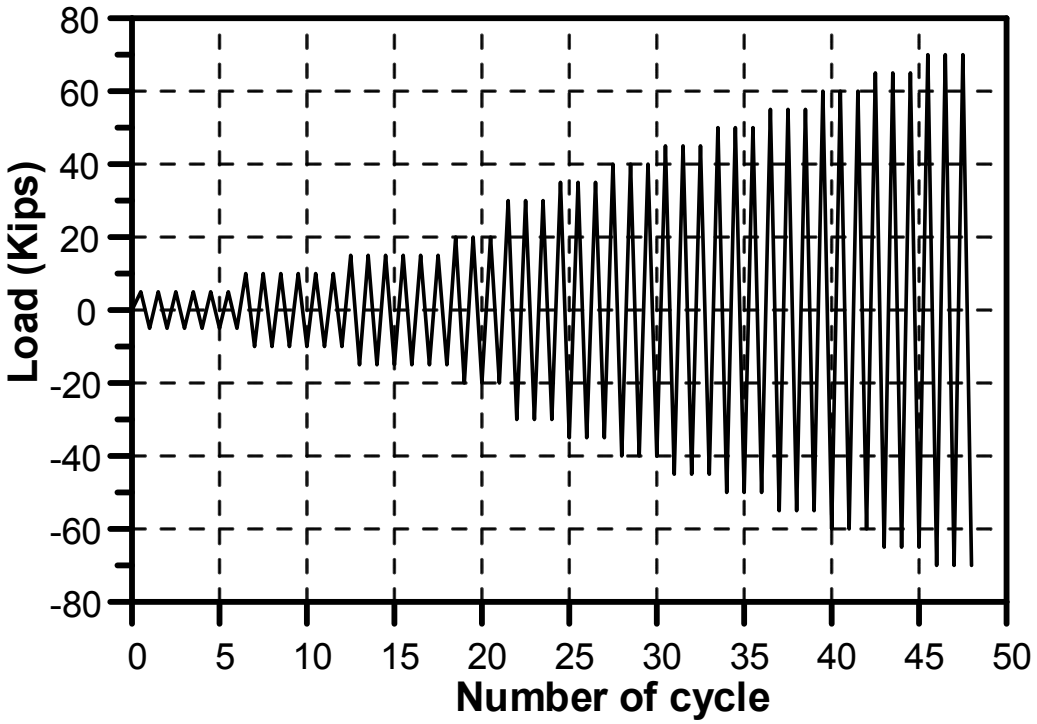

Figure 4-28 Loading protocol.

4.3 Cyclic in-plane shear deformation Test

The specimen was prepared as described in section 3.3 and the setup before starting the test is shown in Figure 3-57 . The loading protocol that was developed in the above section and shown in Figure 4-28 was used in this test.

The test was started by applying cyclic load according to the loading protocol. The first crack occurred at -30 Kips (cycle # -24) and the relative displacement is (-0.005 in.) as it can be seen in Figure 4-29 . The crack started at the contact of the plank (roller side) with the connection and the width of first crack is 0.1 mm. It's parallel to the direction of loading and it occurred at east side of the connection. The east side is the closest side to the actuator and the west side is the far side as shown in Figure 4-29.

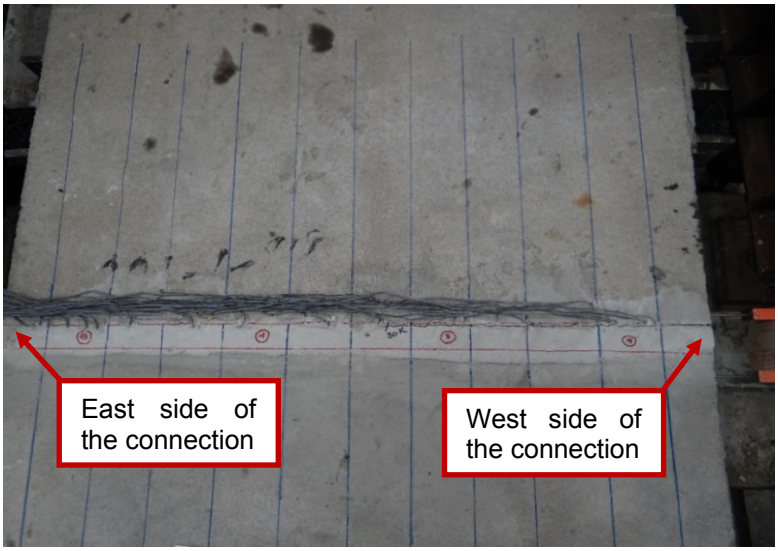

Figure 4-29 The first crack in the connection (at 30 Kips) for cyclic in-plane shear deformation Test.

A new crack developed at +35 Kips (cycle # +25) and the relative displacement is (-0.005"). The crack started at the contact of the plank (Fixed side) with the connection as shown in Figure 4-30. It's parallel to the direction of loading and it occurred at west side with width 0.1mm.

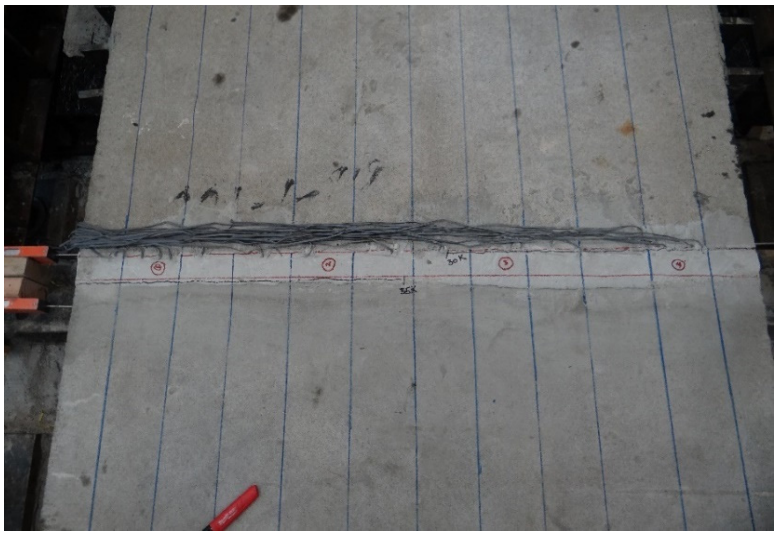

Figure 4-30 The crack in the east side at +35 Kips.

The propagation of crack and a diagonal crack at the west side were noticed at -35 Kips (cycle # -27) as it can be seen in Figure 4-31. The relative displacement is (-0.0079") and the width of cracks is 0.1mm.

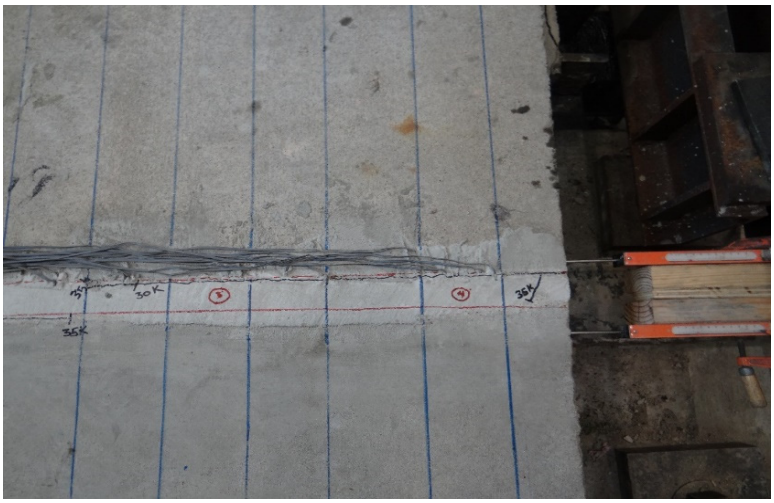

Figure 4-31 The developing and propagation of cracks at -35 Kips.

The propagation of cracks continued at -40K (cycle # -30), the relative displacement is (0.014") and the width of crack is 0.1 mm as shown in Figure 4-32.

Figure 4-32 The propagation of cracks at -40 Kips.

The propagation of crack and diagonal crack at the east end were noticed at -45K (cycle # -33) as illustrated in Figure 4-33. A crack in the plank (fixed side) was noticed at the first opening in the west side and the relative displacement is (0.012”).

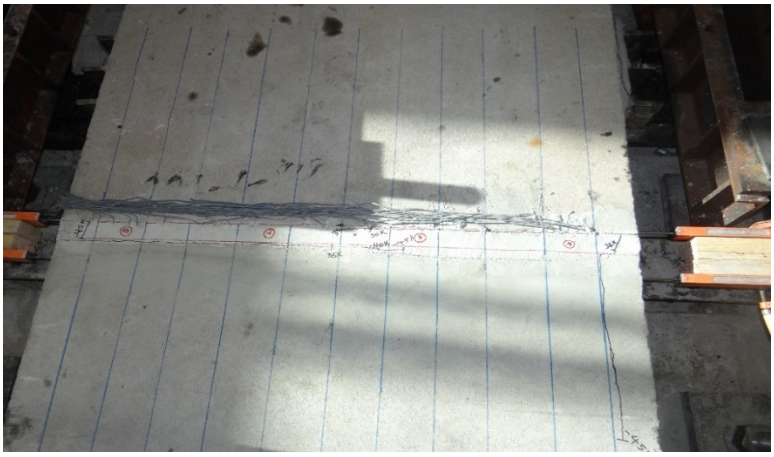

Figure 4-33 The propagation of cracks and a crack in the fixed side at -40 Kips.

Some diagonal cracks were noticed at -50K (cycle # -36) as shown in Figure 4-34. A crack in the plank (roller side) was also occurred at the first opening in the east side as illustrated in Figure 4-35. The relative displacement is (0.03”).

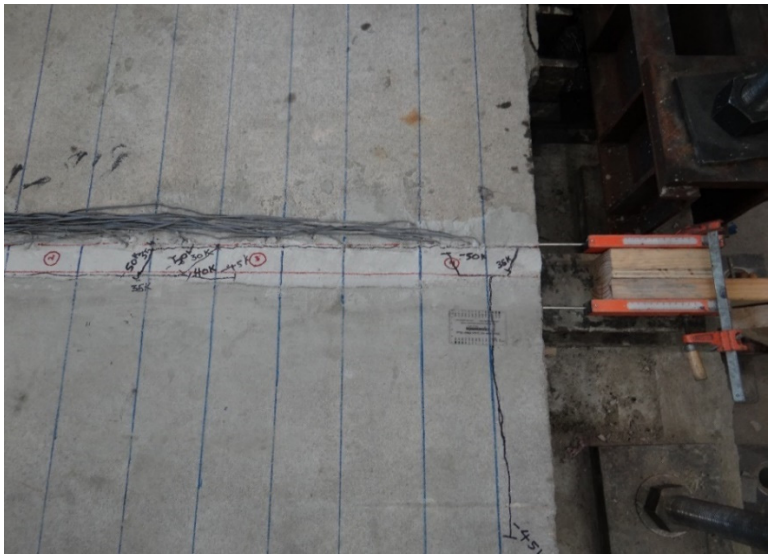

Figure 4-34 Developing some diagonal cracks -50K.

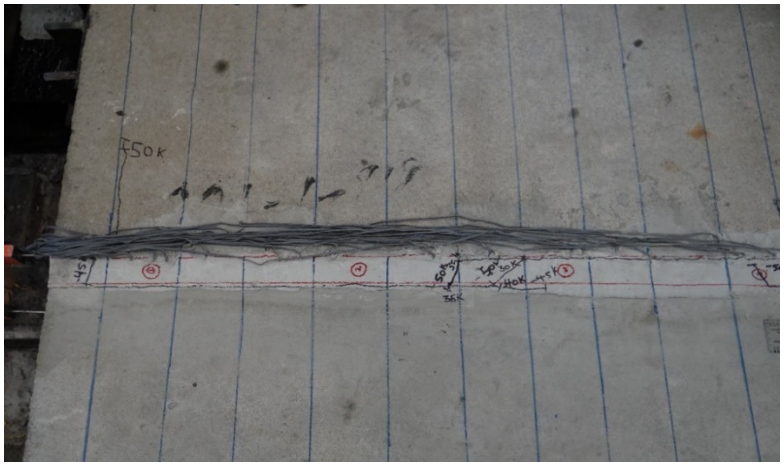

Figure 4-35 Crack in the plank (roller side) at the first opening in the east side at 50 Kips.

Many new cracks were noticed at +55K (cycle # +37) and the relative displacement is (0.005”). The cracks were noticed in both planks (along the openings of the planks) in addition to some diagonal cracks at the connection as illustrated in Figure 4-36. Moreover, some propagation of cracks and diagonal cracks (in the area of load point) were noticed as shown in Figure 4-37.

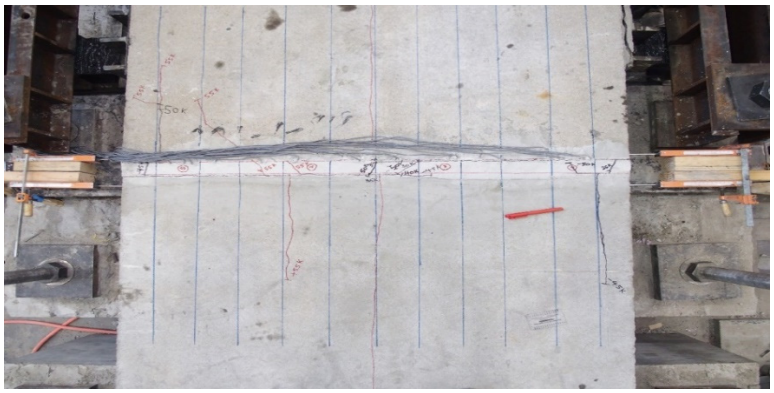

Figure 4-36 Overview of the cracks at +55 Kips.

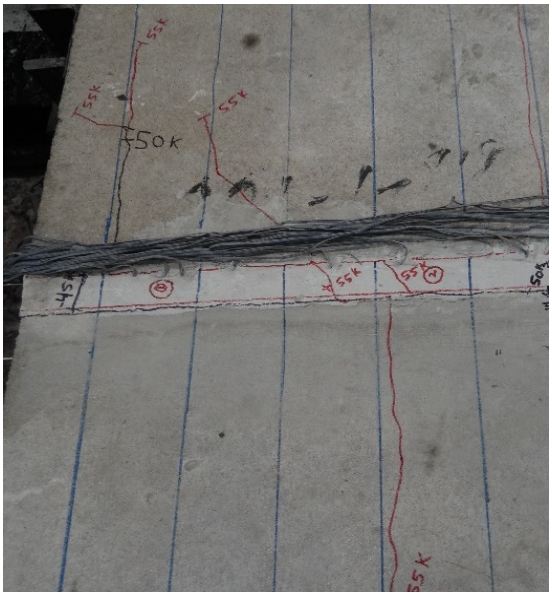

Figure 4-37 Propagation of cracks (in the area of load point) at +55 Kips.

The propagation of cracks was noticed at -55 Kips (cycle # -39) and the relative displacement is (0.075”). A new crack in the roller plank (along the opening in the east side) was also observed. Furthermore, a new crack was noticed in the fixed plank, but it is perpendicular to the direction of load. All these cracks can be seen in Figure 4-38.

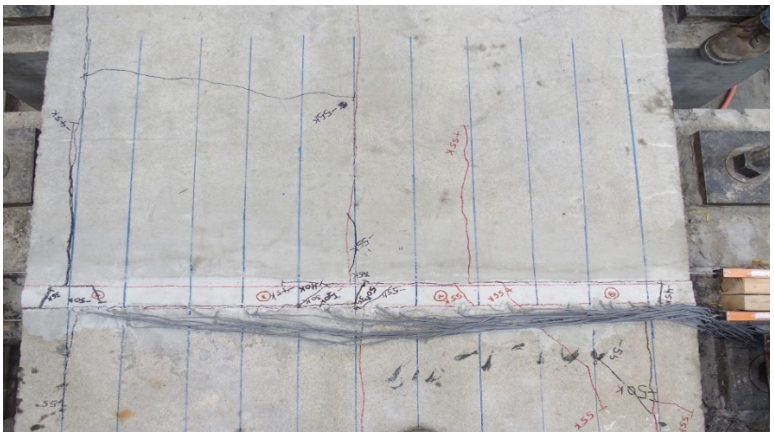

Figure 4-38 Overview of the cracks at -55 Kips.

When the load reached +57 Kips (cycle # +40), many cracks were noticed, the load started dropping, and the width of some cracks was 5 mm. The cracks are described below and shown in Figure 4-39 through Figure 4-41.

- Propagation of the cracks in the planks along the steel rebars.
- New cracks in the plank (roller side) along the steel rebars and perpendicular to the direction of load developed.

However, there was a failure in three of the shear studs as it can be seen in Figure 4-42 . Furthermore, one of the shear stud had a fracture on the top of the welding area as shown in Figure 4-43.

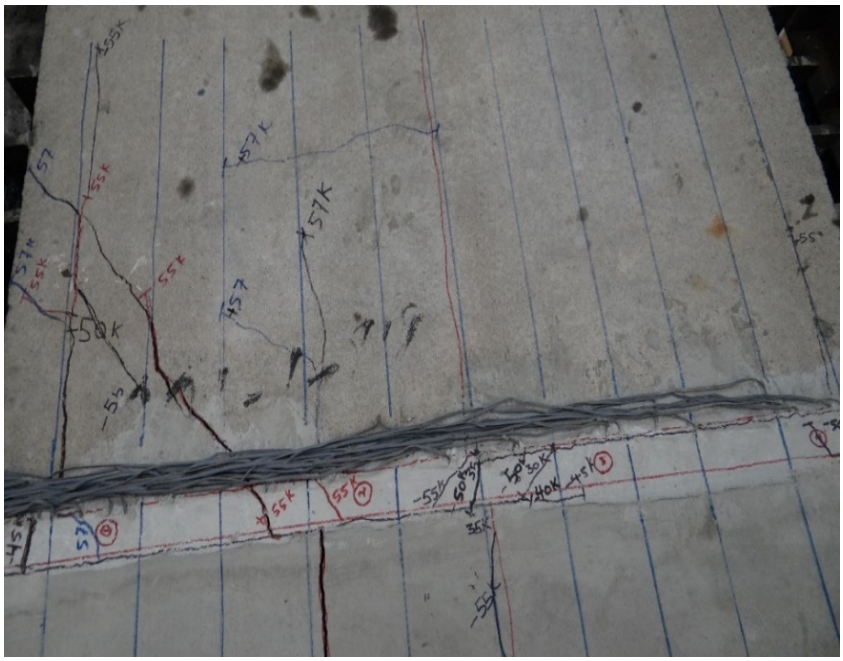

Figure 4-39 Cracks in the roller side plank at (+57 Kips).

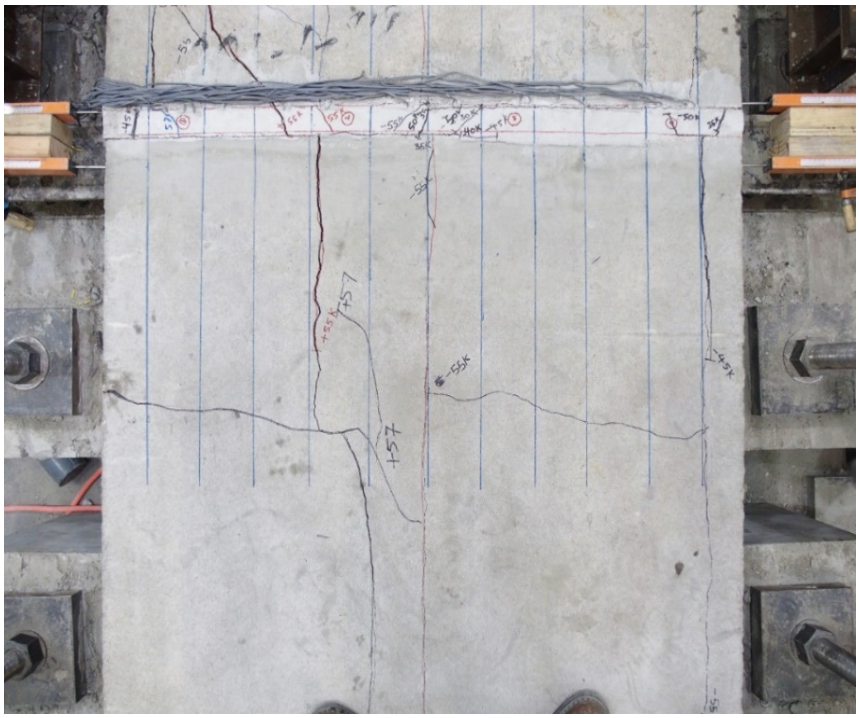

Figure 4-40 Cracks in the fixed side plank at (+57 Kips).

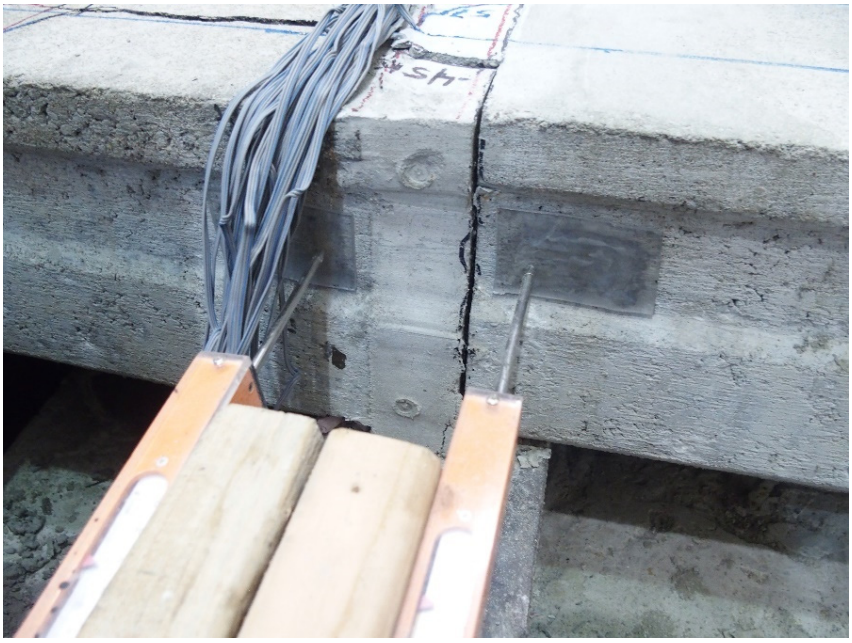

Figure 4-41 Failure in the ends of connection at (+57 Kips)

Figure 4-42 Fractured section of the shear stud after failure.at (+57 Kips).

Figure 4-43 Fracture on the top of welding area of a stud at (+57 Kips).

With reference to Figure 4-44 which shows the locations of LVDTs for this test, the relative displacement was calculated based on the same equation that used in the previous test.

Like the previous test, L4 and L5 were used as backup LVDTs and L1 was used to notice if the middle beam moves during the test. However, the readings of L1 showed that the middle beam did not move during the test.

L6 was used to measure the relative deformation of the hollow core panel in the roller side and it was calculated based on the following equation:

Relative disp.(in) =L6 reading(in.) – L1 reading (in.).

Figure 4-45 shows the relationship between the applied load and the relative displacement of the connection. The maximum shear strength of the connection is 57.5 Kips and the relative displacement is 0.055 in.

Figure 4-46 shows the relationship between the applied load and the deformation of the HCS. The deformation of the HCS at the maximum shear strength is 0.35 in.

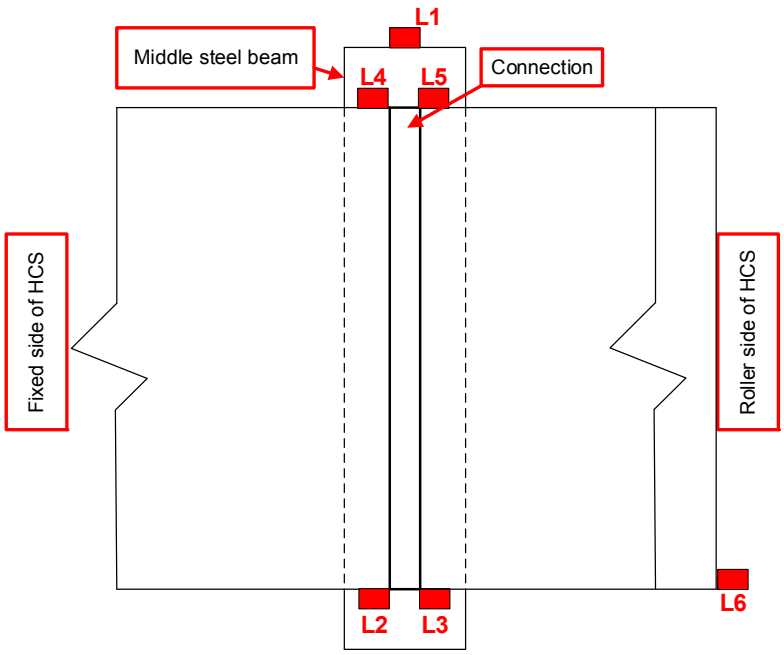

Figure 4-44 LVDTs locations.

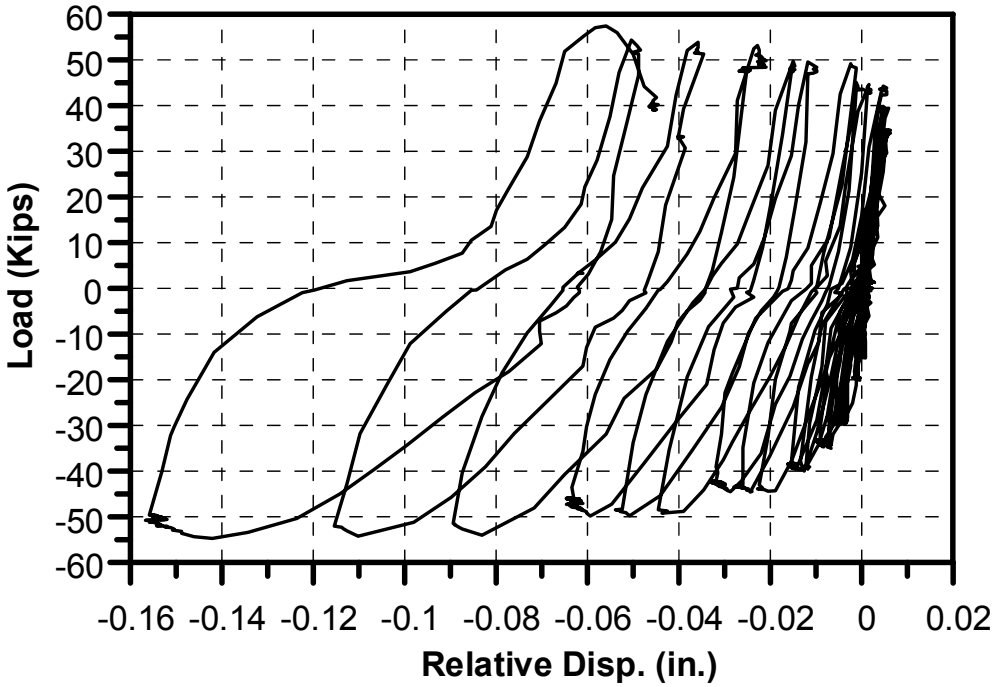

Figure 4-45 Load-Relative displacement loops curve.

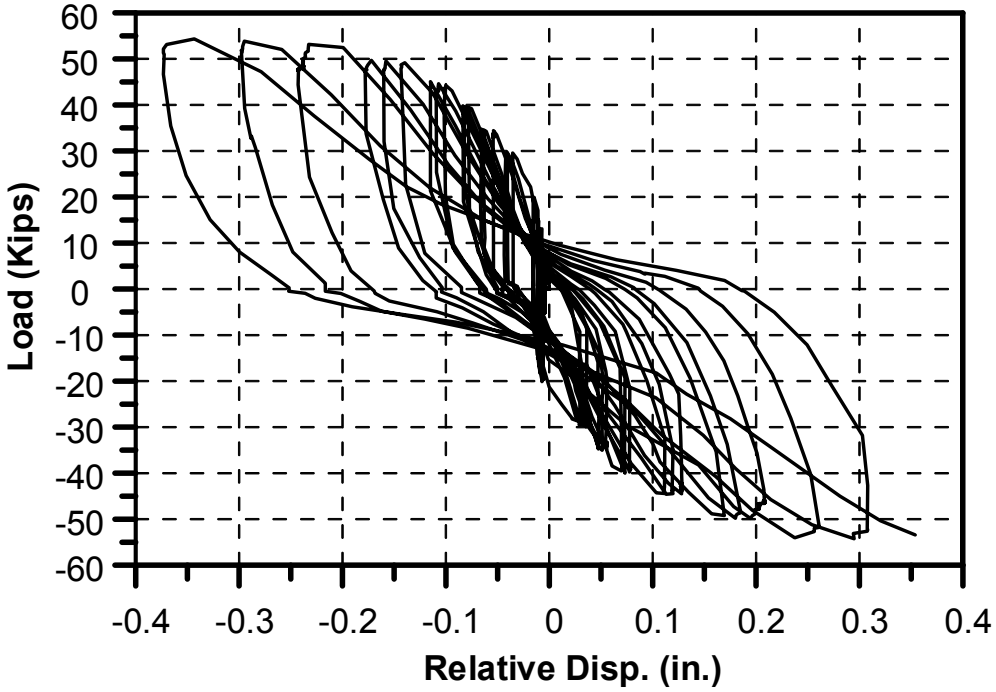

Figure 4-46 Load-Relative deformation HCS curve.

4.3.1 Results of strain gauges on the shear studs

The locations of strain gauges that used in the previous test which are shown in Figure 4-18 are also used in this test. Figure 4-47 through Figure 4-54 illustrate the load-strain curves for the four shear studs that used in this specimen.

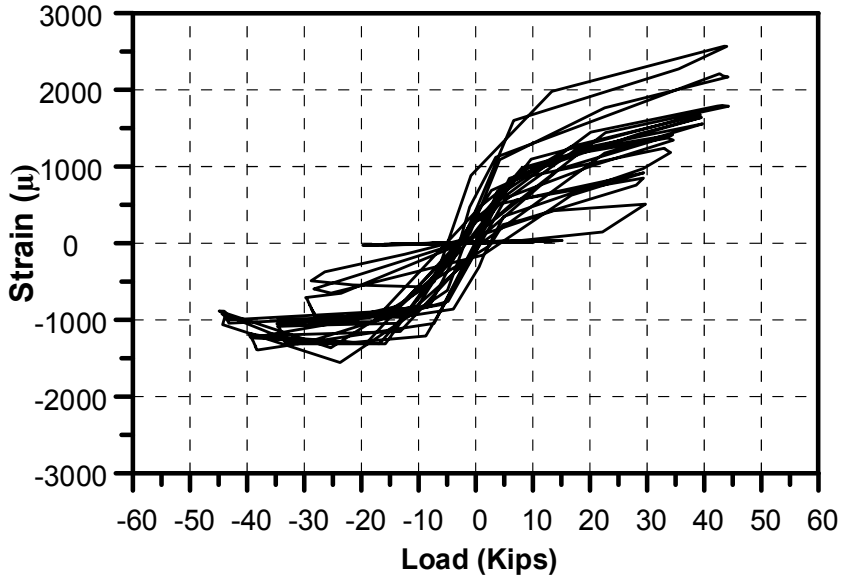

Figure 4-47 Load-strain curve for stud #1 (S1W).

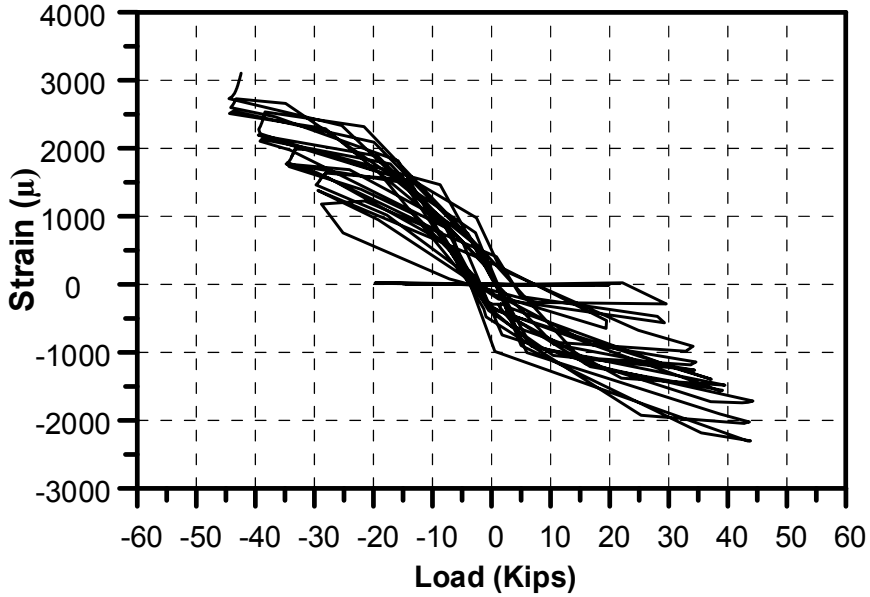

Figure 4-48 Load-strain curve for stud #1 (S1E).

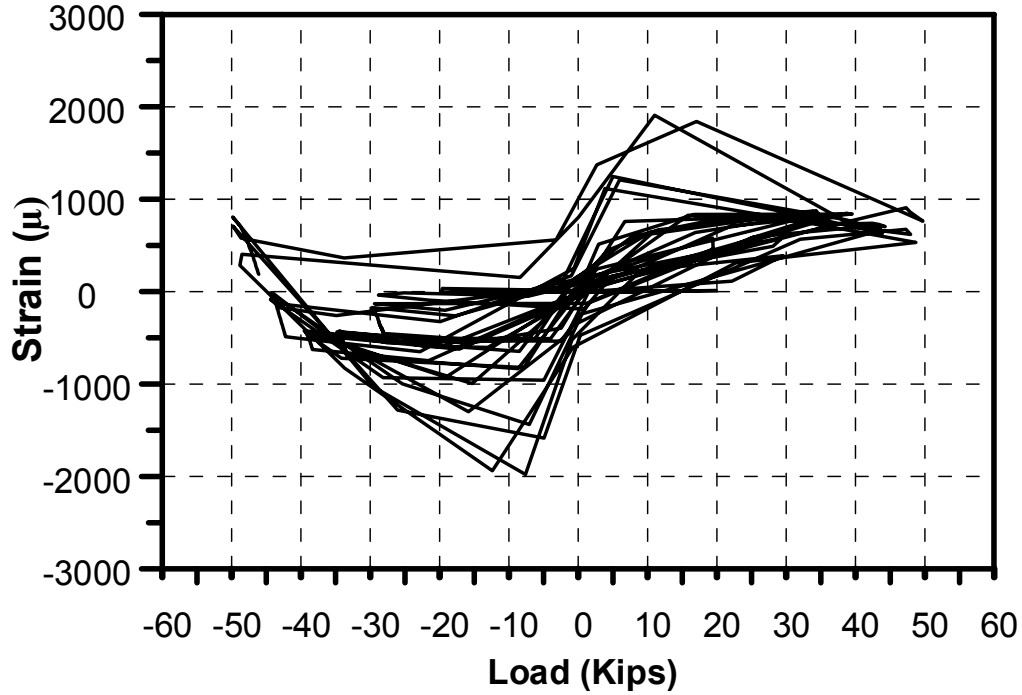

Figure 4-49 Load-strain curve for stud #2 (S2W).

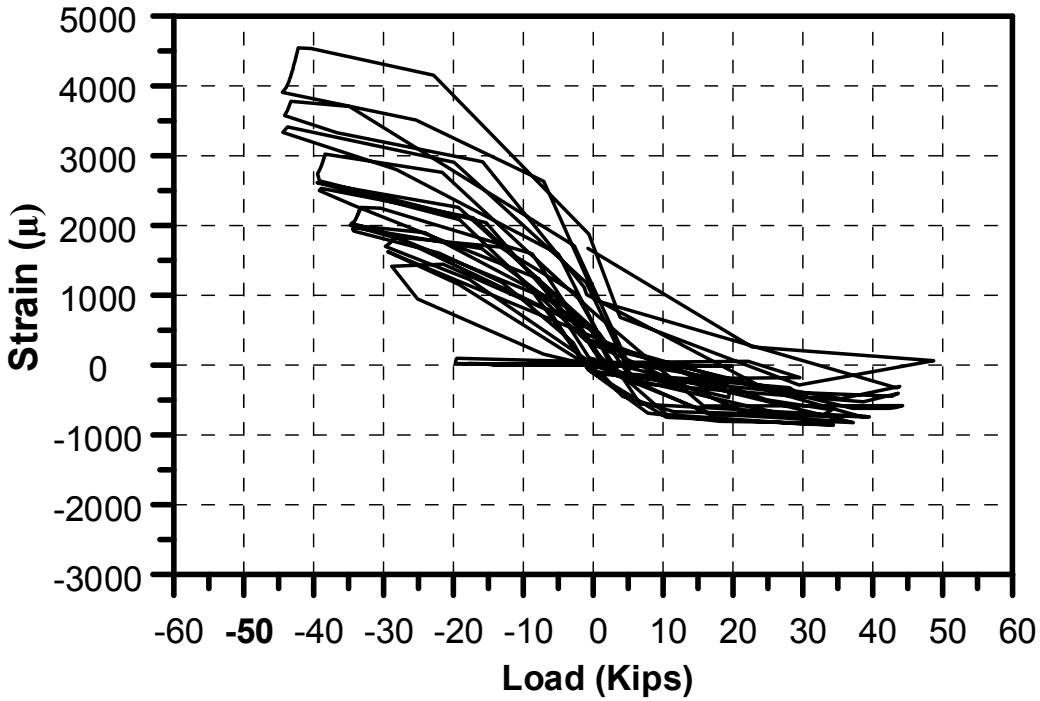

Figure 4-50 Load-strain curve for stud #2 (S2E).

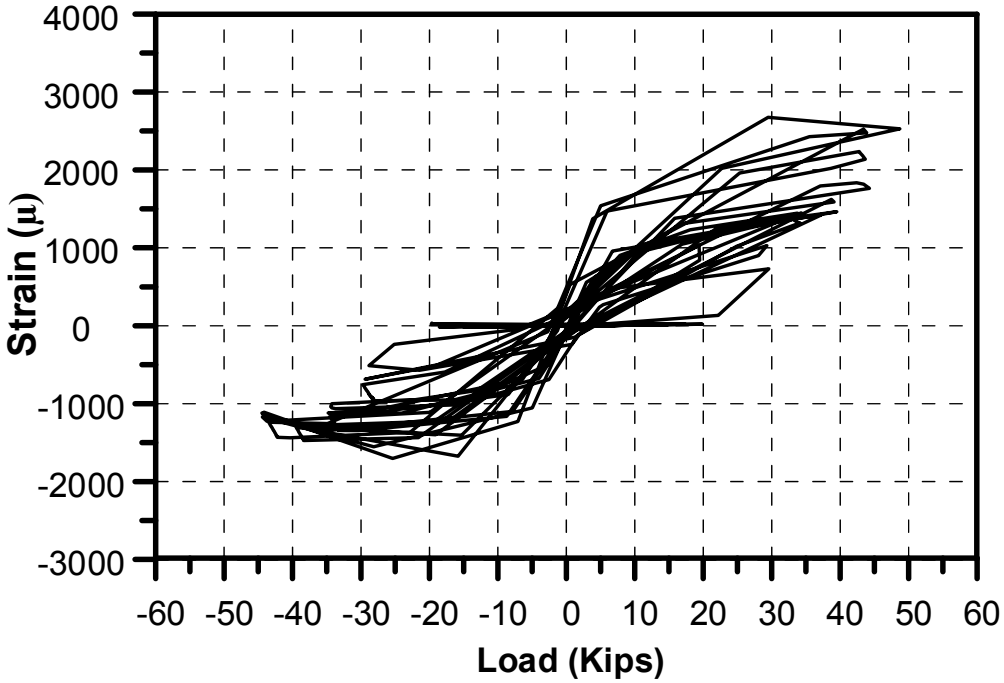

Figure 4-51 Load-strain curve for stud #3 (S3W).

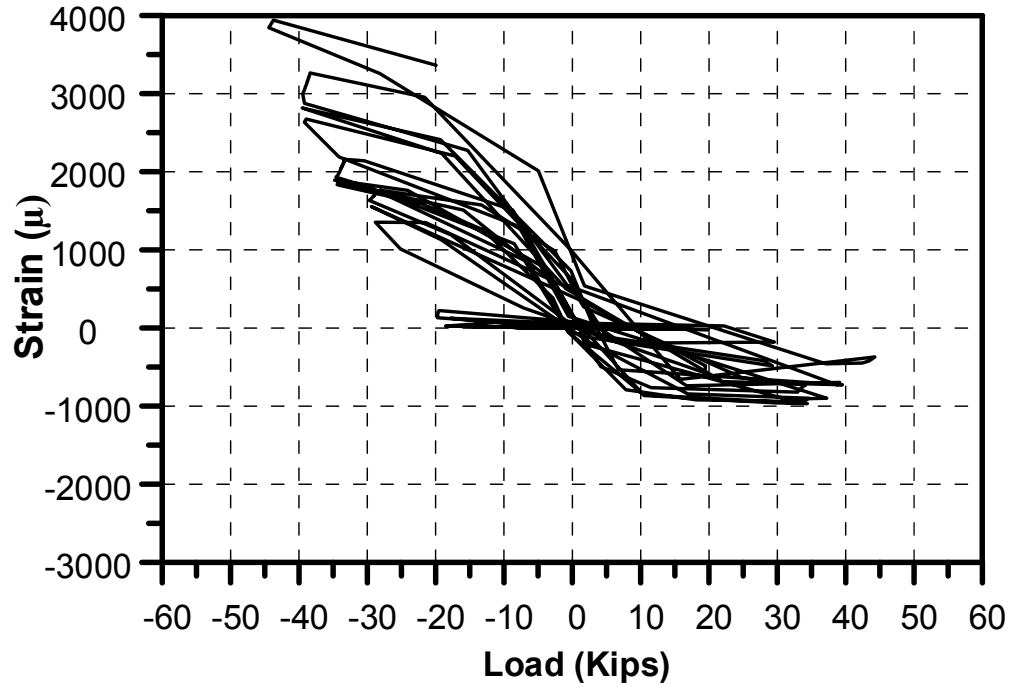

Figure 4-52 Load-strain curve for stud #3 (S3E).

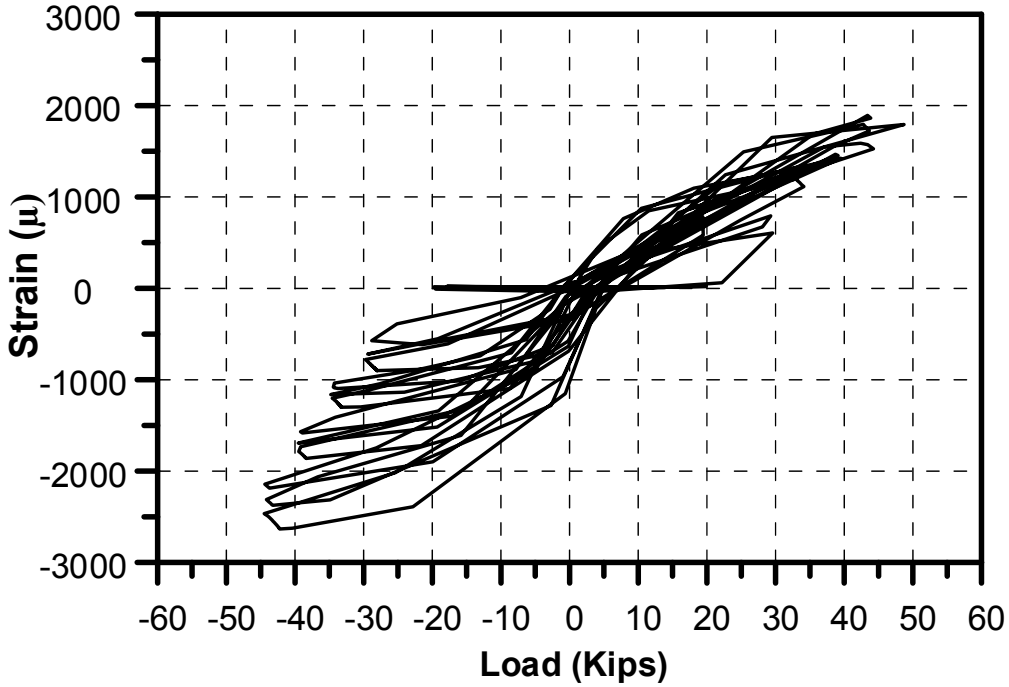

Figure 4-53 Load-strain curve for stud #3 (S4W).

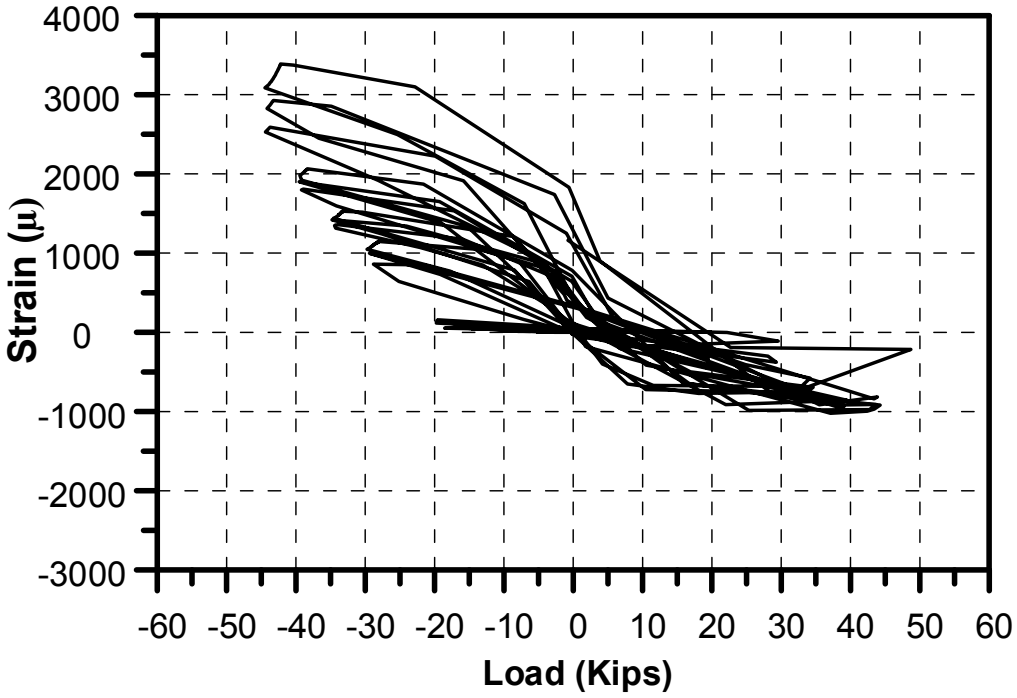

Figure 4-54 Load-strain curve for stud #4 (S4E).

4.3.2 Results of strain gauges on the steel rebars

The steel rebars that were used in this test is grade 60, therefore the yielding strength is 60 Ksi. The yielding strain of the steel rebars is calculated using Hook's law formula as shown below:

$$\varepsilon_y = \frac{F_y}{E_s}$$

Where: ε_s: steel rebar Stain.

E_s: Young's modulus of steel (29,000 Ksi).

F_y: Yielding strength of the steel rebar (60 Ksi).

$$\varepsilon_y = \frac{60}{29{,}000} = 2069\ \mu$$

With reference to Figure 4-55 which shows the locations of the strain gauges on the steel rebars, Figure 4-56 through Figure 4-70 show the load-strain curve for all the rebars used in this test.

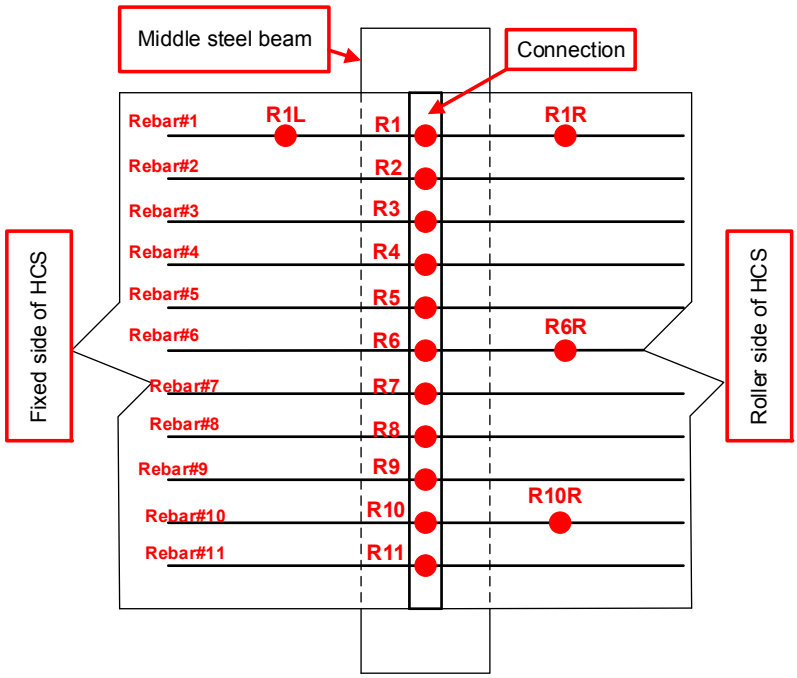

Figure 4-55 steel rebars locations.

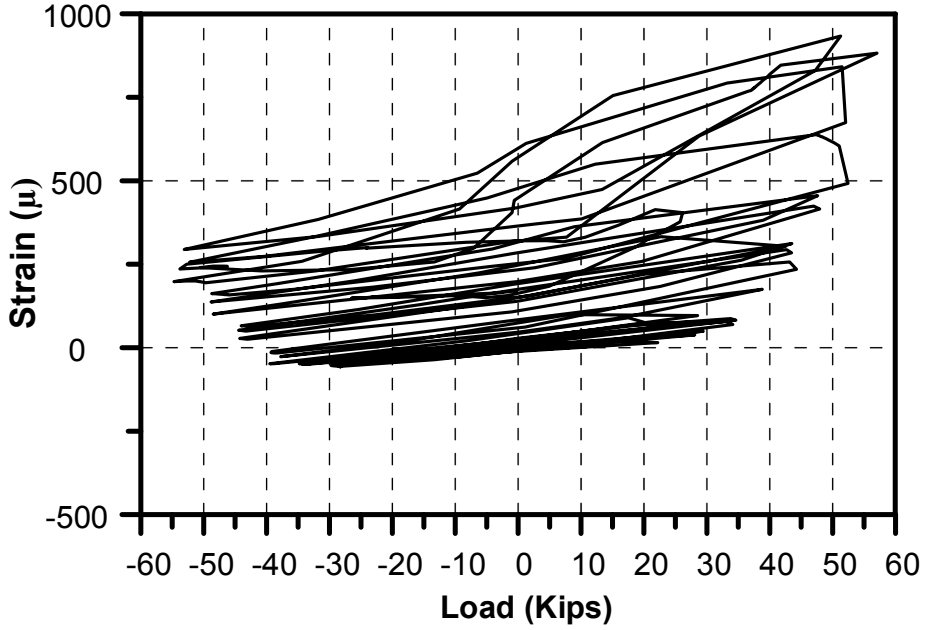

Figure 4-56 Load-strain curve for rebar#1 (fixed side)-R1L.

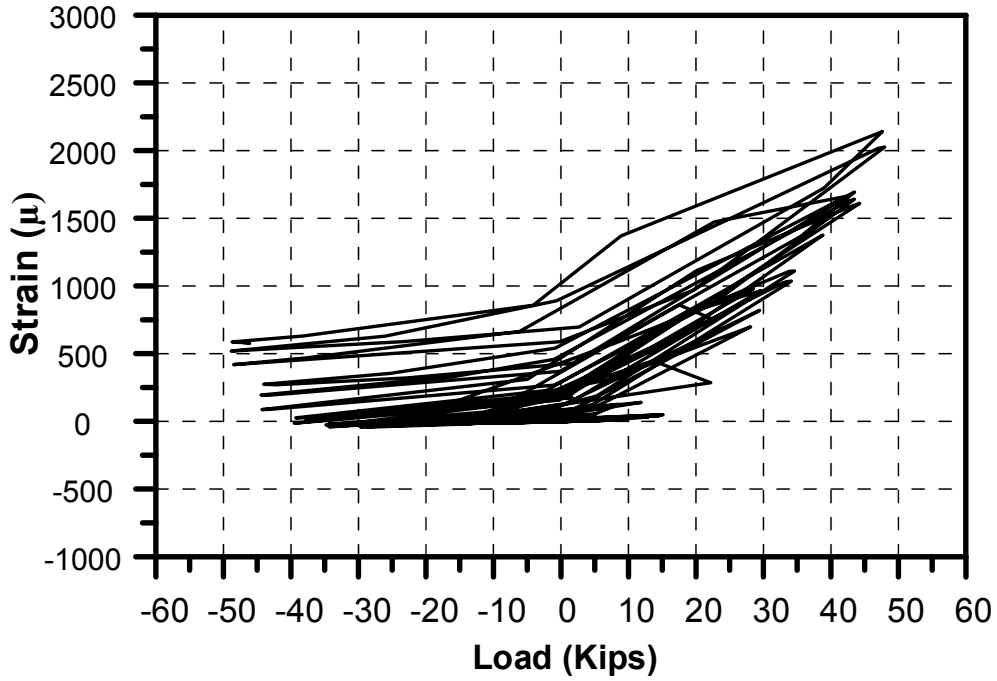

Figure 4-57 Load-strain curve for rebar#1 (middle side)-R1.

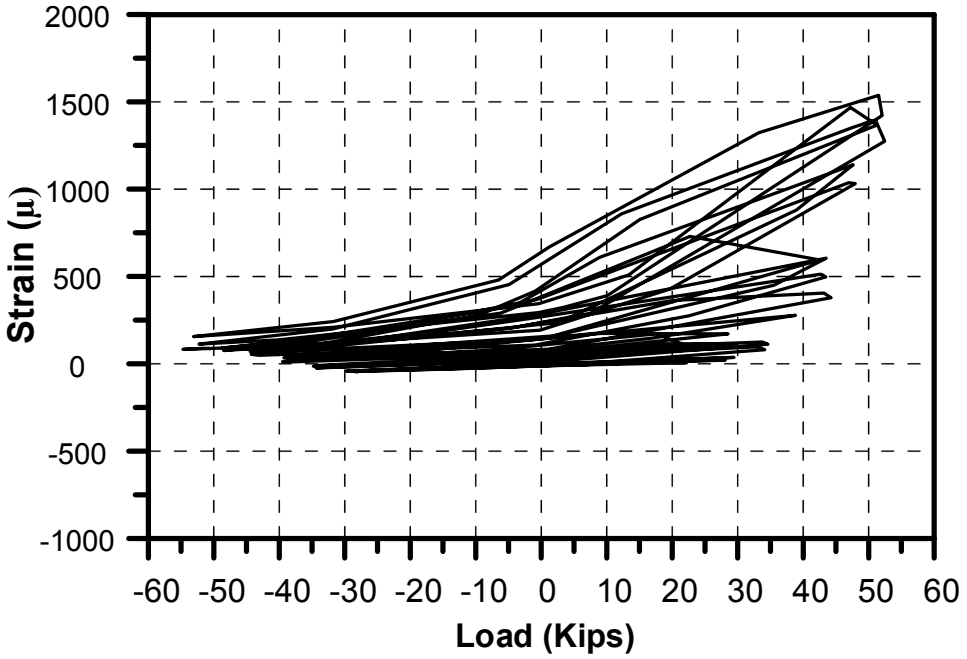

Figure 4-58 Load-strain curve for rebar#1 (roller side)-R1R.

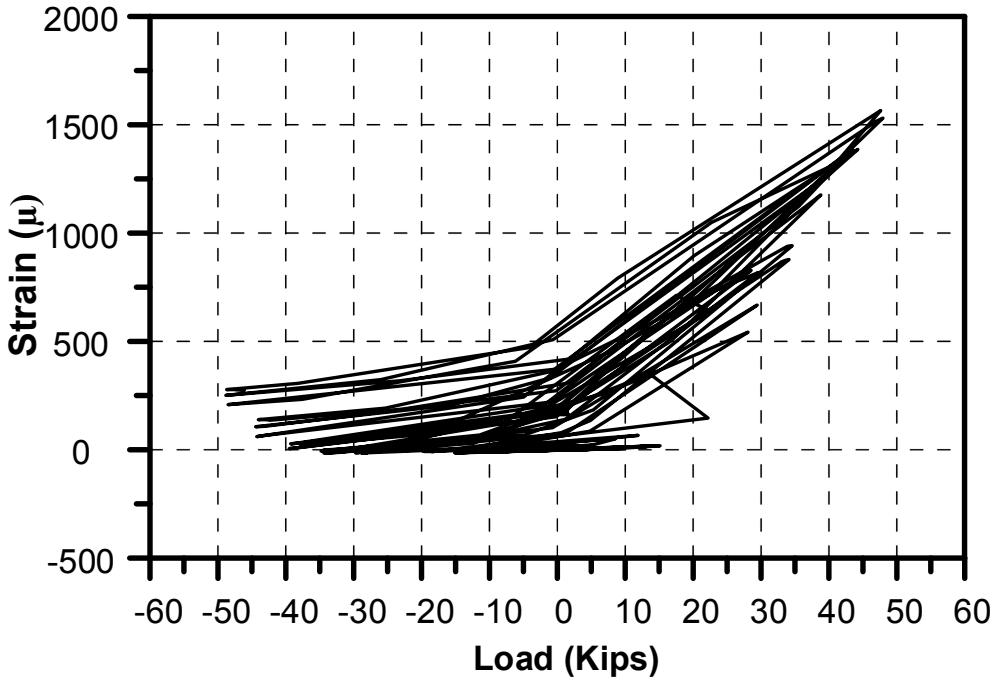

Figure 4-59 Load-strain curve for rebar# 2-R1.

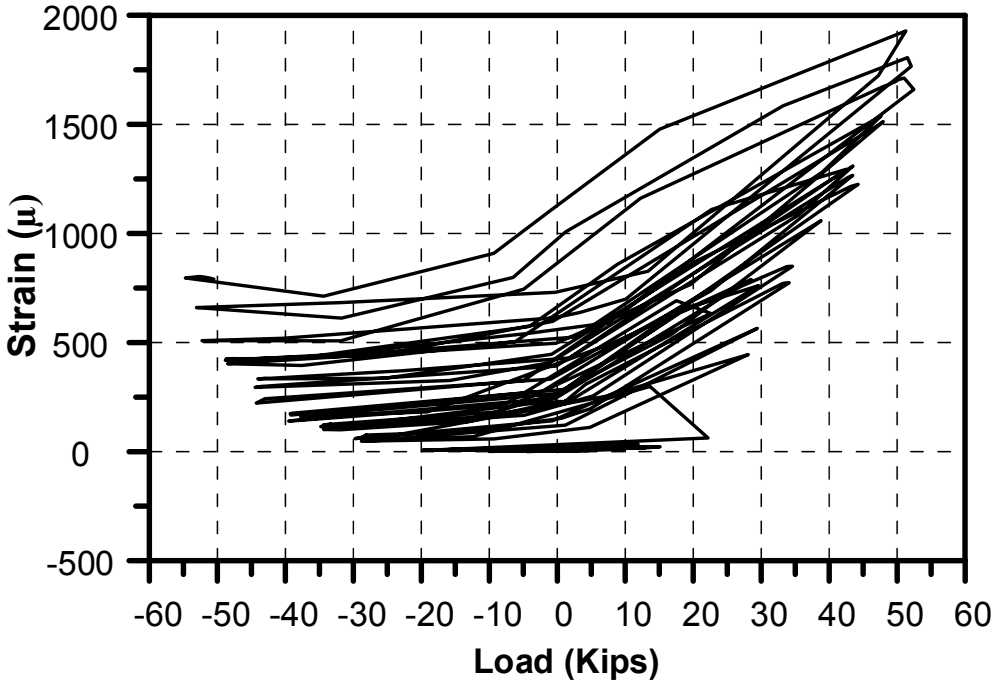

Figure 4-60 Load-strain curve for rebar# 3-R3.

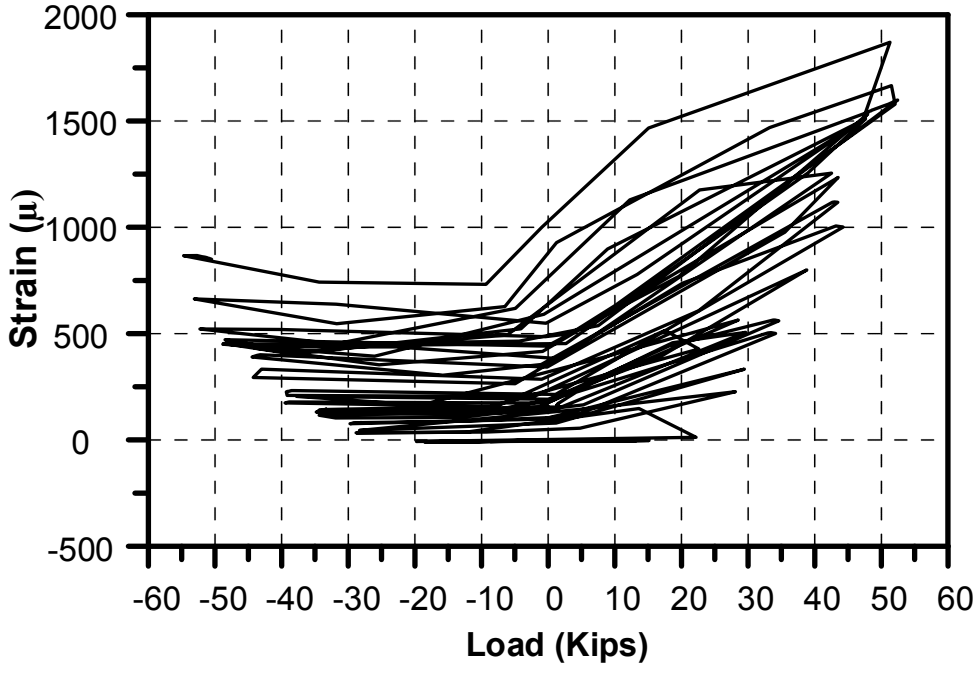

Figure 4-61 Load-strain curve for rebar# 4-R4.

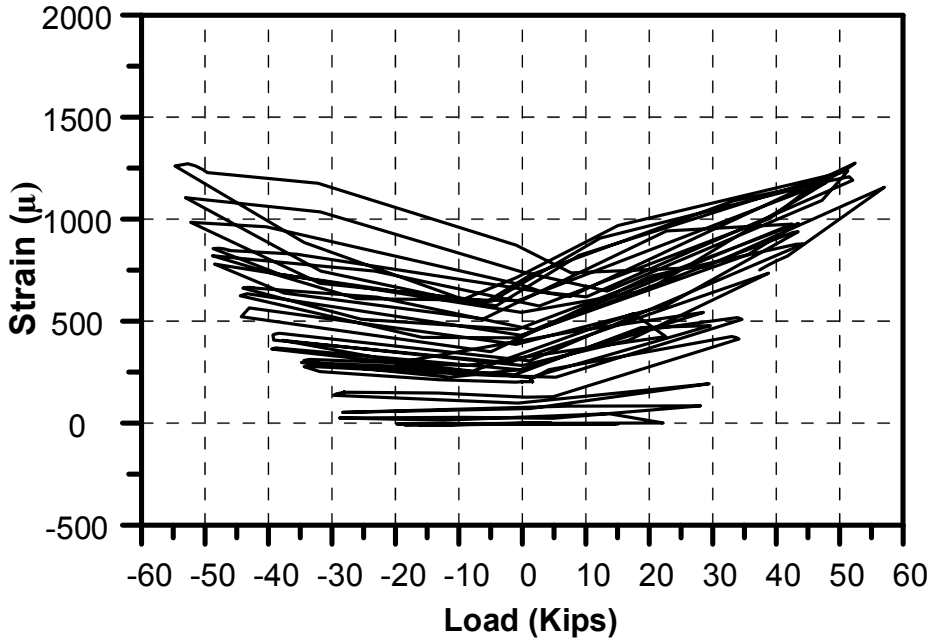

Figure 4-62 Load-strain curve for rebar# 5-R5.

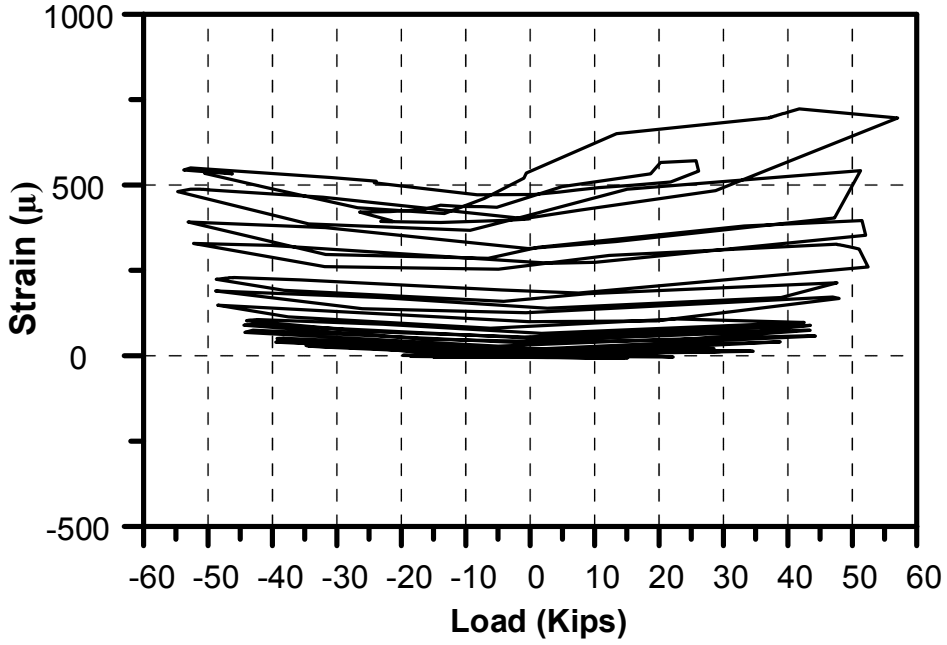

Figure 4-63 Load-strain curve for rebar#6-(roller side)-R6R.

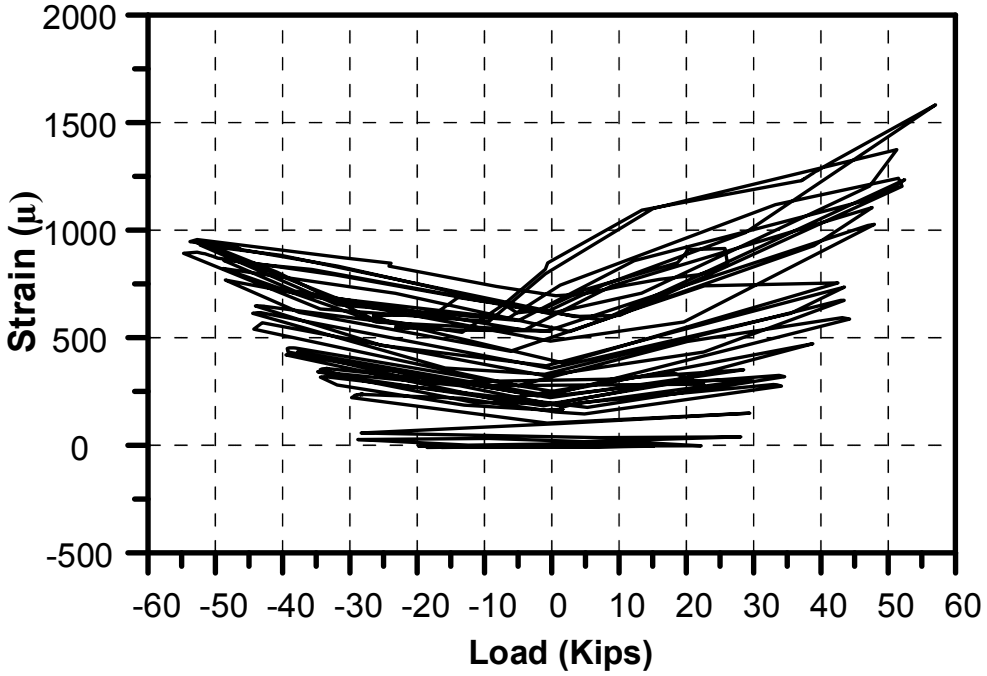

Figure 4-64 Load-strain curve for rebar#6-R6.

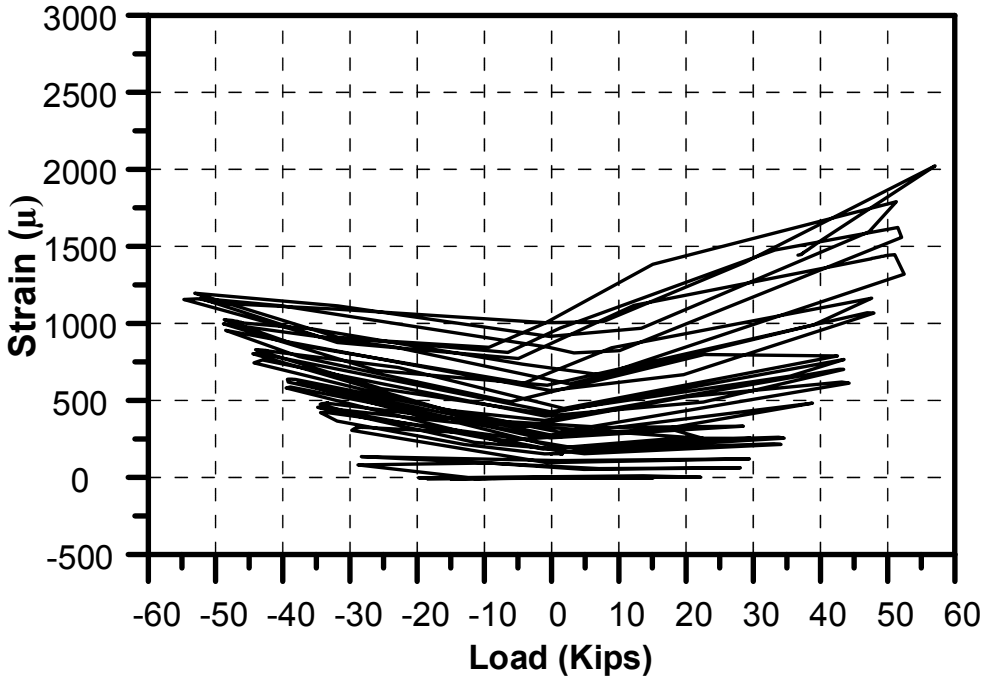

Figure 4-65 Load-strain curve for rebar# 7-R7.

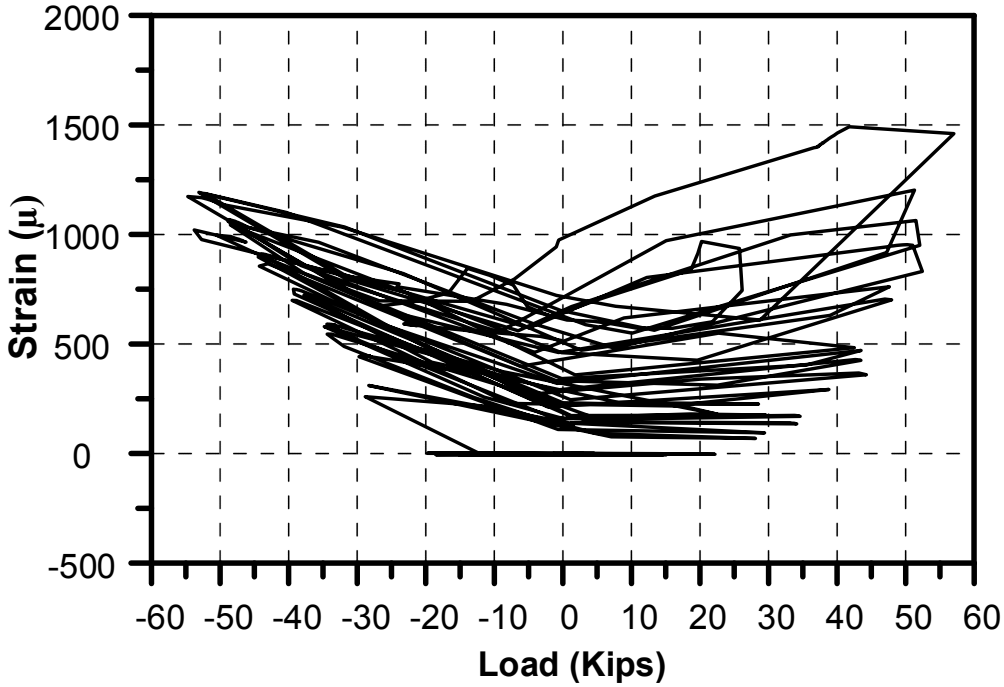

Figure 4-66 Load-strain curve for rebar# 8-R8.

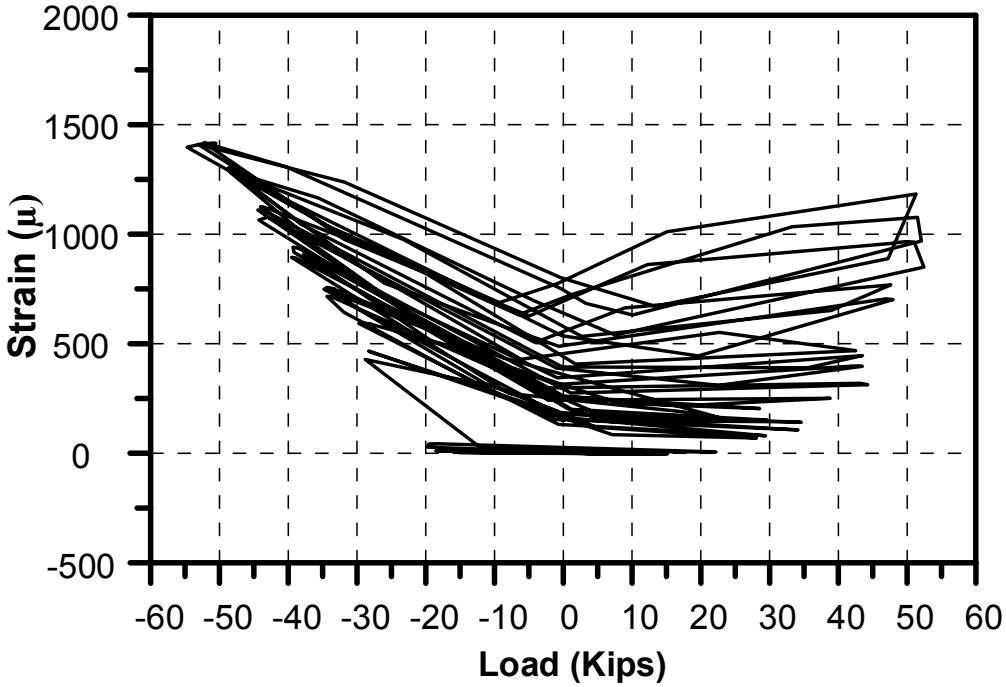

Figure 4-67 Load-strain curve for rebar# 9-R9.

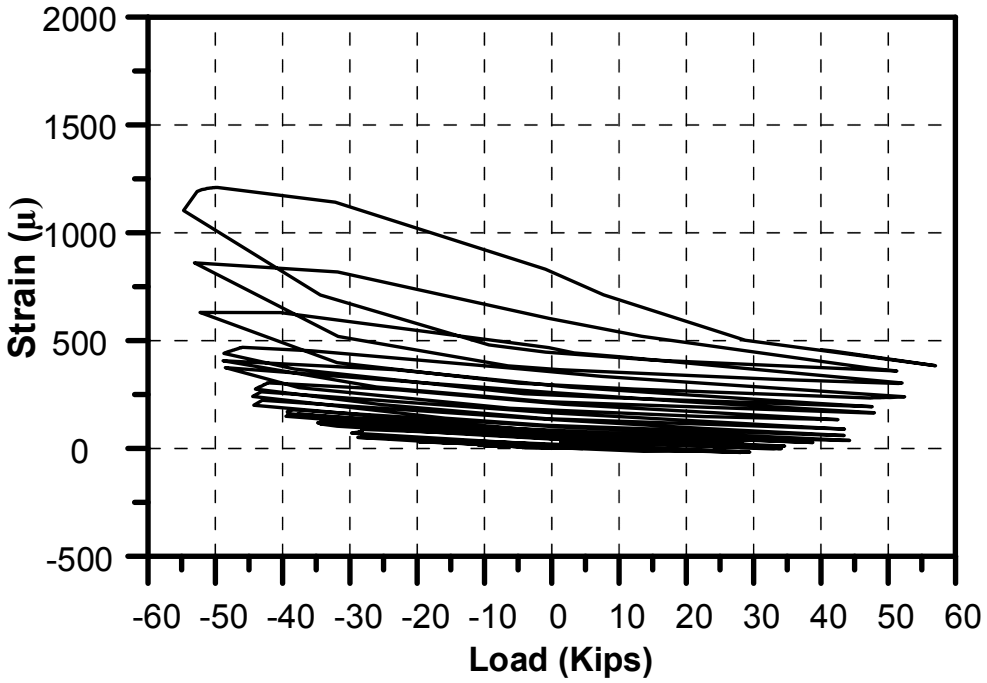

Figure 4-68 Load-strain curve for rebar#10 (roller side)-R10R.

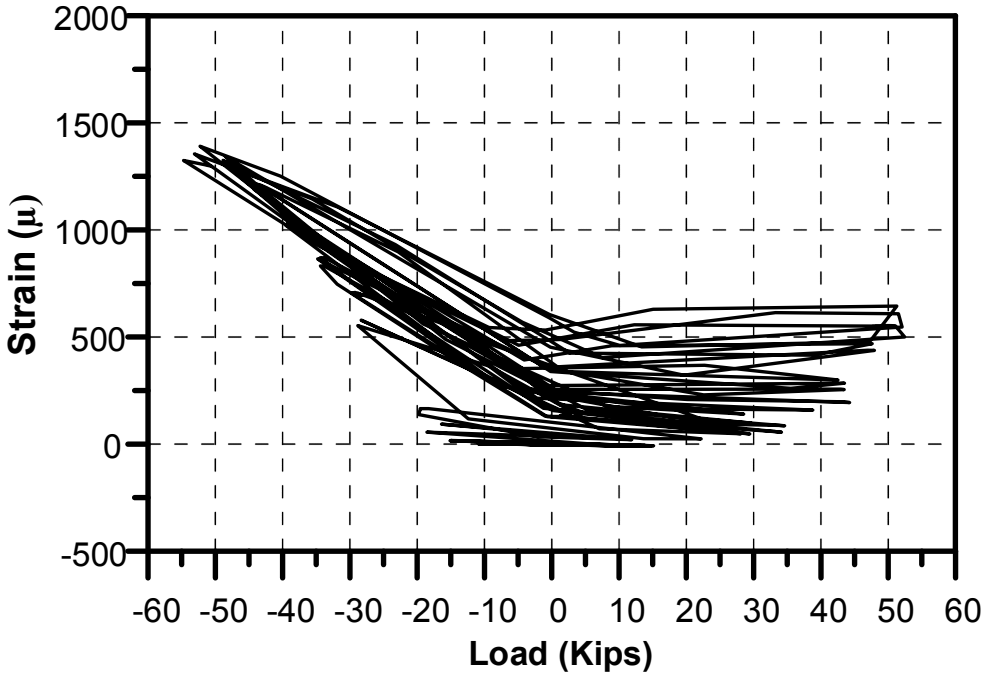

Figure 4-69 Load-strain curve for rebar#10-R10.

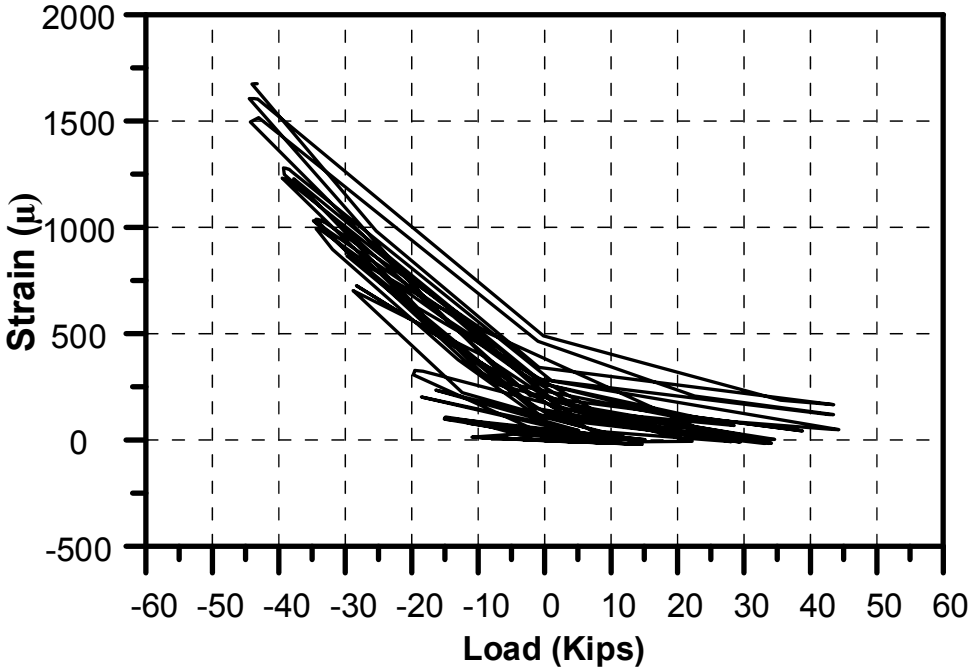

Figure 4-70 Load-strain curve for rebar#11-R11.

4.3.3 Analysis and discussion of the results

The results of this test showed that there was no crack developed before 30 Kips. Furthermore, the relative displacement of the first crack at 30 Kips was 0.005 in. That means the shear resistance of the of the connection before onset the cracks is 7.5 Kips/ft.

The maximum load that the connection resisted before failure was 57.5 Kips and the relative displacement at that load was 0.055 in. Like the pervious test under monotonic loading, the failure in the hollow core panel occurred along the steel rebars which is also due to debonding between grout and steel rebars.

All the shear studs yielded in this test and they started yielding at load range (45 Kips-50 Kips). Three of shear studs failed completely in this test whereas the other one had a fracture on the top of welding area. However, all of the fractures were observed on the top of welding area and this type of failure is mostly common in the shear studs.

In general, it can be concluded that the failure of this specimen is due to the followings:

- Insufficient amount of shear studs to resist the shear force.
- Debonding between the grout and steel rebars inside the plank's holes, this leads to an increase the volume of grout and consequently cracks and failure of the planks.

Yielding in steel rebars occurred in rebars 1,2,3,4,7 and 11 and it occurred at load range (50 Kips -57 Kips). Moreover, the maximum strain values were noticed at the middle of rebars compared with roller and fixed sides. However, the roller side of rebars has more strains compared with fixed side.

4.4 Cyclic in-plane shear deformation Test (6 Studs+180^o hooked rebars)

The results of the previous cyclic in-plane shear deformation test showed that the failure in the specimen is due to the failure in the shear studs and the hollow-core planks. The failure in the planks is due to the debonding between the steel rebar and the grout. Therefore, in order to increase the strength of the shear studs, the amount of shear studs increased by two, so the total of shear studs is four. Furthermore, in order to increase the bond between the rebars and the grout, the ends of rebars were hooked up to 180^o.

The specimen was prepared as described in section 3.4 and the setup before starting the test is shown in Figure 3-61 . The same loading protocol that used in the previous test which is shown in Figure 4-28 was also used in this test.

The test began by applying cyclic load according to the loading protocol. The first crack occurred at +30 Kips (cycle # +24) and the relative displacement is (-0.0008 in.) as shown in Figure 4-71 . The crack started at the contact of the plank (fixed side) with the connection, it's parallel to the direction of loading and it occurred at east side and the width of crack is 0.1mm.

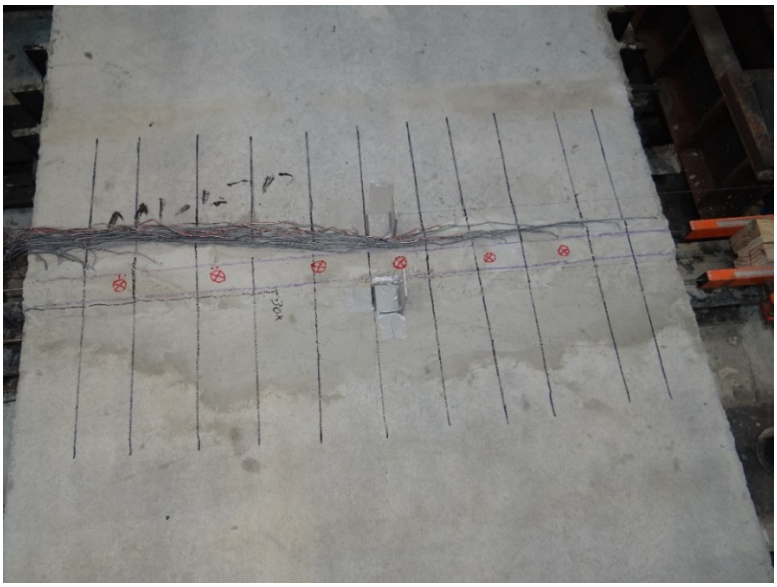

Figure 4-71 The first crack in the connection (at +30 Kips) for cyclic in-plane shear deformation (6 Studs,180^{o} hooked rebars) test.

A new crack occurred at -30 Kips (cycle # -24) and the relative displacement is (+0.0067 in.) as it can be seen in Figure 4-72. The crack started at the contact of the plank (roller side) with the connection, it's parallel to the direction of loading and it occurred at the west end of the connection and the width of crack is 0.1mm.

Figure 4-72 A new crack occurred in the roller side –west end at -30 Kips

The propagation of crack at the west end was noticed at +35 Kips (cycle # +27) as illustrated in Figure 4-73 . the relative displacement is (+0.0028 in.) and the width of crack is 0.1mm.

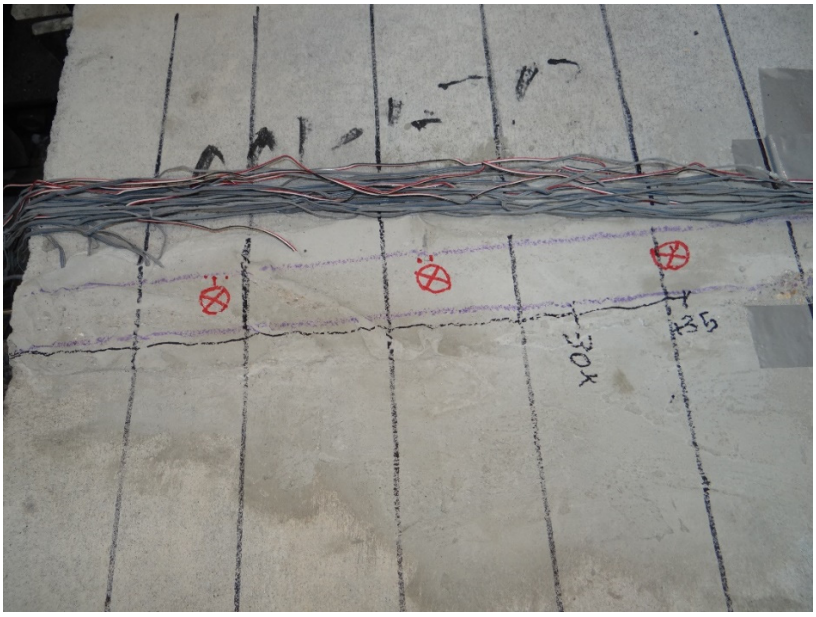

Figure 4-73 Propagation of crack +35 Kips.

The propagation of crack in the east end was noticed at -35 Kips (cycle # -27) as illustrated in Figure 4-74. The relative displacement is (+0.0028 in.) and the width of crack is 0.1mm.

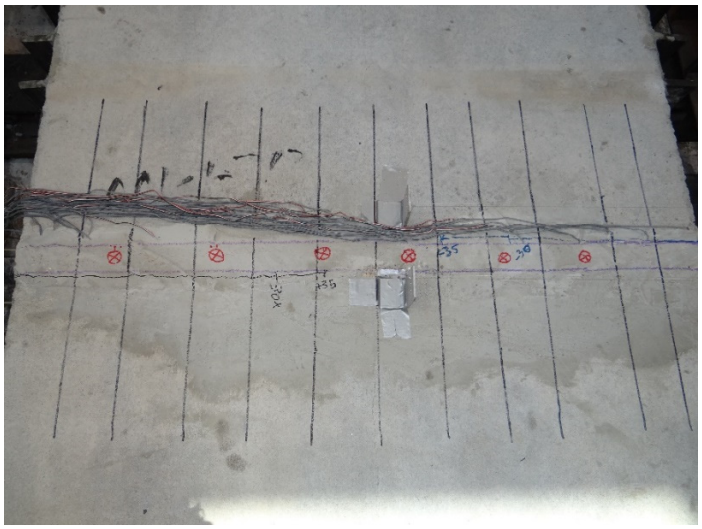

Figure 4-74 Propagation of crack -35 Kips.

No new cracks or propagation were noticed at +40K (cycle # +30) and -40 Kips (cycle # -30). The relative displacement is (0.0024in.) and (0.0028 in) respectively, and the width of crack is 0.1mm.

A new crack occurred at +45 Kips (cycle # +33) in the middle of connection (Fixed side) as shown in Figure 4-75. The relative displacement is (-0.0114”). The width of crack is 0.1mm.

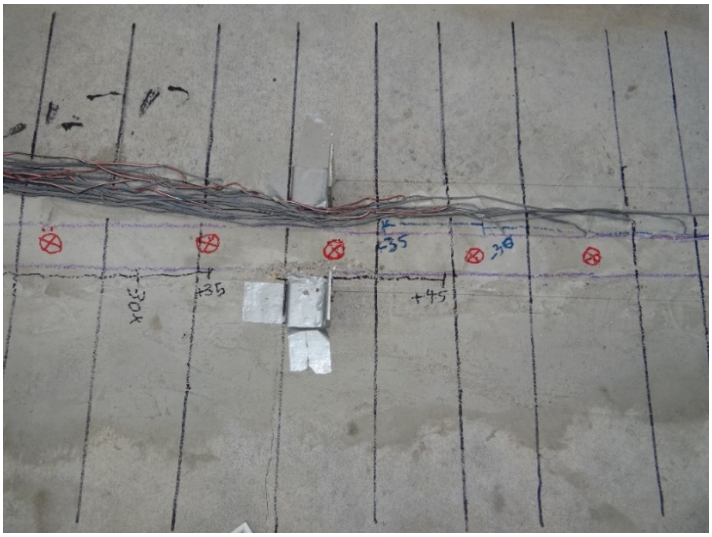

Figure 4-75 A new crack occurred at +45 Kips.

The propagation of crack in the middle of connection was noticed at -45 Kips (cycle # -33) in the fixed side as it can be seen in Figure 4-76 . The relative displacement is (-0.0094") and the width of crack is 0.1mm.

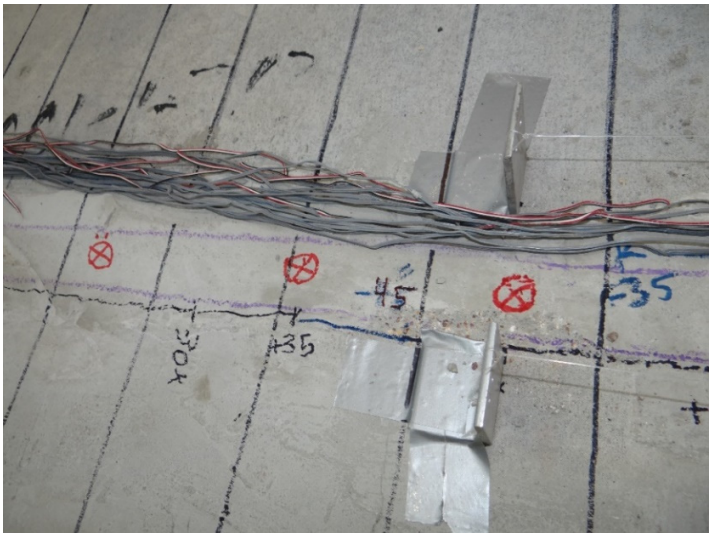

Figure 4-76 The propagation of crack at -45 Kips.

Some diagonal cracks were noticed at +50 Kips (cycle # +36) as it can be seen in Figure 4-77. The relative displacement is (-0.0181").

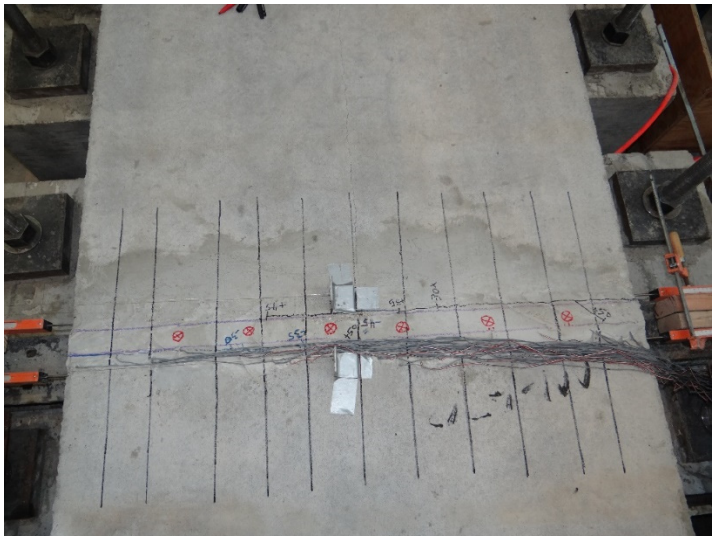

Figure 4-77 diagonal cracks at +50 Kips

Some diagonal cracks also were also noticed at -50 Kips (cycle # -36) as shown in Figure 4-78. The relative displacement is (-0.0067”).

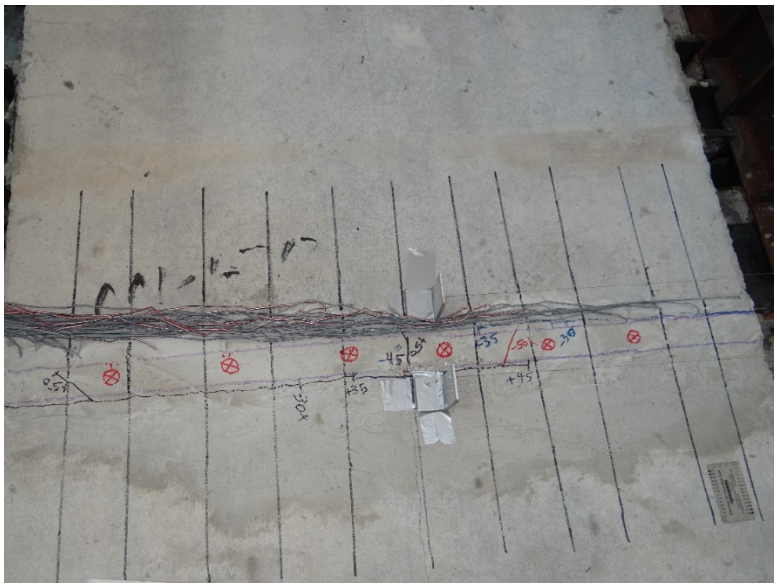

Figure 4-78 Diagonal cracks also at -50 Kips.

Some diagonal cracks also were also noticed at +55 Kips (cycle # +39) as illustrated in Figure 4-79. The relative displacement is (-0.0244”).

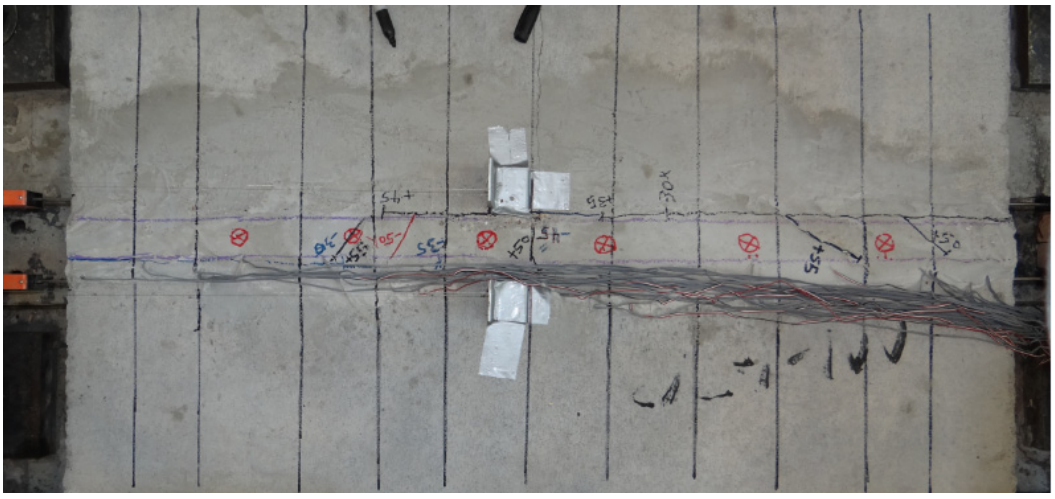

Figure 4-79 Diagonal cracks also at +55 Kips.

When the load reached -55 Kips (cycle # -39) , many cracks were noticed and the load started dropping:

- Propagation of the cracks in the planks along the steel rebar.
- New cracks in the plank (roller side) along the steel rebars and perpendicular to the direction of load were noticed.
- The width of some cracks was 5mm.

Figure 4-80 Overview of the cracks at -55 Kips.

Based on Figure 4-81 which shows the locations of LVDTs for this test, the relative displacement and the deformation of the hollow-core planks were calculated using the same equations that used in the previous test.

(L4, L5) and (L7,L8) are LVDTs were used as backups to measure the relative displacements and L1 was used to notice if the middle beam moves during the test. However, the readings of L1 showed that the middle beam did not move during the test.

Figure 4-82 through Figure 4-84 show the relationship between the applied load and the relative displacement of the connection. The maximum shear strength of the connection is -55 Kips and the relative displacement is 0.0228 in.

Figure 4-85 shows the relationship between the applied load and the deformation of the HCS. The deformation of the HCS at the maximum shear strength is 0.23 in.

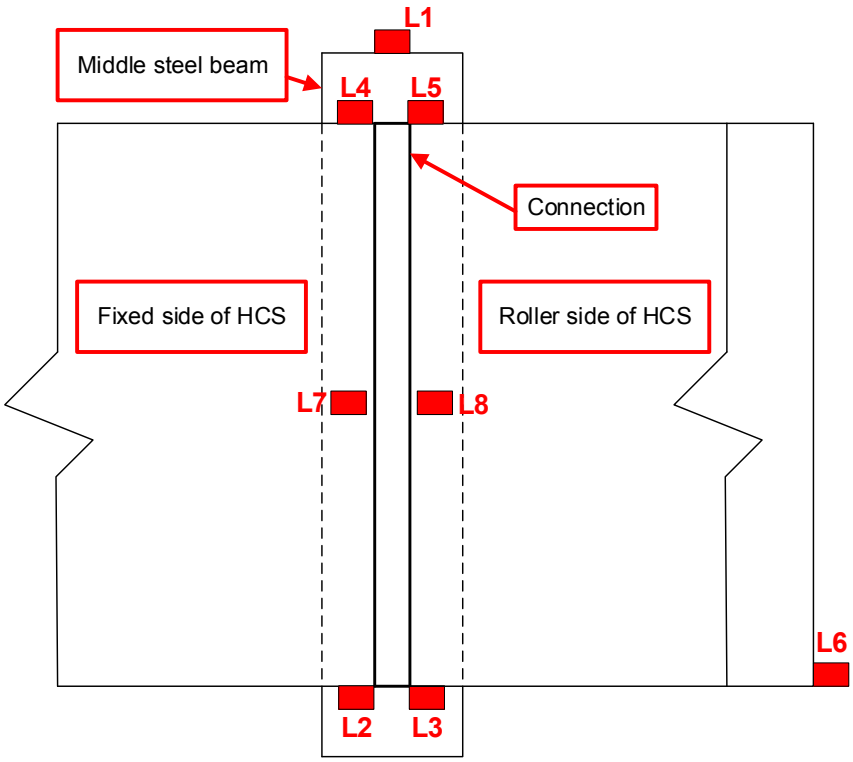

Figure 4-81 LVDTs locations.

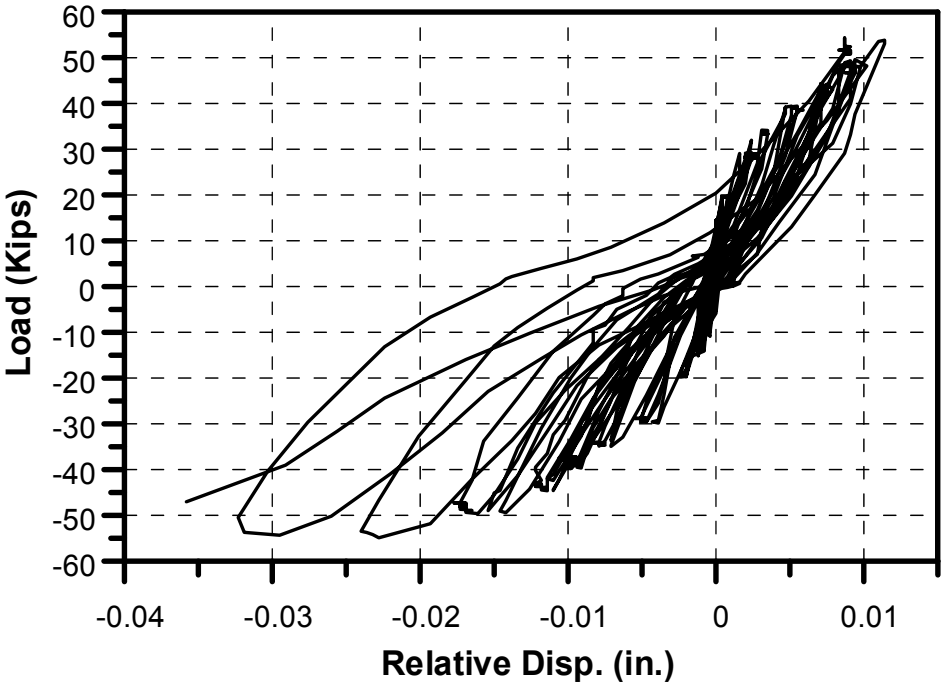

Figure 4-82 Load-Relative displacement loops curve.

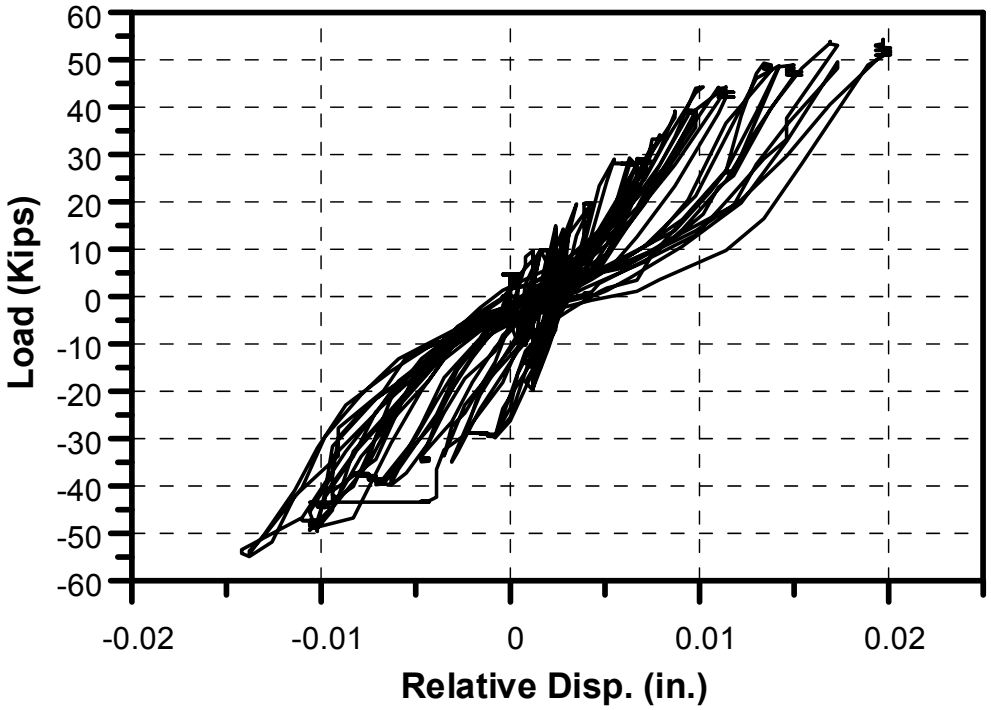

Figure 4-83 Load-Relative displacement loops curve (Backup).

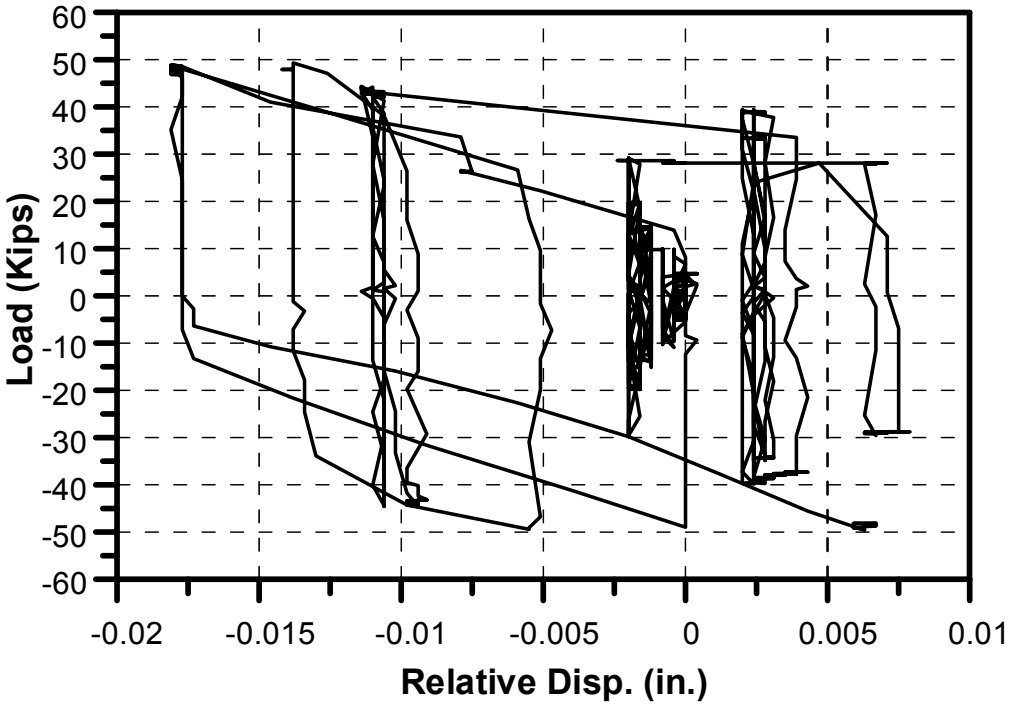

Figure 4-84 Load-Relative displacement loops curve (Backup).

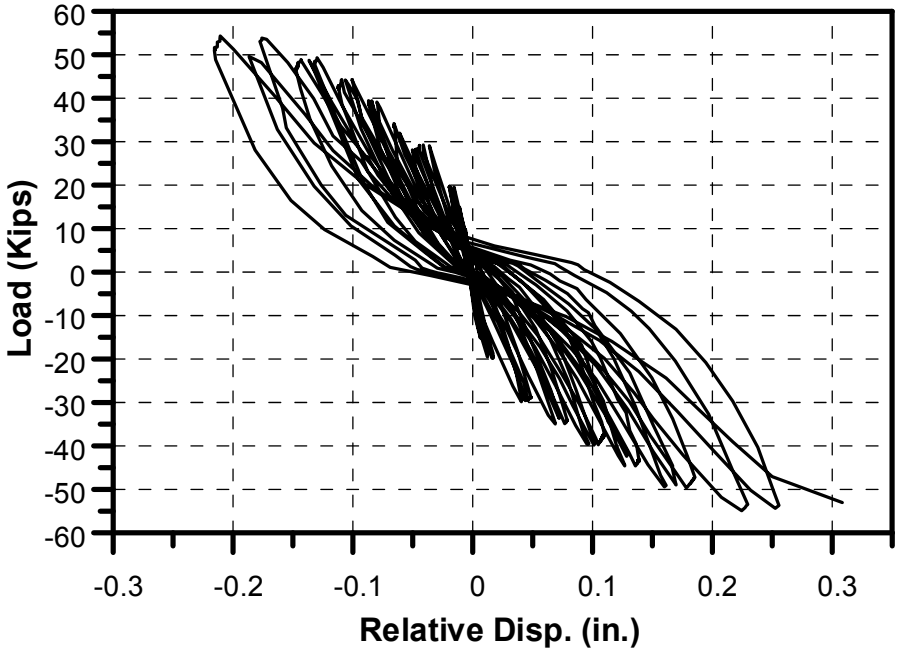

Figure 4-85 Load-Relative deformation HCS curve

4.4.1 Results of strain gauges on the shear studs

With reference to Figure 4-86 which shows the locations of shear studs, Figure 4-87 through Figure 4-98 show the load-strain curve for all the shear studs that used in this test.

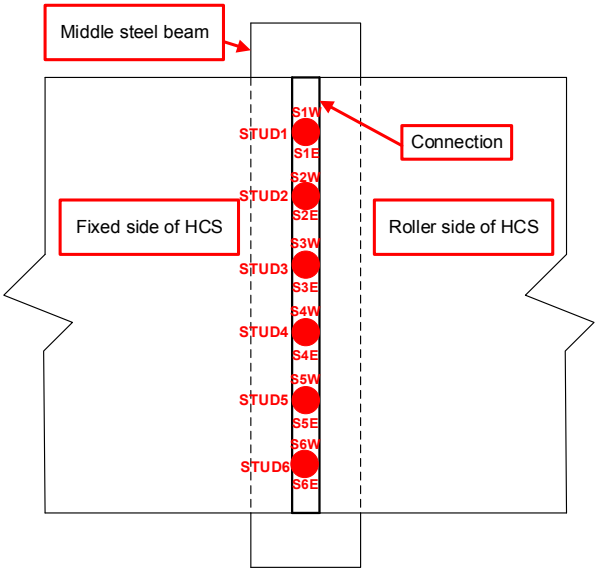

Figure 4-86 Shear studs' locations.

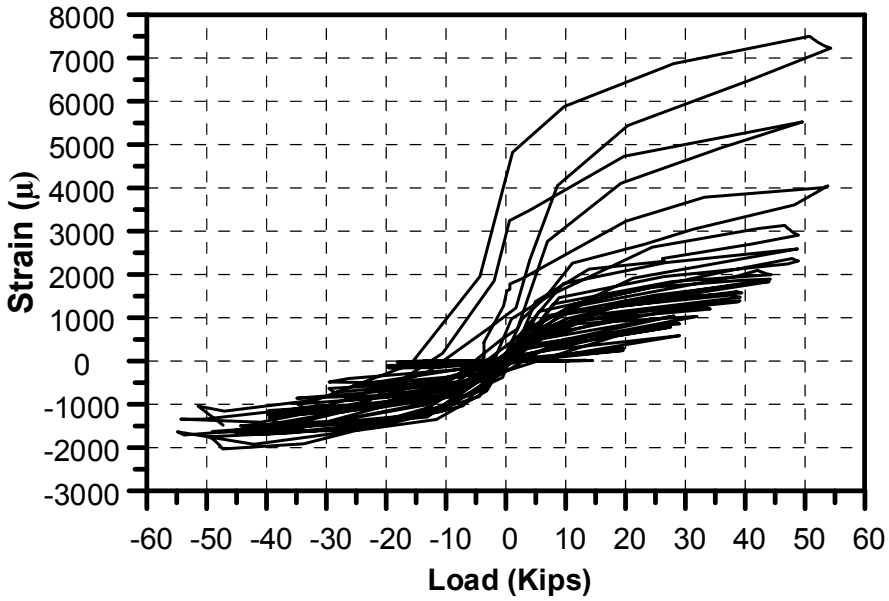

Figure 4-87 Load-strain curve for stud #1 (S1W).

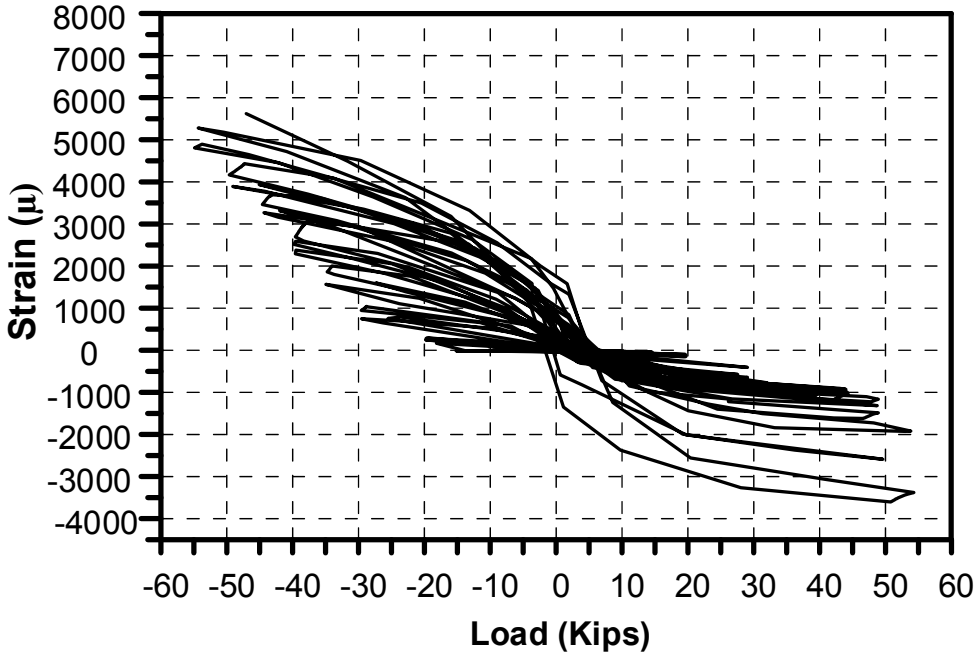

Figure 4-88 Load-strain curve for stud #1 (S1E).

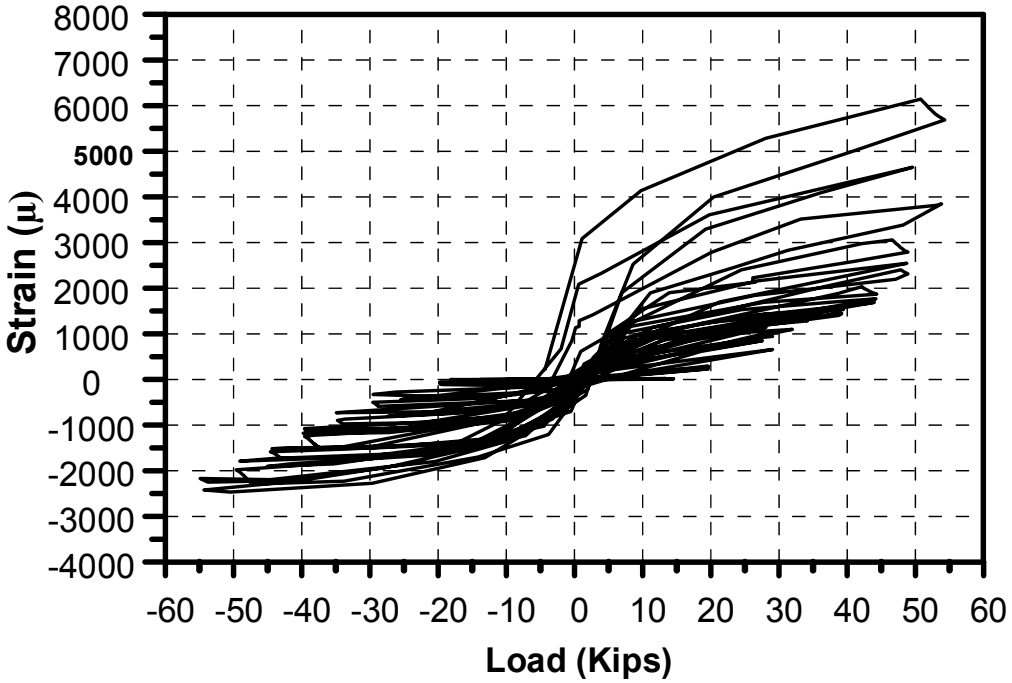

Figure 4-89 Load-strain curve for stud #2 (S2W).

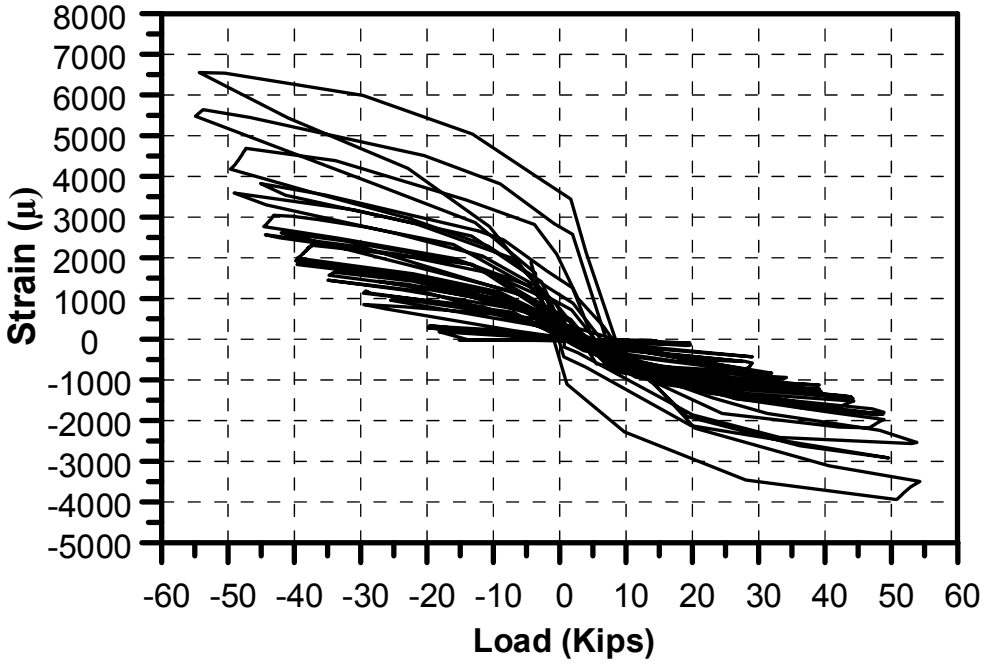

Figure 4-90 Load-strain curve for stud #2 (S2E).

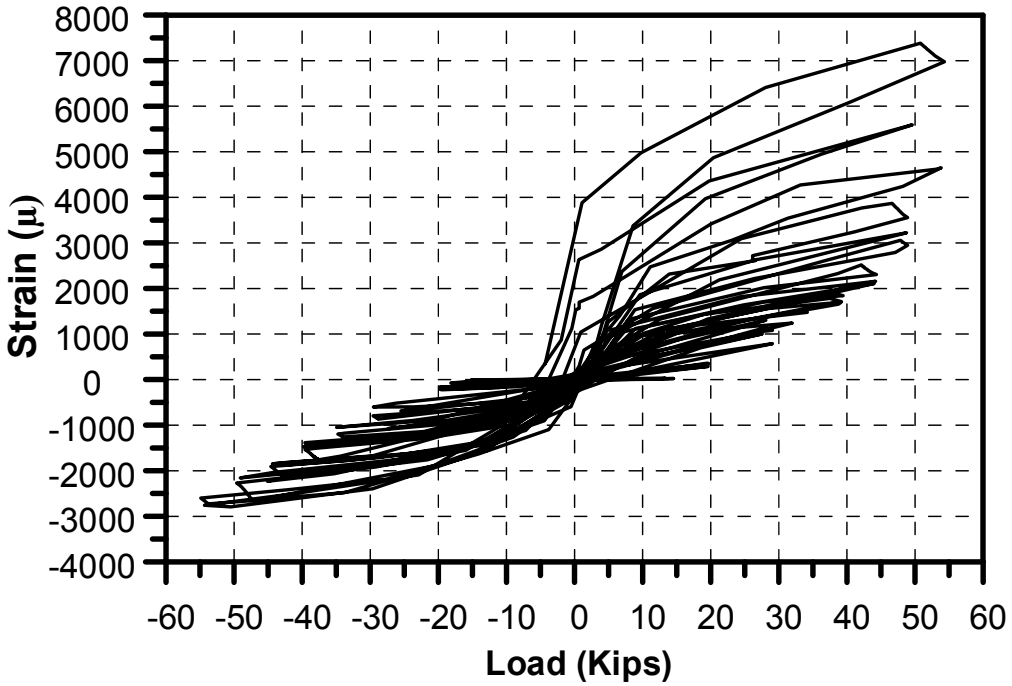

Figure 4-91 Load-strain curve for stud #3 (S3W).

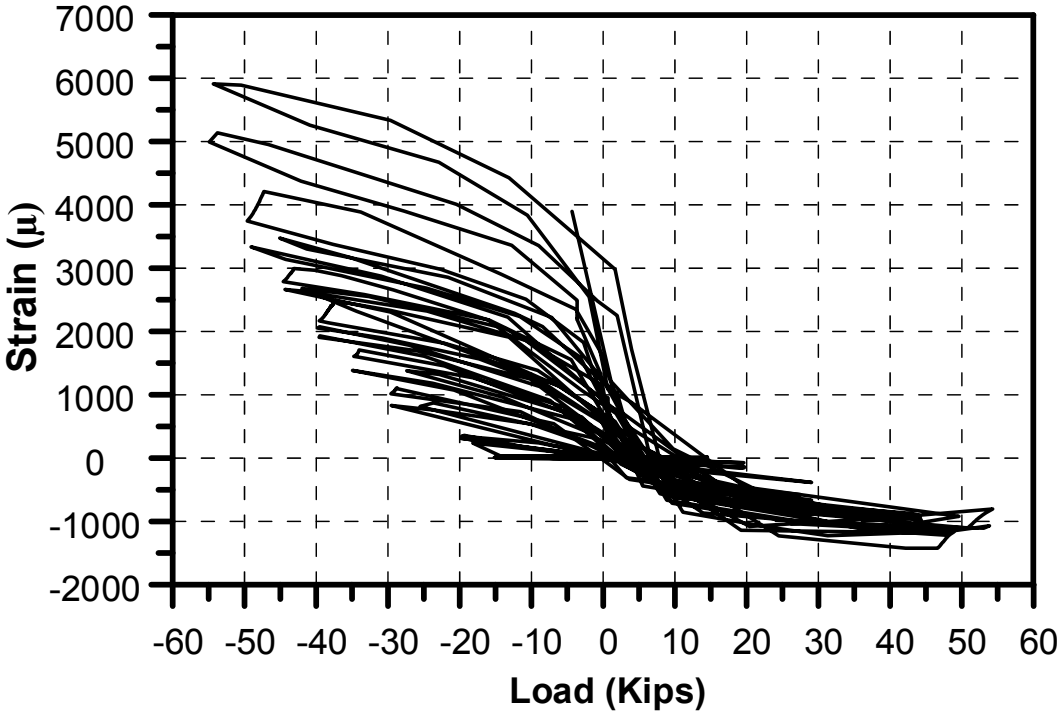

Figure 4-92 Load-strain curve for stud #3 (S3E).

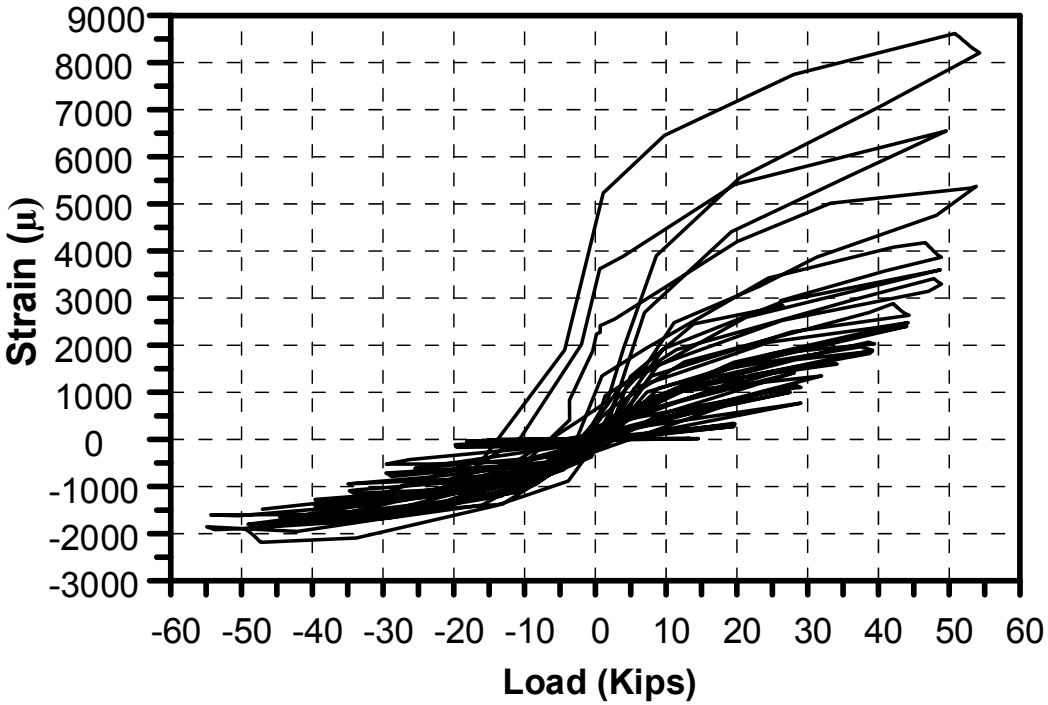

Figure 4-93 Load-strain curve for stud #4 (S4W).

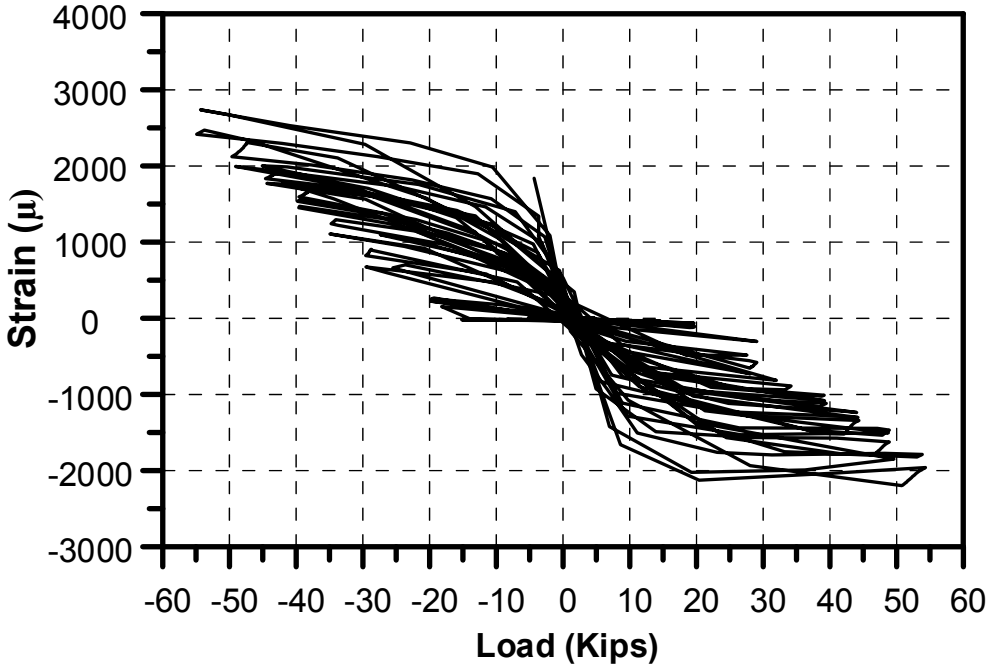

Figure 4-94 Load-strain curve for stud #4 (S4E).

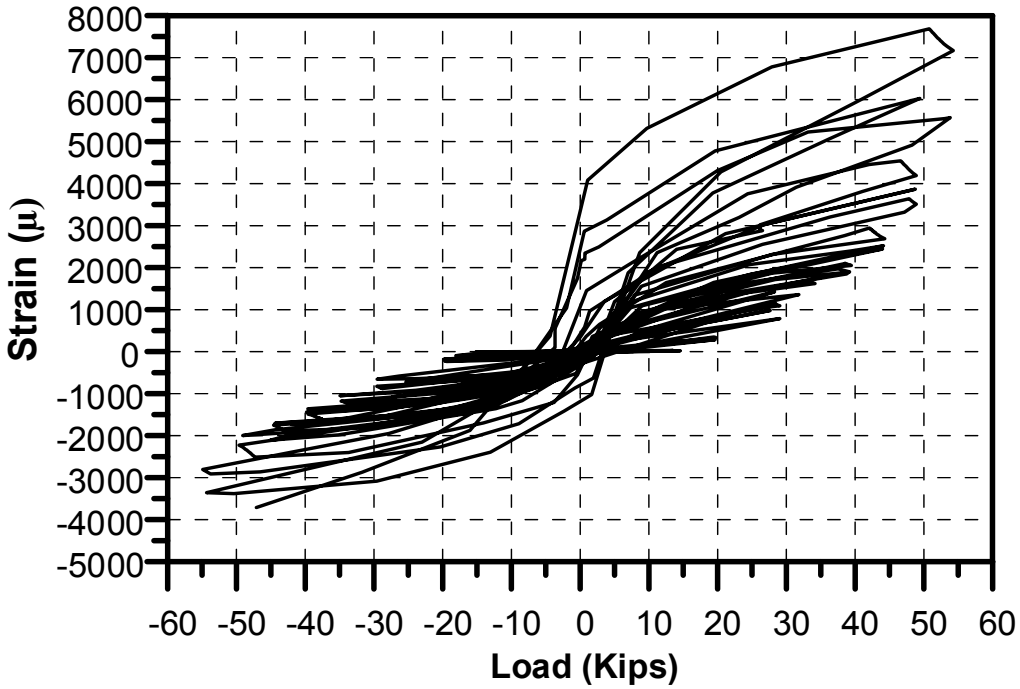

Figure 4-95 Load-strain curve for stud #5 (S5W).

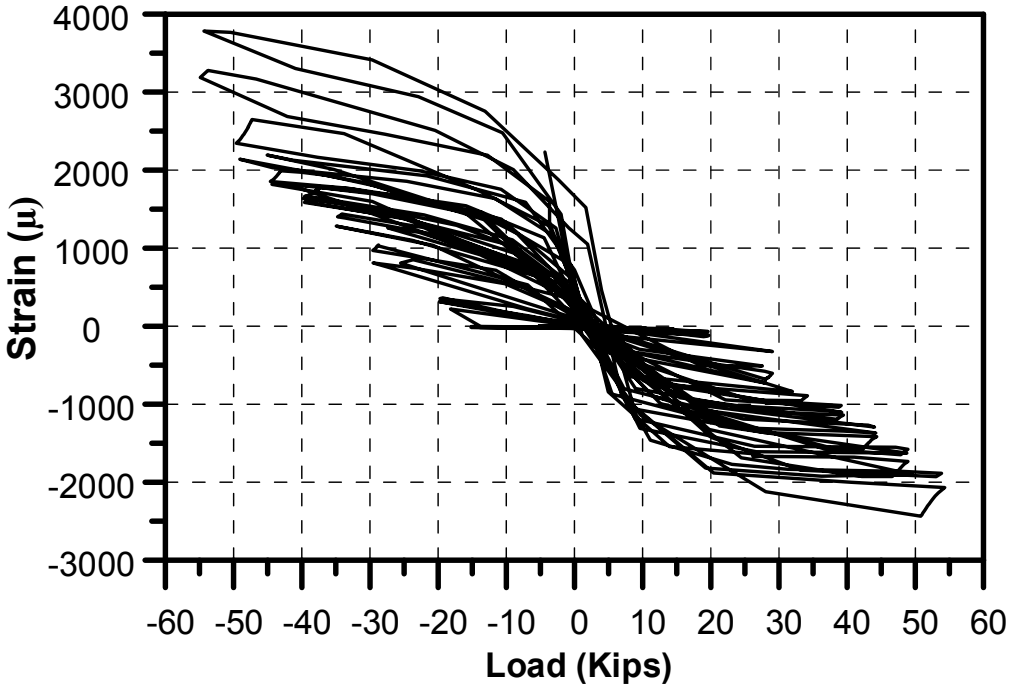

Figure 4-96 Load-strain curve for stud #5 (S5E).

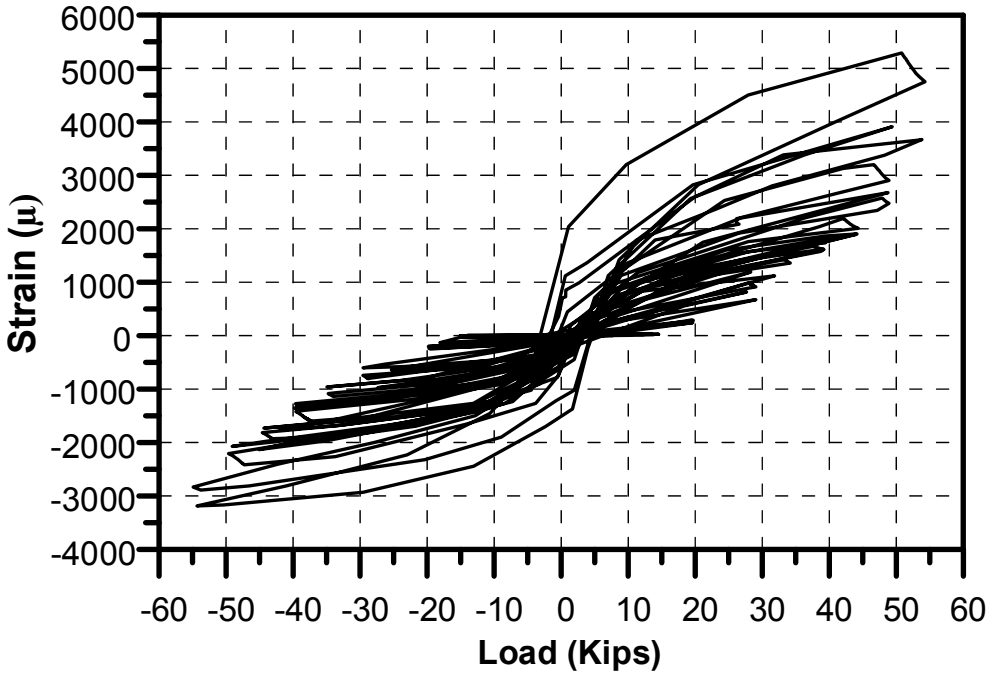

Figure 4-97 Load-strain curve for stud #6 (S6W).

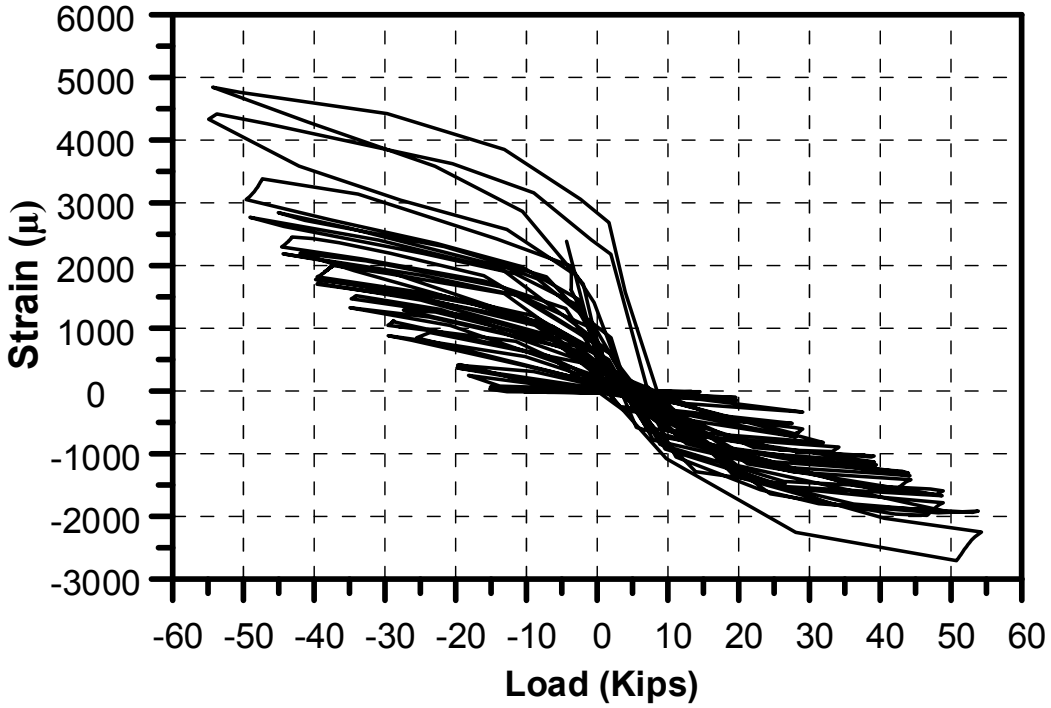

Figure 4-98 Load-strain curve for stud #6 (S6E).

4.4.2 Results of strain gauges on the steel rebars

The same locations of steel rebars in the previous test is also used in this test. Therefore, with reference to Figure 4-55, the Figure 4-99 through Figure 4-111 show the load-strain curve for all the rebars that used in this test. However, the two strain gauges on rebar #10 were not measuring due to damage during the setup or the test.

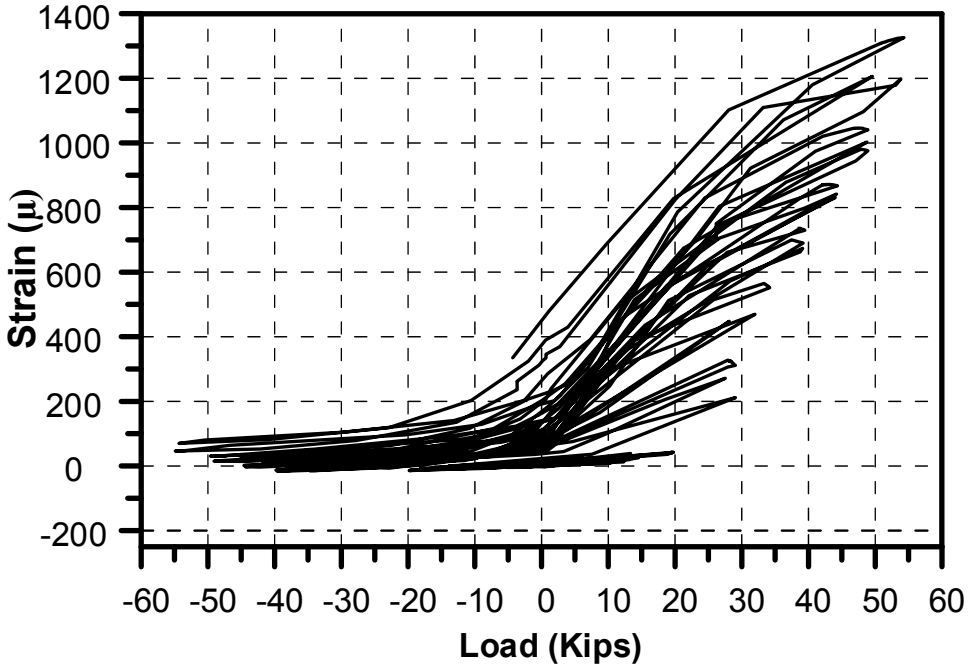

Figure 4-99 Load-strain curve for rebar#1 (fixed side)-R1L.

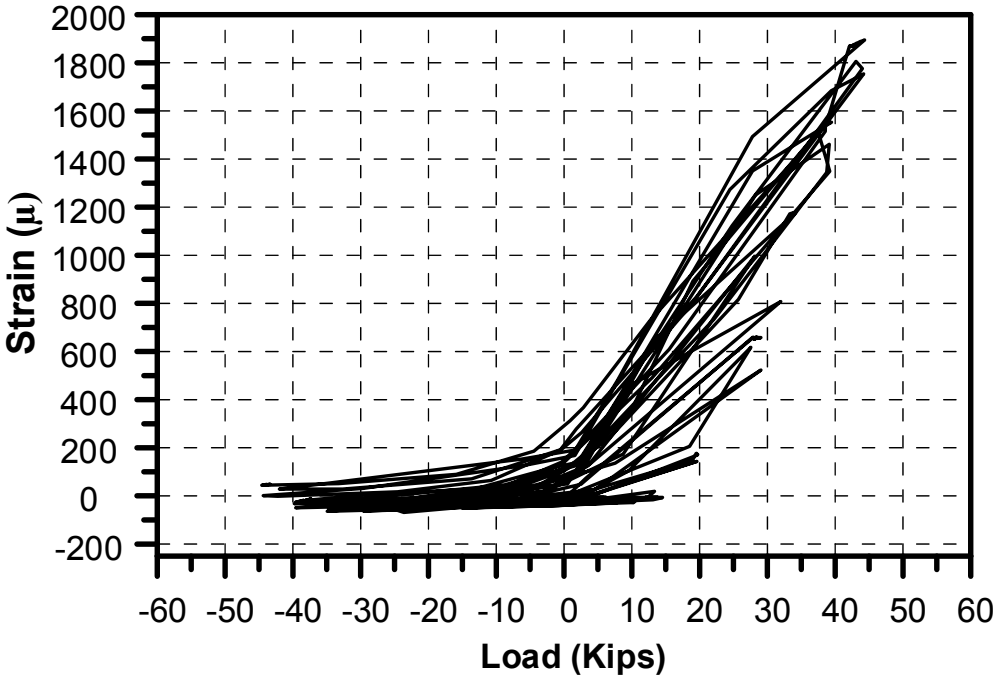

Figure 4-100 Load-strain curve for rebar#1 (middle)-R1L.

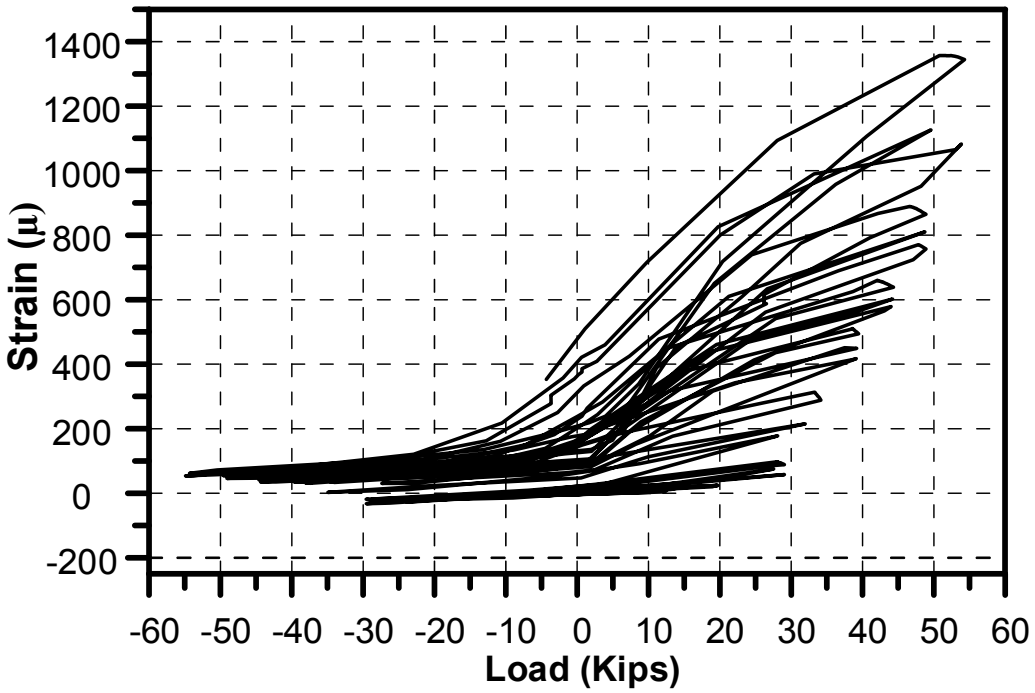

Figure 4-101 Load-strain curve for rebar#1 (roller side)-R1R.

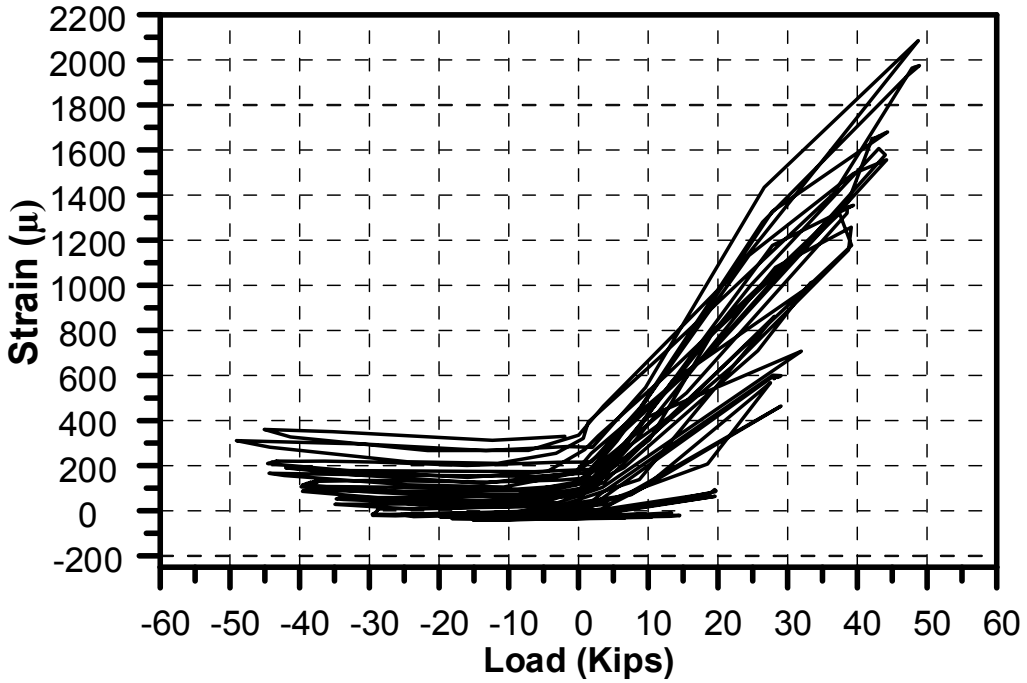

Figure 4-102 Load-strain curve for rebar#2-R2.

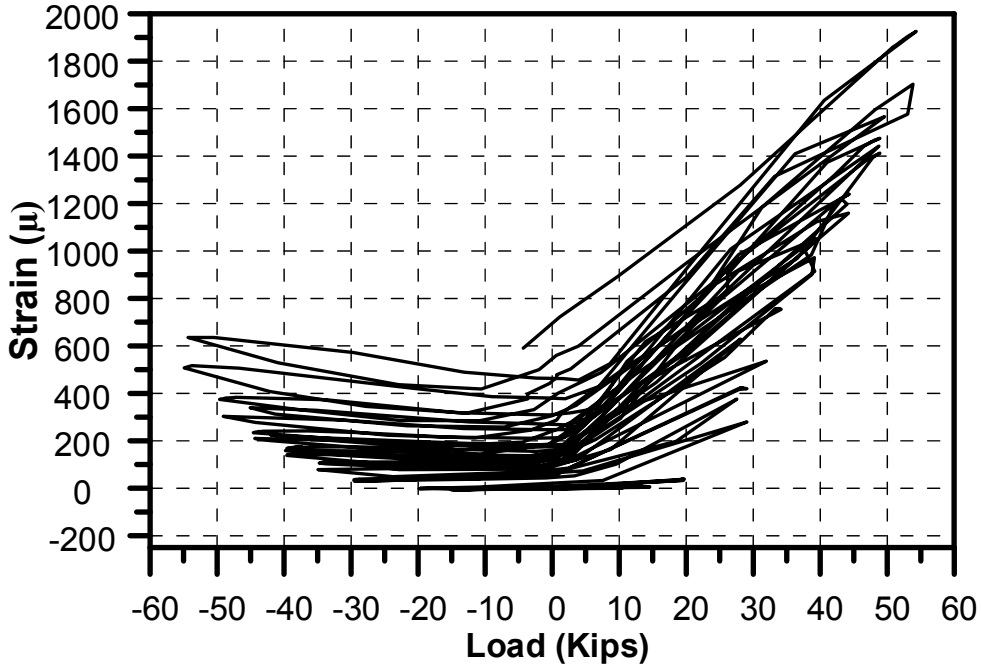

Figure 4-103 Load-strain curve for rebar#3-R3.

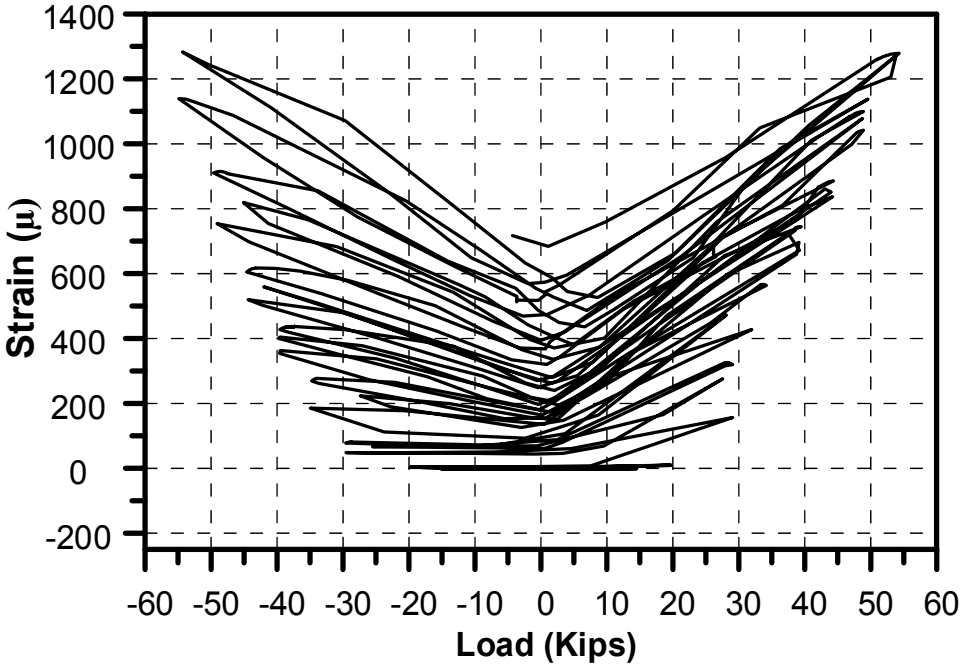

Figure 4-104 Load-strain curve for rebar#4-R4.

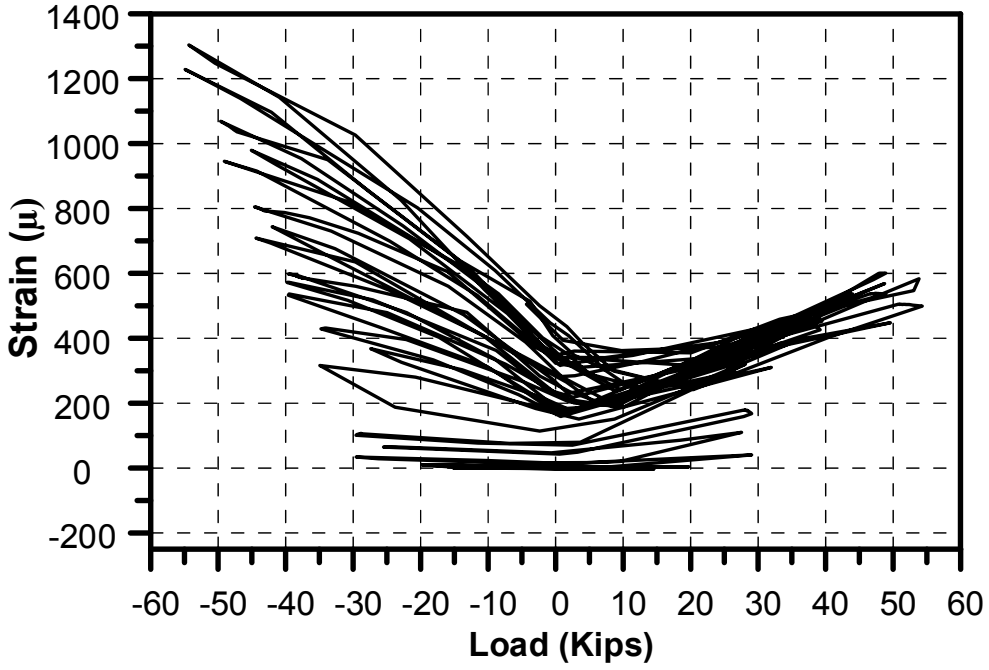

Figure 4-105 Load-strain curve for rebar#5 -R5.

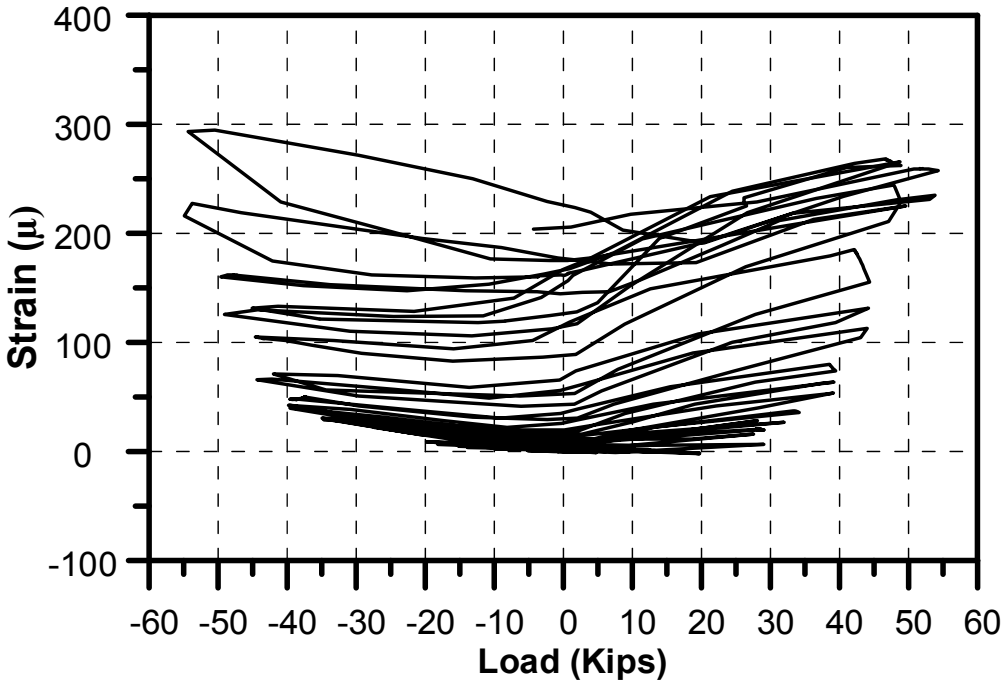

Figure 4-106 Load-strain curve for rebar#5 (roller side)-R6R

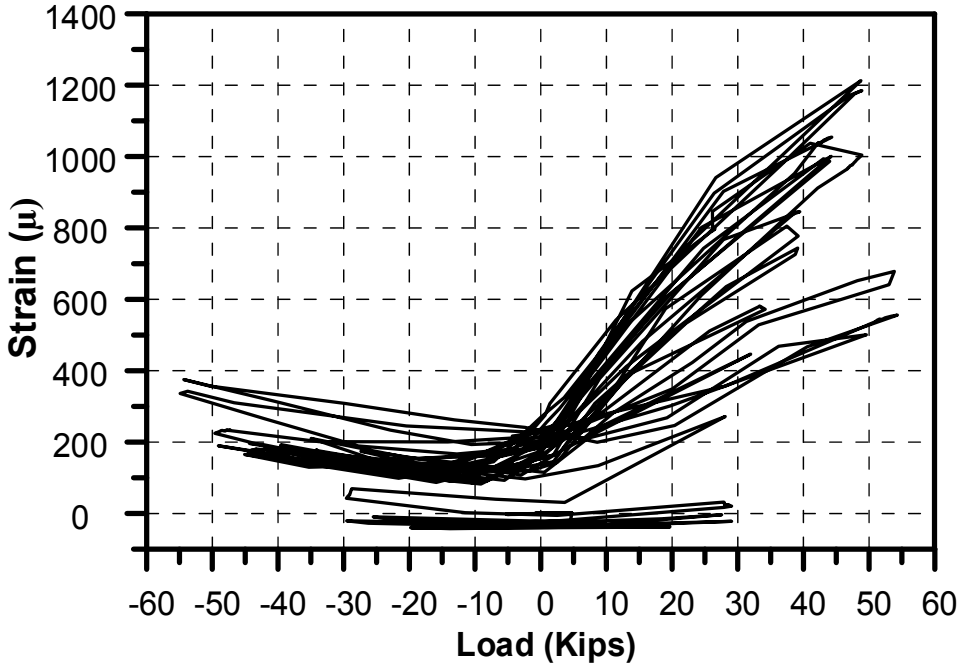

Figure 4-107 Load-strain curve for rebar#6 (middle)-R6.

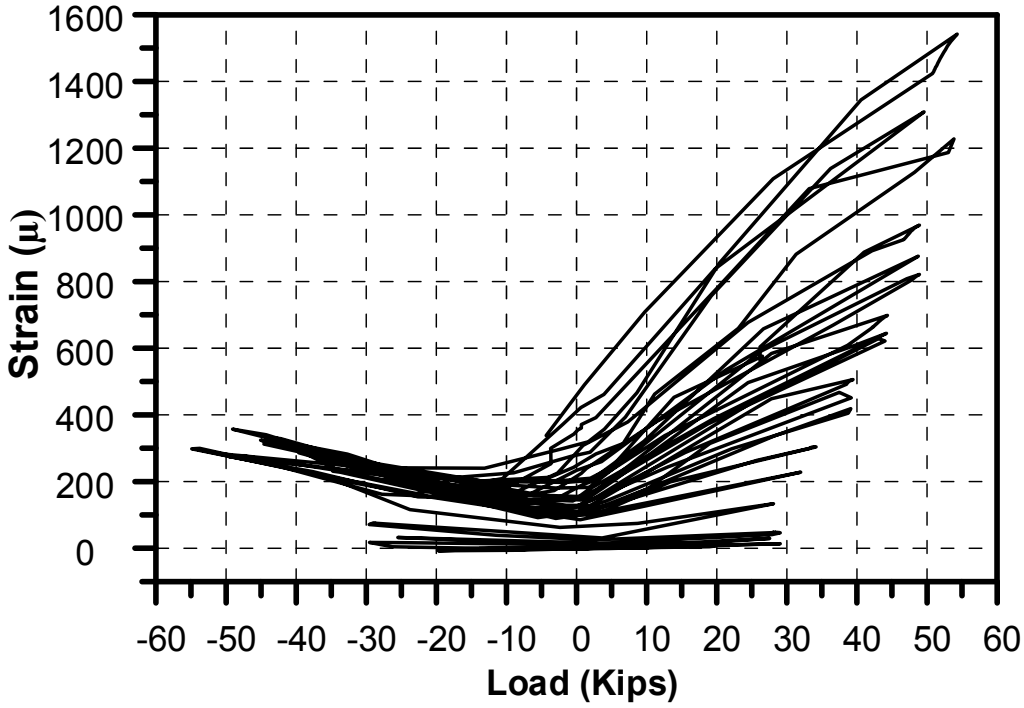

Figure 4-108 Load-strain curve for rebar#7-R7.

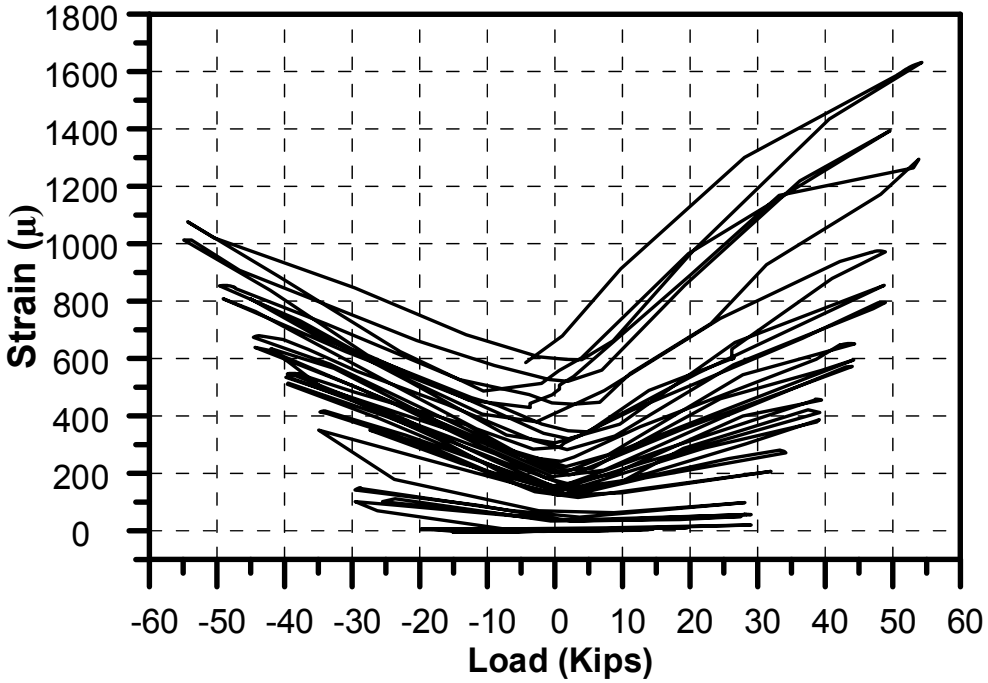

Figure 4-109 Load-strain curve for rebar#8-R8.

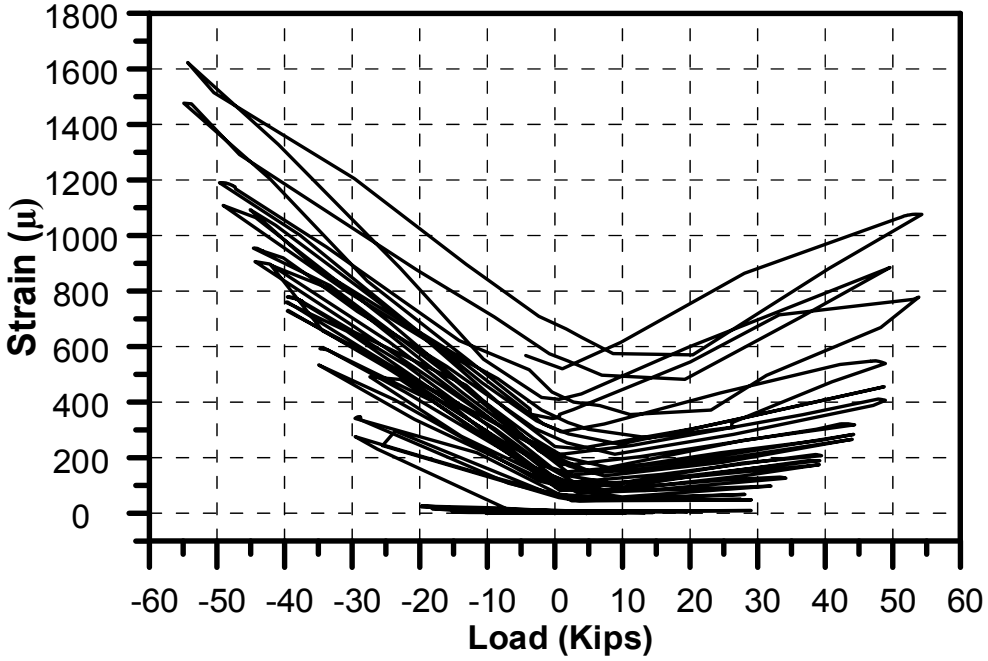

Figure 4-110 Load-strain curve for rebar#9-R9.

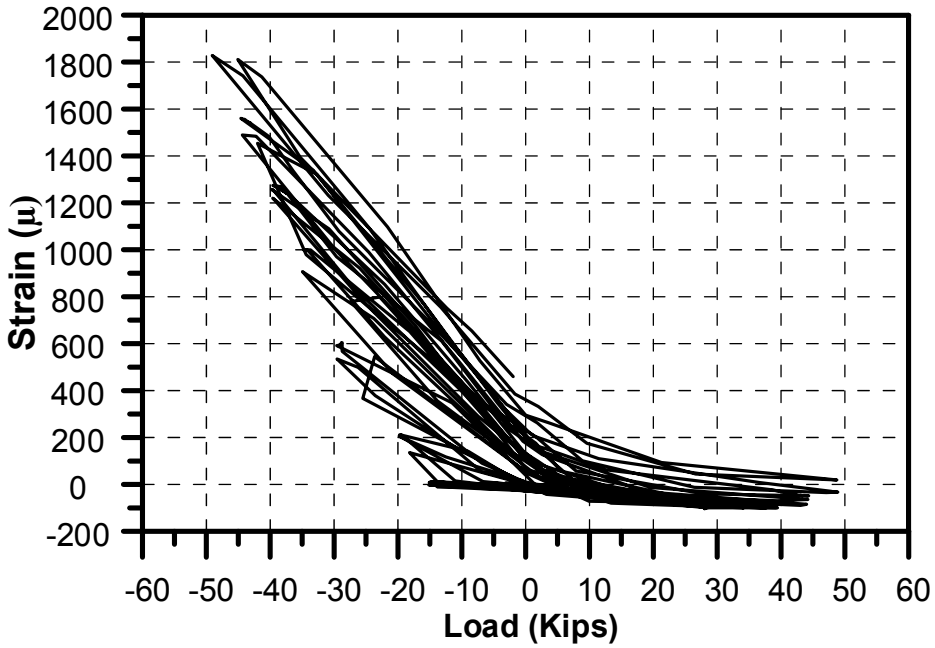

Figure 4-111 Load-strain curve for rebar#11-R11.

4.4.3 Analysis and discussion of the results

The results also showed that there was no crack developed before 30 Kips. The relative displacement of the first crack at 30 Kips was 0.0008 in. That means the shear resistance of the of the connection before onset the cracks is 7.5 Kips/ft.

The maximum load that the connection resisted before failure was 55 Kips and the relative displacement at that load was 0.0228 in. However, the failure in the hollow core panels occurred along the steel rebars and at the ends of steel rebars inside the openings of the planks.

All the shear studs yielded in this test and they started yielding at load range (45 Kips-50 Kips). However, no fracture was noticed in the shear studs. Therefore, it can be concluded that the failure of this specimen is only due to insufficient strength of the hollow-core planks to resist the shear force at the connection area.

Yielding in steel rebars occurred in rebars 1,2,3, and 11. Moreover, the maximum strain values were also noticed at the middle of rebars compared with roller and fixed sides. However, the roller side of rebars has more strains compared with fixed side.

4.5 Cyclic in-plane shear deformation Test (6 Studs+180^o hooked rebars+2" topping)

Based on the results of the previous test which showed that the hollow-core planks have insufficient strength to resist the shear force at the connection area, 2 in. concrete topping was casted over the hollow-core panels to investigate if that increases the shear strength of the planks and the connection as well.

The specimen was prepared as described in section 3.5 and the setup before starting the test is shown in Figure 3-69 and Figure 3-70. The same loading protocol that used in the previous test was also used in this test.

The test was begun by applying cyclic load according to the loading protocol. No cracks were noticed on the topping slab or the hollow-core planks before reaching -55 Kips. However, there were relative displacements measured as shown in Table 4- 1 below.

Table 4- 1 Load-relative displacements before failure at (-55 Kips)

Cycle Number	Force (Kips)	Relative Displacement (in.)
(+) 24	(+) 30 K	(+) 0.002
(-) 24	(-) 30 K	(-) 0.0045
(+) 27	(+) 35 K	(+) 0.0059
(-) 27	(-) 35 K	(-) 0.0035
(+) 30	(+) 40 K	(+) 0.0091
(-) 30	(-) 40 K	(-) 0.0039
(+) 33	(+) 45 K	(+) 0.0091
(-) 33	(-) 45 K	(-) 0.0051
(+) 36	(+) 50 K	(+) 0.013
(-) 36	(-) 50 K	(-) 0.0051

(+) 39 (+) 55 K (+) 0.023

When the load reached -55 Kips cycle # (-39) with relative displacement 0.0065 in., dropping in force was noticed as it can be seen in Figure 4-112 through Figure 4-116 and they are:

- Damage in the planks at the location of applied load (local damage).
- Separation between the topping and the planks.
- Hairlines cracks were noticed on the top of topping slab.
- After removing the topping slab, many cracks were noticed in the plank.

Figure 4-112 Local damage at the location of applied load.

Figure 4-113 Separation between the topping and the planks at (-55 Kips).

Figure 4-114 Failure in the ends of connection at (-55 Kips).

Figure 4-115 Cracks on the top of topping slab at (-55 Kips).


Figure 4-116 Cracks in the planks after removing topping slab.

The same locations of LVDTs which are illustrated in Figure 4-81 were also used in this test. However, the readings of L1 showed that the middle beam did not move during the test.

Figure 4-117 through Figure 4-119 show the relationship between the applied load and the relative displacement of the connection. The maximum shear strength of the connection is -55 Kips and the relative displacement is 0.007 in.

Figure 4-120 shows the relationship between the applied load and the deformation of the HCS. The deformation of the HCS at the maximum shear strength is 0.1 in.

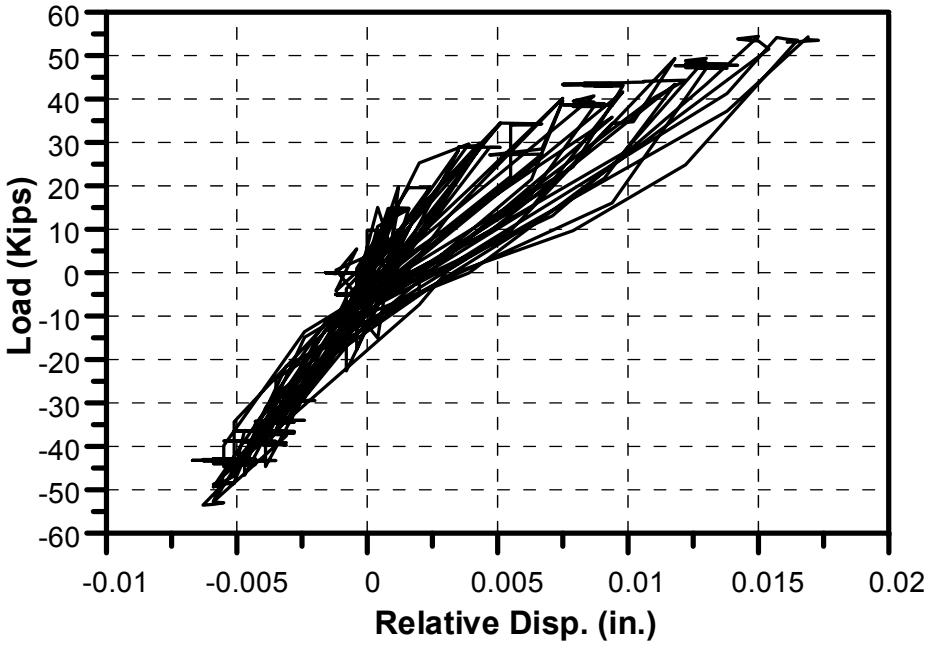

Figure 4-117 Load-Relative displacement loops curve.

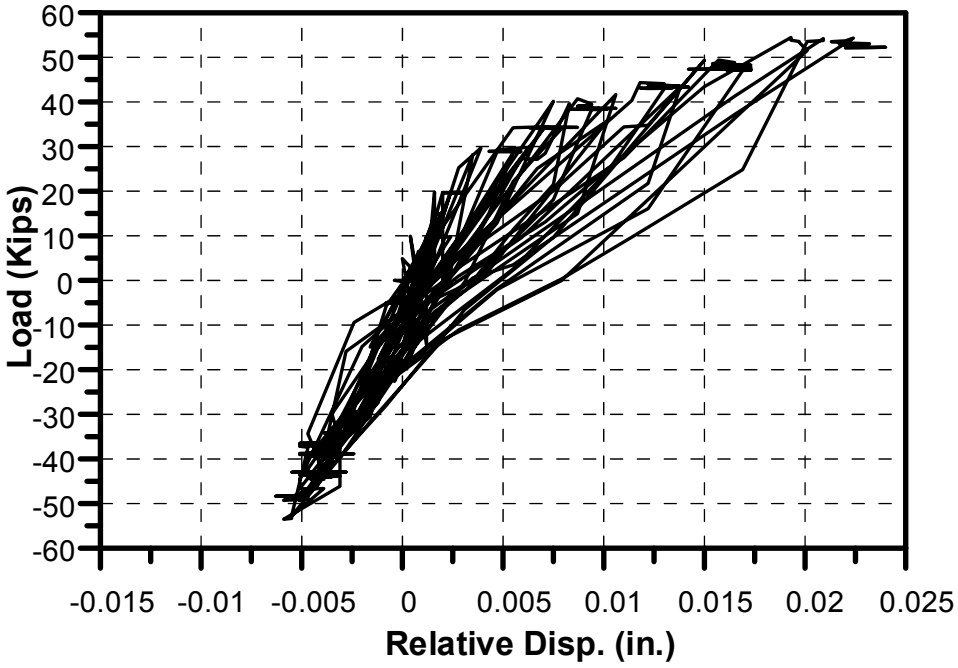

Figure 4-118 Load-Relative displacement loops curve (backup).

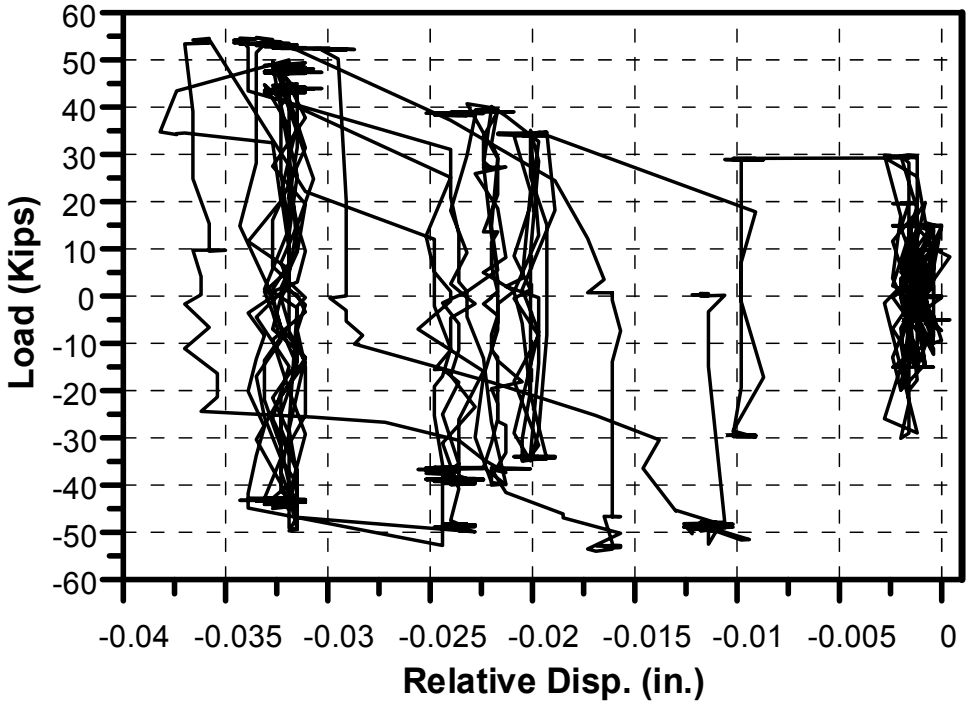

Figure 4-119 Load-Relative displacement loops curve (backup).

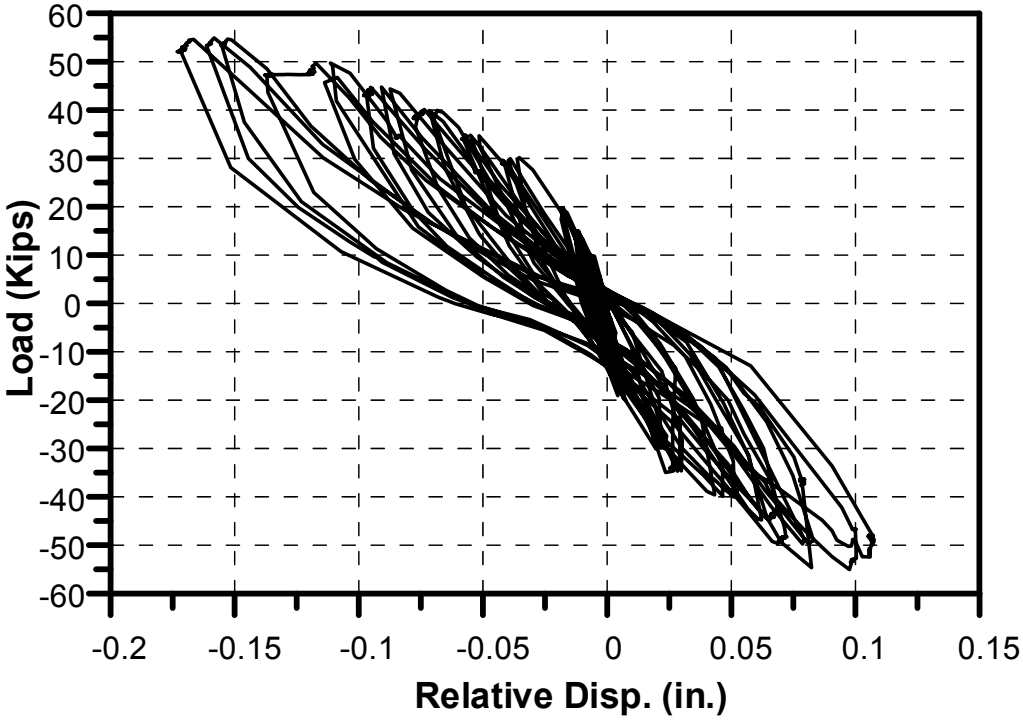

Figure 4-120 Load-Relative deformation HCS curve

4.5.1 Results of strain gauges on the shear studs

The same locations of shear studs which are illustrated in Figure 4-86 were also used in this test .Figure 4-121 through Figure 4-132 show the load-strain curve for all the shear studs that used in this test.

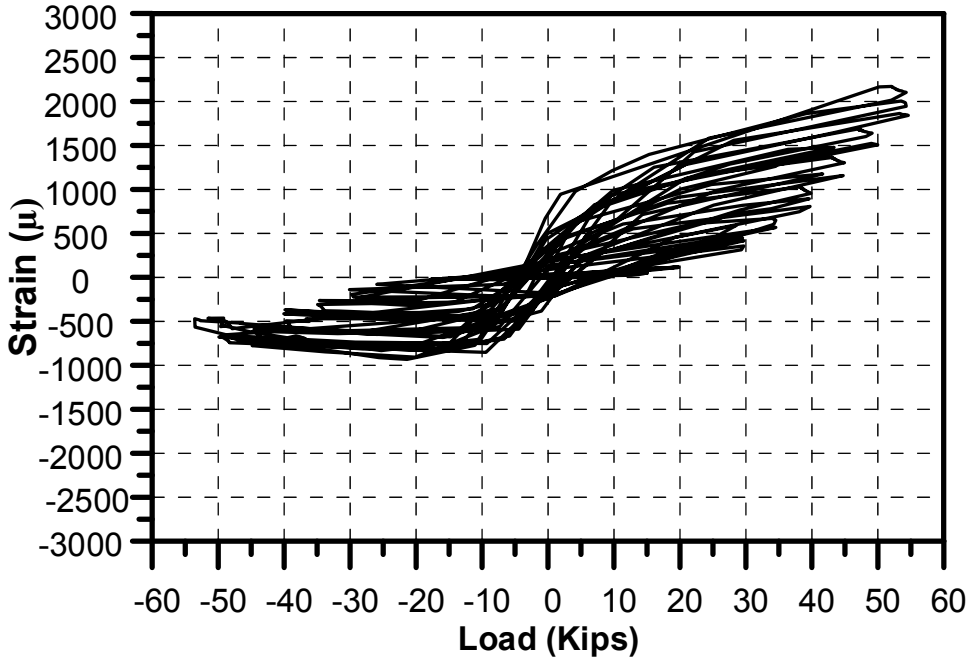

Figure 4-121 Load-strain curve for stud #1 (S1W).

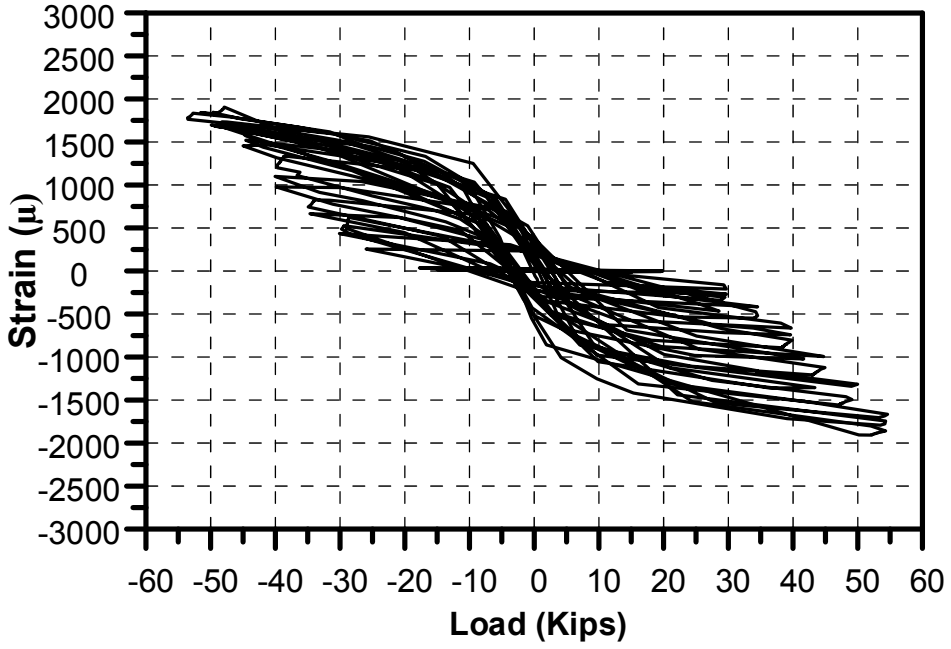

Figure 4-122 Load-strain curve for stud #1 (S1E).

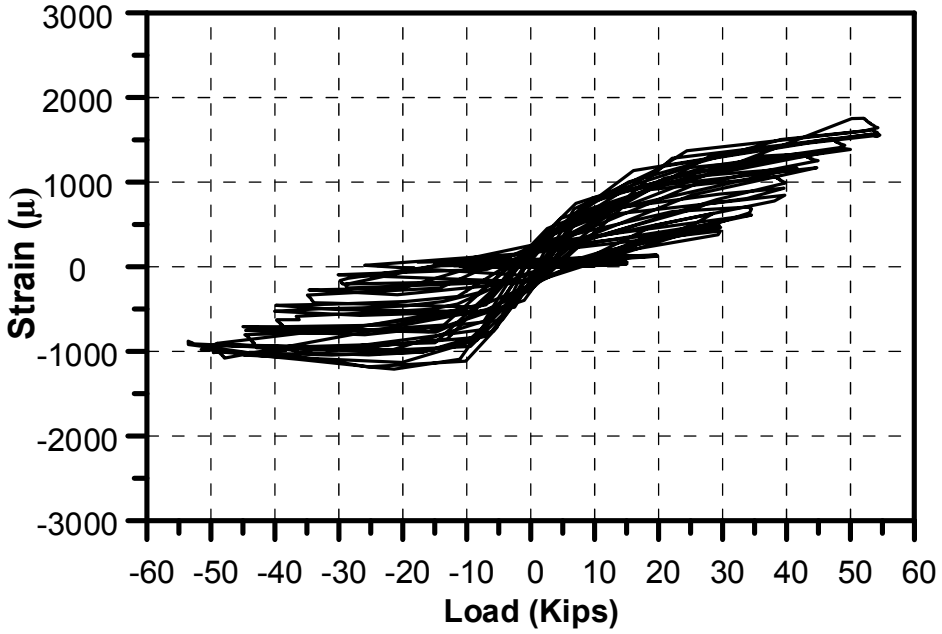

Figure 4-123 Load-strain curve for stud #2 (S2W).

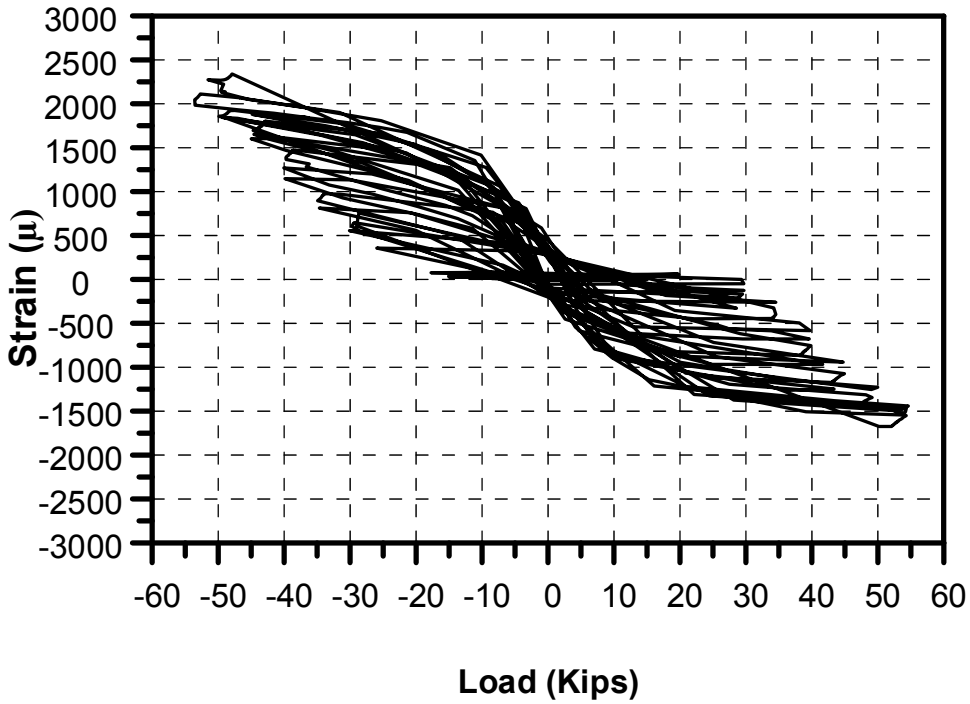

Figure 4-124 Load-strain curve for stud #2 (S2E).

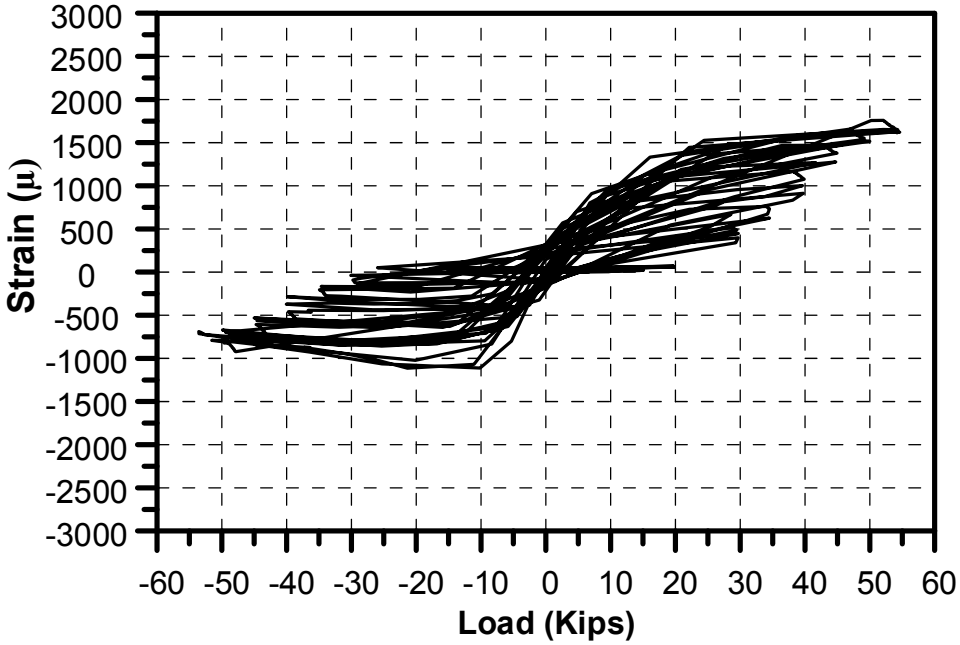

Figure 4-125 Load-strain curve for stud #3 (S3W).

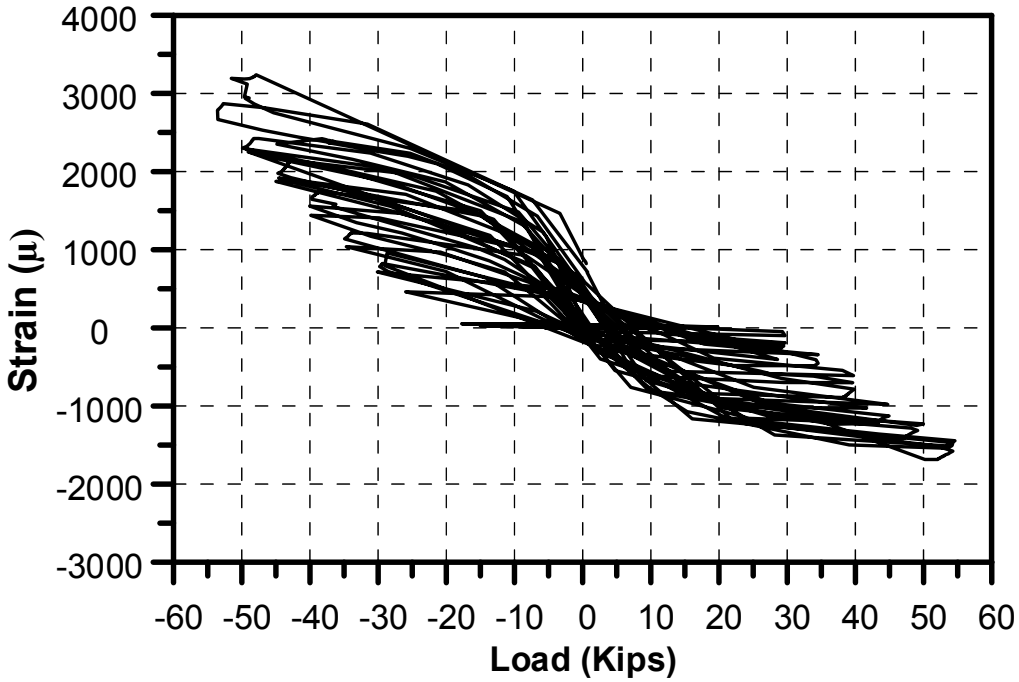

Figure 4-126 Load-strain curve for stud #3 (S3E).

.

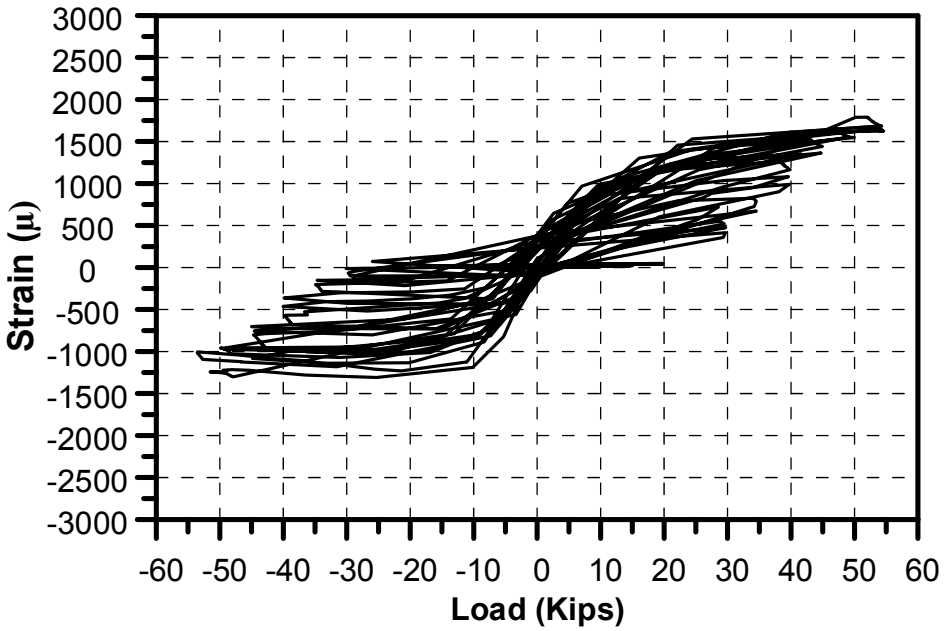

Figure 4-127 Load-strain curve for stud #4 (S4W).

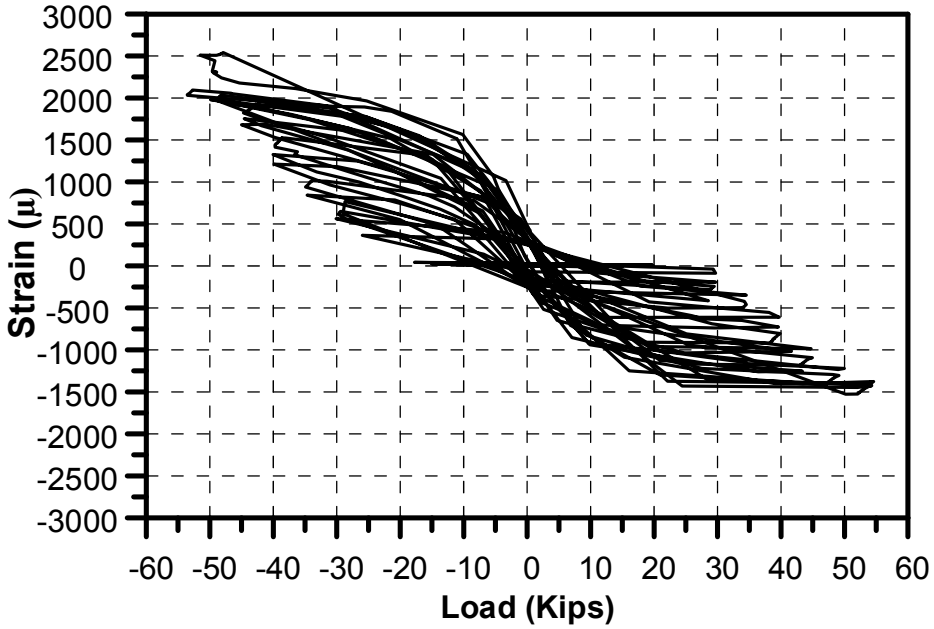

Figure 4-128 Load-strain curve for stud #4 (S4E).

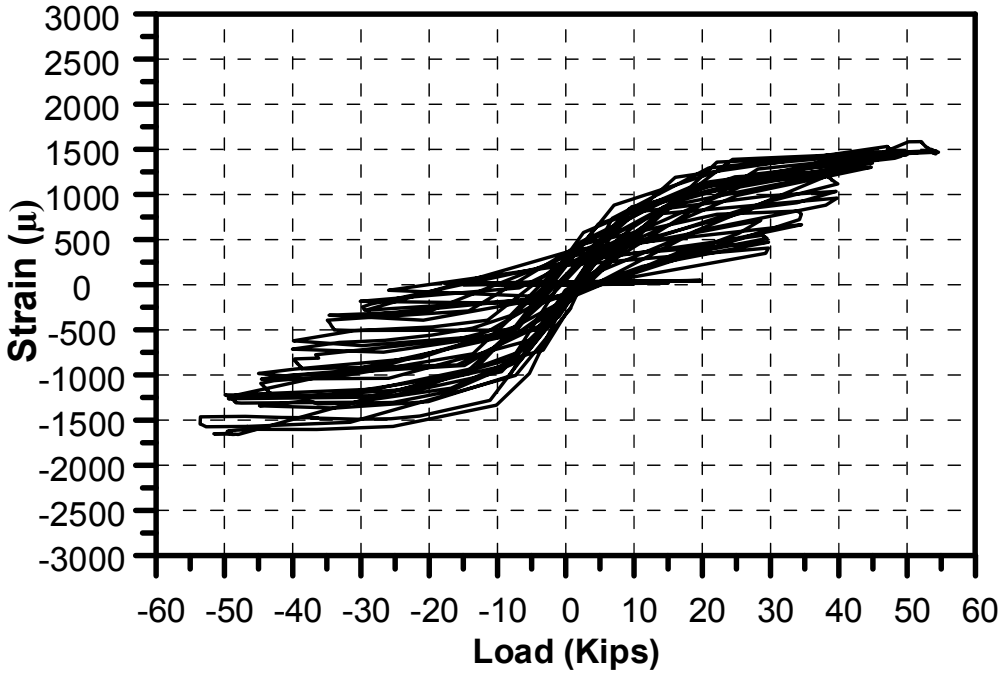

Figure 4-129 Load-strain curve for stud #5 (S5W).

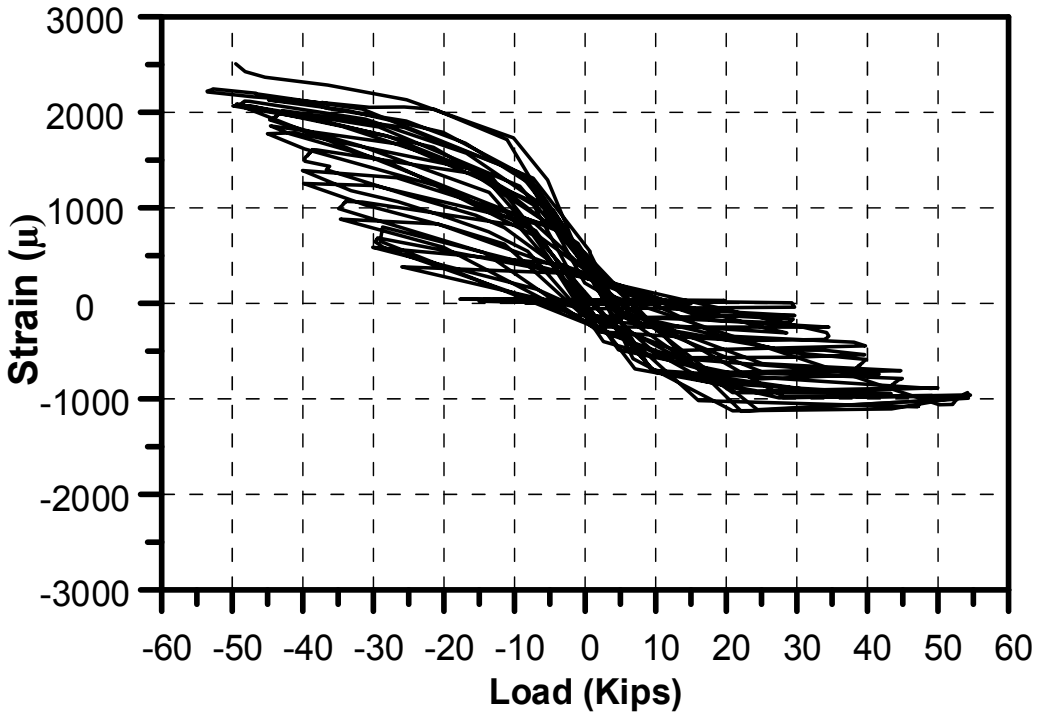

Figure 4-130 Load-strain curve for stud #5 (S5E).

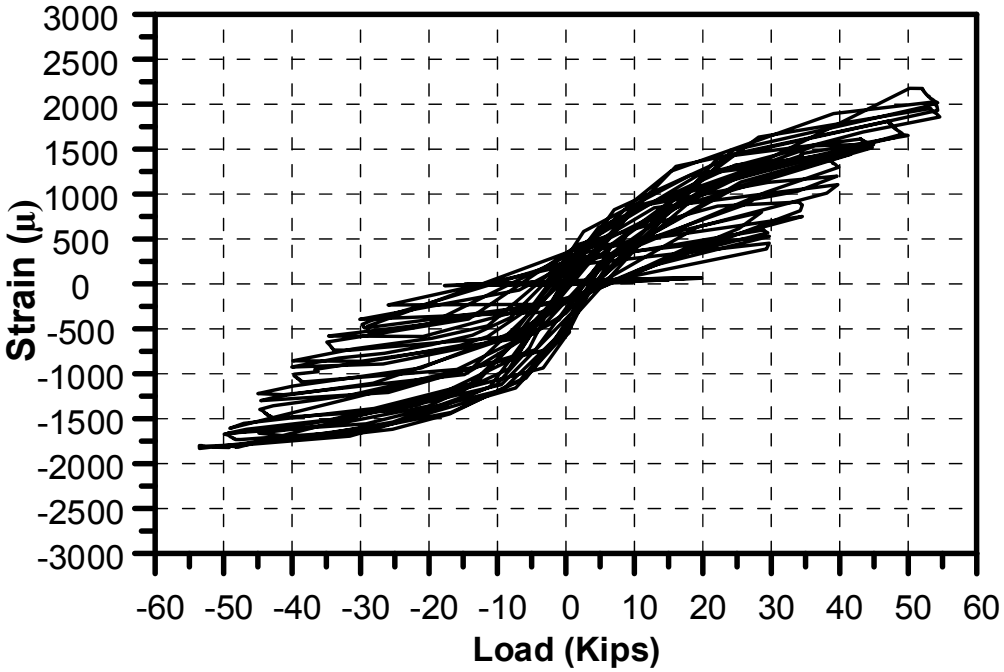

Figure 4-131 Load-strain curve for stud #6 (S6W).

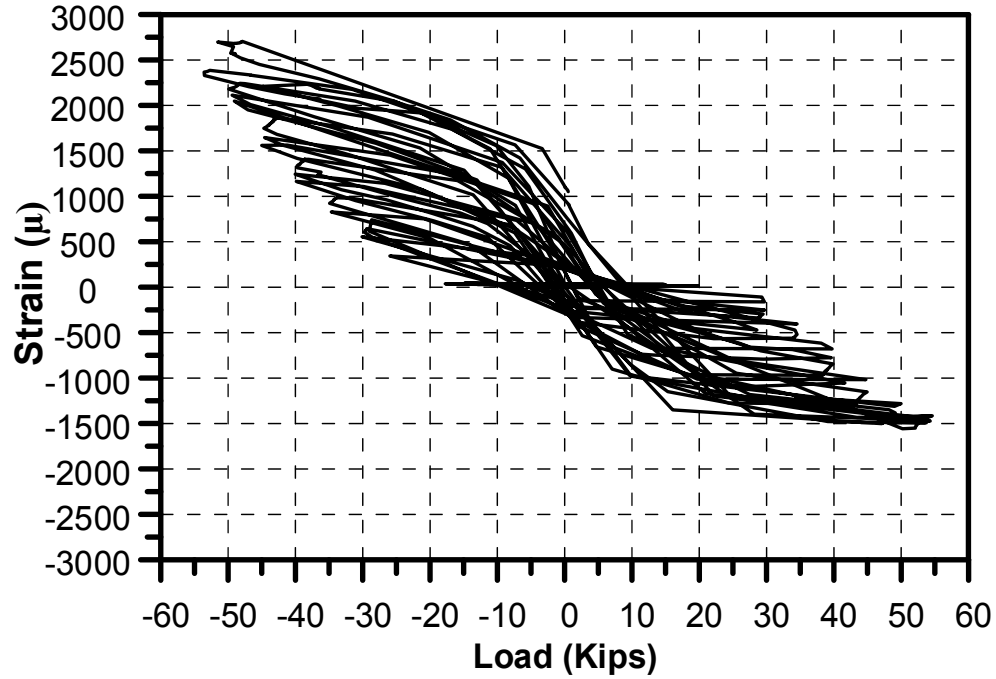

Figure 4-132 Load-strain curve for stud #6 (S6E).

4.5.2 Results of strain gauges on the steel rebars

With reference to Figure 4-133 which shows the locations of the strain gauges on the steel rebars. Figure 4-134 through Figure 4-139 show the load-strain curve for all the rebars used in this test.

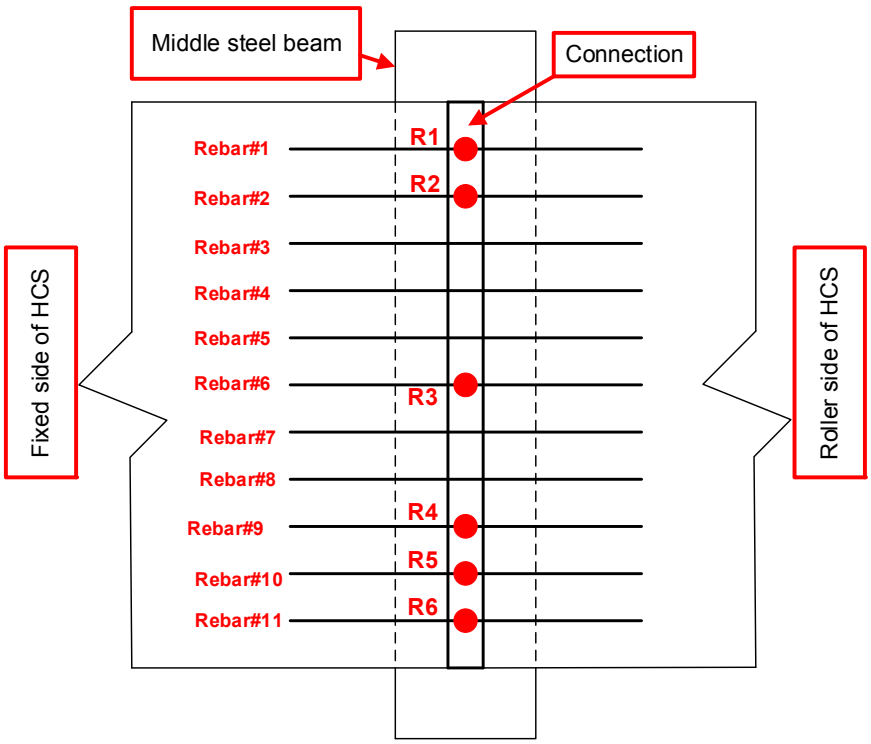

Figure 4-133 Steel rebars locations.

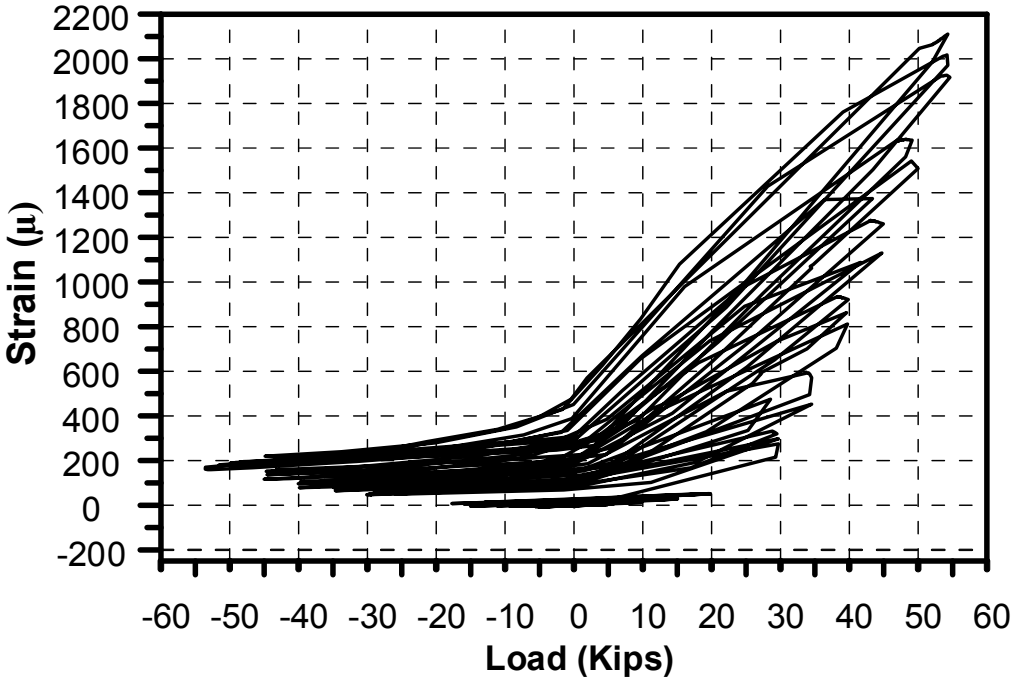

Figure 4-134 Load-strain curve for rebar#1-R1.

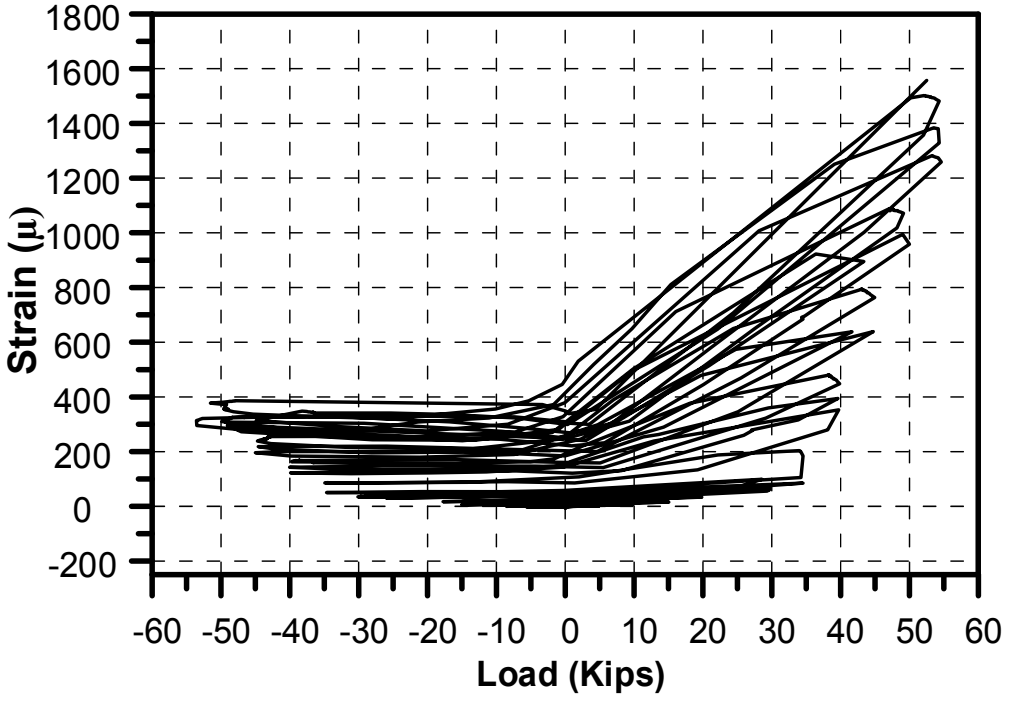

Figure 4-135 Load-strain curve for rebar#2-R2.

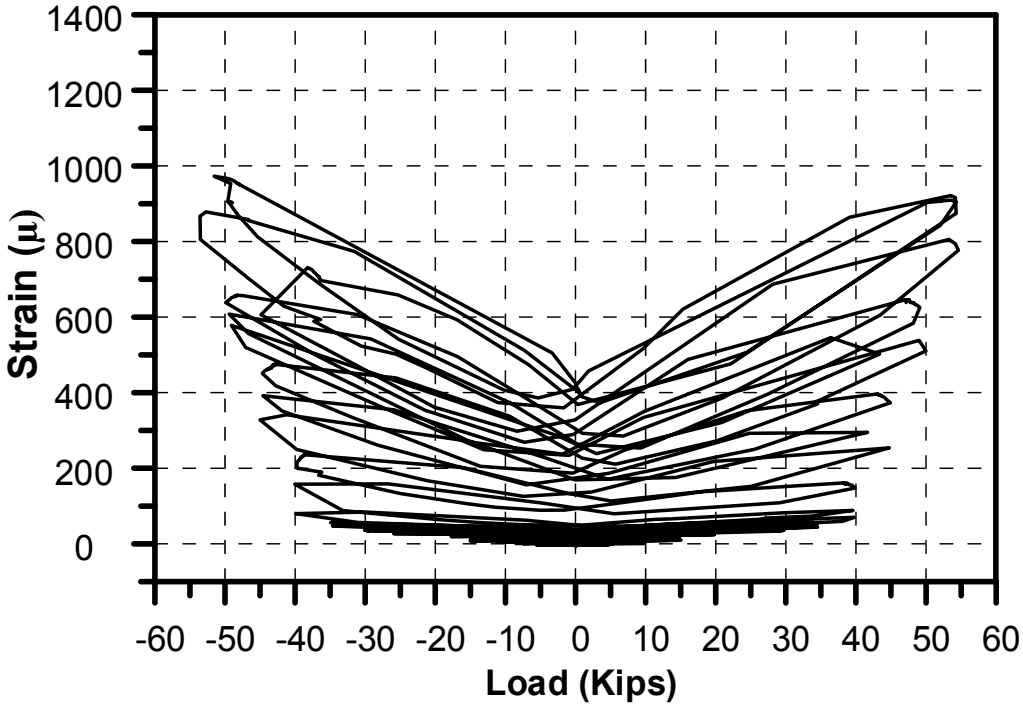

Figure 4-136 Load-strain curve for rebar#6-R3.

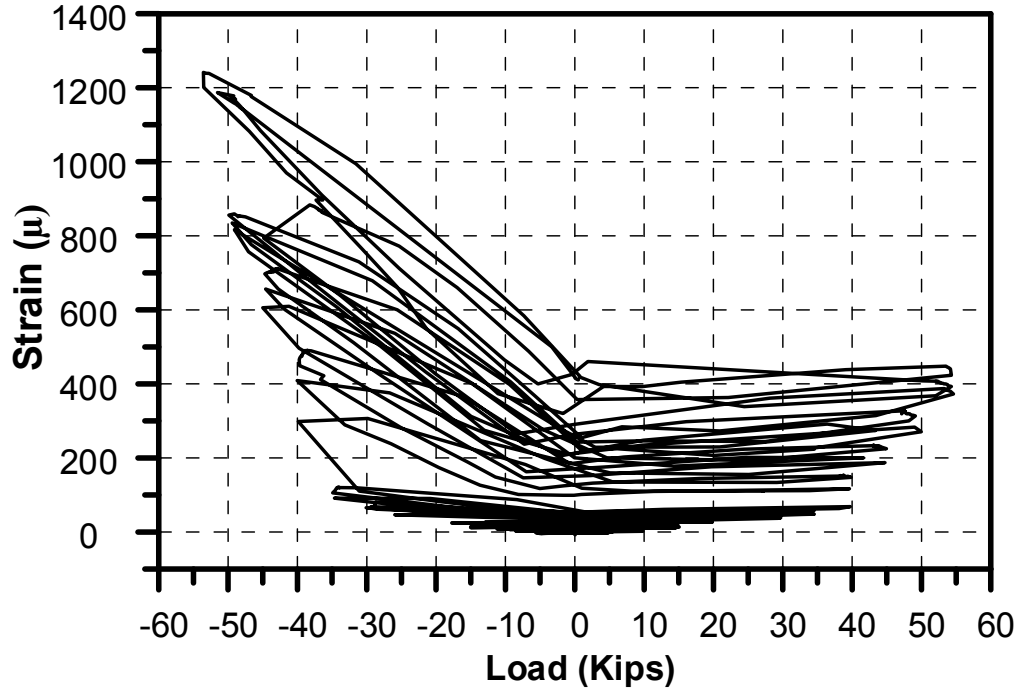

Figure 4-137 Load-strain curve for rebar#9-R4.

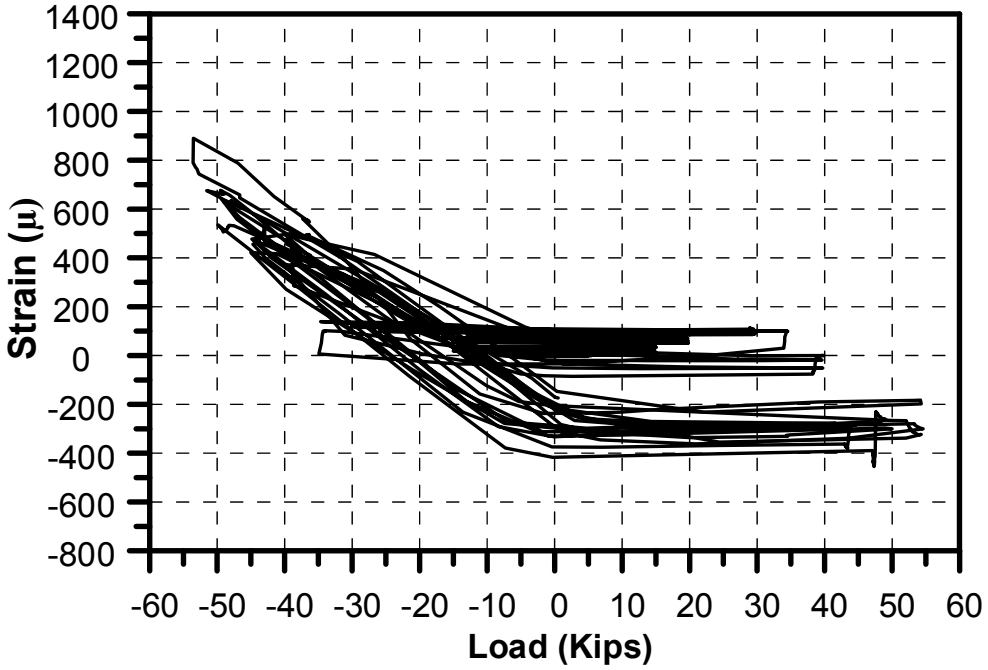

Figure 4-138 Load-strain curve for rebar#10-R5.

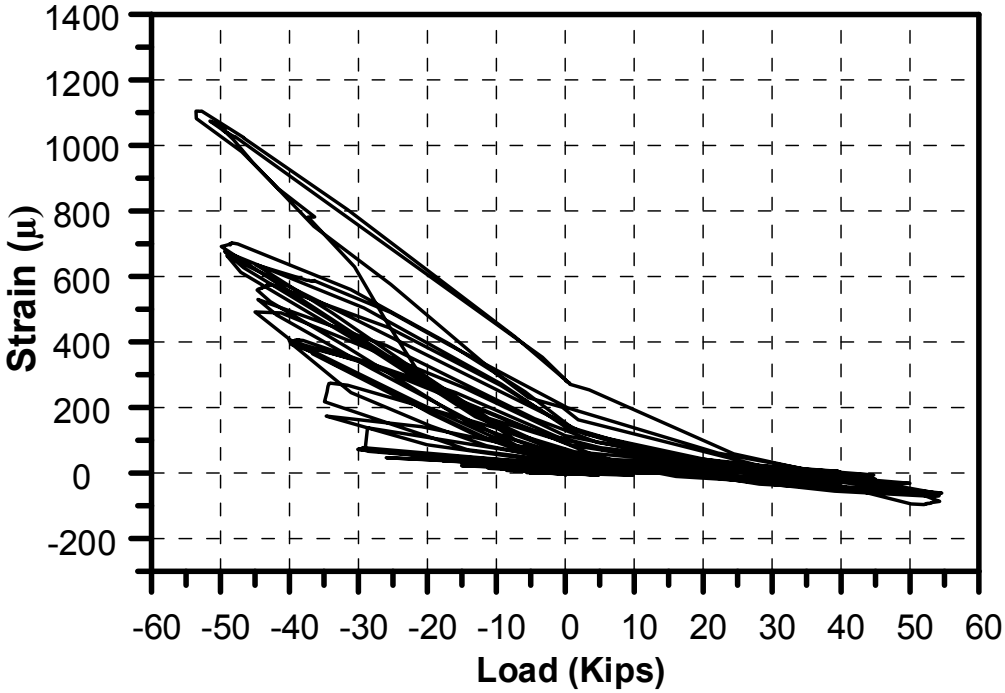

Figure 4-139 Load-strain curve for rebar#11-R6.

4.5.3 Analysis and discussion of the results

The results of this test showed that no cracks were observed on the top surface of topping before -55 Kips. However, the dropping in force was noticed after local damage in the location of applied force at -55 kips and the relative displacement at that load was 0.007 in. Therefore, the maximum load that the connection resisted before failure was 55 Kips which is similar to the maximum load of the previous specimen (without concrete topping).

There was a separation between the topping slab and the hollow core slabs at the maximum force. Moreover, after removing the topping slab, many cracks were noticed on the hollow core planks.

It can be concluded that the cracks started in the planks and they couldn't be seen because they were covered by the topping slab. However, the failure in the hollow core panels occurred along the steel rebars and at the ends of steel rebars inside the openings of the planks.

All the shear studs yielded in this test and they started yielding at load range (45 Kips-50 Kips). However, no fracture was noticed in the shear studs. On the other hand, the yielding in steel rebars occurred in one rebar (rebar # 1).

Generally, it can be concluded that the topping slab does not increase the strength of connection and the hollow core planks to resist the cyclic load.

4.6 Cyclic in-plane shear deformation Test (Double shear effect)

Because the nonlinear Finite Element Analysis (FEA) results (Chapter 8) showed that there is a double shear effect on some connections in the STF system, this specimen was carried out to investigate that effect.

The specimen was prepared as described in section 3.6 and the setup before starting the test is shown in Figure 3-91 through Figure 3-93. However, loading protocol that used in the previous tests was modified as illustrated in Figure 4-140.

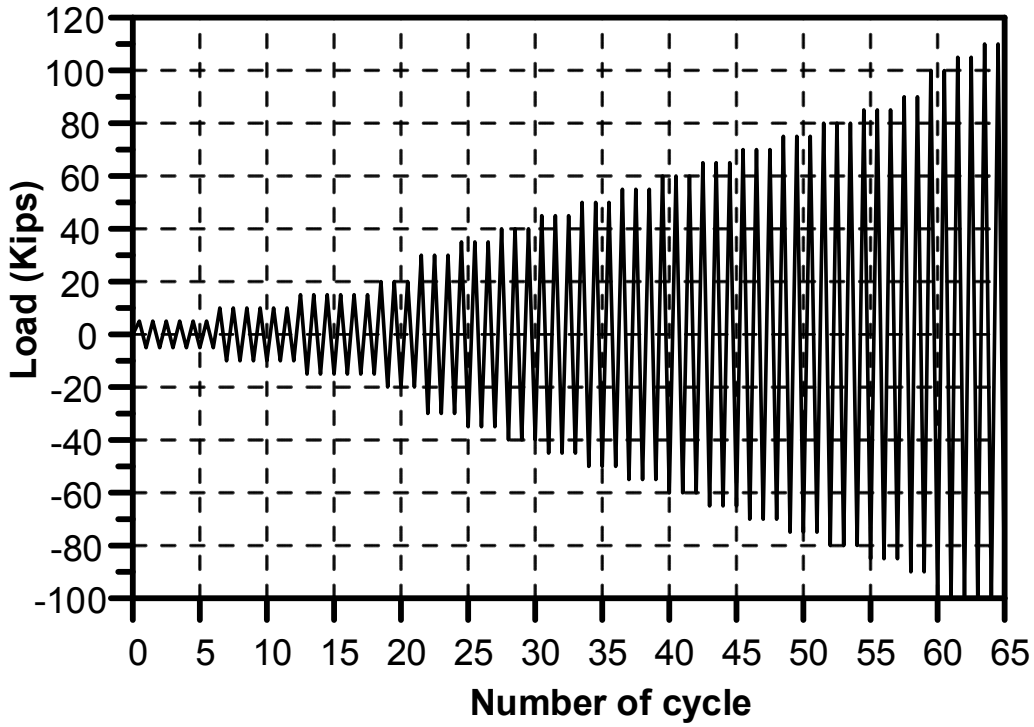

Figure 4-140 Loading protocol for the double shear test.

The test started by applying cyclic load as in the loading protocol. No cracks were noticed before 100 Kips. However, the first crack occurred at +100 Kips with a relative displacement 0.08 in. and the width of the crack was 0.1mm. Furthermore, the crack started between the west side of concrete connection and the hollow-core panel (north

side) and extended diagonally through the connection to the hollow-core panel in the south side as it can be seen in Figure 4-141.

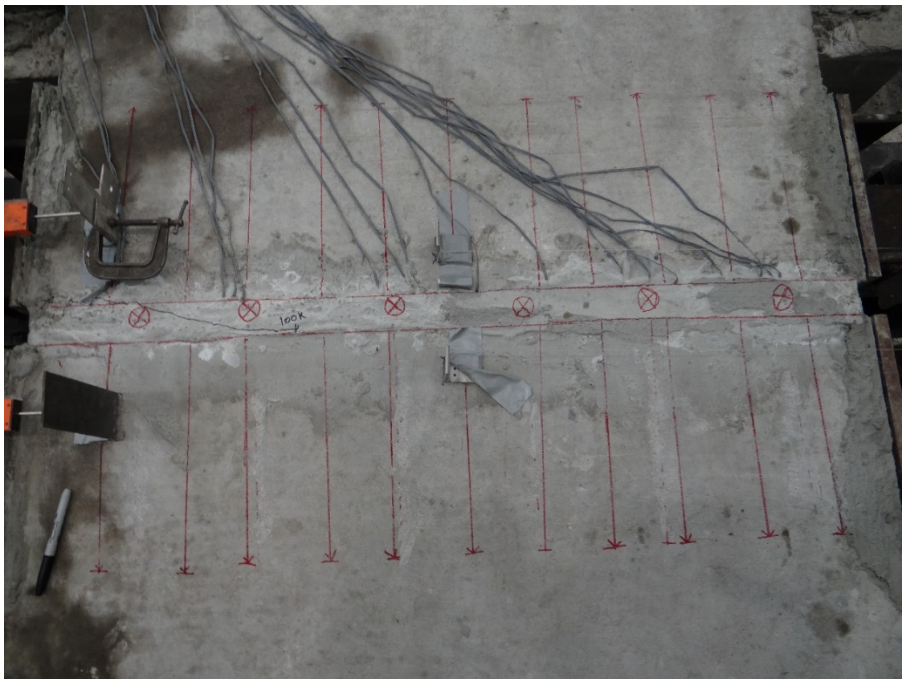

Figure 4-141 First crack of the double shear test at +100 Kips.

Crack propogation ocurred at +105 Kips with relative displacement 0.08” and the width of the crack is 0.1 mm. The propogation extended through the hollow core-slab (south side).

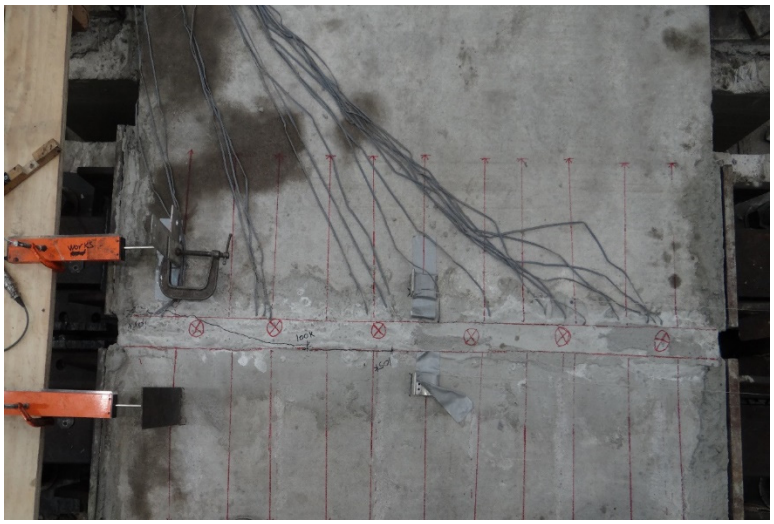

Figure 4-142 First crack propogation +105 Kips.

When the load reached -100 Kips as shown in Figure 4-143 and Figure 4-144, a dropping in force was noticed and there were:

- Separation between the hollow-core panel (north side) and the connection, where the crack propagated along the connection.
- Cracks occurred at the end of steel rebars in the hollow-core panel (south side).
- The relative displacement is (0.15”), (0.18”) respectiveley an the width of the crack is 0.3 mm.

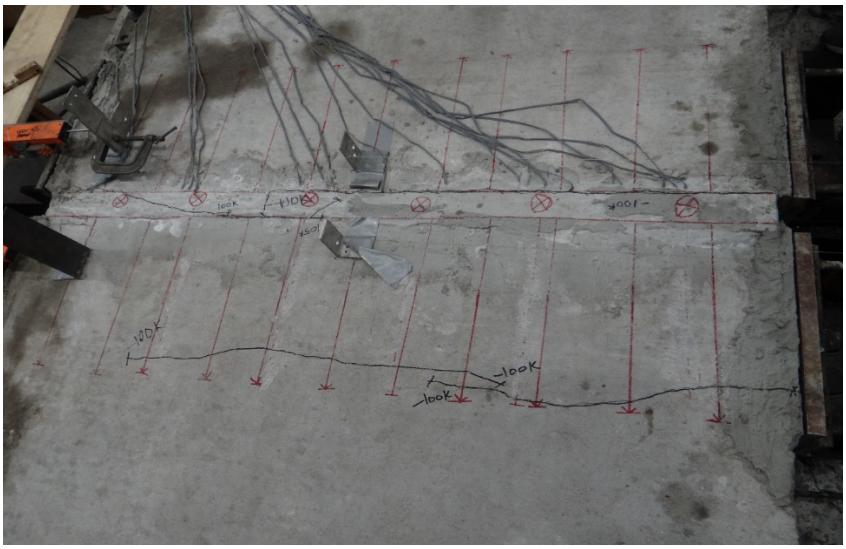

Figure 4-143 Overview of the specimen's failure at -100 Kips.

Figure 4-144 Separation between the plank (north side) and the connection; Crack at the end of steel rebars.

Figure 4-145 shows a portion of the loading protocol which demonstrates the progress of cracks and failure of the specimen.

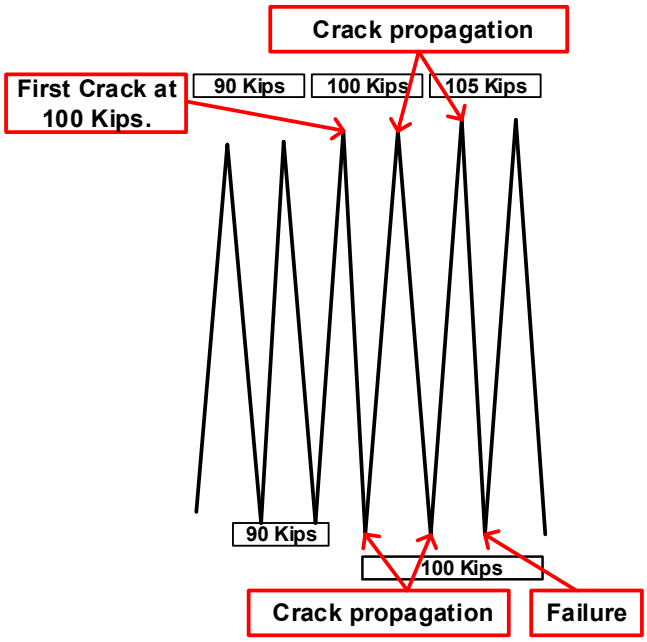

Figure 4-145 The progress of cracks and failure of the specimen.

By continue applying force, cracks occurred at the end of steel rebars in the hollow-core panel (north side) as it can be seen in Figure 4-146 and Figure 4-147.

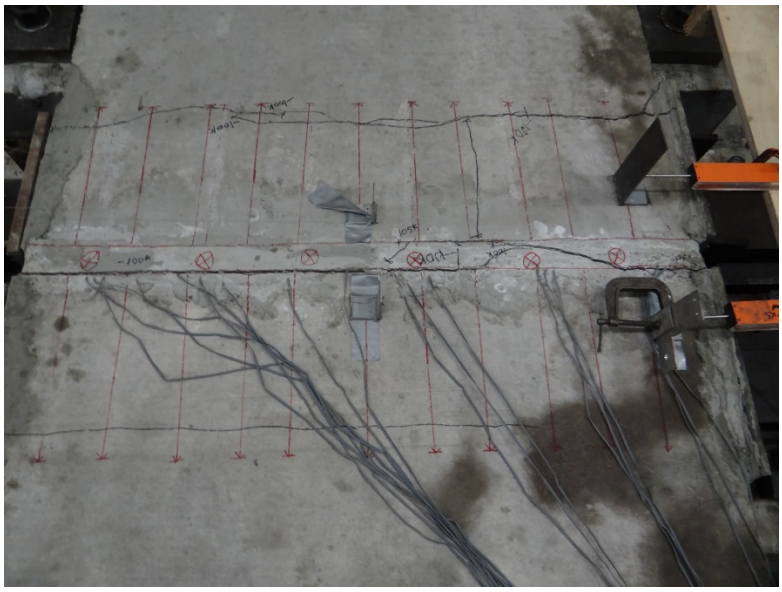

Figure 4-146 Overview of the specimen at the end of test.

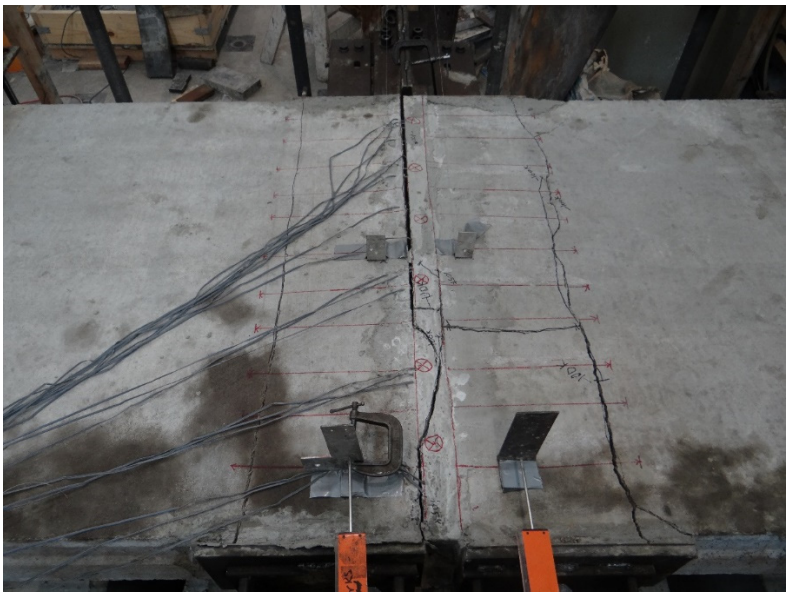

Figure 4-147 Cracks at the end of steel rebars in the hollow-core panel (north side).

With reference to Figure 4-148 which shows the locations of LVDTs for this test, L1 and L2 represent the displacements at the ends of the connection and the Load-displacement relationship for both of them are illustrated in and respectively. On the other hand, L3 and L4 represent the displacements at the middle of connection. The displacement of the hollow-core planks was calculated using the same equations that used in the previous tests.

(L4, L5) and (L7,L8) are LVDTs were used as backups to measure the relative displacements and L7 was used to notice if the middle concrete block moves during the test. However, the readings of L7 showed that the middle concrete block did not move during the test.

Figure 4-149 through Figure 4-154 show the relationship between the applied load and the relative displacement of the connection. The maximum shear strength of the connection is -100 Kips and the relative displacement is 0.0228 in.

Figure 4-155 and Figure 4-156 show the relationship between the applied load and the deformation of the HCS. The deformation of the HCS at the maximum shear strength is 0.23 in.

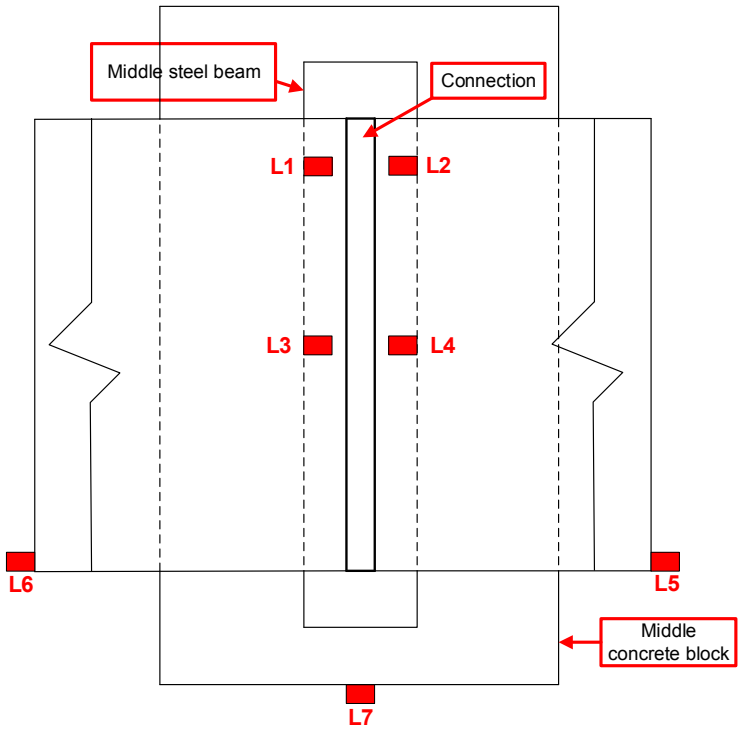

Figure 4-148 LVDTs locations.

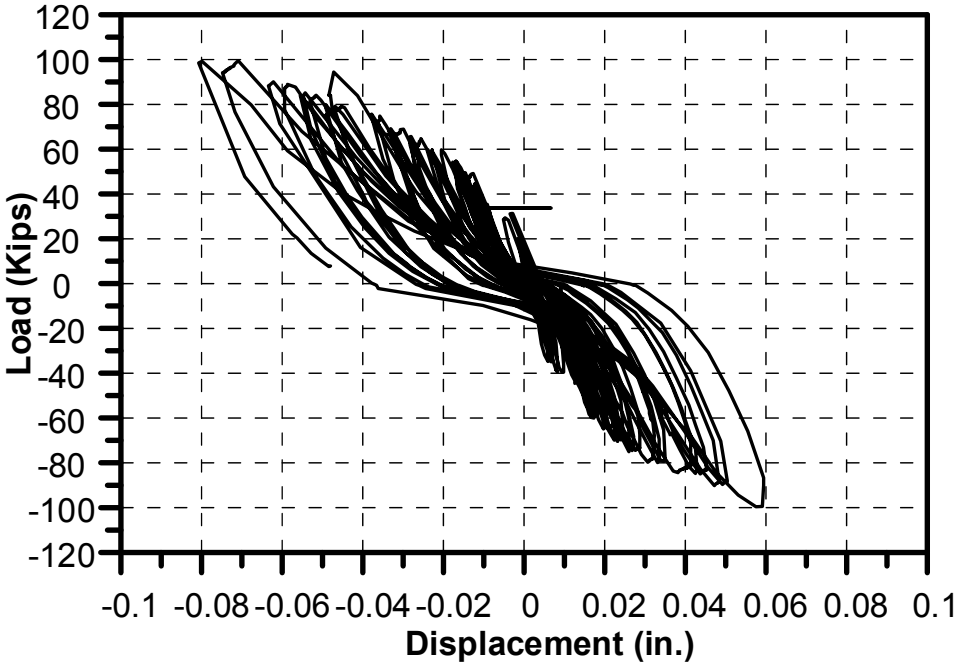

Figure 4-149 Load-Displacement at the end of connection (L1).

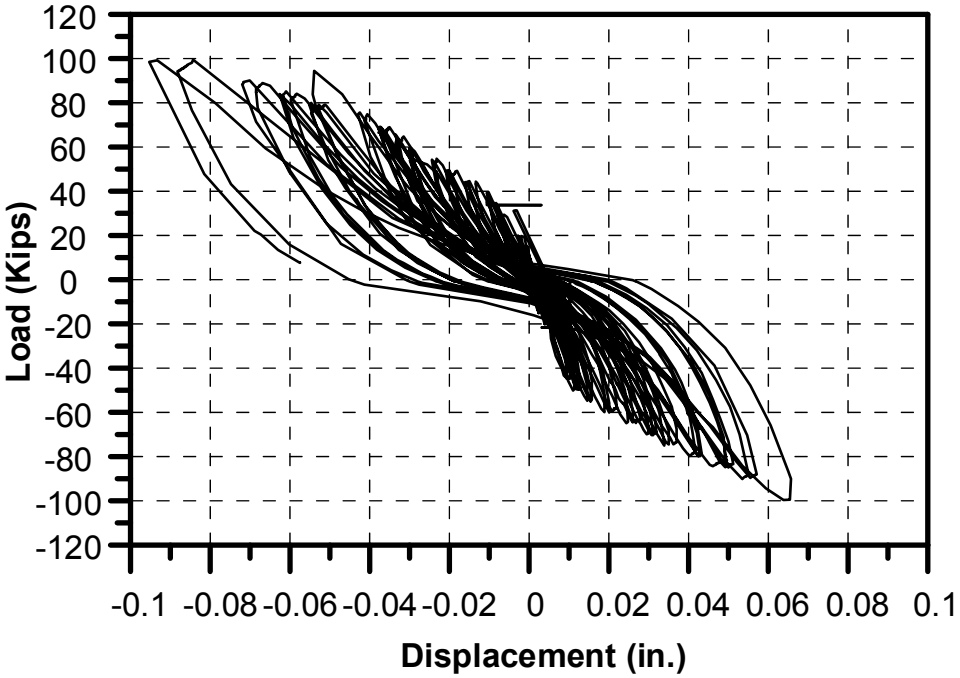

Figure 4-150 Load-Displacement at the end of the connection (L2).

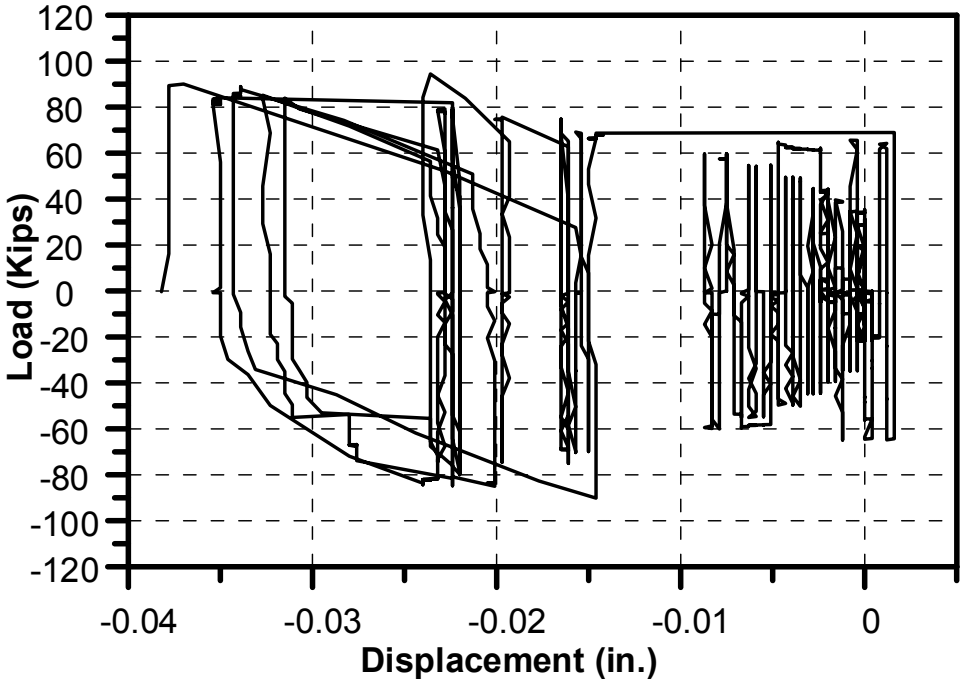

Figure 4-151 Load-Displacement at the middle of the connection (L3).

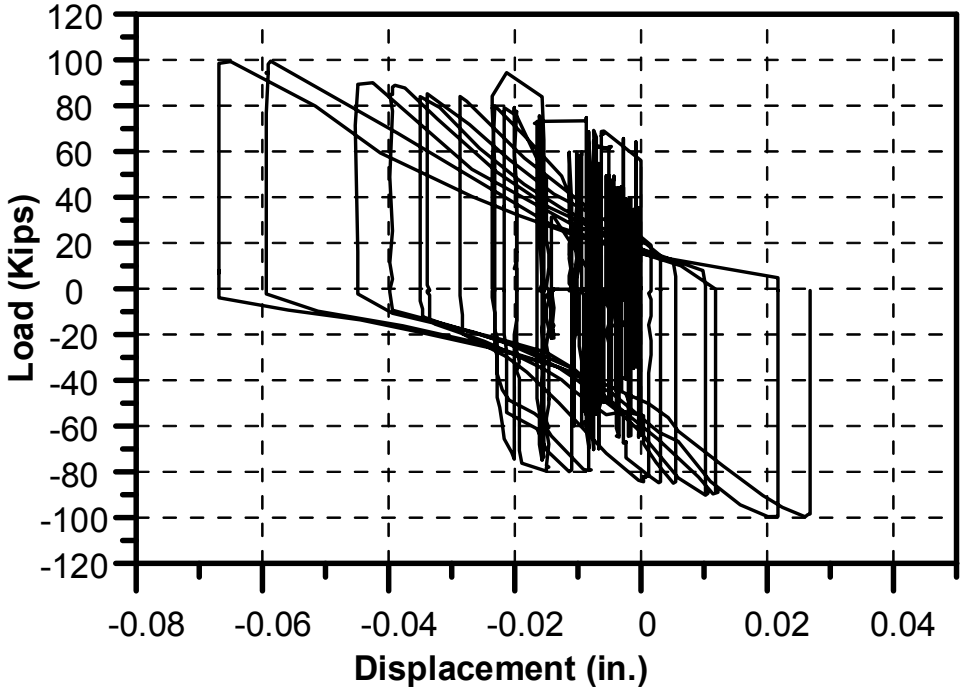

Figure 4-152 Load-Displacement at the middle of the connection (L4).

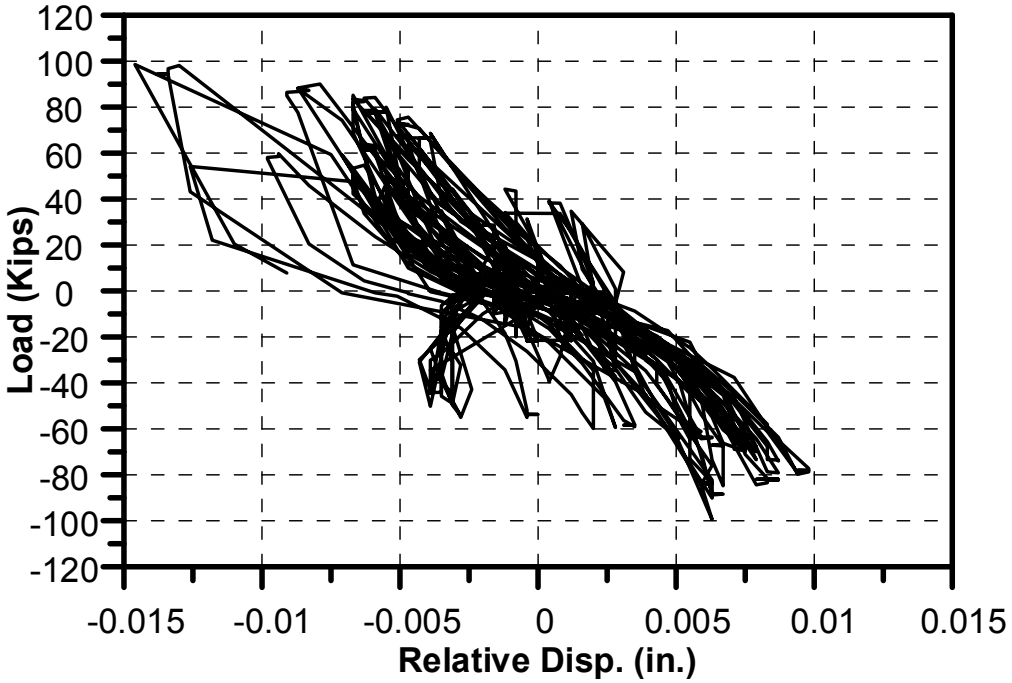

Figure 4-153 Load-Relative displacement at the end of connection.

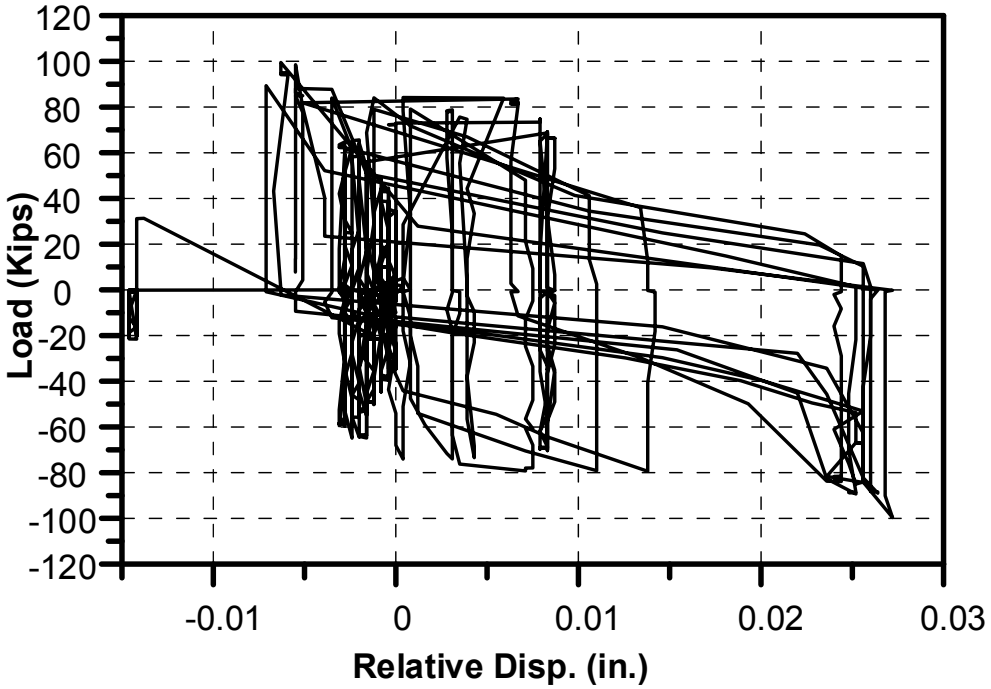

Figure 4-154 Load-Relative displacement at the middle of connection.

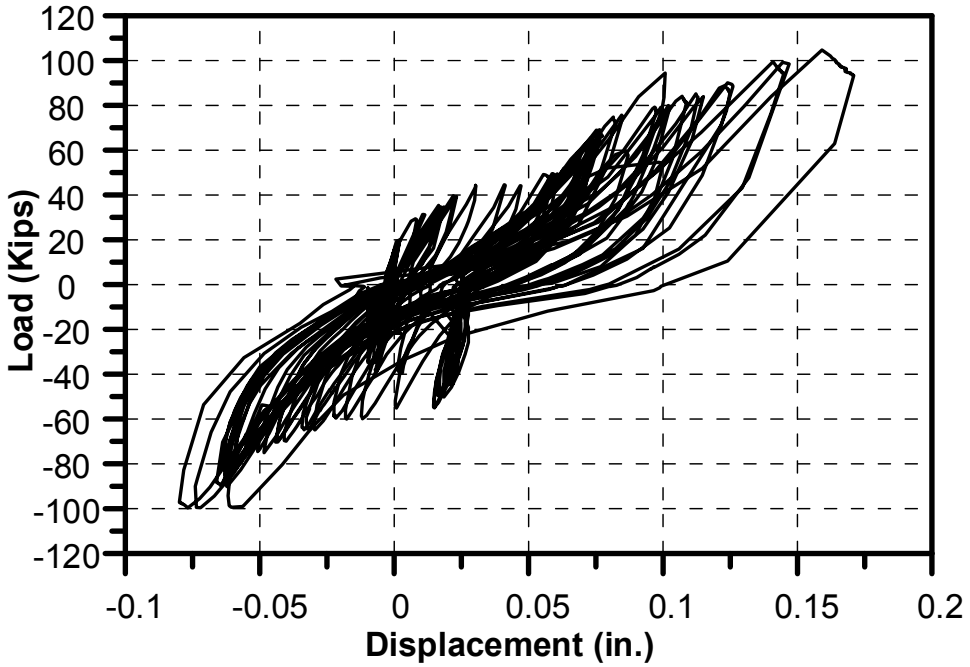

Figure 4-155 Load-HCS deformation (L5).

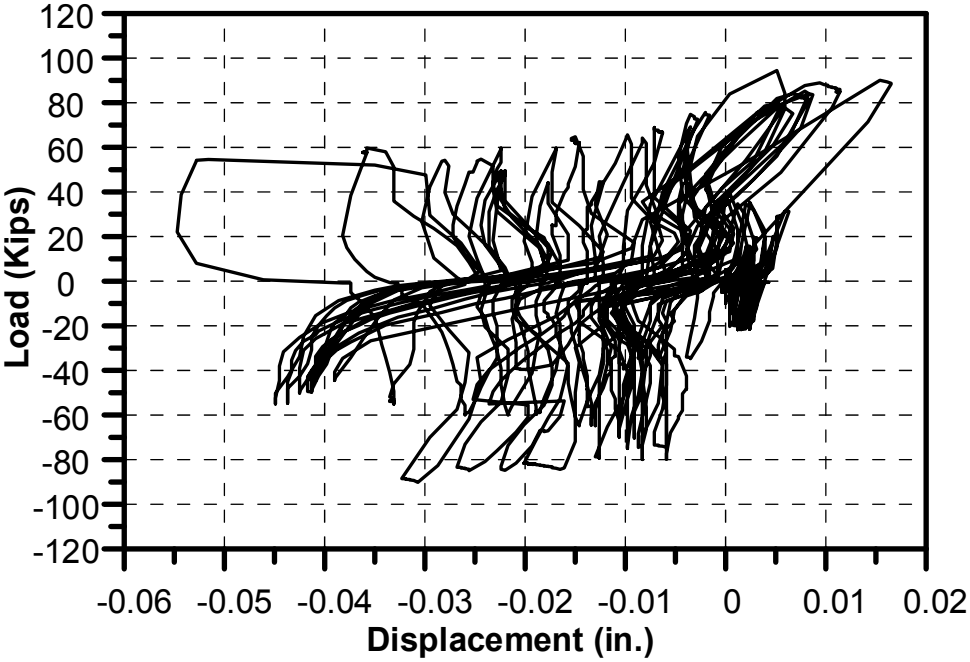

Figure 4-156 Load-HCS deformation (L6).

4.6.2 Results of strain gauges on the shear studs

The same locations of shear studs which are illustrated in Figure 4-86 were also used in this test . However, all shear studs yielded and one of them started rupture at the base (top of welding region) as illustrated in Figure 4-157.

Figure 4-158 Figure 4-167 show the load-strain curves for all the shear studs that used in this test.

Figure 4-157 Yielding and fracture of shear studs.

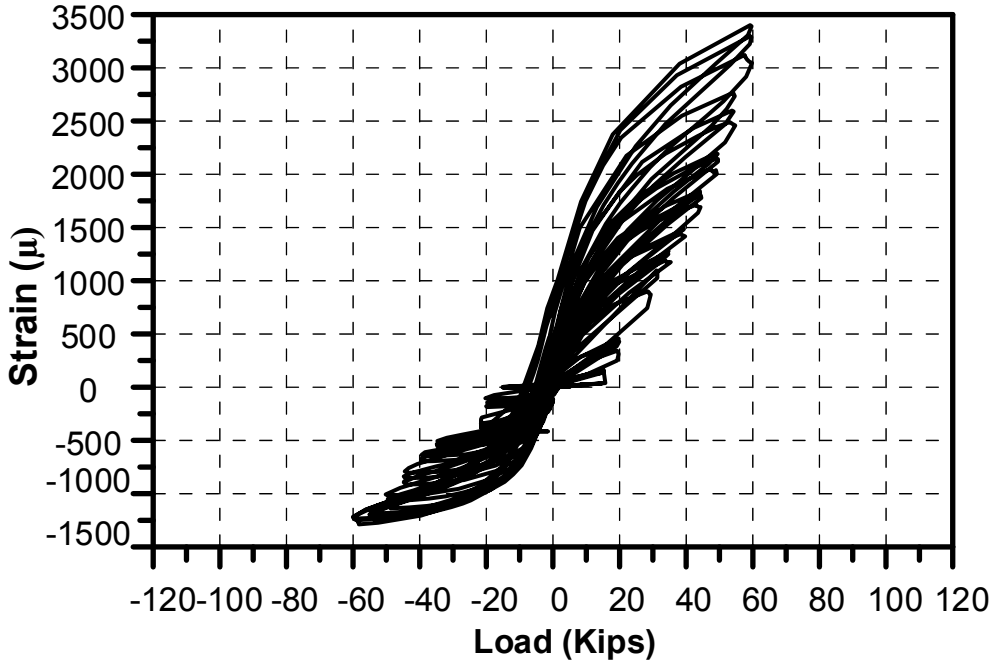

Figure 4-158 Load-strain curve for stud #1 (S1W).

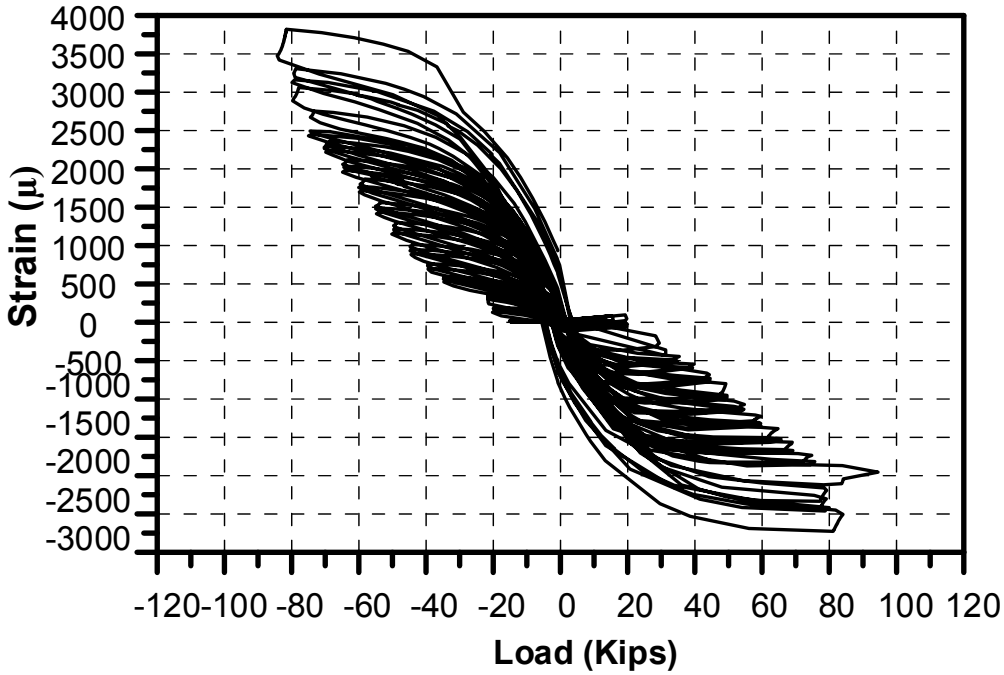

Figure 4-159 Load-strain curve for stud #1 (S1E).

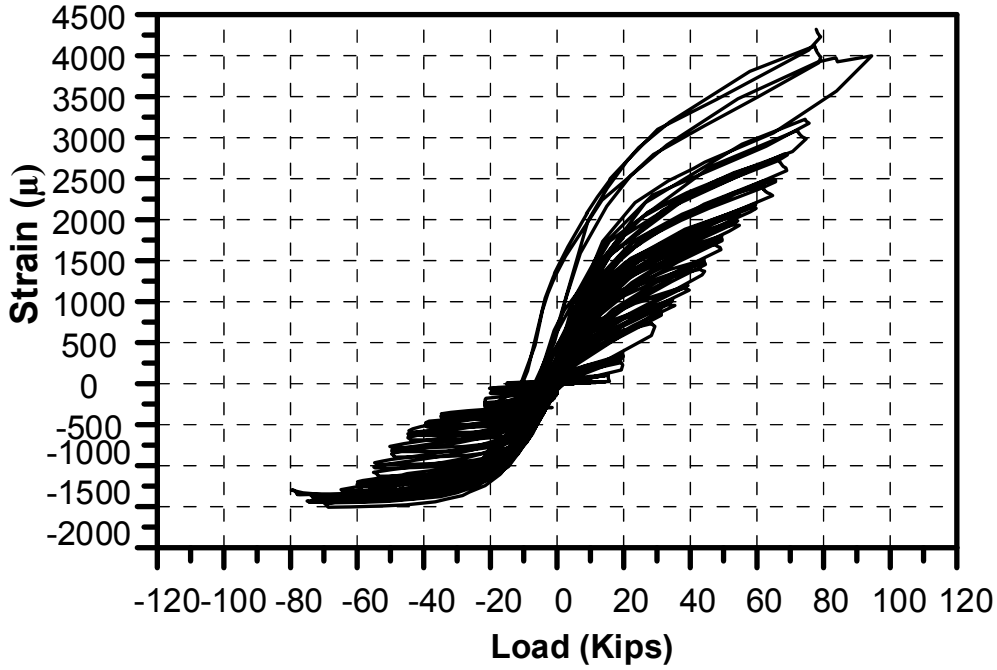

Figure 4-160 Load-strain curve for stud #2 (S2W).

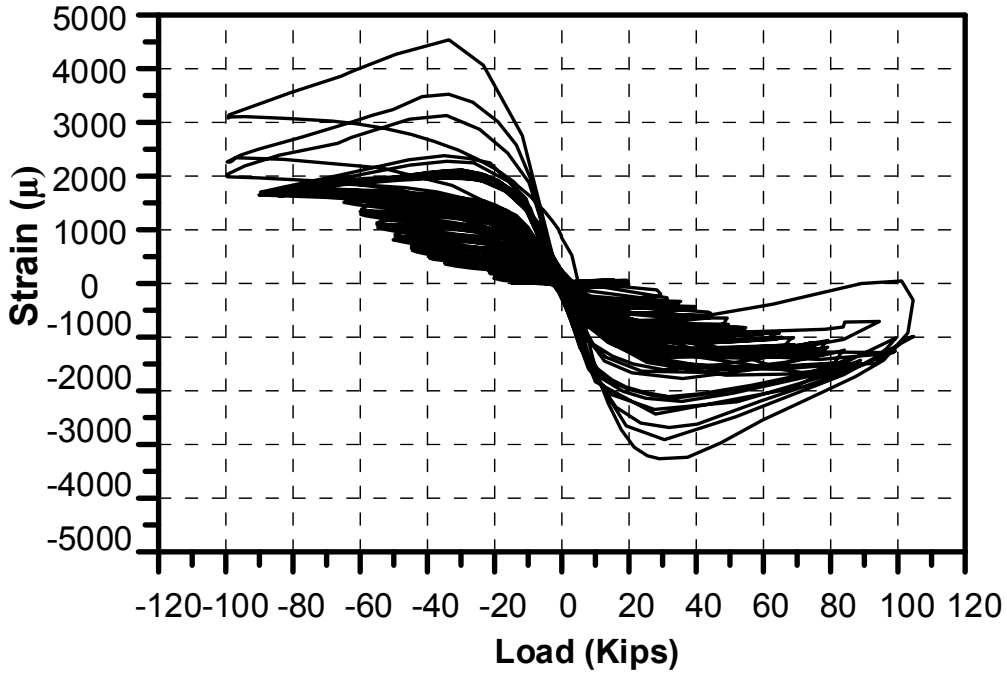

Figure 4-161 Load-strain curve for stud #2 (S2E).

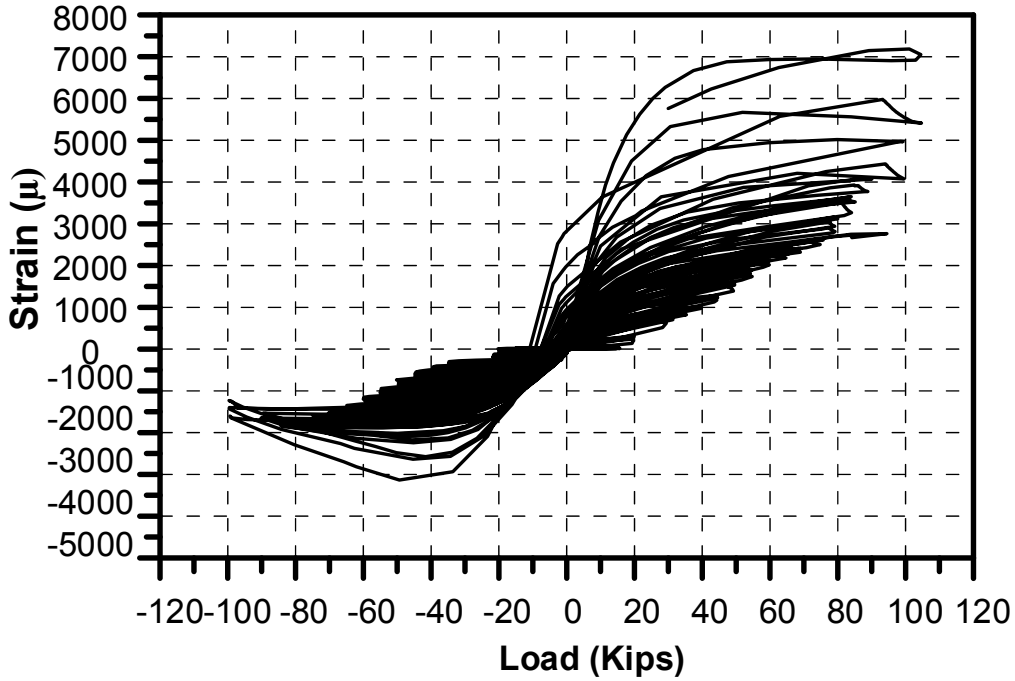

Figure 4-162 Load-strain curve for stud #3 (S3W).

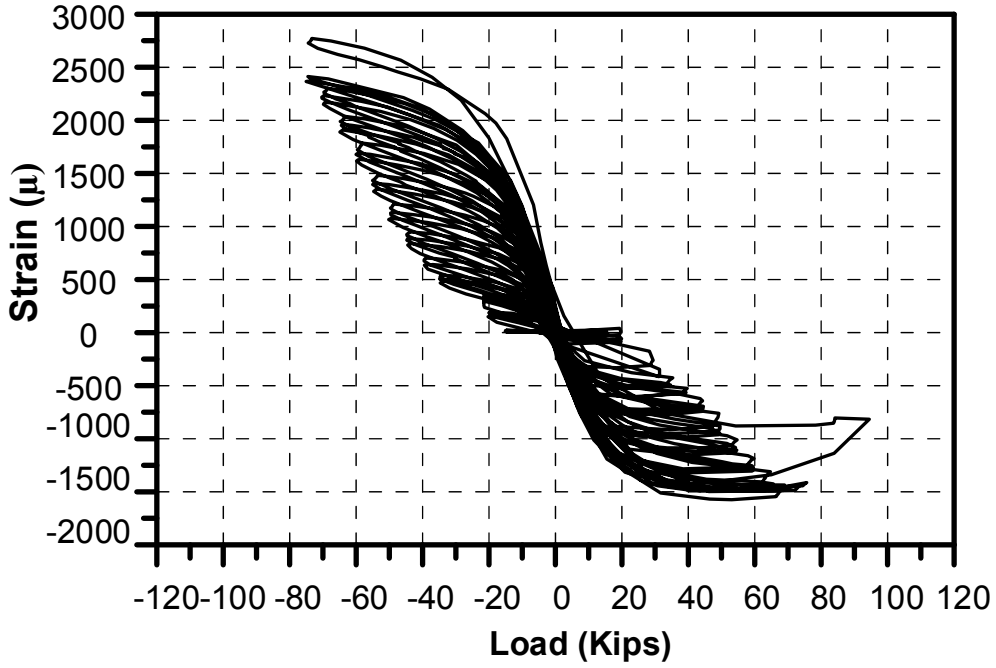

Figure 4-163 Load-strain curve for stud #3 (S3E).

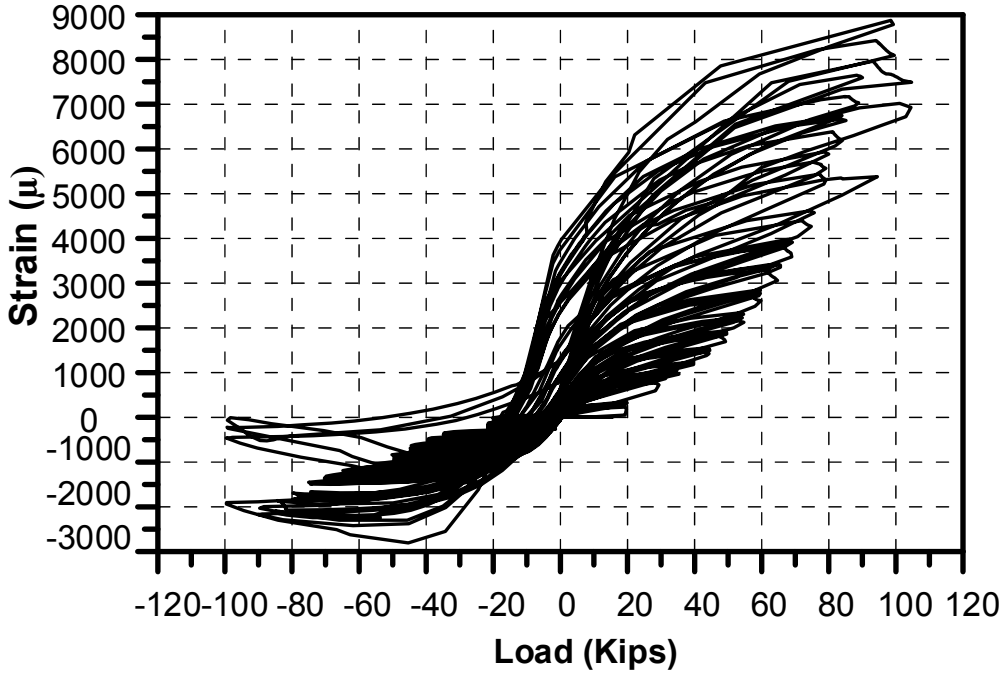

Figure 4-164 Load-strain curve for stud #4 (S4W).

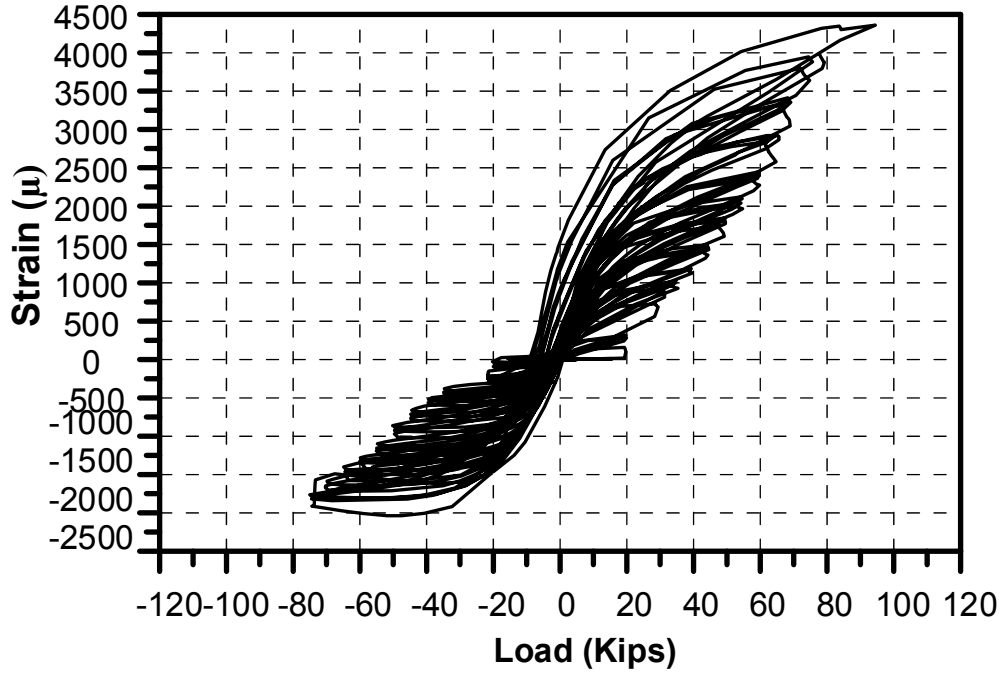

Figure 4-165 Load-strain curve for stud #5 (S5W).

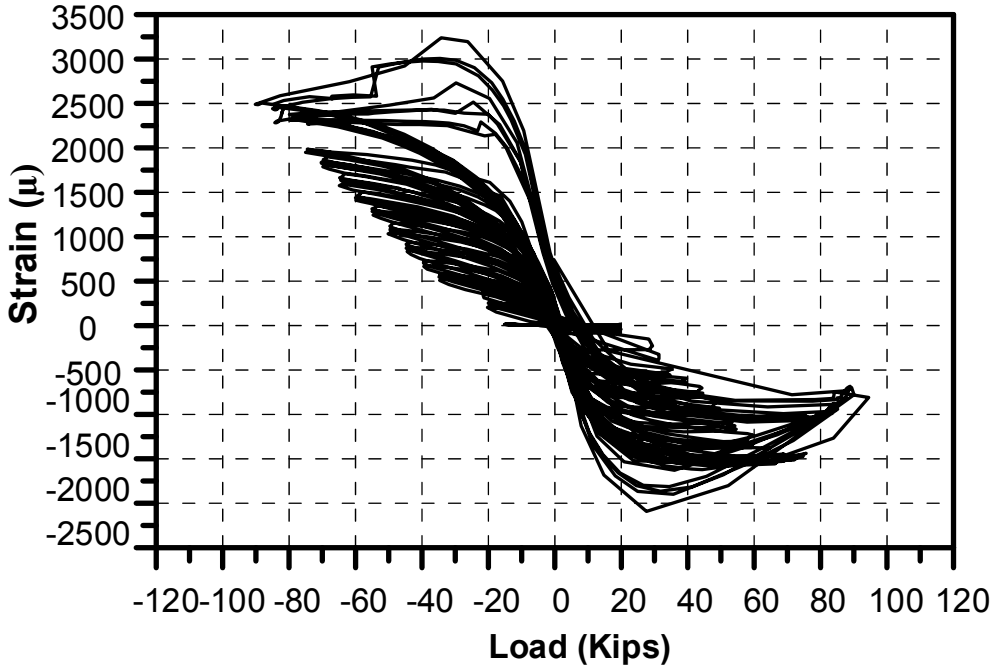

Figure 4-166 Load-strain curve for stud #5 (S5E).

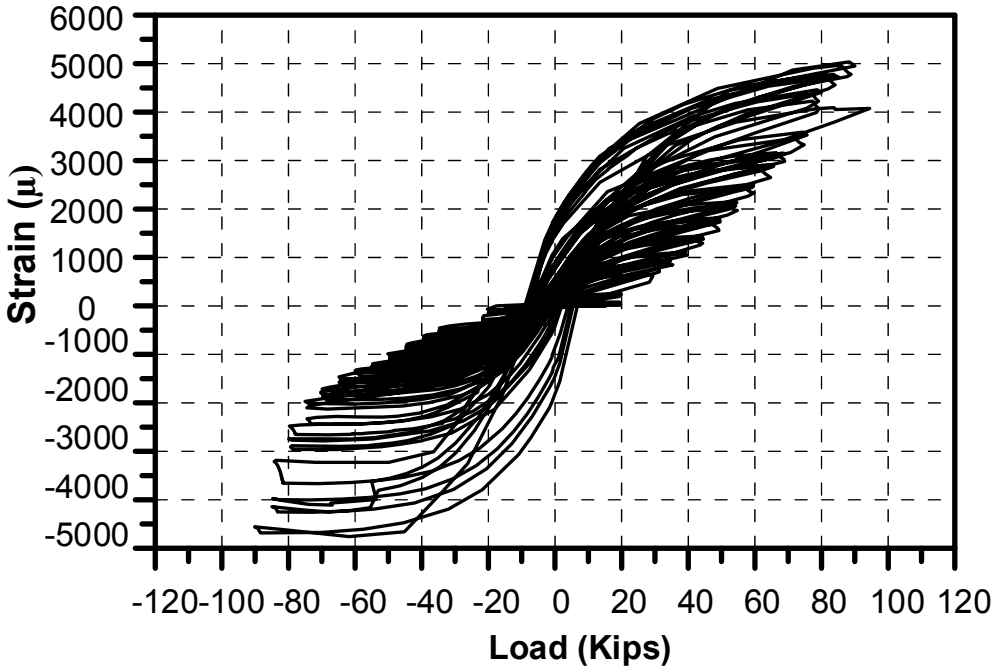

Figure 4-167 Load-strain curve for stud #6 (S6W).

4.5.2 Results of strain gauges on the steel rebars

With reference to Figure 4-133 which shows the locations of the strain gauges on the steel rebars, Figure 4-168 through Figure 4-173show the load-strain curve for all the rebars used in this test.

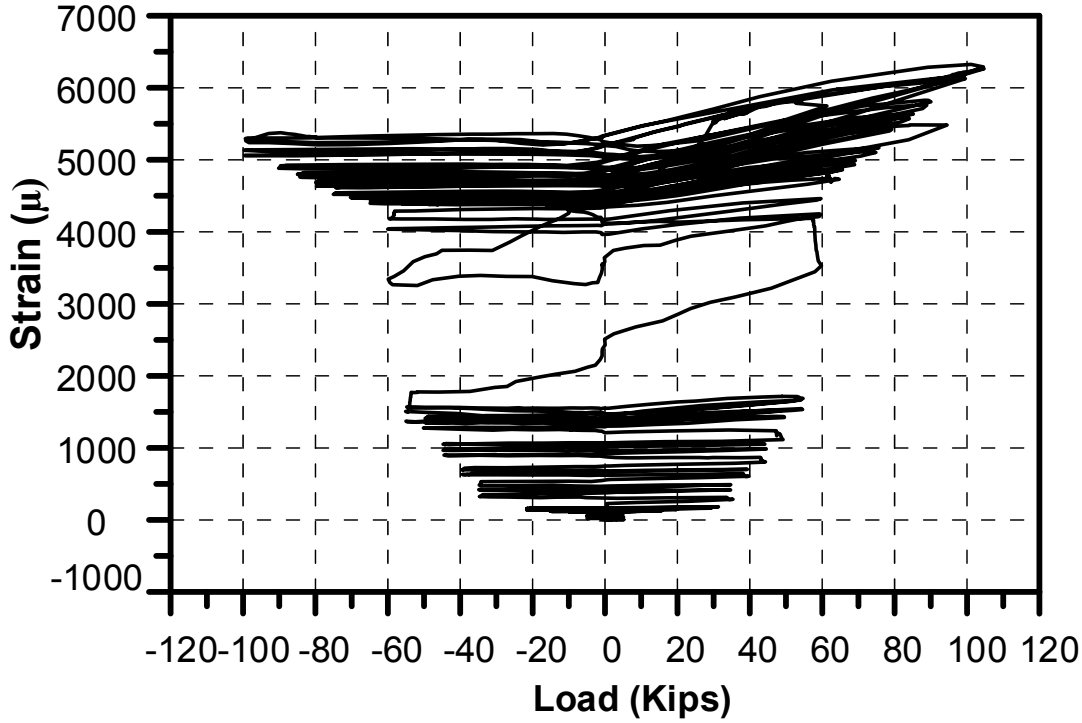

Figure 4-168 Load-strain curve for rebar#1-R1.

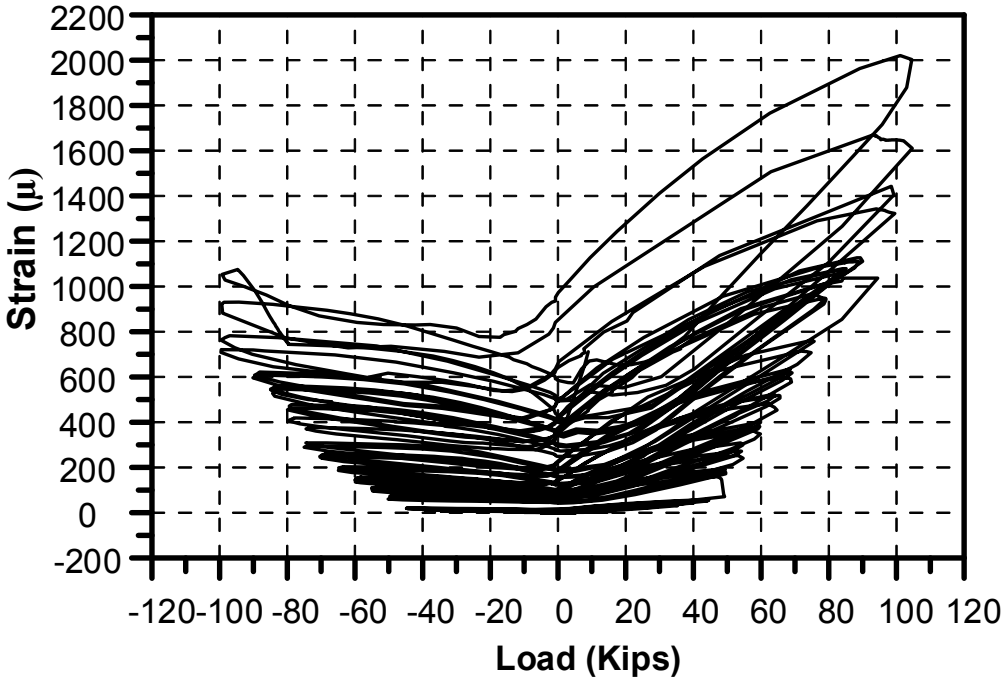

Figure 4-169 Load-strain curve for rebar #3-R3.

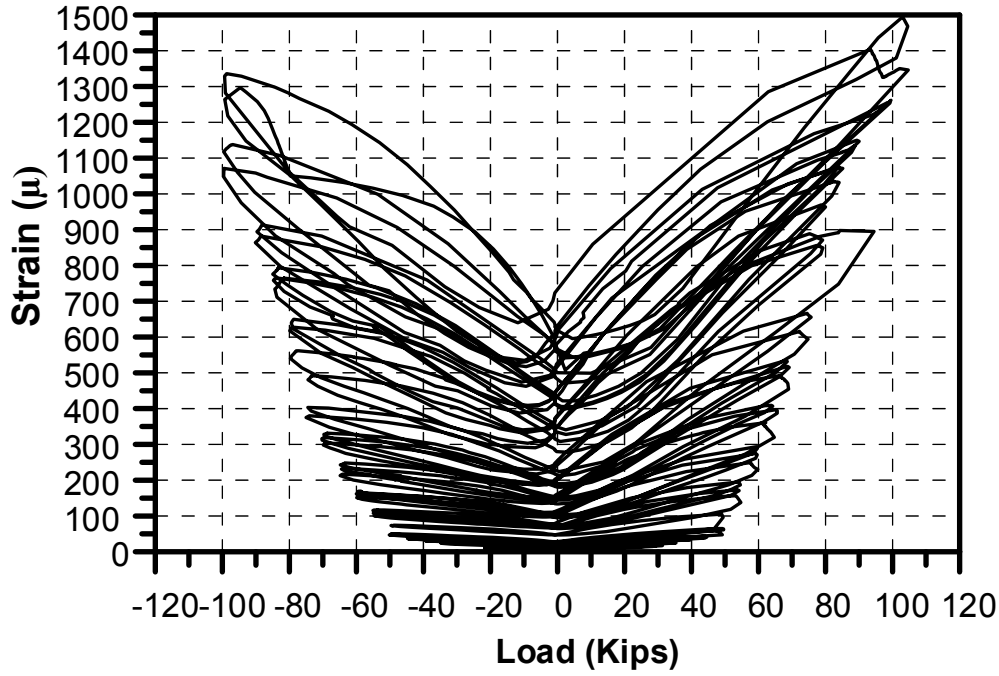

Figure 4-170 Load-strain curve for rebar #6-R6.

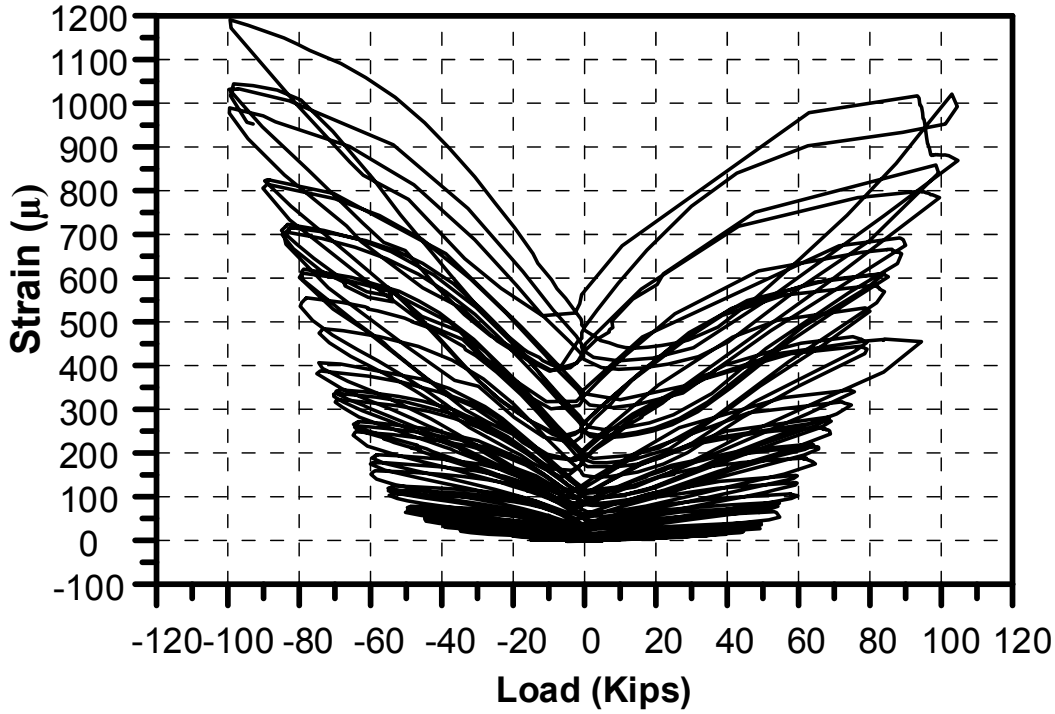

Figure 4-171 Load-strain curve for rebar #9-R9.

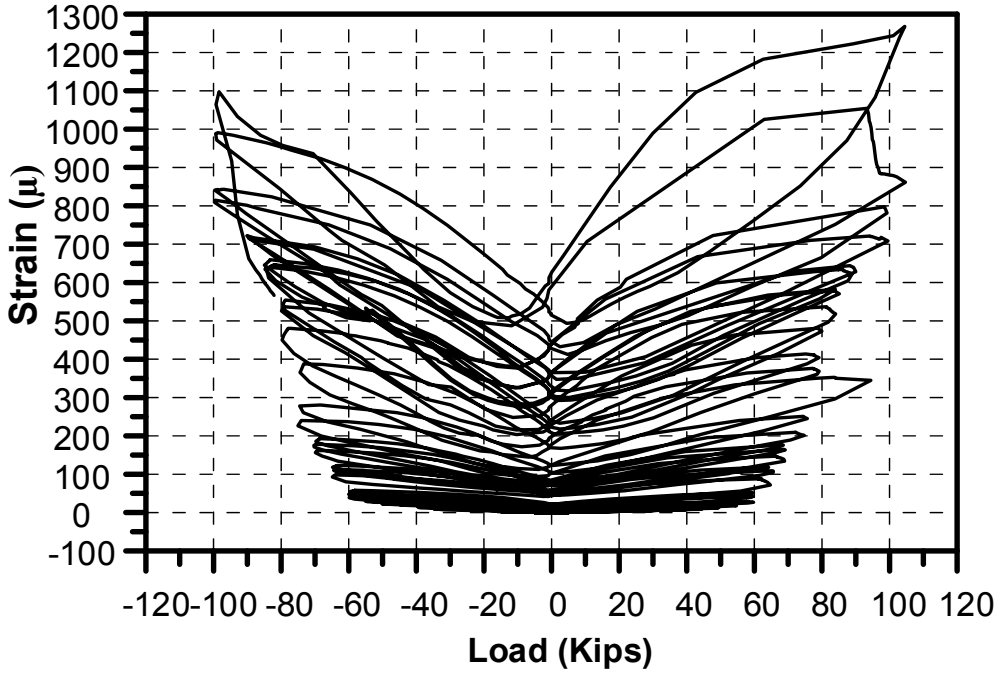

Figure 4-172 Load-strain curve for rebar #9-R9.

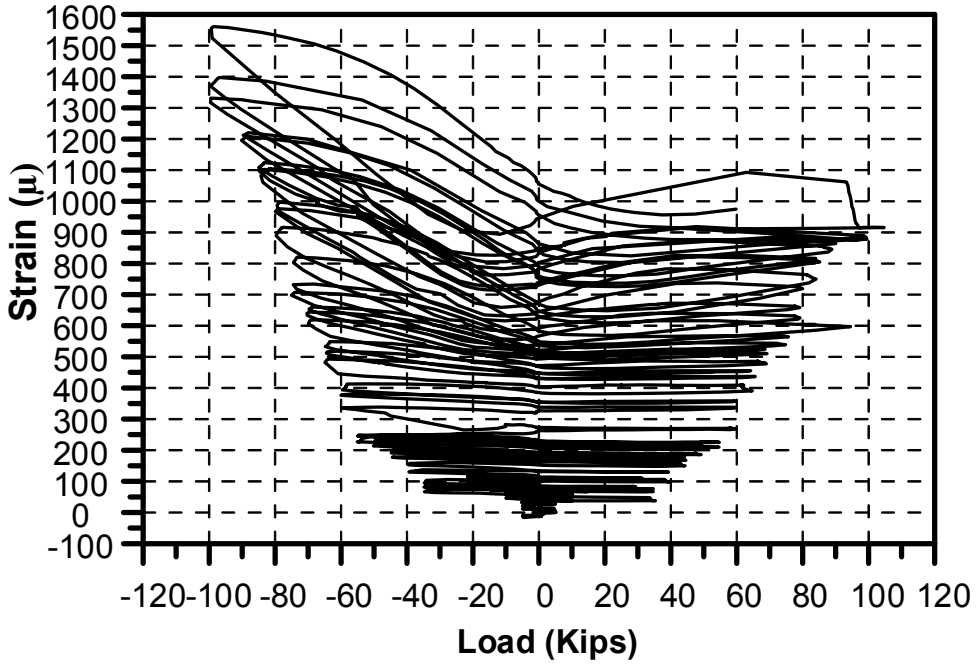

Figure 4-173 Load-strain curve for rebar #9-R9.

4.6.3 Analysis and discussion of the results

The results of this test showed that the first crack was noticed at +100 Kips. After two cycles at (-100 Kips) from the first crack, a dropping in force was noticed in which a separation between the hollow-core panel and the connection occurred first, then the crack propagated along the connection. Therefore, it can be concluded that the maximum shear force that the STF connection can resist under double shear fore is 100 Kips (25 kips/ft.).

The cracks that occurred at the end of steel rebars in the planks are due to insufficient strength of the hollow-core panels to resist a shear force more than 50 kips (12.5 Kips/ft) at the connection.

All shear studs yielded and one of them started rupture at the base (top of welding region) which is common failure in the shear studs. However, they started yielding at load range (45 Kips-50 Kips). On the other hand, the yielding in steel rebars occurred in one rebar (rebar # 1).

Chapter 5

PERFORM-3D Modeling

5.1 Introduction

Nonlinear static pushover and time-history analyses were carried out using a computer program, Perform-3D (CSi, 2011), to evaluate the seismic performance of the STF structures.

In PERFORM-3D the displacement-based (or deformation-based) design can be used. This design considers the inelastic behavior using nonlinear inelastic analysis where the inelastic deformation (or ductility) can be more important than strength. On the other hand, PERFORM-3D permit to apply capacity design principles. The Capacity design is a design process in which the designer selects locations within a structural system to yield (ductile components) by permitting inelastic behavior. However, the other locations will remain elastic and can be less ductile. This design process improves reliability, reduces the amount of damage, and reduce construction costs.

5.2 General considerations

In all STF structures that are designed in chapter 6, the top and bottom chords of the trusses were considered as continuous members. Furthermore, the chord members were assumed to be rigidly connected to the columns except where there was no diagonal web member connecting to the column at that location as shown in Figure 5-1 .In such case, typical construction details suggest that the chord members are more appropriately assumed to be pin-connected to the columns (Marstellar and Faraone, 2002). However, the web members were rigidly connected to the chord members.

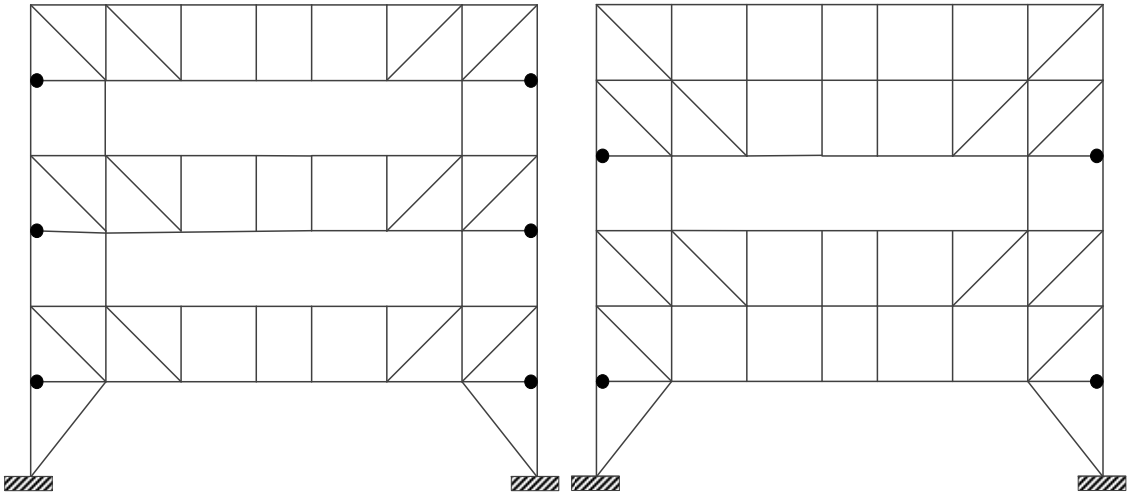

Figure 5-1 Locations of pin connections between chord members and columns in the six-story STF building: (a) odd bay; (b) even bay

All of the horizontal truss members were considered pin-connected to the STF system and spandrel beams. Because the spandrel beams are part of the moment-resisting frames, they were treated as rigidly connected to the columns in their strong axis direction. Interior beams were considered pin-connected to the truss chords to minimize force transfer from the horizontal trusses to the STF system when the building is displaced along the longitudinal direction.

The column sizes were kept within the typical W-shape columns. All of the members were selected such that all compression elements in the members were non-slender elements as defined in AISC 360-16.

5.3 Members modeling properties

All the members except the diagonal web members in the STF trusses and the braces for the ground floor were modeled as standard frame (beam-column type) elements. Moreover, the truss members and columns were modeled with both axial-moment (P-M-M) and moment-rotation plastic hinges at both ends as illustrated in Figure 5-2.

The flexure yielding properties also include the interaction between axial force and moment. The expected yield and ultimate strengths can be determined by applying the material overstrength factor (Ry), and the strain hardening adjustment factor (ω). The respective values are considered to be 1.1 for both of them in the wide flange and single hollow structural section members, while they are considered to be 1.3 for both of them in the double hollow structural section members.

Figure 5-3 through Figure 5-6 show the hysteresis model properties which were used in the nonlinear pushover and time-history analyses of typical columns, beams, vertical members outside of the Vierendeel panels (Special segments), and vertical members in the Vierendeel panels (Special segments).

The maximum rotational capacity of the column and beams is considered to be 0.03 rad before strength degradations occur (Newell and Uang, 2008). On the other hand, it is considered to be 0.04 and 0.02 for the vertical members in the Vierendeel panels (Special segments) outside of the Vierendeel panels respectively.

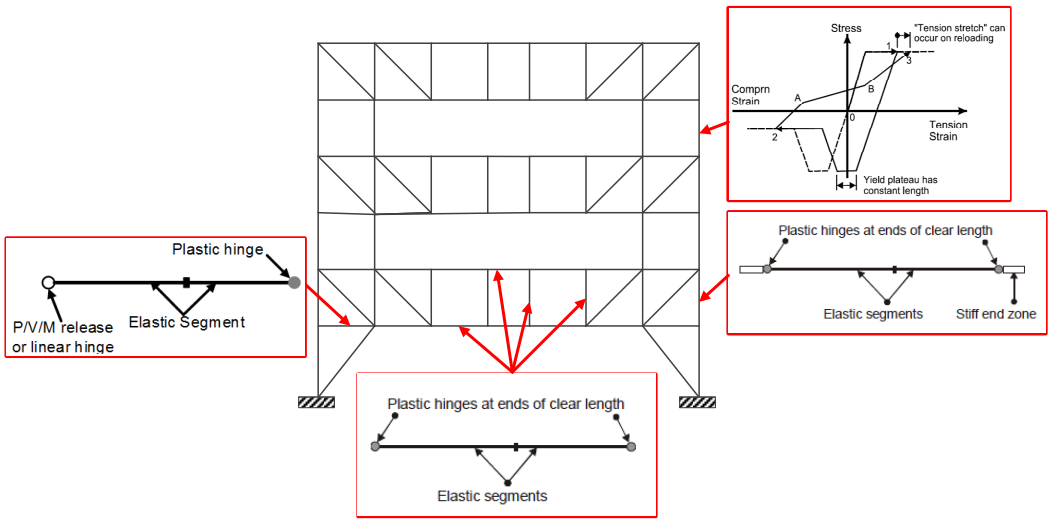

Figure 5-2 Component models for design and nonlinear analyses of STF system.

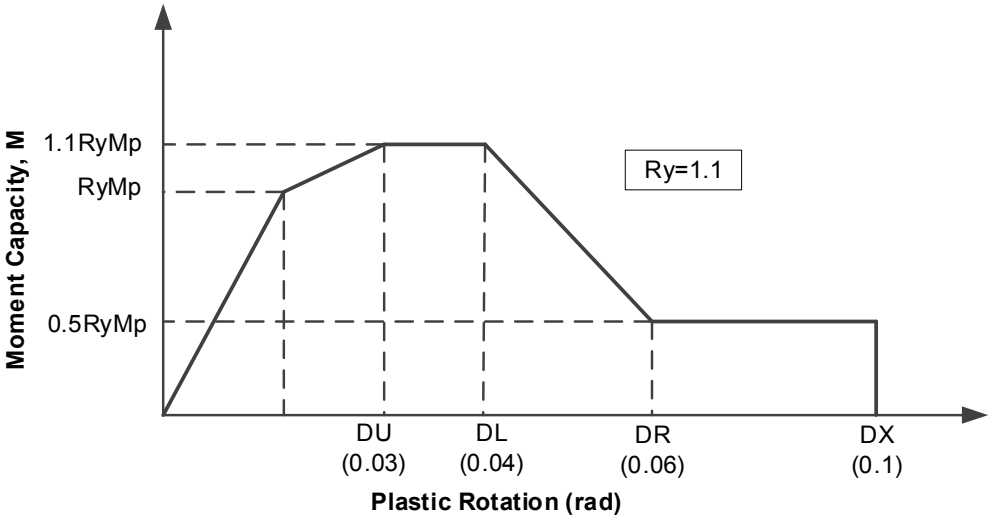

Figure 5-3 Member modeling properties of typical column element.

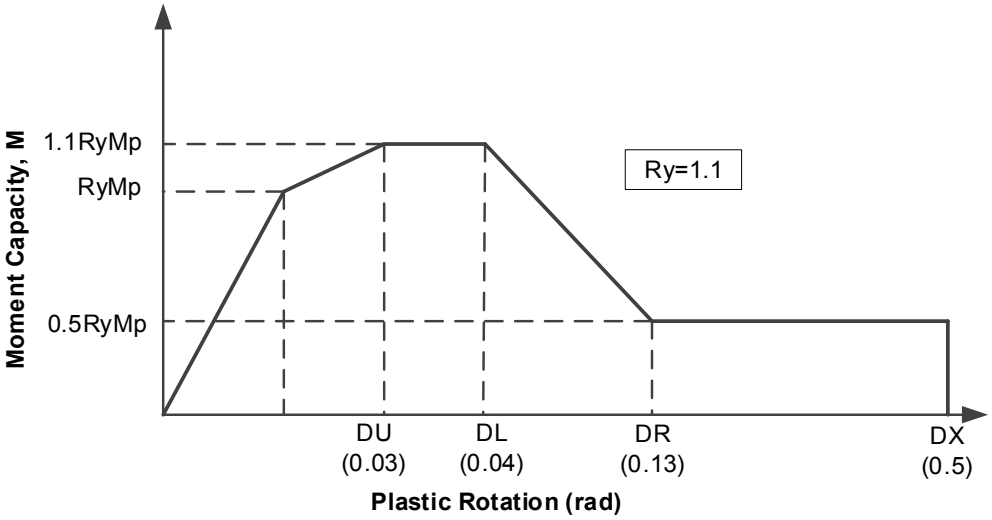

Figure 5-4 Member modeling properties of typical beam element.

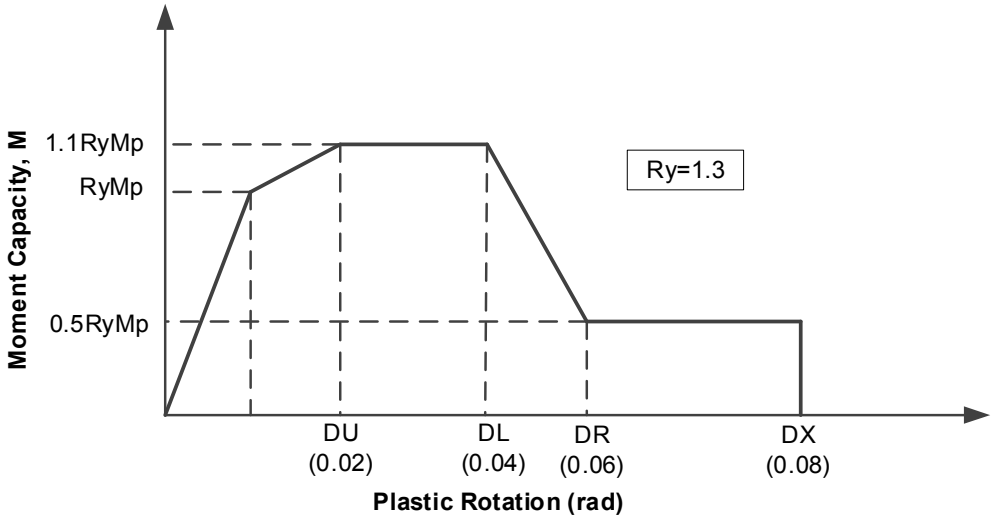

Figure 5-5 Member modeling properties of typical vertical members outside of the Vierendeel panels (Special segments).

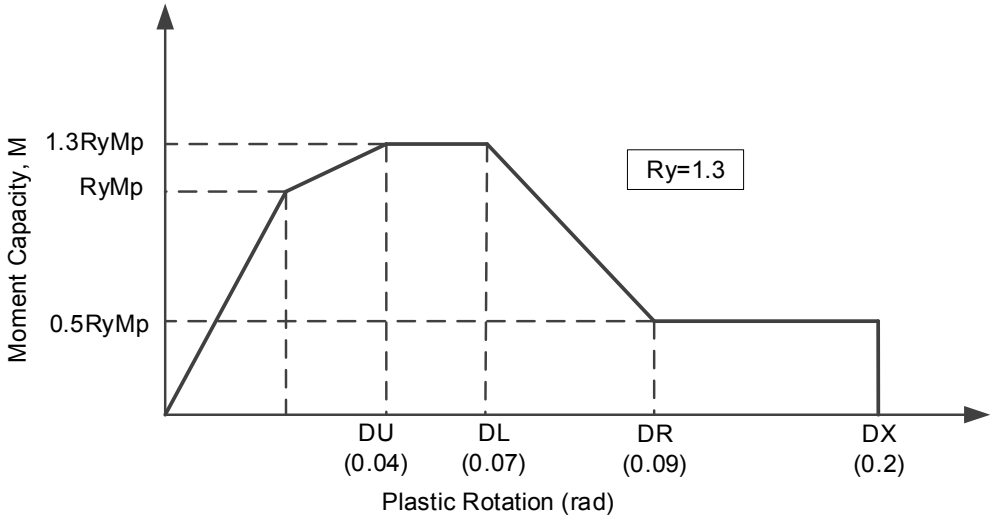

Figure 5-6 Member modeling properties of typical vertical members in the Vierendeel panels (Special segments).

The diagonal web members in the STF trusses, hangers, and posts were modeled as buckling-type steel strut. The expected yield and ultimate strengths of those members were determined in accordance with brace members as per AISC 341-10. The lengths of

yielding or buckling segments of the diagonal web members and the diagonal braces were taken as 85% of their working point lengths to account for the gusset plates and rigid zones of columns or chord members at the ends of those members. This effective length, 0.85L, was used in the computation of the compressive strength of the buckling type members. P-Delta effect due to gravity loads was included in the analyses. The Rayleigh damping (combination of the mass and stiffness proportion damping) matrix suggested by Perform-3D (CSi, 2011) as shown in Figure 5-7 and the recommended damping ratio for welded steel structure of 2% is used throughout the analysis (Chopra, 2007).

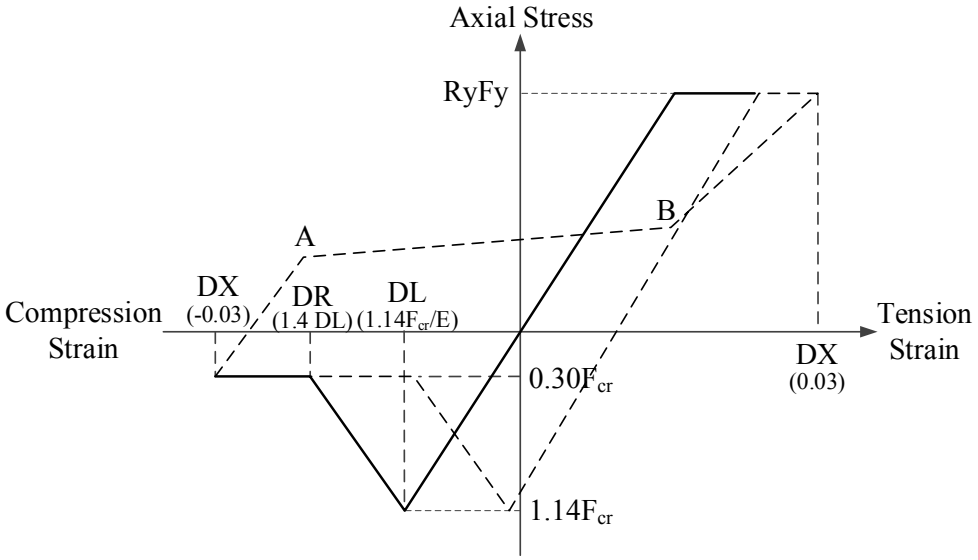

Figure 5-7 Member modeling properties of typical buckling-type element.

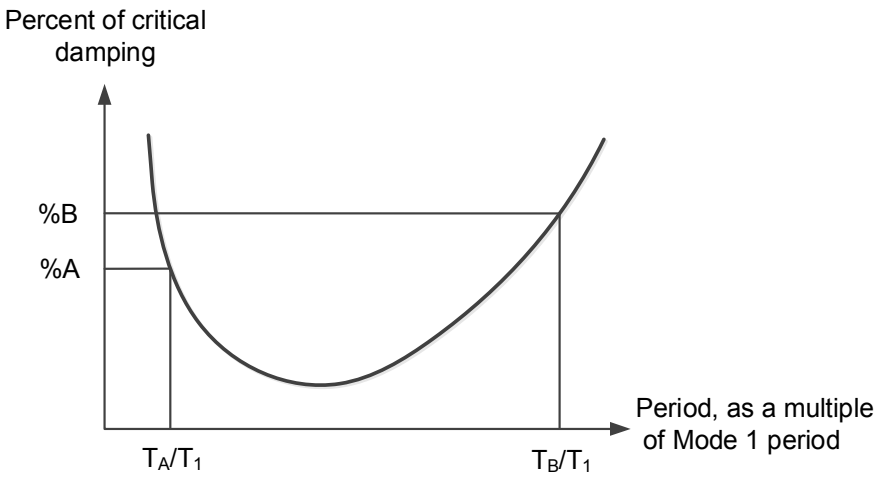

Figure 5-8 Rayleigh damping matrix.

Table 5-1 Rayleigh damping matrix

	Point A	Point B
Damping, %	2	2
Period ratio, T/T1	1	2

Chapter 6

Design Procedure and Nonlinear Analyses.

6.1 Introduction

This chapter presents a design procedure for the STF system and a seismic performance evaluation of the proposed modified layout for mid-to high-rise STF buildings. Six-story modified prototype STF with vertical members at the ends of the non-story levels were designed first, then the same procedure was followed to design two different heights STF buildings, twelve-story and twenty-story. For comparison purposes, six-story STF building with diagonal braces (kickers) at the ends of the non-story levels which were proposed by Simasathien et al. (2014) and a six-story conventional STF were also designed.

All the structures were designed and analyzed based on ASCE's Minimum Design Loads for Buildings and Other Structures (ASCE 7) (ASCE 2016). A nonlinear static pushover analysis was performed using the program PERFORM-3D to design the structures through elastic and inelastic behavior of the structure up to a target drift. Nonlinear static pushover and time-history analyses for all structures were carried out using PERFORM-3D to evaluate their seismic performance. The results of the analyses are discussed in chapter 7.

6.2 Structures geometry and gravity loads

The six-story is (64 ft. 1½ in.) by (180 ft.) in plan and (64 ft. 6 in.) in height. The floor height on the first level is 12 ft. where the upper levels are 10.5 ft. There are six bays with 36 ft. spacing on centers in the transverse direction. The horizontal trusses are shifted to avoid the direct gravity loading on the Vierendeel panels as illustrated in Figure 6-1.The STF system serves as the seismic force-resisting system in the transverse direction. In the

longitudinal direction, conventional moment-resisting frames are used along the perimeter as the seismic force resisting system.

Figure 6-2 and Figure 6-3 show the structural geometries of the 6-story STF system (kickers) and the 6-story conventional STF respectively which were designed for the comparison purposes in this study.

The twelve-story and twenty-story have the same plan dimensions as in the six-story. However, the heights are (127 ft. 6 in.) and (211 ft. 6 in.) for the twelve-story and the twenty-story as shown in Figure 6-4 and Figure 6-5, respectively.

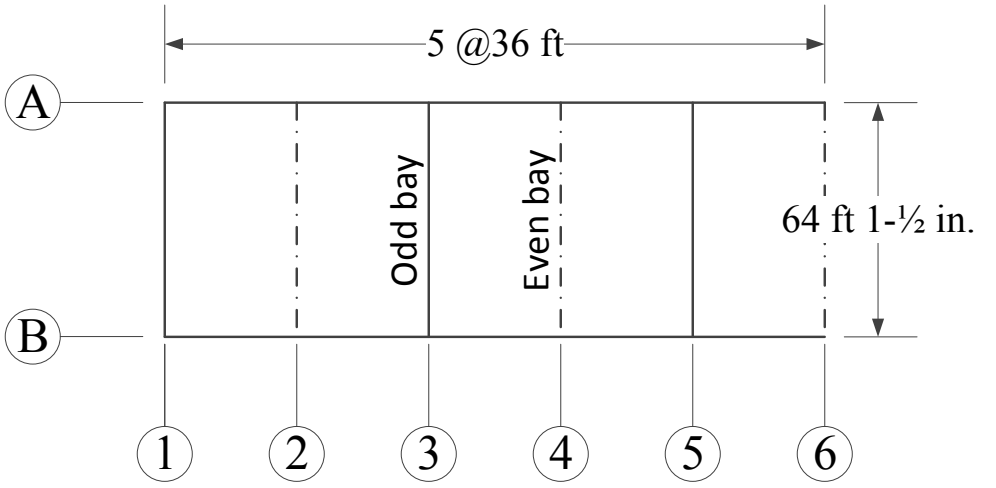

(a)

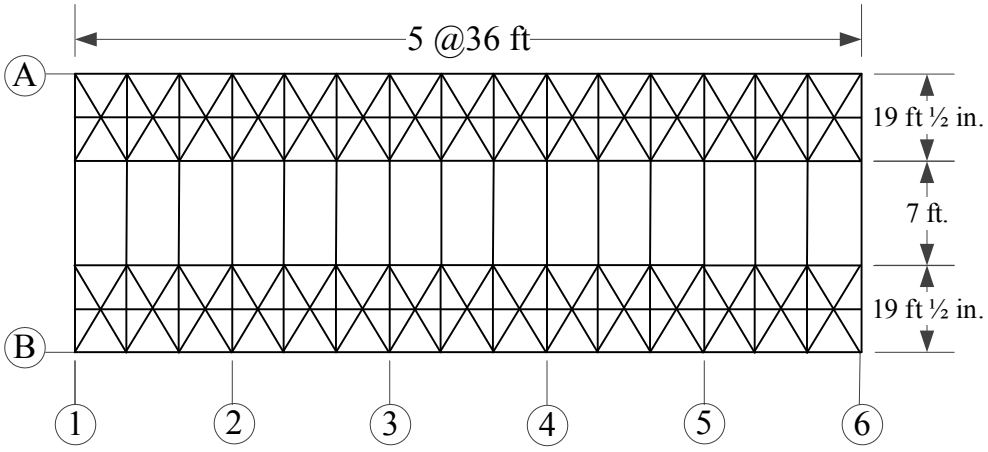

(b)

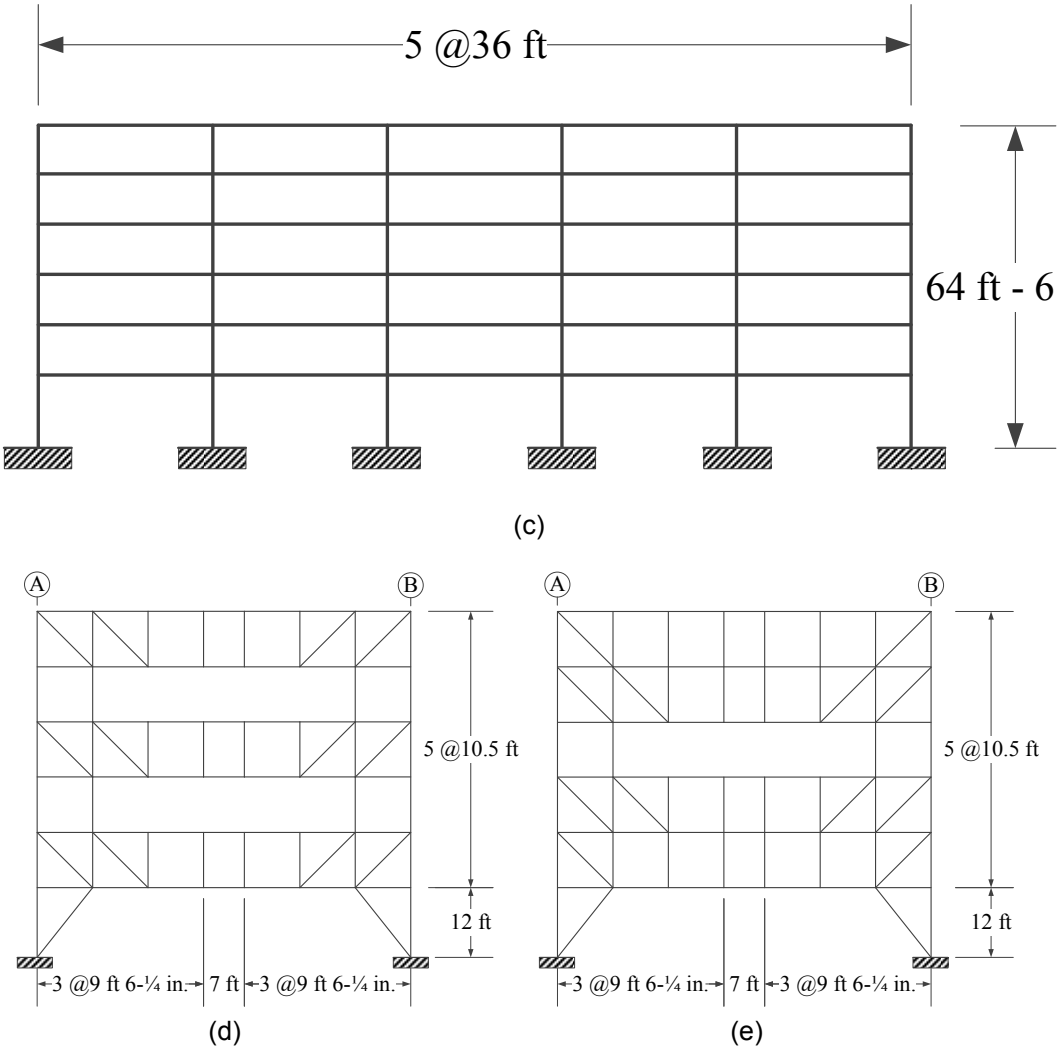

Figure 6-1 Structural geometry of the 6-story modified STF system (vertical members): (a) plan view horizontal trusses not shown for clarity ; (b) horizontal trusses plan (c) longitudinal side (moment frame) view; (d) elevation view of odd bay; (e) elevation view of even bay

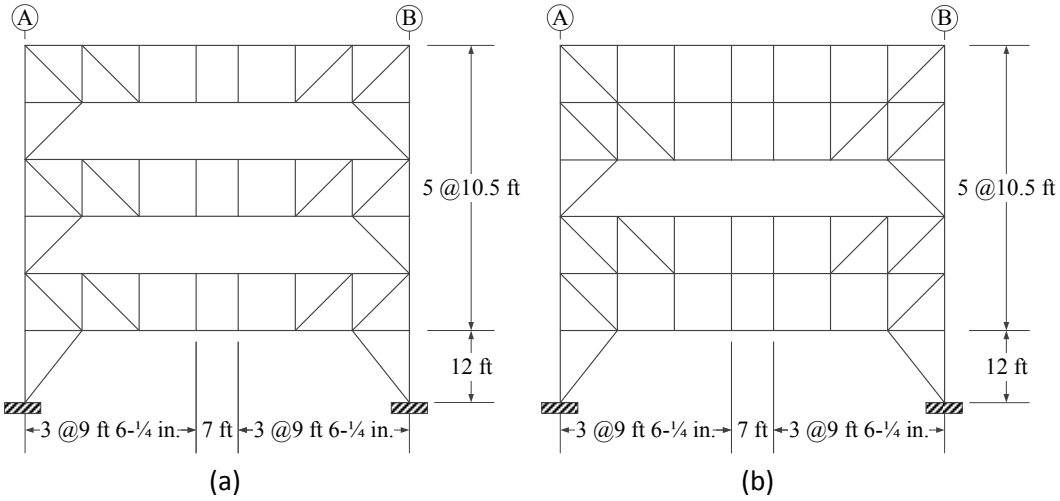

Figure 6-2 Structural geometry of the 6-story STF system (kickers): (a) elevation view of odd bay; (b) elevation view of even bay.

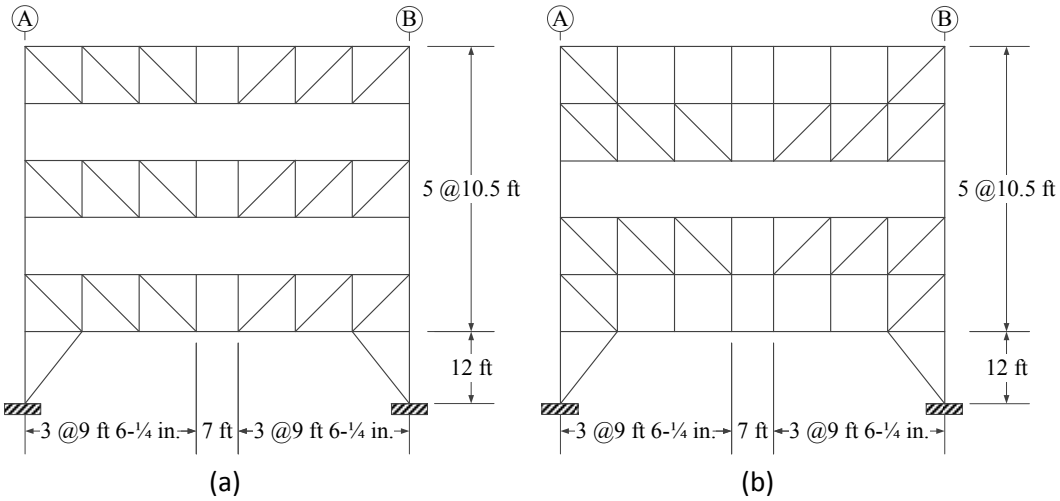

Figure 6-3 Structural geometry of the conventional 6-story STF system: (a) elevation view of odd bay; (b) elevation view of even bay.

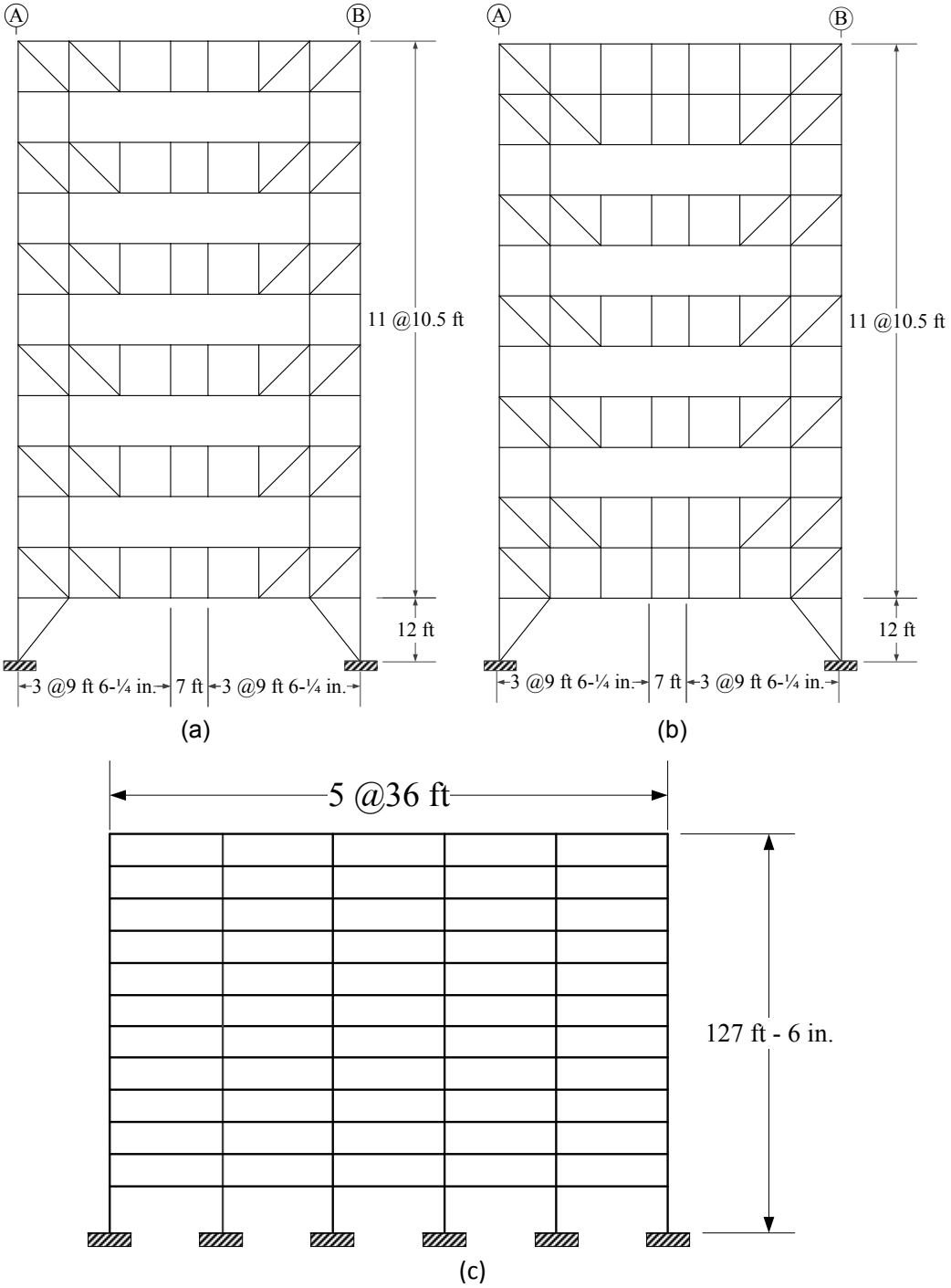

Figure 6-4 Structural geometry of the 12-story STF system: (a) elevation view of odd bay; (b) elevation view of even bay; (c) longitudinal side (moment frame) view.

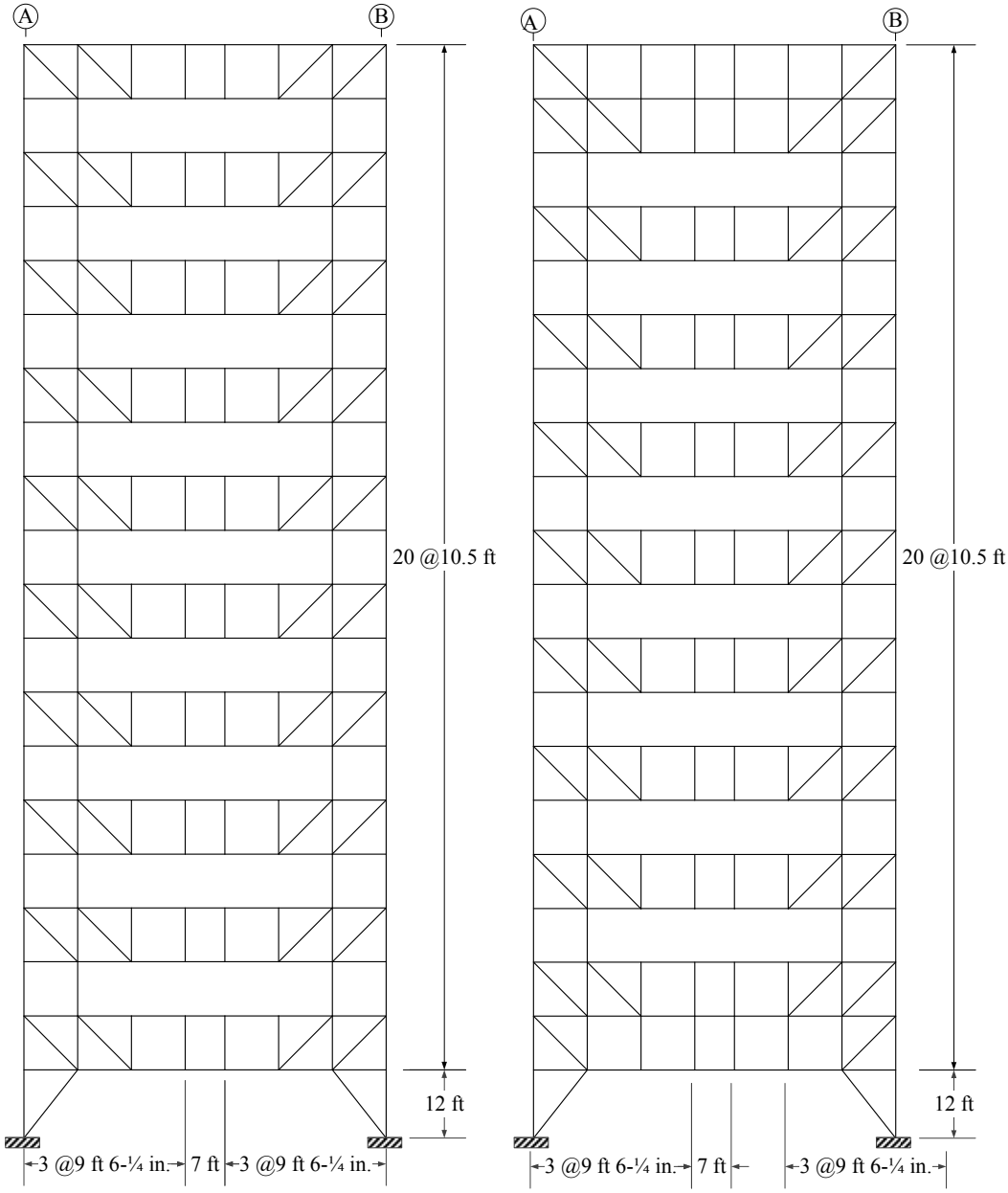
A
B
20 @10.5 ft
12 ft
3 @9 ft 6-¼ in.
7 ft
3 @9 ft 6-¼ in.
A
B
20 @10.5 ft
12 ft
3 @9 ft 6-¼ in.
7 ft
3 @9 ft 6-¼ in.

(a) (b)

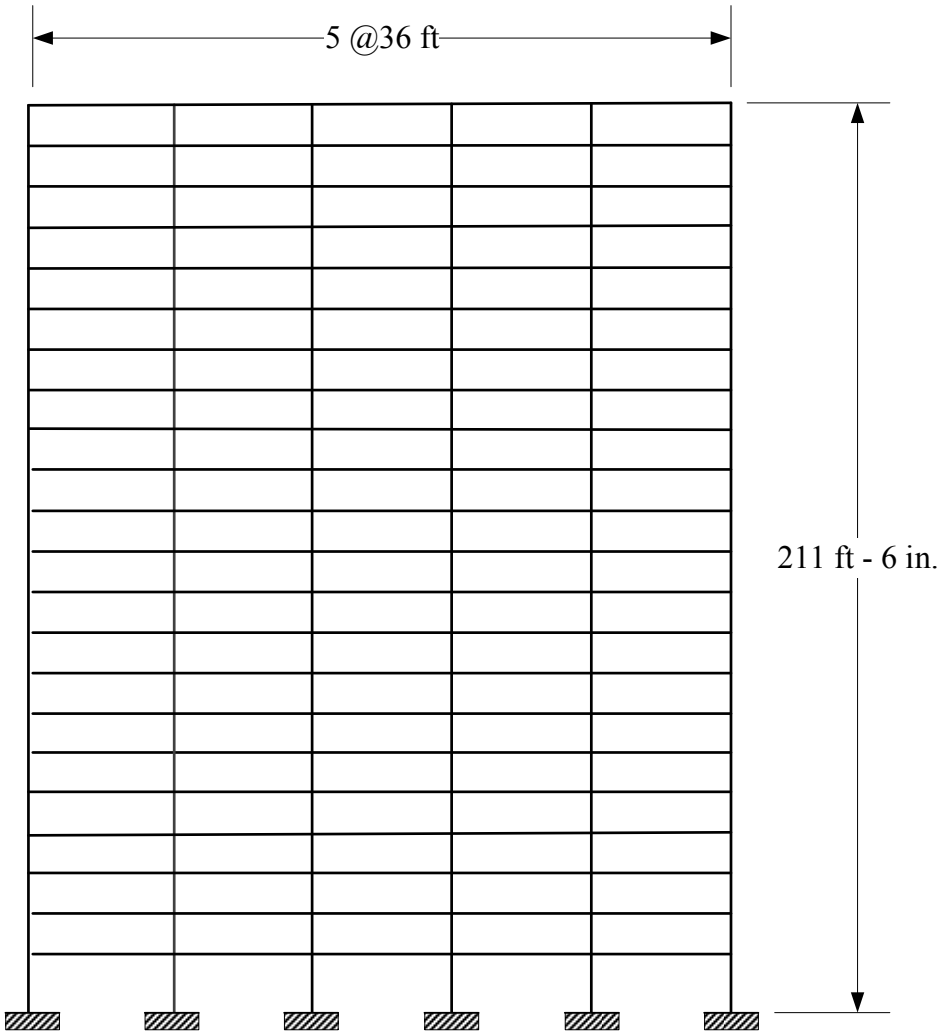

(c)

Figure 6-5 Structural geometry of the 20-story STF system: (a) elevation view of odd bay; (b) elevation view of even bay; (c) longitudinal side (moment frame) view.

The design gravity loads for the model structures are shown in , the dead load of 97 psf and live load of 40 psf were used as gravity load. Structural member design was carried out according to the load and resistance factor design (LRFD) of AISC 360-16 with ASTM A992 for the wide flange section steel and ASTM 500 Gr.C for the hollow structural steel.

Table 6-1 Gravity loads used in the design of structures.

Dead Load	**97 psf**
- 8” precast hollow core plank.	60 psf
- Leveling compound.	5 psf
- Structural steel (Including horizontal trusses)	20 psf
- Partitions.	12 psf
Live Load	**40 psf**

6.3 Equivalent Lateral Force (ELF)

The Equivalent Lateral Force (ELF) method is a simplified technique in which the effect of dynamic loading of an expected earthquake is substituted by a static force (base shear) which is distributed laterally on a structure for design purposes. Equivalent Lateral Force (ELF) analysis of section 12.8 in ASCE 7-16 was used for the seismic design of the STF system. San Francisco, California was selected because there is seismic activity and the USGS maps website was used to determine the seismic design parameters. Because the soil properties are not known in sufficient detail to determine the site class, site class D was selected (Section 11.4-3-ASCE 7-16).

Based on Table 1.5-1 in ASCE 7-16 and Table 1604.5 in IBC-2018, risk category II was selected for 6 and 12 stories structures and risk category III was selected for the 20 stories. Both tables 11.6-1 and 11.6-2 in ASCE 7-16 were used to determine the Seismic Design Category (SDC).

Table 6-2 shows the seismic design parameters which were used in the seismic design for the STF structures for risk categories II and III.

Table 6-2 Seismic design parameters.

MCE Short Period Spectral Response Acc., S_s	1.5g
MCE One-second Spectral Response Acc., S_1	0.60g
Acceleration Site Coefficient, F_a	1.0
Velocity Site Coefficient, F_v	1.7
Short Period Design Spectral Response Acc., S_{DS}	1.0g
One-second Design Spectral Response Acc., S_{D1}	0.68g
Site Class	D
Seismic Design Category (SDC)	D
Long-period transition period in seconds, T_L	12

6.3.1 Calculation of the fundamental period (T)

The approximate fundamental period (T_a), in second, was determined in accordance with the following equation (Eq. 12.8-7) ASCE 7-16:

$$T_a = C_t h_n^x$$

where the value of the coefficients C_t and x were taken from (Table 12.8-2) ASCE 7-16 for "All other structural system" category,0.02 and 0.75 respectively. h_n (ft) is the structural height measured from the base to the highest level of the structure.

Assuming from computer analysis that $T_{computed} > C_u T_a$, where Cu is a coefficient for upper limit on calculated period taken from Table 12.8-1-ASCE 7-16. Therefore, the following equation was used to calculate the fundamental period:

$$T = C_u T_a = C_u C_t h_n^x$$

6.3.2 Calculation of seismic base shear (V):

The seismic base shear, V, was determined using the following equation (Eq. 12.8-7) ASCE 7-16:

$$V = C_s W$$

Where W is the effective seismic weight of the system; C_s ,the seismic response coefficient, is determined using the following equation (Eq. 12.8-2) ASCE 7-16:

$$C_s = \frac{S_{DS}}{\left(\frac{R}{I_e}\right)}$$

where S_{DS} is the design spectral response acceleration parameter in the short period range, R is the response modification factor, and I_e is the importance factor. Because the STF system is not addressed as a seismic force-resisting system in ASCE 7-16 Table 12.2-1, a response modification factor of the Steel Special Concentrically Braced Frames (SCBF), was conservatively used in the seismic design. Table 1.5-2 was used to determine the importance factor.

The value of C_s which is computed in accordance with the (Eq. 12.8-2) needs not exceed the value of C_s in (Eq. 12.8-3, Eq. 12.8-4) ASCE 7-16

$$C_s = \frac{S_{D1}}{T\left(\frac{R}{I_e}\right)} \qquad T \le T_L$$

$$C_s = \frac{S_{D1} T_L}{T^2\left(\frac{R}{I_e}\right)} \qquad T \ge T_L$$

Where S_{D1} is the design spectral response acceleration parameter at a period of 1.0 second and T is the fundamental period of the structure.

Table 6-3 shows the values of all design parameters that are used to determine the Seismic Response Coefficient calculations (Cs) based on the procedure and equations that mentioned above.

Table 6-3 Design parameters for the 6-Story,12-Story, and 20-Story Prototype STF Buildings.

parameters	Story Level		
	6	12	20
Building Height (ft.)	64.5	127.5	211.5
The approximate fundamental period, Ta (s)	0.455	0.759	1.109
Coefficient for upper limit on calculated period, Cu	1.4	1.4	1.4
The fundamental period of the structure, T (s)	0.637	1.063	1.552
Occupancy Importance Factor, I	1.0	1.0	1.25
Response Modification Factor, R	6.0	6.0	6.0
Seismic Response Coefficient, Cs	0.167g	0.107g	0.091g
Total Building Weight, W (Kips).	6720	13440	22400

Vertical lateral seismic force distribution over the height of the structure was carried out according to ASCE (Eq.12.8-11 and Eq.12.8-12) which are shown below:

$$F_x = C_{vx} V$$

$$C_{vx} = \frac{w_x h_x^k}{\sum_{i=1}^{n} w_i h_i^k}$$

where

C_{vx} : Vertical distribution factor;

V :Total design lateral force or shear at the base of the structure (kip);

w_i and w_x : Portion of the total effective seismic weight of the structure (W) located or assigned to level i or x;

h_i and h_x = height [ft (m)] from the base to level i or x; and

k = an exponent related to the structure period as follows:

- For structures that have a period of 0.5 s or less, k = 1;
- For structures that have a period of 2.5 s or more, k = 2; and
- For structures that have a period between 0.5 and 2.5 s, k=0.75+0.5T.

The lateral force distribution for 6-Story, 12-Story, and 20-Story STF are presented in the Table 6-4 through Table 6-6.

Table 6-4 Lateral force distribution for 6-story prototype buildings.

Level	h_i (ft)	w_i (kips)	$w_i h_i^k$	C_{vi}	F_i (kips)
2	12	1120	15934	0.0479	53.7
3	22.5	1120	31191	0.0937	105.2
4	33	1120	46962	0.1411	158.4
5	43.5	1120	63088	0.1896	212.8
6	54	1120	79484	0.2389	268.1
Roof	64.5	1120	96102	0.2888	324.1
Total	64.5	6720	332761	1	1122.2

k=1.0685

Table 6-5 Lateral force distribution for 12-story prototype building.

Level	h_i (ft)	w_i (kips)	$w_i h_i^k$	C_{vi}	F_i (kips)
2	12	1120	27051	0.0083	11.9
3	22.5	1120	60540	0.0186	26.7
4	33	1120	98899	0.0304	43.7
5	43.5	1120	140910	0.0433	62.2
6	54	1120	185901	0.0571	82.1
7	64.5	1120	233437	0.0717	103.1
8	75	1120	283210	0.0870	125.0

9	85.5	1120	334991	0.1028	147.9
10	96	1120	388596	0.1193	171.6
11	106.5	1120	443881	0.1363	196.0
12	117	1120	500724	0.1537	221.1
Roof	127.5	1120	559023	0.1716	246.8
Total	127.5	13440	3257162	1	1438.1

K= 1.2815

Table 6-6 Lateral force distribution for 20-story prototype building.

Level	h_i (ft)	w_i (kips)	$w_i h_i^k$	C_{vi}	F_i (kips)
2	12	1120	49665	0.0015	3.0
3	22.5	1120	129613	0.0039	7.9
4	33	1120	232525	0.0069	14.1
5	43.5	1120	354448	0.0106	21.5
6	54	1120	493005	0.0147	29.9
7	64.5	1120	646556	0.0193	39.3
8	75	1120	813882	0.0242	49.4
9	85.5	1120	994027	0.0296	60.3
10	96	1120	1186216	0.0353	72.0
11	106.5	1120	1389804	0.0414	84.4
12	117	1120	1604241	0.0478	97.4
13	127.5	1120	1829054	0.0545	111.0
14	138	1120	2063828	0.0615	125.3
15	148.5	1120	2308196	0.0687	140.1
16	159	1120	2561828	0.0763	155.5
17	169.5	1120	2824431	0.0841	171.5
18	180	1120	3095736	0.0922	187.9
19	190.5	1120	3375497	0.1005	204.9
20	201	1120	3663492	0.1091	222.4
Roof	211.5	1120	3959512	0.1179	240.4
Total	211.5	22400	33575556	1	2038.4

K= 1.526

6.4 Design of members

The prototypes STF buildings first modeled using PERFORM-3D as explained in chapter 5. The gravity load was determined according to its respective tributary area and load path, then it was applied as a distributed load over the beams as shown in Figure 6-6.

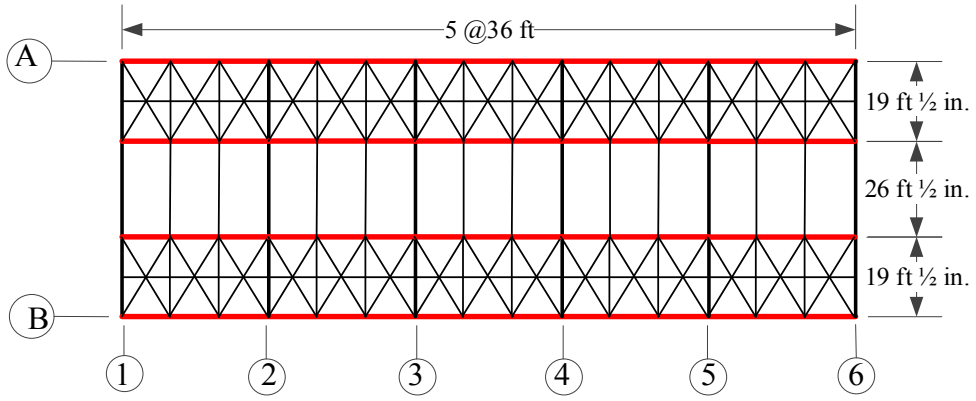

Figure 6-6 Locations of beams (red color) where gravity load was applied.

The members of the STF buildings were first designed elastically based on the load combinations as defined in ASCE7-16. The critical gravity load combination of $((1.2+0.2S_{DS})D+\rho Q_E+0.5LL)$ which includes the vertical seismic load effect ($0.2S_{DS}$) with redundancy factor, ρ, and overstrength factor, Ωo, equal to 1.0 were used in the design.

The lateral earthquake forces that were calculated above based on the Equivalent Lateral Force (ELF) method according to ASCE7-16 were applied. The calculated lateral load for each floor was divided and applied equally on the joints of the horizontal trusses as it can be seen in Figure 6-7.

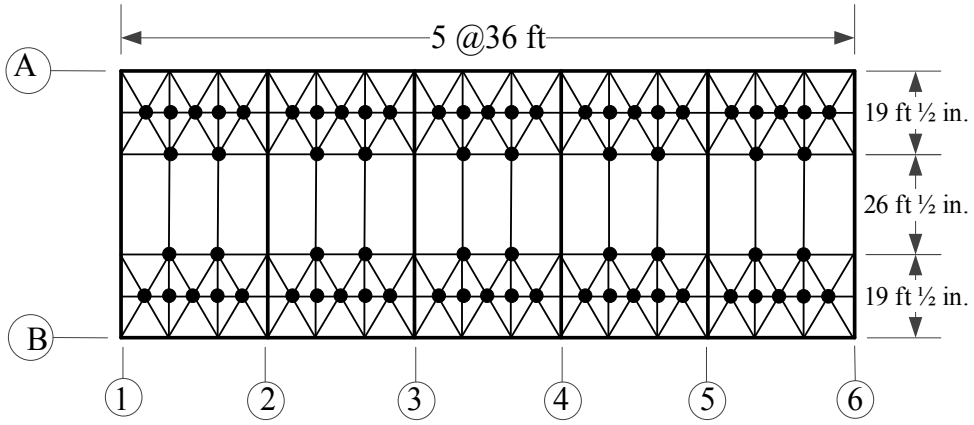

Figure 6-7 Locations of the applied lateral earthquake forces on the steel horizontal trusses.

In the final design of members, the sizes of chords and vertical members of the Vierendeel panels (Special segments) were kept with the same size sections as in the elastically design as illustrated in Figure 6-8. However, the truss members outside the Vierendeel panels including chords and vertical members, diagonal web members, horizontal truss members, interior and spandrel beams, and columns were redesigned using the capacity design approach based on lateral forces corresponding to 1% roof drift (as shown in Figure 6-9) from pushover analysis considering plastic hinge properties of the truss members in the Vierendeel panels.

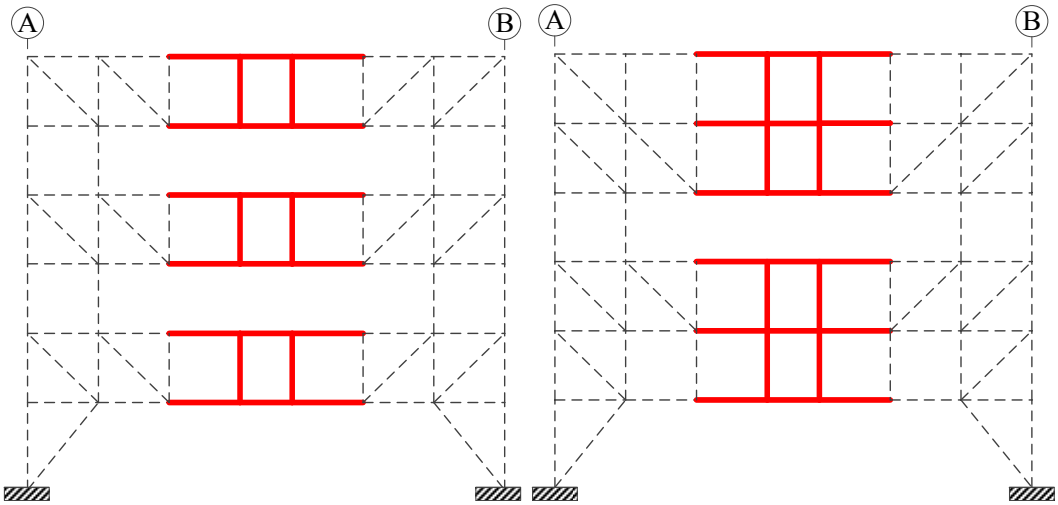

Figure 6-8 Locations of members that were kept with the same size sections as in the elastically design (a) Odd bays (b) Even bays.

However, if the pushover analysis shows that any yielding occurs outside of the SS, except at the base of the columns, such nonyielding member needs to be redesigned to ensure that it remains elastic. In other words, a nonlinear pushover of 1% roof drift was performed until the chord members within the SS and intermediate vertical members fully yielded and the members outside, except at the base of the columns, remain elastic.

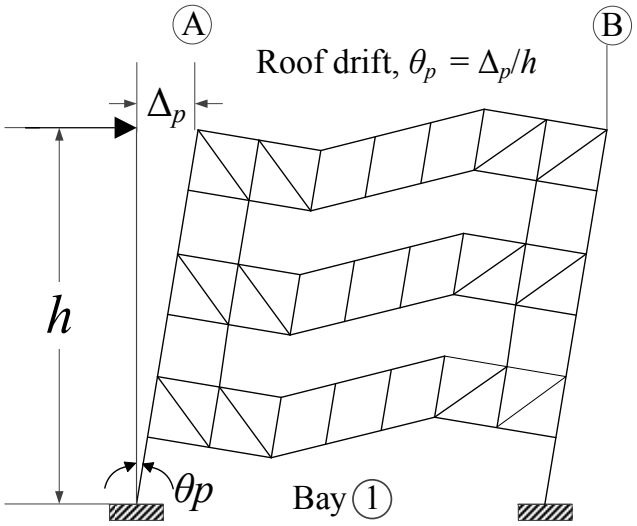

Figure 6-9 Roof drift calculation.

However, the 1% value was selected based on preliminary nonlinear time-history analyses using the DBE level ground motions, which indicated that the average interstory drift ratios were approximately 1%. This design approach was similar to that for the special segments with Vierendeel panels in the Special Truss Moment Frames (STMFs) (Chao and Goel, 2008), in which the yielding of members is limited within the Vierendeel panels of the STF system under large lateral forces.

Moreover, the gravity load combination of $((1.2+0.2S_{DS})$ D +0.5LL) was used in this capacity design approach. However, the pushover load was applied as in the ASCE7-16 where the load at the roof is 1.0 Kip. Furthermore, the pushover load for each floor was divided and applied uniformly on the same joints of the steel horizontal trusses that the lateral earthquake forces were applied (Figure 6-7).

Based on the above design procedure, Figure 6-10 through Figure 6-12 show the sizes of members for the 6-Story modified STF (Vertical members) for the 6-Story,12-Story,and 20-Story, respectively.

Figure 6-13 and Figure 6-14 show the sizes of members for the 6-Story modified STF (Kickers) and the 6-Story conventional STF, respectively. However, the sizes of members that were used in the horizontal trusses and the beams in the moment frame direction were used for both structures.

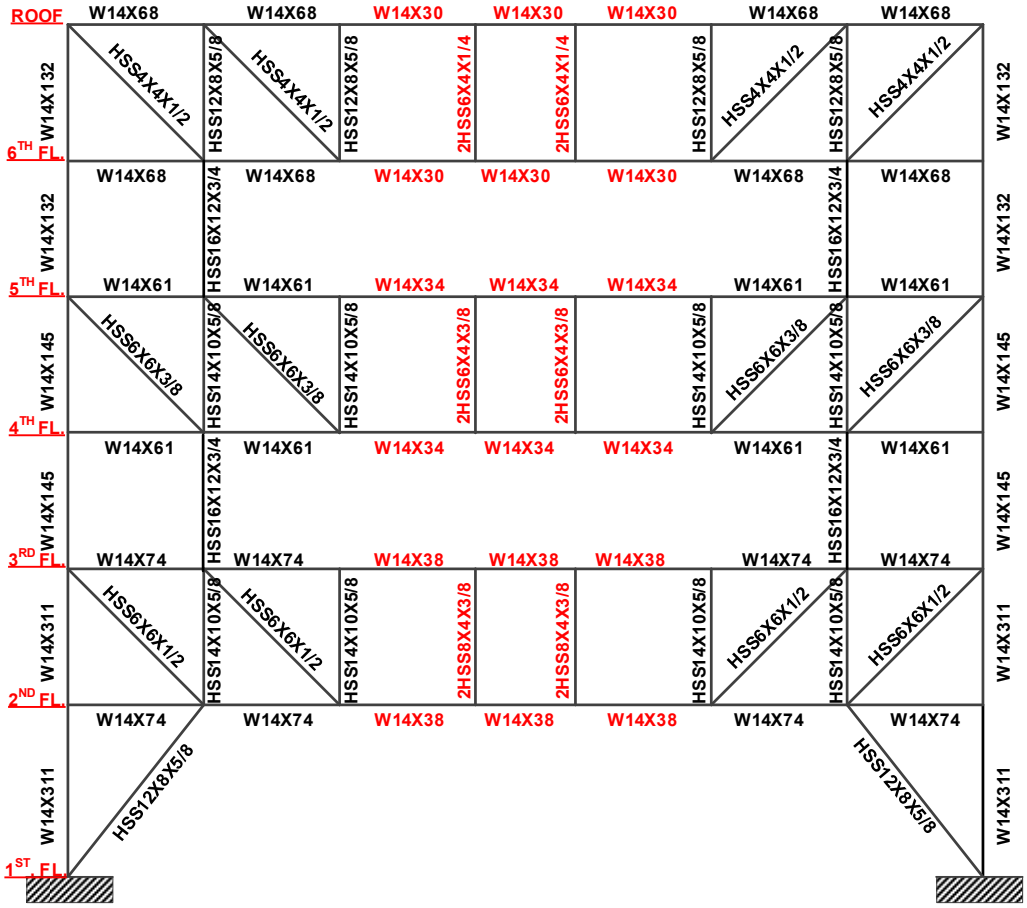

(a)

Figure 6-10 Typical member sections of the six-story building (vertical members): (a) odd bays; (b) even bays; (c) moment frame (d) Horizontal trusses(The members in red color are those which were kept the same as in the elastically design).

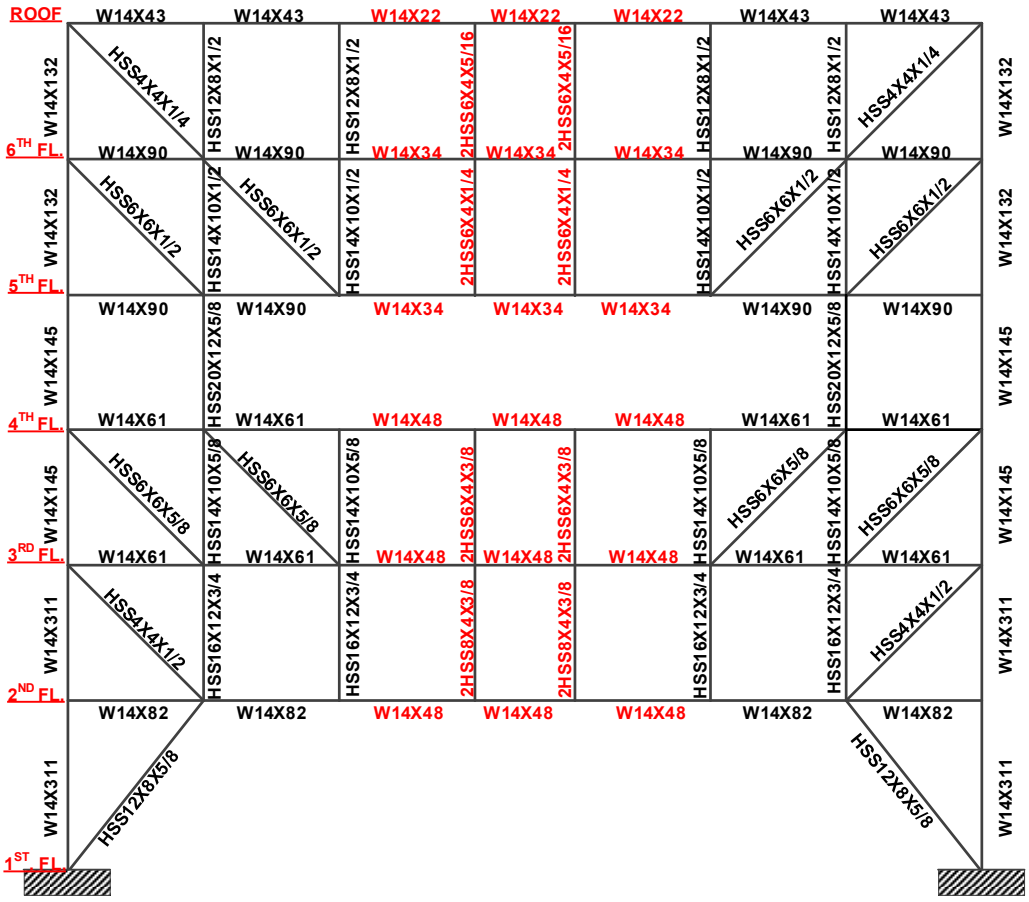

(b)

Figure 6-10 Continued.

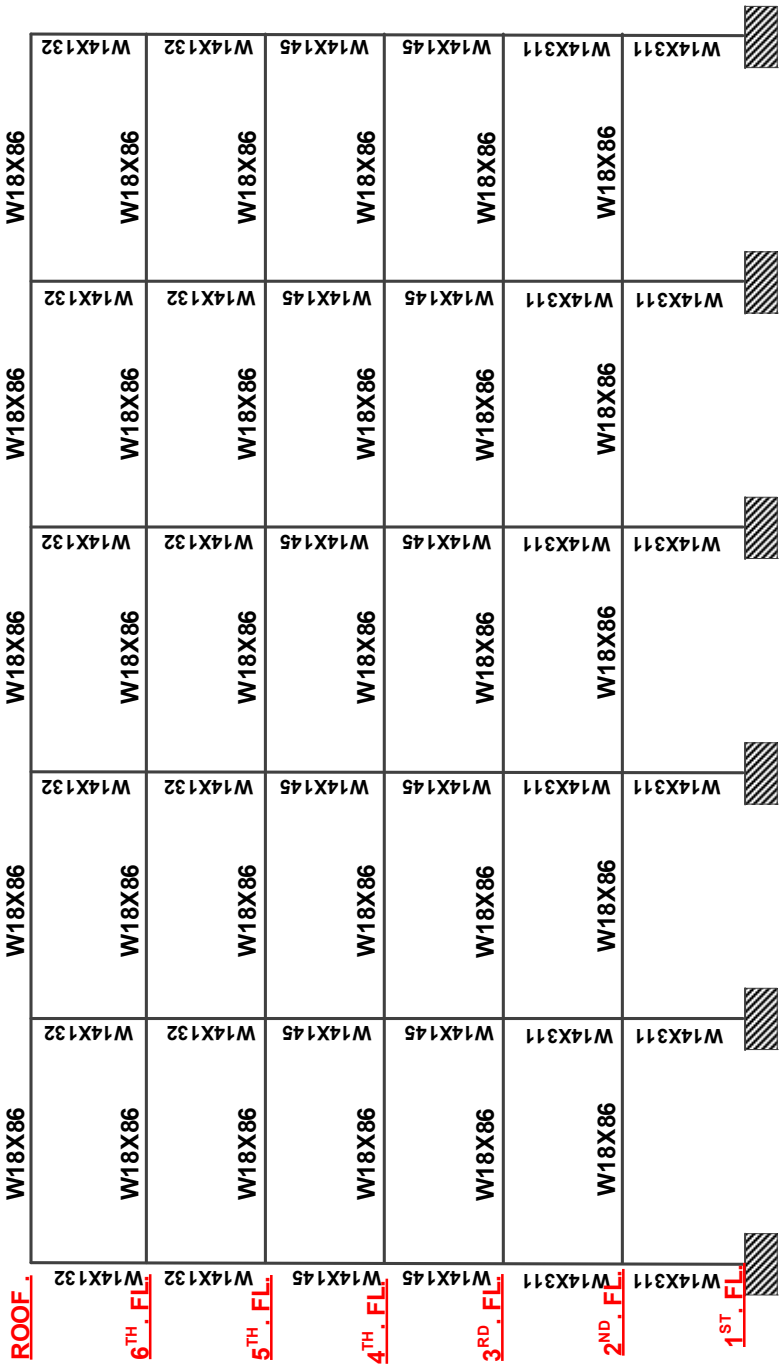

(c)

Figure 6-10 Continued.

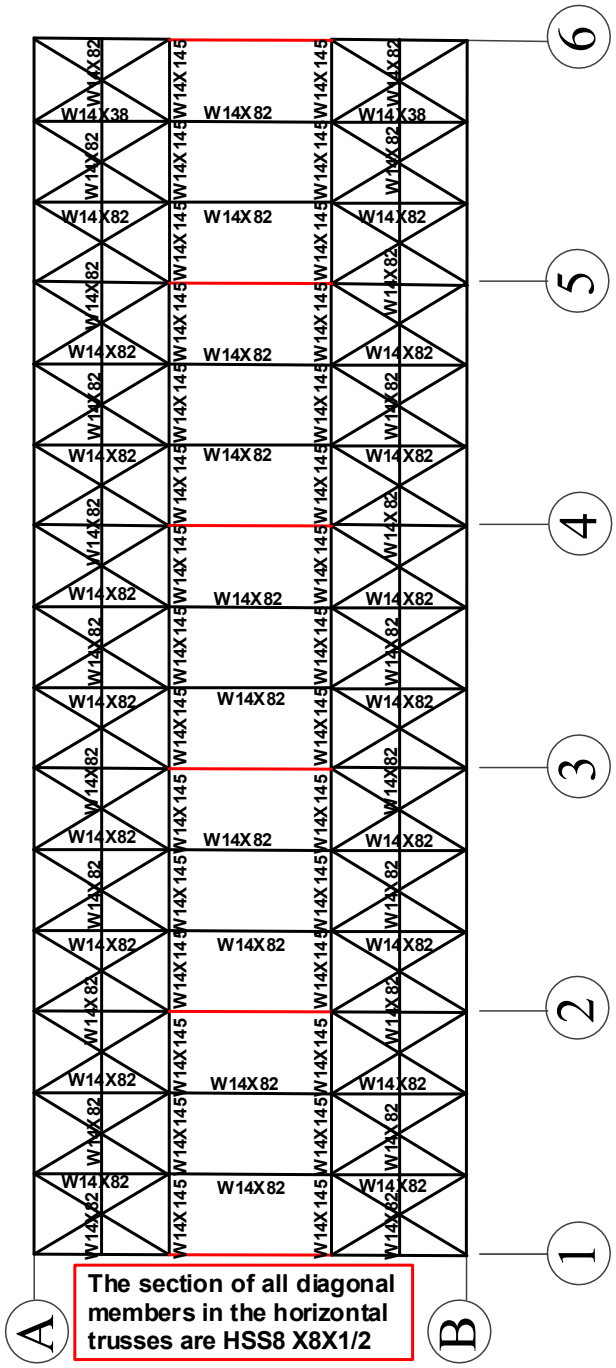

(d)

Figure 6-10 Continued.

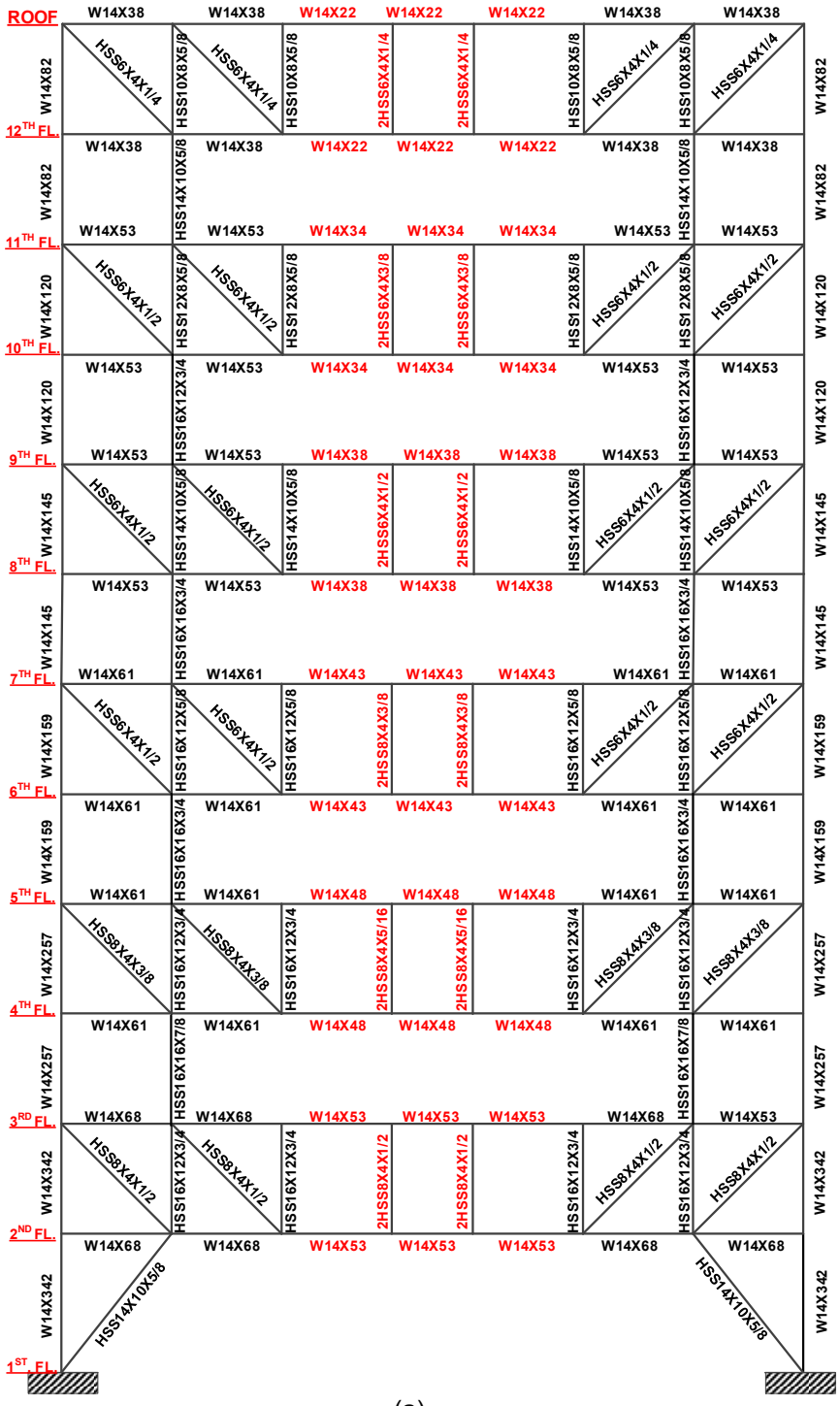

(a)

Figure 6-11 Typical member sections of the twelve-story building (vertical members): (a) odd bays; (b) even bays; (c) moment frame (d) Horizontal trusses.

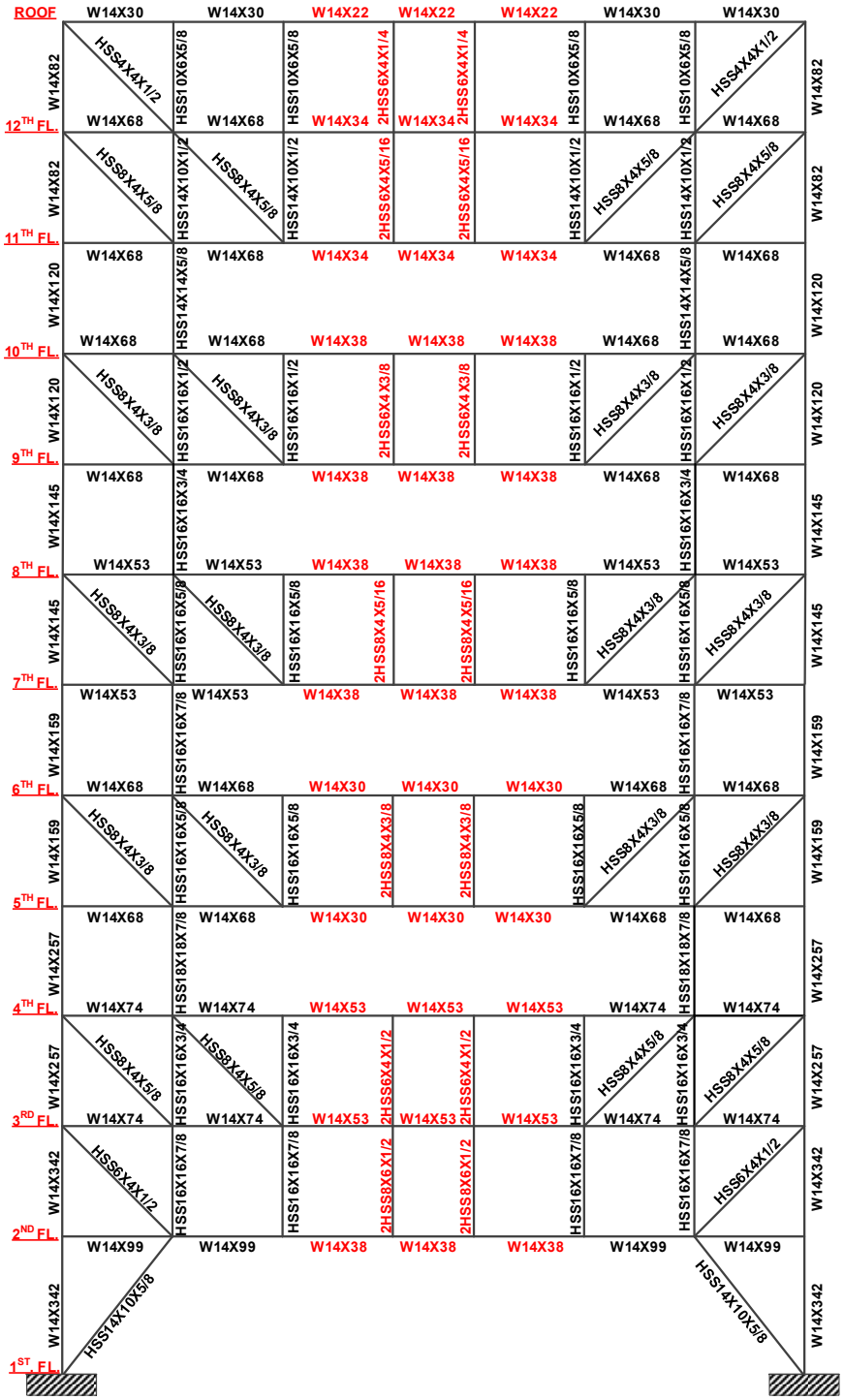

(b)

Figure 6-11 Continued.

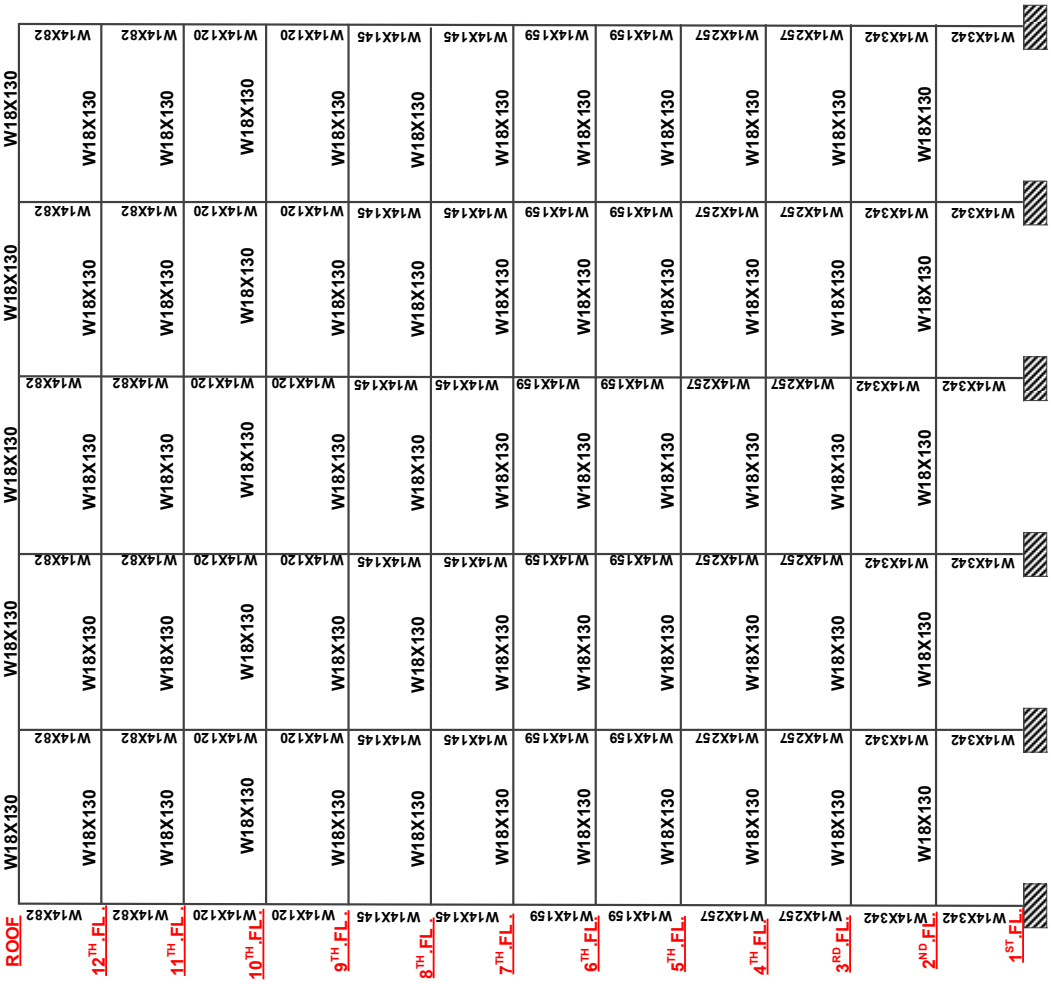

(b)

Figure 6-11 Continued.

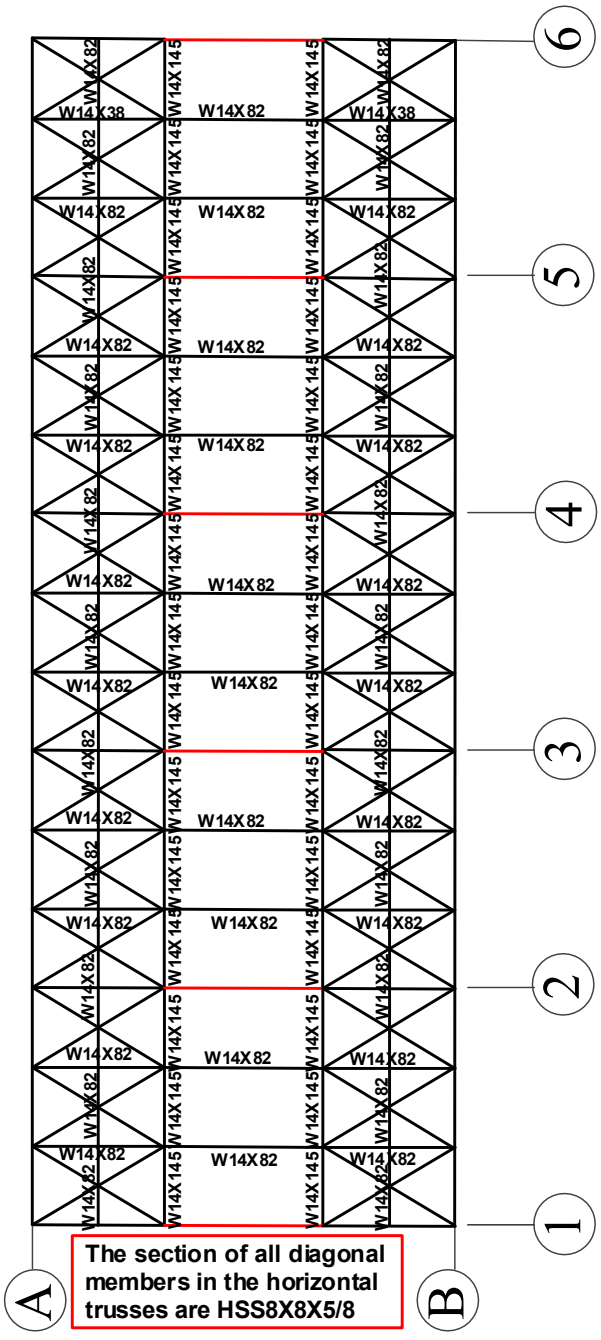

(d)

Figure 6-11 Continued.

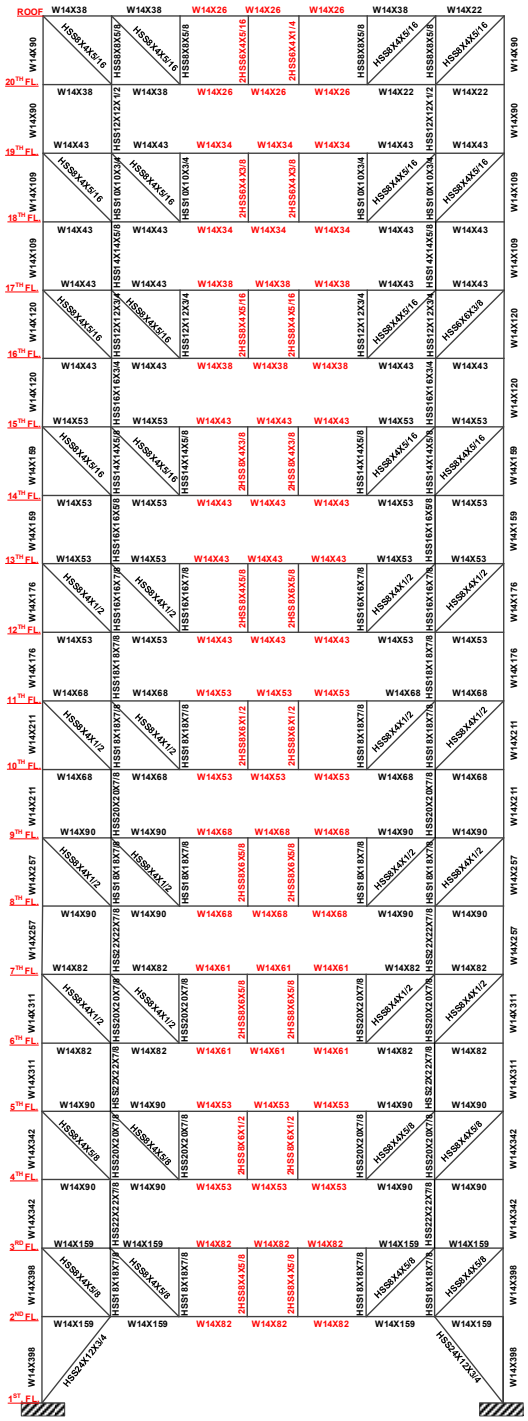

(a)

Figure 6-12 Typical member sections of the twenty-story building (vertical members): (a) odd bays; (b) even bays; (c) moment frame (d) Horizontal trusses.

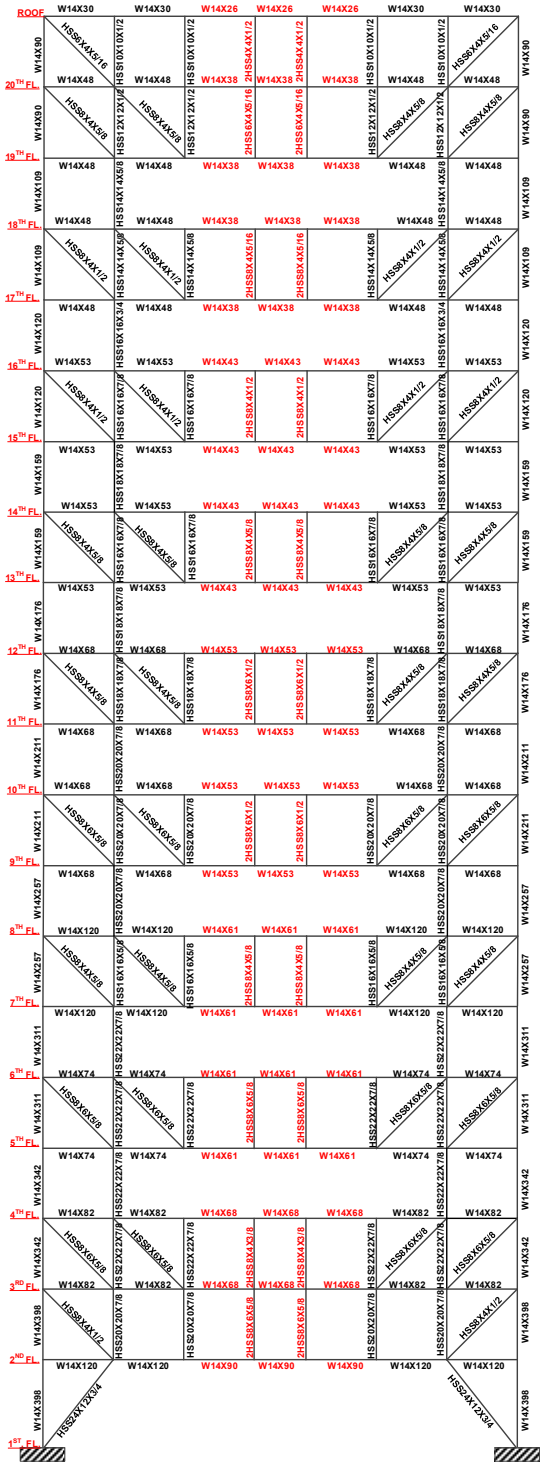

(b)

Figure 6-12 Continued.

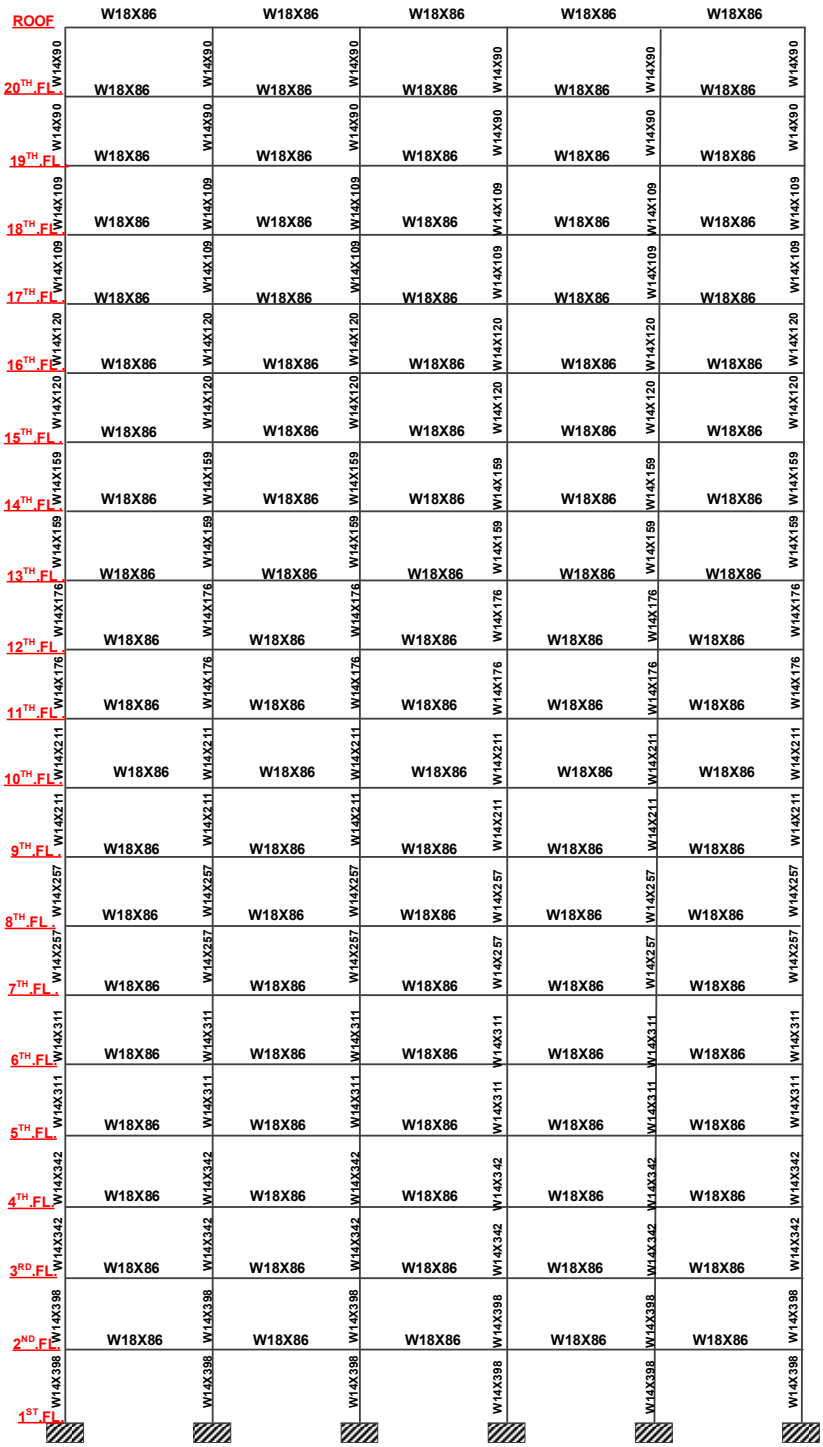

(c)

Figure 6-12 Continued

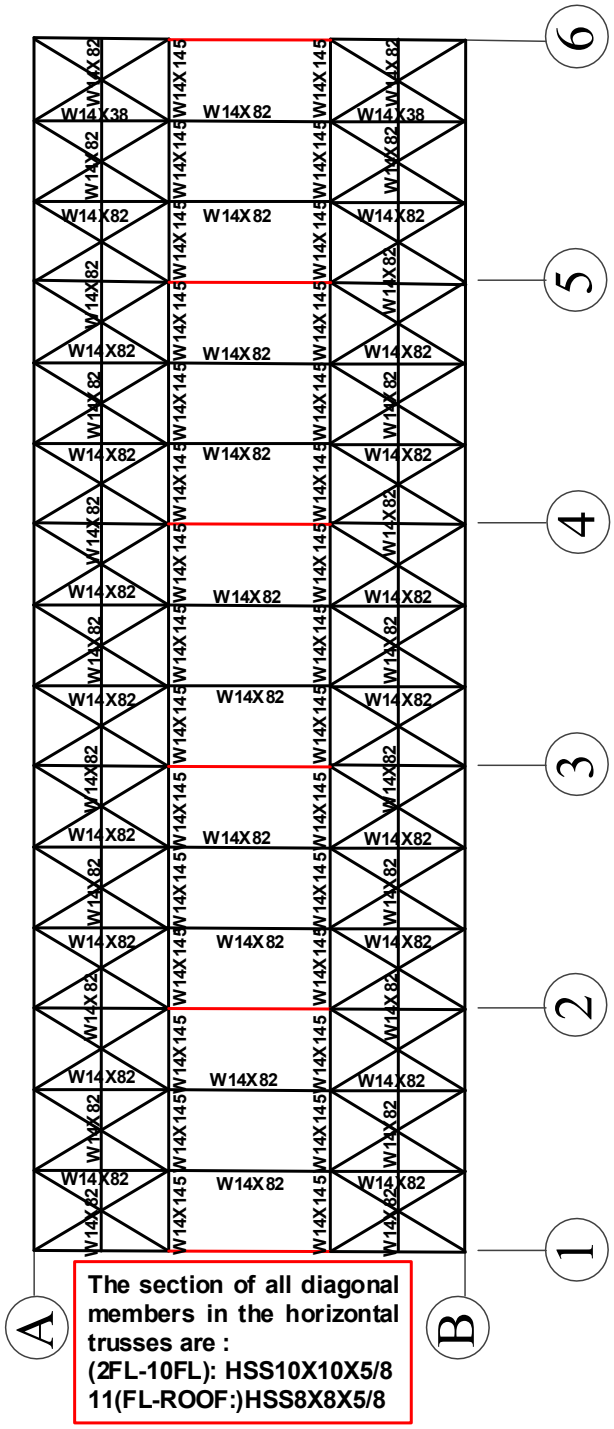

(d)

Figure 6-12 Continued

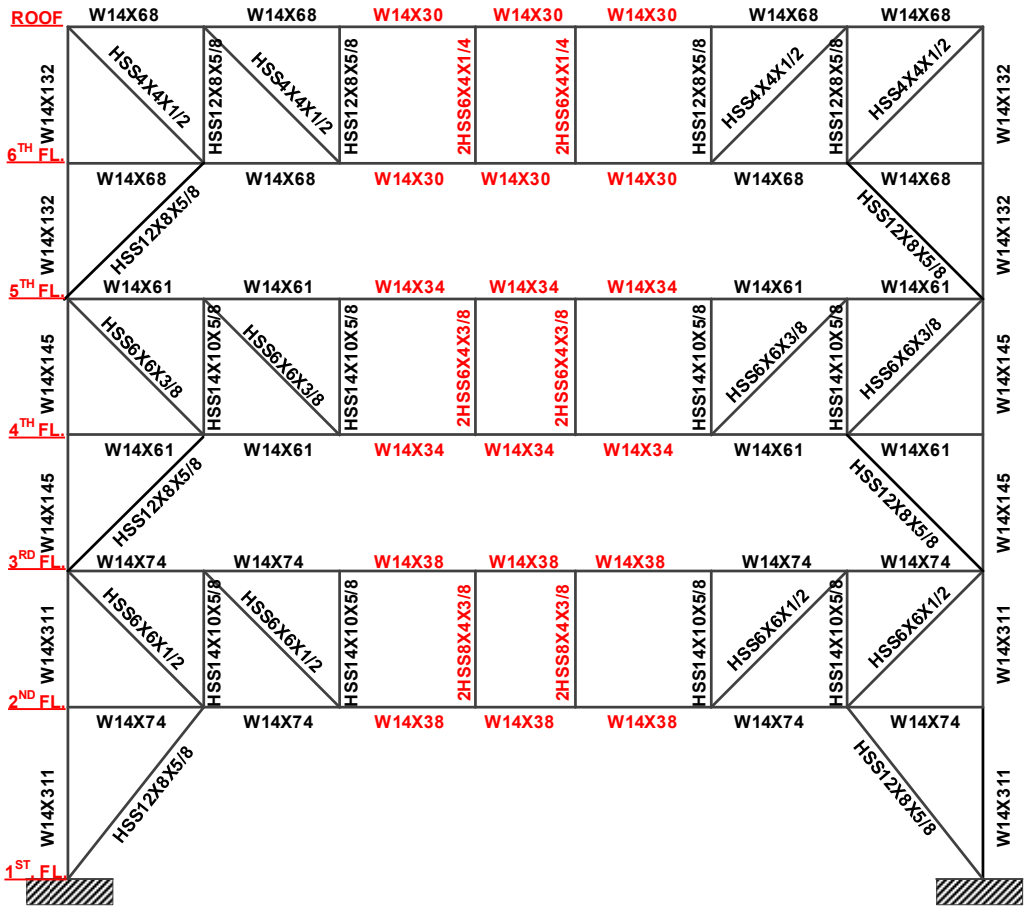

(a)

Figure 6-13 Typical member sections of the 6-Story modified STF (Kickers) : (a) odd bays; (b) even bays.

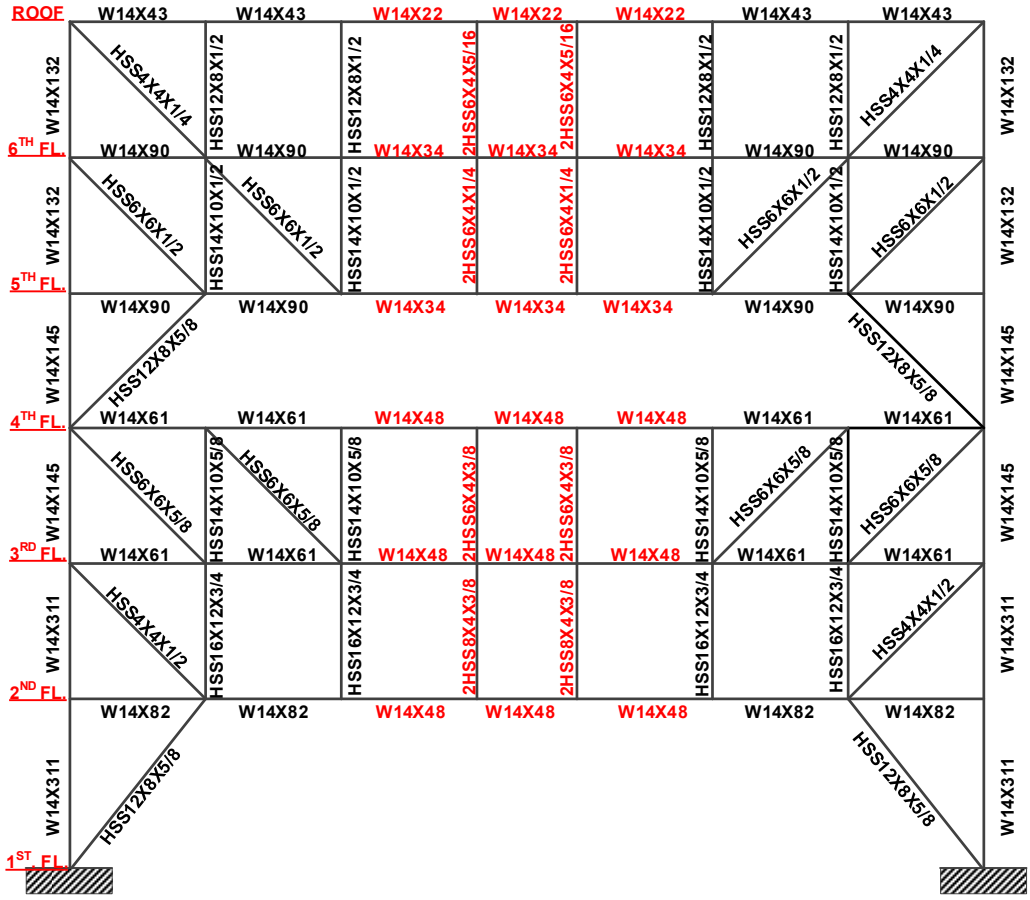

(b)

Figure 6-13 Continued

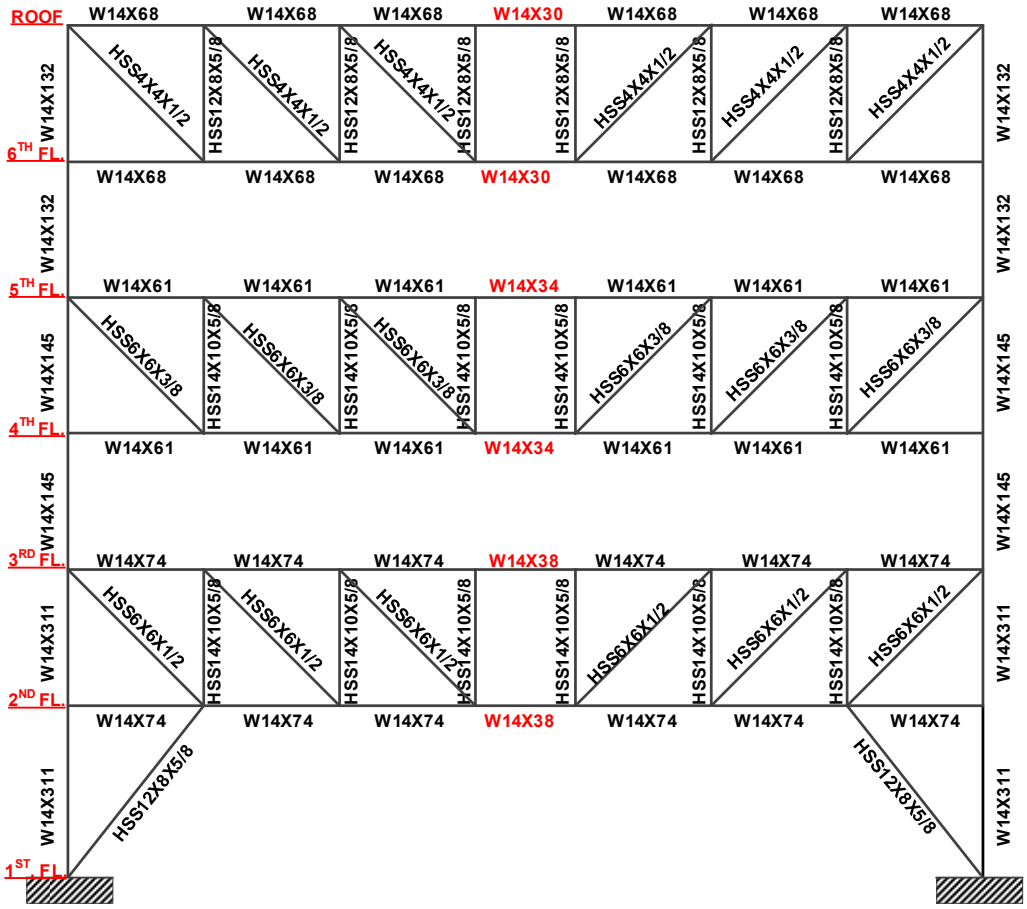

(a)

Figure 6-14 Typical member sections of the 6-Story conventional STF: (a) odd bays; (b) even bays.

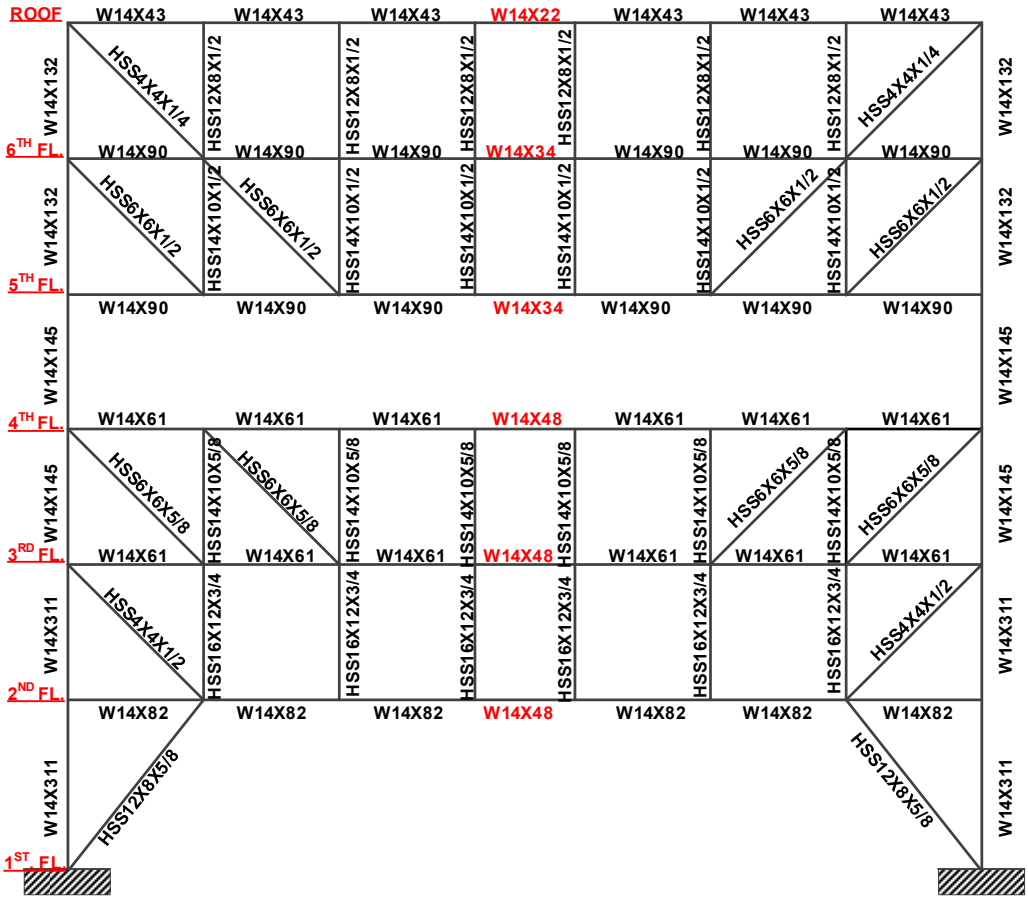

(b)

Figure 6-14 Continued

6.5 Pushover analysis

Pushover is a static-nonlinear analysis method where a structure is subjected to gravity loading and gradually increasing lateral loads through elastic and inelastic behavior up to a target displacement or the failure of structure. The equivalent lateral loads approximately represent earthquake induced forces. Load-deformation curve, known as the pushover curve, is obtained by this analysis to indicate any premature failure or weakness.

Furthermore, this analysis enables monitoring of plastic rotation and determination of collapse load and ductility capacity. However, pushover analyses were carried out to evaluate the seismic performance of all STF structure in this study using PERFORM-3D program to evaluate their seismic performance and the results are discussed in chapter 7.

6.6 Nonlinear time-history analysis

The STF buildings in this study were designed and analyzed for their seismic responses through a series of nonlinear time-history analyses for the maximum considered earthquake (MCE, 2% probability of exceedance in 50 years) level ground motions in the transverse direction of the structure. However, the gravity load combination that was used in the NTH is (1.0 D +0.5LL) and the requirements of (ASCE 7-2016)-Chapter 16 were followed for selection and scaling of the MCE ground motions.

6.6.1 Selection of the ground motions:

Based on the requirements of ASCE7-16 section 16.2.2 and the assumption that the STF structures are located in San Francisco, California with a site class D, the following events which are shown in Table 6-7 for the ground motions were selected with their abbreviation that were used in this study.

Table 6-7 Earthquake ground motions used in analyses.

Earthquake Name	Station Name	Year	Magnitude	PGA (g)	Rjb (km)	Abbreviation
San Fernando	LA - Hollywood Stor FF	1971	6.61	0.2248	22.77	MCE-1
Imperial Valley-06	Delta	1979	6.53	0.2357	22.03	MCE-2
Imperial Valley-06	El Centro Array #11	1979	6.53	0.3668	12.56	MCE-3
Superstition Hills-02	El Centro Imp. Co. Cent	1987	6.54	0.3573	18.2	MCE-4
Superstition Hills-02	Poe Road (temp)	1987	6.54	0.2862	11.16	MCE-5
Loma Prieta	Capitola	1989	6.93	0.5111	8.65	MCE-6
Loma Prieta	Gilroy Array #3	1989	6.93	0.5591	12.23	MCE-7
Landers	Coolwater	1992	7.28	0.2837	19.74	MCE-8
Landers	Yermo Fire Station	1992	7.28	0.2245	23.62	MCE-9
Northridge-01	Beverly Hills - 14145 Mulhol	1994	6.69	0.4434	9.44	MCE-10
Northridge-01	Canyon Country - W Lost Cany	1994	6.69	0.4036	11.39	MCE-11

6.6.2 Scaling of the ground motions

The seismic design parameters which are shown in Table 6-2 were used to develop the design response spectrum (MCE) and Figure 6-15 below shows the design response spectrum-MCE (Target response).

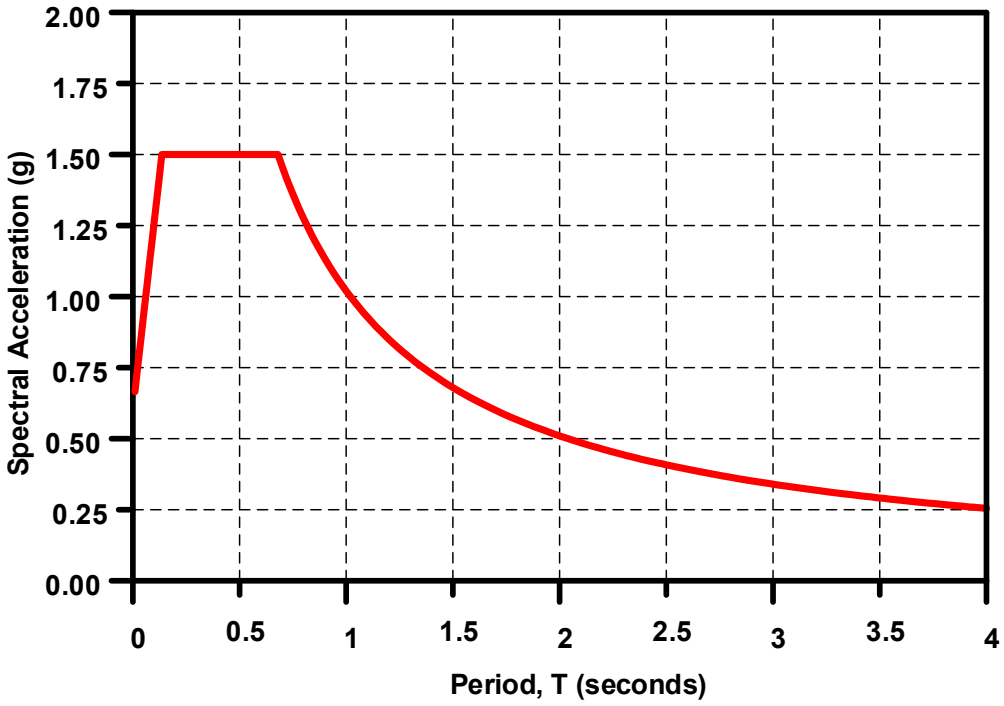

Figure 6-15 Design response spectrum (Target response spectrum).

6.6.2 Unscaled ground motions

The records of the selected ground motions were taken from the PEER Ground Motion Database. Then the spectral acceleration versus period were developed.

It can be noticed from Figure 6-16 which shows the target spectrum and the unscaled ground motions and their average that the ground motions must be scaled based on ASCE7-16 section 16.2.3.1,16.2.3.2 and 16.2.3.3 requirements.

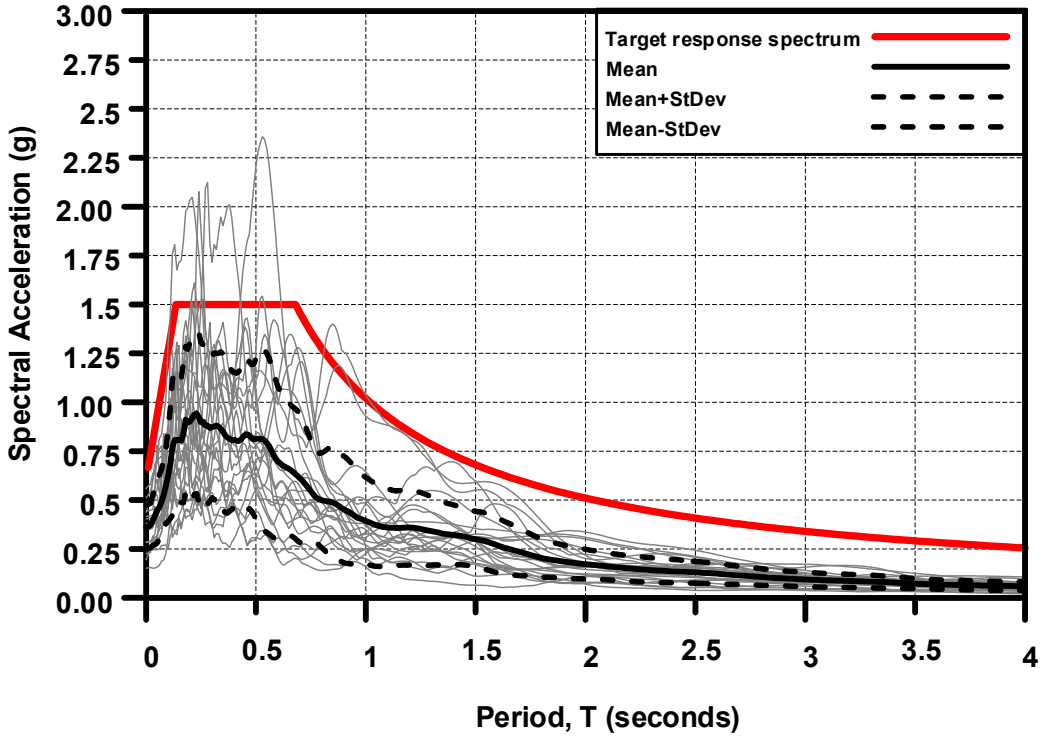

Figure 6-16 Design response spectrum and the unscaled ground motions

6.6.3 Period range for scaling

The requirements in ASCE 7-16 section 16.2.3.1 were followed to determine the period range for scaling. However, the periods in Table 6-8 which are calculated based on ASCE 7-16 equations were used here.

..

Table 6-8 The period range for scaling.

Parameters	STF Structure		
	6-Story	12-Story	20-Story
The fundamental period of the structure, T (s).	0.637	1.063	1.552
Lower bound period (0.2T) (s).	0.1274	0.2126	0.3104
Upper bound period (2T) (s).	1.274	2.126	3.104

6.6.4 Amplitude scaling

Based on section 16.2.3.2, for each horizontal ground motion pair, a maximum-direction spectrum shall be constructed from the two horizontal ground motion components. To achieve that, (RotD100) which is the maximum response spectrum over all rotation angles was selected in the scaling procedure.

The first iteration of scaling was carried out by using the tool that available in the he the Pacific Earthquake Engineering Research Center (PEER) website .First, the response spectrum (target spectrum)-similar to response spectrum in Figure 6-15- was defined. Second, the required ground motions selected. Third, the range of period and their weights were entered. Finally, RotD100 for spectral ordinate and damping Ratio of 5% were selected. Additionally, Minimize MSE was selected to be the scaling Method.

Figure 6-17 through Figure 6-19 show the result of scaling using PEER website for the STF buildings (6,12, and 20 stories). Furthermore, Table 6-8 shows the scaled factors which obtained from the PEER website.

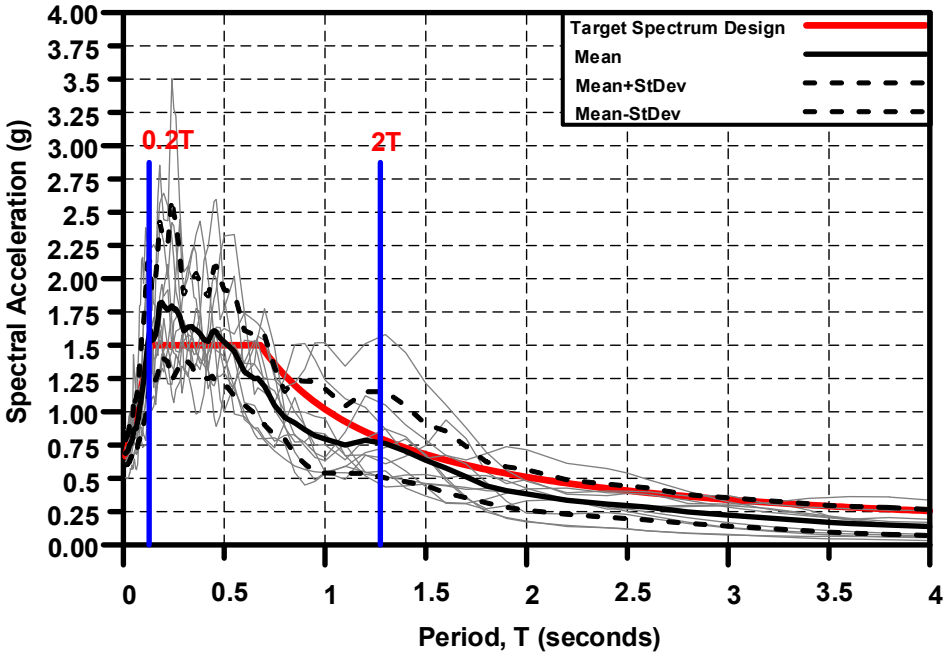

Figure 6-17 Scaling of the selected ground motion for 6-story STF based on PEER website.

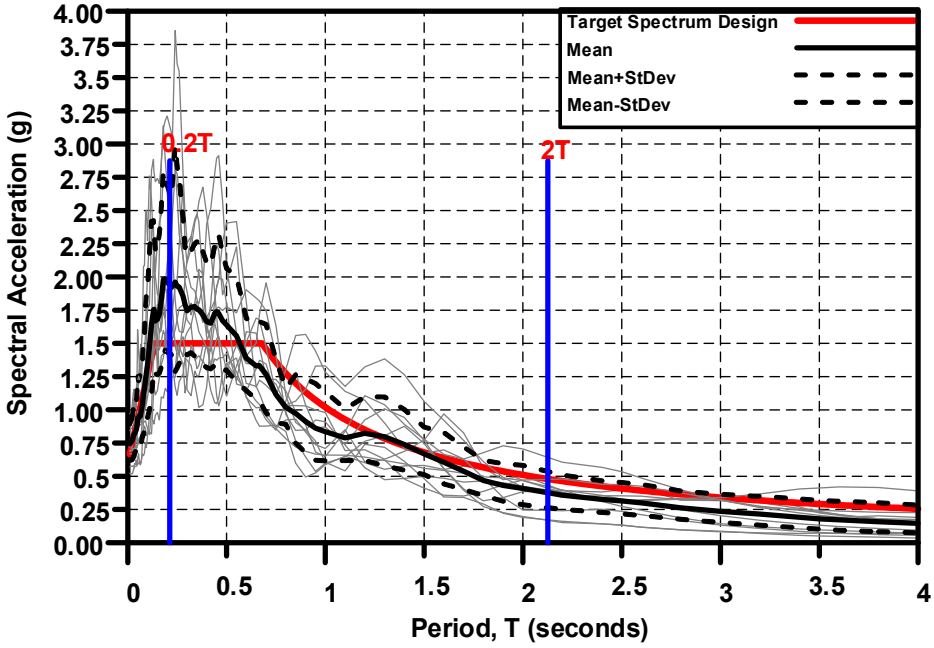

Figure 6-18 Scaling of the selected ground motion for 12-story STF based on PEER website

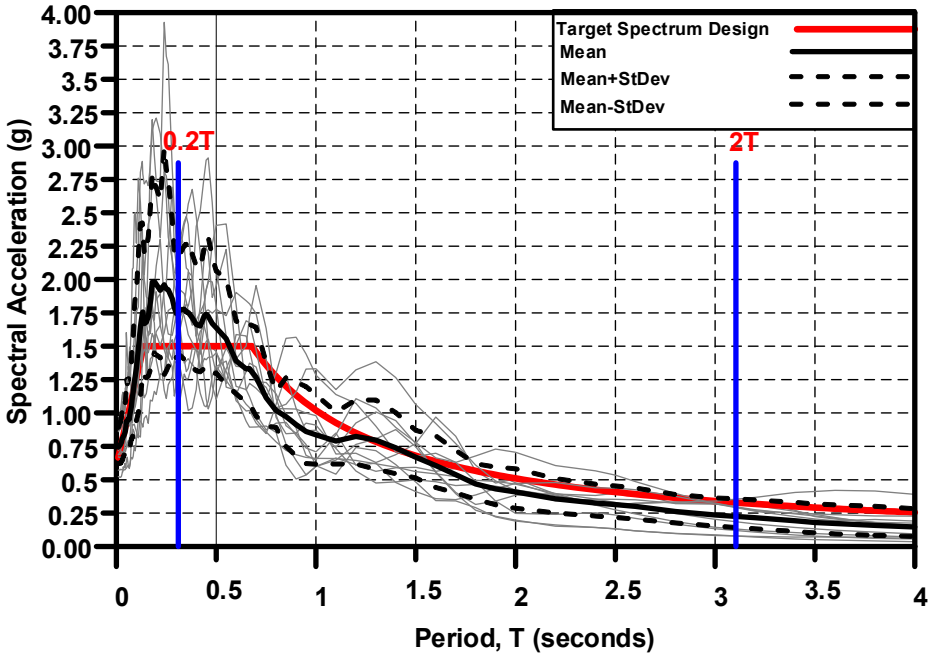

Figure 6-19 Scaling of the selected ground motion for 20-story STF based on PEER website.

Table 6-9 The scaled factors based on PEER website.

Ground motion	STF structure-Scale factor		
	6-Story	12-Story	20-Story
MCE-1	3.025	3.453	3.501
MCE-2	1.951	2.017	2.015
MCE-3	1.589	1.748	1.782
MCE-4	2.021	2.000	1.997
MCE-5	1.812	2.031	2.033
MCE-6	1.100	1.176	1.211
MCE-7	1.277	1.519	1.552
MCE-8	1.468	1.577	1.618
MCE-9	2.643	2.307	2.314
MCE-10	0.992	1.014	1.029
MCE-11	1.231	1.325	1.344

Based on the requirement of sections 16.2.3.2 and 16.2.3.3, the average of the maximum-direction spectra from all the ground motions shall not fall below 90% of the target response spectrum for any period within the same period range.

Therefore, the ground motion re-scaled again and Figure 6-20Figure 6-22below show the rescaling of the ground motions. Table (6-2) show the DBE scale factor that should be used for the selected ground motion in the design of the three STF structures.

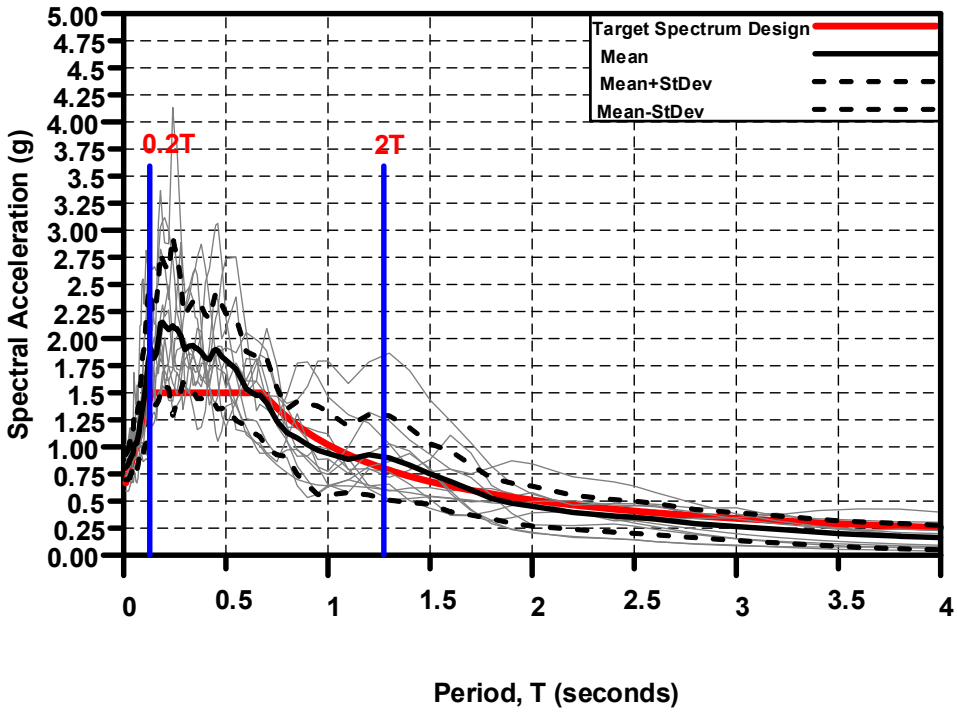

Figure 6-20 Re-scaling of the selected ground motion for 6-story STF.

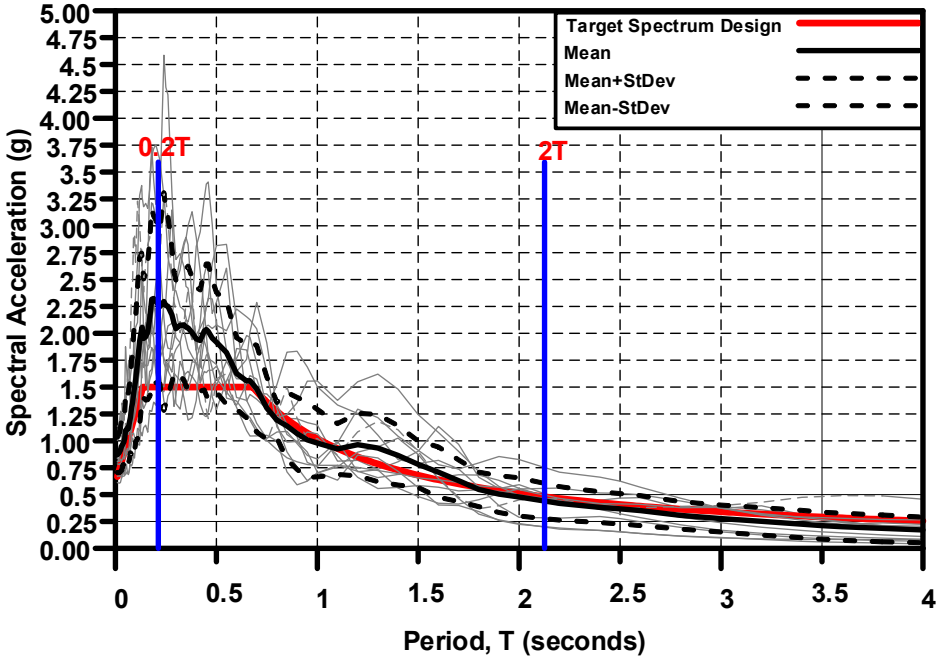

Figure 6-21 Re-scaling of the selected ground motion for 12-story STF.

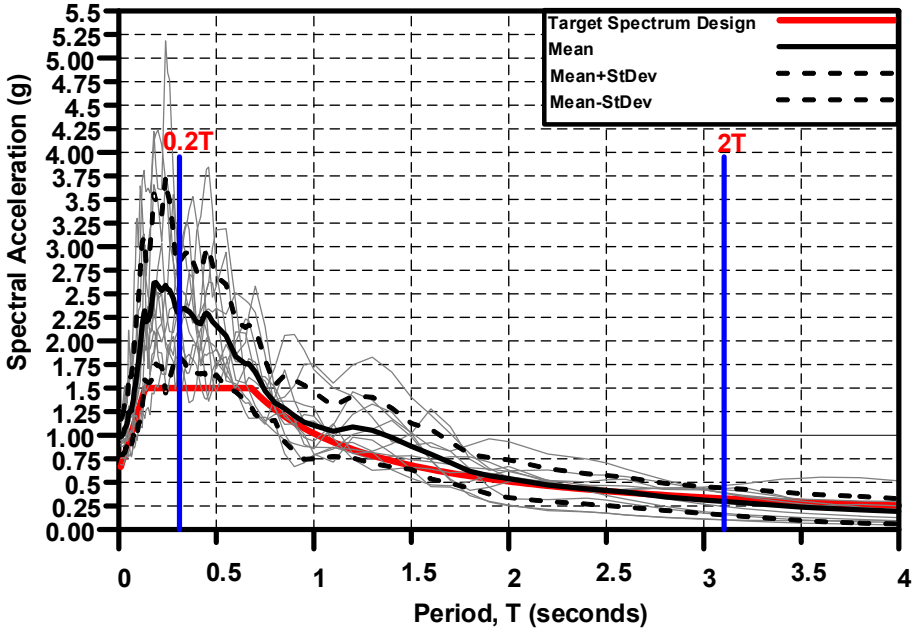

Figure 6-22 Re-scaling of the selected ground motion for 20-story STF.

Table 6-10 The MCE scaled factors after rescaling.

Ground motion	STF structure-Scale factor		
	6-Story	12-Story	20-Story
MCE-1	3.569	4.109	4.621
MCE-2	2.302	2.400	2.659
MCE-3	1.875	2.080	2.352
MCE-4	2.384	2.380	2.636
MCE-5	2.138	2.417	2.683
MCE-6	1.298	1.399	1.598
MCE-7	1.507	1.808	2.048
MCE-8	1.732	1.876	2.135
MCE-9	3.118	2.745	3.054
MCE-10	1.171	1.207	1.358
MCE-11	1.452	1.576	1.774

Chapter 7

Non-linear Analyses Results and Discussion

7.1 Introduction

This chapter discusses the results on the non-linear analyses based on the modeling and the design procedure which were discussed in chapter 5 and chapter 6, respectively. The forces transfer based on the linear analysis and the non-linear time history analyses for the 6-story modified STF (Vertical members), (Kickers), and conventional STF are discussed and compared. Moreover, the results of pushover analyses are presented which include the pushover curves, the story shear forces, and the plastic hinge rotations for 6-story,12-story and 20-story STF structures. However, the deflected shapes for one bay (Bay 1) are shown in this chapter and the other bays are shown in Appendix A.

The results of the Non-Linear Time History (NTH) analyses are discussed in the second part of this chapter. The results include the average Maximum Interstory Drift Ratio (MIDR) for the 6-story,12-story and 20-story STF structures. Furthermore, the deflected shape of Bay 1 with the MIDR and the plastic hinge rotations under a selected MCE ground motion are discussed and compared. The deflected shapes for other bays are shown in Appendix B.

7.2 Change of the force transfer pattern in the modified STF

During the linear preliminary design process and the non-linear time history analyses, it was observed that when the vertical members and the diagonal braces (Kickers) are introduced to the non-story level of the STF system, the story shear forces were transferred in a more direct manner (i.e., most forces were transferred directly from upper truss to the lower non-truss and so forth) and no longer primarily depended on

staggered manner via the diaphragms to transfer the lateral forces, as in the conventional STF system.

This largely reduced the demands in the diaphragms as well as the connections between the diaphragms and trusses in the STF system. The story shear distributions in each bay of the modified and conventional 6-story STF structures when subjected to ASCE7 specified lateral forces elastically designed models are summarized in Table 7- 1.

In order to investigate the story shear distribution in each bay under MCE hazard level , a ground motion (MCE 11) was selected and the results are shown in

Table 7-2. The maximum story shear for each bay at the same level was calculated using the greater of the absolute maximum or absolute minimum shear force.

However, the rigid floor diaphragm was modeled to represent the story shear transfer mechanism of the hollow core planks in the conventional model whereas the horizontal truss was used as the shear diaphragm in the modified structural layouts during the preliminary design process for its simplicity of obtaining the story shear forces.

Table 7- 1 Story shear in individual bay based on elastically designed models (kips).

Story	Bay 1			Bay 2		
	(Modified) (Vertical members)	(Modified) (Kickers)	Conven-tional STF	(Modified) (Vertical members)	(Modified) (Kickers)	Conven-tional STF
6	50	75	40	51	35	52
5	*65	*82	*29	157	120	207
4	141	118	142	*78	*142	*23
3	*101	*119	*48	264	227	339
2	163	166	149	175	171	163
1	183	180	163	182	196	186
Story	Bay 3			Bay 4		
	(Modified) (Vertical members)	(Modified) (Kickers)	Conven-tional STF	Conven-tional STF	(Modified) (Kickers)	Conven-tional STF
6	62	75	238	51	38	*52
5	*43	*78	*16	158	124	213
4	201	135	288	*72	*136	*19
3	*59	*99	*22	261	221	335
2	186	187	236	173	169	163
1	199	183	217	186	197	201
Story	Bay 5			Bay 6		
	(Modified) (Vertical members)	(Modified) (Kickers)	Conventi onal STF	(Modified) (Vertical members)	(Modified) (Kickers)	Convent ional STF
6	55	70	61	50	44	40
5	*43	*75	*17	112	101	105
4	188	127	278	*100	*128	*41
3	*61	*96	*24	186	175	178
2	171	174	203	168	168	139
1	188	176	194	184	190	161

* indicates non-truss bay

Note: The total base shear of the conventional and the modified models are the same (1122 kips) which is the total lateral applied to the structures as shown in Table 6-4 although the individual bays of the models had different base shear.

Table 7-2 Story shear in individual bay under MCE 11 ground motion.

Story	Bay 1			Bay 2		
	(Modified) (Vertical members)	(Modified) (Kickers)	Conven-tional STF	(Modified) (Vertical members)	(Modified) (Kickers)	Conven-tional STF
6	282	158	221	338	196	229
5	*324	*235	*229	869	321	842
4	518	319	375	*292	*368	*132
3	*245	*264	*228	549	601	1059
2	411	374	311	562	415	528
1	517	396	180	694	454	674
Story	Bay 3			Bay 4		
	(Modified) (Vertical members)	(Modified) (Kickers)	Conven-tional STF	Conven-tional STF	(Modified) (Kickers)	Conven-tional STF
6	487	219	375	416	243	228
5	*280	*227	*108	889	354	842
4	721	461	977	*251	*364	*99
3	*138	*367	*83	545	615	*948
2	615	439	611	622	388	583
1	828	450	707	870	371	750
Story	Bay 5			Bay 6		
	(Modified) (Vertical members)	(Modified) (Kickers)	Conventi onal STF	(Modified) (Vertical members)	(Modified) (Kickers)	Convent ional STF
6	357	221	311	279	170	229
5	*258	*231	*106	534	293	375
4	677	397	934	*357	*317	*228
3	*139	*354	*106	420	456	311
2	511	415	548	459	389	180
1	582	426	641	565	423	229

* indicates non-truss bay

7.3 Pushover analysis results

In the pushover analysis for all structures, roof drifts of all the bays were used during the analysis as the drift limits. The analysis stopped when the displacement at roof elevation in any bay reached the 3% limit. However, the bay on grid 1 (as shown in Figure 6-1) reached 3% roof drift before other bays and was chosen as the controlling bay. Figure 6-9 shows the detail of how the roof drift was calculated for this study. For the conventional 6-story STF, the analysis failed to converge and was terminated at 0.80% roof drift due to excessive deformation.

Nonlinear pushover analysis results of the 6-story modified STF and conventional STF structures are shown in Figure 7-1 through Figure 7-3.The pushover curves of 12-story and 20-story modified (vertical members) STF structures are shown in Figure 7-4 and Figure 7-5 respectively.

It can be seen from the pushover curves of the 6-story STF structures that the ultimate strength capacity of the conventional STF is 3281 Kips which is much higher than the modified STF (Kickers) and (vertical members) which are 2648 Kips and 2350, respectively. This increase is due to the high stiffness of the conventional STF compared with the modified structures under the same ASCE7 specified lateral load (1122 Kips). On the other hand, the modified STF structures show much more ductility than the conventional STF structures.

The pushover curves of the 12-story and 20-story modified STF structures show that the ultimate strength capacities are 2393 Kips and 3343 Kips under ASCE7 specified lateral load (2393 Kips) and (3343 Kips), respectively. Moreover, both structures show appropriate ductility.

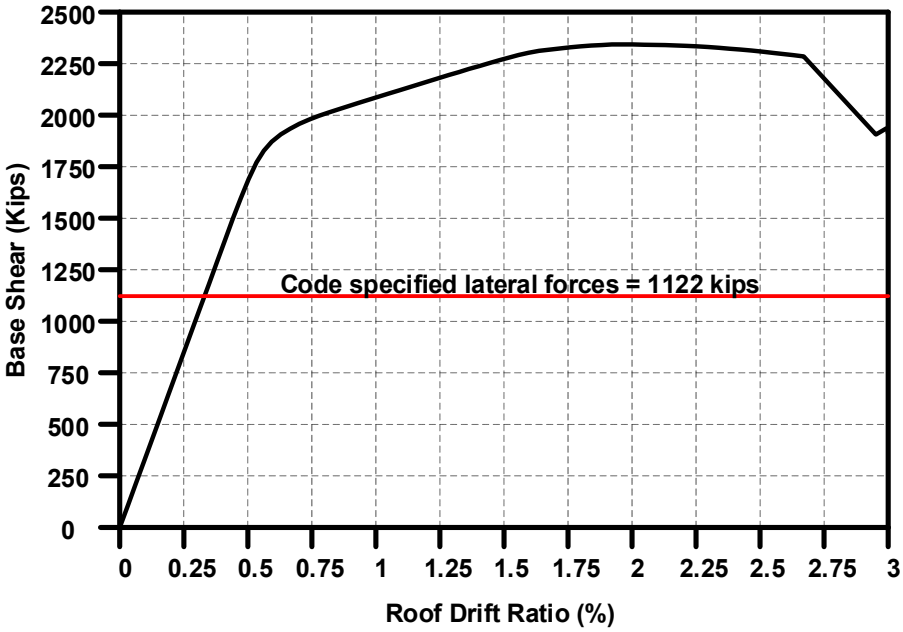

Figure 7-1 Base shear vs. roof drift response up to 3% roof drift for 6-Story Modified STF (Vertical members) building.

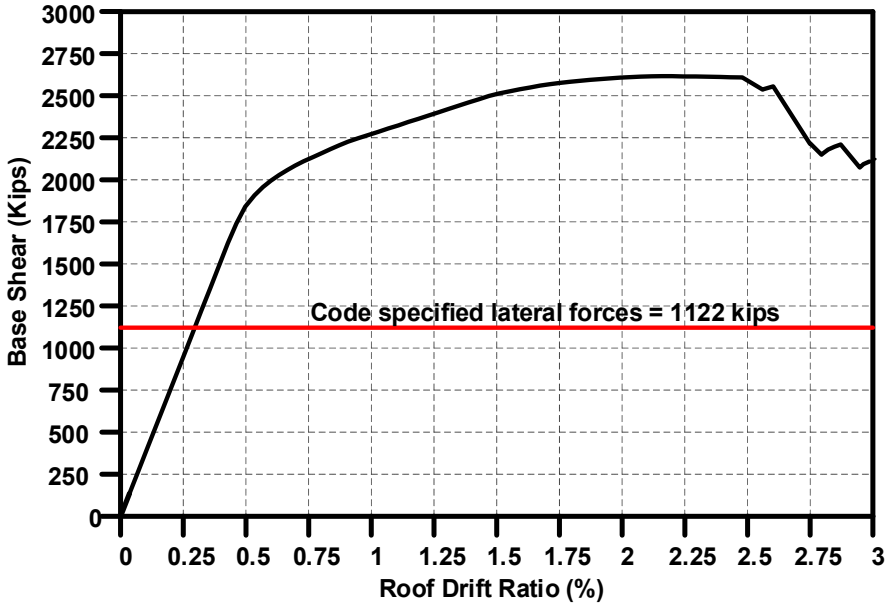

Figure 7-2 Base shear vs. roof drift response up to 3% roof drift for 6-Story Modified STF (Kickers) building.

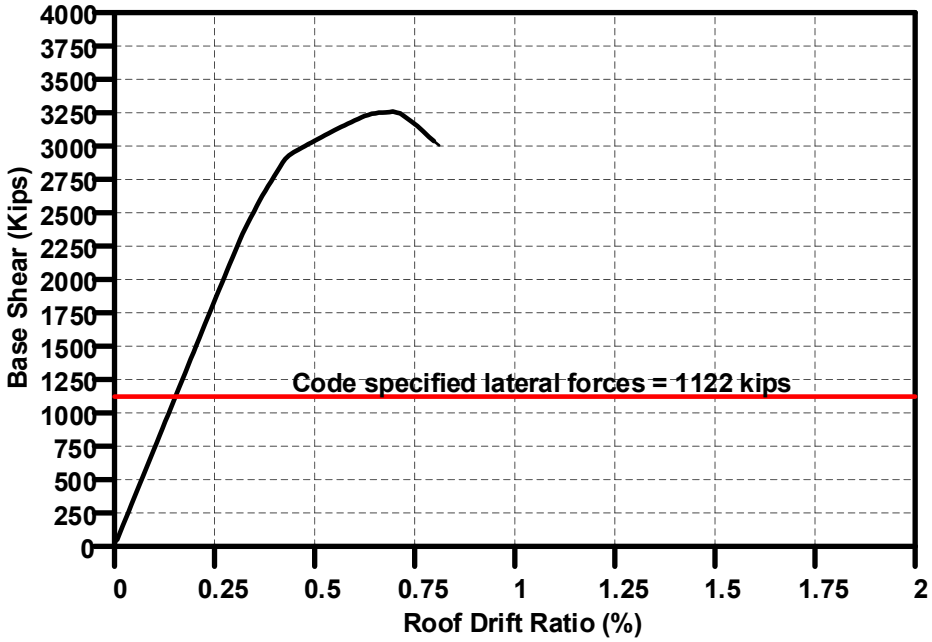

Figure 7-3 Base shear vs. roof drift response up to 0.80% roof drift for 6-Story conventional STF building.

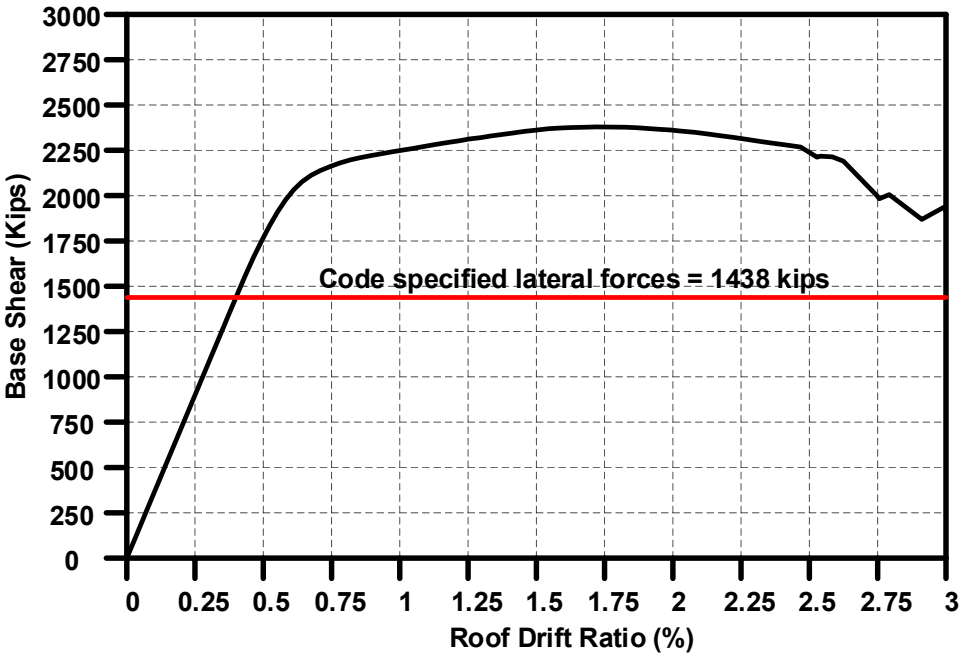

Figure 7-4 Base shear vs. roof drift response up to 3% roof drift for 12-Story Modified (Vertical members) STF building.

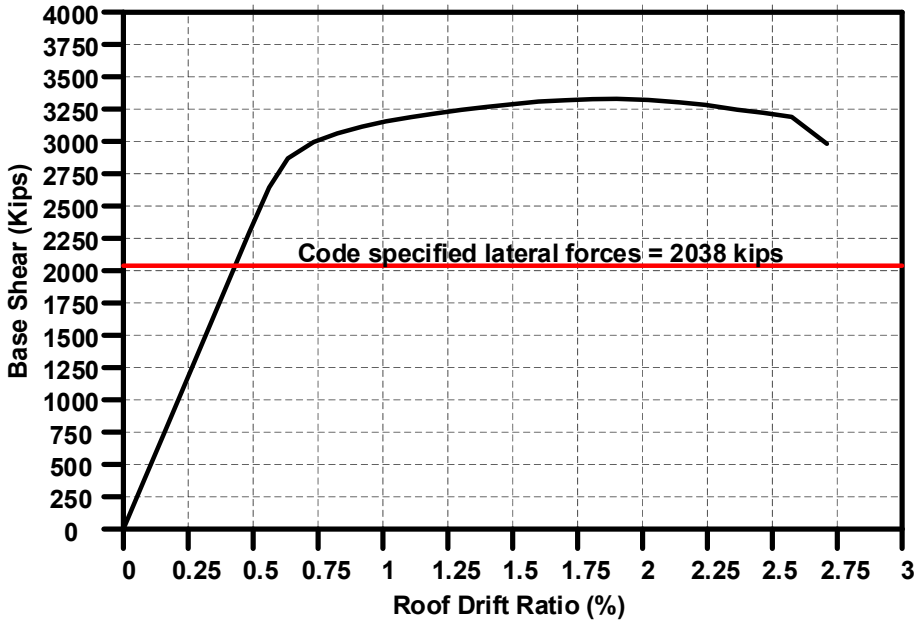

Figure 7-5 Base shear vs. roof drift response up to 3% roof drift for 20-Story Modified (Vertical members) STF building.

The story shear for individual bay in each story of all five structures from the pushover analysis is summarized in Table 7-3.

Table 7-3 Story shear in individual bay from pushover analysis (kips).

	Bay 1	Bay 2	Bay 3	Bay 4	Bay 5	Bay 6	Total
6-Story Modified STF (Vertical members)							
6th Story	118	95	127	97	122	115	673
5th Story	152	324	81	326	90	259	1231
4th Story	321	155	414	142	408	239	1679
3rd Story	236	559	111	549	123	436	2014
2nd Story	380	352	384	353	374	397	2240
1st Story	411	355	398	368	394	423	2350
6-Story Modified STF (Kickers)							
6th Story	163	58	190	77	188	104	780
5th Story	214	251	197	279	195	247	1383
4th Story	251	479	267	356	272	333	1958
3rd Story	283	573	354	503	239	439	2390
2nd Story	410	394	454	425	428	426	2537
1st Story	430	436	416	485	419	463	2648

6-Story conventional STF

6th Story	122	150	217	145	174	123	931
5th Story	97	598	43	598	48	323	1707
4th Story	457	61	806	52	815	151	2342
3rd Story	191	985	56	924	58	588	2803
2nd Story	498	511	565	524	535	502	3136
1st Story	537	557	515	596	515	561	3281

12-Story Modified STF (Vertical members)

12th Story	77	37	88	36	97	59	395
11th Story	70	225	20	207	22	160	704
10th Story	214	56	280	52	283	123	1008
9th Story	162	340	74	348	82	272	1277
8th Story	318	106	398	102	392	205	1521
7th Story	238	429	123	446	136	361	1732
6th Story	405	132	501	126	500	258	1921
5th Story	295	492	163	510	178	428	2066
4th Story	448	192	534	176	521	323	2193
3rd Story	301	609	132	594	144	508	2287
2nd Story	438	342	409	337	395	423	2344
1st Story	460	335	410	345	403	439	2393

20-Story Modified STF (Vertical members)

20th Story	67	36	75	36	63	56	333
19th Story	61	202	18	189	20	146	636
18th Story	192	56	254	50	254	116	921
17th Story	133	346	49	345	37	263	1173
16th Story	288	116	368	106	352	205	1435
15th Story	201	467	87	466	94	368	1683
14th Story	367	193	446	176	418	293	1892
13th Story	259	579	116	575	126	462	2117
12th Story	450	229	538	210	511	353	2290
11th Story	342	607	185	622	200	522	2478
10th Story	521	262	607	246	585	406	2626
9th Story	408	638	229	674	256	581	2786
8th Story	604	230	721	217	720	415	2908
7th Story	471	641	287	687	318	607	3011
6th Story	651	252	763	238	764	452	3120

5th Story	490	702	288	734	318	658	3191
4th Story	648	355	711	328	691	529	3262
3rd Story	488	780	261	782	282	718	3310
2nd Story	614	507	550	494	541	620	3326
1st Story	633	480	571	475	558	627	3343

Note: The cell colors indicate story frame as shown below.

Truss
Hanger
Post
Non-story level with vertical members.
Story with braces

Some members are selected to compare the plastic hinge rotation of the chord and vertical members in the trusses in bay 1 of all the 6- story structures. The locations of the selected members are illustrated in Figure 7-6. The maximum plastic hinge rotations of the selected members are listed in Table 7-4.

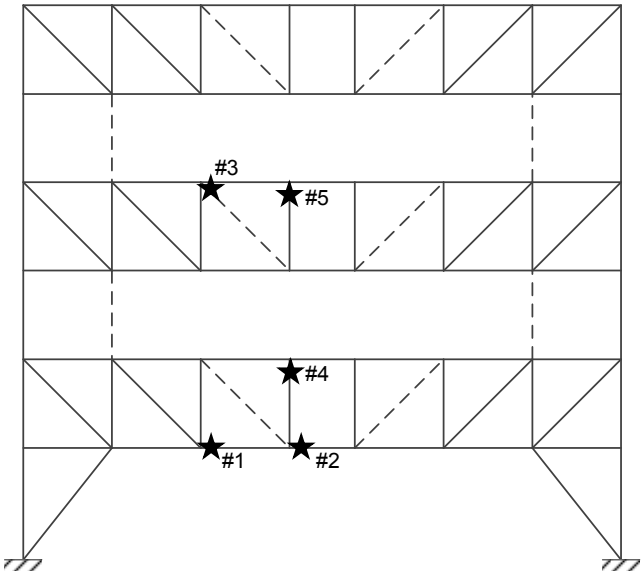

Figure 7-6 Locations of the selected chord and Vierendeel vertical members in bay 1.

Note: The member locations are the same for all models even though the member layouts are different for the conventional STF model.

Table 7-4 Plastic hinge rotation of the selected members from pushover analysis (kips).

Member number	(Modified) (Vertical members)		(Modified) (Kickers)		Conventional STF	
	3% Drift	0.80% Drift	3% Drift	0.80% Drift	3% Drift	0.80% Drift
1	5.80	0.63	6.83	0.94	NA	0.00
2	0.00	0.00	0.00	0.00	NA	7.63
3	5.73	0.52	6.09	0.61	NA	0.00
4	-11.24	-0.82	-12.99	-1.20	NA	0.00
5	-12.13	-0.87	-12.29	-1.10	NA	0.00

Note: For the conventional STF model, the analysis failed to converge and was terminated at 0.80% roof drift due to excessive deformation.

It can be seen that the Vierendeel chord members of the conventional STF model have higher rotational than the modified models at the same level of roof drift (0.80%). On the other hand, the Vierendeel chord and vertical members of the modified (Kickers) have slightly higher rotational than the modified (Vertical members) at the same roof drifts (0.80% and 3%).

The early yielding in Vierendeel chord members in the conventional STF model led to force redistribution to the kickers and the columns, thus much higher member force demands in the columns and the kickers at the same level of roof drift. This also leads to the failure of the conventional STF at much lower roof drift than the other modified models.

Figure 7-7 through Figure 7-11 show the deflected shapes of the members in bay 1 for the 6-story modified STF (Vertical members), 6-story modified STF (Kickers), and the 6-story conventional STF maximum plastic hinge rotations of the yielded members, and member minimum usage ratios at 3% roof drift and 0.80% roof drift. For the conventional STF Model, only the deflected shape of bay 1 at 0.80% roof drift is included since the

analysis failed to converge and was terminated at 0.80% roof drift. The deflected shapes of bay 1 at 3% for the 12-story (modified) and 20-story (modified) with maximum plastic hinge rotations are shown in Figure 7-12 and Figure 7-13,respectively. However, the deflected shapes of bay 2 through bay 6 are shown in Appendix A.

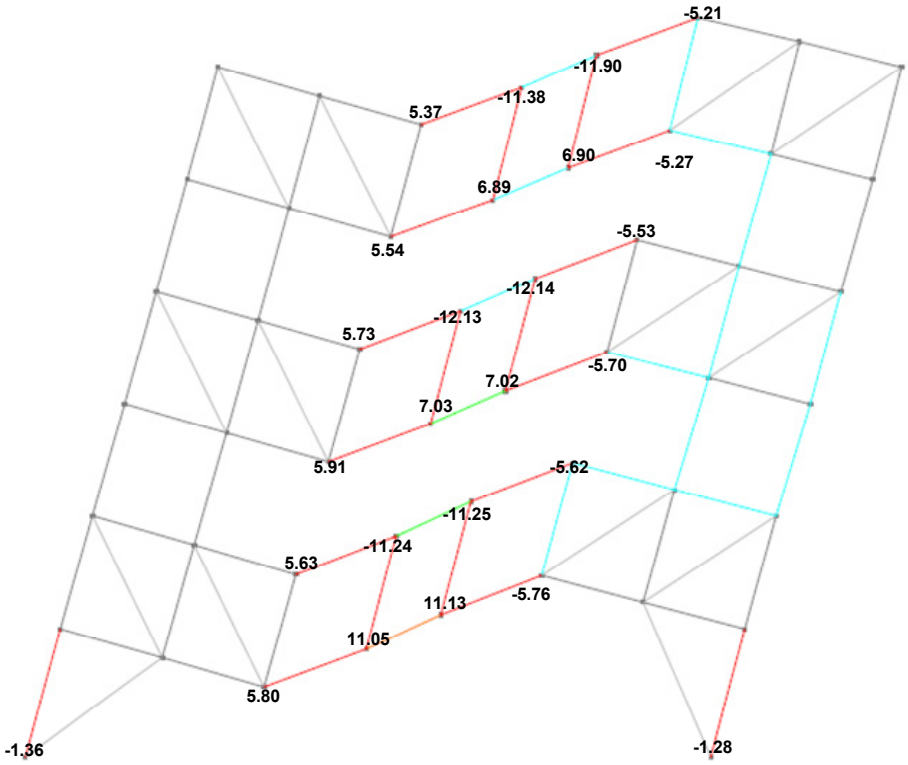

Figure 7-7 Bay 1 deflected shape with plastic hinge rotations (%) of the 6-Story building at 3% roof drift.

The member colors indicate the minimum usage ratio (demand versus capacity of the member) as followed:

Color	Usage Ratio
Grey	0.0
Teal	0.4
Green	0.6
Orange	0.8
Red	1.0

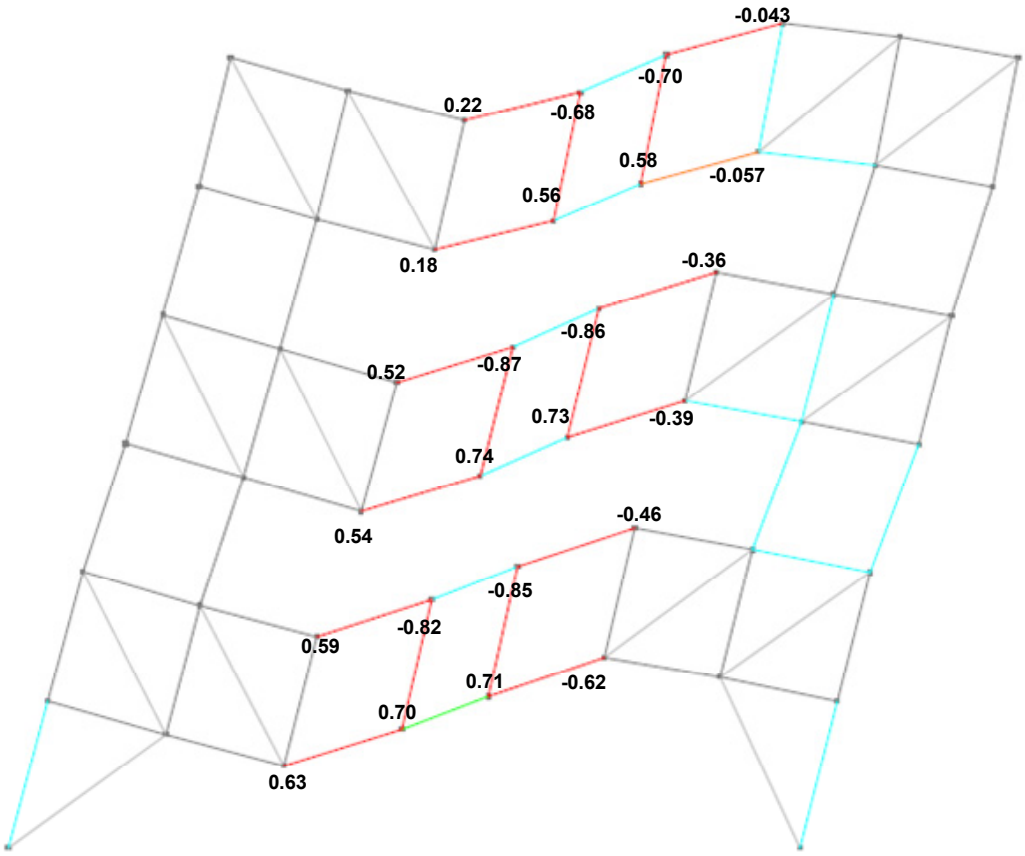

Figure 7-8 Bay 1 deflected shape with plastic hinge rotations (%) of the 6-Story building at 0.80 % roof drift.

The member colors indicate the minimum usage ratio (demand versus capacity of the member) as followed:

Color	Usage Ratio
Grey	0.0
Teal	0.4
Green	0.6
Orange	0.8
Red	1.0

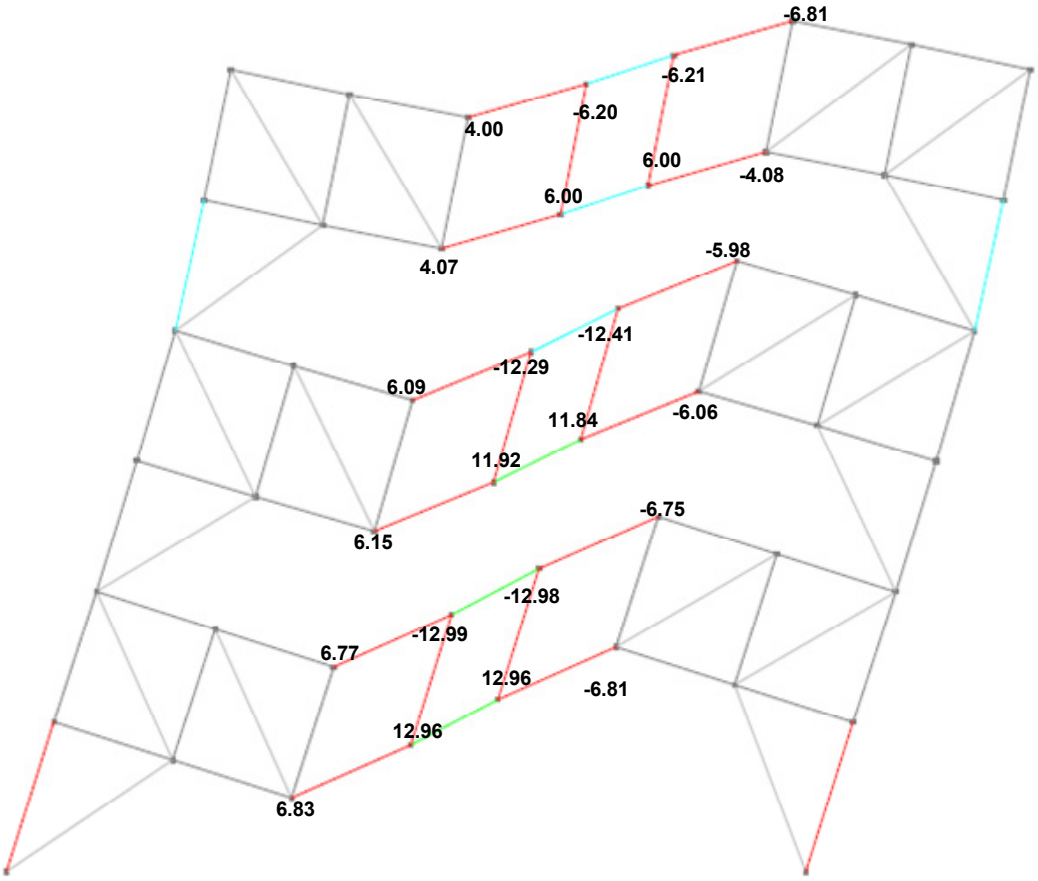

Figure 7-9 Bay 1 deflected shape with plastic hinge rotations (%) of the 6-Story (With kickers) building at 3% roof drift.

The member colors indicate the minimum usage ratio (demand versus capacity of the member) as followed:

Color	Usage Ratio
Grey	0.0
Teal	0.4
Green	0.6
Orange	0.8
Red	1.0

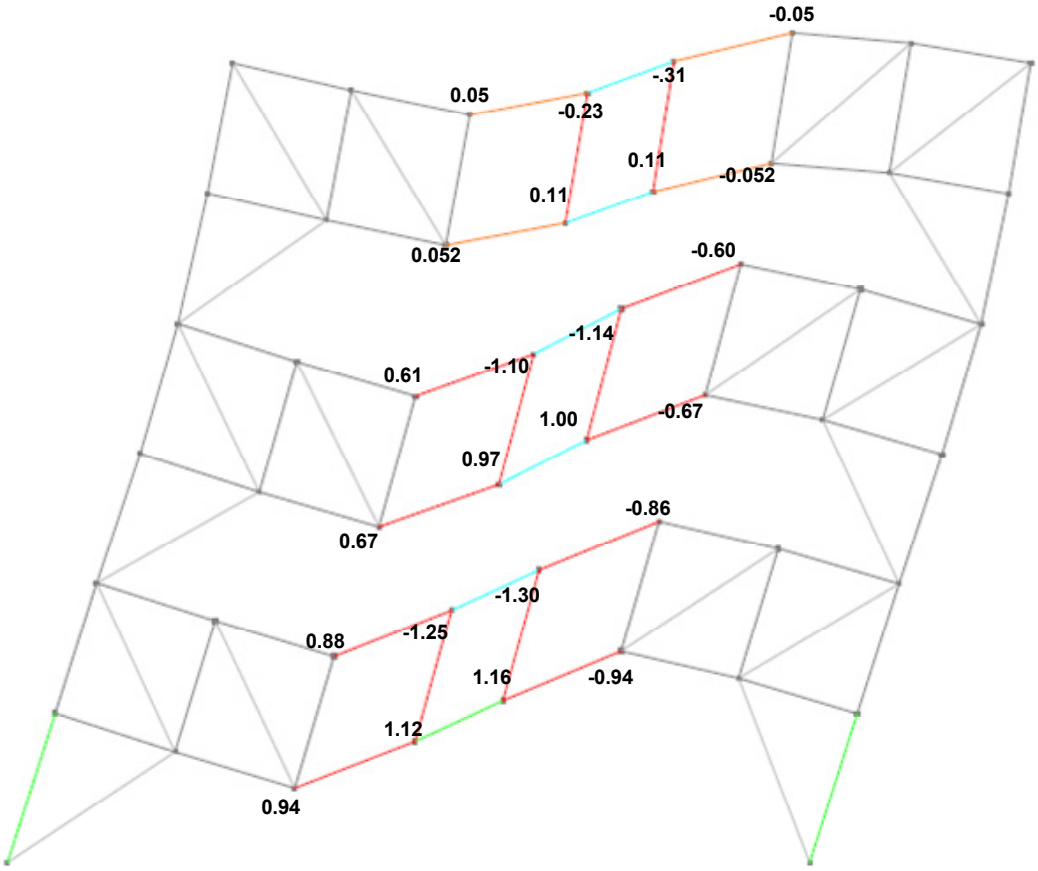

Figure 7-10 Bay 1 deflected shape with plastic hinge rotations (%) of the 6-Story (With kickers) building at 0.80 % roof drift.

The member colors indicate the minimum usage ratio (demand versus capacity of the member) as followed:

Color	Usage Ratio
Grey	0.0
Teal	0.4
Green	0.6
Orange	0.8
Red	1.0

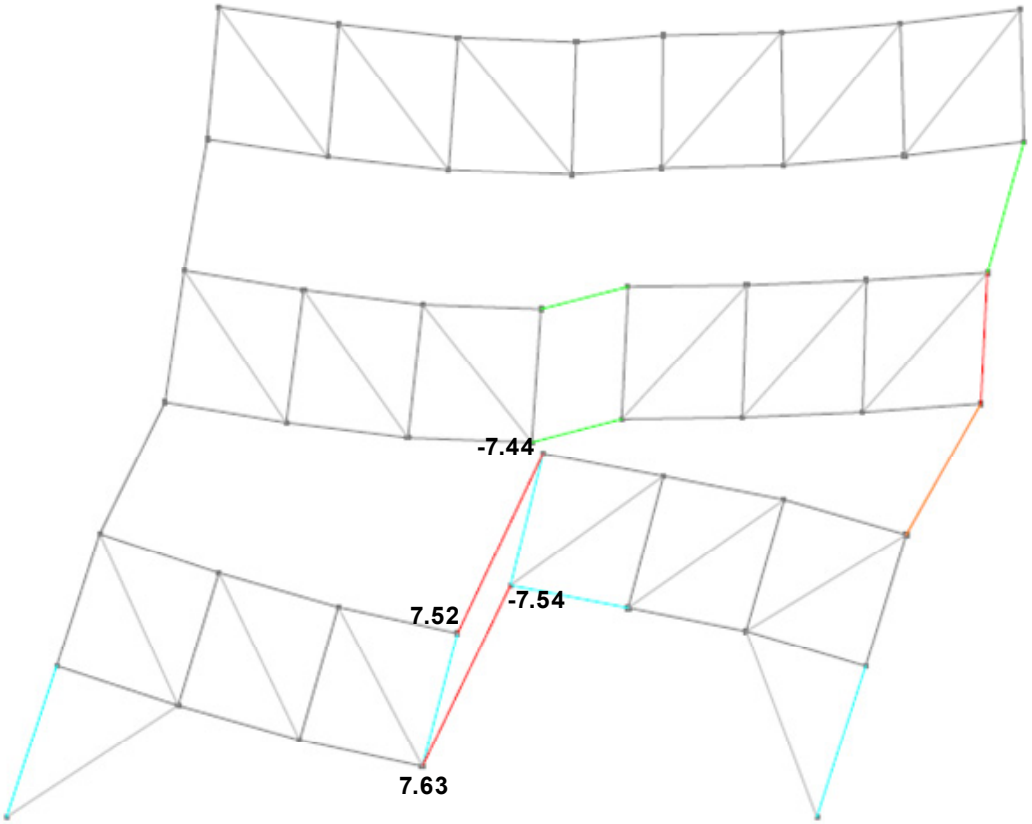

Figure 7-11 Bay 1 deflected shape with plastic hinge rotations (%) of the 6-Story (SVP, Without vertical members) building at 0.80% roof drift.

The member colors indicate the minimum usage ratio (demand versus capacity of the member) as followed:

Color	Usage Ratio
Grey	0.0
Teal	0.4
Green	0.6
Orange	0.8
Red	1.0

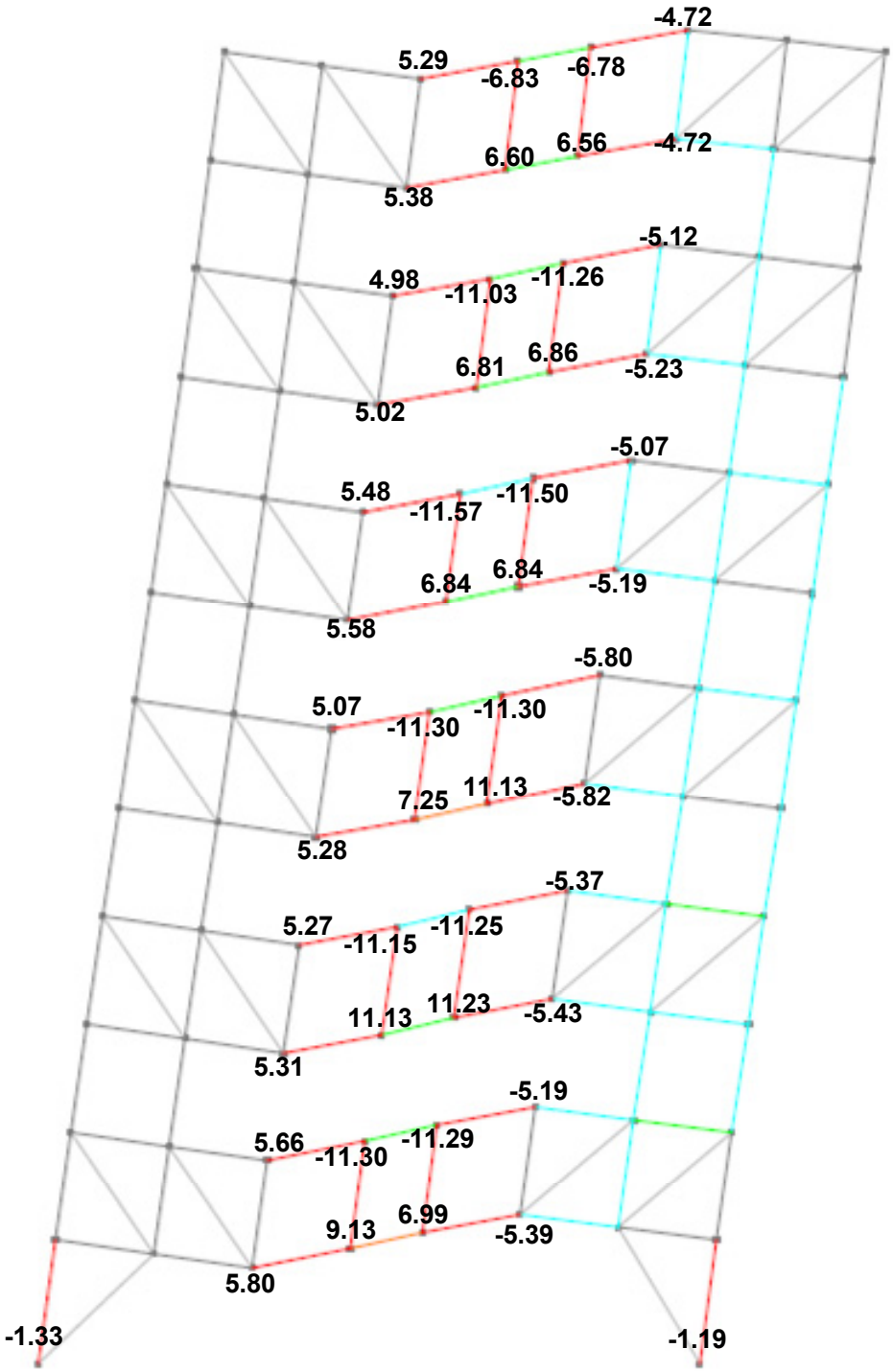

Figure 7-12 Bay 1 deflected shape with plastic hinge rotations (%) of the 12-Story building at 3% roof drift.

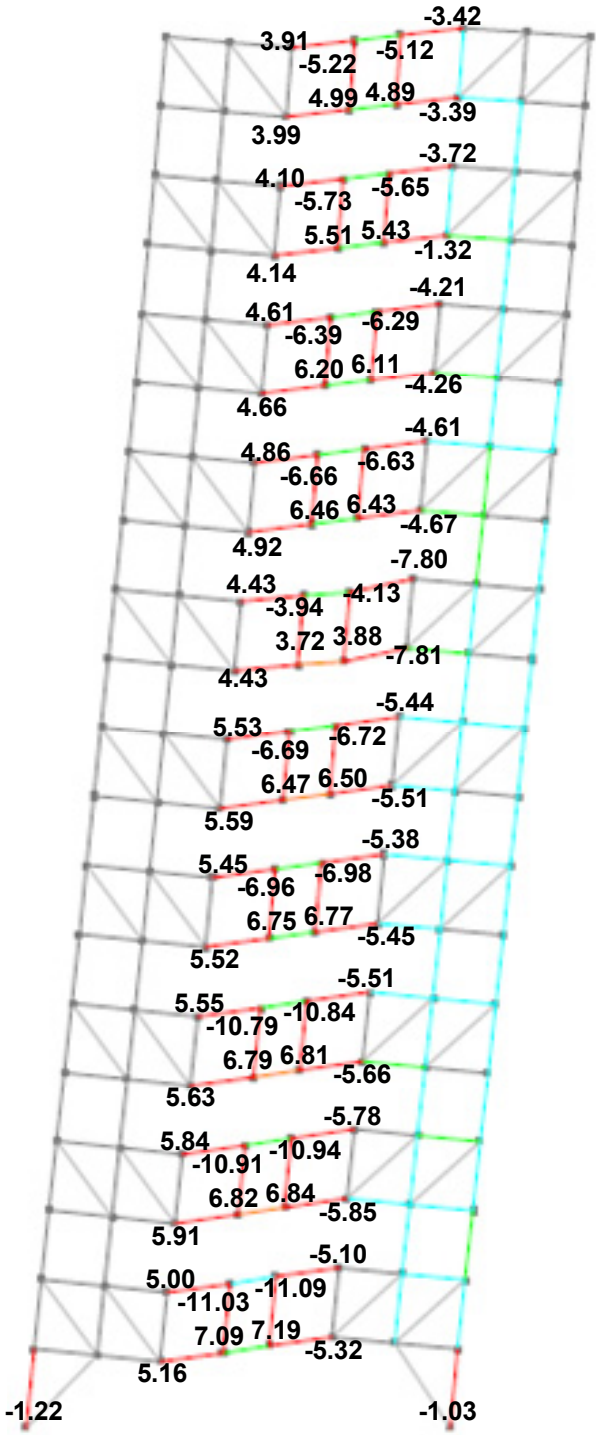

Figure 7-13 Bay 1 deflected shape with plastic hinge rotations (%) of the 20-Story building at 3% roof drift.

Generally, it can be observed that the plastic hinge rotation angles of the vertical members in the Vierendeel panels are larger than those of the chord members at the end of the Vierendeel panel. This is due to the long rigid end zones of the vertical members which are connected to the chord members via gusset plates illustrated in Figure 7-14.

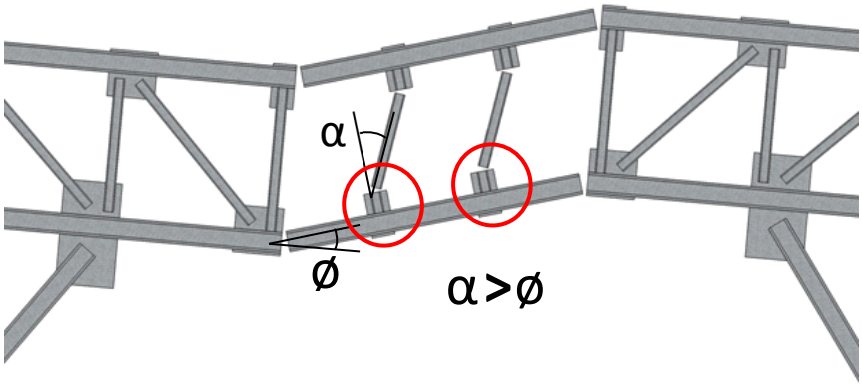

Figure 7-14 Rigid end zones of the vertical members in Vierendeel panels.

However, because of their high rotational demands, the vertical members in the Vierendeel panel yield and fail before the chord members. This behavior could be useful because if only the vertical members are damaged in a moderate seismic event, they can be easily replaced. This yield mechanism is similar to the Special Truss Moment Frame (STMF) as shown in Figure 7-15 in which the Intermediate Vierendeel Members (IVM) have large rotational demands than the chord member according to the two following proposed equations by Chao et al. (2019).

$$\theta_{p,chord}(rad) = \gamma + \theta = \frac{L}{0.9L_s}\theta$$

$$\theta_{p,IVM}(rad) = \gamma + \theta' = 1.2\left[\theta\frac{(L-0.9L_s}{0.9L_s} + \frac{l}{l-2e}\theta\right]$$

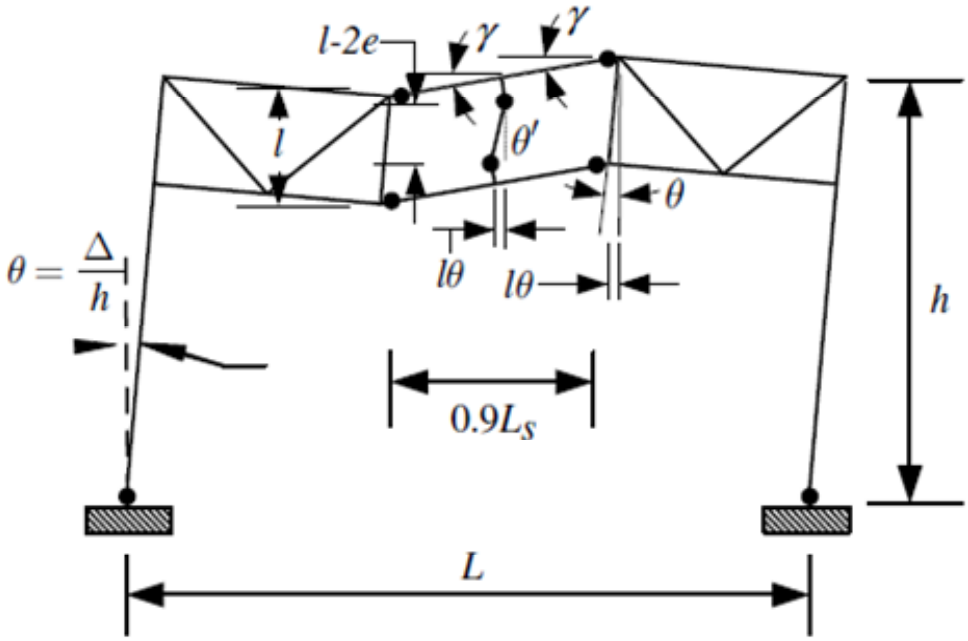

Figure 7-15 Relationship between story drift ratio, chord rotation, and intermediate vertical member rotation (Chao et al, 2020)

where ɵ is the plastic story drift ratio (PSDR), l is the depth of the truss, between horizontal chord member centerlines and e is the distance from centerline of the chord member to the end of welds of the IVM.

7.4 Nonlinear time-history analysis results

Nonlinear time-history analyses for all studied structures were carried out using Perfrom-3D computer program. All of the models were analyzed to evaluate the seismic performance under eleven ASCE7 code scaled MCE ground motions recorded in the transverse direction.

The main investigating parameter is the interstory drift ratio response in the direction of the truss (transverse direction of the structures). The fundamental periods of

the structures obtained from Perform-3D modal analyses of all models are summarized in Table 7-5.

Table 7-5 Fundamental periods of the structures (seconds).

Model	Transverse direction
6-Story modified STF (Vertical members)	0.993
6-Story modified STF (Kickers)	0.974
6-Story conventional STF	0.683
12-Story modified STF (Vertical members)	1.776
20-Story modified STF (Vertical members)	2.453

7.4.1 Maximum interstory drift ratios

The Maximum Interstory Drift Ratio (MIDR) demand are an important seismic design parameter because it is used to evaluate seismic hazard levels and performance of structural and non-structural elements for structures located in seismic areas. The stiffness in the STF system varies from bay to bay within the same floor because of the staggered pattern arrangement. This leads to significant differences in the story drifts of each bay in the same level. Therefore, the interstory drifts from all the bays on both sides of the frame (grid A and B as shown in Figure 6-1) were collected from the time-history analysis for each MCE ground motion. The maximum interstory drift ratios (MIDR) of each ground motion were calculated using the greater of the absolute maximum or absolute minimum interstory drift ratios from all the bays within each story.

The average values of MIDR for each hazard level were also calculated for all models. The results of the time-history analysis for 6-story STF models under MCE ground motions are illustrated in Figure 7-16 through Figure 7-18. It can be seen that the average values of MIDR of the modified STF (Vertical members) and (Kickers) range from 1.26-

1.64% and 1.29-1.49% for the MCE hazard levels respectively, whereas the values of the conventional STF range from 0.44-1.91%.

Figure 7-19 shows comparison between the average values of the 6-story STF models. It can be observed that the average values of MIDR of the 6-story modified STF (vertical members) and (kickers) models do not differ significantly. Comparing to the conventional STF system the modified STF system gives relatively uniformed MIDR throughout the height of the structure This is due to the yielding members in the Vierendeel panels which control the rotational capacity of the structures.

Figure 7-20 and Figure 7-21 show the results of the time-history analysis for 12-story and 20-story modified STF (vertical members) respectively. It can be seen that the average values of MIDR of the 12-story and 20-story modified STF (Vertical members) range from 1.25-2.03% and 1.13-2.16% for the MCE hazard levels respectively.

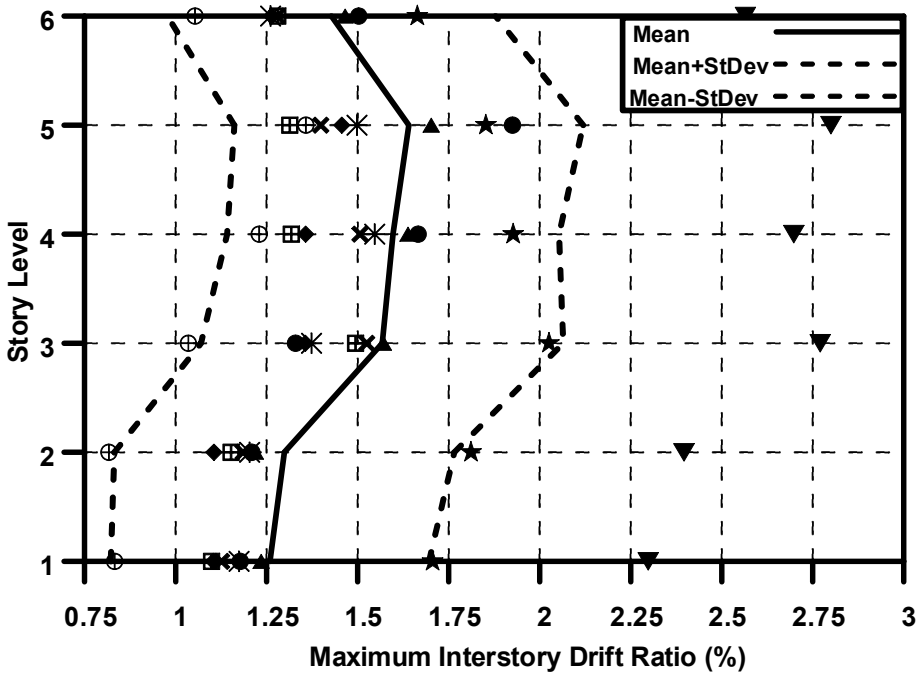

Figure 7-16 Maximum interstory drift ratios subjected to MCE ground motions for 6-Story modified STF (Vertical members).

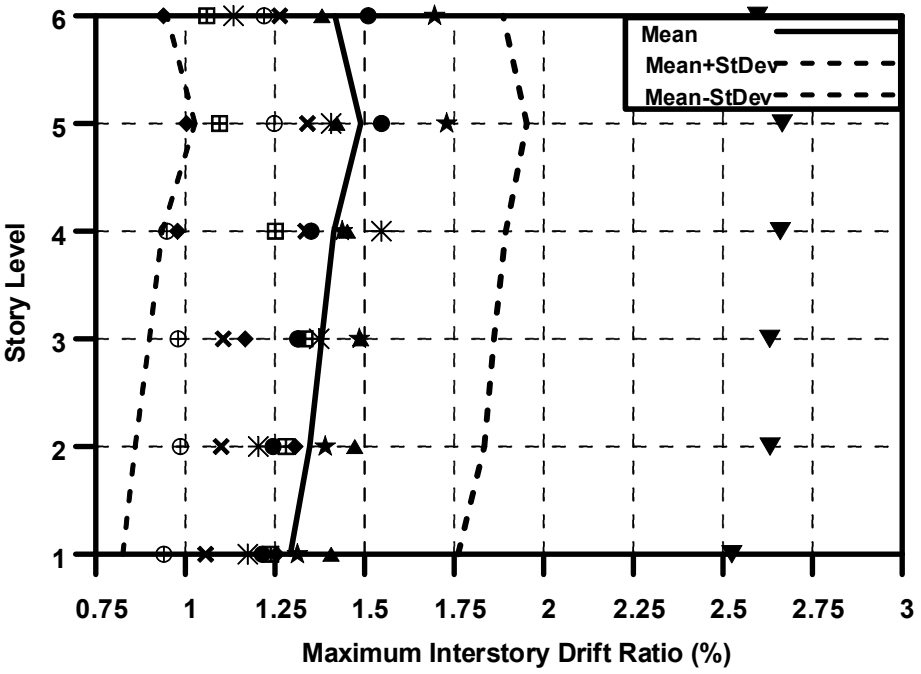

Figure 7-17 Maximum interstory drift ratios subjected to MCE ground motions for 6-Story modified STF (Kickers).

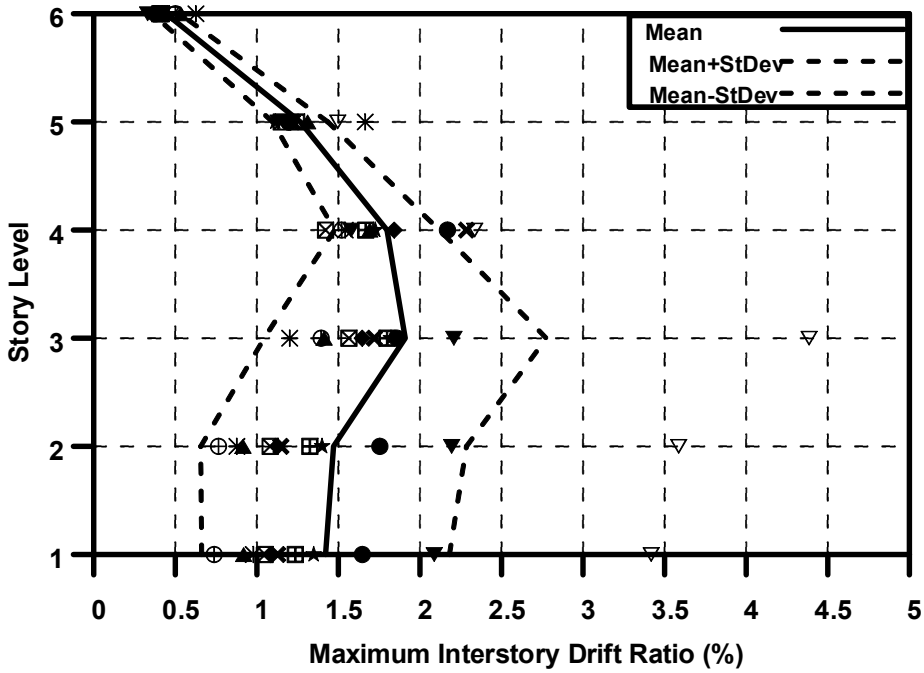

Figure 7-18 Maximum interstory drift ratios subjected to MCE ground motions for 6-Story conventional STF

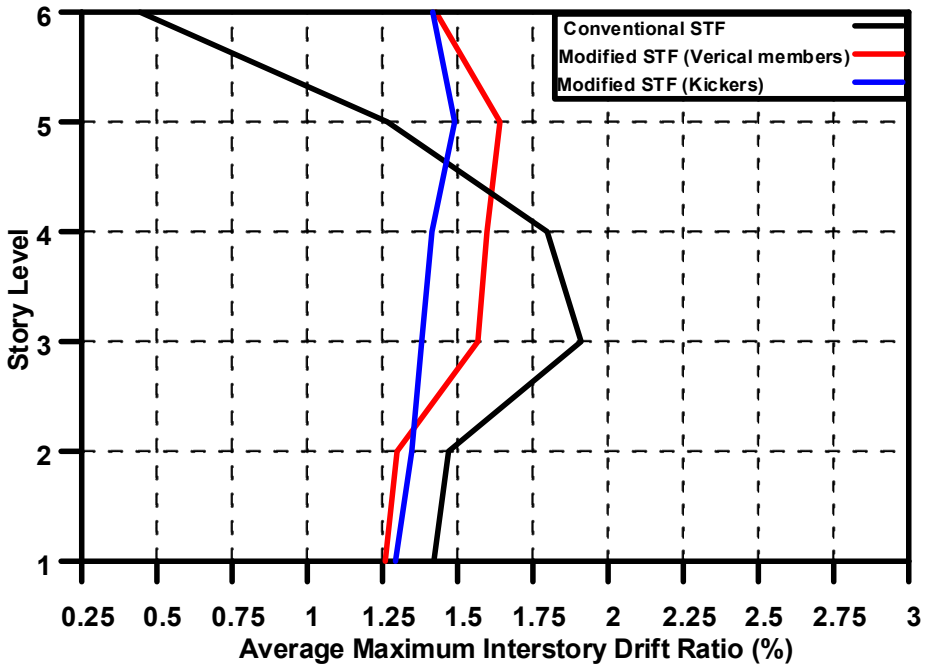

Figure 7-19 Average maximum interstory drift ratios subjected to MCE ground motions for 6-Story modified STF (Vertical members)and (Kickers); conventional STF.

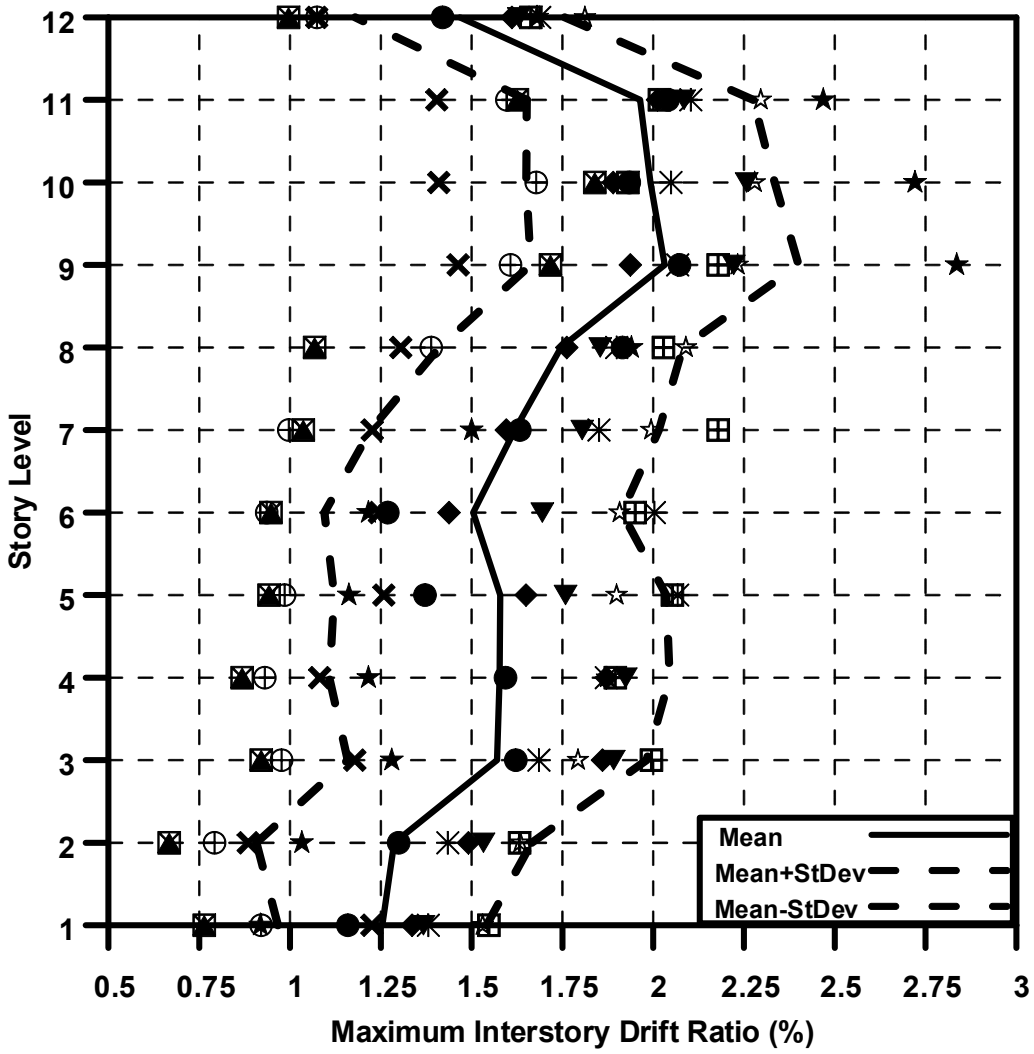

Figure 7-20 Maximum interstory drift ratios subjected to MCE ground motions for 6-Story modified STF (Vertical members).

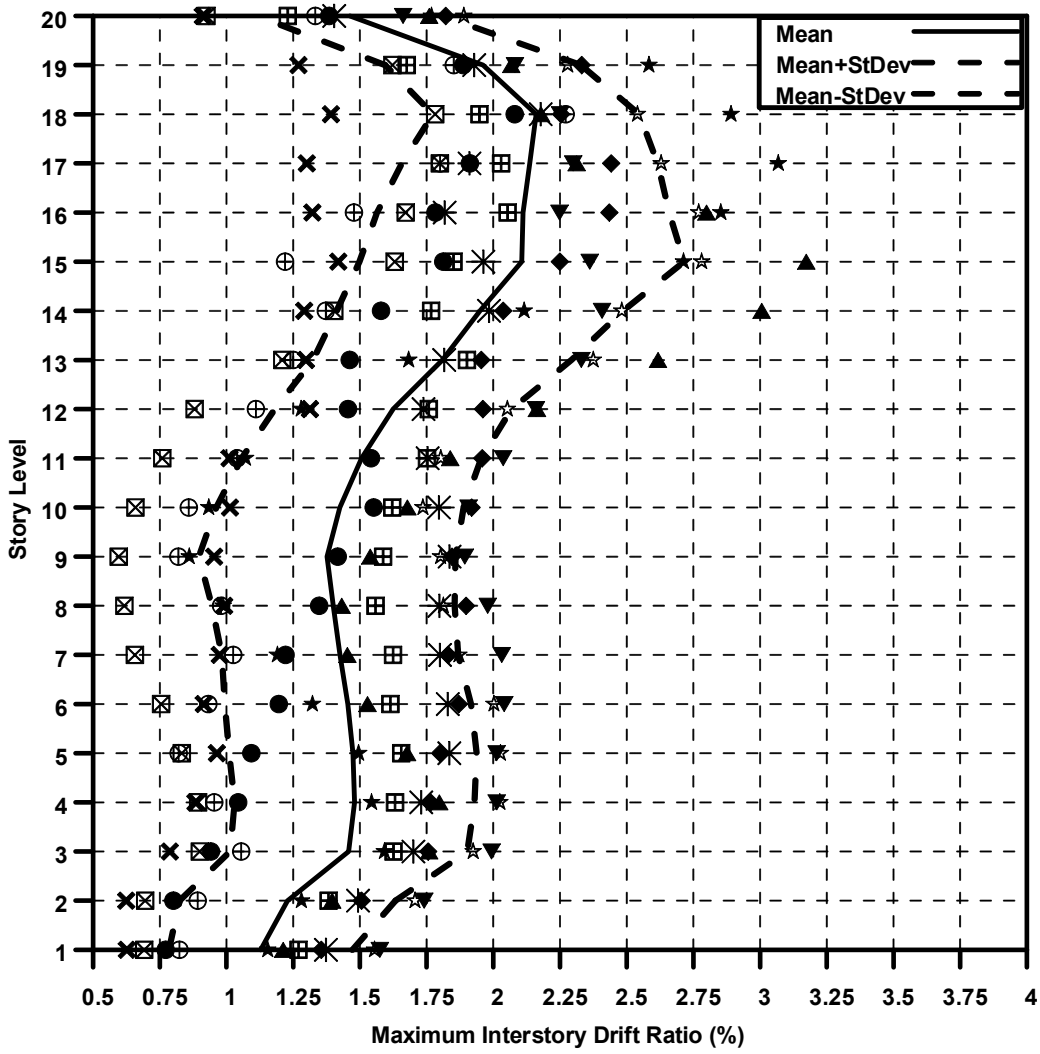

Figure 7-21 Maximum interstory drift ratios subjected to MCE ground motions for 6-Story modified STF (Vertical members).

7.4.2 Plastic hinge rotation

The plastic hinge rotation of the selected members that shown in Figure 7-6 were collected and the average maximum plastic hinge rotations of the these selected members from all ground motions are summarized as in Table 7-6.

Figure 7-22 through Figure 7-24 show plastic hinge locations, the maximum plastic hinge rotations, and the maximum interstory drift ratios along with the minimum usage ratios of the members in the deflected shape of bay 1 at the maximum roof drift ratio under a selected ground motion (MCE 11) for the 6-story modified STF (Vertical members), (Kickers), and conventional STF the, respectively. The plastic hinge rotations and the interstory drift ratios for the modified 12-story and 20-story STF (vertical members) are illustrated in Figure 7-25 and Figure 7-26, respectively.

It can be observed that in the modified STF, the rotational demands of the chord members in the Vierendeel panels are much high compared with the conventional STF. On the other hand, the plastic hinge rotations of the chords and vertical members in the modified (Kickers) are slightly higher than modified (vertical members).

It was noticed that in the modified STF, the vertical members in the Vierendeel panels started to yield first then followed by the chord members. Therefore, the rotation demands of the vertical member are high compared with the chord members. On the contrary, the chord members stated to yield first in the conventional STF, and high rotation demands in the chord members which led to redistribution of the forces and thus the columns yielded under high force demand.

Table 7-6 Average maximum plastic hinge rotation of the selected members from nonlinear time-history analyses of MCE hazard levels (kips).

Member number	Average maximum plastic hinge rotation (%)		
	6-Story modified STF (Vertical members)	6-Story modified STF (Kickers)	6-Story conventional STF
1	1.53	1.77	0.00
2	0.00	0.00	7.32
3	1.33	1.40	0.00
4	2.02	1.86	0.00
5	2.13	2.13	0.00

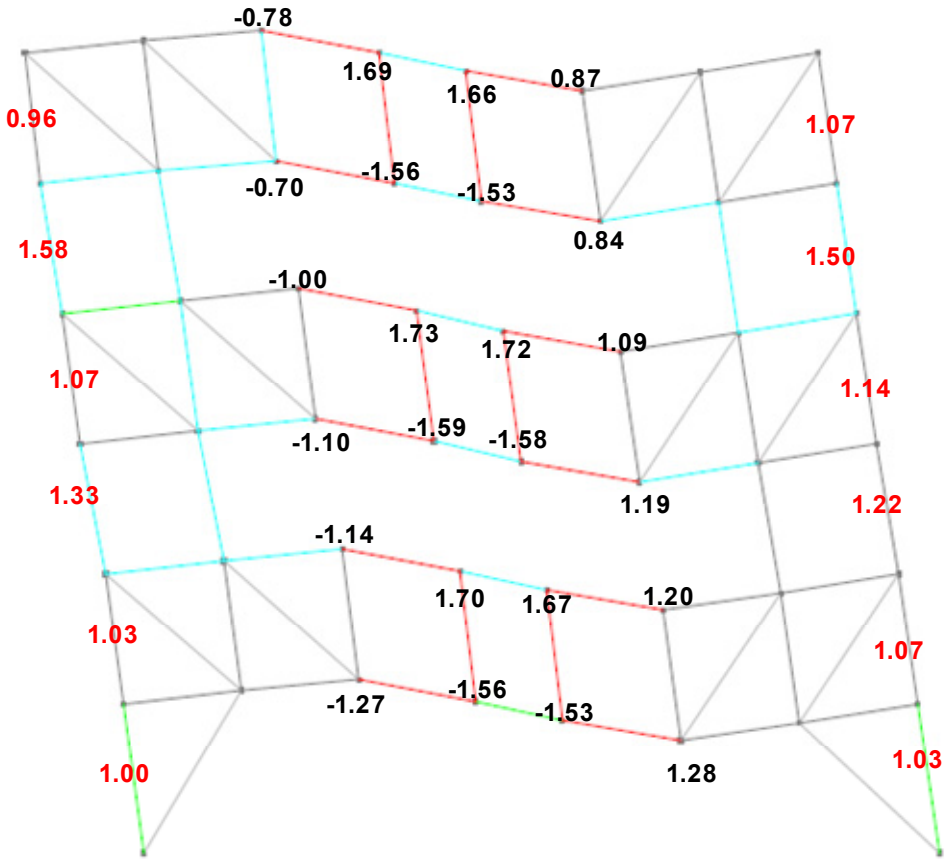

Figure 7-22 Bay 1 deflected shape with interstory drift ratios (%) (red color) and plastic hinge rotations (%) (black color) of the 6-Story modified STF (Vertical members) building under MCE11 ground motion.

The member colors indicate the minimum usage ratio (demand versus capacity of the member) as followed:

Color	Usage Ratio
Grey	0.0
Teal	0.4
Green	0.6
Orange	0.8
Red	1.0

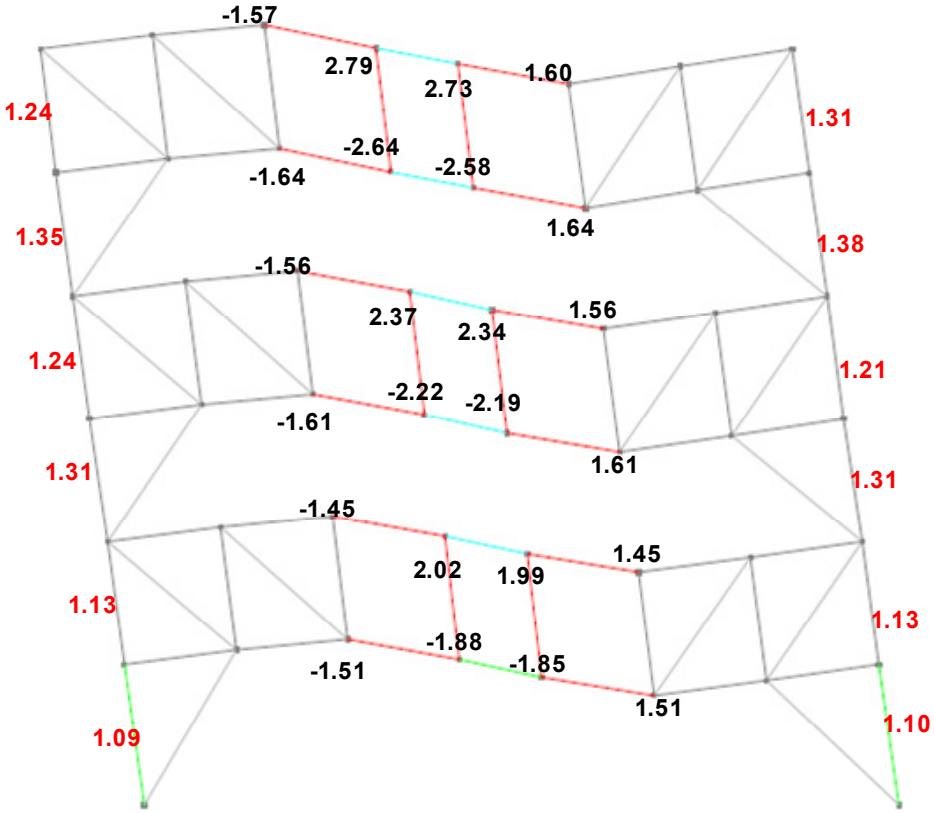

Figure 7-23 Bay 1 deflected shape with interstory drift ratios (%) (red color) and plastic hinge rotations (%) (black color) of the 6-Story modified STF (Kickers) building under MCE11 ground motion.

The member colors indicate the minimum usage ratio (demand versus capacity of the member) as followed:

Color	Usage Ratio
Grey	0.0
Teal	0.4
Green	0.6
Orange	0.8
Red	1.0

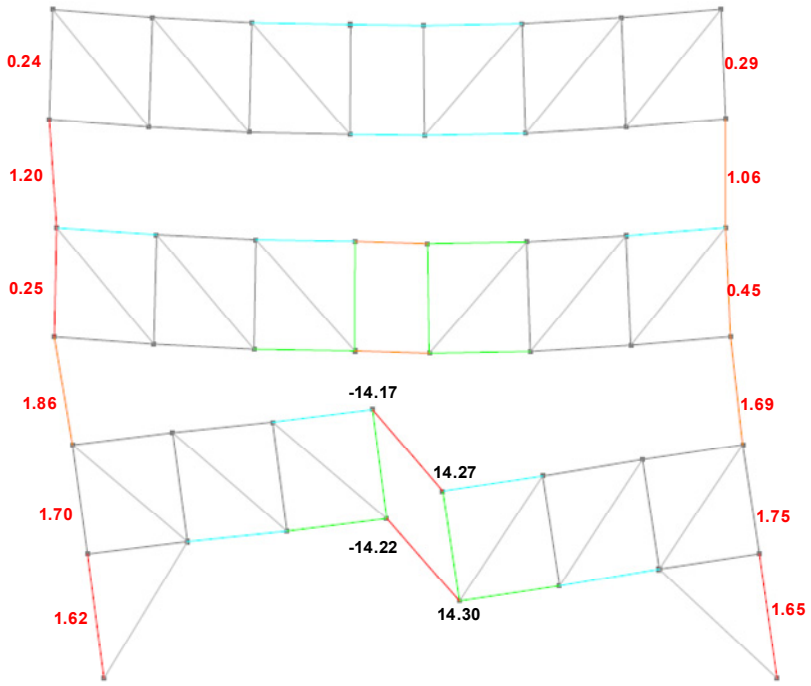

Figure 7-24 Bay 1 deflected shape with interstory drift ratios (%) (red color) and plastic hinge rotations (%) (black color) of the 6-Story modified STF (Kickers) building under MCE11 ground motion.

The member colors indicate the minimum usage ratio (demand versus capacity of the member) as followed:

Color	Usage Ratio
Grey	0.0
Teal	0.4
Green	0.6
Orange	0.8
Red	1.0

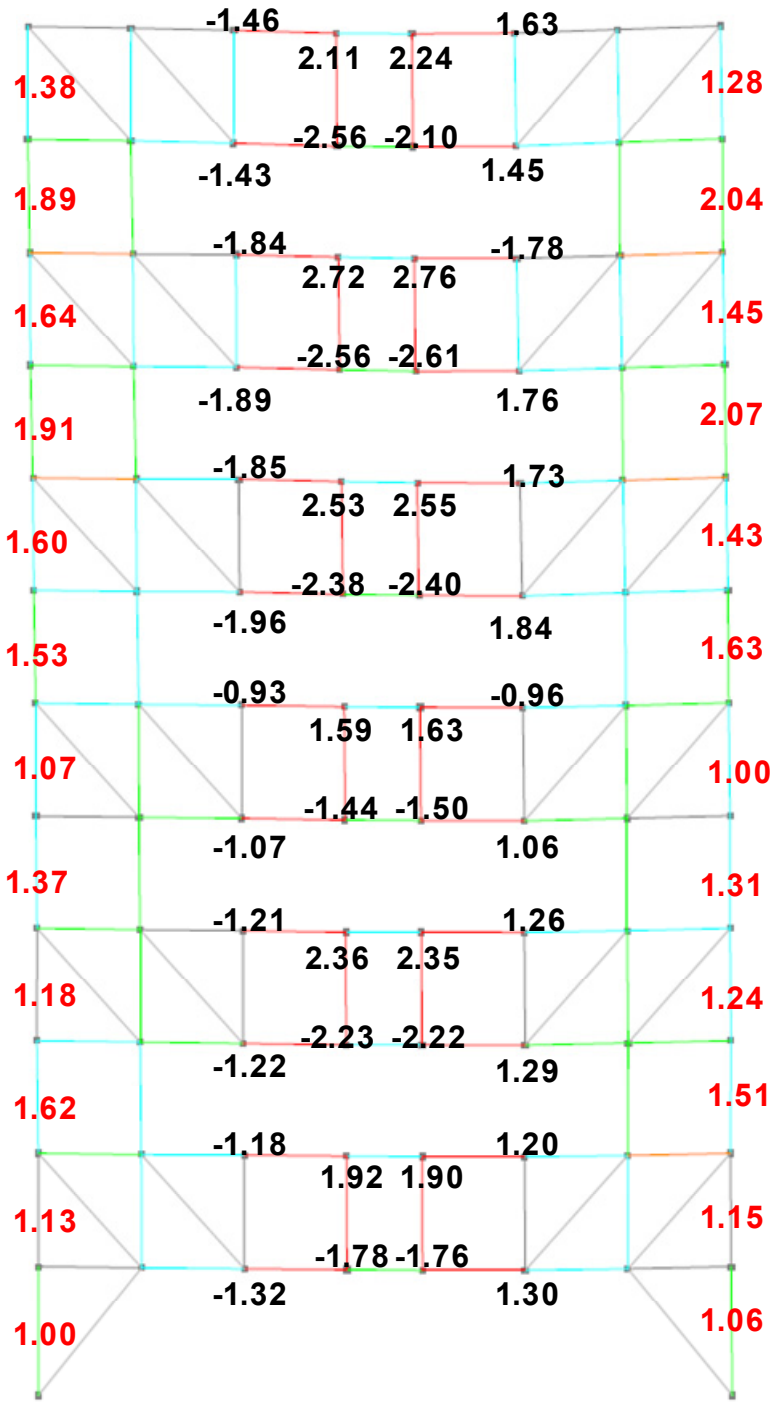

Figure 7-25 Bay 1 deflected shape with interstory drift ratios (%) (red color) and plastic hinge rotations (%) (black color) of the 12-Story modified STF(Vertical members) building under MCE11 ground motion.

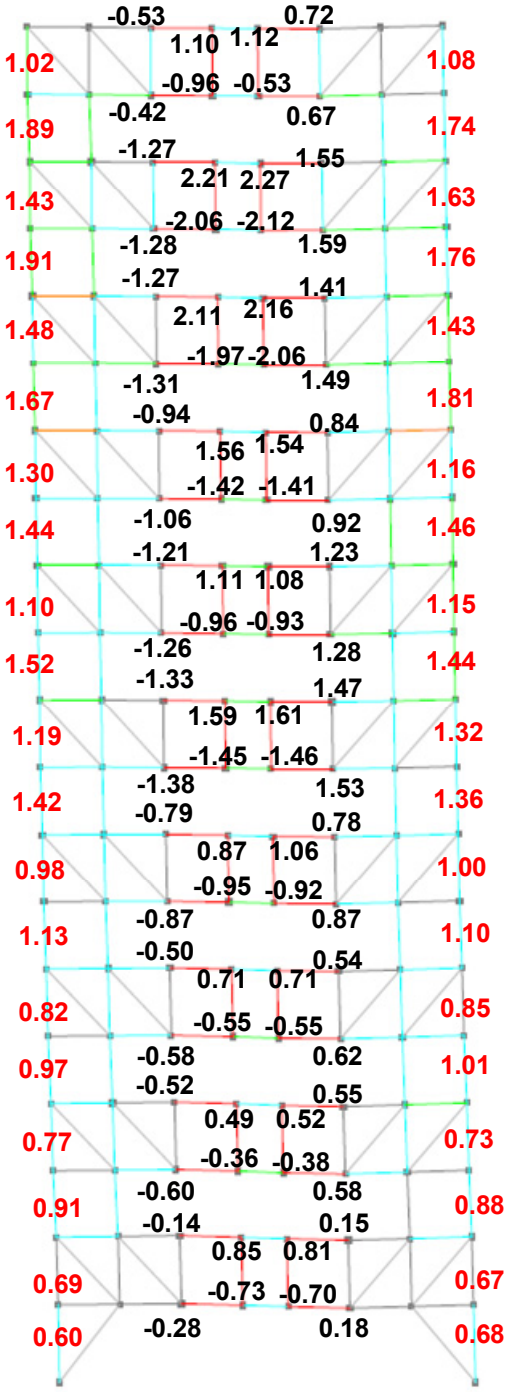

Figure 7-26 Bay 1 deflected shape with interstory drift ratios (%) (red color) and plastic hinge rotations (%) (black color) of the 20-Story modified STF(Vertical members) building under MCE11 ground motion.

Chapter 8

Finite Element Analysis

8.1 Introduction

Finite Element Analysis (FEM) was carried out using ABAQUS software to investigate the stress transfer mechanism across trusses members and the slabs. Furthermore, shear demands in the connections between precast hollow-core slab diaphragm to steel truss members were studied and determined. Moreover, the effect of deformation that comes from the lateral displacement along the moment (or braced) frame in the longitudinal direction of the STF system on these connections was investigated.

The exterior connections in the STF are under single shear effect, but the interior connections might be under the effect of single or double sheer. Therefore, they were investigated in this analysis.

8.2 Structure geometry and members section

6-Story 6- bays modified STF (Vertical members) was modeled using ABAQUS Version 6.14 as shown in Figure 8-1 through Figure 8-3. The sections which were used in the truss members: chords are W10X88, vertical and diagonal members are HSS6X6X0.5. On the other hand, the section used in the columns is W12X230, and W12X190 for the beams in longitudinal direction. The thickness of the slab is 8" and the connections between slabs and truss chords were created at 2' spacing. Five concrete slabs were used in each story.

8.3 Material properties

Material properties used in the model are summarized in Figure 8-1. For concrete material properties, compressive strength of the concrete was assumed 5000 psi (slabs) and 2600 psi (connections).

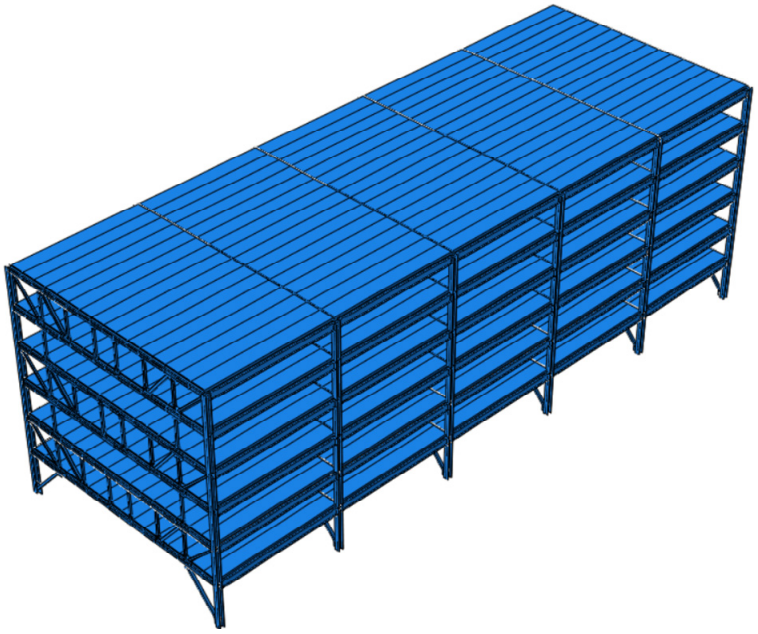

Figure 8-1 Overview of the STF model.

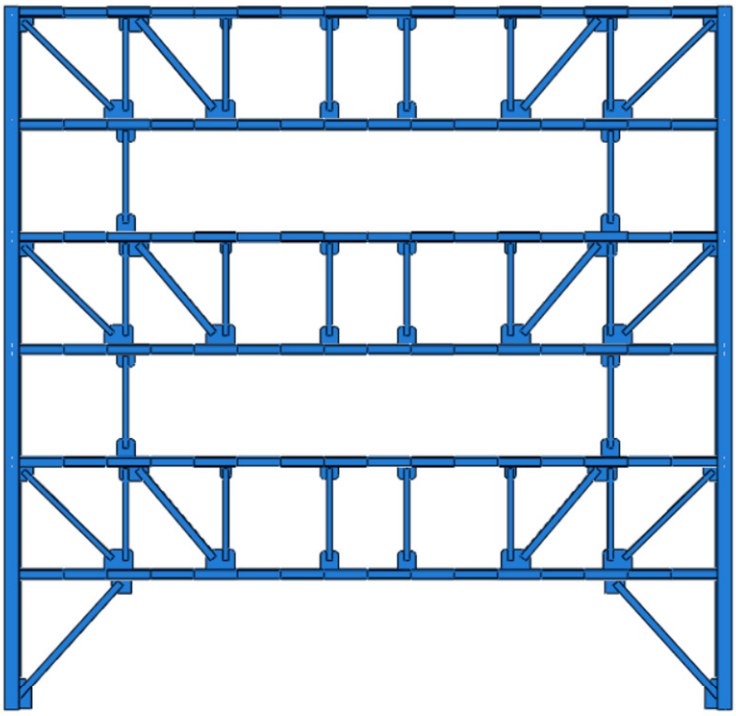

Figure 8-2 Odd bays in the STF model.

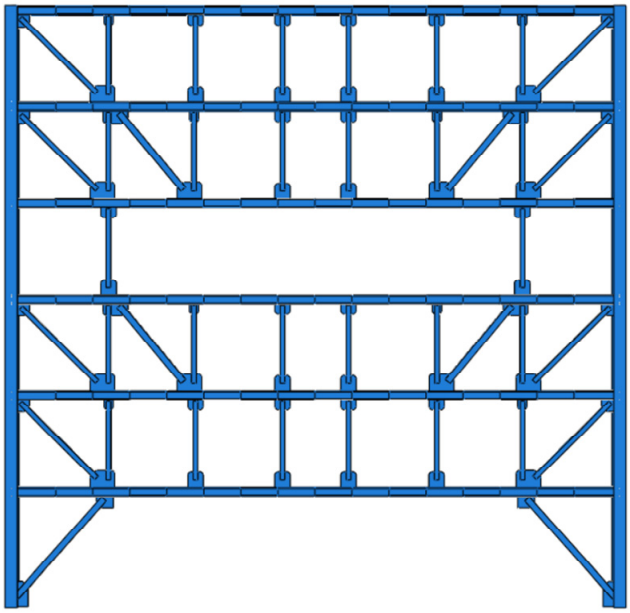

Figure 8-3 Even bays in the STF model.

Table 8-1 Material properties.

Material	Applied members	Density (lb/in^3)	Modulus of Elasticity (psi)	Poisson's ratio
Steel	Trusses (Chords), columns, and longitudinal beams. (WF section)	0.284	29,000,000	0.3
Steel	Trusses (Vertical and diagonal members). (HSS section)	0.284	31,400,000	0.3
Concrete	Slab	0.0868	4,030,509 [1]	0.2
Concrete	Connection	0.0868	2,906,441 [1]	0.2

[1] $57000\sqrt{f`_c}$ ($f`_c$=4000 psi)

Table 8-2 shows the stresses and plastic stains that used in the inelastic modeling of the Trusses (Chords), columns, and longitudinal beams which are wide flange section (WF).

Table 8-2 Stresses and plastic stains (WF)

Stress (psi)	Plastic Strain
55000	0
55000	0.02301
65000	0.04801
73000	0.09801

Table 8-3 shows the stresses and plastic stains that used in trusses (Vertical and diagonal) (HSS).

Table 8-3 Stresses and plastic stains (HSS)

Stress (psi)	Plastic Strain
77000	0
81000	0.02625
52000	0.19755

The concrete damaged plasticity model was used to model the slab of the structure. Table 8-4 show the stresses and inelastic stains of the compressive behavior of the concrete. Additionally, Table 8-5 shows the stresses and cracking strains of the tensile behavior of the concrete.

Table 8-4 Compressive behavior of the concrete

Stress (psi)	Inelastic Strain
1750	0
3000	0.0005
5000	0.0015
2500	0.006
500	0.02

Table 8-5 Tensile behavior of the concrete

Stress (psi)	Inelastic Strain
275	0
180.07	0.001
113.83	0.002
78.34	0.003
61.97	0.004
50.12	0.005
75	0.008
94.04	0.009
100	0.02

8.3 Load and boundary conditions

Distributed gravity and lateral loads were applied on the top of all diaphragm in the transverse direction until the first yielding of members in the Vierendeel panels occurred. Fixed boundary condition was applied to column depicted in Figure 8-4.

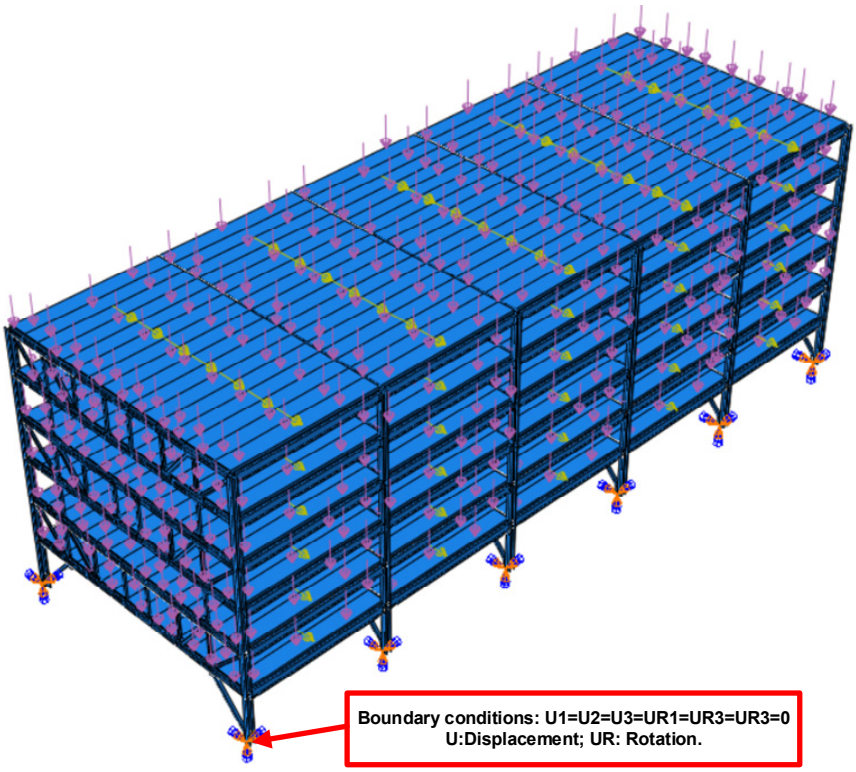

Figure 8-4 Load and boundary condition

8.4 Finite element constraints and mesh

The components were connected at the contact surfaces using tie constrains. The structure is composed of eleven components. They are chord, column, beam in the MF direction, Vertical member out of SS, Vertical member in the SS, Vertical member in non-story level, brace in the ground floor, diagonal member out of SS, concrete slab, concrete connection, and gusset plate.

The components of the structure were modeled as separate parts as presented in Figure 8-5 and Figure 8-6. Two types of element discretization shapes are used in the model. Hexahedral solid element was used for the chord, column, beam in the MF direction, concrete slab, concrete connection whereas the tetrahedral solid element was used for the Vertical member out of SS, Vertical member in the SS, Vertical member in non-story level, brace in the ground floor, diagonal member out of SS, and gusset plate.

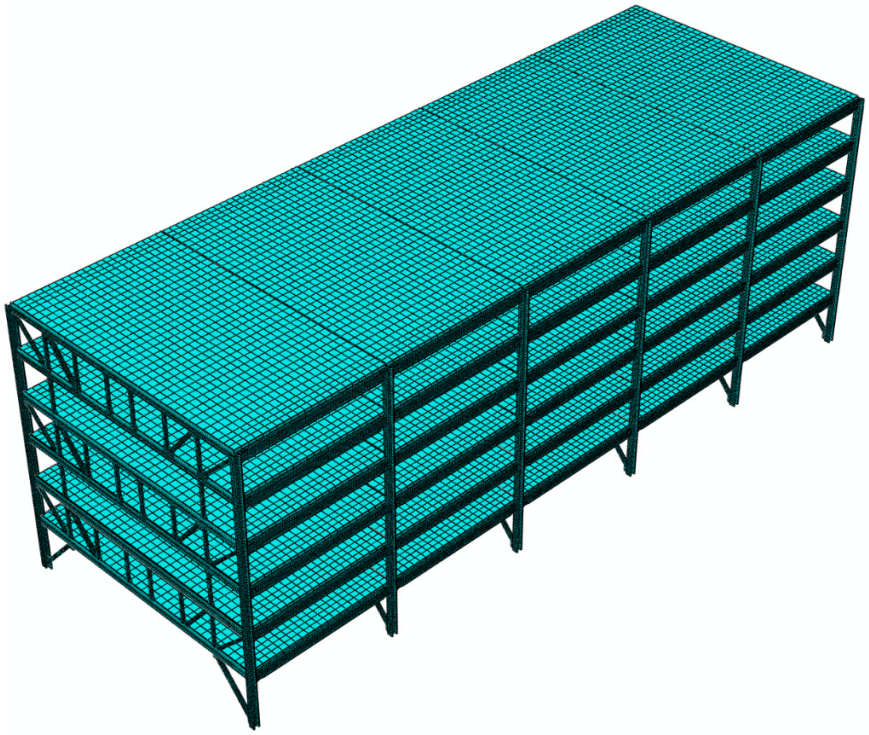

Figure 8-5 Overview of the finite element mesh.

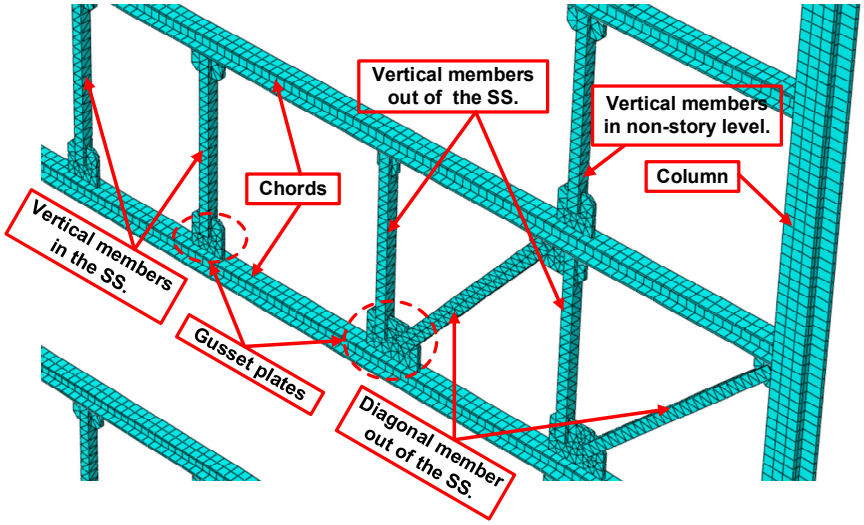
Vertical members out of the SS.
Vertical members in non-story level.
Column
Chords
Vertical members in the SS.
Gusset plates
Diagonal member out of the SS.

(a)

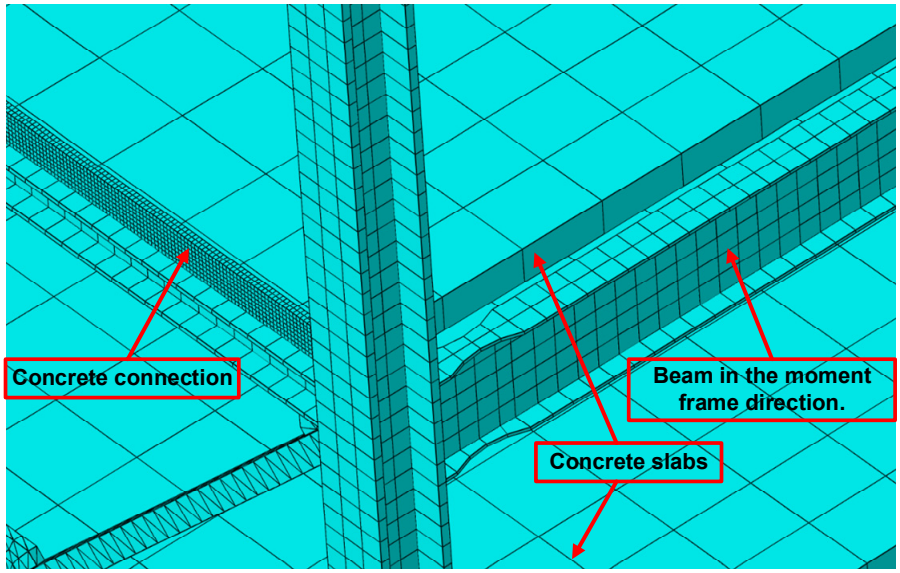
Concrete connection
Beam in the moment frame direction.
Concrete slabs

(b)

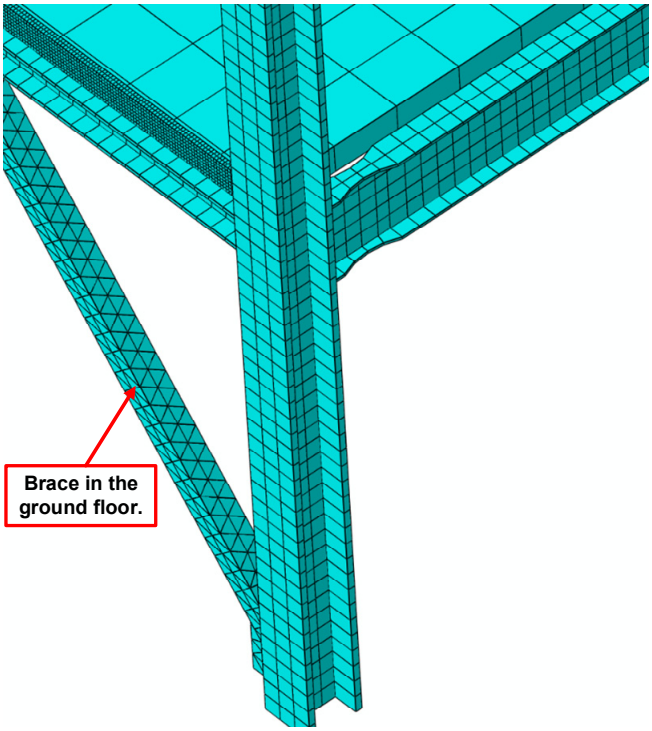

(c)

Figure 8-6 Finite element type and mesh for the (a) Column, Chord, Gusset plate, vertical and diagonal members (b) Concrete slab, Concrete connection, and Beam in MF direction(c) Brace in the ground floor.

8.5 Finite element results

The STF structure model was pushed up to failure and Figure 8-7 shows the overview of the deflected shape of the structure. It was observed that the first yielding started at about 0.34% roof drift which is similar to that of a typical Concentrically Braced Frame (CBF) which is expected to yield and buckle at rather moderate story drifts of about 0.3% to 0.5% (AISC,2016b).

The first members that started to yield (plastic hinge formation) at 0.34% roof drift were the vertical members in the Vierendeel panels as illustrated in Figure 8-8. Then followed by the ends of the chord members in the Vierendeel panels which were yielded at 0.87% as shown in Figure 8-9. These members represent the Special Segments (SS)

which dissipate the seismic energy during the earthquakes. Therefore, the plastic hinge locations are confined within the Vierendeel panels which is preferred yielding mechanism (Moore,2005).

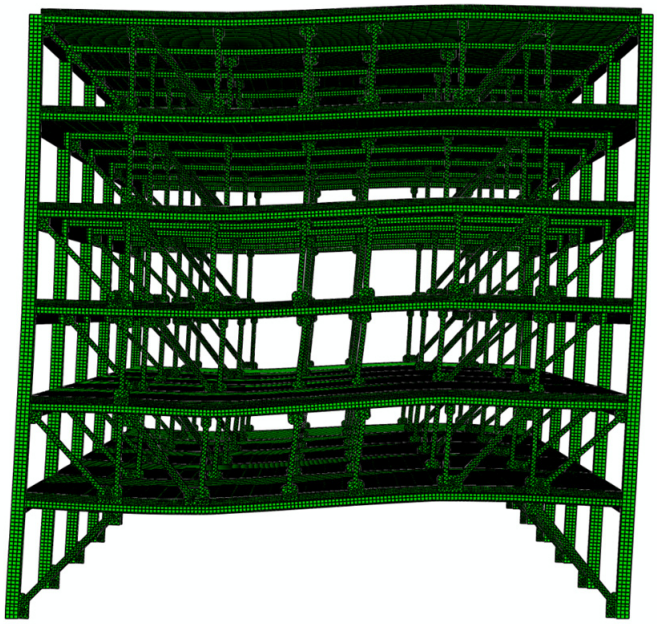

Figure 8-7 Overview of the deformed shape.

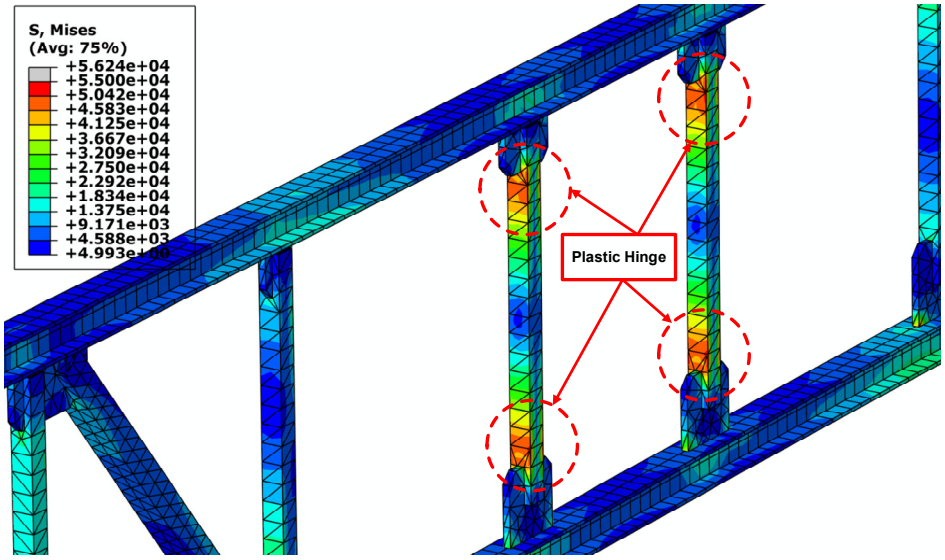

Figure 8-8 Formation of plastic hinges in the vertical members of Vierendeel panels at 0.34% roof drift.

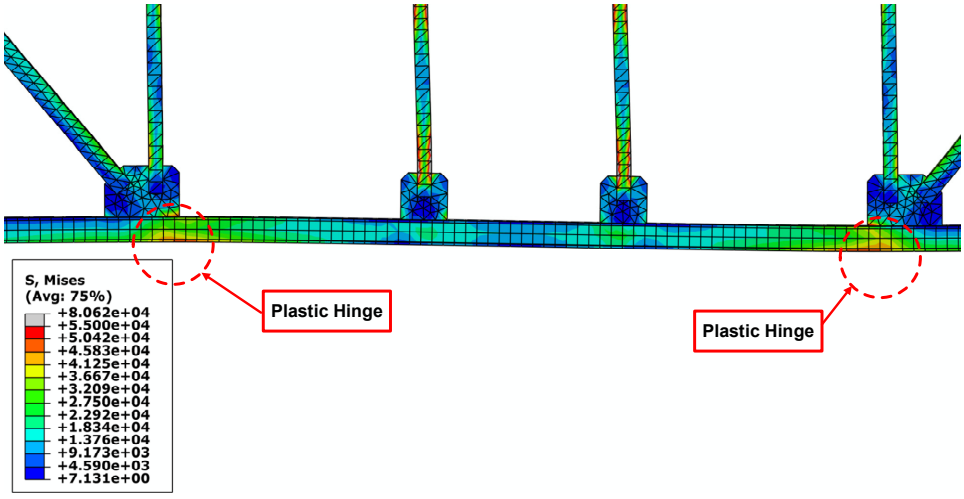

Figure 8-9 Formation of plastic hinges at the ends of chords in the Vierendeel panels at 0.87% roof drift.

The results of analysis showed that the maximum principal stress in slab (diaphragm) reduced and become nearly constant beyond a short distance from the trusses as it can be seen in Figure 8-10.

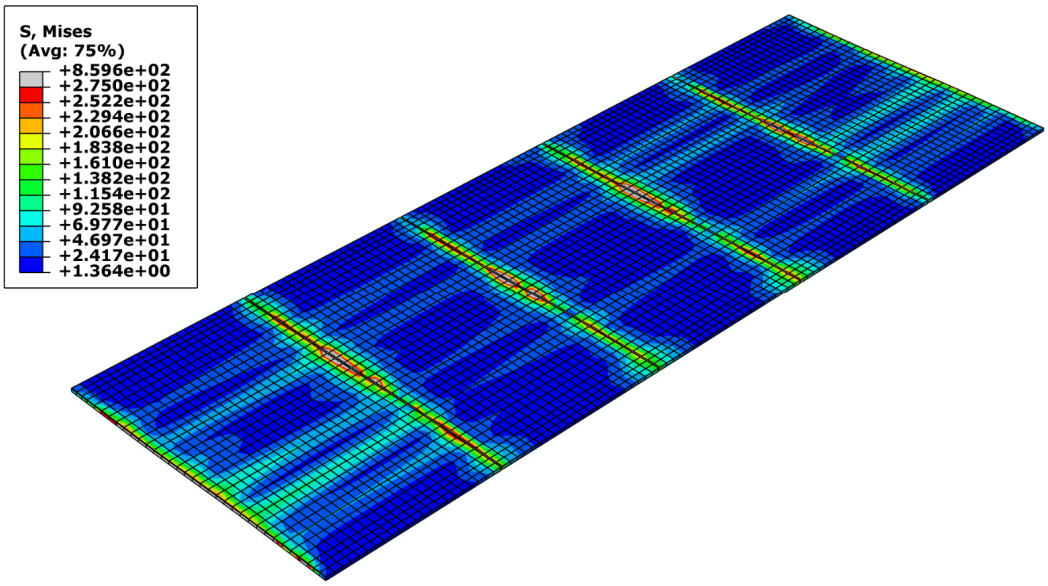

Figure 8-10 Principal stress in the diaphragm and the connection at 2% roof drift.

The shear behavior and demand at the exterior and interior connections were studied. The results showed that the exterior connection which is under single shear has maximum shear demand (695 Kips) which represents (10.77 K/ft.) as shown in Figure 8-11.

On the on the hand, the results showed that the interior connection is under double shear effect as shown in Figure 8-12.

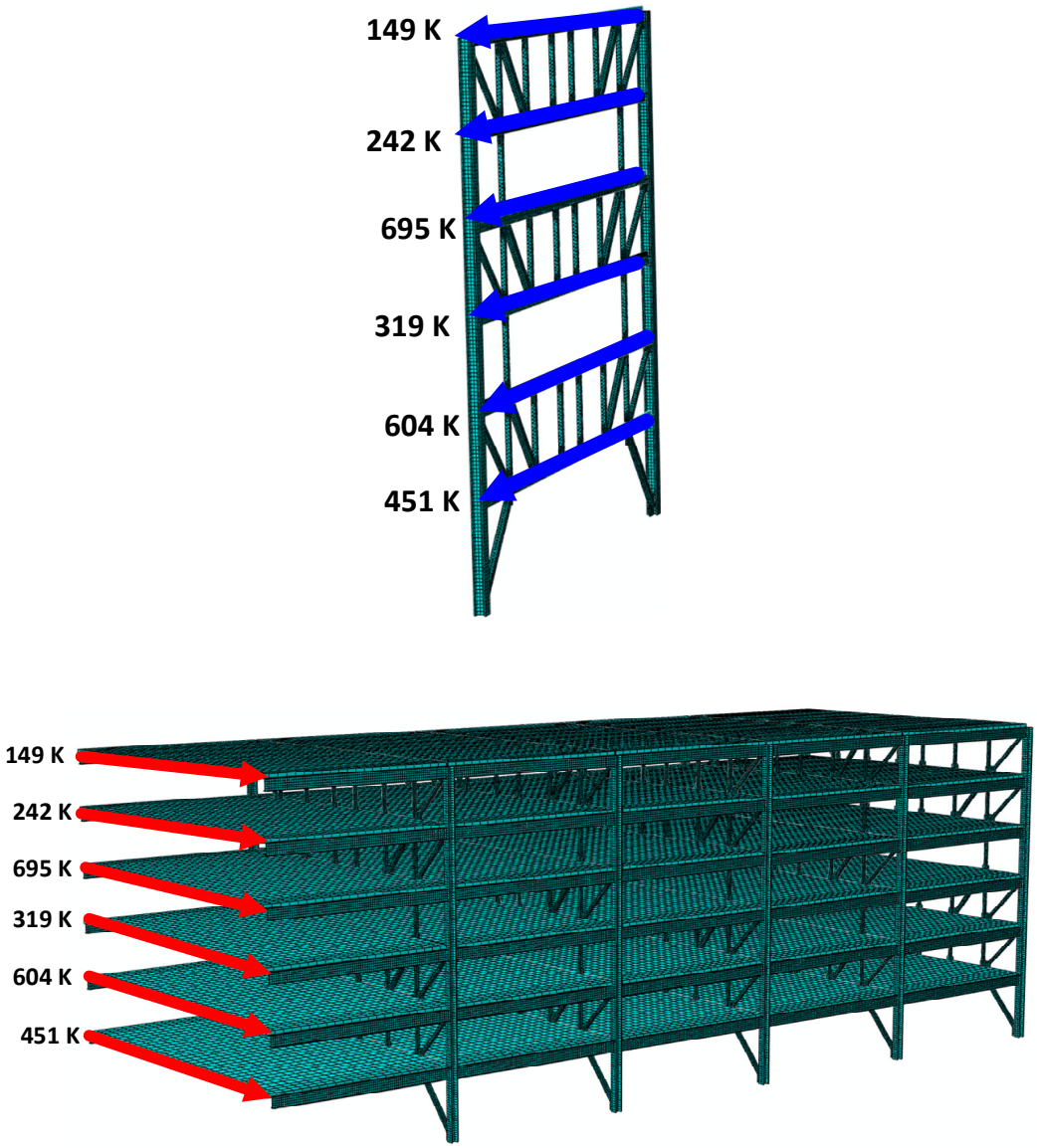

Figure 8-11 Free-body diagram in an exterior connection shows the single shear effect.

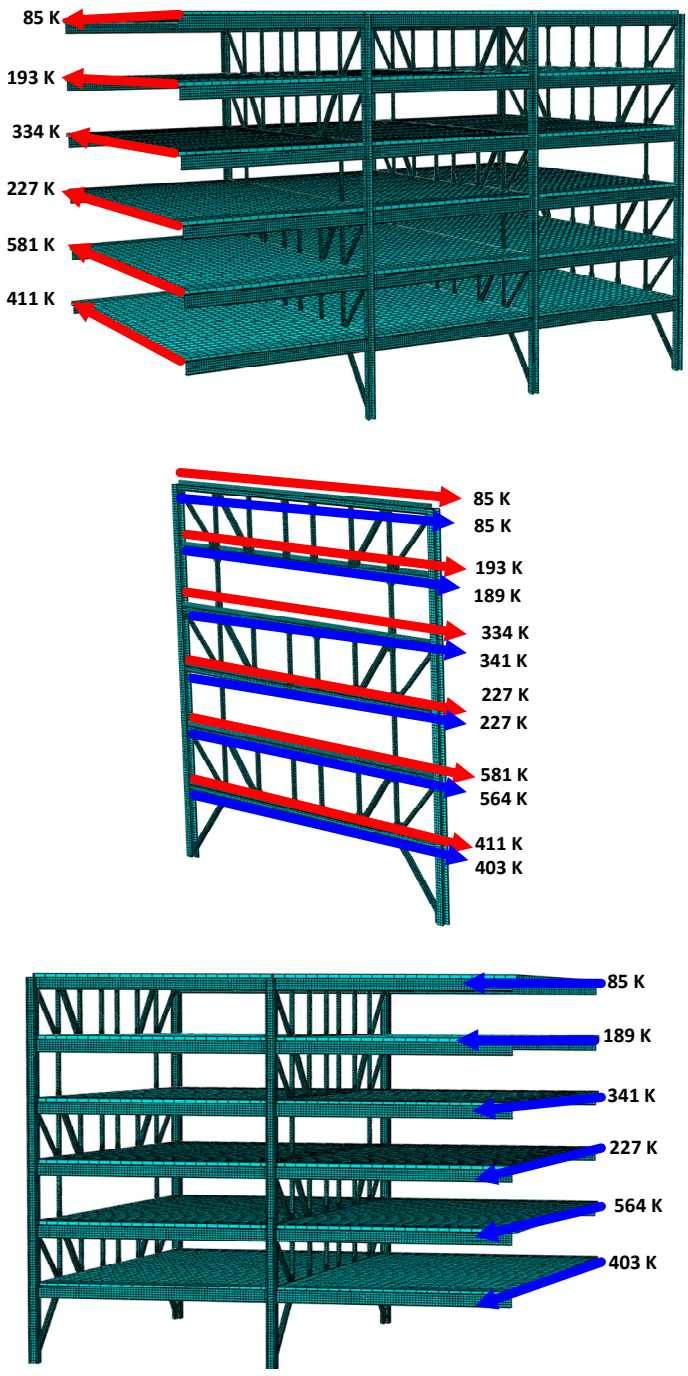

Figure 8-12 Free-body diagram in an interior connection shows the double shear effect.

8.6 The bending rotation deformation

The nonlinear analyses of a three-dimensional 6-story STF building model (Simasathien, 2016) indicated that the hollow-core slab diaphragms and the diaphragm-to-truss connection is subjected to a bending rotation (θ) deformation. This deformation comes from the lateral displacement along the moment (or braced) frame in the longitudinal direction of the building as shown in Figure 8-13. The bending rotation, θ, is resulting from the compatibility deformation and its magnitude is close to the story drift ratio of the moment frame (or braced frame) in the longitudinal direction.

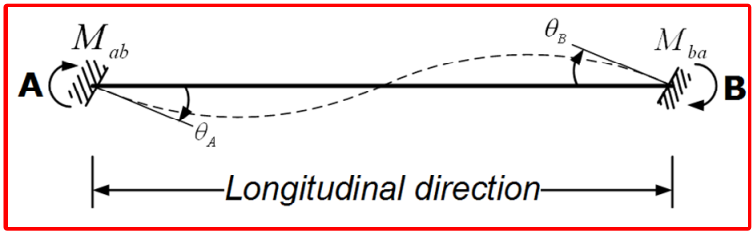

Figure 8-13 Bending rotation, θ, of the hollow-core diaphragm and its connections.

In order to investigate the effect of the bending deformation on the hollow-core slab diaphragms and the diaphragm-to-truss connection, the same structure that modeled above with distributed gravity and lateral loads which was applied on the top of all diaphragm in the longitudinal direction was pushed up to 2%.

The results showed that the effect of the bending rotation, θ, is concentrated locally at the end of chords as shown in Figure 8-14.

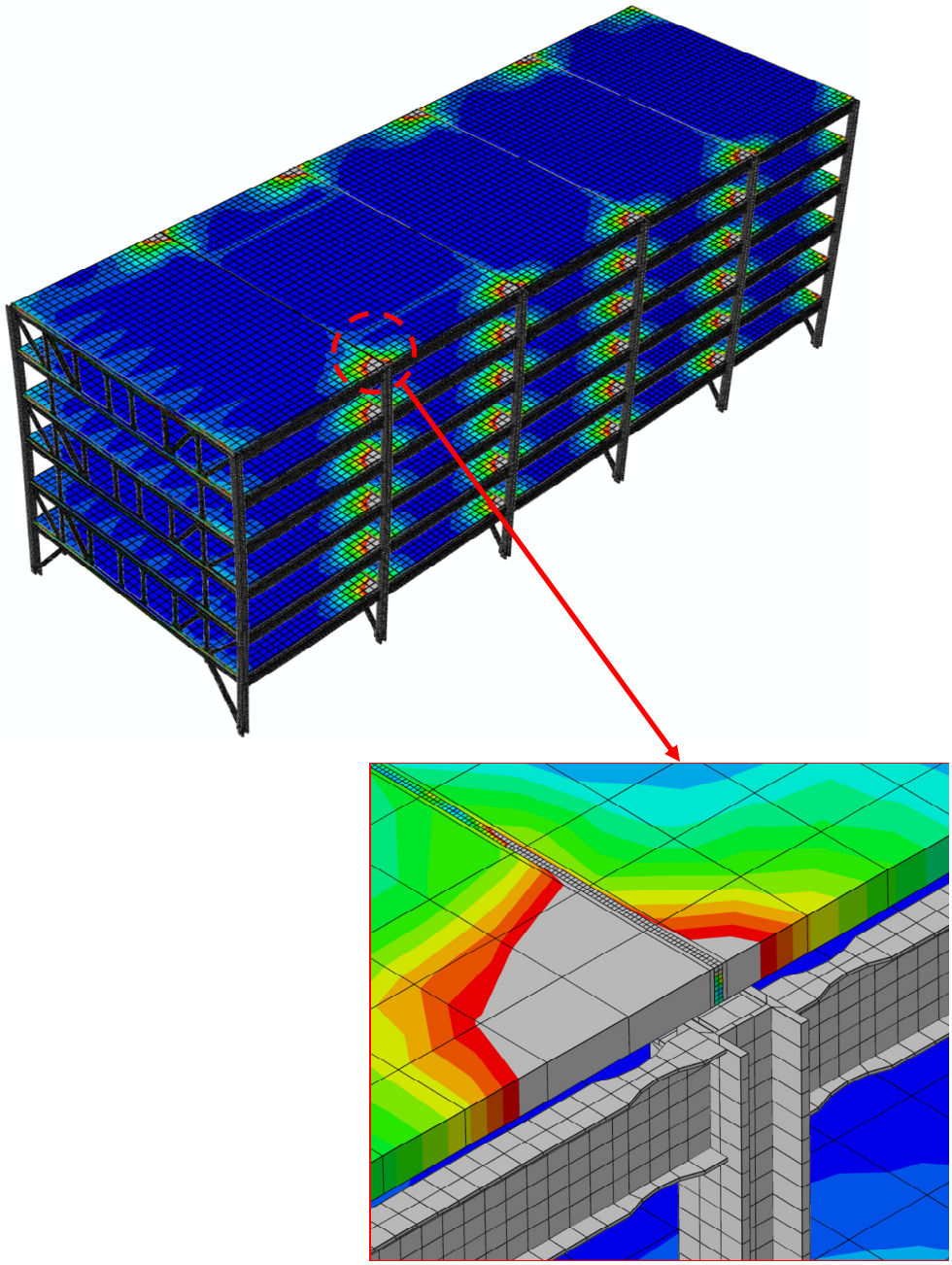

Figure 8-14 Bending rotation, θ, of the hollow-core diaphragm and its connections.

Chapter 9

Summary and Conclusions

The main purposes of this study are to investigate the cyclic behavior of the connection between precast hollow-core slab diaphragm to steel truss in the STF system, to present a design procedure for the STF system, and to evaluate the seismic performance of the proposed modified STF by nonlinear time-history (NTH) analyses.

Five large scale specimens were prepared and tested to evaluate the cyclic behavior of the connection under the effect of single and double shear forces. A modified STF was proposed by adding vertical members in the non-story levels of the STF structure and using the horizontal trusses as a diaphragm to transfer the high shear forces especially in the lower floors.

A design procedure was presented and followed to design the proposed STF with different level heights 6,12 and 20-story, then the 6-story modified STF was compared with a 6-story conventional STF. On the other hand, Finite Element Analysis (FEA) was carried out to investigate the effect of double shear on the connection in the transverse direction and the bending rotation effect in the longitudinal direction.

The following conclusions are drawn from the study:

1. No crack occurred in the connection before 30 kips (or 7.5 k/ft) under the effect of cyclic single shear; the maximum capacity of the hollow-core plank to steel connection was 13.5 k/ft.
2. The failure in the hollow-core plank occurred along the steel rebars which was due to debonding between grout and steel rebars.
3. Fracture at bottom of the shear stud was observed when a smaller number of studs was used.

4. Severe damage occurred in hollow-core planks at a shear of approximately 50 kips (12.5 k/ft), regardless single-shear or double-shear effect.
5. Based on full-scale hollow-core plank to steel chord tests, the failure mode was either due to fracture of the shear studs or severe damage in the concrete hollow-core. Neither of the failure modes are desired in the connection.
6. The modified STF has clearly defined yield mechanism and structural fuses.
7. NTH analyses indicated the modified STF showed stable responses under MCE ground motions.
8. The addition of vertical members to the non-truss levels can effectively reduce the demands of the columns in the non-truss stories.
9. The addition of vertical members helps to reduce the staggered load transfer pattern thus decrease the cumulative forces in the connections.
10. The modified STF system gives relatively uniformed MIDR throughout the height of the structure than the conventional STF system. This is due to the clearly defined yielding members in the special segments and the capacity design which keep the members outside of the yielding members elastic.
11. Nonlinear analyses showed that the new horizontal trusses can effectively transfer the seismic forces through steel connections, which can be designed to remain elastic during a major earthquake.
12. NTH analyses indicated that the modified STF could be a viable seismic force-resisting system in seismically active areas.

Appendix A

In Appendix A the deflected shapes under pushover analysis of the bay 2 through bay 6, the horizontal trusses of each floor, the two moment frames for the 6-story modified STF (Vertical members), 6-story modified STF (Kickers),6-story conventional STF , 12-story modified STF (Vertical members), 20-story modified STF (Vertical members) are shown in the following figures.

For all figures, the member colors indicate the minimum usage ratio (demand versus capacity of the member) as followed:

Color	Usage Ratio
Grey	0.0
Teal	0.4
Green	0.6
Orange	0.8
Red	1.0

A1. Deflected shapes of pushover analysis for 6-story modified STF (Vertical members).

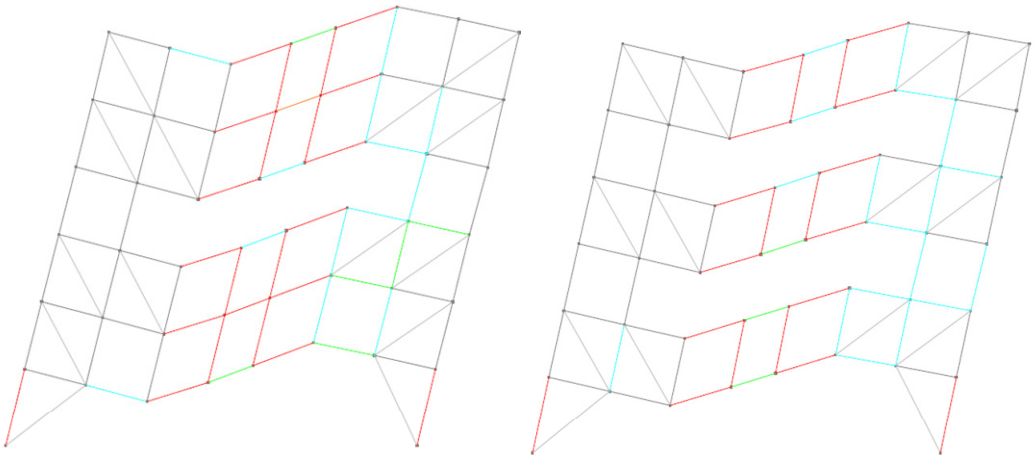

(a) (b)

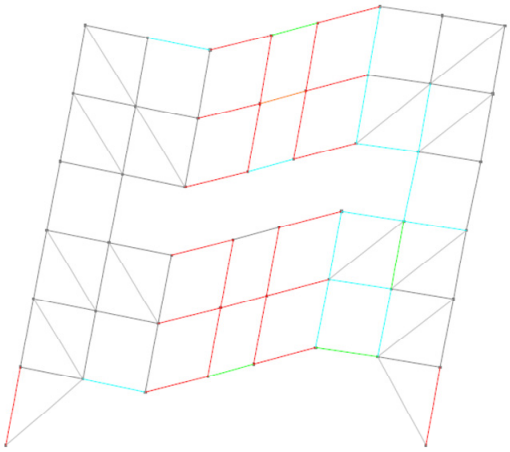

(c)

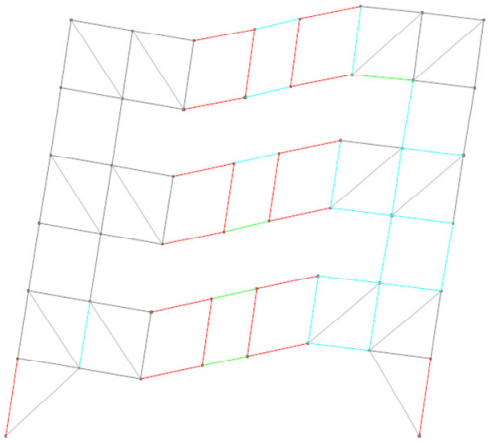

(d)

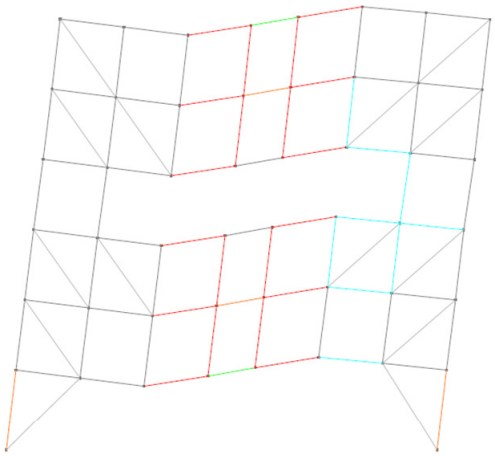

(e)

A- 1 Deflected shape of the 6-Story modified STF (Vertical members) model at 3% roof drift: (a) bay 2 ;(b) bay 3;(c) bay 4;(d) bay 5; (e) bay 6.

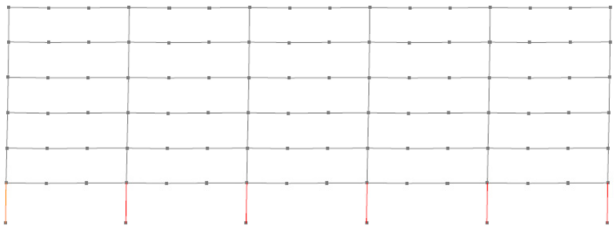

(a)

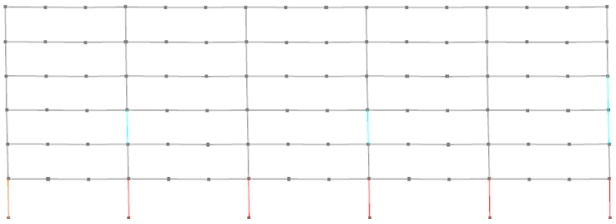

.(b)

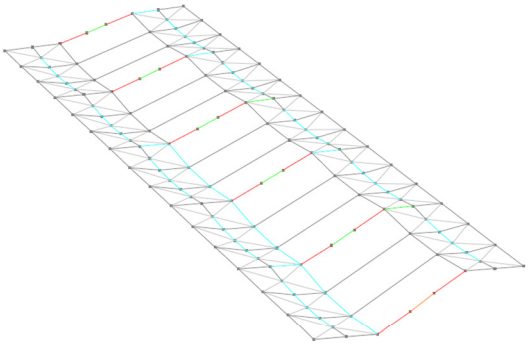

(c)

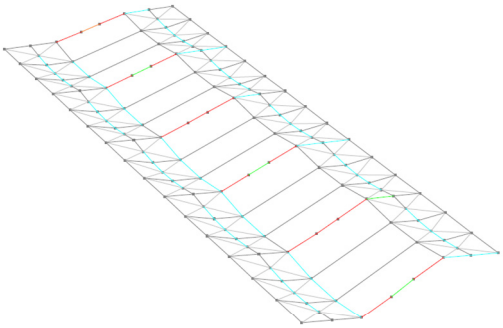

(d)

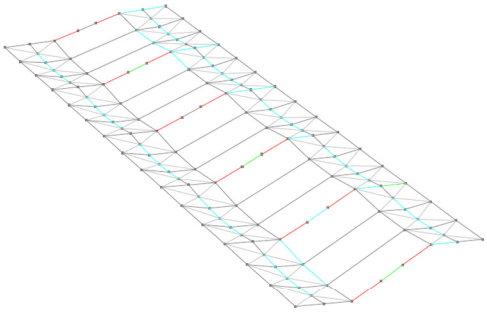

(e)

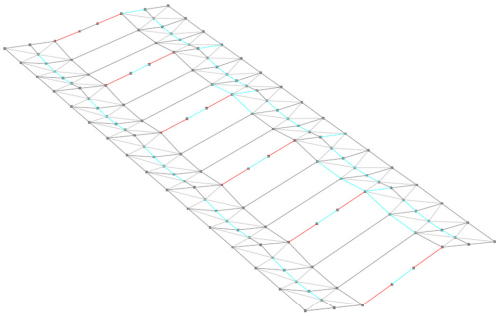

(f)

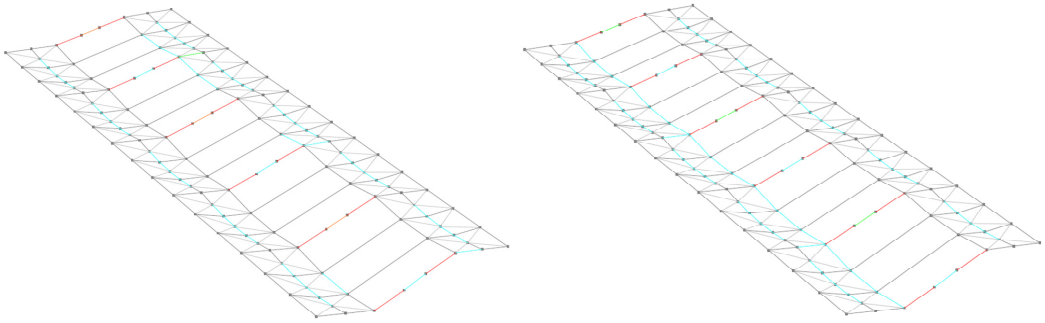

(g) (h)

A-2 Deflected shapes of the moment frames (a)MF1 (b) MF2; and the horizontal truss members on the (c) 2nd floor (d) 3rd floor (e) 4th floor (f) 5th floor (g) 6th floor (h) roof floor for the 6-Story modified STF (Vertical members) model.

A2. Deflected shapes of pushover analysis for 6-story modified STF (Kickers).

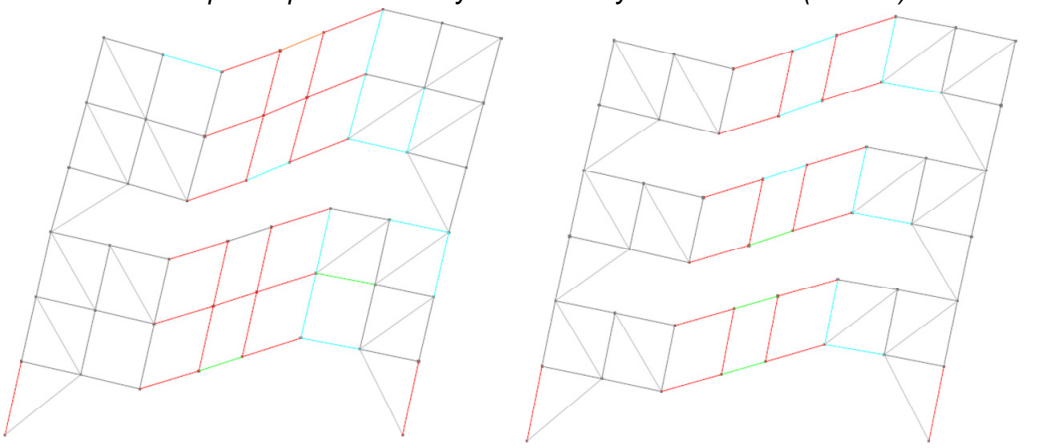

(a) (b)

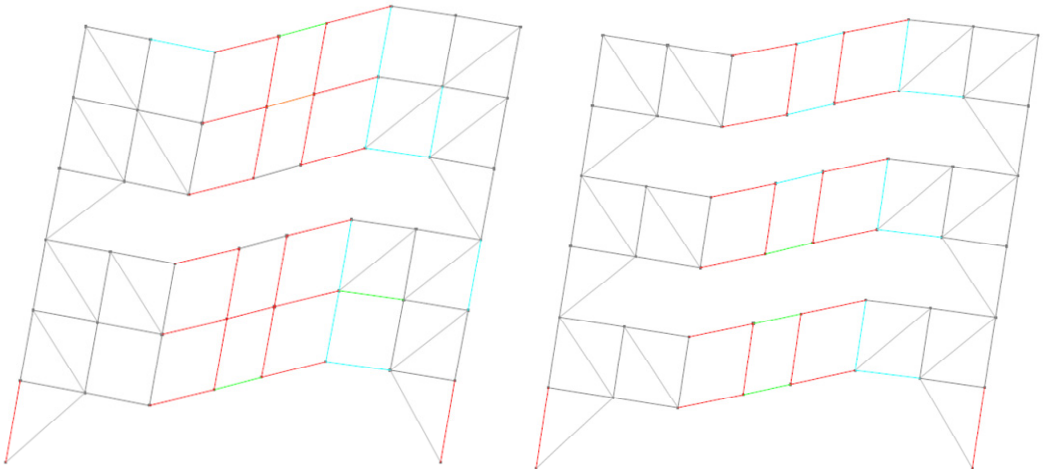

(c) (d)

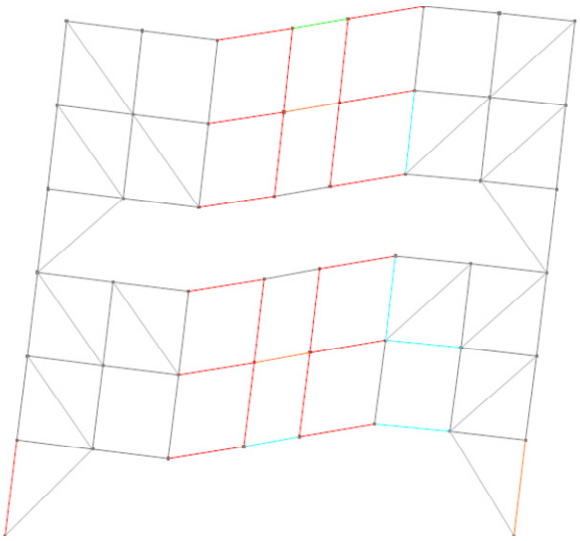

(e)

A-3 Deflected shape of the 6-Story modified STF (Kickers) model at 3% roof drift: (a) bay 2 ;(b) bay 3;(c) bay 4;(d) bay 5; (e) bay 6.

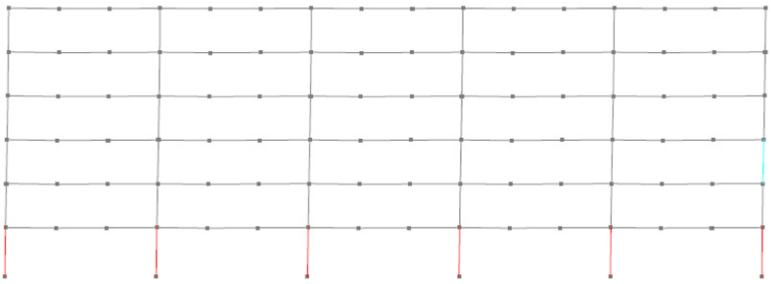

(a)

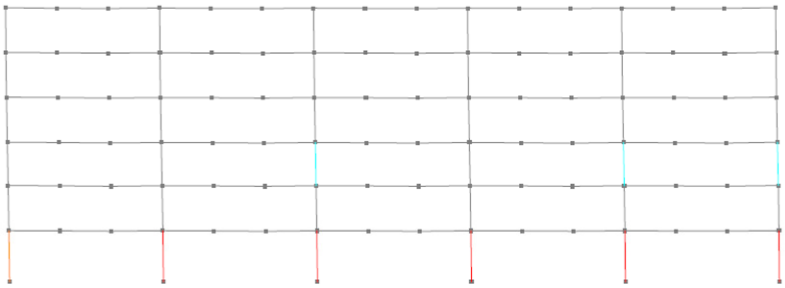

(b)

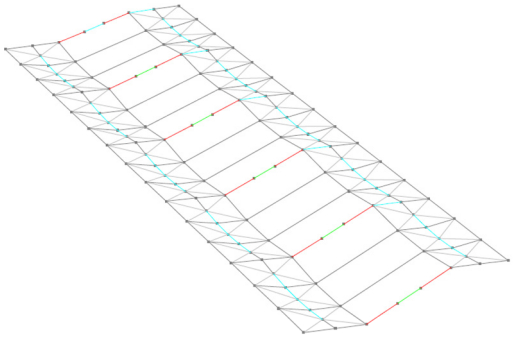

(c)

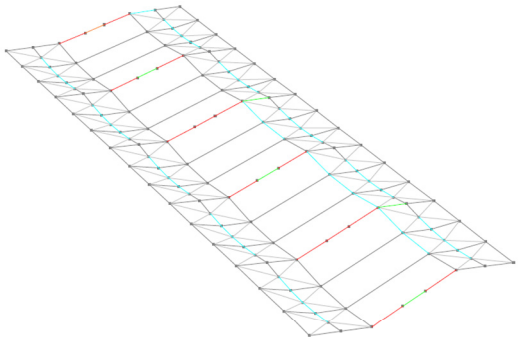

(d)

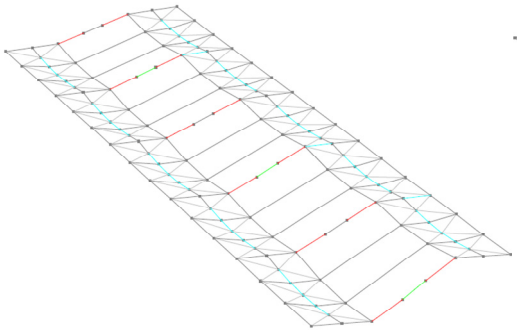

(e)

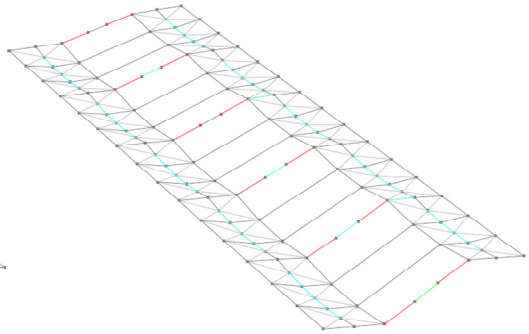

(f)

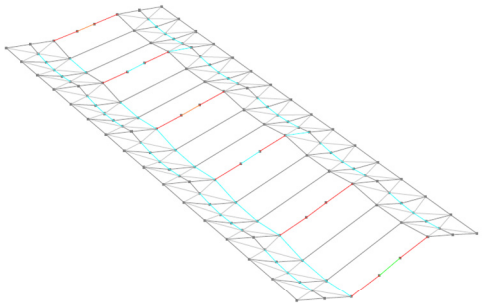

(g)

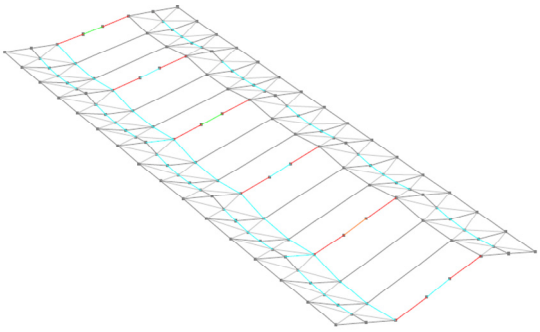

(h)

A-4 Deflected shapes of the moment frames (a)MF1 (b) MF2; and the horizontal truss members on the (c) 2nd floor (d) 3rd floor (e) 4th floor (f) 5th floor (g) 6th floor (h) roof floor the 6-Story modified STF (Kickers) model.

A3. Deflected shapes of pushover analysis for 6-story conventional STF

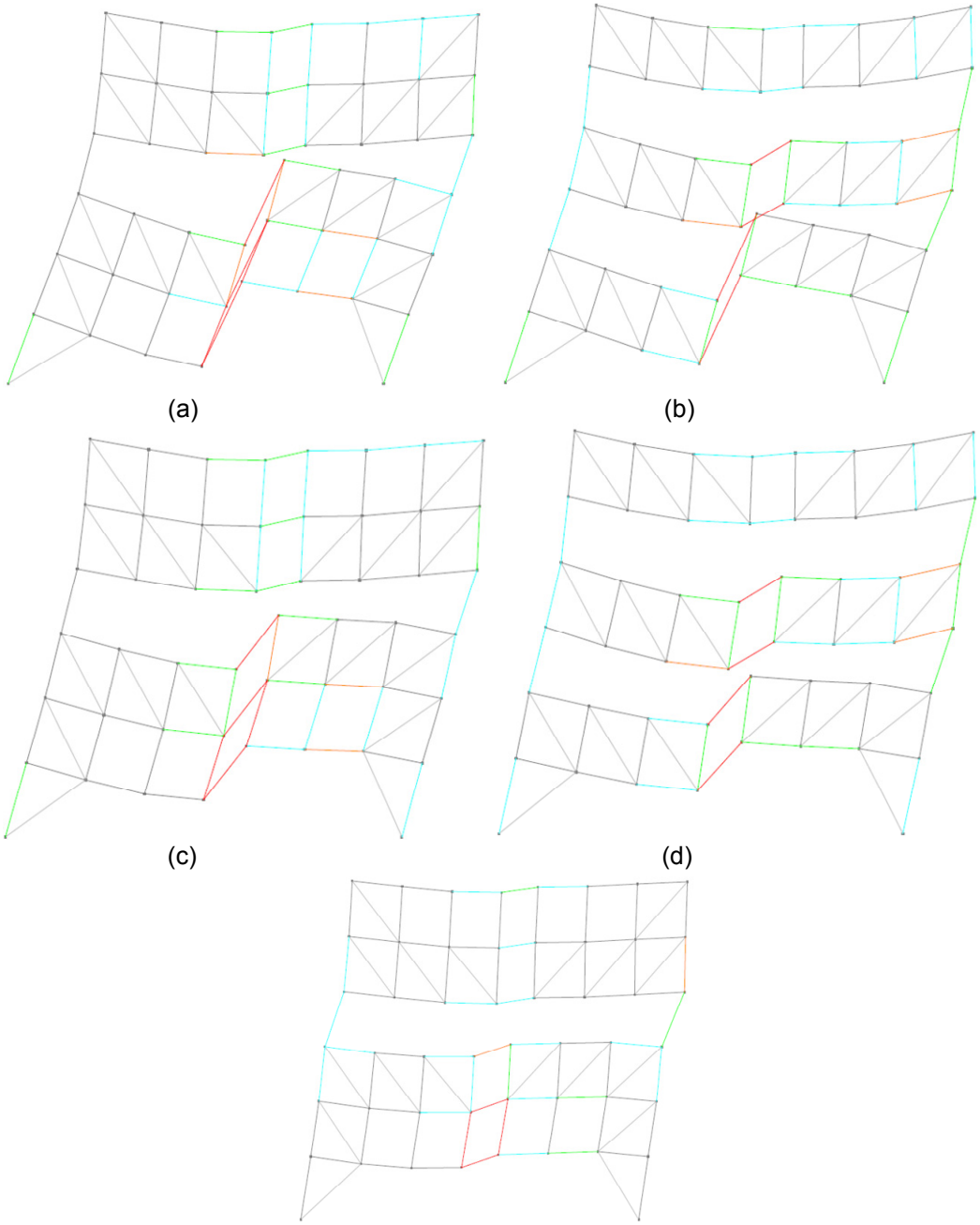

A-5 Deflected shape of the 6-Story modified STF (Kickers) model at 3% roof drift: (a) bay 2 ;(b) bay 3;(c) bay 4;(d) bay 5; (e) bay 6.

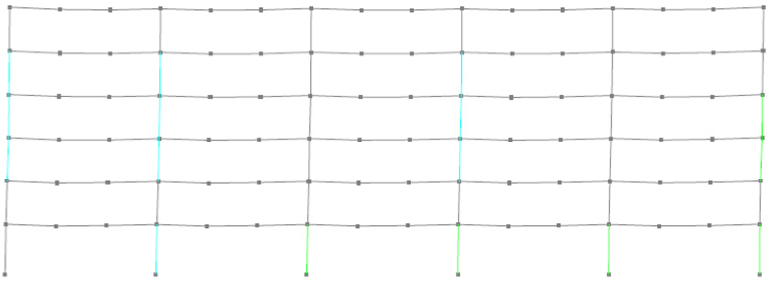

(a)

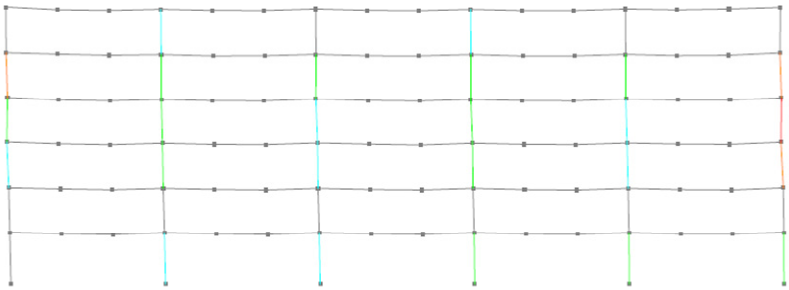

(b)

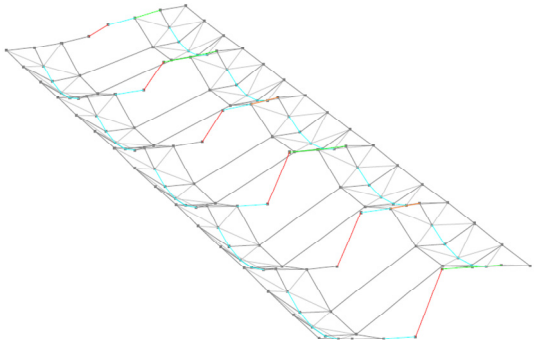

(c)

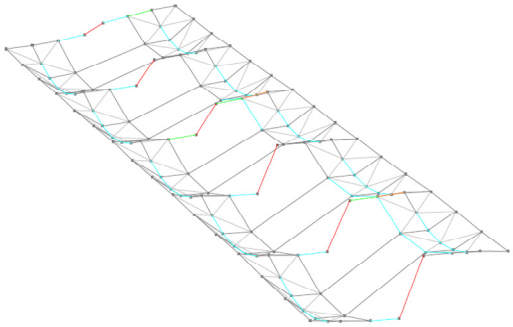

(d)

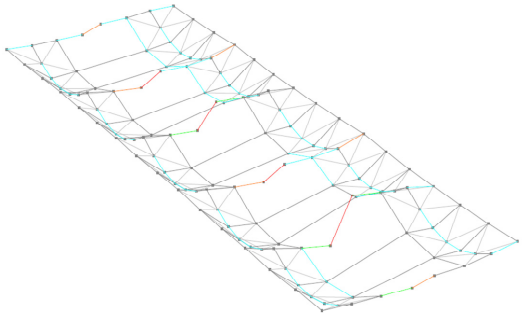

(e)

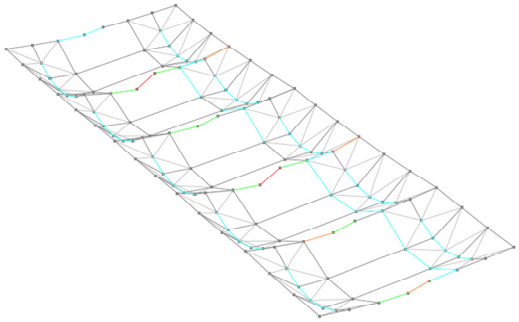

(f)

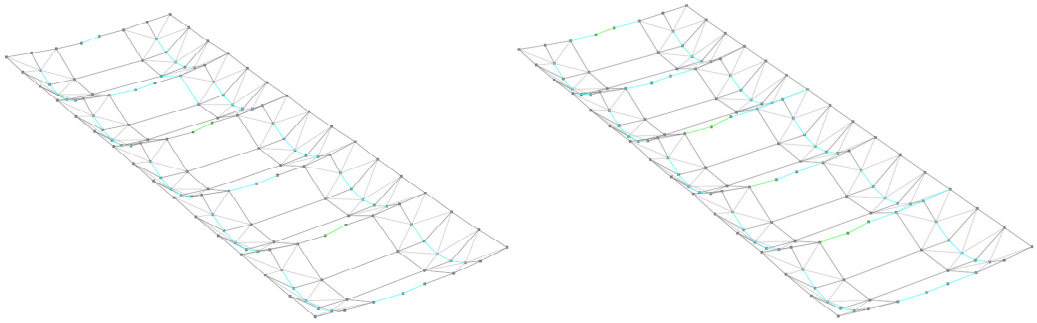

(g) (h)

A-6 Deflected shapes of the moment frames (a)MF1 (b) MF2; and the horizontal truss members on the (c) 2nd floor (d) 3rd floor (e) 4th floor (f) 5th floor (g) 6th floor (h) roof floor the 6-Story modified STF (Kickers) model.

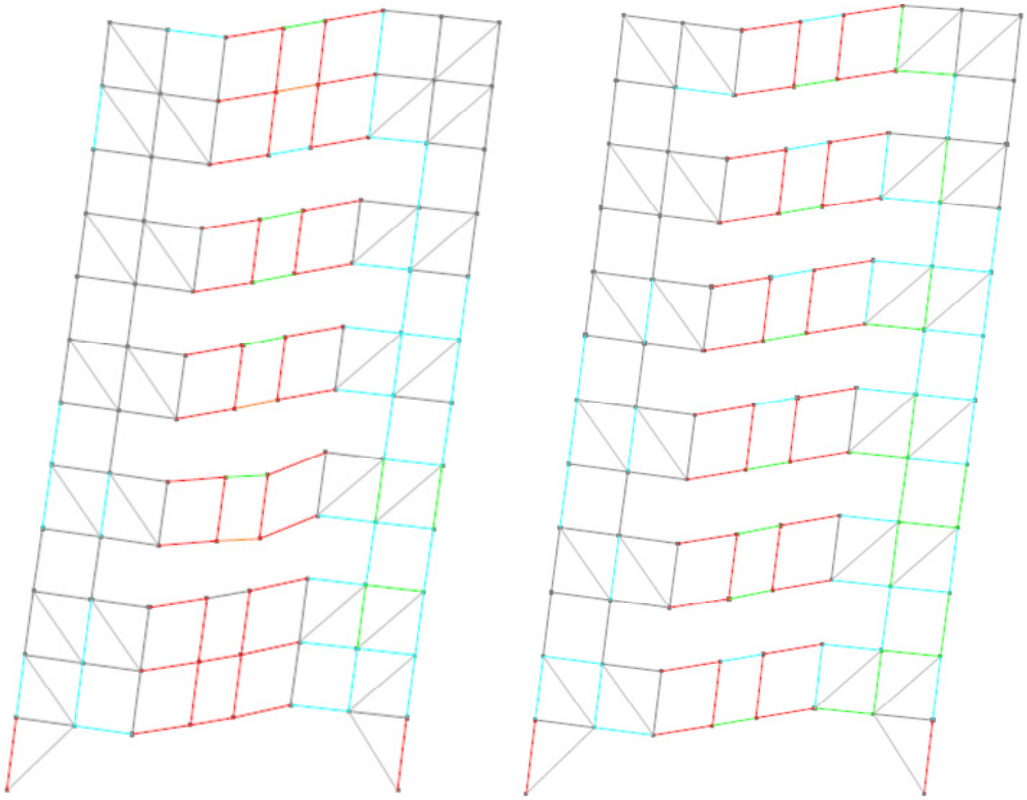

(a) (b)

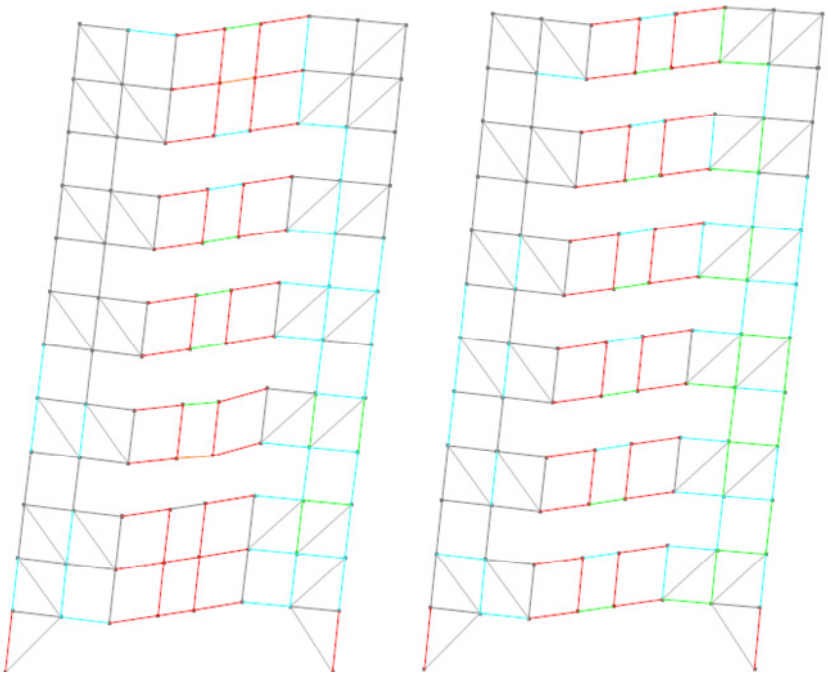

(c)

(d)

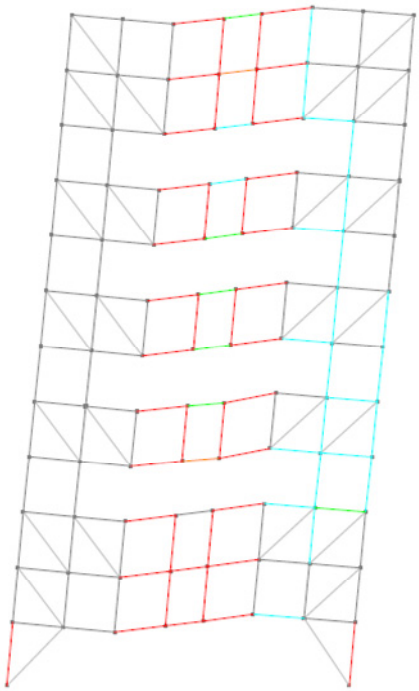

(e)

A-7 deflected shape of the 12-Story building at 3% roof drift: (a) bay 2 ;(b) bay 3;(c) bay 4;(d) bay 5; (e) bay 6.

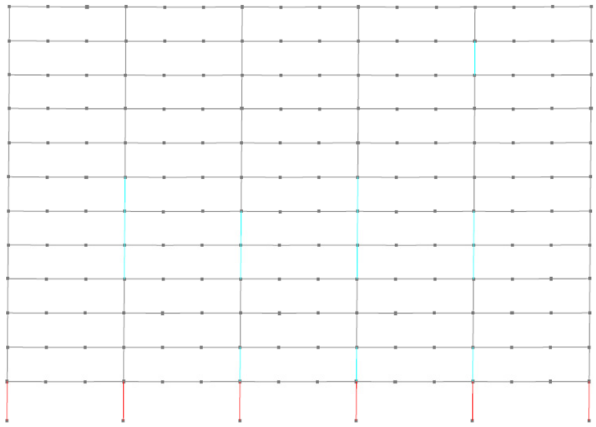

(a)

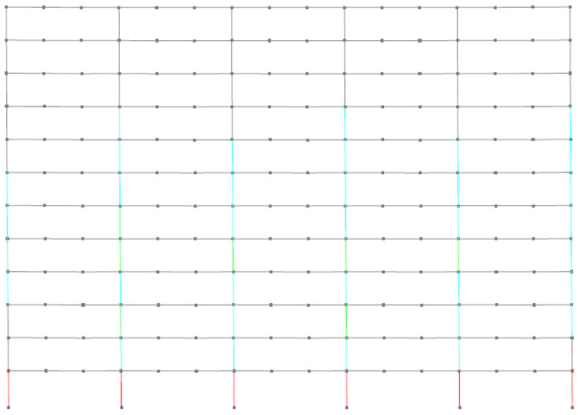

(b)

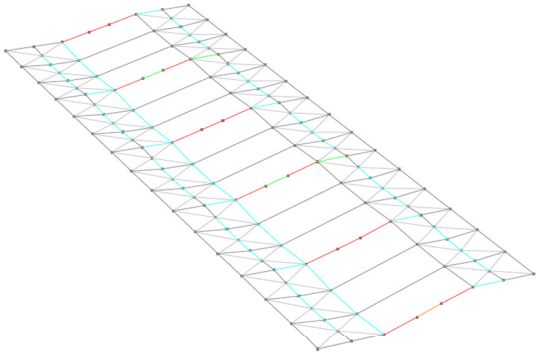

(c)

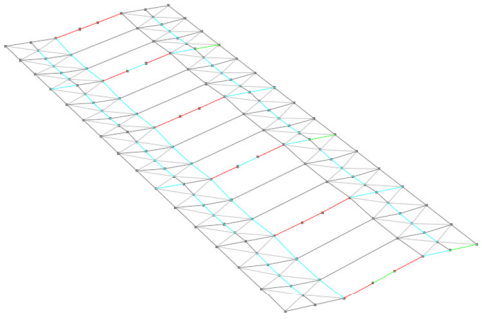

(d)

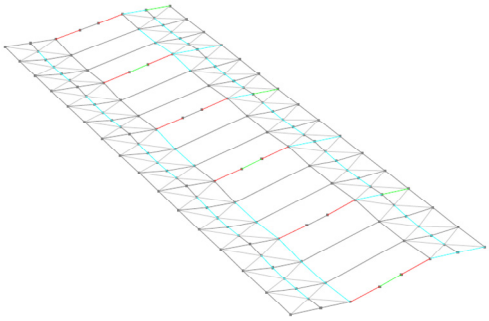

(e)

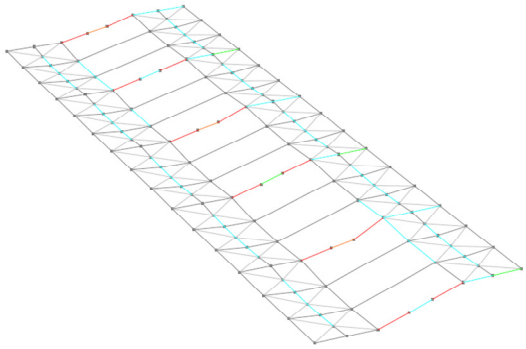

(f)

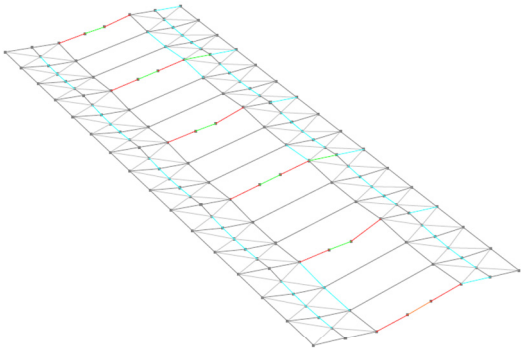

(g)

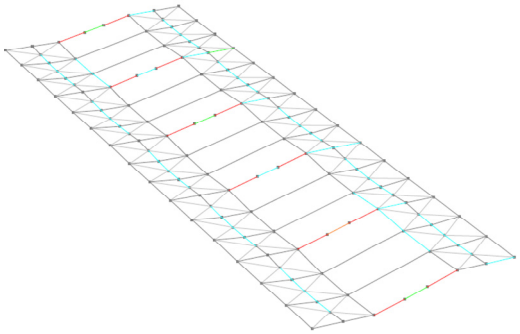

(h)

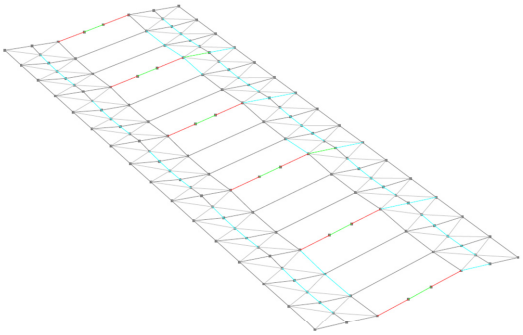

(i)

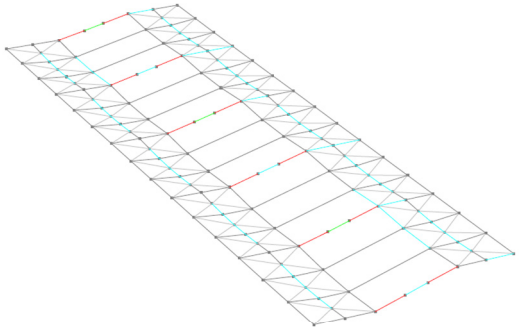

(j)

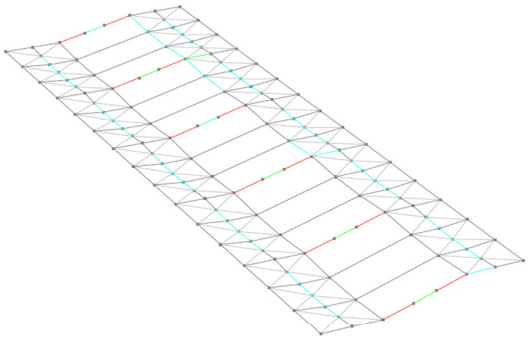

(k)

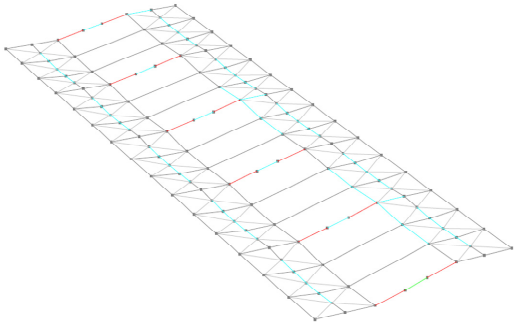

(l)

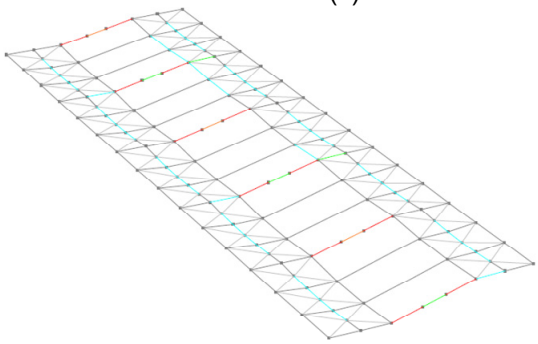

(m)

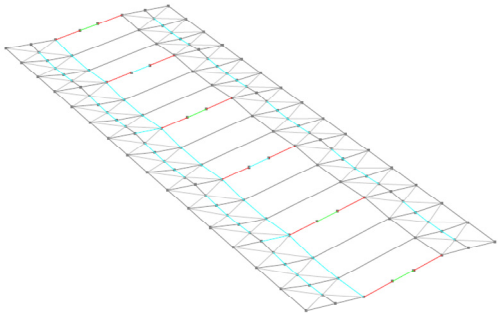

(n)

A-8 Deflected shapes of the moment frames (a) MF1 (b) MF2; and the horizontal truss members on the (c) 2nd floor (d) 3rd floor (e) 4th floor (f) 5th floor (g) 6th floor (h) 7th floor(i) 8th floor (j) 9th floor (k) 10th floor (l) 11th floor (m) 12th floor (n) Roof floor for the 6-Story STF.

A4. Deflected shapes of pushover analysis for 20-story modified STF (Vertical members).

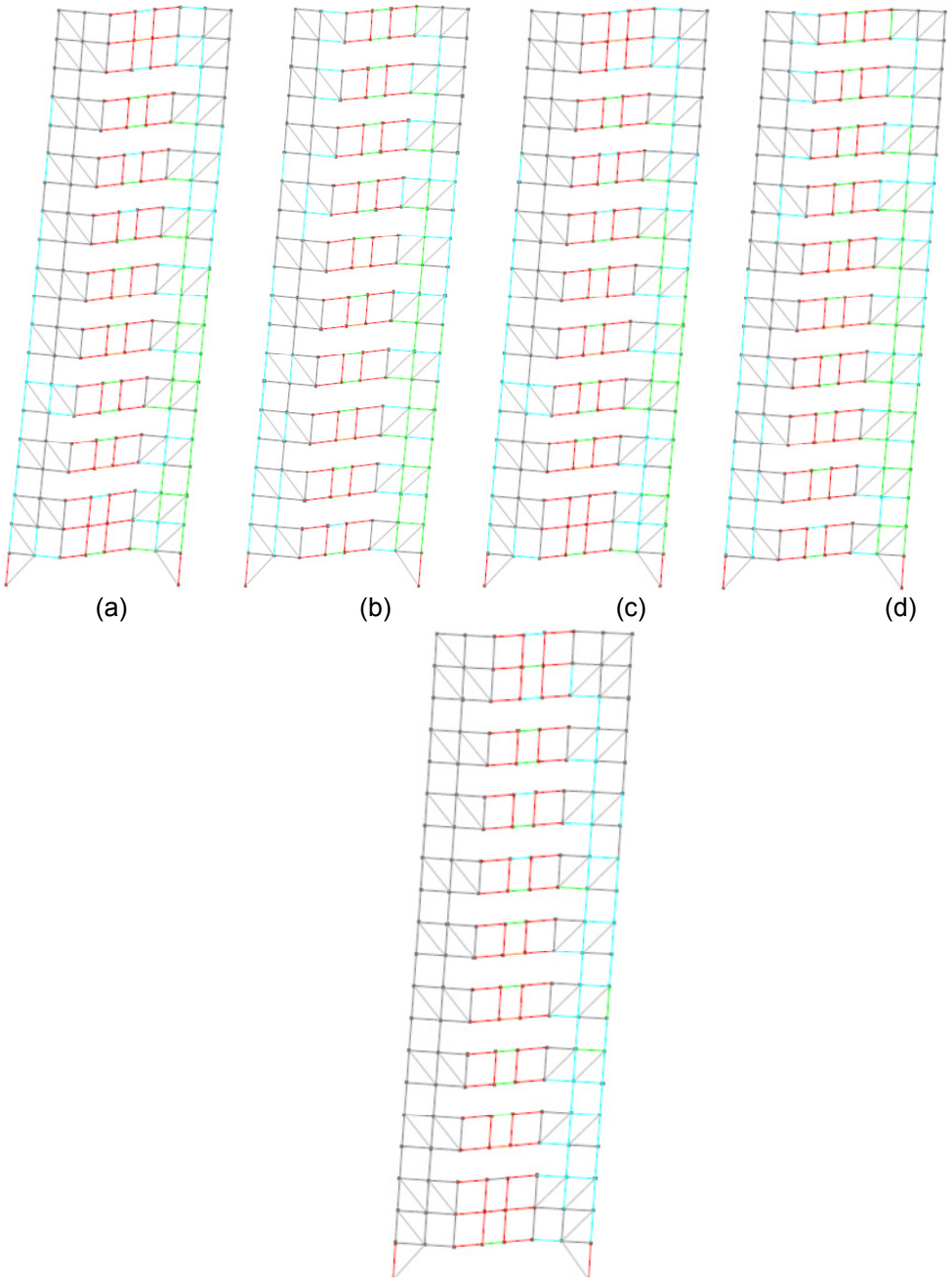

(a) (b) (c) (d)

(e)

A-9 deflected shape of the 6-Story building at 3% roof drift: (a) bay 2 ;(b) bay 3;(c) bay 4;(d) bay 5; (e) bay 6.

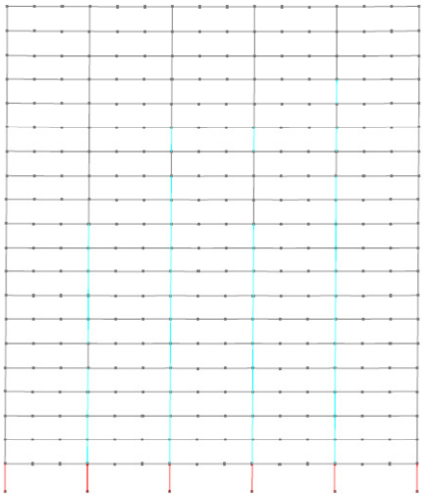

(a)

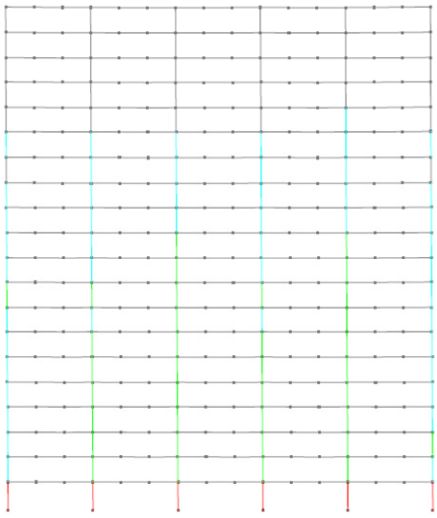

(b)

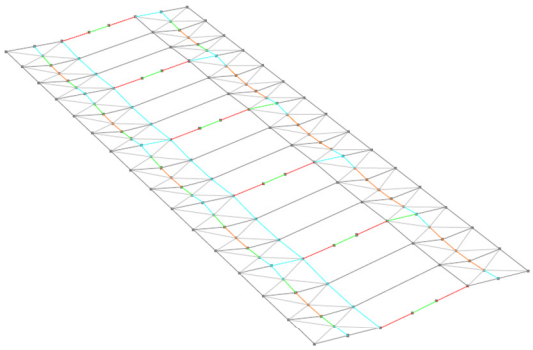

(c)

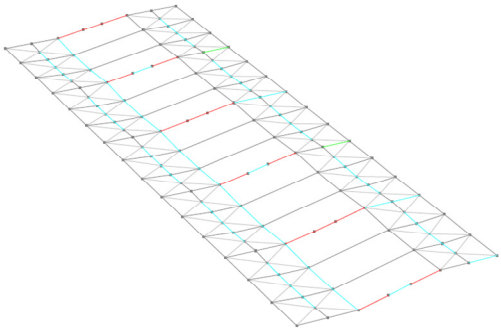

(d)

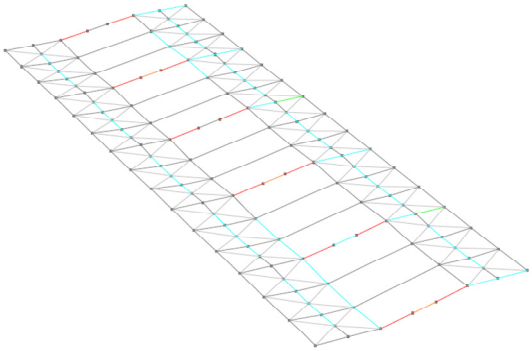

(e)

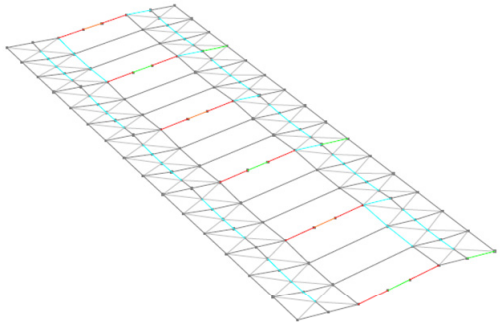

(f)

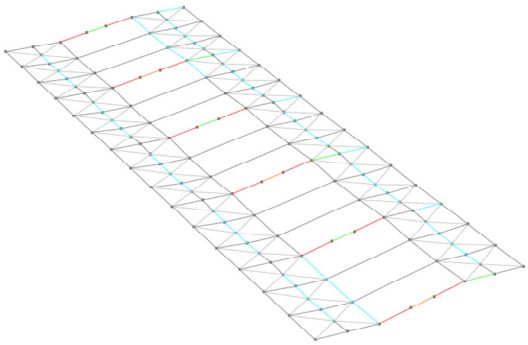

(g)

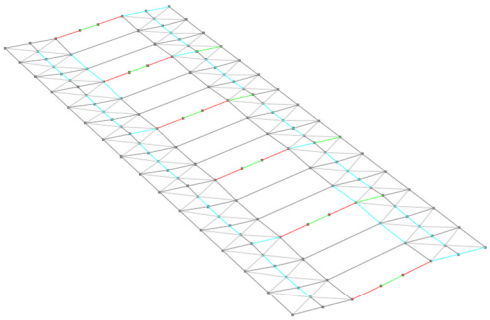

(h)

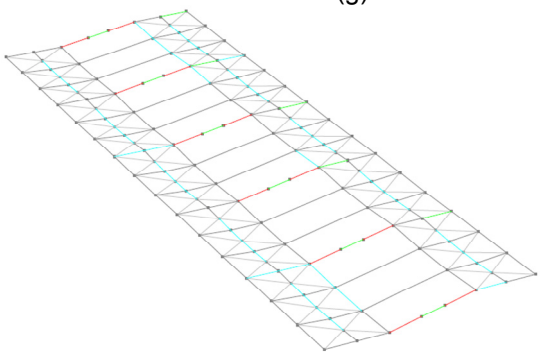

(i)

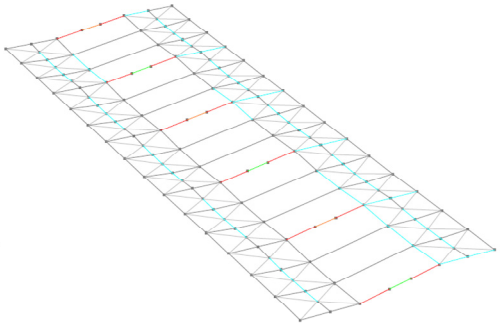

(j)

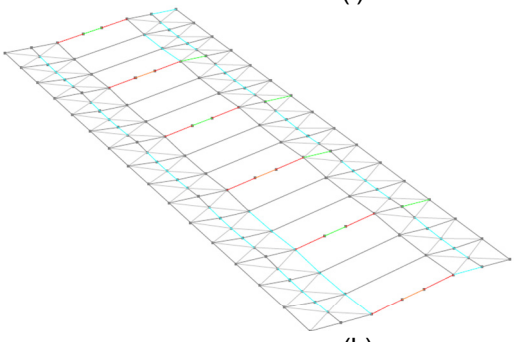

(k)

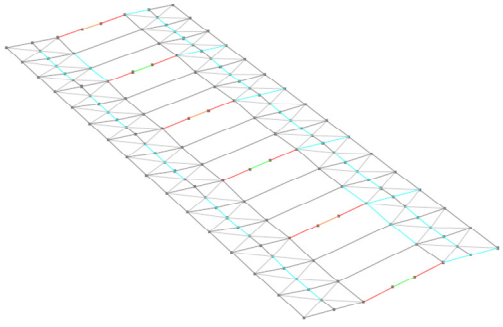

(l)

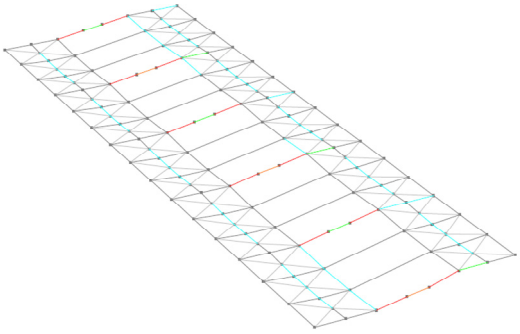

(m)

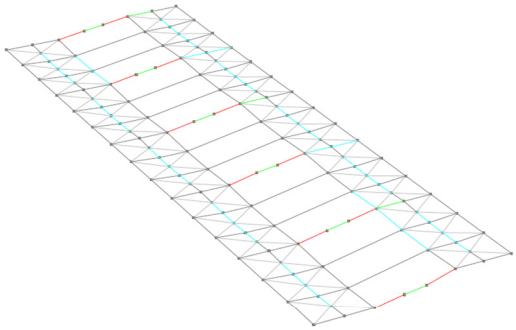

(n)

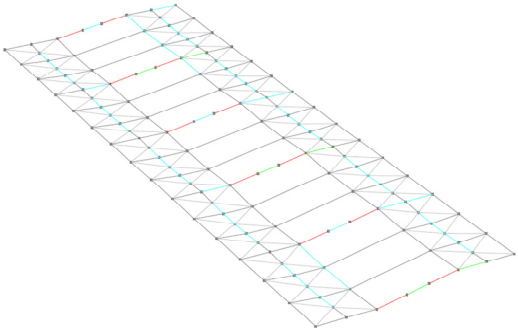

(o)

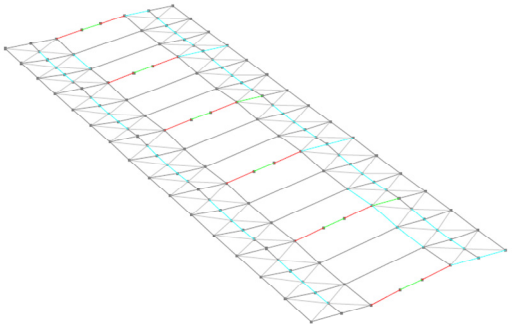

(p)

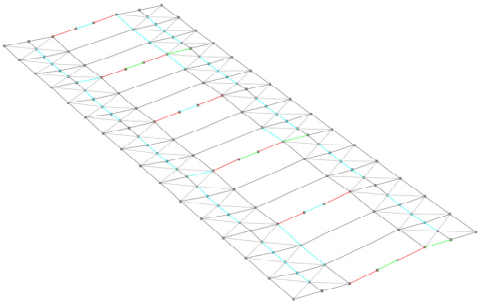

(q)

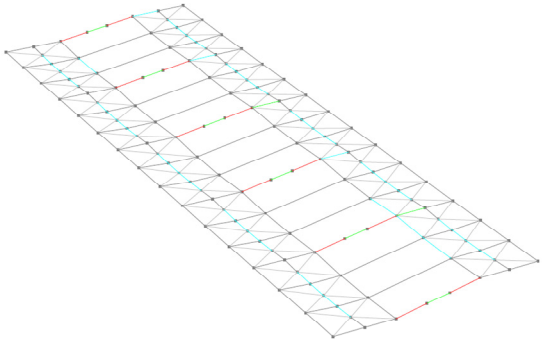

(r)

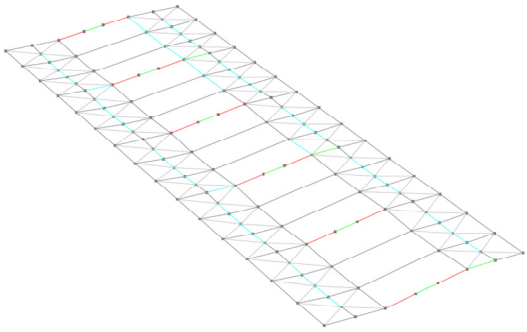

(s)

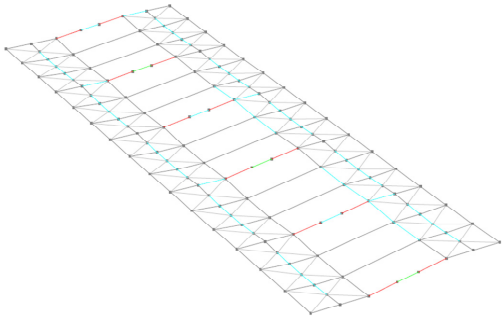

(t)

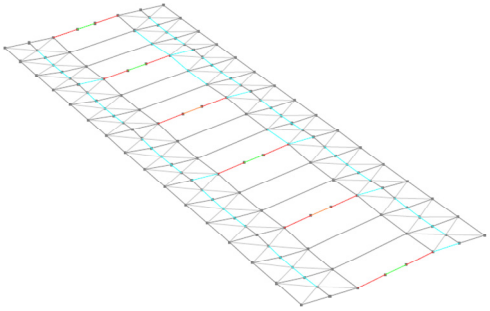

(u)

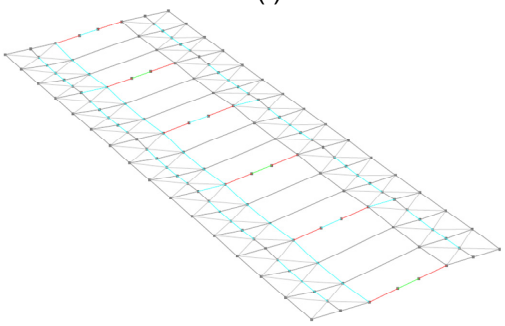

(v)

A-10 Deflected shapes of the moment frames (a) MF1 (b) MF2; and the horizontal truss members on the (c) 2nd floor (d) 3rd floor (e) 4th floor (f) 5th floor (g) 6th floor (h) 7th floor(i) 8th floor (j) 9th floor (k) 10th floor (l) 11th floor (m) 12th floor (n) 13th floor (o) 14th floor (p)15th floor (q) 16th floor (r) 17th floor (s) 18th floor (t) 19th floor (u) 20th floor (v) roof floor for the20-Story STF.

Appendix B

In Appendix B the deflected shapes under Nonlinear Time-History (NTH) analysis of the bay 2 through bay 6, the horizontal trusses of each floor, the two moment frames for the 6-story modified STF (Vertical members), 6-story modified STF (Kickers),6-story conventional STF , 12-story modified STF (Vertical members), 20-story modified STF (Vertical members) are shown in the following figures.

For all figures, the member colors indicate the minimum usage ratio (demand versus capacity of the member) as followed:

Color	Usage Ratio
Grey	0.0
Teal	0.4
Green	0.6
Orange	0.8
Red	1.0

B1. Deflected shapes of 6-story modified STF (Vertical members) under MCE-2.

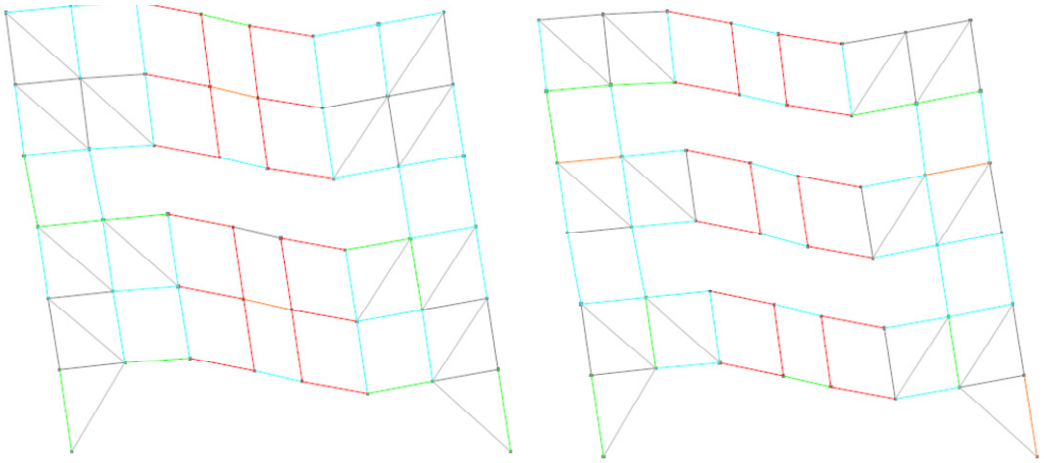

(b) (b)

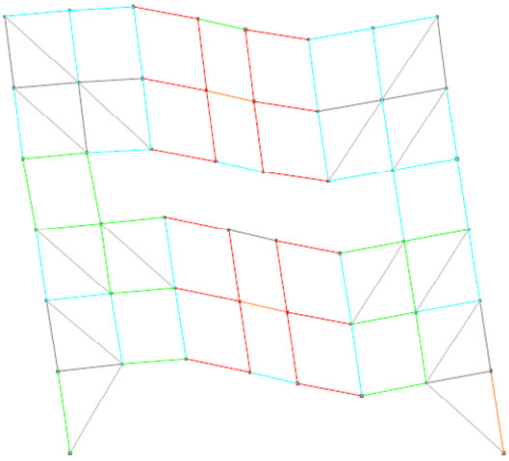

(c)

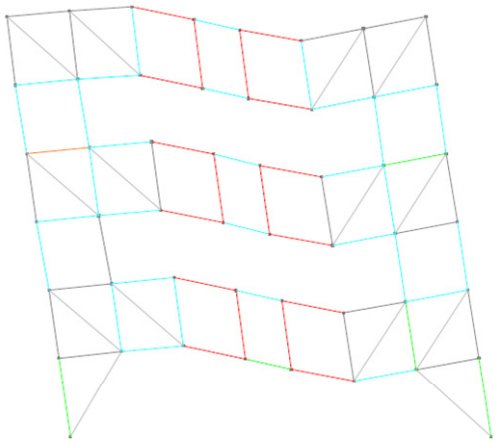

(d)

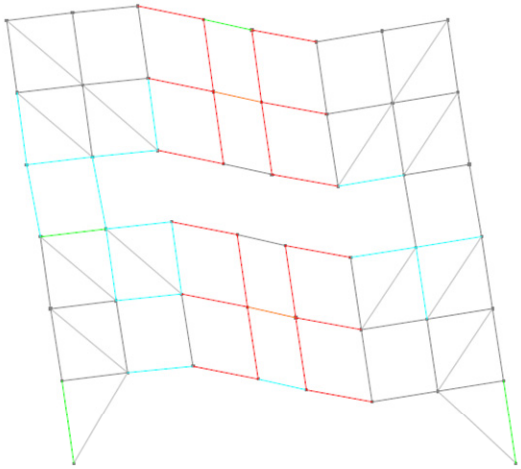

(e)

B- 1 Deflected shape of the 6-Story modified STF (Vertical members) model at 3% roof drift: (a) bay 2 ;(b) bay 3;(c) bay 4;(d) bay 5; (e) bay 6.

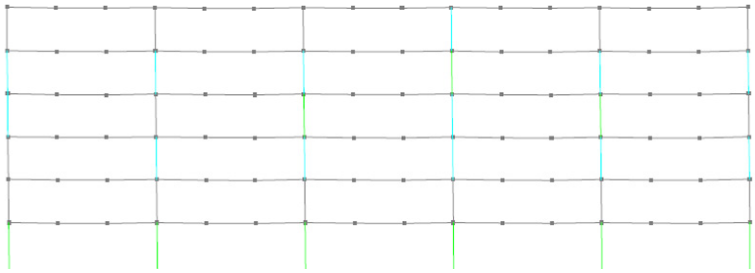

(b)

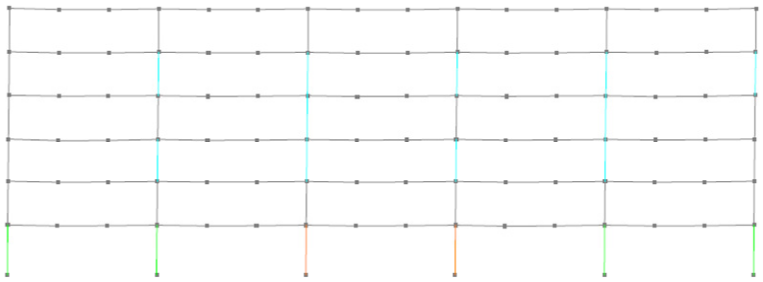

.(b)

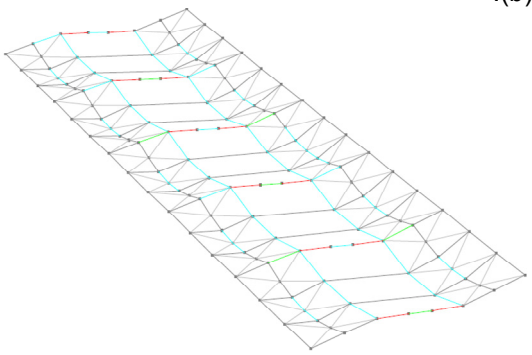

(c)

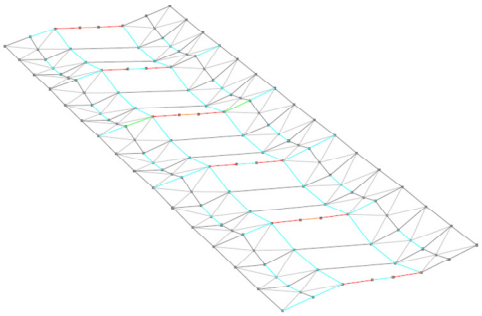

(d)

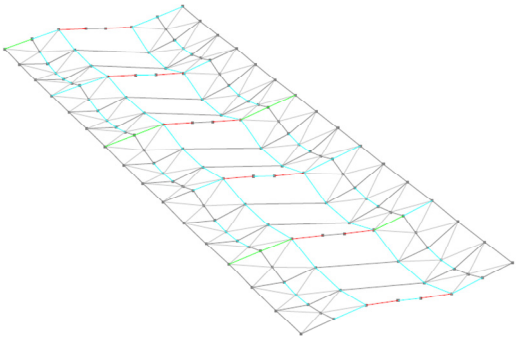

(e)

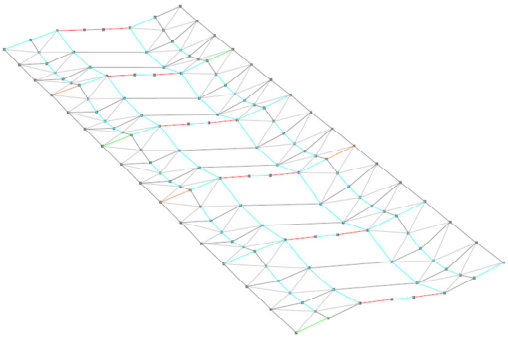

(f)

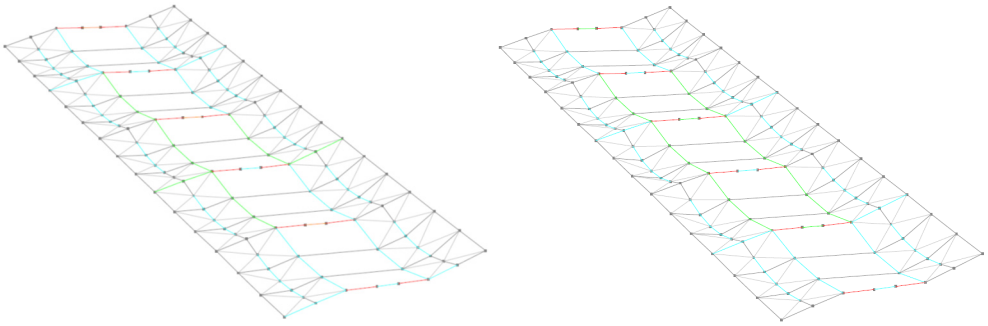

(g) (h)

B-2 Deflected shapes of the moment frames (a)MF1 (b) MF2; and the horizontal truss members on the (c) 2nd floor (d) 3rd floor (e) 4th floor (f) 5th floor (g) 6th floor (h) roof floor for the 6-Story modified STF (Vertical members) model.

B2. Deflected shapes of pushover analysis for 6-story modified STF (Kickers).

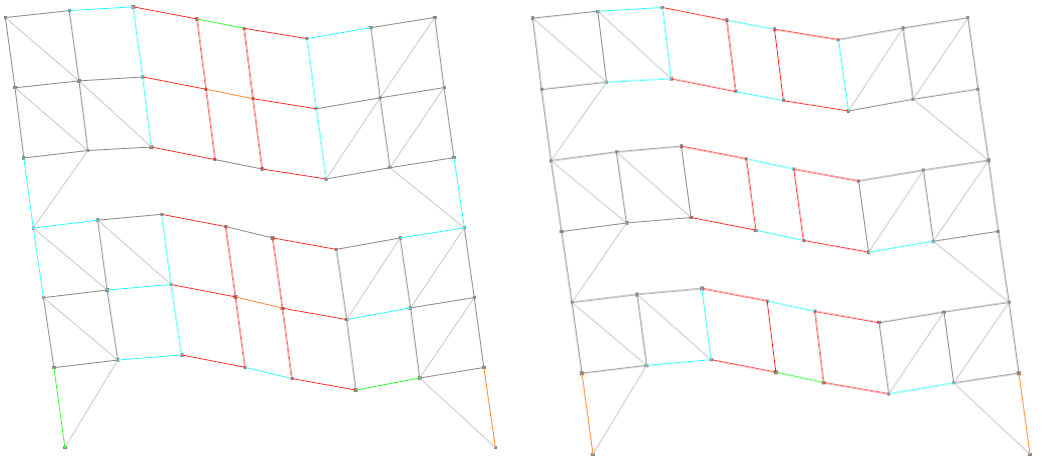

(a) (b)

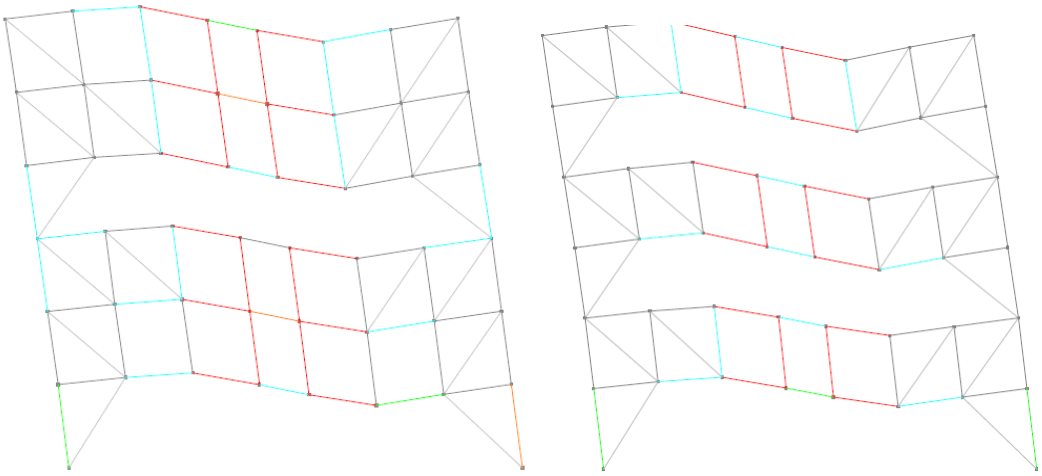

(c) (d)

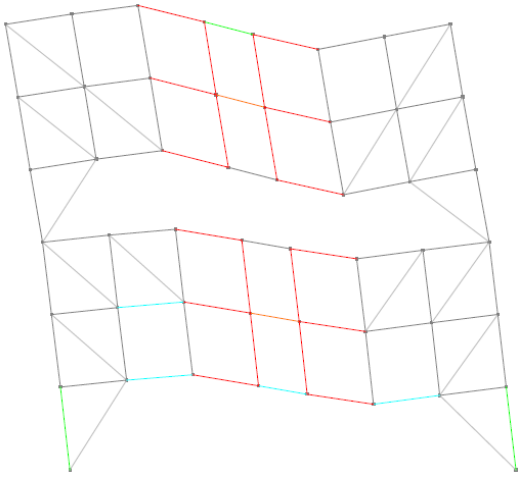

(e)

B-3 Deflected shape of the 6-Story modified STF (Kickers) model at 3% roof drift: (a) bay 2 ;(b) bay 3;(c) bay 4;(d) bay 5; (e) bay 6.

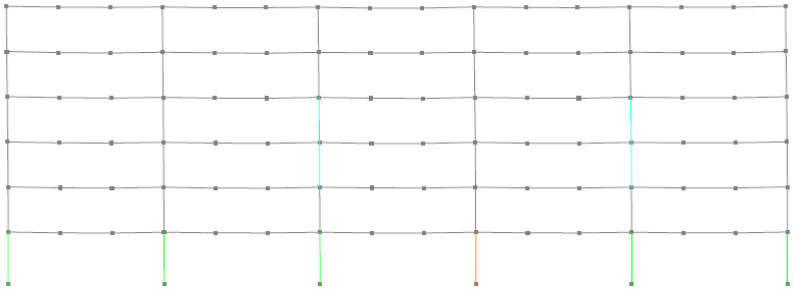

(a)

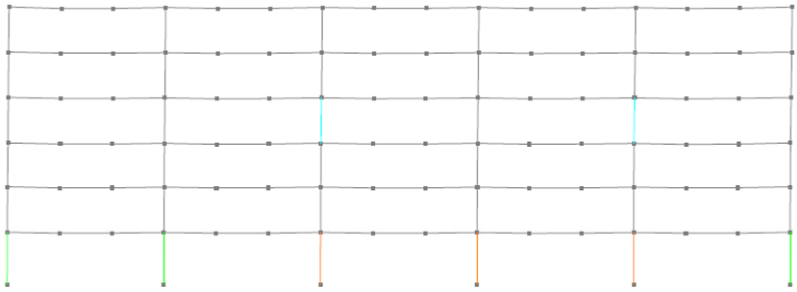

(b)

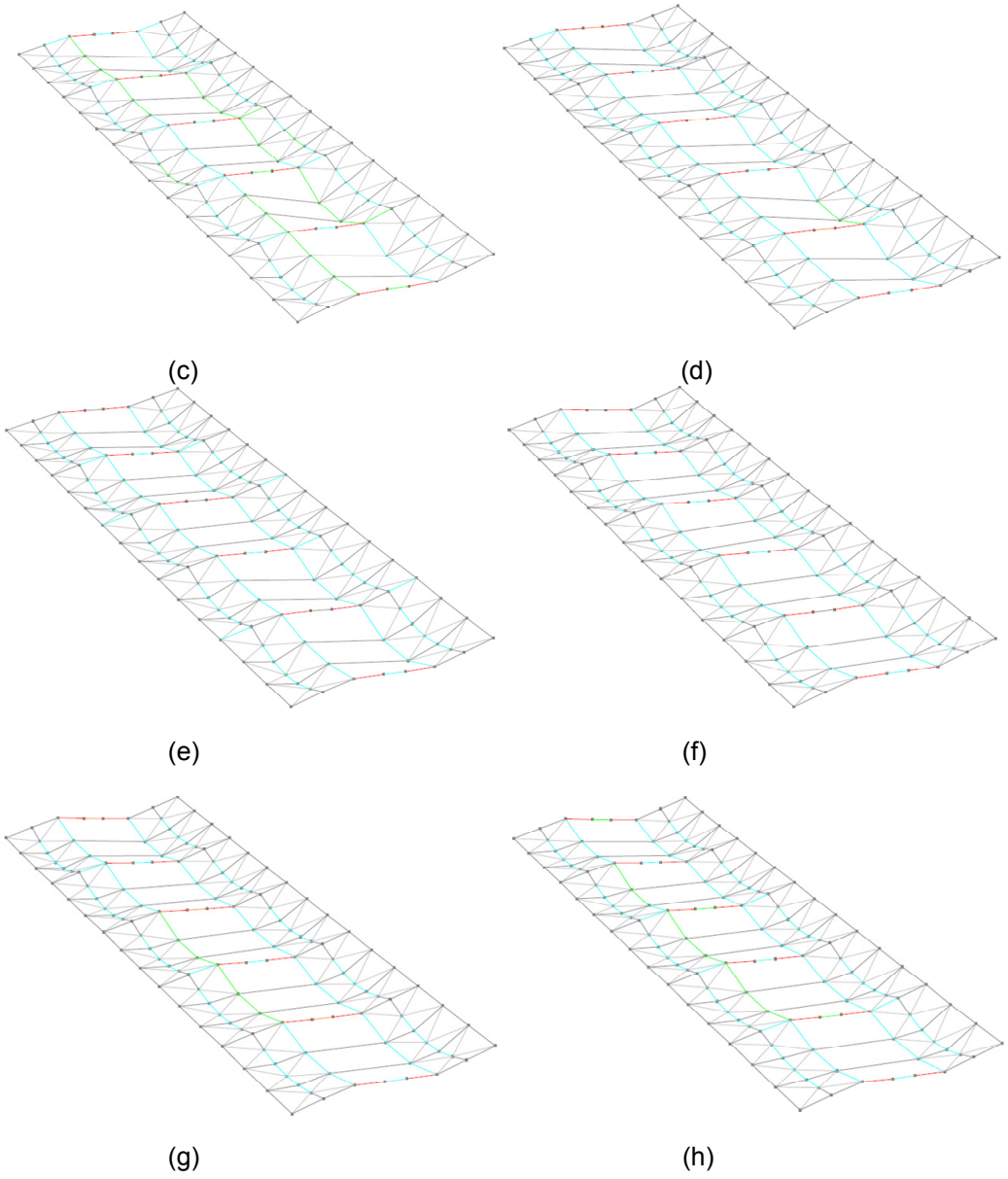

(c) (d)

(e) (f)

(g) (h)

B-4 Deflected shapes of the moment frames (a)MF1 (b) MF2; and the horizontal truss members on the (c) 2nd floor (d) 3rd floor (e) 4th floor (f) 5th floor (g) 6th floor (h) roof floor the 6-Story modified STF (Kickers) model.

B3. Deflected shapes of pushover analysis for 6-story conventional STF

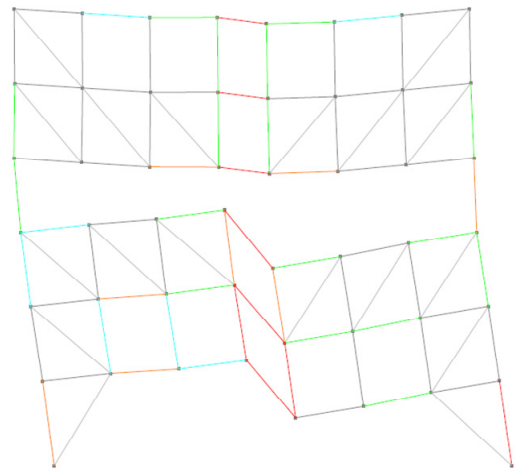

(b)

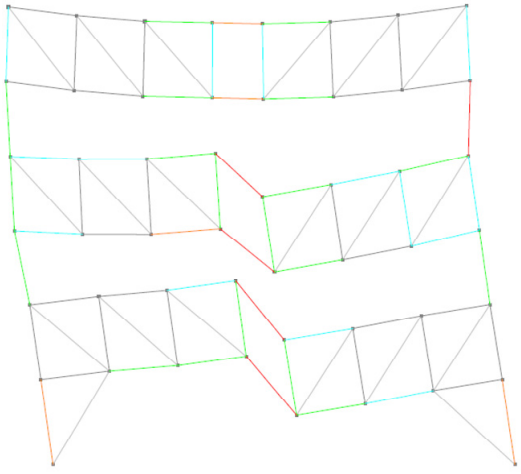

(b)

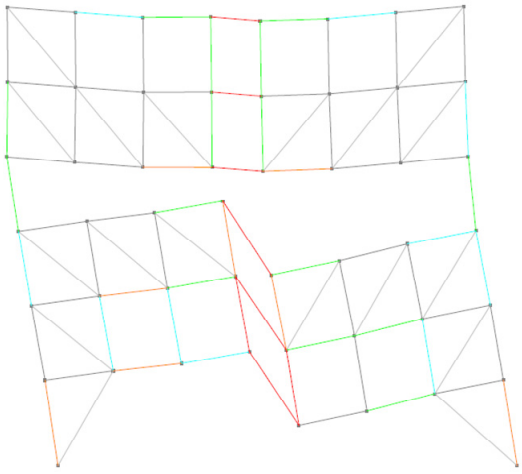

(c)

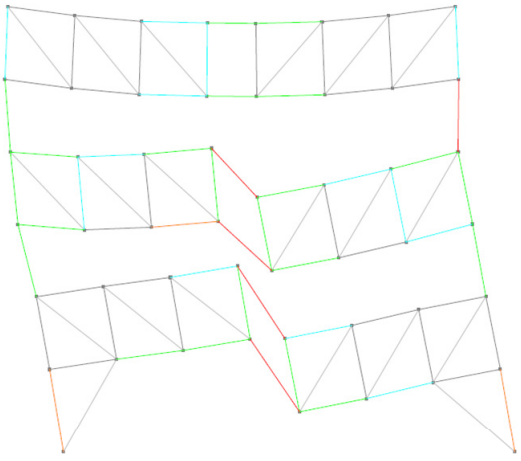

(d)

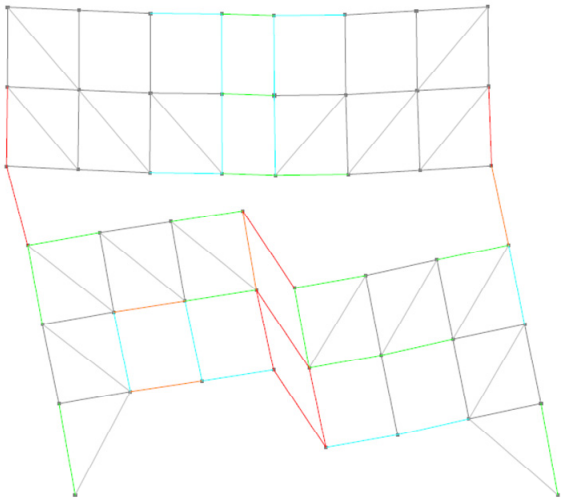

(e)

B-5 Deflected shape of the 6-Story modified STF (Kickers) model at 3% roof drift: (a) bay 2 ;(b) bay 3;(c) bay 4;(d) bay 5; (e) bay 6.

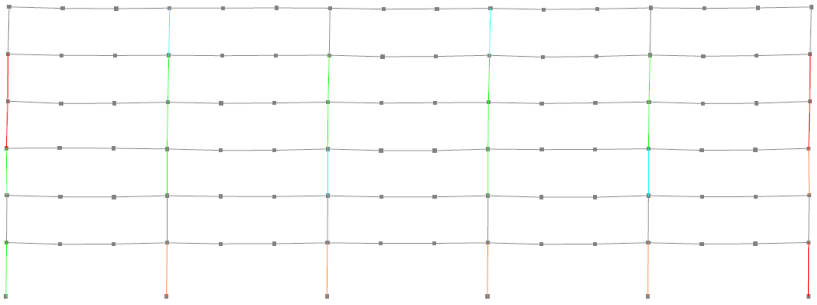

(a)

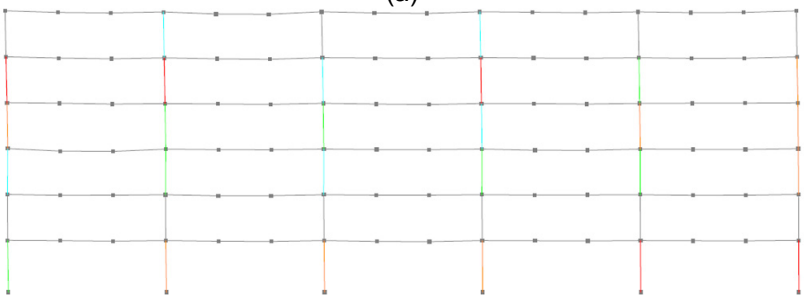

(b)

(c)

(d)

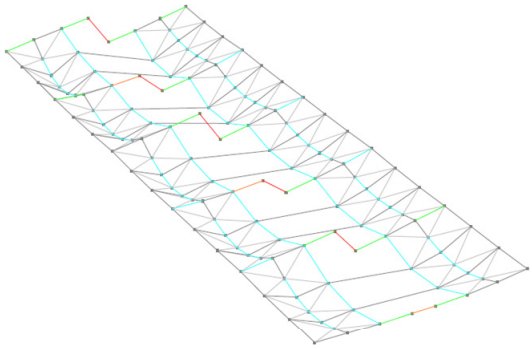

(e)

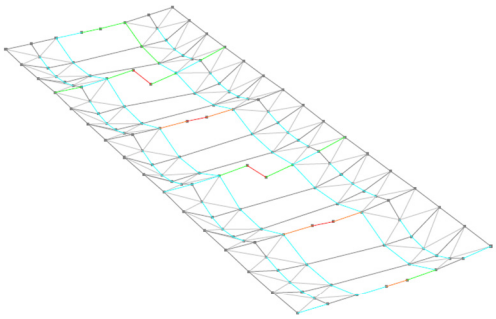

(f)

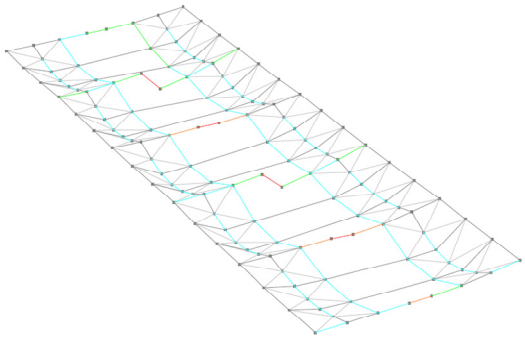

(g)

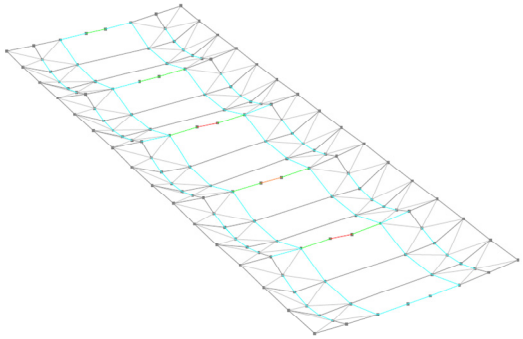

(h)

B-6 Deflected shapes of the moment frames (a)MF1 (b) MF2; and the horizontal truss members on the (c) 2nd floor (d) 3rd floor (e) 4th floor (f) 5th floor (g) 6th floor (h) roof floor the 6-Story modified STF (Kickers) model.

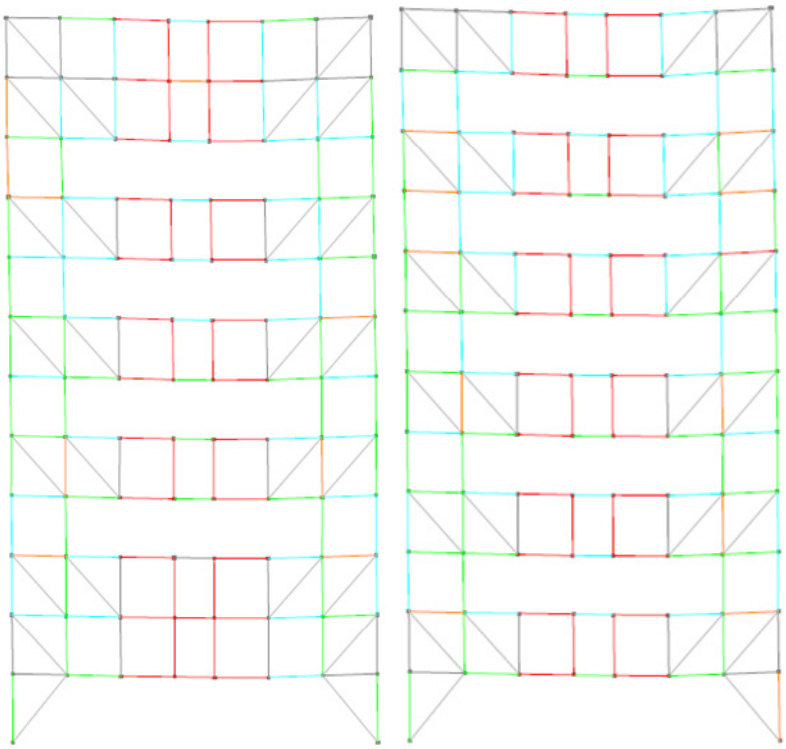

(a) (b)

(c) (d)

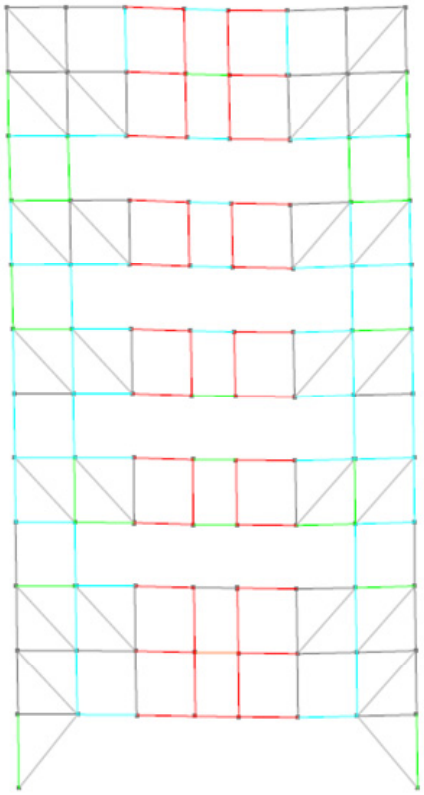

(e)

B-7 deflected shape of the 12-Story building at 3% roof drift: (a) bay 2 ;(b) bay 3;(c) bay 4;(d) bay 5; (e) bay 6.

(a)

(b)

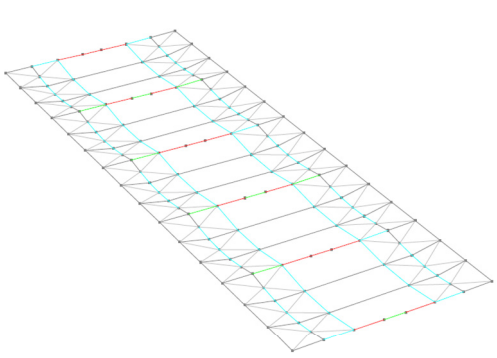

(c)

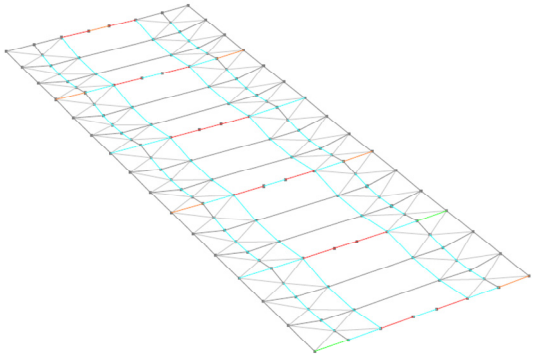

(d)

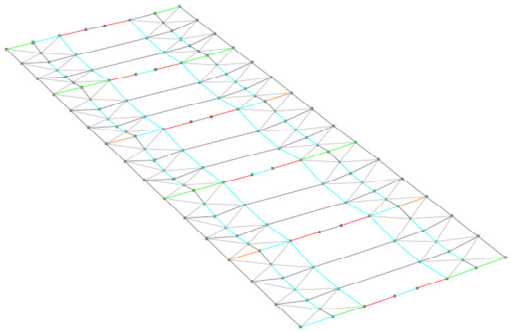

(e)

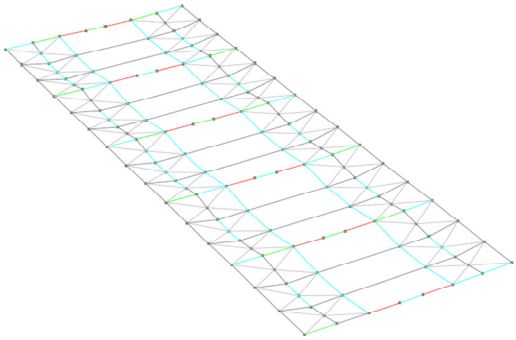

(f)

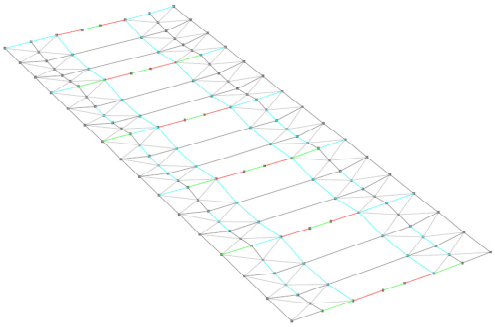

(g)

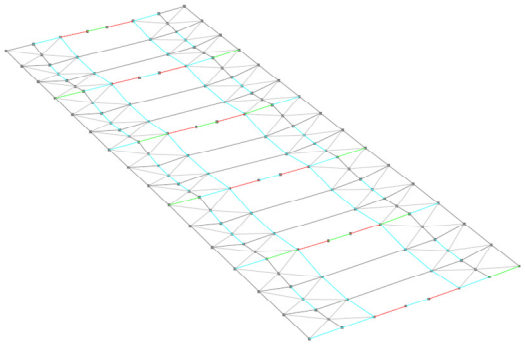

(h)

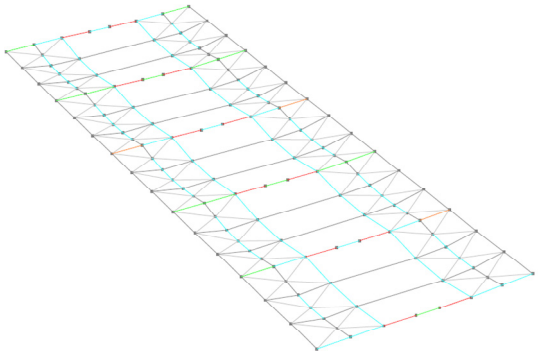

(i)

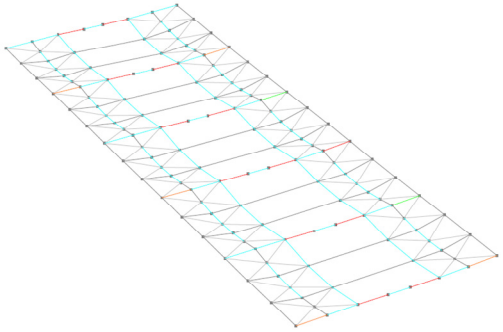

(j)

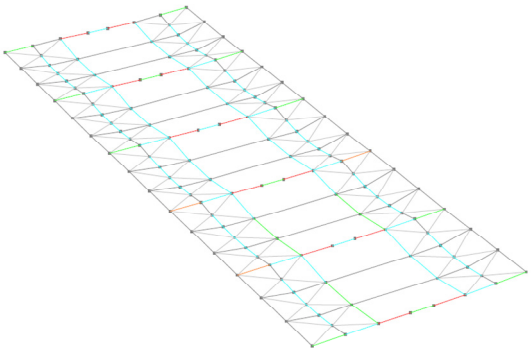

(k)

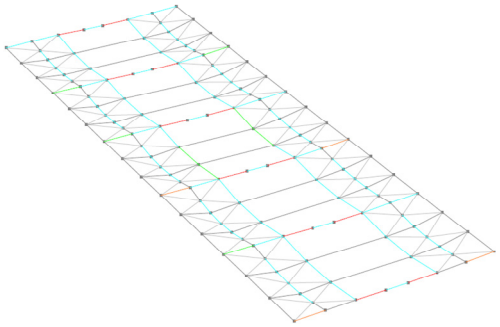

(l)

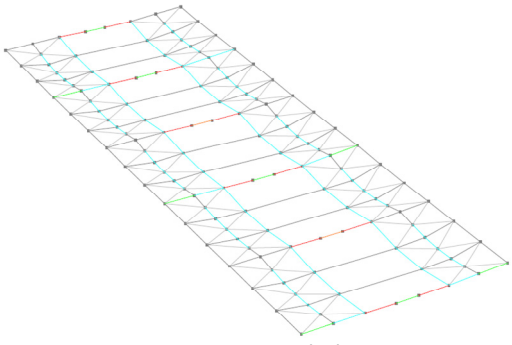

(m)

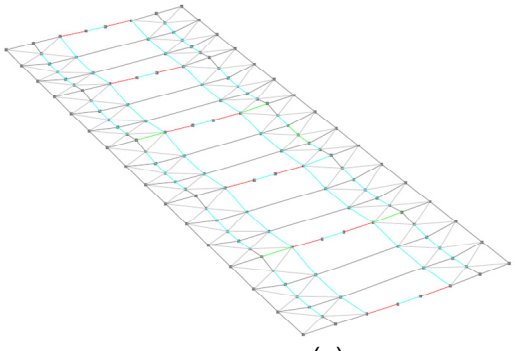

(n)

B-8 Deflected shapes of the moment frames (a) MF1 (b) MF2; and the horizontal truss members on the (c) 2nd floor (d) 3rd floor (e) 4th floor (f) 5th floor (g) 6th floor (h) 7th floor(i) 8th floor (j) 9th floor (k) 10th floor (l) 11th floor (m) 12th floor (n) Roof floor for the 6-Story STF.

B4. Deflected shapes of pushover analysis for 20-story modified STF (Vertical members).

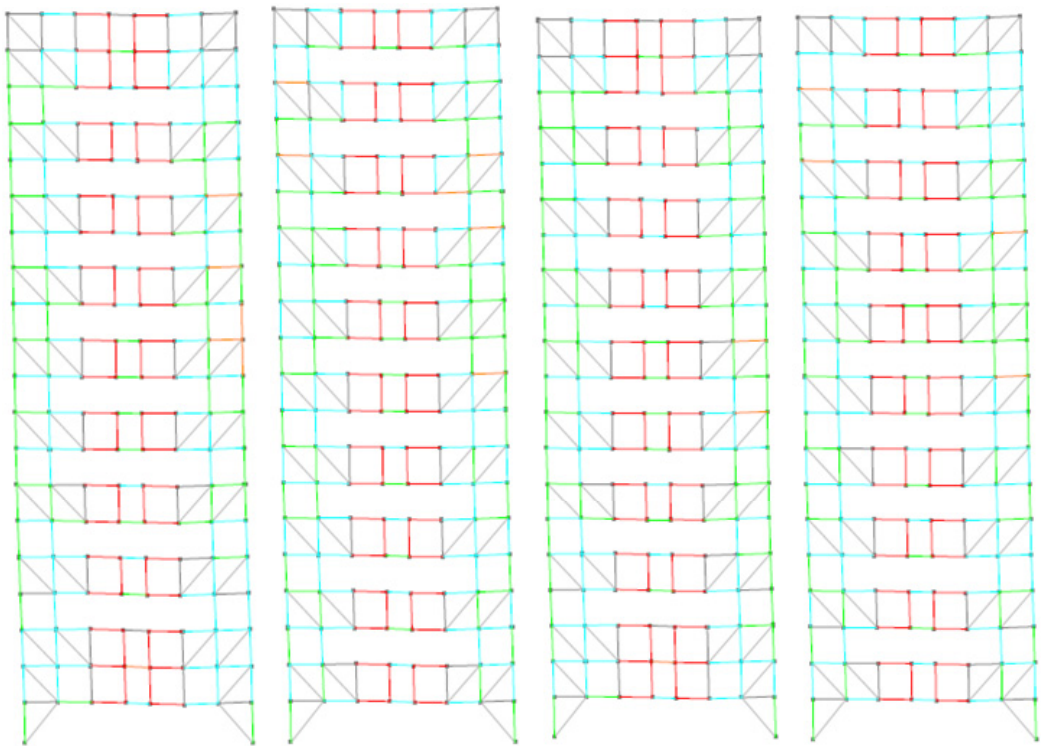

(b) (b) (c) (d)

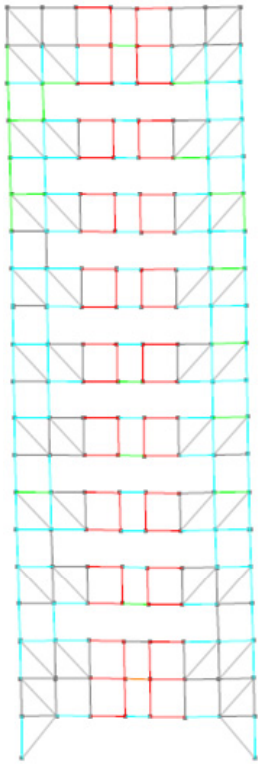

(e)

B-9 deflected shape of the 6-Story building at 3% roof drift: (a) bay 2 ;(b) bay 3;(c) bay 4;(d) bay 5; (e) bay 6.

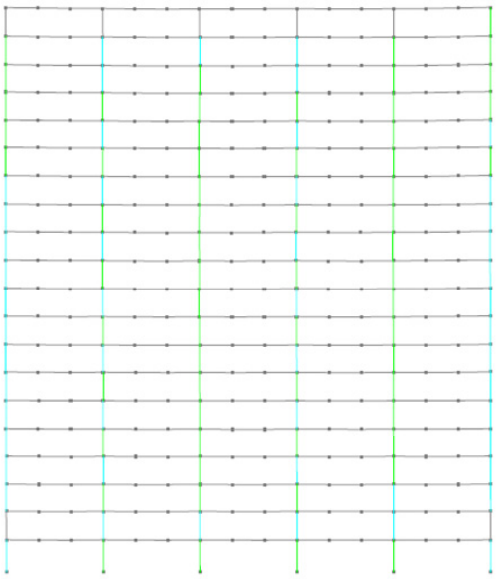

(b)

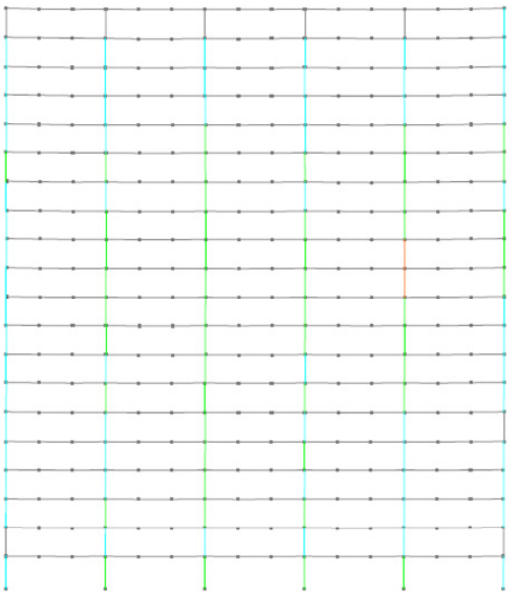

(b)

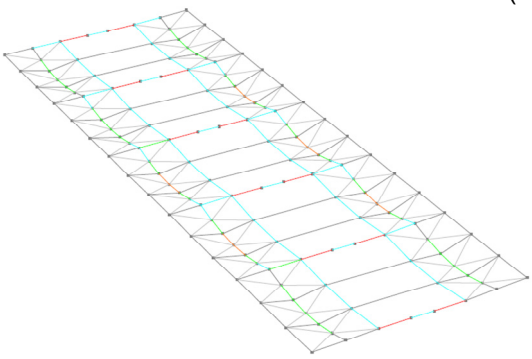

(c)

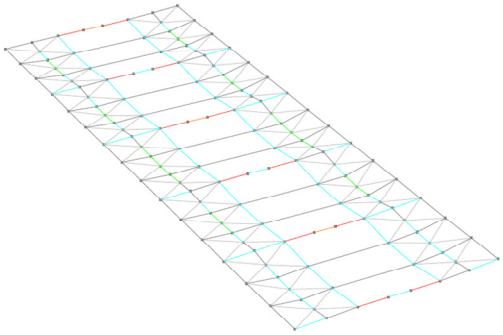

(d)

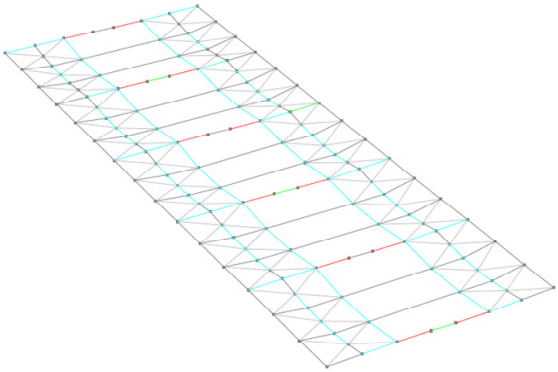

(e)

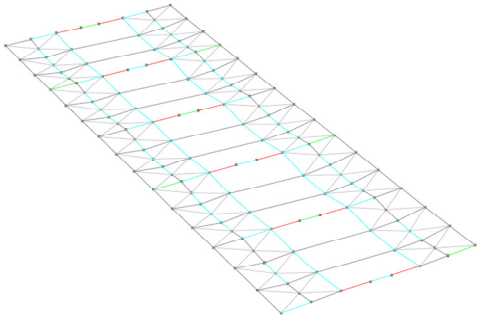

(f)

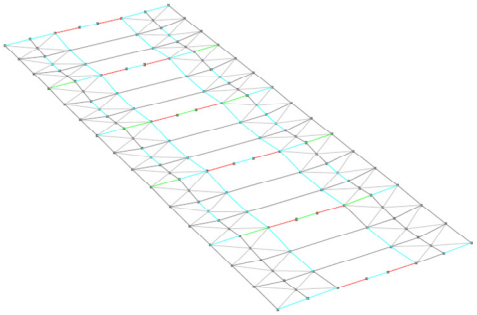

(g)

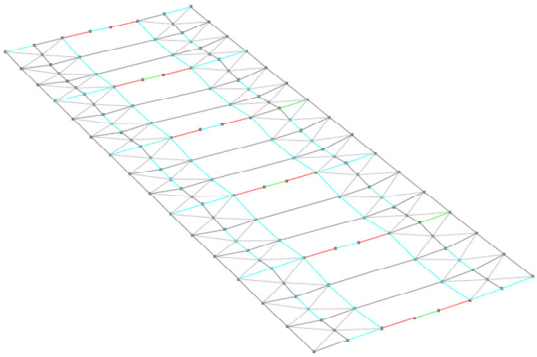

(h)

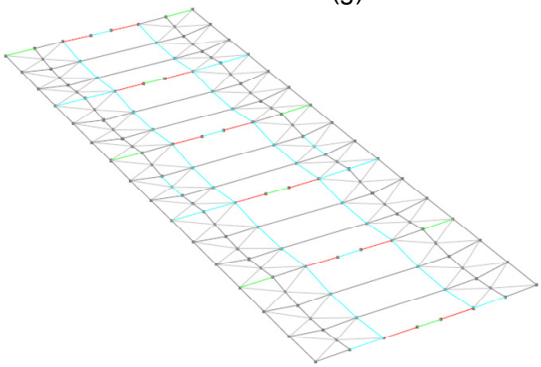

(i)

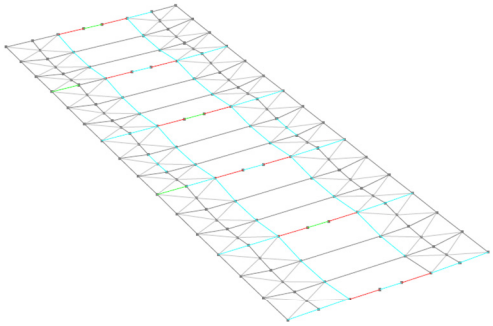

(j)

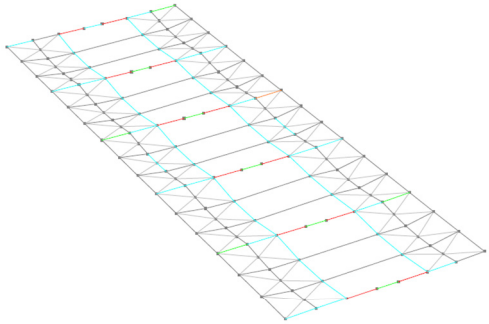

(k)

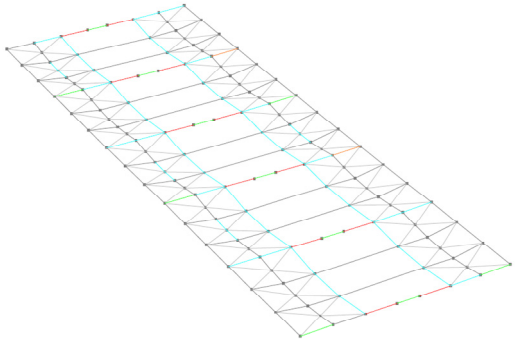

(l)

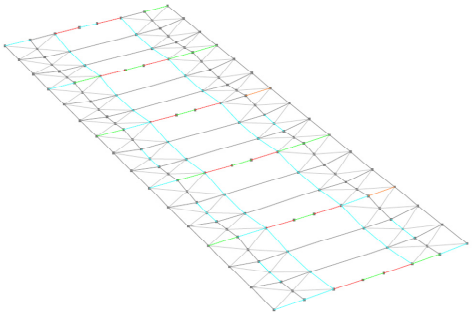

(m)

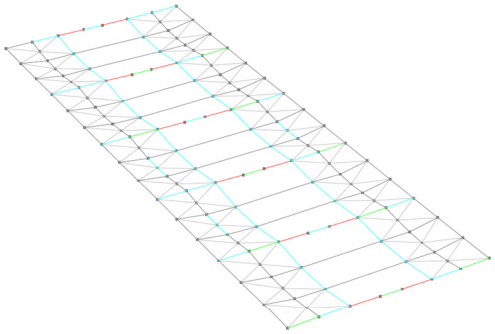

(n)

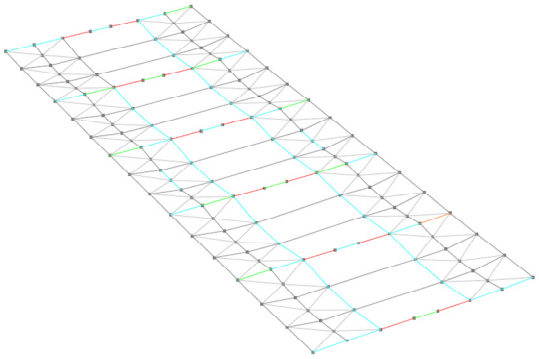

(o)

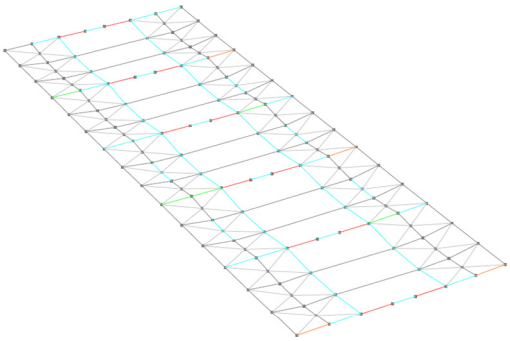

(p)

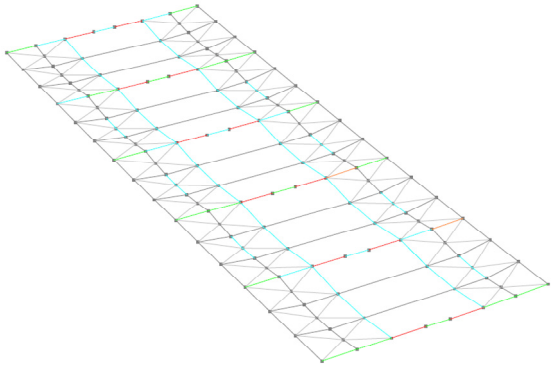

(q)

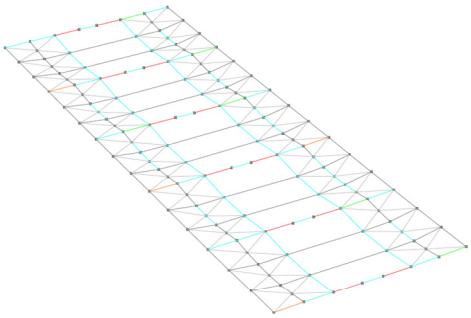

(r)

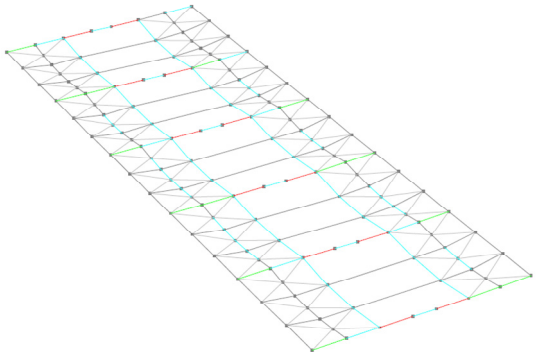

(s)

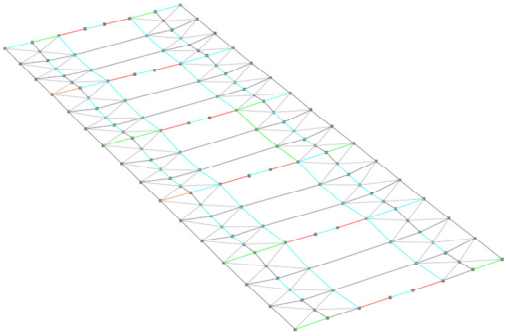

(t)

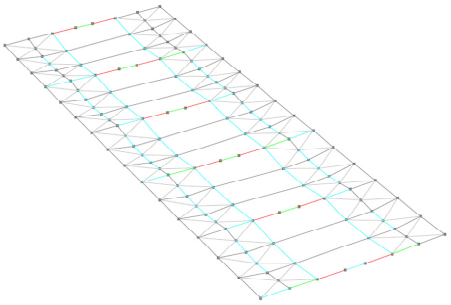

(u)

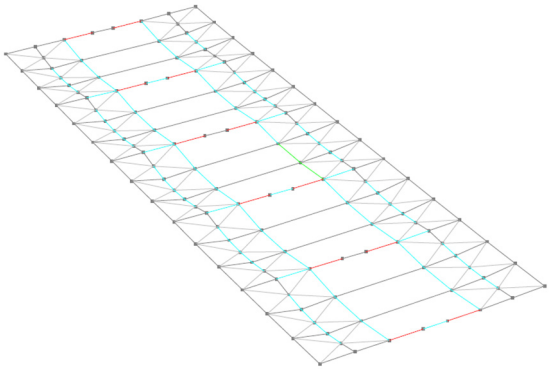

(v)

B-10 Deflected shapes of the moment frames (a) MF1 (b) MF2; and the horizontal truss members on the (c) 2nd floor (d) 3rd floor (e) 4th floor (f) 5th floor (g) 6th floor (h) 7th floor(i) 8th floor (j) 9th floor (k) 10th floor (l) 11th floor (m) 12th floor (n) 13th floor (o) 14th floor (p)15th floor (q) 16th floor (r) 17th floor (s) 18th floor (t) 19th floor (u) 20th floor (v) roof floor for the20-Story STF.

References

1. American Institute of Steel Construction (AISC) (2016a), “Specification for Structural Steel Buildings”, ANSI/AISC 360-10, Chicago, IL.
2. American Institute of Steel Construction (AISC). (2016b), “Seismic provisions for structural steel buildings.” ANSI/AISC 341-16, Chicago, IL.
3. American Institute of Steel Construction (AISC). (2016c), “Seismic Design Manual”, third edition.
4. American Society of Civil Engineers (ASCE). (2016), Minimum Design Loads for Buildings and Other Structures, ASCE/SEI 7-16, Reston, VA.
5. Basha, H.S., and Goel, S.C. (1994), “Seismic resistance truss moment frames with ductile Vierendeel segment,” Report No. UMCEE 94-29, Department of Civil and Environmental Engineering, University of Michigan, Ann Arbor, MI.
6. Brazil, A. (2000), “Staggered Truss System Proves Economical for Hotels.” Modern Steel Construction. AISC 40 (9), September 2000, pp. 32-38.
7. Bursi, O. S., and Gramola, G. (1999). “Behaviour of headed stud shear connectors under low-cycle high amplitude displacements.” Material and structures, 32 (4): 290–297.
8. Chao, S.-H. (2012), “Modified Structural Layouts for Staggered Truss Framing Systems Used in Seismically Active Areas,” Presentation at 2012 Structures Congress, Chicago, March 29, 2012.
9. Chao, S.-H. , Jiansinlapadamrong, C., Simasathien, S., and Okazaki, T. (2020), “Full-Scale Testing and Design of Special Truss Moment Frames for High-Seismic Areas,” ASCE Journal of structural engineering, 146(3).

10. Chao, S.-H., and Goel, S. C. (2006), "A Seismic Design Method for Steel Concentric Braced Frames for Enhanced Performance," Proceedings, Fourth International Conference on Earthquake Engineering, Taipei, Taiwan.
11. Chopra, A.K. (2011), “Dynamics of structures – Theory and Applications to Earthquake Engineering”, 4th Ed., Pearson Prentice Hall, Upper Saddle River, NJ.
12. Ciutina, A.L. and stratan, A. (2011), “Cyclic performances of shear connectors”, Composite Construction in Steel and Concrete VI, pp. 52-64.
13. Civjan, S. A., and Singh P. (2003), “Behavior of shear studs subjected to fully reversed cyclic loading”, Journal of Structural Engineering, ASCE,129(11), pp.1466–1474.
14. Cohen, M.P. (1986), “Design Solutions Utilizing the Staggered-steel Truss System.” Engineering Journal. AISC, 23 (3), pp 97-106.
15. Computers and Structures, Inc. (CSi). Components and elements for PERFORM-3D and PERFORM-COLLAPS. CSi: Berkeley, California, 2011.
16. Driscoll G and Slutter R. (1961), “Research on Composite Design at Lehigh University”. Proceedings of the national engineering conference. Chicago (IL), American Institute of Steel Construction, pp.18-24.
17. Eurocode 4 (EC-4) (2004), “Eurocode 4-Design of composite steel and concrete structures Part 1.1: General rules and rules for buildings”, European Standard, ENV 1994-1-1-ver-2004; 1994.
18. Gattesco, N., and Giuriani, E. (1996), “Experimental study of stud shear connectors subjected to cyclic loading”, Journal of construction steel research, 38 (1), pp. 1–21.
19. Goody, M. E., Hansen, R. J., LeMessurier, W. J., Pahl, P. J., Pelletier, R. J., Doyen, J. H., Opitz, C. F., Sarno, J. S., Schildknecht, R., Schwarz, K. W., and Kayser, F. (1967), High Rise Housing in Steel: the Staggered Truss System : a research

project, Massachusetts Institute of Technology. Department of Civil Engineering. United States Steel Corporation, 227 pages.

20. Gupta, R. P. (1971) “Seismic Behavior of Staggered Truss Framing System.” , Department of Civil Engineering, University of Michigan, Ann Arbor, December 1971, 130 pages.
21. Gupta, R. P. and Goel, S. C. (1972), “Dynamic Analysis of Staggered Truss Framing System,” Journal of the Structural Division, 1972, 98 (7), pp. 1475-1492.
22. Habibullah, Ashraf. “Staggered Truss Framing Systems Using ETABS.” Computer and Structures, Inc. Berkeley, California, website article.
23. Hanson, R. D. and Berg, G. V. (1973), “A seismic Design Procedure for Staggered Truss Framed Buildings.” Preprints, Fifth World Conference on Earthquake Engineering. International Association for Earthquake Engineering, Rome, 4 pages.
24. Hanson, R. D. and Berg, G. V. (1974), “A seismic Design of Staggered Truss Buildings,” Journal of the Structural Division, ASCE,100 (1), pp.175-193.
25. Hanson, R. D., Goel, S. C., Berg, G. V. (1972), “Seismic Behavior of Staggered Truss Framing System Design Procedure for Earthquake Loading.” Department of Civil Engineering, University of Michigan, Ann Arbor, January 1972, 86 pages.
26. Hassler, A.E. (1986), “Erecting the Staggered-truss System: A View from the Field.” Engineering Journal. AISC, Vol.23, pp 166-172.
27. Hawkins, N. M. and Mitchell, D. (1984), “Seismic response of composite shear connections.” Journal of Structural Engineering, 110 (9), pp. 2120–2136.
28. Hossli, R. and Flucker, R. (2013), “William LeMessurier: Educator and Innovative Engineer”, Structure magazine, June 2013, pp. 46-47.
29. ICBO. “Uniform Building Code.” International Conference of Building Officials, Whittier, California, 1997.

30. Jiansinlapadamrong, C., Park, K.-S., Hooper, J.D., and Chao, S.-H., (2019), “Seismic Design and Performance Evaluation of Long-Span Special Truss Moment Frames,” ASCE Journal of Structural Engineering.
31. Kim, J., Lee, J.-H., and Kim, Y.-M. (2007), “Inelastic behavior of staggered truss systems”, The Structural Design of Tall and Special Buildings,16 (1), March 2007, pp. 85–105.
32. Lam, D. (2007), “Capacities of headed stud shear connectors in composite steel beams with precast hollowcore slabs”, Journal of Constructional Steel Research, 63, pp. 1160–1174.
33. Leffler, R.E. (1983), “Calculation of Wind Drift in Staggered-Truss Buildings.” Engineering Journal. AISC, 20(1), pp 1-28.
34. Levy, M. (2000), “Staggered truss system earns an A+”, Modern Steel Construction, November 2000.
35. Makino, M. (1984), “Design of framed steel structures with infill reinforced concrete walls”. In: Roeder CW, editor. Composite and mixed construction, New York (NY), ASCE, pp. 279–287.
36. Marstellar, B. and Faraone, T. (2002), “Anatomy of a Staggered Truss.” Modern Steel Construction, AISC, 42 (9), September 2002, pp. 35.
37. McMullin, K., and Astaneh-Asl, A. (1994), “Cyclical behavior of welded steel shear studs”, Structures Congress XII: Proceedings of Papers Presented at the Structures Congress ‘94. Atlanta, GA, April 24–28; pp. 1024–1029.
38. McNamara, R.J., (1999), “Aladdin Hotel: a 38-story Design-build Steel Structure Features a Staggered-truss Frame”, Modern Steel Construction. AISC 39, 5, May 1999, pp 28-34.

39. Moore, K.S. (2005), “Staggered Truss Framing System in Areas of Moderate-High Seismic Hazard,” Proceedings of the 2005 North American Steel Construction Conference, Montreal, Canada.
40. Newell, J.D., and Uang, C.-M. (2008), “Cyclic behavior of steel wide-flange columns subjected to large drift,” Journal of Structural Engineering, American Society of Civil Engineering, vol. 134, no. 8, pp.1334-1342.
41. Ollgaard J., Slutter R., and Fisher J. (1971), “Shear strength of stud connectors in lightweight and normal-weight concrete”, Engineering Journal,8(2), pp. 55-64.
42. Pallarés, L., and Hajjar, J.F. (2010), “Headed steel stud anchors in composite structures, Part I: Shear”, Journal of Constructional Steel Research, 66, pp.198-212.
43. PCFOG committee. (2009). Seismic Performance of Hollow-Core Floor Systems: Preliminary draft. Department of Building and Housing, Wellington, New Zealand.
44. Pollak, B. (2003), “Staggered truss solution”, Modern Steel Construction, July 2003.
45. Saari, W., Hajjar, J., Schultz, A., & Shield, C. (2004), “Behavior of shear studs in steel frames with reinforced concrete infill walls”, Journal of Constructional Steel Research, 60(10), 1453-1480.
46. Scalzi, J. B. (1971). “The staggered truss system – Structural considerations,” AISC Engineering Journal, October, pp. 138-143.
47. SEAOC. (2009). SAEOC Blue Book—"Seismic Design Recommendations on Staggered Truss Frames”, Article 8.03.010.
48. Simasathien, S. (2016), “Enhanced Seismic Performance of Special Truss Moment Frames and Staggered Truss Framing System for Seismically Active Areas”, Doctoral Dissertation, the University of Texas at Arlington, May 2016, 434 pages.
49. Simasathien, S., Chao S.-H., Moore, K., and Okazaki, T. (2014a). “Modified Structural Layouts for Staggered Truss Framing Systems Used in Seismically Active Areas,”

Proceedings of the 10th National Conference in Earthquake Engineering, Earthquake Engineering Research Institute, Anchorage, AK.

50. Simasathien, S., Jiansinlapadamrong, C., and Chao, S.-H. (2017), “Seismic Behavior of Special Truss Moment Frame with Double Hollow Structural Sections as Chord Members,” Engineering Structures,131(15), pp. 14–27.
51. Simasathien, S., Jiansinlapadamrong, C., Okazaki, T., Chao, S.-H., (2014b). “Cyclic loading performance of special truss moment frame with double-channel chord members,” Proceedings of the 10th National Conference in Earthquake Engineering, Earthquake Engineering Research Institute, Anchorage, AK, 2014.
52. Stringer, D. (1982), “Staggered Truss and Stub Girder Framing Systems in Western Canada”, Canadian structural engineering conference, pp. 3-8.
53. Taranath, B. S. (2012), “Structural analysis and design of tall buildings: Steel and composite construction”, Taylor & Francis, CRC Press, New York, N.Y., USA.
54. Viest IM. (1956), “Investigation of stud shear connectors for composite concrete and steel T-beams”, Journal of the American Concrete Institute,27(8), pp. 875-891.
55. Wexler, N. and Lin, F.-B. (2003), “Staggered Truss Framing Systems. Steel Design Guide No. 14”, American Institute of Steel Construction, Inc., Chicago, IL.

Biographical Information

Ra'ed Al-mazaidh obtained a Bachelor of Science in Civil Engineering with a specialization in Structures from Jordan University of Science and Technology (JUST) at Irbid, Jordan in 2003. He got a Master of Science in Structural Engineering from the University of Jordan at Amman in 2013.

After he received his Bachelor of Science, he first worked for two years as a head of the technical department in the Ministry of Municipal Affairs (Jordan). Then, he worked for ten years as a head of the civil engineering department in the Electricity Distribution Company (EDCO) in Jordan.

In 2014, he got a scholarship from the Hashemite University (HU) in Jordan to get the PhD degree in Structural Engineering from the U.S. He enrolled in the Civil Engineering PhD program / Structures and Applied Mechanics at the University of Texas at Arlington, in spring 2015. His research interests include Self-Consolidating Concrete (SCC), seismic-resistant steel frames especially the Staggered Truss Framing System (STF), Non-linear analysis, Performance-based seismic engineering and Finite Element Analysis (FEA).